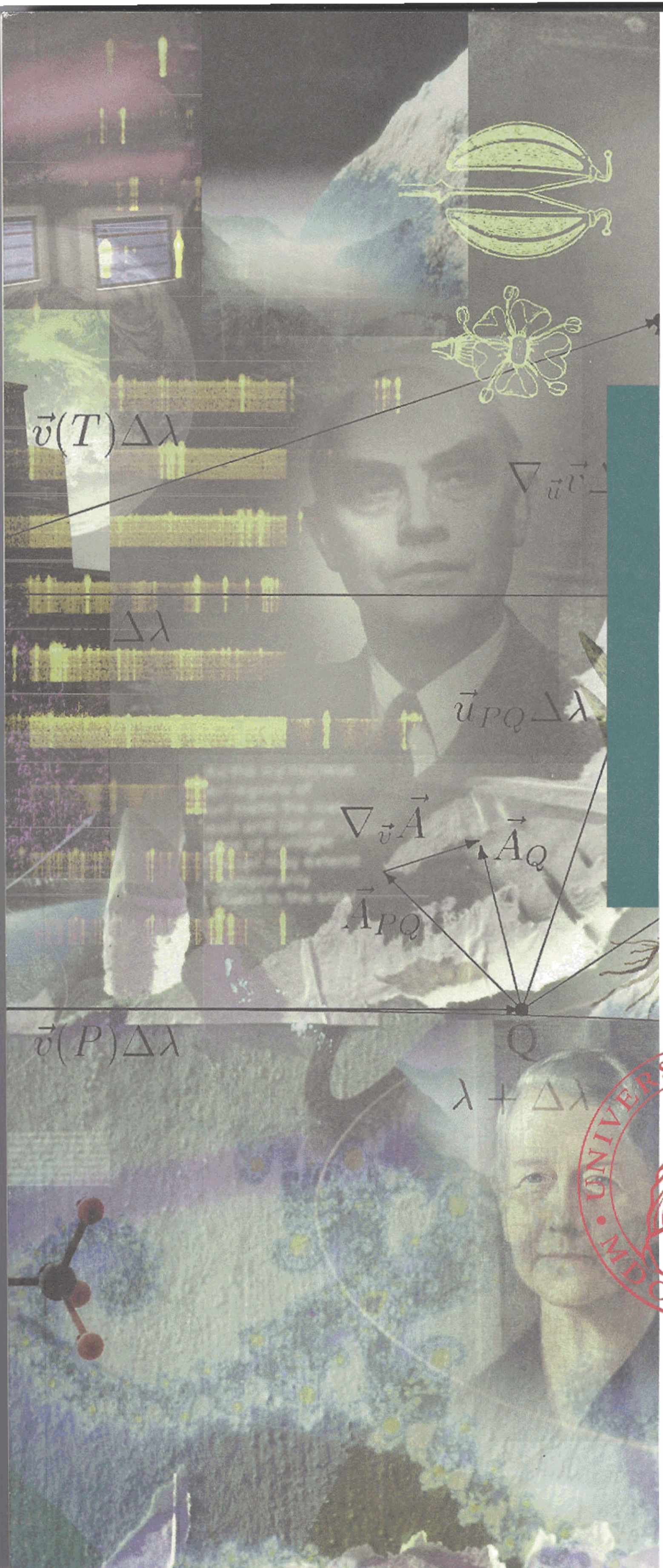

Ravindran Vidya

Theoretical Investigations on Mixed-valence Transition-metal Oxides

Faculty of Mathematics
and Natural Sciences
University of Oslo
2005

Theoretical Investigations on Mixed-valence Transition-metal Oxides

by

RAVINDRAN VIDYA

Dissertation presented for the degree of Doctor Scientiarum
2005

Department of Physics
Faculty of Mathematics and Natural Sciences
University of Oslo
Norway

To my Family

What we have learned is a handful
of sand.
What we have yet to learn is the
whole world.
- Tamil poetess Avvaiyar
(ca. 200 B.C.)

Preface

If I have been able to see farther than others it is
because I stood on the shoulders of giants.
Sir Isaac Newton

I am truly honored to submit my thesis for the degree of Dr. Scient. at the Department of Physics, Faculty of Mathematics and Natural Sciences, University of Oslo. This thesis is a fruit of four years of dedicated research. It would not have been made possible or had not taken the shape it has now, without the help and support of many people. I feel this is the right time and place to pay my tribute for these contributions.

First of all, I wish to express my sincere thanks to Prof. Leif Veseth for accepting me as his Ph.D student. Even though I have registered my doctor project at the Department of Physics, the actual research work has been carried out at the Department of Chemistry under the daily guidance of Prof. Helmer Fjellvåg, Prof. Arne Kjekshus, and Dr. P. Ravindran. I render my sincere gratitude to Helmer for his many insightful discussions, showing keen interest in my works, and providing me the necessary infrastructure facilities. I am most indebted to Arne for many scientific discussions (especially enlightening me on magnetism among many other subjects), his skilful guidance, and caring enquiries on the progress of the project. I am ever grateful to Arne for being patient and devoting his valuable time in improving the quality of the manuscripts (in fact, toward the end I flooded him with too many manuscripts in too short a time). I am truly privileged to sit beside a living “encyclopedia", Dr. P. Ravindran who formulated the main-stream project, giving new ideas and directions to move ahead in addition to providing computational tools from his treasury. The letter “P" in his name must certainly stand for perseverance, who taught me that perseverance and determination are most important in life. I kindly acknowledge him for actively participating in discussions and continuously motivating me to use different tools to bring out the real truth and thereby understand the underlying physics.

I also extend my warm thanks to Dr. P. Vajeeston for fruitful colloboration and many helps with the PC. I wish to gratefully acknowledge Professors O.K Anderson, O. Jepsen, J.M. Wills, and O. Eriksson, for allowing me to use their computational codes. I wish to thank Prof. P. Blaha, Prof. G. Kresse, Prof. Bjørn Hauback, Dr. Pavel Korzhavyi, Dr. Karel

Knizek, Dr. Smagul Zh. Karazhanov, Dr. Anna Delin, Dr. Alexei Grechnev, Laila Offernes, Ole Bjørn Karlsen, and Arne Klaveness for useful communications.

I kindly acknowledge the Research Council of Norway (NFR) and the Department of Physics for providing me the financial support. The project has been successfully carried out using the Norwegian Supercomputer facilities (NOTUR). I express sincere thanks to NFR for providing the supercomputer time and the staff at NOTUR consortium for their support. I also acknowledge the computer supports provided by our friends at local edb@kjemi and USIT. I take this opportunity to thank all my friends in “Seksjon A" for providing a pleasant working environment.

Next my greatest gratitude goes to my parents and brother who are always there to share my pleasure and pain. I should admit that without their constant support and encouragement, this could not have been made possible. I extend my warm thanks to all my relatives and friends (here in Oslo and elsewhere) who through their loving calls from miles away enquired my progress and encouraged me. I also take this opportunity to thank all my school, college, and university teachers who have sown in me a keen interest for science which actually has taken me thus far in life.

Last but certainly not the least, I am ever grateful to my husband Ravi for his patience and understanding. I wish to appreciate the love of my two year old son Vighnesh, who with his pure innocent smiles refreshes my mind and recharges my brain. I owe a lot to both of you.

I thank one and all and wish the readers a happy reading.

University of Oslo, November 2005

Vidya

CONTENTS

CHAPTER 1

Introduction

Knowledge advances by steps and not by leaps.
Lord Macaulay

1.1 Materials Science

An important and widely acclaimed feature of materials science has been the recognition of the fundamental similarities underlying the structures, phenomena, and properties of a wide variety of interesting and technologically important materials. This has led to an unusually large degree of cross-fertilization of ideas and approaches among several different traditional scientific and engineering fields.

Not only all properties and qualities of matter but also all fields of human concern are involved in the interaction between the macro- and microscopic levels of the atomic architecture. To the age-old question: “which comes first, the chicken or the egg?", a probable response of a materials scientist would be: “neither”. In material science there is a synergism between what exists and what needs to exist. Materials are mostly designed with a particular application in mind.[1]

Owing to the capacity of man for immediate aesthetic interaction with materials, quite subtle materials were discovered very early. It began simply with the collection of beautiful natural objects and the discovery that heating and mixing changed their qualities to yield materials that could be used for more than “mere” enjoyment. This aesthetic involvement spurred continual search, and quite advanced materials technology were developed long before mechanical technology. Until about 1800 AD knowledge of materials and the practical control of their composition and properties to achieve a desired result were more advanced in the Far Eastern than in Western cultures [1]. One may venture a guess that this was because Eastern culture put slightly greater emphasis upon an aesthetic approach to the

---

[1] Indeed some new materials, such as nylon, the first polymer, were discovered simply by chance.

world rather than a logical advance.

It has long been recognized that ingenious developments of materials coincide with important stages in the development of civilizations. The current efflorescence of materials science and engineering is certainly coincident with great social changes. Materials were handled in accordance with their nature that has been learned sensitively, but theoretical understanding of the reasons for their properties developed slowly and had little or no effect on the practice until the last century [1]. For a long period of time structure-sensitive properties other than magnetism were invisible to physicists, and it was mainly practical artisans and a few more theoretically inclined chemists and metallurgists who kept alive knowledge of real solids and slowly accumulated facts that eventually forced the birth of the new physics of solids.

1.2 Computational Materials Science

Medieval alchemists dreamed of transmuting common base metals into gold, but such miraculous conversions proved impossible, of course. One of the most promising developments in materials research – computational materials science – is sometimes referred as "computational alchemy" Today, thanks to discoveries in the fields of computational physics and computational chemistry, researchers are making startling progress in understanding and manipulating matter at the atomic and molecular level. This has been fueled by the increasing performance of state-of-the-art supercomputers and high performance workstations. Researchers in this field have acquired enough confidence in their arsenal of computational methods in order to make bold predictions that have run ahead of experiments or in some cases, even corrected them.

The opportunities for computational research are as broad as they are deep. All kinds of materials are dealt with, without any restriction. Ultimately, we hope that new understanding of all of these materials will be transferred to making new materials with properties that mankind can use. Because of the detailed perspective they offer into the behavior of atoms and electrons, we can often significantly enhance and deepen our understanding of how materials function. This approach of using only knowledge of the composition of a material to predict properties is often referred to as *first-principles* or *ab-initio* calculation. An obvious advantage of successful first-principles methods is that, since no experimental input is needed, the behavior of a material can be predicted even before it is synthesized. With the increasing capabilities of first-principles methods, some researchers have started to think about computer-based design of new materials. In principle, this should be possible, because all the properties of a material are determined by the constituent atoms and the basic laws of physics. Hence, when material scientists attempt to design new materials, they can quickly focus on promising systems.

Moreover, computational experiments have the advantage over real experiments that one has full control over *almost all* the experimental variables. This level of control makes it possible to design experiments that are optimized to understand the influence of a specific variable. As these calculations are not limited to physically realizable states of a material, they can be used to conduct “what-if” experiments. In a calculation it is reasonably simple to change the crystal structure, move or substitute an atom, change the applied pressure, make arbitrary deformations, and so forth, and then to evaluate the effect of these modifications on the properties of interest.

1.2.1 Density-functional theory

Since the beginning of quantum mechanics in the 1920’s, one of the most spectacular advances in physics is perhaps the formulation of the density-functional theory (DFT) which enables one to handle many-electron systems with ease. It was constructed by Hohenberg and Kohn [2] in the 1960’s, for which Kohn was awarded the Nobel Prize in chemistry 1998. Since its introduction DFT has evolved into a powerful tool that is widely used in condensed matter theory and computational materials science for the calculation of electronic, magnetic, and structural properties of solids.

First-principles simulations using DFT have proved to be a reliable and computationally tractable tool in condensed matter physics. These simulations have now impacted virtually every area of this broad field. Along with the advances in computing technology that have occurred during the last decade, there have been important algorithmic improvements, and for certain classes of materials it is now feasible to simulate systems containing 100 or more atoms in a unit cell. This opens the door for the direct application of these techniques to study a substantial amount of real materials problems. This method has been remarkably successful in reproducing, explaining, and in some cases predicting a wide variety of materials phenomena. Specific examples range from early predictions of phase transitions in silicon under pressure [3] to determination of stable and metastable adsorption geometries on metal surfaces [4], as well as many successes in understanding magnetic materials.

The fundamental concept of DFT is that all the ground-state properties of a material are completely determined by the electron charge density $\rho(\mathbf{r})$ – the real space distribution of electrons around the atoms. The contribution of DFT to the science of multi-particle quantum systems (such as molecules and condensed matter) is two-fold. The first contribution is one of understanding; since the inception of quantum mechanics theoreticians were used to think in terms of single-particle orbitals, but when high accuracy is required, the number of Slater determinants increases so much that the comprehension becomes difficult. However, the approach of DFT is different, it focusses on the real three-dimensional space using the electron density $\rho(\mathbf{r})$, a tangible and easily understood entity. The second contribution of DFT is of practical nature. In the conventional quantum mechanics, the handling of systems with many particles (N more than 10-20) becomes cumbersome, since the number of Slater determinants are intractable and hence impossible to handle in practical calculations. As DFT uses $\rho(\mathbf{r})$, it allows for handling of fairly large systems ($N \approx 100-1000$), with computational efforts that rise much more moderately with the increasing number of atoms.

1.3 Thesis outline

The scientific world is broadly divided into basic (or fundamental) research and applied research. For materials scientists involved in basic research, the goal is most often to determine why certain kinds of materials have a particular set of properties. Sometimes predictions of materials properties are made even before the materials themselves are synthesized.

On the other hand, applied research involves fashioning materials for real-life applications. It involves knowledge about the conditions under which a material will be used and identifying candidate materials for this purpose. There is always a real need for better materials – the issue is how much better they have to be and at what cost. An applied scientist, with a particular application in mind, will scour lists of known materials looking for one that meets the expected needs. If existing materials are unsuitable, the applied and basic scientist must work together to develop new materials. This synergism between what is available and what needs to be developed reflects the important and complementary roles of the basic and applied sciences in the materials field.

This thesis is intended to appeal to both fundamental and applied researchers. The problems have been carefully selected so that, our computational efforts will attempt to answer some of the most fundamental questions relating to technologically-significant materials. Exploring their properties is expected to lead to more understanding and hence to new materials. We believe that with a fundamental understanding at the electronic level of a system comes, a basic scientific appeal and a more complete control over the properties and mechanisms governing any system. This understanding gives the power of prediction which is perhaps the ultimate goal of all sciences.

The thesis presented here deals with theoretical calculations of properties like phase stability, electronic structure, magnetic properties, ordering phenomena such as spin, charge, and orbital ordering, and excited-state properties for perovskite-like and complex oxides. The objective of the study has been of a threefold nature: First, to gain further knowledge on a fundamental scientific level of the properties of matter and how these are governed by the electronic structure. Second, to demonstrate the versatility and increased applicability of theoretical calculations as complement to experiments. Third the last, but not the least, objective has been to answer some of the most intricate questions concerned with mixed-valence oxides.

1.3.1 Spin, charge, and orbital Ordering

The past few years have seen a flurry of activities in the study of magnetic materials, which previously had an image of "musty physics laboratories peopled by old codgers with iron filings under their fingernails" [5]. In particular, advances in atomic- and nanoscale growth and characterization techniques have led to the production of modern magnetic materials that reveal a range of fascinating phenomena. These phenomena derive from the fact that electrons have spin as well as charge, giving an extra level of complexity to the physics and an extra degree of freedom in device design. Today, the science and technology of magnetism have undergone a renaissance, driven both by the urge to understand the new physics, and by demand from industry for better materials. The potential impact on society of the recent advances in magnetic materials is extensive and evidenced by the dramatic enhancement in data-storage density. The discoveries of colossal magnetoresistance (CMR) or [giant magnetoresistance (GMR)] materials, in which magnetic fields cause orders of magnitude changes in conductivity have been particularly significant. Sensors, read heads, and memories based on GMR are already commercially available in the market.

In addition to the salient property of magnetoresistance, the CMR (GMR) materials also possess exotic properties such as charge and orbital ordering. Charge ordering is the ordering of valence electrons in a particular fashion below a characteristic transition temperature ($T_{\rm co}$). In the canonical picture of magnetic insulators known since the 1950's, the electrons occupy fixed atomic orbitals, and the magnitude and sign of the magnetic interaction between neighboring electron spins depend on the relative orientation of the orbitals in which the spin density resides. Orbital order (the fixed pattern of orbital occupations at every atomic site) is usually either built into the crystal structure or changes only at temperatures much exceeding the magnetic ordering temperature ($T_{\rm C}$). One of the main objectives of this project has been to gain understanding of such ordering phenomena. The basic requirement for charge ordering to take place is the presence of an element (usually a transition-metal constituent) in different valence states. Even though a lot of attention has been paid to mixed-valence manganese oxides, it should be noted that the orbital physics is universal in transition-metal oxides. Hence we have attempted to analyze compounds (particularly perovskite-like and complex oxides) containing mixed-valence transition-metal constituents such as Cr, Mn, Fe, and Co. We believe that a basic understanding of mixed valence and hence charge and orbital ordering will provide new understanding and in turn new materials.

The thesis has been disposed of as three main segments. The first part should appeal to readers with a general background and broad-line interests. The second part deals with introductions to the theoretical background and the topics covered in the present project. The third part is more detailed and intended to give a thorough analysis of the results obtained from the theoretical studies. This part is further complemented by direct access to the articles and publications themselves together with relevant references. In all segments, the aim is to spark the basic curiosity of the readers and make them dwell deeper with the science.

CHAPTER 2

Theoretical Background – Many-body Problem

Make things as simple as possible, but not simpler.
Albert Einstein

Condensed matter physics and materials science are concerned with the fundamental understanding and exploitation of properties of systems with interacting electrons and atomic nuclei. The electrons and nuclei that compose a given material constitute a strongly interacting many-body system. The properties of matter are governed by the behavior of the almost mass-less electrons that move around the much heavier nuclei. This has been well known since the early days of quantum mechanics. With this comes the recognition that, at least in principle, almost all properties of materials can be addressed given suitable computational tools. In order to describe real matter, we need to device theoretical tools that are capable of dealing with the interactions between a very large number of particles, typically of the order of moles, i.e., 10^{23} particles; which is a Herculean task to exploit indeed. Hence we need to resort to approximations and simplifications.

The Schrödinger equation is the basic tool to study the properties of a given material. The time-independent Schrödinger equation has the operator form [6]

$$H\psi = E\psi \tag{2.1}$$

where H is the Hamiltonian operator, E is energy, and ψ is the wave function. Eq. 2.1 can be exactly solved in the case of one nucleus and one electron, viz. for hydrogen and hydrogen-like systems. However, a more realistic situation comprises a many-particle wave function $\psi(r_1, r_2, ..r_i, ..r_N)$, where r_i denotes the position of particle i. The 10^{23} ingredients of a typical solid make the problem complicated. The Hamiltonian for the whole bulk system is

$$H = -\frac{\hbar}{2}\sum_k \frac{\nabla^2}{M_k} + \frac{1}{2}\sum_{k\neq l}\frac{Z_k Z_l}{|R_k - R_l|} - \frac{\hbar^2}{2m}\sum_i \nabla_i^2 + \frac{1}{2}\sum_{i\neq j}\frac{e^2}{|r_i - r_j|} - \sum_{i,k}\frac{Z_k}{|r_i - R_k|}. \tag{2.2}$$

In this Hamiltonian $\hbar$ (= $h/2\pi$, h is the Planck constant), m and r_k denote the electron mass and the respective coordinates, M_k and R_k nuclear masses and the respective coordinates, and Z is the charge of the constituent nuclei. The indices i and j number the electrons and k and l the nuclei. The first term in Eq. 2.2 denotes the kinetic energy of the nuclei, the second term the Coulomb energy between the nuclei, the third term the kinetic energy of the electrons, the fourth term the interaction among the electrons, and the last term denotes the electrostatic interaction between the electrons and the nuclei [which can be regarded as an external potential (V_{ext}) acting upon the electrons]. The motions of the nuclei, notably originating from lattice vibrations, in most materials is on a much larger time scale than typical electronic scale, so that the electrons may be considered to be in their instantaneous ground state as the nuclei move. Hence, in this so-called "Born-Oppenheimer" approximation, the nuclei are considered to be stationary, and Eq. 2.2 has to be solved for the electrons around these stationary nuclei. This allows us to remove the first term in Eq. 2.2. The second term is only a constant (since the nuclear positions are known), and is not to be considered until we actually calculate the total energy. Now, the total energy Hamiltonian can be expressed as

$$H = -\sum_i \nabla_i^2 + \sum_{i \neq j} \frac{1}{|r_i - r_j|} - \sum_{i,k} \frac{2Z_k}{|r_i - R_k|}. \tag{2.3}$$

Here we have also introduced the Rydberg atomic units, i.e., $e^2 = 2$, $\hbar = 1$, and $m = \frac{1}{2}$. In order to solve the Schrödinger equation for all the interacting electrons, we have to solve a system of around 10^{23} simultaneous differential equations. Such a calculation is beyond the capabilities of present-day computers, and is likely to remain so for the foreseeable future.

2.1 The Hartree approximation

The Hartree approximation provides a way to simplify Eq. 2.2 so that it can be solved somewhat easily. In Eq. 2.2, the potential experienced by an electron depends on the positions of the other electrons. However, this potential can be approximated by an average single-particle potential called the Hartree potential which is not coupled to the individual motions of all the other electrons, but depends simply upon the time-averaged electron distribution of the system. It is given by

$$V_d(\mathbf{r}_i) = e^2 \sum_{j \neq i} n_j \frac{|\psi_j(\mathbf{r}_j)|^2}{|\mathbf{r}_i - \mathbf{r}_j|}, \tag{2.4}$$

where n_j are the orbital occupation numbers and $\psi_j(\mathbf{r}_j)$ is a single-particle wave function, *i.e.*, a solution to the one-particle wave-equation:

$$\Big[-\frac{\hbar^2}{2m}\nabla^2 + V_{ext} + V_d(\mathbf{r}_i)\Big]\psi_i(\mathbf{r}_i) = \varepsilon_i \psi_i(\mathbf{r}_i) \tag{2.5}$$

Thus, the set of equations now becomes separable. However, the equations are still non-linear and have to be solved self consistently by iteration. Even though the Hartree approximation allows one to calculate the approximate single-particle wavefunctions for the electrons in solids, it has a few drawbacks.

According to the Pauli-exclusion principle, two electrons can not exist at the same point in space with the same set of quantum numbers. However, the wave function in Hartree theory

$$\Psi(\mathbf{r}_1\sigma_1, \mathbf{r}_2\sigma_2, ..., \mathbf{r}_N\sigma_N) = \prod_i^N \psi_i(\mathbf{r}_i, \sigma_i) \tag{2.6}$$

is not antisymmetric for interchange of electron coordinates and accordingly does not follow the Pauli-exclusion principle. Moreover, the Hartree approximation fails to describe how an electron is affected by the configuration of the $N-1$ other electrons. These defects have been rectified by the Hartree−Fock theory.

2.2 Hartree−Fock approximation

Already in 1930 Fock pointed out that, any approximation to the true wave function should explicitly include spin and should be antisymmetric to interchange of electrons. Hence, instead of the "simple" spatial orbitals, one must use spin orbitals and moreover take into account antisymmetric linear combinations of products of spin orbitals. We assert that a solution of Eq. 1 is given by any state Ψ that makes the following quantity stationary:

$$E = \frac{(\Psi, H\Psi)}{\Psi, \Psi} \tag{2.7}$$

According to the variational principle [7], the normalized expectation value of energy is minimized by the ground-state wave function Ψ.

A better description is to replace the wave function in Eq. 2.6 by a Slater determinant of one-electron wave functions

$$\Psi(\mathbf{r}_1\sigma_1, \mathbf{r}_2\sigma_2, \ldots, \mathbf{r}_N\sigma_N) = \frac{1}{\sqrt{N!}} \begin{vmatrix} \Psi_1(\mathbf{r}_1\sigma_1) & \Psi_1(\mathbf{r}_2\sigma_2) & \ldots & \Psi_1(\mathbf{r}_N\sigma_N) \\ \Psi_2(\mathbf{r}_2\sigma_2) & \Psi_2(\mathbf{r}_2\sigma_2) & \ldots & \Psi_2(\mathbf{r}_N\sigma_N) \\ \vdots & \vdots & \ddots & \vdots \\ \Psi_N(\mathbf{r}_N\sigma_N) & \Psi_N(\mathbf{r}_N\sigma_N) & \ldots & \Psi_N(\mathbf{r}_N\sigma_N) \end{vmatrix}. \tag{2.8}$$

This is a linear combination of products of the form given by Eq. 2.6 and all corresponding products are obtained by permutation of $\mathbf{r}_i\sigma_i$ among themselves. The Hartree−Fock equation which follows from energy-minimization is given by:

$$\Big[-\frac{\hbar^2}{2m}\nabla^2 + V_{ext} + V_d(\mathbf{r}_i)\Big]\psi_i(\mathbf{r}_i) - \sum_j \int d' \frac{e^2}{|\mathbf{r}-\mathbf{r}'|}\psi_j^\star(\mathbf{r}')\psi_i(\mathbf{r}')\psi_j(\mathbf{r})\delta_{s_i s_j} = \varepsilon_i\psi_i(\mathbf{r}_i) \tag{2.9}$$

Hence, in addition to the Hartree potential, another potential called the *exchange potential* (the last term on the left hand side of Eq. 2.9) operates only between electrons with the same spin. In addition, there should also be a correlation interaction (resulting from simple electrostatic interaction between the electrons), which is not included here. Consequently, the correlation energy can be described as the difference between the exact energy for the system and the Hartree–Fock energy.

2.3 Density-functional theory (DFT)

Since the ground-state electronic structure is the most important quantity in determining the material properties, we need a robust and very accurate method to describe the electronic structure. It is well known that the properties of matter are governed by the electrons surrounding the atomic nuclei and interactions between them. Hence, if one could get hold of the real space distribution of these electrons [viz. the electron charge density $\rho(\mathbf{r})$] then almost all physical properties can be predicted. The objective of the electronic structure calculations is to obtain the electron density. The most important milestone of modern day quantum mechanics is the development of DFT [8]. By far, the most accurate "first-principles" quantitative calculation of $\rho(\mathbf{r})$ is based on DFT which is able to distinguish small energy differences between very different phases of a given material. DFT is so successful that it has now become one of the most widely used modern theories to understand the properties of matter.

Hohenberg and Kohn suggested in 1964 that the many-electron wavefunction is a too complicated entity to deal with as a fundamental variable in a variational approach. Hence, in their density-functional formalism which is based on two theorems first introduced by Hohenberg and Kohn [2] and later extended by Kohn and Sham [9], they suggested a different quantity.

2.3.1 Theorem 1

For an interacting system of electrons in an external potential, $V_{ext}(\mathbf{r})$, there exists a universal functional of the charge density, $F[\rho(\mathbf{r})]$, independent of $V_{ext}(\mathbf{r})$, that provides the electronic energy:

$$E = \int V_{ext}(\mathbf{r})\rho(\mathbf{r})d\mathbf{r} + F[\rho(\mathbf{r})]. \tag{2.10}$$

2.3.2 Theorem 2

The functional $F[\rho(\mathbf{r})]$ obtains its minimum value (viz. the ground-state energy) for the actual electron-charge density of the system [2].

The electron-charge density can be obtained from the solution of an associated single-particle problem, whose effective single-particle potential $V_{eff}[\mathbf{r}, \rho(\mathbf{r})]$, is the sum of the external potential, and a unique functional of ρ as given below. As a consequence, the calculation of the energy in terms of $\rho(\mathbf{r})$ is reduced to the self-consistent solution of a system of coupled, non-linear, one-electron-like Schrödinger equations:

$$\left[-\frac{1}{2}\nabla^2 + V_{ext}(\mathbf{r}) + \int \frac{\rho(\mathbf{r}')}{|\mathbf{r}-\mathbf{r}'|}d\mathbf{r}' + \frac{\delta E_{xc}[\rho]}{\delta \rho_(\mathbf{r})}\right] \phi_i(\mathbf{r}) = \epsilon_i \phi_i(\mathbf{r}), \tag{2.11}$$

The so-called Kohn-Sham (KS) wavefunctions, ϕ_i, are single-particle eigenfunctions that are strictly meaningful only for determining $\rho(\mathbf{r})$. The KS eigenvalue ϵ_i, which is the derivative of the total energy with respect to the occupation of state i, is used in determining which one-electron states are occupied: states are filled from the lower eigenvalues to the higher, without regard to the spin parameter. The eigenvalues are not strictly related to single-particle excitation energies, although further theoretical considerations can explain why KS-band structures become a useful tool in the interpretation of spectroscopic (especially photoemission) data.

For an arbitrary electron-charge density there is no simple explicit expression for the exchange correlation energy E_{xc}. The widely used local-density approximation (LDA) is a simple approach, exact within the limit of a homogeneous electron density, and leads to remarkably accurate results for many classes of materials. Within the LDA, E_{xc} is written as

$$E_{xc}(\rho) = \int \rho(\mathbf{r}) E_{xc}[\rho(\mathbf{r})] d\mathbf{r}, \tag{2.12}$$

where $E_{xc}(\rho)$ is the exchange-correlation energy of a uniform interacting electron gas of density ρ. The use of LDA is strictly speaking, justified only if $\rho(\mathbf{r})$ is a slowly varying function, and a number of extensions exist which give improved accuracy for systems with more localized electrons.

2.4 Spin-polarized systems

In the generalization of DFT to spin-polarized systems, the charge density $\rho(\mathbf{r})$ is decomposed into the two spin densities ($\rho_\uparrow$ and $\rho_\downarrow$) as

$$\rho(\mathbf{r}) = \rho_\uparrow(\mathbf{r}) + \rho_\downarrow(\mathbf{r}) \tag{2.13}$$

The Hohenberg-Kohn theorem in this case postulates that the ground-state total energy is a functional of the spin densities.

$$E = E[\rho_\uparrow, \rho_\downarrow] \tag{2.14}$$

The total energy consists of terms like those for the non-spin-polarized case. The Coulomb terms remain functionals of the total energy, but E_s (viz. single-particle kinetic energy) and E_{xc} become functionals of the two spin densities. There are separate sets of KS orbitals for the two spin components, and two sets of single-particle equations need to be solved to obtain them. The variational principle is invoked to generate the spin-polarized KS equations of spin-density-functional theory.

$$(T + V_{ei}(\mathbf{r}) + V_H(\mathbf{r}))\phi_{i\sigma}(\mathbf{r}) = \epsilon_{i\alpha}\phi_{i\sigma}(\mathbf{r}) \tag{2.15}$$

where σ is the spin index and the density is given by a sum over the occupied orbitals.

$$\rho_\sigma(\mathbf{r}) = \sum_{occ} \phi^\star_{i\sigma}(\mathbf{r})\phi_{i\sigma}(\mathbf{r}) \tag{2.16}$$

and the highest occupied orbital is determined by the electron count. V_{xc} is the only term in the single-particle Hamiltonian that is explicitly spin dependent.

$$V_{xc,\sigma} = \frac{\delta E_{xc}[\rho_\uparrow, \rho_\downarrow]}{\delta \rho_\sigma(\mathbf{r})} \tag{2.17}$$

The total-energy expression then becomes,

$$E = E_{ii} + \sum_{occ} \epsilon + E_{xc}[\rho_\uparrow, \rho_\downarrow] - \frac{1}{2}\int d^3\mathbf{r} V_H(\mathbf{r})\rho(\mathbf{r}) - d^3\mathbf{r}(\rho_\uparrow(\mathbf{r})V_{xc,\uparrow}(\mathbf{r}) + \rho_\downarrow(\mathbf{r})V_{xc,\downarrow}) \tag{2.18}$$

These equations are to be solved self-consistently as in the non-spin-polarized case. In the above expression, E_{ii} is the electron-electron interaction energy and E_{xc} is a functional of the two spin densities. E_{xc} favors spin-polarized solutions and T_s opposes such an outcome. A balance between these two terms determines whether a material is magnetic or not (neglecting diamagnetism).

Because of the additional degrees of freedom contained in the spin-density case, spin-polarized KS equations often have multiple self-consistent solutions, corresponding to different stable spin configurations. Hence, in order to determine the real ground state (corresponding to the lowest energy), all possible spin configurations should be considered in the calculations. Moreover, the dimension of the matrix corresponding to the Hamiltonian operator for a magnetic system will be twice the dimension of the matrix representing the non-magnetic system. The upper left quarter of the matrix represents one spin channel and the lower right quarter of the matrix represents the other spin channel. The off-diagonal elements correspond to hybridization between different spins and / or rotated spin coordinates.

2.4.1 Exchange-correlation energy

The exchange potential for a system of variable density can be approximated by a term $[\rho(\mathbf{r})]^{1/3}$, where $\rho(\mathbf{r})$ represents the *local density*. This $[\rho(\mathbf{r})]^{1/3}$ dependence is a consequence of the *exchange (Fermi) hole*. The Fermi hole is a region surrounding each electron in which the probability of finding another electron with the same spin is small. In other words, this hole is the region near an electron which is avoided by electrons with the same spin. Modern DFT approximates the full non-local exchange with a term based on the local density, hence called the *local density approximation* (LDA). The exchange-correlation term is to some extent approximated in the current theoretical framework. Since the electrons interact with each other, they correlate their motion so that they tend to avoid each other.

The *correlation (Coulomb) hole* is the region surrounding each electron in an atom in which the probability of finding another electron is small. An electron at **r** reduces the probability of finding another electron at a nearby position $\mathbf{r}'$, and every electron is surrounded by a hole in the electron density of equal and opposite charge [10]. In the *local spin density approximation* (LSDA) the exchange-correlation energy is written as

$$E_{xc}^{LDA} = \int d\mathbf{r}\rho(\mathbf{r})\epsilon_{xc}[\rho_{\uparrow}(\mathbf{r}), \rho_{\downarrow}(\mathbf{r})], \tag{2.19}$$

where ϵ_{xc} is the exchange-correlation energy per particle in a homogeneous spin-polarized electron gas. We can also describe an exact term for the exchange-correlation energy using exchange-correlation holes [10]:

$$E_{xc} = \frac{1}{2}\int d(\mathbf{r})\rho(\mathbf{r})\int d\mathbf{r}'\frac{1}{|\mathbf{r}' - \mathbf{r}|}\rho_{xc}(\mathbf{r}, \mathbf{r}' - \mathbf{r}), \tag{2.20}$$

where $\rho_{xc}(\mathbf{r}, \mathbf{r}' - \mathbf{r})$ is the exchange correlation hole which obeys the sum rule (total charge equals to -1):

$$\int d\mathbf{r}'\rho_{xc}(\mathbf{r}, \mathbf{r}' - \mathbf{r}) = -1. \tag{2.21}$$

It can be shown that on making a variable substitution $\mathbf{R} = \mathbf{r}' - \mathbf{r}$, E_{xc} can be written as [10]:

$$E_{xc} = \frac{1}{2}\int d(\mathbf{r})\rho(\mathbf{r})\int_0^{\infty} d\mathbf{R}\mathbf{R}^2\frac{1}{|\mathbf{R}|}\int d\Omega\rho_{xc}(\mathbf{r}, \mathbf{R}), \tag{2.22}$$

which in turn implies that the exchange energy depends only on the spherical average of ρ_{xc}. Here lies the answer to why the LDA approximation works so well. The point is that even if LDA does not give the right form for the exchange-correlation hole it does give a spherical average which is very close to the real charge distribution [10].

The LDA is widely used in solid state physics, but there are more modern improvements suitable to treat the full non-local exchange such as the *generalized gradient approximation* (GGA), where E_{xc} has become more composite on introduction of contributions also from the gradient of the local density.

2.4.2 Generalized-gradient approximation

One of the promising avenues for refinement of the LDA is the GGA approach. In GGA, the function $E_{xc}(\rho)$ is replaced by a local function of the charge density and the magnitude of its gradient, $E_{xc}(\rho, |\nabla\rho|)$; the rational is that a better description might result from incorporation of the additional information contained in the local gradient. GGA-based calculations have been reported for a wide variety of materials using several different parameterizations of the GGA functionals. From these calculations it is found: (1) GGAs significantly improve the ground-state properties for the light elements, molecules and solids composed of these, (2) many properties of the $3d$ transition metals are improved, for example the correct bcc ground state for Fe is obtained, (3) magnetic energies for the $3d$ transition metals may be overestimated, and (4) the GGAs lead to excessive increases in the unit-cell parameters for some materials containing heavy elements, and consequently degraded agreement with experiment compared to the LDA [11].

The exchange-correlation energy is given as a (spin) density gradient of the form:

$$E_{xc}^{GGA}[\rho_\uparrow, \rho_\downarrow] = \int d\mathbf{r} f(\rho_\uparrow(\mathbf{r}), \rho_\downarrow(\mathbf{r}), \nabla\rho_\uparrow(\mathbf{r}), \nabla\rho_\downarrow(\mathbf{r})), \tag{2.23}$$

where the function f is chosen according to certain criteria. Exchange-correlation approximations in the above form are *semilocal* in the sense that the energy density at **r** depends on the electron density in an infinitesimal neighborhood of **r**. There are quite a few GGA functionals available, named after the inventors as Langreth-Mehl, Perdew-Wang 86, Becke-Perdew, Lee-Yang-Parr etc. However, in the present project we have used only the PW91 and PBE GGA functionals.

Perdew-Wang 91 (PW91)

The PW91 [12] approach is similar to LSDA as well as gradient expansion approximation (GEA) but it is purely *ab initio*. It is constructed using only uniform electron-gas data for exact conditions. PW91 includes a real space cut-off also for the correlation functional and takes the Becke exchange with only small refinements. It fulfills almost all of scaling relations, including those found after the formulation of functional.

Perdew-Burke-Ernzerhof (PBE)

The PBE [13] approach simplifies the cumbersome derivation of PW91 and corrects some of its minor flaws such as the spurious wiggles in the exchange-correlation potential for small and large (dimensionless) density gradients. However, the resulting energies change only marginally.

2.5 Limitations of density-functional theory

Every theory has its own advantages as well as limitations, like two sides of a coin. DFT provides no exception. Fundamentally, DFT only concerns the electronic ground-state structure and underestimates band gaps, which for some semiconductors come out incorrect by 10–30%. A famous (and for this project very relevant) error is also found for transition-metal oxides that are predicted to be metallic, whereas they actually are semiconductors/insulators. Other traditional short-comings of the DFT have been attributed to failures of the specific exchange-correlation functions used, e.g., the failure to predict the bcc ground-state structure of Fe. When GGA is used instead of LDA, the correct ground-state structure is expectedly obtained. In practice, it is a complicated matter to single out the exact reason for the failure in a given calculation, since there are usually an appreciable number of approximations involved. However, it should be stressed that although there are limitations to the applicability of the DFT (along with exchange-correlation functionals), one should not to be too pessimistic. Instead, one should view these procedures as computational exercises and simply try to push the limits of the theory, of course always trying to validate the findings with experimental facts.

CHAPTER 3

Computational Techniques

Do not worry about your difficulties in mathematics. I can assure you mine are still greater.

Albert Einstein

DFT based electronic structure methods are classified according to the representations that are used for the density, potential and, most importantly the Kohn-Sham orbitals. The choice of representation is made to minimize the computational costs of the calculations, while maintaining sufficient accuracy. These competing material- and application-dependent goals have led to the development and use of a wide variety of techniques. In this chapter, we will briefly explain some of the techniques for solving the single-particle equations for crystalline solids and outline the difference between methods that have been used in this thesis.

$$[-\nabla^2 + V_{eff}(\mathbf{r})]\psi_i(\mathbf{r}) = \varepsilon_{\mathbf{i}}\psi_{\mathbf{i}}(\mathbf{r}). \tag{3.1}$$

From this equation we can find the electron charge density $\rho(\mathbf{r})$

$$\rho(\mathbf{r}) = \sum_{j=1}^{N} |\psi_j|^2. \tag{3.2}$$

Because both the electrostatic potential (Φ) and V_{xc} depend on $\rho(\mathbf{r})$ we can calculate a new $V_{eff}(\mathbf{r})$ using the local-density approximation, GGA etc. for the exchange-correlation and the Poisson equation for the electrostatic contribution:

$$\nabla^2\Phi(\mathbf{r})_i = -4\pi \sum_{j=1, j\neq i}^{N} |\psi_j|^2. \tag{3.3}$$

We repeat this process until self-consistency is reached [viz. the difference between $V_{eff}(\mathbf{r})$ in the m and $m{-}1$ iterations is less than a predetermined value; the difference being the only chosen convergence criterion]. When self-consistency has been reached, we calculate the total energy of the system of electrons and nuclei using the total-energy expression of the functionals Eq.(2.10)

3.1 Periodicity and crystal symmetry

It would have been an impossible task to solve the equations if we had to perform the calculations for all electrons in a given material. The calculations performed by DFT is usually for a unit cell of a crystal. (A crystal is an ordered state of matter in which the positions of the nuclei and consequently all properties are repeated in space.) Fortunately the potential is periodic for an infinite crystal, i.e., invariant under lattice translation **T** and hence solving the equations in some reduced part of the system will provide the solution for the entire system since the solution will necessarily repeat itself with the translational symmetry of the crystal.

$$V(\mathbf{r}+\mathbf{T}) = V(\mathbf{r}), \tag{3.4}$$

$$\mathbf{T} = m_1\mathbf{a}_1 + m_2\mathbf{a}_2 + m_3\mathbf{a}_3. \tag{3.5}$$

The vectors $\{\mathbf{a_i}\}$ are the real-space Bravais lattice vectors that span the crystal structure and $\{m_i\}$ are integers. According to the Bloch theorem, the eigenstates can be chosen to takes the form of a plane wave times a function with the periodicity of the Bravais lattice;

$$\psi_{\mathbf{k}}(\mathbf{r}+\mathbf{T}) = e^{i\mathbf{k}.\mathbf{T}}\psi_k(\mathbf{r}) \tag{3.6}$$

where **k** is the Bloch wave vector. Now, the one-electron function can be characterized by the Bloch vector **k**. As a consequence, Eq. (3.1) can be rewritten as

$$H_{eff}(\mathbf{r})\psi_n(\mathbf{k};\mathbf{r}) = \varepsilon_n(\mathbf{k})\psi_n(\mathbf{k};\mathbf{r}), \tag{3.7}$$

where the index i in Eq. (3.1) has been replaced by the quantum number n. The one-electron wave function ψ_n and the corresponding eigenvalues ε_n are now characterized by the Bloch wave vector **k**.

The phase factor takes the value 1 for some electronic states. This happens when the wave-vector corresponds to a $reciprocal$ lattice vector defined by

$$\mathbf{g} = 2\pi(n_1\mathbf{b}_1 + n_2\mathbf{b}_2 + n_3\mathbf{b}_3) \tag{3.8}$$

where n_i are integers and $\mathbf{b_i}$ are the basis vectors of the reciprocal lattice, i.e.,

$$(\mathbf{a_i}.\mathbf{b_j}) = \delta_{ij} \tag{3.9}$$

For **k** = g

$$e^{i\mathbf{k}.\mathbf{T}} = e^{i\mathrm{g}.\mathrm{T}} = e^{2\pi i m_i n_i} = 1. \tag{3.10}$$

Thus a periodicity in real space also introduces a periodicity in reciprocal space ($\mathbf{k}$), and an electron state with wave vector $\mathbf{k}' = \mathbf{k} + \mathbf{g}$ will consequently satisfy the Bloch condition. To describe the electronic structure of a solid it is thus not necessary to consider the vectors, we can consider only the wave vectors contained inside the region of the reciprocal space known as Brillouin zone (BZ). In addition to the translation symmetry, the crystal also obeys symmetries under rotations, implying that there are symmetry operations which transform one wave vector into another wave vector and that reduces our problem further. The smallest possible zone which defines a complete set of symmetry independent wave vectors is called the irreducible part of the BZ. For example, in a simple cubic lattice, the irreducible part of the BZ is only 1/48 of the full BZ and this is the only part we need to find a solution for in such an electronic structure problem.

3.2 Electronic structure methods

In order to solve Eq. 3.7 we need to expand it in a basis of known functions, and we have to resort to one of the available electronic structure methods.

The choice of basis-functions is crucial for the efficiency of a given computational method and the first step in the implementation of a DFT method is to find a suitable basis set.

(1) Basis sets that obey the Bloch condition explicitly, viz. the expansion involves basis functions that are fixed and the coefficients c_n are chosen to minimize the energy.

$$\psi(\mathbf{r}) = \sum_n c_n \phi_n(\mathbf{r}) \tag{3.11}$$

One disadvantage of this approach is that the wave functions are fixed, which often leads to considerable difficulties in obtaining a sufficiently converged basis set.

(2) The other group involves wave functions that can be varied. The variation is promoted by introducing energy-dependent wave functions $\phi_n(\varepsilon, \mathbf{r})$ of the form

$$\psi(\varepsilon, \mathbf{r}) = \sum_n c_n \phi_n(\varepsilon, \mathbf{r}), \tag{3.12}$$

However, the Bloch conditions are no longer automatically fulfilled. The solutions in one unit cell are now chosen to fit smoothly to those of the neighboring cells, thus fulfilling the Bloch condition "indirectly". As the wave function can be modified to the problem at hand, these techniques converge very fast for the number of required basis functions. Every $\mathbf{k}$ point of the band structure must be solved for a large number of ε. Solutions only exist when ε are actual eigenvalues. While computation based on these methods are accurate, they are also time consuming. A solution to this problem is to linearize the energy dependent orbital basis. The basis is introduced in the form of a Taylor expansion in ε so that the orbitals themselves are energy independent, although the expansion retains the energy dependence.

The variational equation (3.7) thus has to be solved only once for each **k** point. Such methods are extremely rapid and slightly less accurate than other non-linear methods.

3.3 The LMTO method

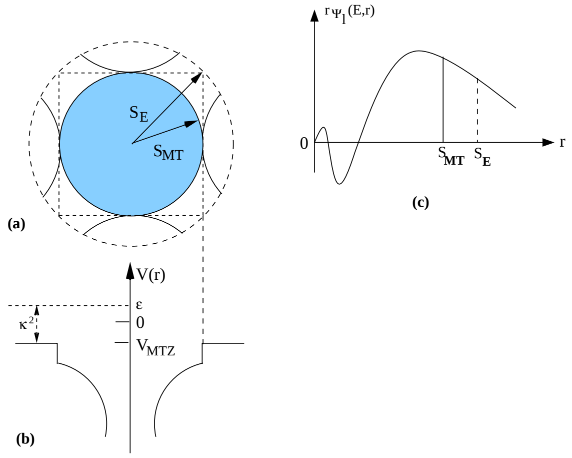

Figure 3.1: The muffin-tin approximation. (a) the muffin-tin sphere with radius S$_{MT}$, and the describing sphere of radius S$_E$. (b) the muffin-tin part of the crystal potential $V(r)$, and (c) the radial part of the wave function.

During the last decades, the linear-muffin-tin-orbital (LMTO) [14] method has become very popular for the calculation of the electronic structure for crystalline systems. The LMTO method combines the following advantages: (a) It uses a minimal basis, which leads to high efficiency and makes calculations possible for large unit cells. (b) In this method all elements are treated in the same way, so that atoms with a large number of core states can be considered (say, phases containing d and f metals). (c) This method is very accurate, due to the augmentation procedure which gives the wave function the correct shape near the nuclei. (d) It uses atom-centered basis functions with well-defined angular momentum, which makes the calculation transparent [15].

3.3.1 Muffin-tin orbitals

The crystal is divided into non-overlapping muffin-tin[1] spheres surrounding the atomic sites and an interstitial region outside the spheres. Inside the muffin-tin sphere the potential is assumed to be spherically symmetric while in the interstitial region the potential, V$_{MTZ}$, is assumed to be constant or slowly varying. Because the potential in the interstitial is constant we can shift the energy scale and set it to zero. In the following overview of the method we

---

[1] The picturesque name of muffin-tin derives from the fact that it looks like a pan for cooking muffins.

consider a crystal with only one atom per primitive cell. Within a single muffin-tin well we define the potential by

$$V_{MT}(\mathbf{r}) = \begin{cases} V(\mathbf{r}) - V_{MTZ} & , \quad |\mathrm{r}| < S_{MT} \\ 0 & , \quad |\mathrm{r}| > S_{MT} \end{cases} \tag{3.13}$$

Here $V(\mathbf{r})$ is the spherically symmetric part of the crystal potential. The radii of the muffin-tin spheres are chosen such that they do not touch each other. In the following S_{MT} is expressed by S.

To solve the Schrödinger equation for the muffin-tin potential

$$[-\nabla^2 + V_{MT}]\psi(\varepsilon, \mathbf{r}) = (\varepsilon - V_{MTZ})\psi(\mathbf{r}) \tag{3.14}$$

one introduces the kinetic energy κ^2 in the interstitial region by

$$\kappa^2 = (\varepsilon - V_{MTZ}) \tag{3.15}$$

For an electron moving in the potential from an isolated muffin-tin well embedded in the flat potential V_{MTZ}, the spherical symmetry can extend throughout all space and the wave functions become

$$\psi_L(\varepsilon, \mathbf{r}) = i^l Y_l^m(\hat{\mathbf{r}})\psi_l(\varepsilon, r) \tag{3.16}$$

using the convention that $r = |\mathbf{r}|$ and $\hat{\mathbf{r}}$ is the direction of $\mathbf{r}$ and including a phase factor i^l.

To obtain basis functions which are approximately independent of energy, reasonably localized, and normalizable for all values of κ^2, Andersen [16] used muffin-tin orbitals. The spherical Bessel functions added to the wavefunction for r < S cancels the divergent part of $\psi_l(\varepsilon, k, r)$ and simultaneously reduce the energy and potential dependence at the tails. Moreover, it incorporates the effects due to the neighbors into the wavefunction so that a minimal basis set of LMTO functions can accurately describe the system [17]. Hence, the muffin-tin orbitals can take the form

$$\chi_{lm}(\varepsilon, \mathbf{r}) = i^l Y_l^m(\hat{\mathbf{r}}) \begin{cases} \psi_l(\varepsilon, \mathbf{r}) + P_l(\varepsilon)\frac{(r/S)^l}{2(2l+1)} & , \quad |\mathrm{r}| < S \\ (r/S)^{-l-1} & , \quad |\mathrm{r}| > \mathrm{S} \end{cases} \tag{3.17}$$

where $\psi_l(\varepsilon, \mathbf{r})$ is a solution of the radial Schrödinger equation inside the atomic sphere.

$$P_l(\varepsilon) = 2(2l+1)\frac{D_l(\varepsilon) + l + 1}{D_l(\varepsilon) - l} \tag{3.18}$$

The potential function and the normalization of $\psi_l(\varepsilon, \mathbf{r})$ are determined by satisfying differentiability and continuity of the basis function on the sphere boundary. Here the term $D_l(\varepsilon)$ is the logarithmic derivative of the wave function. The tail of the basis function, *i.e.*, the part outside the muffin-tin sphere is in general introduced as Neumann function, but in Eq. (3.15) the kinetic energy of this tail (known as k^2) is simply chosen to be zero. Therefore the Neumann function has a simple form like the above.

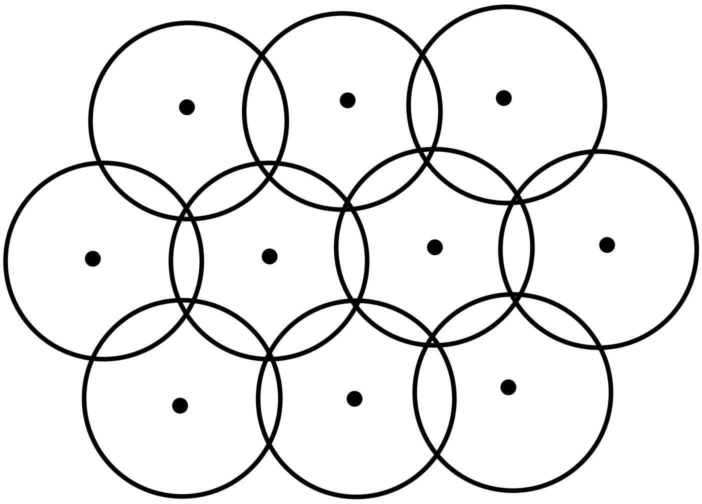

Figure 3.2: The atomic sphere approximation (ASA) in which the muffin-tin spheres are chosen to have the same volume as the Wigner-Seitz cell, resulting in overlapping spheres.

3.3.2 The LMTO $-$ atomic sphere approximation method

In the LMTO-atomic sphere approximation (LMTO-ASA) [18], the muffin-tin spheres are overlapping in such a way that the total volume of the muffin-tin sphere equals the atomic volume. This means that the muffin-tin radius S is equal to the Wigner$-$Seitz radius S_{WS} where the total volume per atom is given by $V = (4\pi/3)S_{WS}^3$. In the ASA, the potential is also assumed to be spherically symmetric inside each muffin-tin sphere, and the kinetic energy of the basis functions in the interstitial is restricted to be constant, actually zero in the calculation.

In order to construct a linear method, the energy dependent terms in the muffin-tin spheres of Eq. (3.17) are replaced by the energy independent function Φ. The function is defined as a combination of radial functions and their energy derivative

$$\Phi(D,r) = \phi_l(r) + \omega(D)\dot{\phi}_l(r), \tag{3.19}$$

where $\omega(D)$ is a function of the logarithmic derivative. $\omega(D)$ should make the energy dependent orbitals $\chi_{lm}(\varepsilon,\mathbf{r})$, defined in Eq. (3.17), continuous and differentiable at the sphere boundary S. The boundary condition is determined as $D = -(l+1)$. The thus obtained energy independent orbital can now be written as

$$\chi_{lm}(\varepsilon,\mathbf{r}) = i^l Y_l^m(\hat{\mathbf{r}}) \begin{cases} \Phi_l(D,r) & , \ |\mathrm{r}| < \mathrm{S} \\ (r/S)^{-(l+1)} & , \ |\mathrm{r}| > \mathrm{S} \end{cases} \tag{3.20}$$

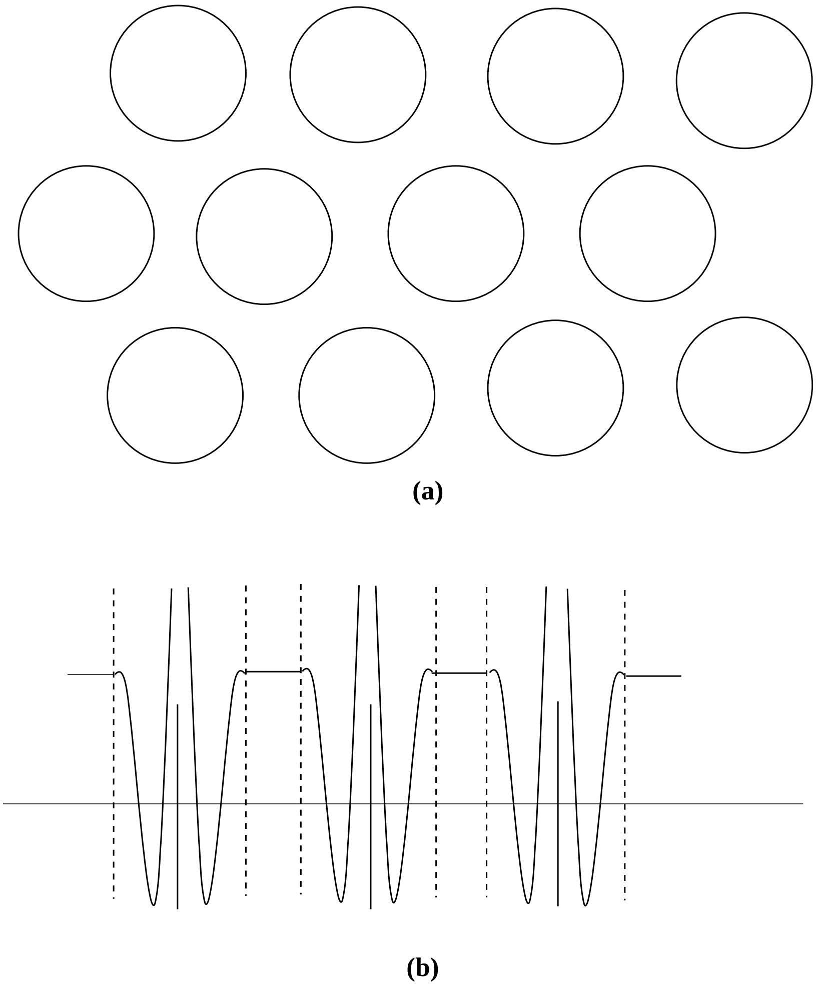

Figure 3.3: (a) The muffin-tin division of space into spheres and interstitial regions. (b) Schematic representation of the wave function inside the sphere (by a radial function) and in the interstitial region (by a Hankel and Neumann function or by a plane-wave). The vertical dotted lines indicate the sphere boundaries.

3.4 Full potential methods

All electron methods with localized basis functions, or with more intricate basis sets, such as the linearized augmented plane-wave (LAPW) and LMTO methods are widely used since they are more precise. However, the most accurate all-electron methods can be more computationally demanding than pseudopotential techniques. In the full-potential methods space is divided into two types of regions: non-overlapping spheres surrounding the atomic sites called *muffin-tin spheres* and region outside these spheres called *interstitial* region. Since the linearized methods have been derived in terms of matrix elements of the Hamiltonian in a fixed basis, one simply has to calculate matrix elements of the full non-spherical potential in the sphere and the full spatially varying potential in the interstitial. The basis functions are the same in LMTO, LAPW or projected-augmented-wave (PAW) functions which are derived from a spherical approximation to the full potential. However, the spheres merely denote convenient boundaries defining the regions where the basis functions and the potential have different representations. Various calculational schemes differ from each other only in the treatment of the interstitial regions.

In the self-consistent calculation one also needs to calculate the potential arising from the density. This necessitates a procedure in which the Poisson equation is solved taking into account the sharply varying charge density inside the spheres. The field inside can be expanded in spherical harmonics and outside the spheres can be represented by smooth functions.

3.4.1 The full potential LMTO method

The FP-LMTO calculations [19] are all electron and fully relativistic, without shape approximation to the charge density or potential. The crystal is divided into non-overlapping muffin-tin spheres and interstitial regions outside the spheres. The wave function is then represented differently in these two types of regions. Inside a muffin-tin sphere, the basis functions are as in the LMTO-ASA method, viz. a Bloch sum of linear muffin-tin orbitals expanded by structure constants [$\phi_\nu(r)$ and $\dot{\phi}_\nu(r)$]. In the interstitial region, Hankel and Neumann functions are used to describe the spatially varying potential. But unlike the ASA (where kinetic energy is resticted to be zero in the interstitial region) the kinetic energy is not a constant. For simplicity, here we only consider a mono-atomic solid and suppress the atomic site index. The κ dependent linear muffin-tin orbitals can now be written as,

$$\psi_{klm}(\mathbf{k},\mathbf{r}) = \chi_{klm}(\mathbf{r}) + \sum_{lm} J_{klm}(\mathbf{r}) S_{klm,l'm'}(\mathbf{k}), \tag{3.21}$$

where

$$\chi_{lm}(\mathbf{r}) = i^l Y_l^m(\hat{\mathbf{r}}) \begin{cases} -ikh_l(\kappa S)\frac{\Phi(D_h,r)}{\Phi(D_h,S)} & , \quad |\mathrm{r}| < \mathrm{S} \\ -ikh_l(\kappa r) & , \quad |\mathrm{r}| > \mathrm{S} \end{cases} \tag{3.22}$$

and

$$J_{klm}(\mathbf{r}) = i^l Y_l^m(\hat{\mathbf{r}}) \begin{cases} J_l(\kappa S)(\kappa S)\frac{\Phi(D_J,r)}{\Phi(D_J,S)} & , \quad |\mathrm{r}| < \mathrm{S} \\ J_l(\kappa r) & , \quad |\mathrm{r}| > \mathrm{S} \end{cases} \tag{3.23}$$

Inside the muffin-tin sphere at τ, we can also expand the electron density and potential in spherical harmonics times a radial function,

$$n_\tau(\mathbf{r})|_\tau = \sum_h n_\tau(h; r_\tau) D_h(\hat{\mathbf{r}}_\tau), \tag{3.24}$$

$$V_\tau(\mathbf{r})|_\tau = \sum_h V_\tau(h; r_\tau) D_h(\hat{\mathbf{r}}_\tau), \tag{3.25}$$

where D_h are linear combinations of spherical harmonics, $Y_l^m(\hat{\mathbf{r}})$. D_h are chosen here because we need an invariant representation of the local point group of the atomic site contained in the muffin tin. The expansion coefficients $n_\tau(h;\, r_\tau)$ and $V_\tau(h;\, r_\tau)$ are numerical functions given on a radial mesh.

In the interstitial region, the basis function, charge density, and potential are expressed as Fourier series,

$$\psi(\mathbf{k}; \mathbf{r})|_I = \sum_{\mathbf{G}} e^{i(\mathbf{k}+\mathbf{G}).\mathbf{r}} \psi(\mathbf{k}+\mathbf{G}), \tag{3.26}$$

$$n_I(\mathbf{r})|_I = \sum_{\mathbf{G}} n_{\mathbf{G}} e^{i(\mathbf{k}+\mathbf{G}).\mathbf{r}}, \tag{3.27}$$

$$V_I(\mathbf{r})|_I = \sum_{\mathbf{G}} V_{\mathbf{G}} e^{i(\mathbf{k}+\mathbf{G}).\mathbf{r}}, \tag{3.28}$$

where **G** are reciprocal lattice vectors spanning the Fourier space.

3.4.2 The basis set

Envelope functions form a suitable basis in interstitial regions. By choosing the appropriate envelope function, e.g., plane waves, Gaussians, and spherical waves (Hankel functions), one can utilize various electronic structure methods (LAPW, LMTO, etc.). The LMTO envelope function is represented as

$$K_{lm}(\kappa; \mathbf{r}) = -\kappa^{l+1} i^l Y_l^m(\hat{\mathbf{r}}) \begin{cases} -h_l^+(\kappa\mathbf{r}) & \kappa^2 \le 0 \\ n_l(\kappa\mathbf{r}) & \kappa^2 > 0 \end{cases} \tag{3.29}$$

where n_l is a spherical Neumann function and h_l^+ is a spherical Hankel function of the first kind. The envelope function is singular Hankel or Neumann functions with regards to the sign of the kinetic energy. This introduces a κ dependence for the basis functions inside the muffin-tin sphere through the matching conditions at the sphere boundary. Using variational method, the ground state still has several basis functions with the same quantum numbers, n, l, and m, but different κ^2. This is called a double-basis approach.

The basis can always contain different basis sets corresponding to the atomic quantum number l, but with different principal quantum numbers n. A basis constructed in this way forms a fully hybridizing basis set, rather than a set of separate energy panels.

3.4.3 The LMTO matrix

We now introduce a convenient notation for the basis functions:

$$|\chi_i(\mathbf{k})\rangle = |\phi_i(\mathbf{k})\rangle + |\psi_i(\mathbf{k})\rangle, \tag{3.30}$$

where $|\phi\rangle$ is the basis function inside the muffin-tin spheres and $|\psi_i(\mathbf{k})\rangle$ represents the tails of basis-function outside the spheres.

A wave function $\Psi_{kn}(\mathbf{k})$ is then constructed by a linear combination of the LMTO basis functions, χ_i. The linear combination can be written as

$$|\Psi\rangle = \sum_i A_i|\chi_i\rangle \tag{3.31}$$

The Hamiltonian operator is

$$\hat{H} = H_0 + V_{nmt} + V_I \tag{3.32}$$

where H_0 is the Hamiltonian operator containing the kinetic energy operator and the spherical part of the muffin-tin potential, V_{nmt} represents the non-spherical part of the muffin-tin potential, and V_I is the interstitial potential. Then by using the variational principle for the one-electron Hamiltonian, the LMTO secular matrix follows as

$$\sum_j [\langle\chi_i(\mathbf{k})|H_0 + V_{nmt} + V_I|\chi_j(\mathbf{k})\rangle - \varepsilon(\mathbf{k})\langle\chi_i(\mathbf{k})|\chi_j(\mathbf{k})\rangle]A_j = 0 \tag{3.33}$$

which can be reduced to

$$\sum_j [H^0_{ij} + H^1_{ij} - \varepsilon(\mathbf{k})O_{ij}]A_j = 0 \tag{3.34}$$

where

$$H^0_{ij} = \langle\phi_i(\mathbf{k})|H_0|\phi_j(\mathbf{k})\rangle \tag{3.35}$$

$$O_{ij} = \langle\phi_i(\mathbf{k})|\phi_j(\mathbf{k})\rangle + \langle\psi_i(\mathbf{k})|\psi_j(\mathbf{k})\rangle \tag{3.36}$$

and

$$H^1_{ij} = \langle\phi_i(\mathbf{k})|V_{nmt}|\phi_j(\mathbf{k})\rangle + \frac{1}{2}(\kappa_i^2 + \kappa_j^2)\langle\psi_i(\mathbf{k})|\psi_j(\mathbf{k})\rangle + \langle\psi_i(\mathbf{k})|V_I|\psi_j(\mathbf{k})\rangle \tag{3.37}$$

where $|\psi_j(\mathbf{k})\rangle$ is an eigenfunction to ∇^2 with eigenvalue κ_j^2, H^0_{ij} is the spherical muffin-tin part of Hamiltonian matrix, O_{ij} is the overlap between the orbitals inside the sphere as well as in the interstitial region, and H^1_{ij} contains the corrections to the Hamiltonian matrix coming from the muffin-tin and interstitial regions. The first term in Eq. (3.37) is the non-spherical potential matrix, the next term is the expectation value of the kinetic energy operator in the interstitial region, and the last term is the interstitial potential matrix.

Total energy

The total energy for the whole crystal can be expressed as [20]

$$E_{tot} = T_{val} + T_{cor} + E_c + E_{xc} \tag{3.38}$$

where T_{val} and T_{cor} are the kinetic energy for the valence and core electrons, respectively, E_c is the electrostatic energy including electron-electron, electron-nucleus, and nucleus-nucleus contributions, and E_{xc} is an exchange energy term. The kinetic energy is usually expressed as the expectation value of the kinetic energy operator $-\nabla^2$. According to the eigenvalue equation the expectation value can be expressed as a sum over one-electron energies minus the effective potential energy. The core eigenvalues $\varepsilon_{i\tau}$ are obtained as an exact solution to the Dirac equation with the spherical part of the muffin-tin potential

$$\begin{aligned} E_{tot} &= \sum_{\mathbf{k}n}^{occ} w_{n\mathbf{k}} \varepsilon_{\mathbf{k}n} + \sum_{\mu\tau} f_{i\tau}\varepsilon_{i\tau} + \int_{Vc} n(\mathbf{r}) \Big[\frac{1}{2} V_c(\mathbf{r}) - V_{in}(\mathbf{r})\Big] d\mathbf{r} \\ &\quad -\frac{1}{2} \sum_j Z_{\tau j} V_c(\tau_j; 0) + \int_{V_c} \rho(\mathbf{r}) \varepsilon_{\mathrm{xc}}(\rho(\mathbf{r})) d\mathbf{r}, \end{aligned} \tag{3.39}$$

where the integral run over the unit cell [16]. The term with summation over j covers the core states. The density $\rho(\mathbf{r})$ is the total charge density, including valence as well as core electrons. V_{in} is the input potential obtained from LDA. The Madelung term $V_c(\tau; 0)$ describes the Coulomb potential at the nucleus (excluding the Z/r self contribution) and $\varepsilon_{\mathrm{xc}}$ is the exchange-correlation energy.

3.5 Full potential LAPW method

Some of the calculations in the present project have been carried out using the FP-LAPW program package WIEN97 and WIEN2K [21]. The LAPW method is a very accurate calculational scheme for electronic-structure investigations. This approach is characterized by the use of a basis set which is especially adapted to the problem. The method is basically derived from the augmented-plane-wave (APW) approach. The construction of APW developed by Slater is motivated by the fact that near an atomic nucleus the potential and wavefunctions are similar to those in an atom; strongly varying, but nearly spherical. Conversely, between the atoms both the potential and wavefunctions are smoother. Accordingly, space is divided into two regions and different basis expansions are used in these regions: radial solutions of Schrödinger's equation inside non-overlapping atom-centered spheres and plane-waves in the remaining interstitial regions.

$$\varphi(\mathbf{r}) = \begin{cases} \frac{1}{\Omega^{1/2}} \sum_G C_G e^{i(G+k)r} & r \in interstitial \\ \sum_{lm} A_{lm} u_l(r) Y_{lm}(r) & r \in inside - sphere \end{cases} \tag{3.40}$$

where φ is the wave function, Ω the cell volume and u_l the regular solution of the Eq. 3.40. Here C_G and A_{lm} are expansion coefficients, E_l is a parameter (introduced equal to the band energy) and V is the spherical component of the potential inside the sphere:

$$\Big[-\frac{d^2}{dr^2}+\frac{l(l+1)}{r^2}+V(r)-E_l\Big]ru_l(r)=0 \tag{3.41}$$

The particular choice of these functions was motivated by Slater who noted that plane-waves are the solutions of Schrödinger equation for a constant potential, while the radial functions are solutions for a spherical potential, provided that E_l is equal to the eigenvalue. This approximation known as muffin-tin approximation is commonly used in APW codes and is very good for close-packed (like fcc and hcp) materials.

The dual representation defined by Eq. 3.40 is not guaranteed to be continuous on the sphere boundaries, as it should be, for the kinetic energy to be well defined. Therefore a constraint is imposed in the APW method, by defining the A_{lm} in terms of $C_{\mathbf{G}}$ through the spherical harmonic expansion of the planewaves. The coefficient of each lm component is matched at the sphere boundary. Thus,

$$A_{lm}=\frac{4\phi i^l}{\Omega^{1/2}u_l(R)}\sum_{\mathbf{G}}C_{\mathbf{G}}j_l(|\mathbf{k}+\mathrm{g}|R)\mathrm{Y}^{\star}_{\mathrm{lm}}(\mathbf{k}+\mathbf{G}) \tag{3.42}$$

where the origin is taken at the center of the sphere and R is the sphere radius. Thus the A_{lm} are completely determined by the plane-wave coefficients $C_{\mathbf{G}}$ and the energy parameters E_l. The individual functions which are labeled by **G** and consist of single plane-waves in the interstitial matched to radial functions in the spheres are the augmented plane-waves (APWs).

3.5.1 The LAPW basis and its properties

In the LAPW method, the basis functions inside the spheres are linear combinations of a radial function $\mathrm{u}_l(\mathrm{r})\mathrm{Y}_{lm}(\mathbf{r})$ and their energy derivatives. The u_l are defined with a fixed E_l. The energy derivative $\dot{u}_l(r)Y_{lm}$ satisfies

$$\Big[-\frac{d^2}{dr^2}+\frac{l(l+1)}{r^2}+V(r)-E_l\Big]r\dot{u}_l(r)=ru_l(r) \tag{3.43}$$

in the non-relativistic case. These functions are matched to the values and derivatives of the plane waves on the sphere boundaries. Plane waves augmented in this way are called LAPW basis functions. In terms of this basis the wavefunctions,

$$\varphi(\mathbf{r})=\begin{cases}\frac{1}{\Omega^{1/2}}\sum_G C_G e^{i(G+k)r} & r\in interstitial\\ \sum_{lm}[A_{lm}u_l(r)+B_{lm}\dot{u}_l(r)]Y_{lm}(r) & r\in inside-sphere\end{cases} \tag{3.44}$$

where the B_{lm} are coefficients for the energy derivatives analogous to the A_{lm}. The LAPWs are plane waves in the interstitial region of the unit cell, and they match the numerical radial functions inside the spheres with the requirement that the basis functions and their derivatives are continuous at the boundary. In this method no shape approximations are made and consequently such a procedure is often called "full-potential LAPW" (FP-LAPW). The LAPW method has more advantages than the APW method. In the former, accurate energy bands (at a given **k** point) are obtained with a single diagonalization, while in the APW method the diagonalization is needed for each band. Moreover, the LAPW basis has more flexibility inside the spheres, i.e., two radial functions instead of one. This means that there is no difficulty in treating non-spherical potentials inside the spheres; although the optimum value of E_l is not known *a priori*, the flexibility arising from $\dot{u}_l$ allows an accurate solution. There is however a price to be paid for this flexibility. This arises from the requirement that the basis functions should have continuous derivatives. Higher plane wave cut-offs are required to achieve a given level of convergence.

In the WIEN2K package the total energy is calculated according to the Weinert scheme [22]. The convergence of the basis set is controlled by the cut-off parameter $R_{mt}K_{max}$ (determining the size of the matrix of the system), which usually assumes values between 6 and 9. The R_{mt} represents the smallest of all atomic sphere radii in the unit cell and K_{max} is the magnitude of the largest K vector (plane-wave cut-off).

There is a quantitative difference between the LAPW and LMTO approaches in the requirements of the full potential. Since the minimal basis for LMTO only involves functions with l_{max} given by the actual angular momenta or the primary states making up the band, only angular momenta up to $2l_{max}$ are relevant. However, for the LAPW methods, much higher angular momenta in the wavefunctions are required (typically $l_{max} \approx 8$ to 12 for accurate calculations) to satisfy the continuity conditions accurately. The difference results from the fact that, the LAPW basis is much larger; in order to represent the interstitial region accurately, many plane waves are required.

3.6 Pseudopotential Method

In 1934, Fermi first introduced the concept of pseudopotential. He interpreted the measured optical spectra of alkali atoms arising from transitions to high-lying electronic energy levels using the so-called pseudopotential and argued that for high-lying states the oscillations of the wave function near the atomic core played a very small role. Therefore he built a potential that gave a nodeless pseudo-wave-function which had the correct large-distance behavior. In most materials the core electrons do not contribute to the bonding, but only their absolute energy is affected by the average electrostatic potential in the vicinity of the core (core level shift). A fundamental idea is therefore the “frozen-core approximation”. The pseudopotential approximation treats each nucleus plus its core electrons as a “frozen core” that does not change in response to changes in its environment. The interactions of the valence electrons with this core are then described by a pseudopotential, usually constructed from all-electron calculations to reproduce the eigenvalues, and the wavefunctions outside the core. The core electrons are calculated for a reference configuration (in general, spherical) and are kept fixed thereafter. The wave functions for the valence electrons are treated (pseudized) so as to give the same energy levels as the all-electron wavefunctions. The pseudo wavefunctions differ from the all-electron wavefunctions only inside a region around the nucleus and are constructed to be nodeless. Nodeless pseudo-wavefunctions reduce the number of required plane waves considerably. It is implicit within the pseudo potential approach that the exchange-correlation potential, V_{xc}, like the direct Coulomb potential is separable into a core part and a valence part.

The main advantage of the pseudo potential method is that one does not need the complicated all-electron wave functions but only the pseudo wavefunctions which are tailored to be well-behaving numerically. Another advantage is that one needs to calculate the properties of ion only once in an environment such as a free atom and use it throughout all other DFT calculations. The frozen-core approximation allows one to transfer the properties of the free atom to an atom bound in a solid.

One of the most widely used implementations of DFT is the so-called plane wave pseudopotential method in which the KS wave functions are expanded in a basis of plane waves. Plane wave basis sets offer many advantages in DFT calculations for solids including completeness, unbiased representation, and arbitrarily good convergence accuracy. They also allow for straight forward mathematical formulation and implementation, which is convenient for the calculation of Hellmann-Feynmann forces in DFT perturbation calculations and for linear response calculations [23].

Having determined the pseudopotential, the total structural energy E_{str} can be evaluated. The contributions to E_{str} include the Madelung core-core energy, the electron-core energy, the kinetic energy of the electrons (which can be evaluated from the pseudopotential and wave functions), the electron-electron Hartree energy, and the exchange-correlation energy (which can be evaluated using the charge density). The input is the atomic number for each constituent atoms and the crystal structure. For a given structure, the volume for which E_{str} has a minimum that determines the lattice constants, and the curvature yields the bulk modulus. Although molecular dynamics schemes have been developed and are improving, at present one has to generally rely on the comparison of candidate crystal structures to predict or explain properties of different solid phases. Future molecular dynamics techniques will likely allow the predictions of new non-equilibrium solid phases with interesting and useful properties.

The fact that the total-energy pseudopotential method could predict the existence of a solid phase and its ground-state properties gave a significant boost to the research in this field [24]. The added claim that only the atomic number, atomic mass, and candidate crystal structures are used as input provided credence for the proposition that the total-energy pseudopotential approach is a first-principles method that could serve as a useful standard model of solids.

3.7 The projected augmented wave (PAW) method

In the pseudopotential methods a potential and its corresponding pseudo wave functions are constructed to reproduce the atomic scattering properties in an energy window around the atomic eigenvalues. They are then used as input parameters to the many-particle DFT calculations. The PAW method is in principle a frozen-core all-electron method that aims at adding the advantages and accuracy of all-electron methods to the more simple and computationally less demanding pseudopotential method.

Blöchl [25] developed the projected-augmented wave method (PAW) by combining ideas from the pseudo potential and linear augmented-plane-wave (LAPW) methods. The PAW method starts from a simple linear transformation that connects the exact valence wave function $|\psi\rangle$ to a pseudo (PS) wavefunction $|\tilde{\psi}\rangle$ which is expanded into plane waves,

$$|\psi\rangle = |\tilde{\psi}\rangle - \sum\nolimits_{N,i} |\tilde{\phi_{N,i}}\rangle\langle\tilde{p_{N,i}}|\tilde{\psi}\rangle + \sum\nolimits_{N,i} |\phi_{N,i}\rangle\langle\tilde{p}_{N,i}|\tilde{\psi}\rangle \tag{3.45}$$

All quantities related to the PS representation of the wave function are indicated by the tilde symbol. The ϕ are local wave functions, the index N goes over all sites, and i over the quantum numbers n, l, and m. The $\tilde{p}_i$ are localized projector functions that have to fulfill the condition

$$\sum_i |\tilde{\phi}\rangle\langle\tilde{p}_i| = 1. \tag{3.46}$$

Defining the character $c_{N,i}$ of an arbitrary wave function $\tilde{\psi}$ at the atomic site N as

$$c_{N,i} = \langle\tilde{p}_{N,i}|\tilde{\psi}\rangle, \tag{3.47}$$

the pseudo- and all-electron wavefunctions at an atomic site N can be easily reconstructed from the plane-wave expanded pseudo wave functions as,

$$|\tilde{\psi}_N\rangle = \sum_i |\tilde{\phi}_{N,i}\rangle c_{N,i} \tag{3.48}$$

and

$$|\psi_N\rangle = \sum_i |\phi_{N,i}\rangle c_{N,i}. \tag{3.49}$$

The variational quantities that need to be determined during the ground-state calculation are the PS wave function $\tilde{\psi}$. However, contrary to the “simple" pseudopotential methods the operators A representing physical quantities need to be consistently extended to their all-electron forms,

$$\tilde{A} = A + \sum_{N,i,j} |\tilde{p}_{N,i}\rangle \Big(\langle\phi_{N,i}|A|\phi_{N,j}\rangle - \langle\tilde{\phi}_{N,i}|A|\tilde{\phi}_{N,j}\rangle\Big) \langle\tilde{p}_{N,j}|. \tag{3.50}$$

The above equation is valid for local and quasi-local operators such as the kinetic energy.

The valence-only PAW method is implemented in the program package VASP [26]. Its results are almost identical to the most accurate DFT calculations which are based on the FP-LAPW method.

3.7.1 Charge density

The charge density at a point **r** in space is composed of three terms:

$$\rho(\mathbf{r}) = \tilde{\rho}(\mathbf{r}) + \rho'(\mathbf{r}) - \tilde{\rho}'(\mathbf{r}) \tag{3.51}$$

The soft pseudo-charge density $\tilde{\rho}(\mathbf{r})$ is the expectation value for the real-space projection operator $|\mathbf{r}\rangle\langle\mathbf{r}|$ on the pseudo-wave functions.

$$\tilde{\rho}(\mathbf{r}) = \sum_n f_n \langle\tilde{\Psi}_n|\mathbf{r}\rangle\langle\mathbf{r}|\tilde{\Psi}_n\rangle \tag{3.52}$$

The on-site charge densities $\rho'(\mathbf{r})$ and $\tilde{\rho}'(\mathbf{r})$ are treated on a radial support grid. They are given as :

$$\rho'(\mathbf{r}) = \sum_n f_n \langle\tilde{\Psi}_n|\tilde{p_i}\rangle\langle\phi_i|\mathbf{r}\rangle\langle\mathbf{r}|\phi_j\rangle\langle\tilde{p_j}|\tilde{\Psi}_n\rangle = n_{ij}\langle\phi_i|\mathbf{r}\rangle\langle\mathbf{r}|\phi_j\rangle \tag{3.53}$$

where n_{ij} is the occupancy of each augmentation channel (i, j) which is obtained from the pseudo-wave functions on applying the projector functions:
$n_{ij} = \sum_n f_n \langle\tilde{\Psi}_n|\tilde{p_i}\rangle\langle\tilde{p_j}|\tilde{\Psi}_n\rangle$.

Similarly for $\tilde{\rho}'(\mathbf{r})$:

$$\tilde{\rho}'(\mathbf{r}) = \sum_n f_n \langle\tilde{\Psi}_n|\tilde{p_i}\rangle\langle\tilde{\phi_i}|\mathbf{r}\rangle\langle\mathbf{r}|\tilde{\phi_j}\rangle\langle\tilde{p_j}|\tilde{\Psi}_n\rangle = n_{ij}\langle\tilde{\phi_i}|\mathbf{r}\rangle\langle\mathbf{r}|\tilde{\phi_j}\rangle \tag{3.54}$$

We will focus on the frozen-core case, where $\tilde{\rho}$, $\tilde{\rho}'$, and ρ' are restricted to valence quantities. Besides that, we introduce four quantities that will be used to describe the core charge density: ρ_c, $\tilde{\rho}_c$, ρ_{Zc}, and $\tilde{\rho}_{Zc}$. ρ_c denotes the charge density of the frozen core all-electron wave function at the reference atom. The partial-core density $\tilde{\rho}$ is introduced to calculate the nonlinear core corrections. ρ_{Zc} is defined as the sum of the point charge of the nucleus ρ_z and the frozen core AE charge density ρ_c: $\rho_{Zc} = \rho_z + \rho_c$.

The pseudized core density is a charge distribution that is equivalent to ρ_{Zc} outside the core radius and with the same moment as ρ_{Zc} inside the core region.

$$\int_{\Omega r} \rho_{Zc}(\mathbf{r}) d^3\mathbf{r} = \int_{\Omega r} \tilde{\rho}_{Zc}(\mathbf{r}) d^3\mathbf{r} \tag{3.55}$$

The total charge density ρ_T [27] is decomposed into three terms:

$$\begin{aligned} \rho_T &= \rho + \rho_{Zc} \\ &= (\tilde{\rho} + \hat{\rho} + \tilde{\rho}_{Zc}) + (\rho' + \rho_{Zc}) - (\tilde{\rho}' + \hat{n} + \tilde{n}_{Zc}) \\ &= \tilde{\rho}_T + \rho'_T - \tilde{\rho}'_T \end{aligned} \tag{3.56}$$

A compensation charge $\hat{\rho}$ is added to the soft charge densities $\tilde{\rho} + \tilde{\rho}_{Zc}$ and $\tilde{\rho}' + \tilde{\rho}_{Zc}$ to reproduce the correct multiple moments of the AE charge density $\rho' + \rho_{Zc}$ in each augmentation region. Because ρ_{Zc} and $\tilde{\rho}_{Zc}$ have exactly the same monopole $-Z_{ion}$ (the charge of an electron being new +1), the compensation charge must be chosen such that $\tilde{\rho}'$+$\hat{\rho}$ has the same moments as the AE valence-charge density ρ' within each augmentation sphere.

3.7.2 Total energy

The final expression for the total energy can also be split into three terms:

$$E(\mathbf{r}) = \tilde{E}(\mathbf{r}) + E'(\mathbf{r}) - \tilde{E}'(\mathbf{r}) \tag{3.57}$$

where $\tilde{E}(\mathbf{r})$, $E'(\mathbf{r})$, and $\tilde{E}'(\mathbf{r})$ are given by

$$\begin{aligned} \tilde{E}(\mathbf{r}) \;=\;& \sum_n f_n \langle\tilde{\Psi}_n| -\frac{1}{2}\Delta|\tilde{\Psi}_n\rangle + E_{xc}[\tilde{\rho}+\hat{\rho}+\tilde{\rho}_c] + E_H[\tilde{\rho}+\hat{\rho}] + \\ & \int v_H[\tilde{\rho}_{Zc}][\tilde{\rho}(\mathbf{r})+\hat{\rho}(\mathbf{r})]d\mathbf{r} + U(R, Z_{ion}) \end{aligned} \tag{3.58}$$

where $U(R, Z_{ion})$ is the electrostatic energy of the point charges Z_{ion} in an uniform electrostatic background.

$$\begin{aligned} E'(\mathbf{r}) \;=\;& \sum_{ij} n_{ij}\langle\phi_i| -\frac{1}{2}\Delta|\phi_j\rangle + \overline{E_{xc}[\rho'+\rho_c]} + \overline{E_H[\rho']} + \\ & \int v_H[\tilde{\rho}Z_c]\rho'(\mathbf{r})d\mathbf{r} \end{aligned} \tag{3.59}$$

where $\int v_H[\tilde{\rho}Z_c]\rho'(\mathbf{r})d\mathbf{r}$ is the electrostatic interaction between core and valence electrons and E_H is electrostatic energy

$$E_H[\rho] = \frac{1}{2}(\rho)(\rho) = \frac{1}{2}\int d\mathbf{r}\int d\mathbf{r}'\frac{\rho(\mathbf{r})\rho(\mathbf{r}')}{|\mathbf{r}-\mathbf{r}'|} \tag{3.60}$$

$$\begin{aligned} \tilde{E}^1(\mathbf{r}) \;=\;& \sum_{ij} n_{ij}\langle\tilde{\phi}_i| -\frac{1}{2}\Delta|\tilde{\phi}_j\rangle + \overline{E_{xc}[\tilde{\rho}'+\hat{\rho}+\tilde{\rho}_c]} + \overline{E_H[\tilde{\rho}'+\hat{\rho}]} \\ +\;& \int v_H[\tilde{\rho}Z_c][\tilde{\rho}'(\mathbf{r})+\hat{\rho}(\mathbf{r})]d\mathbf{r} \end{aligned} \tag{3.61}$$

The overlining signalizes that the corresponding terms must be evaluated on the radial grid within each augmentation region.

3.8 Brillouin zone integration

In order to determine the charge density and other quantities such as total energy, forces etc. it is necessary to evaluate sums over the occupied states. As discussed in Sec.3.1, for crystals this can be done over the Brillouin zone and by the application of crystal symmetry, can be reduced to integrals over the irreducible wedge of the zone (IBZ). Following the variational principle (minimizing the total energy), and the Pauli-exclusion principle, eigenstates with eigenvalues $\varepsilon_i(\mathbf{k})$ are filled starting from the energetically lowest eigenvalue. The energy of the highest filled eigenstate is called the Fermi energy (E_F). The Fermi energy is given from

$$N = \int_{-\infty}^{\varepsilon_F} D(\varepsilon) d\varepsilon, \tag{3.62}$$

where N is the number of valence electrons and $D(\varepsilon)$ is the density of the states (DOS),

$$D(\varepsilon) = \frac{2}{8\pi^3} \int_{S(\varepsilon)} \frac{dS}{|\nabla\varepsilon(\mathbf{K})|.} \tag{3.63}$$

The integration is carried out all over a surface of constant energy, $S(\varepsilon)$, in the IBZ. The one-electron states most relevant for physical properties are those with energies around the Fermi level. These states are important for the stability of the crystal structure, transport properties, magnetic susceptibility, etc. The integrals are necessarily calculated numerically using wavefunctions and eigenvalues at a finite number of **k** points in the zone. The two commonly used methods are briefly discussed below.

3.8.1 Special points method

In this method integrations are performed as weighted sums over a grid of representative **k** points. The locations of the representative (or special) points and the corresponding weights are independent of the band energies, and are chosen to yield optimum convergence for smooth functions.

This method is well suited for insulators. In metals, bands intersect the Fermi level leading to discontinuities in the occupation and therefore in the integrands on the Fermi surface. In order to overcome this difficulty an artificial broadening of the Fermi surface is used.

3.8.2 Tetrahedron method

In the tetrahedron approach, the zone is divided into tetrahedra and the band energies and wave functions are computed at **k** points on the vertices. This is particularly useful because tetrahedra can be used to fill all space for any grid. The band energies are interpolated linearly between the vertices, and this interpolation is used to determine the Fermi energy. Each band at each **k** point is then assigned a weight based on the volume of the tetrahedron for which it occurs below E_{F}, and the charge density is calculated by summing the individual contributions with these weights. The tetrahedron method is very important in calculations on transition metals, rare earths etc., where there are exquisite details of the Fermi surfaces that must be resolved.

CHAPTER 4

Ground-state Properties and their Analyses

The end of all our exploration will be to arrive where we started.

T.S. Eliot

The properties of matter are usually determined by the electronic ground and excited states. Ground-state properties include: cohesive energy, equilibrium crystal structure, phase transitions between different structural arrangements, elastic constants, charge density, magnetic order, static electric and magnetic susceptibilities, etc.

Since typical energy scales for electrons are much greater than those associated with the degrees of freedom for the more massive nuclei, the lowest energy ground state of the electrons determines the structure and low-energy motions of the nuclei. The vast array of forms of matter - from the hardest diamond to soft lubricants like graphite or the many complex crystals formed by the elements of the Periodic Table - are largely manifestations of the ground-state of the electrons involved.

4.1 Structural stability and Phase transitions

In the area of phase-stability and phase-diagram prediction, first-principles calculations have made an impact on the understanding of real materials. The equation of state as a function of pressure and temperature is perhaps one of the most fundamental relations in condensed matter.

The stable structure at a given pressure (P) and temperature (T) determines all the other properties of the material. The total energy (E) at $T = 0\,\mathrm{K}$ as a function of the volume (Ω) is the most convenient quantity for theoretical analysis because it is quite straightforward to carry out electronic structure calculations at fixed volume. In other words, volume is a convenient “knob” that can be tuned to control the system theoretically. Comparison of theoretical and experimental volume is one of the touchstones of “*ab initio*” electronic-structure research.

The total energy E and Ω per unit cell, together with P and bulk modulus B are related by the equations,

$$E = E(\Omega), P = -\frac{dE}{d\Omega}, B = -\Omega\frac{dP}{d\Omega} = \Omega\frac{d^2E}{d\Omega^2}. \tag{4.1}$$

One has to first determine the equilibrium volume of the cell where E is minimum or P = 0, and bulk modulus (B) for the zero-pressure crystal structure. The most commonly used approach (and that used in this project) is, to calculate E for several different Ω values, and fit these to an analytic function, e.g., the Murnaghan equation of state [28, 29, 30] or the so-called universal equation of state [31] (used here). The minimum gives the corresponding equilibrium volume and total energy, and the second derivative, the bulk modulus.

The major challenge for computational materials science is the prediction of crystal structure. While the properties of a material in a given structure can be predicted, it is still very difficult to demonstrate that a particular chosen structure will be stable or even metastable. With all the sophistication of first-principles theory, structure prediction still has to be approached with brute (but ineffective) force. To “predict” the structure of a compound, we have to compute, at best the total energy for a few “reasonable” candidate arrangements and then proclaim the one with the lowest total energy to represent the ground-state structure. While such an approach may be reasonable when working on well-known systems, it may be of little benefit when dealing with novel or complex multicomponent materials. In a substantial part of this project we have, e.g., studied structural stability and predicted crystal structures for a series of mixed-valence chromium oxides which turned out to be one of the most demanding projects dealt in this thesis. The actual structures considered for the prediction and detailed results are given in Publications VI to IX.

4.2 Electronic Structure

As outlined in Chapter 2, the electronic structure of materials determines ground-state properties such as electrical conductivity. An electronic structure is often visualized by a band-structure plot. A band is the track of an eigen value in reciprocal space.

4.2.1 Classification of materials

Based on the intrinsic electronic structure and the filling of bands, materials can be classified as metals, insulators, semiconductors, and half metals.

Metals
Metals are characterized by a band structure in which the highest occupied band (the valence band; VB) is partially filled. The highest occupied energy level is called the Fermi level (E_{F}). Metals usually have some vacant levels just below the E_{F} whereas some occupied levels occur above E_{F} at T = 0 K. Since metals do not have to be overcoming excitation gaps, the band electrons in singly occupied states close to the E_{F} are able to move around

relatively freely and these electrons are responsible for the conductivity of metals.

Insulators
The VB of an insulator is completely filled. The highest energy level of VB is separated from the lowest energy level of conduction band (CB) by a forbidden energy gap (E_g) of the order of some 5 eV. Even at appreciable temperatures very few electrons from the VB have sufficient thermal energy to be promoted to the CB, hence insulators have zero or negligible conductivity.

Semiconductors
Semiconductors have a similar band structure to insulators, but the E_g is smaller, say, in the range of 0.2 to 2.0 eV. At low temperatures a few electrons have sufficient thermal energy to be promoted to CB and hence create conductivity in an electric field. However, the excitation process is described by an exponential function of temperature and the conductivity may accordingly reach appreciable values at higher temperatures.

It should be noted that insulators are really special cases of semiconductors, distinguished by a much larger size of E_g. Note that for many purposes the Fermi level (E_F) of insulators and semiconductors are postulated to be located midway between VB and CB.

Half metals
Half metals constitute an unique class of magnetic materials in which one of the spin channels (usually postulated as the majority-spin channel) has metallic character and the other spin channel has insulating (semiconducting) character with a distinct band gap extending from the top of the highest filled energy level to the lowest empty energy level (at 0 K).

4.2.2 Density of states

An important description of the electronic structure for many purposes is provided by the density of states (DOS) which is another way to visualize and analyze the electronic structure. In a DOS diagram the abscissa axis is usually chosen as energy and the ordinate axis is the number of eigenvalues (states) at a particular energy level. The energy scale is conveniently chosen so that the E_F is located at zero energy.

$$\rho(E) = \frac{1}{N_k}\sum_{i,\mathbf{k}} \delta(\epsilon_{i,\mathbf{k}} - E) = \frac{\Omega}{(2\pi)^d}\int_{BZ} d\mathbf{k}\delta(\epsilon_{i,\mathbf{k}} - E). \tag{4.2}$$

Assuming independent-particle states, and taking $\epsilon_{i,k}$ as the energy of an electron, Eq.4.2 provides the number of independent-particle states per unit energy. The DOS provides us with the ground-state electronic structure of a given material and helps us to classify materials in the categories metals, insulators, semiconductors and half metals.

For example, Fig. 4.1 presents the electronic structure of $\mathrm{Ca_3Co_2O_6}$ in various magnetic configurations. In the ground-state ferrimagnetic configuration, $\mathrm{Ca_3Co_2O_6}$ has a distinct

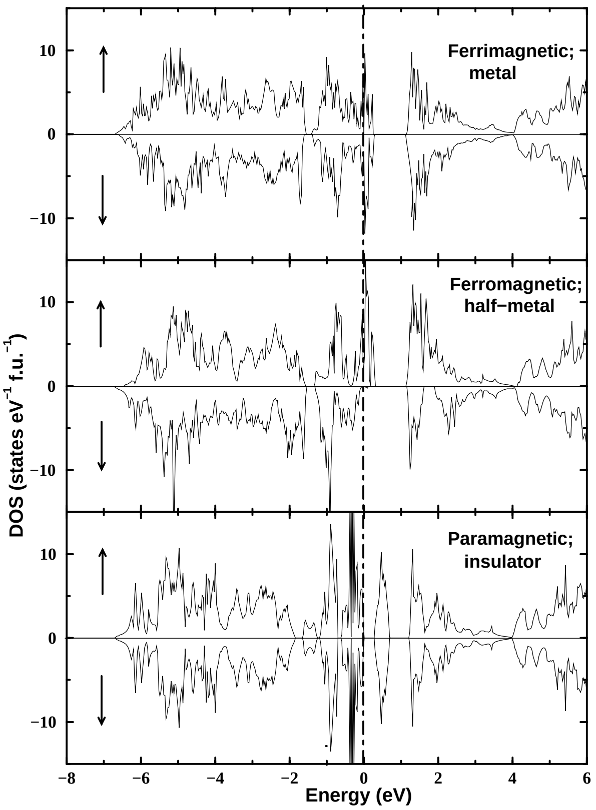

Figure 4.1: Total density of states plots for $Ca_3Co_2O_6$ in different magnetic configurations.

number of states at the E_F implying metallic character. On the other hand, in the higher-energy ferromagnetic configuration, the majority-spin channel still exhibits electronic states at E_F whereas the minority-spin channel shows an energy gap of around 1.15 eV, implying half-metallic character. Further, in the paramagnetic configuration, both majority- and minority-spin channels show gaps of around 0.29 eV, indicating semiconducting behavior. It is worthwhile to note here that we can also extract excited state properties of a material from the DOS and derived quantities thereof.

4.3 Bonding Characteristics

The stable structures of solids are most naturally considered in terms of the electronic ground state which determines the bonding of nuclei. The lowest energy state of the electrons determines the location of the nuclei in space and, conversely, the spatial structure of nuclei provides the external potential that determines the Schrödinger equation for the electrons. When atoms combine to form a solid, the repulsion between the positive ion cores of the atoms is overcome by the attractive forces of the valence electrons that holds the material together. While the ion cores occupy fixed positions (in the structural framework) the valence electrons “whiz” around and between them, forming a kind of electrostatic glue known as “bonding”.

4.3.1 Types of bonding

Bonding in materials is classified according to the four idealized types of bond.

Ionic bonding
Ionic bonding is found in compounds formed by combination of elements with a large difference in electronegativity. This type of bonding occurs when some of the valence electrons from one atomic species are donated wholesale to another atomic species. The ionic systems can be characterized by charge transfer to form closed-shell ions, often leading to structures with the larger sized anions in close-packed arrangements and small cations in intermediate positions to maximize Coulomb attraction (or minimize anion-anion repulsion). Unlike the other bonding types the idealized ionic bonding can be understood and rationalized in terms of the Coulomb law from classical physics. The cohesive energy for an idealized ionic compound is completely determined by the attractive and repulsive forces between the ions.

Covalent bonding
Covalent bond can only be accounted for in terms of quantum mechanical concepts. This type of bonding involves a complete change of electronic states from, say, isolated atom (or ion) to well-defined bonding states in solids. Covalent bonds are directional bonds that result from the formation of localized electronic states with pairing of electrons. One of the main requirements for a covalent bond to be formed is the presence of degenerate energy levels of the constituents so that they can be shared between the constituents. (The essential feature is pairing process whether or not a pair of electrons are involved).

Metallic bonding
Metallic bonding is visualized as itinerant conduction electrons spread among the ion cores forming homogeneous electron gas. Unlike in covalent bonds, the electronic states are essentially delocalized but the crucial features of the covalent bonding (viz. the paired distribution of electrons) is the same. Metals are usually good conductors because there is no energy gap for electronic excitation, when the bands are partially filled they can easily accept different number of electrons which can drift easily between the ion cores. This also enables metals to form alloys among atoms with different valency.

Van der Waals bonding
Van der Waals bonding is sometimes referred to as closed-shell bonding and may be exemplified by rare gas and molecular solids. Phases with van der Walls bonding have electronic states qualitatively similar to those of free atoms, weak van der Waals attraction being bal-

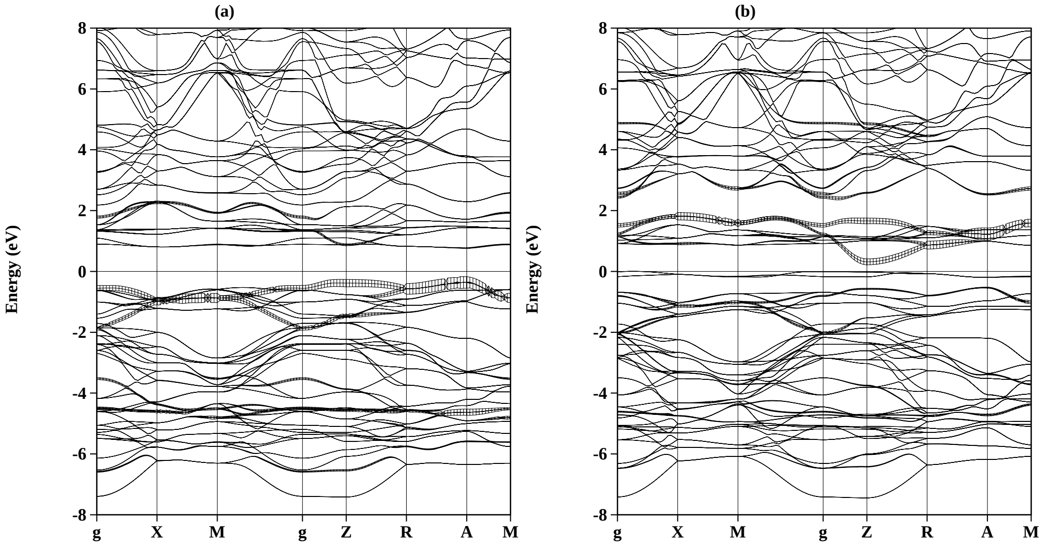

Figure 4.2: Illustration of (a) majority-spin and (b) minority-spin bandstructures of one type of Mn in the ferrimagnetic insulator $YBaMn_2O_5$. The d_{z^2} orbital is highlighted with fat band notation.

anced by repulsion from orbital overlap.

Hydrogen bonding, which is thought to be crucial within many molecules and of important biological activity, is not considered here.

The bonding in a real material is, in general, a combination of all three main types described above. For example, in a metal there can be directional covalent bonding as well as contributions of ionic character due to local charge transfer. In this thesis, we will see a generous number of systems displaying an admixture of the different types of bonding.

The challenge for electronic-structure theory is to provide universal methods that can accurately describe real systems. A theoretical method must not be limited to any particular type of bonding, otherwise it would be rather unproductive. The theory should provide understanding, and not merely numerical values for more or less well-chosen parameters. Different analytical tools (based on DFT) used to visualize and characterize different types of bonding in this thesis are described below.

4.3.2 Partial density of states

Band structures and density of states are common tools for investigating the physical properties of solids. In order to obtain a more local picture of bonding, one can use projected band structure ("fat bands" which display the contribution of one given atom (or one given atomic orbital) in each band for selected directions in reciprocal space (see for example, Fig. 4.2 where d_{z^2} orbital in one of the Mn atoms in $YBaMn_2O_5$ is shown as fat band). DOS

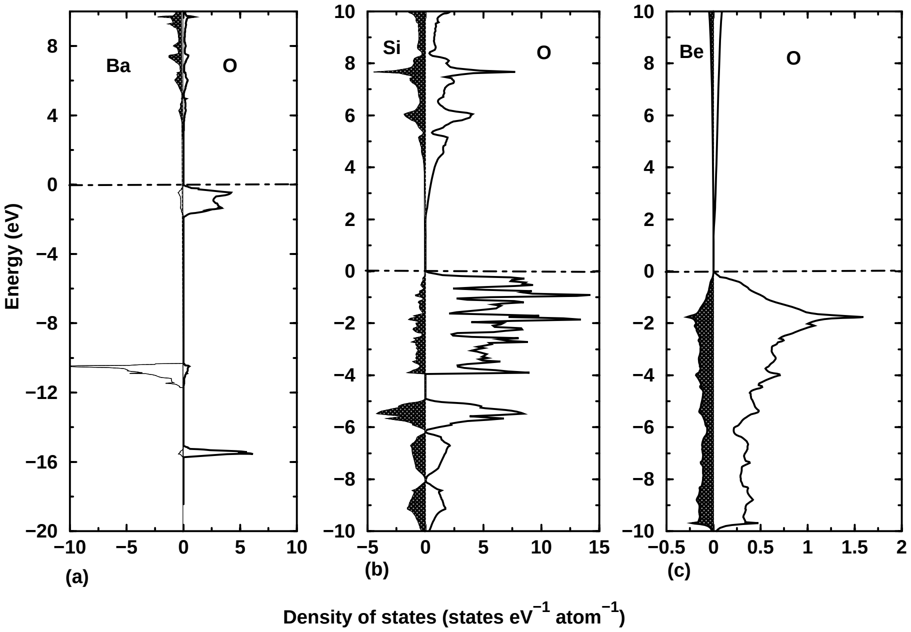

Figure 4.3: Site-decomposed density of states plots for (a) ionic BaO, (b) covalent SiO_2, and (c) semi-covalent BeO. The horizontal dotted line marks (E_F). The region below E_F is the valence band and above E_F is the conduction band.

plots, on the other hand, allow one to calculate atomic gross contributions to the bonding in the whole Brillouin zone. Since the materials studied in this project are mostly multicomponent with large number of atoms, analysis of their electronic structure by means of "fat bands" becomes cumbersome. Hence we have mainly preferred DOS analysis.

The site-projected DOS gives an overview picture of the nature of the bonding between the constituents of a solid. By studying the electronic DOS decomposed according to site and angular momentum one can, in principle, distinguish between ionic and covalent bonding in a compound. If the bonding is strongly ionic, there is little mixing of states from one atom into states of other atoms [see, Fig. 4.3a, where the Ba and O states in BaO are well separated from each other]. If the bonding is primarily covalent, the states of different atoms are mixed together and one would expect to find similar decomposed state densities for all sites [32]. When two atoms interact, their states hybridize with one another to form bonding and antibonding states. Only when the valence states of the constituents are approximately degenerate, does a strong covalent hybridization occur. For SiO_2 in Fig. 4.3b one can see the Si and O states in the same energy region, indicating energetic degeneracy and hence, the covalent interaction. The hybridization between the d electrons of the transition metal with the s and p electrons of the main group elements lead to sp-d bonding and antibonding hybrids, as well as nonbonding d states. Filling of bonding orbitals increases bond strength, filling non-bonding orbitals has little effect, whereas filling antibonding orbitals reduces the

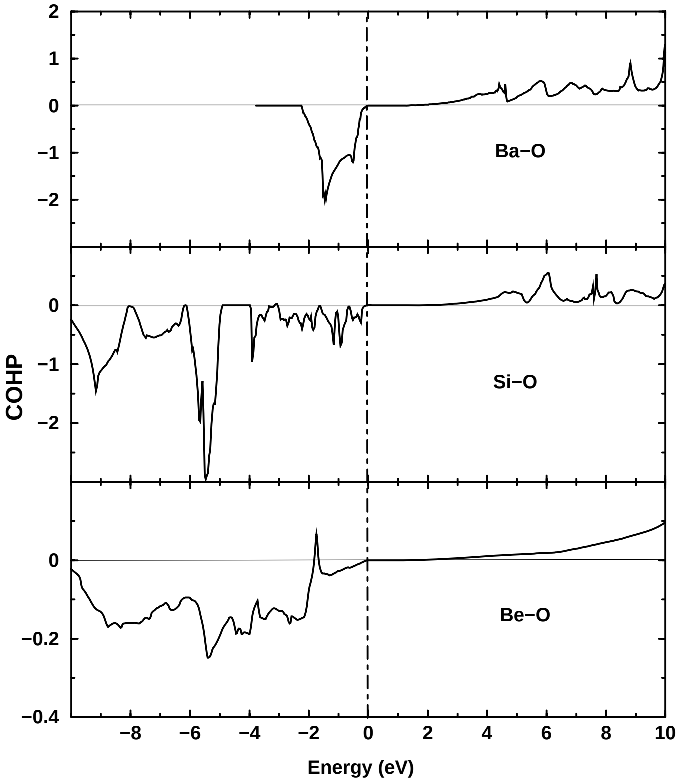

Figure 4.4: Crystal orbital Hamiltonian population plotted for BaO, SiO_2 and BeO. The vertical dotted line indicates the Fermi level.

bond strength. In Fig. 4.3c we display the DOS for the semi-covalent case BeO which exhibits mainly covalent bonding with a woof of ionic bonding interaction.

One of the main tasks of this project has been the study of mixed-valent transition-metal oxides. In order to determine the actual valence states of elements and thereby explore the difference between formal and actual valence states, orbital-decomposed DOS is particularly useful. The orbital-projected DOS provides the occupation of different orbitals with respect to energy. Hence the higher energy orbitals which lead to orbital ordering can be explored (see various publications of this thesis).

4.3.3 Crystal-orbital-Hamiltonian-population (COHP) plot

Another useful tool to distinguish bonding, antibonding, and nonbonding interaction between atoms is the crystal-orbital population. According to this COHP concept, negative COHP values indicate bonding, positive values antibonding, and zero COHP together with finite DOS values suggests nonbonding states. COHP is a quite meaningful way to measure the effective strength of bond interactions. It is calculated by weighing the crystal-orbital-overlap-population with crystal-orbital eigenvalues. Since the latter is less basis-set dependent, COHP should be appropriate in cases with highly degenerated systems. A detailed description of the COHP method can be found in Ref. [33].

The COHP contours should reflect the number of states in a particular energy interval. The integrated COHP (ICOHP) up to the E_F represents the total overlap population of the bonds concerned and this can be taken as a measure of bond strength. For example the ICOHP values (from Fig. 4.4) for BaO, SiO_2, and BeO are 0.54, 2.08, and 1.77, respectively. It should be noted that COHP analysis provides the location of bonding, antibonding, and nonbonding electrons. In order to establish the nature of bonding, COHP should be combined with site-decomposed DOS and other bonding-analysis tools.

4.3.4 Charge-density plot

The electron density $\rho(\mathbf{r})$ plays a fundamental role in the theory and understanding of systems comprised of electrons and nuclei. Since it is the fundamental quantity in the DFT calculations, an understanding of different bonding can be obtained by plotting the charge density distribution in real space. Fig. 4.5a depicts a typical example of ionic bonding in NaCl; Na^+ exhibits reduced charge density whereas Cl^- rules over the enhanced charge density. Fig. 4.5b reproduces covalently bonded Si with significant charge density mid way between the Si atoms. In metallic Al charges are seen to be homogenously distributed in the interstitial region (Fig. 4.5c).

The charge density is in principle, an indicator for the chemical bonding in a given system, but comes normally out as rather featureless, with charge maxima around the atoms, similar to the charge density for overlapping free atoms. Moreover, it gives the overall charge density including contributions from non-bonding electrons. Hence, one needs additional tools for analysis of the bonding character in the real materials.

4.3.5 Charge-transfer plot

If one now (instead of charge density) displays the difference between the electron density of the compound and the electron density of the constituent atoms (viz. *difference* between the crystal density and that of a sum of superimposed neutral spherical atoms), one obtains an impression of how electrons are shifted around when the solid is formed. This allows one to see how the actual chemical bond is formed in the real space. Mathematically the charge-transfer density is the self-consistent electron density of a solid in a particular plane ($\rho_{comp.}$), minus the electron density of the corresponding free atoms ($\rho_{f.a.}$) in an identical structural arrangement,

$$\Delta\rho(r) = \rho(r)_{comp.} - \rho(r)_{f.a.}, \tag{4.3}$$

which allows one to visualize how electrons are redistributed in a particular plane of the structure compared to free atoms.

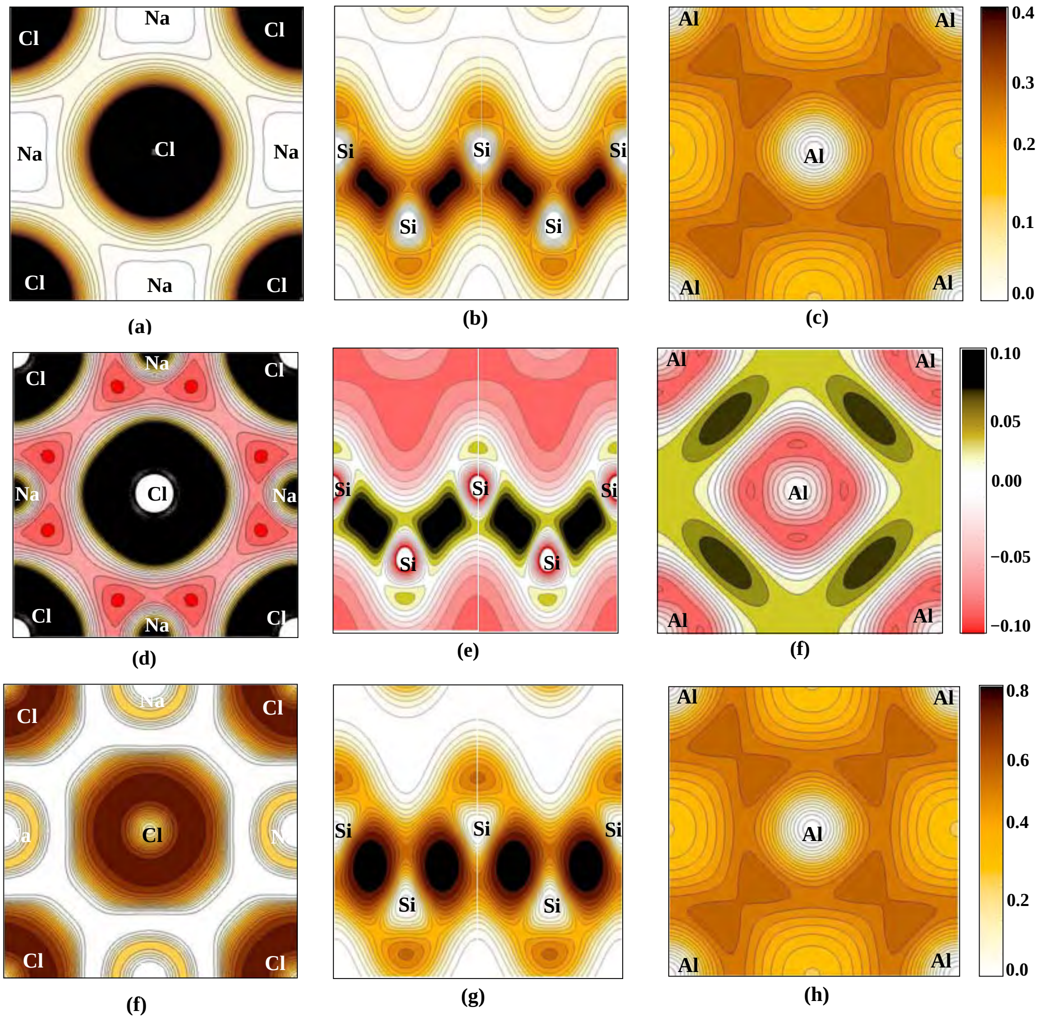

Figure 4.5: Charge-density plots for (a) ionic NaCl, (b) covalent Si, and (c) metallic Al. Charge transfer and electron localization function (ELF) plots are shown in the same order for the above materials in (d), (e), (f) and (g), (h), (i), respectively.

Fig. 2(d−f) shows the charge transfer in ionic NaCl, covalent Si, and metallic Al, respectively. The negative charge-transfer around Na and positive charge-transfer around Cl indicate the transfer of charges from Na to Cl while forming ionic bonding. On the other hand, in the Si case charge has been transferred to the mid-way region between the Si atoms. An experimental charge difference plot based on scattering by x-rays and high-energy electrons [34] has been found to provide a fully comparable picture with theoretical charge-transfer plot. This suggests that the charge transfer plot may be a very valuable tool to visualize bonds, in particular covalent bonds. In metallic Al, we can see that Al has lost electrons to the interstitial regions. Unlike the other two types of bonding, the directional-character of covalent bonding is clearly exposed from charge-density and charge-transfer plots.

In addition, attention may be drawn to the charge difference plotted between $LiCr_3O_8$ and Cr_3O_8 in the same structural arrangement (Fig. 8 in Paper.VII). Such plots have proved very useful to analyze the effect of Li-intercalation in Cr_3O_8, viz, changes in the lattice, bonding character etc as Li enters the Cr_3O_8 lattice. Such an analysis throws some light on the usefulness of $LiCr_3O_8$ and Cr_3O_8 as cathode materials in the rechargeable Li-ion batteries.

4.3.6 Electron-localization function

ELF provides a measure of the local influence of Pauli repulsion on the behavior of electrons and permits the mapping in real space of core, bonding and non-bonding regions in a crystal [35]. ELF is a ground-state property which discriminates between different kinds of bonding interaction for the constituents of a solid [35, 36, 37]. In the implementation for DFT, this quantity depends on the excess of local kinetic energy t_p originating from the Pauli principle.

$$ELF = \{1 + [t_{p(r)}/t_{p,h}(\rho(r))]^2\}^{-1} \tag{4.4}$$

where:

$$t_p = \tau - 1/8[(\nabla\rho)^2/\rho] \tag{4.5}$$

is the Pauli-kinetic-energy density of a closed-shell system. $(\nabla\rho)^2/(8\rho)$ is the kinetic energy density of a bosonic-like system, where orbitals are occupied proportional to $\sqrt{\rho}$. t_p is always positive, and for an assembly of fermions, it describes the additional kinetic energy density required to satisfy the Pauli principle. The total electron density (ρ)

$$\rho = \sum_i^n |\psi_i|^2 \tag{4.6}$$

as well as the kinetic energy density(τ)

$$\tau = 1/2 \sum_i^n |\nabla\psi_i|^2 \tag{4.7}$$

are computed from the orbitals ψ_i, the index i running over all occupied orbitals.

According to Eqn. 4.4, the ELF takes the value one either for a single-electron wave function or for a two-electron-singlet wave function. In a many-electron system ELF is close to one in regions where electrons are paired such as in covalent bonds, or for lone electrons (dangling bonds) while the ELF is small in regions with low density of electrons. In a homogeneous electron gas ELF equals 0.5 at any electron density, and ELF values of this order in homogeneous systems indicates regions where the bonding has metallic character. The ELF distribution for the typical examples of bonding discussed above are shown in Fig. 4.5(g−i). For the NaCl case ELF is around 0.8 at the Cl site and only a non significant ELF value is found at the Na site, thus clearly reflecting ionic bonding. In the Si case, a ELF value just below 1 is found where the shared electrons are located between the Si atoms. In the Al case, maximum values of ELF$\sim$0.5 are found in the interstitial region where the delocalized electrons rule.

In addition to these tools, bonding interaction has been analyzed with the help of concepts like “atoms-in-molecule´´ of Bader [38] and Born-effective charges [39, 40]. These method provide a somewhat quantitative measure of charges present in each atomic site in a lattice. From the thus calculated values we can draw conclusions on nature of bonding as well as valence states of individual constituents. A brief description of these methods and the resulting analysis are dealt with in Publications IV and XI, respectively.

CHAPTER 5

Excited-state Properties

I will love the light for it shows me the way, yet I will
endure the darkness for it shows me the stars.
Og Mandino

A common physical phenomena such as magnetism required the development of civilization to proceed whereas the much more elementary concept of light appeared before mankind—the first primitive experiments can be traced back to the taming of fire by man. However, it was first after the renaissance that mankind started to consider light as a scientific matter of importance.

Dielectric functions and conductivity are the most important response functions in condensed matter physics because they determine the optical properties of materials, electrical conductivity, and a host of technological applications. In addition, optical spectra are perhaps the most widespread tools for studying the electronic excitations themselves. With the preceding chapters as a background we will now proceed to the study of excited-state properties.

5.1 Excitations in Density-Functional Theory

Excitations in condensed matter are usually small perturbations on the entire system. Using perturbation techniques, one can calculate excitation spectra and the real and imaginary parts of the response function. Nevertheless, one needs to know the ground state, since the excitations are perturbations on the ground state.

Spectroscopic techniques such as photoemission spectroscopy are very common in the study of ground-state properties of materials. In photoemission spectroscopy, high-energy photons are bombarded on a system, producing a current of photoelectrons. The energy of these photoelectrons is a measure of their binding energy in the material. The higher the energy of photons or electrons, the more is the perturbation of the ground-state electronic structure.

In general, if the perturbation due to the experimental procedure is kept to a minimum, then the results will more closely reflect the ground state of the system. This criterion is satisfied in optical spectroscopy since the energy involved in the excitations is a couple of tens of eV and both the initial and final states belong to the valence bands. However, the resulting spectrum will have a complicated dependence on the dispersion, which makes interpretation difficult and very indirect.

Using modern band-structure calculations, the problem of deconvoluting the optical spectra can be avoided. Instead, a calculated version of the optical spectrum for a system is derived, and if the agreement between experiment and theory is good, the origin of the peaks in the spectrum can be easily extracted from the parameters used to calculate the spectrum. Moreover, if several models of the ground-state electronic structure exist for a system, optical spectra can be calculated for these different models, and compared with the experimental spectrum. Thus a particular model can be validated.

The calculation of DOS, band structures, photo-emission spectra and optical properties using DFT relies on the identification of the KS eigenvalues (eigenfunctions) with the true eigenvalues (eigenfunctions). DFT is often quoted to be a ground-state theory and it is usually believed that it has little bearing on excited states. However, this is not correct. A basic consequence of the Hohenberg-Kohn theorems is that the ground-state density actually determines the Hamiltonian of the system. The reason is that the external potential (which is the only operator in the Hamiltonian that differs from system to system) is given by the ground-state density. Since the Hamiltonian completely characterizes all states of the system, the ground state density determines not only ground-state but also the excited states [41].

In spite of the above fact, it may be argued that the KS eigenvalues and eigenfunctions are just artificial constructions resulting from the one-particle approximation. However, the KS orbital eigen values are not completely devoid of physical meaning [41]. Their difference is a well defined approximation to the excitation energies in the electron-electron interaction of zeroth order.

5.2 Definition of the Conductivity Tensor

The phenomenological formulation of Maxwell's equations in the presence of polarizable or conducting media can be cast in terms of the complex frequency-dependent dielectric function $\epsilon(\omega)$ or conductivity $\sigma(\omega)$. When a system is subjected to a time-dependent electric field **E**(**r**,t), an induced charge current **J**(**r**,t) will appear as a response. In the linear approximation, the relationship becomes:

$$\mathbf{J}(\mathbf{r},t) = \int d^3r' \int_{-\infty}^{t} dt\sigma(\mathbf{r},\mathbf{r}',t,t')\mathbf{E}(\mathbf{r}',t') \tag{5.1}$$

where the kernel σ (**r**,**r**$'$,t,t$'$) is called the conductivity. In an isotropic material, **J** and **E** are parallel, and the conductivity can be described by a scalar. However, in a real crystal, the two fields will not be parallel, and in this case the conductivity is a tensor of rank two.

If the properties of the crystal do not change with time, the conductivity will only depend on the time difference $t-t'$. Furthermore, when translational symmetry is present, the spatial dependence will follow $\mathbf{r}-\mathbf{r}'$, viz. described by a vector in the Wigner-Seitz cell. We can then Fourier transform over both space and time, which gives the much simpler relationship

$$\mathbf{J}(\omega,\mathbf{q}) = \sigma(\omega,\mathbf{q})\mathbf{E}(\omega,\mathbf{q}) \tag{5.2}$$

where ω corresponds to the frequency of a plane electromagnetic wave and **q** is a crystal wave vector in the first Brillouin zone, and corresponds to the momentum transfer in the excitation of the electrons by the photon, i.e., it is the photon momentum.

In the optical energy range, **q** is very small compared to the momentum of the electrons, and is therefore often neglected. For finite **q**, one can divide the conductivity into a transversal and a longitudinal part, depending on the relative orientation of **q** and **E** [42]. Here, we are only interested in the limit **q**$\rightarrow$0, where this distinction disappears.

An equivalent relationship can be obtained for the unitless dielectric function $\epsilon(\omega,\mathbf{q})$, the relation between this entity and the conductivity being

$$\sigma_{ij}(\omega,\mathbf{q}) = \frac{i\omega}{4\pi}[\delta_{\alpha\beta} - \epsilon_{\alpha\beta}(\omega,\mathbf{q})] \tag{5.3}$$

in electrostatic units, which is the unit system used in this chapter, and i,j are Cartesian coordinate indices. A discussion of optical properties can be done using either of these tensors.

5.2.1 Symmetry considerations

The optical conductivity tensor is symmetric in the absence of a magnetic field. In a coordinate system based on the principal axes, the conductivity tensor becomes diagonal. For crystals with high symmetry, some components will be equal. For example, cubic crystals have equal diagonal elements, and the tensor will have the same properties as a scalar. The presence of a magnetic field will change the symmetry properties of the conductivity tensor. It is no longer symmetric. However, the number of independent terms does not increase. As an explicit example, we take the case with the magnetic moment along the z direction, and with at least three-fold rotation symmetry around the z axis. The form of the optical conductivity tensor then becomes:

$$\boldsymbol{\sigma} = \begin{pmatrix} \sigma_{xx} & \sigma_{xy} & 0 \\ -\sigma_{xy} & \sigma_{xx} & 0 \\ 0 & 0 & \sigma_{zz} \end{pmatrix} \tag{5.4}$$

The Kubo formula [43] provides the link between band structure calculations and the macroscopic theory outlined above. A detailed derivation is given in Ref. [44]. The Kubo formula for the conductivity at finite temperature is,

$$\sigma_{ab}(\mathbf{q},\omega) = -\frac{Ne^2}{im\omega}\delta_{ab} + \frac{1}{\hbar\omega}\int_{-\infty}^{0} dt\langle[j_a(\mathbf{q},0), j_b(-\mathbf{q},t)]\rangle_0 e^{-i\omega t}, \tag{5.5}$$

where a and b are Cartesian coordinate indices, N is the number of electrons per unit volume, and j_b(**q**,t) is a component of the electron current operator in the interaction representation. The symbol $\langle\rangle_0$ around the commutator indicates a thermodynamic average with the equilibrium distribution function. This just means that we take the sum over all states $|n\rangle$, weighted with the occupation.

Expanding the commutator, putting in the identity operator $\sum_{n'}|n'\rangle\langle n'|$ between the two current operators, transforming $j_\beta(-\mathbf{q},t)$ to Schrödinger representation, and taking the limit of direct transitions, $\mathbf{q}\rightarrow 0$ gives,

$$\sigma_{\alpha\beta}(\omega) = \frac{1}{\hbar\omega}\frac{1}{Z}\sum_{nn'} e^{-\beta\epsilon_n}\int_{-\infty}^{0} dt(\langle n|j_\alpha|n'\rangle\langle n'|j_\beta|n\rangle e^{i\omega_{n'n}t} - \langle n|j_\beta|n'\rangle\langle n'|j_\alpha|n\rangle e^{-i\omega_{n'n}t})(e^{-i\omega t}-1), \tag{5.6}$$

where $\hbar\omega_{n'n} = \epsilon_{n'} - \epsilon_n$ and $\sum_{nn'} e^{-\beta\epsilon_n}$ is the partition function ($\beta = 1/k_BT$ and ϵ_n is the energy of state $|n\rangle$). The integral over time can be calculated by introducing a positive damping factor which results in Lorentzian broadening of the states, simulating finite lifetimes. The absorbed photon therefore may have slightly higher or smaller energy than the energy difference between the states.

The states $|n\rangle$ and $|n'\rangle$ are many-body states. In the one-particle approximation, the only matrix elements contributing are those between an occupied Bloch state and one that is unoccupied. This means that the sum over many-body states can be replaced by the sum over one-particle states. Thus, $|n\rangle$ can be thought of as denoting occupied one-particle states, whereas $|n'\rangle$ refers unoccupied one-particle states.

The relation between the current and momentum operators, **j** = (e/m)**p**, and the zero temperature limit are taken into account. Furthermore, our wavefunctions are Bloch functions and thus depend not only on **r** but also on crystal momentum **k**. Therefore we have to integrate also over reciprocal space. The real, (or absorptive) part of the conductivity denoted $\sigma^{(1)}_{\alpha\beta}(\omega)$, can thus be written as,

$$\sigma^{(1)}_{ab}(\omega) = \frac{Ve^2}{8\pi^2\hbar m^2\omega}\sum_{nn'}\int d^3k\langle\mathbf{k}n|p_a|\mathbf{k}n'\rangle\langle\mathbf{k}n'|p_b|\mathbf{k}n\rangle \times f_{\mathbf{k}n}(1-f_{\mathbf{k}n'})\delta(\epsilon_{\mathbf{k}n'}-\epsilon_{\mathbf{k}n}-\hbar\omega). \tag{5.7}$$

where $\epsilon_{\mathbf{k}n}$ is the energy eigenvalue corresponding to eigenfunction $|\mathbf{k}n'\rangle$, and $V/(8\pi^2)$ is the normalization constant for the integral over reciprocal space, which is performed using the tetrahedron method. In this formula, the division between occupied and unoccupied states is taken care of through their Fermi distribution functions $f_{\mathbf{k}n}$ and $f_{\mathbf{k}n'}$.

We now have a formula for the absorptive part of the conductivity. In order to calculate reflectivity of Kerr spectra, we also need the imaginary (or dispersive) part. This part of the conductivity denoted as $\sigma^{(2)}_{ab}(\omega)$ can be calculated from the absorptive part using the Kramers-Kronig (KK) transformation since the absorptive and dispersive components of the conductivity are interdependent through the KK relations. These relations are based on the assumption that no current can respond to the electric field before the electric field has arrived, i.e., cause precedes the effect (also known as *causality theorem*).

5.2.2 Broadening

In order to compare the calculated optical spectra with experimental data, it is often necessary to perform broadening, thus simulating the physical mechanisms, which give the smearing of the experimental spectra. The most important effect is probably the finite lifetime of the excited states. Other contributions include temperature effects, indirect transitions, and experimental resolution.

The effect of finite lifetimes can be simulated by convoluting the absorptive conductivity spectrum obtained by Eq. 5.7 with a Lorentzian. The lifetimes are state dependent, since high-lying excited-energy states are found to be more unstable and to have shorter lifetimes than the lower-lying ones. Thus, in principle the width of the Lorentizian should be function of the states involved in the excitation.

Smearing due to temperature effects, indirect transitions and experimental resolution may all together be simulated by convoluting the spectrum with a Gaussian. Naturally, resolution broadening should be performed on the final spectrum, e.g., the reflectivity. In the other cases, it is always safe to perform the broadening on the absorptive spectrum. If the broadening is performed with a constant width, it can also be performed on the dispersive spectrum separately.

5.2.3 Indirect interband and intraband contributions

The expression for the conductivity in Eq. 5.7, only takes direct interband transitions into account. In addition to these transitions, there are *indirect interband and intraband transitions*. Indirect transitions result from momentum conserving interaction between the electronic excitation and lattice imperfections, notably phonons. The effect of the indirect interband transitions is only a slight broadening of the structures in the optical spectra. If the material has an indirect energy gap, the optical gap will obtain a “foot". The calculated optical dielectric tensor for the case of ferrimagnetic $\mathrm{YBaMn_2O_5}$ (Fig. 5.1)displays such a “foot" from 0 to 1 eV due to an indirect band gap.

Intraband transitions can not take place in a material with a band gap (insulator or semiconductor) since no bands are partially occupied. The opposite is true for metals where low-energy intraband transitions constitute an important part of the total response for the diagonal components of the conductivity tensor. They are usually modeled with the Drude formula (which is based on the free-electron model):

$$\sigma_{\mathrm{D}}(\omega) = \frac{\omega_{\mathrm{P}}^2}{4\pi(\gamma_{\mathrm{D}} - i\omega)} \tag{5.8}$$

where γ_{D} is the inverse relaxation time and ω_{P} is the (unscreened) plasma frequency. The plasma frequency can be calculated by integrating over the Fermi surface and can thus be predicted from band-structure calculations. In the free-electron model, the relation between the plasma frequency and the number of electrons per unit volume N is given by

$$\omega_{\mathrm{P}}^2 = \frac{4\pi N e^2}{m}, \tag{5.9}$$

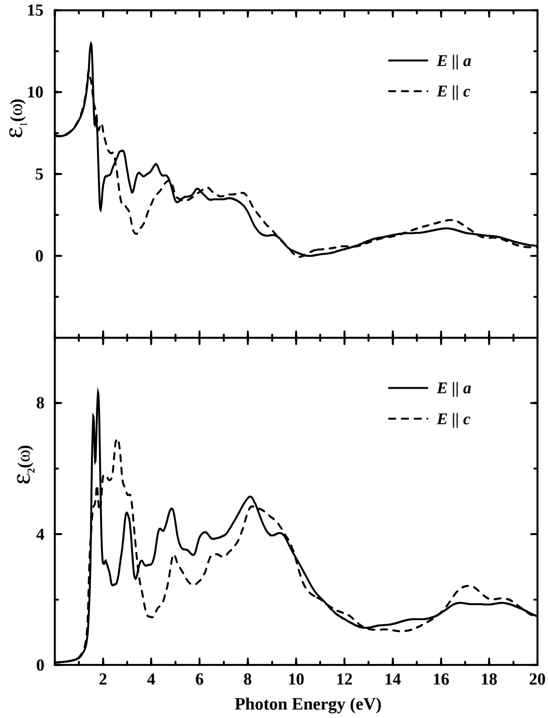

Figure 5.1: Imaginary (upper panel) and real (lower panel) part of the optical dielectric tensor for ferrimagnetic $YBaMn_2O_5$ along the crystallographic a and c directions.

which can be used as a definition of the effective number of electrons N_{eff} per unit volume. The other Drude parameter, $\gamma_{\rm D}$, may change from sample to sample of a given material, since it depends on the amount of impurities and dislocations.

5.3 Extracts of theory of optics

Experimental optical results are reported in the form of reflectivity spectra, energy loss, absorption, refractive indices, and changes in the direction of polarization upon reflection or transmittance. In order to compare calculated and measured spectra, the relations between the conductivity tensor and these quantities must be known. It is useful to start from the expression for a plane wave

$$E(\mathbf{r},t) = E_0 e^{i(\omega t + bfk\dot{r})}. \tag{5.10}$$

In the following formulae, the Cartesian coordinate subscripts and the functional dependence on ω have been suppressed.

5.3.1 Index of refraction

When a plane wave is propagating through a material, the velocity of propagation is different from that of vacuum, and the amplitude may be attenuated. These effects can be described by replacing the wave vector **k** in the plane wave by **Nk**. The function **N** is the (complex) index of refraction, written as **N** = $n + ik$, where n is called the (real) index of refraction and k the extinction coefficient. The relation between **N** and the dielectric function is simply

$$\mathbf{N}^2 = \epsilon \tag{5.11}$$

which follows from Maxwell's equations. Using the relation Eq. 5.3, **N** can be calculated from the conductivity.

5.3.2 Reflectivity

The reflectivity is the ratio between the incident and reflected light intensities. Since the intensity is proportional to the square of the wave amplitude, this can be written as

$$R = r * r \tag{5.12}$$

where r is called the reflection coefficient and is the complex ratio between the incident and the reflected electric field of the plane wave. For a normal incidence, the reflection coefficient is given by [45]

$$r = \frac{\mathbf{N} - 1}{\mathbf{N} + 1} \tag{5.13}$$

and the reflectivity becomes

$$R = \left| \frac{(\mathbf{N} - 1)}{(\mathbf{N} + 1)}^2 \right|. \tag{5.14}$$

5.3.3 Absorption coefficient

The absorption coefficient α is defined as

$$\alpha = -\frac{1}{I}\frac{dI}{dr} \tag{5.15}$$

where I is the intensity of the plane wave at a distance r inside the material. By differentiation of I expressed using the plane wave, one finds that α is proportional to the imaginary part of the refractive index times the frequency:

$$\alpha = \frac{2\omega k}{c}. \tag{5.16}$$

5.3.4 Energy loss

When a beam of mono-energetic electrons impinges on a solid, excitations in the solid, (e.g., plasmon excitations or interband transitions) result in energy losses of the electron beam. In this case, the electric field causing the response is in the direction of propagation of the beam, and not perpendicular to it, as is the case for photons. From dielectric theory one can show that the energy loss of the electron beam is proportional to the energy loss function L, which is defined as

$$L = -Im\frac{1}{\epsilon}. \tag{5.17}$$

5.4 A note on spin-orbit coupling

The spin-orbit coupling is important for heavier elements and is required in the calculation of the magneto-optical effects. The spin-orbit coupling term is written as,

$$\xi(r)\mathbf{l}\cdot\mathbf{s} \tag{5.18}$$

where ξ is the spin-orbit coupling strength

$$\xi(r) = \frac{1}{2m^2c^2}\frac{1}{r}\frac{dV}{dr}. \tag{5.19}$$

Normally, spin-orbit interaction is included in the calculational scheme by incorporating this term in the calculation of the Hamiltonian matrix elements inside the muffin-tin spheres. The operator $\mathbf{l}\cdot\mathbf{s} = l_x s_x + l_y s_y + l_z s_z$ can be rewritten using ladder operators as $s_\pm = s_x \pm i s_y$ and $l_\pm = l_x \pm i l_y$. The spin-ladder operators act on the spin components, for example $s_\pm$ will turn spin down into spin up. Similarly, the orbital-ladder operator acts on the spherical harmonics, increasing or decreasing the magnetic quantum number m by one.

Therefore, direct inclusion of spin-orbit coupling doubles the size of the matrix to be diagonalized since spin up and spin down are mixed. In the LMTO methods relatively little time is consumed for matrix diagonalization. However, in the case of LAPW method, the matrices are large and diagonalisation of them requires substantial computational efforts. Therefore, spin-orbit is usually included as a second variational step, which is workable as long as the coupling is not too large.

5.5 Calculation of Magneto-Optical Properties

Plane-polarized light, when reflected from a metal surface or transmitted through a thin film with non-zero magnetization, will become elliptically polarized, with its major axis slightly rotated with respect to the original direction. The effect due to transmission is called the MO Faraday effect, and that due to reflection is known as the MO Kerr effect (MOKE) [46, 47]. The Kerr effect exists in several different geometries. Of these, the polar Kerr effect (for which the direction of the macroscopic magnetization of the ferromagnetic material and the propagation direction of the linearly polarized incident light-beam are perpendicular to the plane of the surface) is by far the largest. Therefore the polar-Kerr geometry is the most interesting in connection with technological applications. Hence, we performed our theoretical investigations for the polar Kerr effect only. With the magnetic moment in the [001] direction of say, a hexagonal crystal, the optical conductivity tensor will take the form of Eq. 5.4.

Consider a plane-polarized light beam traveling in the z direction which is parallel to the magnetization direction **M**. This light beam can be resolved into two circularly polarized beams with the spinning direction of the corresponding electric field parallel and antiparallel to **M**. We use the sign convention in which right-circular polarized (RCP) light has its electric field vector **E** rotating in a clockwise sense at a given point in space. The signs of Faraday rotation θ_{F} and Kerr rotation θ_{K} are positive for a clockwise rotation of the axes of the polarization ellipse, as viewed by an observer who looks in +z direction when the incoming linearly polarized light from a source is traveling along the +z direction. For the polar geometry, the Kerr rotation and ellipticity are related to the optical conductivity through the following relation,

$$\frac{1+\tan(\eta_K)}{1-\tan(\eta_K)}e^{2i\theta_K} = \frac{(1+n_+)(1-n_-)}{(1-n_+)(1+n_-)}, \tag{5.20}$$

where $n_\pm^2$ are eigenvalues of the dielectric tensor corresponding to Eq. 5.4. In terms of conductivities, they are

$$n_\pm^2 = 1 + \frac{4\pi i}{\omega}(\sigma_{xx} \pm i\sigma_{xy}). \tag{5.21}$$

For small Kerr angles, Eq. 5.20 can be simplified [48] to

$$\theta_K + i\eta_K = \frac{-\sigma_{xy}}{\sigma_{xx}\sqrt{1+\frac{4\pi i}{\omega}\sigma_{xx}}}. \tag{5.22}$$

The magnetic circular birefringence, also called the Faraday rotation θ_{F}, describes the rotation of the polarized plane of linearly polarized light on transmission through matter magnetized in the direction of the light propagation. Similarly, the Faraday ellipticity η_F, which is also known as the magnetic circular dichroism, is proportional to the difference of the absorption for right- and left-handed circularly polarized light [47]. Thus, these quantities are simply given [49] by:

$$\theta_{\mathrm{F}} + i\eta_{\mathrm{F}} = \frac{\omega d}{2c}\left(n_+ - n_-\right), \tag{5.23}$$

where c is the velocity of light in vacuum, and d is the thickness of the film material under investigation.

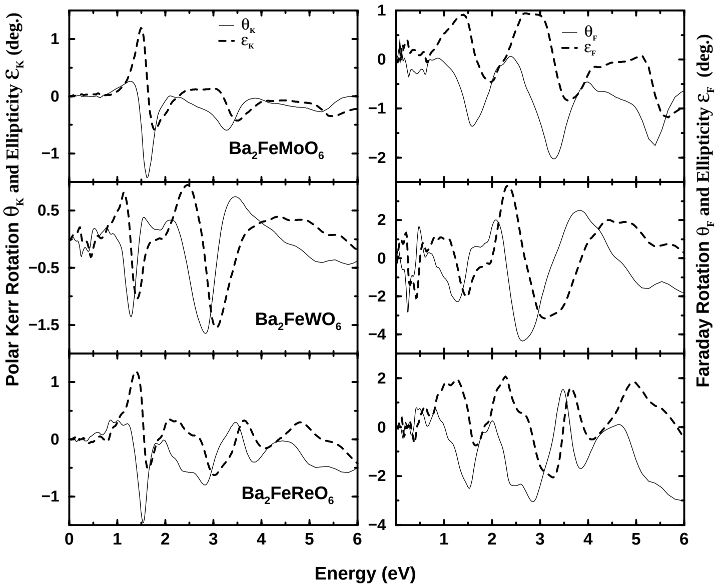

Figure 5.2: The calculated polar Kerr rotation (θ_K), Kerr ellipticity (ϵ_K), Faraday rotation (θ_F), and Faraday ellipticity (ϵ_F) spectra for Ba$_2$FeBO$_6$ with B = Mo, W, and Re.

We have performed extensive calculations on magneto-optical properties for A_2FeBO$_6$ (A = Ca, Sr, Ba; B = Mo, W, and Re) and found that most of the compounds in that series have very high Kerr and Faraday rotations at 0 K. Readers can observe the large magneto-optical effects (of the order of $\sim$1.5° Kerr and 2−4° Faraday rotation) for Ba$_2$FeBO$_6$ (B = Mo, W, and Re) as exemplified in Fig. 5.3. It is worthwhile to recall here that Kerr rotation value of $\sim$2.5° has been observed for one of the Heusler alloys, PtMnSb [50]. However, we believe that our finding of large magneto-optical values may be the highest for any oxide material. As these compounds have magnetic transition temperature (T_C) around 400 K and also half-metallic electronic structure, we anticipate that they may have important technological applications (Publication IVX).

5.5.1 Magneto-optical figure-of-merit

In order to extract the written information in a MO medium easily, and to make the signal-to-noise ratio as high as possible, the MO figure of merit (FOM) [51] should be large. FOM is defined [52] as,

$$FOM \approx \sqrt{R(\theta_K^2 + \epsilon_K^2)}, \tag{5.24}$$

where R is reflectivity and θ_K and ϵ_K are as defined earlier. FOM is often used to characterize and evaluate the performance of a MO medium fabricated by different manufacturers. However, FOM depends on the structure on to which the magnetic material is embedded, a

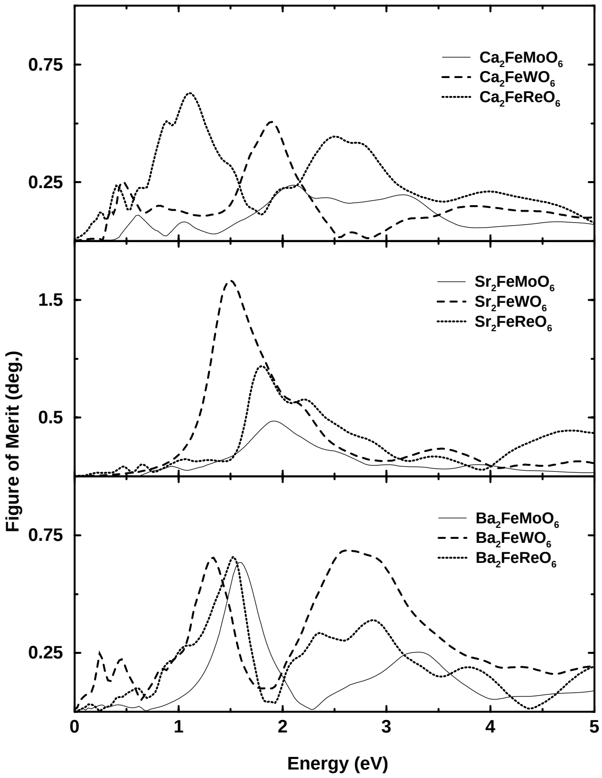

Figure 5.3: Magneto-optical figure-of-merit for A_2FeBO$_6$ with B = Mo, W, and Re.

large FOM value is one of the many indications for applicability of MO materials. The FOM values calculated for the double perovskites A_2FeBO$_6$ (A = Ca, Sr, Ba; B = Mo, Re, and W) compounds are comparable with that for the well-known MO material PtMnSb, and we believe that these large FOM values can motivate more experimental MO studies on these compounds.

5.6 Calculation of XANES

We have computed x-ray absorption spectra in this project for systems like YBaMn$_2$O$_5$ and CaRuO$_3$, within the dipole approximation from the FPLAPW (Wien2K) partial DOS along the lines described by Neckel *et al.* [53] The intensity $I(\omega) = E - E_c$ arising from transitions from initial VB states (energy E and and angular momentum ℓ) to a final core state (E_c,ℓ') is given by:

$$\frac{I_{\tau n'l'}(\omega)}{\omega^3} = \sum_{\ell} W_{\ell\ell'} M_{\tau}^2(\ell, n'\ell', E) D_{\ell}^{\tau}(E) \delta(E - E_{n'\ell'}^{core} - \hbar\omega) \tag{5.25}$$

where the matrix elements are given by

$$M_\tau^2(\ell, n'\ell', E) = \frac{\left[\int_0^{R_\tau} P_\ell^\tau(r,E) r P_{n'\ell^{prime}}(r) dr\right]^2}{\int_0^{R_\tau} P_{\ell^\tau}(r,E)^2 dr}$$

n' and ℓ' represent principal and angular momentum quantum numbers for the core states, $D_\ell^\tau(E)$ is the partial DOS of atom τ with angular momentum ℓ; P_ℓ^τ and R_τ being the radial wave function and atomic sphere radius of atom τ. The transition coefficient $W_{\ell\ell'}$ can be calculated analytically according to the equation,

$$W_{\ell\ell'} = \frac{\ell+1}{2\ell+1}\delta_{\ell,\ell'-1} + \frac{\ell}{2\ell-1}\delta_{\ell,\ell'+1}$$

For absorption spectra $D_\ell^\tau(E > E_F) = 0$. To account for instrumental resolution and lifetime broadening of core and valence states we have broadened the calculated spectra using a Lorentzian function with FWHM of 1 eV.

CHAPTER 6

Magnetism and Spin Ordering

> *Imagination is more important than knowledge.*
> *Albert Einstein*

6.1 Magnetic classes

Inorganic solids that exhibit magnetic effects are characterized by having unpaired electrons. It has long been known that such materials acquire a magnetic moment M when exposed to a magnetic field H. The amount of induced magnetization of the material in an applied field is given by,

$$M = \chi H \tag{6.1}$$

(in general, $\mathbf{M} = \chi\mathbf{H}$) where χ is termed magnetic susceptibility. For a large special class of materials the induced magnetic moment is oppositely aligned to the applied magnetic field viz. $\chi < 0$. This behavior is called **diamagnetism** which is omnipresent in every material including the magnetic materials which are discussed below. Compared with the other forms of magnetism the effect of diamagnetism is small.

The most important magnetic materials have non-zero atomic magnetic moments, i.e., each atom carries a magnetic moment. In large classes of materials these moments will be uncorrelated (under certain conditions: notably in the absence of an external magnetic field), and point randomly in arbitrary directions resulting in a zero net moment (Fig. 6.1a).

$$\mathbf{M} = \sum \mathbf{M}_i = 0 \;\; (random;\; P\; state) \tag{6.2}$$

where $\mathbf{M}_i$ is the magnetic moment of atom i. When a magnetic field of a certain magnitude is applied, these atomic moments will be aligned by the applied field. The total moment behaves according to the above equation with $\chi > 0$ (in general with M and H as vectors and χ as a tensor) and the magnetic susceptibility χ becomes a temperature function. Such

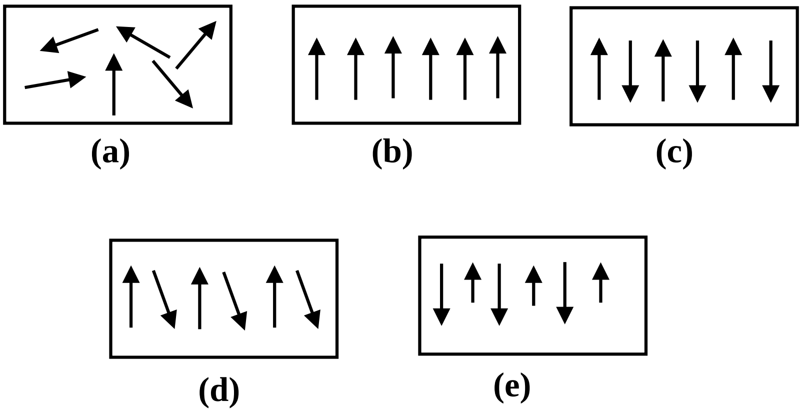

Figure 6.1: Schematic illustration of possible simple arrangements of atomic magnetic moments in (a) paramagnetic, (b) ferromagnetic, (c) collinear antiferromagnetic, (d) canted antiferromagnetic, and (e) ferrimagnetic order. More exotic forms of co-operative magnetism like helimagnetism etc. are not included since such arrangements are not found among the phases included in this study.

materials are called **paramagnetic** materials. While the applied field favors alignment of local moments in its direction, the thermal disordering effect opposes the alignment.

Another class of materials, known as **ferromagnetic** materials, do not need an external magnetic field to get magnetized, they exhibit spontaneous magnetization [Fig. 6.1(b)].

$$\mathbf{M} = \sum_{i}^{N} \mathbf{M}_i = N \cdot \mathbf{M}_i \ \ (F\ state) \tag{6.3}$$

Among the pure elements Fe, Co, Ni, and some rare-earths provide examples of ferromagnetic materials. At sufficiently high temperatures ferromagnetic materials transform into a paramagnetic state and in the absence of a magnetic field their atomic magnetic moments point in arbitrary directions, cancelling each other and resulting in zero net magnetization. At the temperatures concerned the thermal fluctuations of the moments are so high that the aligning tendency of the atomic moments is surmounted. When the temperature is reduced, the interaction between oriented atomic moments start to compete with the thermal disorder effects. When the temperature is further reduced to a value known as Curie temperature T_{C}, a transition to the ferromagnetic state occurs. Below T_{C} the interaction between non-zero atomic moments overcomes the thermal fluctuations, resulting in a net spontaneous magnetic moment even without the application of an external field. The magnetic susceptibility in the paramagnetic state is given by,

$$\chi = \frac{C}{T - \Theta}, for\ \ T > \Theta \approx T_{\mathrm{C}} \tag{6.4}$$

where C is named as the Curie constant and Θ the Weiss constant. The above equation is named as the Curie-Weiss law.

Simple **antiferromagnetic** systems comprise oppositely aligned atomic magnetic moments, the vectorial sum of which becoming zero by symmetry, below an ordering temperature known as the Néel temperature (T_{N}).

$$\mathbf{M} = \sum_{i}^{N} \mathbf{M}_i = 0 \;\; (cancelling;\;\; AF\ state) \tag{6.5}$$

Above T_{N} the paramagnetism rules and the temperature variation of the magnetic susceptibility is also in this case described by equation (2). The Weiss constant is related to T_{N} by $T_{\mathrm{N}} \approx -\Theta$.

A considerable amount of efforts has been made over the years to understand the origin of magnetism using both classical physics and quantum mechanics. It was eventually Dirac's relativistic quantum theory that explained the spin quantum state of electrons. The spin magnetic moment can be regarded as an extra degree of freedom for the electron – it can be either in a "spin up" or in a "spin down" configuration. The concept of spin falls out naturally from the solutions of the eigenvalue problem and is intimately connected with relativity. Electrons are treated as waves in quantum mechanics and the overlap of such waves is reflected as an interaction between the spins of different electrons. If this so-called "exchange interaction" is strong enough, the material will experience co-operative ordering of the spin moments. A common way to handle such exchange interaction is to use the so-called "mean field approximation" In this approach one spin is considered to be influenced by the exchange interaction from the mean field from all other spins. After manipulation, this initially fixed spin is released and treated so that it becomes on equal footing with the other spins.

It should also be noted that the atomic moments comprise contributions from both the spin magnetic moment and the orbital magnetic moment. The latter moment originates from the orbiting of an electron (a charged species) around the positive nucleus (a source of the electric field). The ground state of a free atom or ion (like rare-earth $4f$ ions) with a perfect spherical symmetry has an orbital magnetic moment in accordance with Hund's second rule. For a $3d$-transition-metal atom the electric field from neighboring atoms (the crystal field effect) normally breaks the spherical symmetry conditions and the orbital moment becomes "quenched" and such an atom is said to obey the "spin-only" approximation. When the spin-orbit interaction energy is introduced as an additional perturbation on the system, the spin may, under certain conditions drag some orbital moment along with it [54]. If the sign of the interaction favors parallel orientation of the spin and orbital moments, then the total moment will become larger than the spin-only value. Thus the spin-orbit coupling removes parts of the quenching of the moments at the spin value and results in turn in a directional preference of the spin moment.

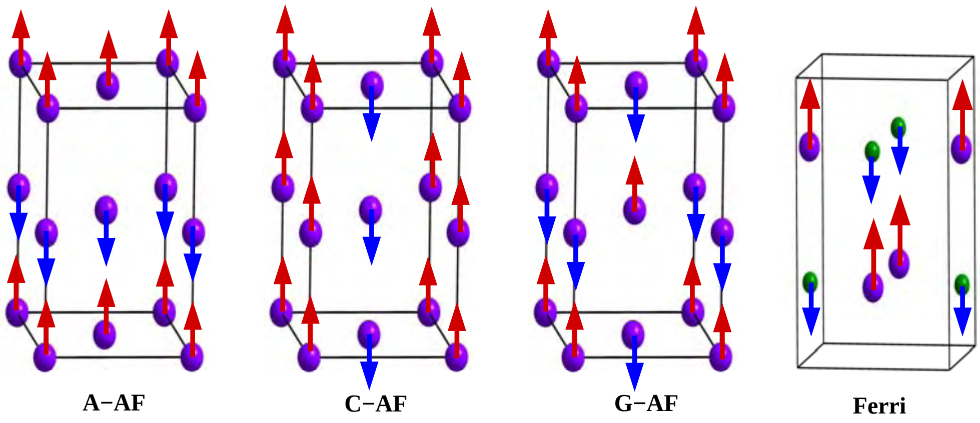

Figure 6.2: Schematic diagram indicating possible different types of antiferromagnetic spin ordering in perovskite-like oxides.

6.2 Types of antiferromagnetic spin ordering

Since one of the aims of the present thesis has been to study transition-metal oxides, performing calculations in the respective co-operative magnetic states has been mandatory. Therefore, we have conducted theoretical simulations for paramagnetic (P), ferromagnetic (F), and antiferromagnetic (AF) configurations of a given system. Sometimes, in addition to the experimentally found or suggested magnetic states, we also considered other possible magnetic orderings in order to obtain a broader platform for judgement of the magnetic arrangement.

In perovskite-like oxides, the AF spin ordering can take different configurations according to the inter- and intraplane spin-couplings as described below.

A-type AF:
This configuration occurs when the interplane coupling is antiferromagnetic and the intraplane coupling within (001) is ferromagnetic, [Fig. 6.2(a)]. (For example, undoped $LaMnO_3$ with orthorhombic structure has an A-AF arrangement).

C-type AF:
This configuration is opposite to A-type ordering, i.e., the interplane coupling is ferromagnetic and intraplane coupling is antiferromagnetic, forming a chain-like ordering [Fig. 6.2(b)]. (The orthorhombic $LaCrO_3$ has and C-AF structure as its ground-state magnetic structure.)

G-type AF:
In this case, both inter- and intraplane couplings are AF [Fig. 6.2(c)]. [This kind of ordering is commonly seen in RBaMn$_2$O$_5$ (R = Y and La; Publications I to V)].

The orthorhombic perovskite-oxide $SrRuO_3$ is found to be a ferromagnetic metal whereas the magnetic ground-state of $CaRuO_3$ is shrouded under controversy. In order to find out the exact magnetic ground-state structure for $CaRuO_3$, and to understand the reason for its distinction from $SrRuO_3$, we have considered all the above magnetic orderings for a series of $Sr_{1-x}Ca_xRuO_3$ (x = 0, 1/4, 1/2, 3/4, and 1). We arrived at a conclusion that $CaRuO_3$ has a spin-glass-like behavior. The results are dealt with in Publications (XII and XIII). We have seen that based on these orderings, the electronic structure also undergoes noticeable changes.

CE-type AF:
In this case the magnetic cell is a quadrupled chemical unit cell with zig-zag arranged F chains of magnetic atoms that are AF coupled with nearest neighboring chains. In optimally doped perovskites (e.g., $La_{1-x}Sr_xMnO_3$, x = 1/2), the most common magnetic order is the CE-type AF order. However, as this type of ordering is computationally very demanding (really too complex to handle), we have not considered it in our calculations.

Canted antiferromagnetic structure and non-collinear magnetic arrangements were not included in our calculations.

Ferrimagnetic:
In *ferrimagnetic* (Ferri) ordering [Fig. 6.2(d)], the situation is basically the same as in a corresponding AF arrangement, but the atoms bearing opposite magnetic moments occur in different quantities and/or their magnetic moments differ in size. As a consequence, the moments do not compensate to give a resulting zero total moment for an individual crystallite. The overall behavior of Ferri materials in a magnetic field is like that of F materials [55]. In the present thesis, one finds several examples of Ferri systems. In $YBaMn_2O_5$ (Publication I), the Ferri state results from differently-sized non-cancelling moments on two crystallographically different Mn sites (formally Mn^{3+} and Mn^{4+}). In Sr_2FeMoO_6 (Publication XIV), the oppositely arranged magnetic moments of Fe and Mo are of different size, again leading to Ferri state. In the case of one-dimensional $Ca_3Co_2O_6$, a triangular network of Co-O chains are formed. The moments of Co are F aligned along the chains. For every two F-aligned chains there is one AF-aligned chain resulting in a Ferri state.

6.3 Exchange interaction

If the magnetic species in a solid do not communicate with each other, Eq.(1) simplifies to Curies Law in which $\Theta = 0\,K$ and co-operative magnetic ordering is prohibited. Magnetic exchange interaction in oxides does normally not involve communication via conduction electrons. In most oxide cases the direct exchange interaction between the moment-carrying transition-metal atoms is out of the question owing to the long metal-to-metal separations in the crystal structure. The only example of a phase with probable direct exchange interaction in this thesis is provided by $Ca_3Co_2O_6$ (Publications X and XI). For the magnetic exchange

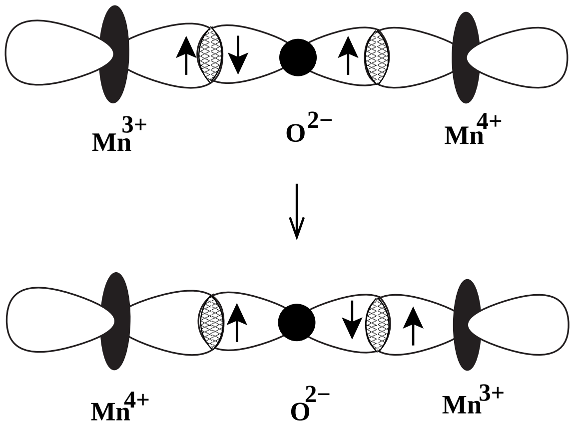

Figure 6.3: Schematic illustration of double-exchange interaction between Mn^{4+} and Mn^{3+} via an intermediate O^{2-}.

information path in oxides one is accordingly left with indirect exchange interactions either of the double- or super-exchange types.

6.3.1 Double-exchange interaction

In order to rationalize the spin-ordering phenomena and associated changes in electrical conductivity in transition-metal oxides, the concept of double-, and super-exchange interactions has been invoked. The most important interaction in magnetic materials is the double-exchange interaction [56, 57]. Transition-metal atoms arranged in a periodic array in a crystal lattice may be subjected to exchange interactions between the spins of unpaired electrons associated with the atoms concerned. For a transition-metal atom contained in a perovskite-type structure surrounded by six O atoms, the wave functions (orbitals) pointing toward the oxygen ions (d_{z^2} and $d_{x^2-y^2}$, denoted as e_g) have higher energy than those pointing between them (d_{xy}, d_{yz}, and d_{zx}, named t_{2g} orbitals) [58]. When electrons occupy these orbitals, the ground state is determined by the semiempirical Hund's rule.

The spins of the e_g electrons of a transition-metal atom are forced to be parallel to the localized t_{2g} spins (by the usually strong) Hund's coupling J_{H}. When an e_g electron hops between atoms, its spin wave function is coupled to the spin direction of the t_{2g} spins at the atom concerned. Therefore, the effective transfer integral (t_{ij}) is considered to be proportional to $\cos(\Theta_{ij}/2)$, (where Θ_{ij} is the angle between the two spin directions). The transfer integral depends on the relative direction of the two spins: it takes a maximum value for parallel spins and zero value for antiparallel spins. Therefore, the kinetic energy gain of the electrons is maximized for parallel spin, which leads to the F interaction between the spins and efficient transfer of electrons between the atoms. This mechanism is called *double-exchange interaction*. For example, for a system containing Mn^{3+} and Mn^{4+} intervened by

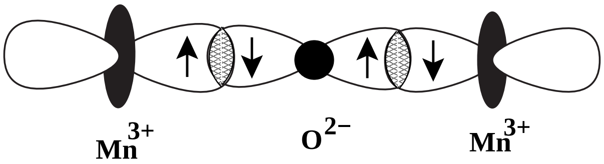

Figure 6.4: Schematic illustration of super-exchange interaction between two Mn^{3+} via O^{2+}.

an O^{2-}, there is simultaneous transfer of one electron between Mn^{3+} and the neighboring O^{2-} and from thereon to Mn^{4+}. The limiting configurations Mn^{3+}-O^{2-}-Mn^{4+} and Mn^{4+}-O^{2-}-Mn^{3+} will be degenerate if the spins of the two d shells are parallel, and represents the lowest energy state of the system at low temperature. It should be emphasized that the F double-exchange interaction is characterized by short-range electron hopping between atoms, and this process can be terminated at any point in the lattice and accordingly preventing a three-dimensional conductivity. Double exchange always results in F configurations unlike super-exchange which involves virtual electron transfer and frequently leads to AF arrangements [59].

6.3.2 Super-exchange interaction

Super-exchange interaction is one of the processes by which coupling of magnetic moments promotes an AF state. For example, let us consider $LaMnO_3$ where Mn^{3+} carry four d electrons and O^{2-} two p electrons. The half-filled e_g orbital is oriented so as to point directly at adjacent oxygen atoms. The unpaired electron in the e_g orbital of Mn^{3+} is able to couple magnetically with electrons in the p orbitals on O^{2-}. This coupling may well involve the formation of an excited state in which the electron is transferred from the e_g orbital to the oxygen p orbital. The p orbitals of O^{2-} contain two electrons each, which are mutually coupled antiparallel. Hence, a chain coupling effect occurs which extends through the entire crystal structure (Fig. 6.4). The net effect of this is that neighboring Mn^{3+} ion in $LaMnO_3$ (along c direction), separated by intervening O^{2-}, are coupled antiparallel [60]. The essential point in the super-exchange mechanism is that the spin moments of the transition-metal atoms on opposite sides of an oxygen atom interact with each other through the p orbital of the latter. The super-exchange interaction is expected to be the strongest for a bond angle of 180^o. The difference between double- and super-exchange lies basically on the filling of intermediate oxygen p orbital, the valence-state of the transition-metal atoms involved, and the position of these atoms relative to one another.

CHAPTER 7

Charge and Orbital Ordering

> *A profound truth is a truth whose opposite is also a profound truth.*
>
> *Niels Bohr*

7.1 Mixed-valence transition-metal oxides

Transition-metal oxides have been intensively studied in recent years in order to elucidate relationships between structure, bonding, and magnetic properties motivated both by intrinsic interest in the subject itself and also owing to the extraordinary technological potential of these materials. The transition-metal oxides are traditionally regarded as compounds formed by oxygen anions with completely-filled valence shells and cations[1] of transition-metals with an incompletely-filled d shell. The situation becomes somewhat messy because the incomplete d shells do not represent universally stable configurations, and the cations tend to exist in various valence states depending on the actual constituents and external factors like temperature, pressure etc. It must be appreciated that the metal atoms are located in an environment consisting of oxygen anions and other cations, and thus subjected to the complex influence of the immediate crystal field and more long-range electrostatic forces as well as magnetic interactions. The combination of all such effects determines the degree of the localization of the outer electrons, viz. their pertinence to definite atoms. Therefore it is appropriate to distinguish between materials exhibiting a high degree of *localization* (as found in magnetic oxides where ions that possess various valences can be present simultaneously in the crystal lattice) and those with itinerant charge carriers (as in superconducting oxides [61]).

Compounds with mixed-valence (MV) transition-metal ions have been widely studied

---

[1] In this chapter, covalent interactions are neglected in a way that the presentation uses a purely ionic language.

for their interesting optical, electrical, and magnetic properties. Robin and Day have classified [62] mixed-valence compounds into three categories: (i) Class-I MV characterized by distinctly different co-ordination environments for constituents in different valence states. Such phases contain localized electrons and exhibit insulating/semiconducting behavior. (ii) Class-II MV are also characterized by different environments for the constituents in differing valence states, but the structural surroundings are sufficiently similar to allow electron transfer between some or all constituents with only a small input of energy. (iii) Class-III MV exhibits delocalization of the valence electrons so that all of the MV atoms obtain the same chemical environment and the same valence state. Of particular interest are compounds that transform from either class-III or class-II MV to class-I MV upon cooling. This type of transition, triggered by electron localization, often leads to a phenomenon known as *charge ordering*.

7.1.1 Determination of valence states

The charge ordering phenomenon which is elaborated on this thesis requires participation of mixed-valence transition-metal ions. For inorganic materials, valence or oxidation states of the constituents are commonly assigned on the basis of an ionic model, viz. electroneutrality is attained as if the compound under consideration is an ionic insulator. For example, in an ABO$_3$ perovskite oxide like LaMnO$_3$, the starting point is the assumption that O acquires a completely filled valence shell (O^{2-}), La should be La^{3+}, and Mn should then be Mn^{3+}. However, as we have seen the bonding in our materials have mixed ionic and covalent character. Hence the assignment of valence states to transition metal atoms may be non-trivial.

Over the years there has been quite a few empirical rules advanced for ascribing valence to binary, ternary etc. compounds like the Pauling rules, Hume-Rothery (8−N) rule etc. However, for compounds comprising of heavy elements, and in particular transition-metals, the participation of electrons in magnetism makes the situation complicated. The valence of any element is determined by the involvement of the outer-most (valence) shell electrons in bonding and magnetism. In order to determine the most stable spin and valence configurations, the semi-empirical Hund rules are used:

(i) The individual electron spins s_i combine to give the maximum value of the spin quantum number S in accordance with the Pauli principle.

(ii) The orbital vectors l_i combine to give the maximum value of L in conformity with the Pauli principle.

(iii) The resultant L and S combine to form J, the value of which is to be taken as $J = L - S$ if the shell is less than half occupied, and $J = L + S$ if the shell is more than half occupied.

The measured magnetic moments at the transition metal sites in a given structure may be viewed in relation to these rules. Even though measurement of magnetic moments and use of concepts like bond-valence sums can provide indications of the presence of mixed-valence states in a compound, such empirical facts do not allow firm conclusions about valence states.

7.1.2 Effects of crystal-field

In addition to exchange interactions, crystal-field effects play an important role in determining the splitting of the d levels, and consequently in the choice between different valence states for transition-metal constituents. In free atomic states, every $3d$ electronic state has the same energy (viz. the energy levels are degenerate). When a transition-metal atom is surrounded by, say, oxygen ligands in tetrahedral, octahedral etc. configurations, the surroundings anions give rise to a strong electric field that splits the d levels into two groups, triply degenerate t_{2g} (d_{xy}, d_{yz}, and d_{xz} with spatial distributions along $xy, yz,$ and xz) and doubly-degenerate e_g levels ($d_{x^2-y^2}$ and d_{z^2} orbitals with spatial distribution along the coordinate axes). The splitting of the d levels varies with respect to the magnitude of the surrounding crystal field as qualitatively illustrated in Fig. 7.1. Note that the population of the thus split d levels also has a deciding effect on the spin states of the atom concerned, referred to as low-spin, intermediate-spin, and high-spin states in the ionic terminology.

In our efforts to determine valence states for transition-metal constituents in the studied systems, we make use of theoretically calculated magnetic moments as well as site- and orbital-projected DOS. For example, in our calculation on $Ca_3Co_2O_6$ which has Co in octahedral and trigonal prismatic environments, we first arrived at the conclusion that the Co atoms exist in Co^{2+} and Co^{4+} states (Publication X). We are pleased to note that our findings stimulated many experimental and theoretical further studies on this compound. As more or less anticipated many of these reports rejected our proposal of a different oxidation state for the Co species and favored instead a common Co^{3+} state in low-spin and high-spin configurations. However, using various analytical tools (Publication XI) we have later found that the problem is not so simple, but most of the controversy seem to originate from use of the ionic terminology on a compound which exhibits an appreciable covalent contribution to the Co-O bonding.

7.2 Influence of structure on ordering phenomena

Within the oxide family, perovskite-type materials[2] (with general formula ABO_3) are among the most exotic, and exhibit a wide spectrum of physical properties such as superconductivity, colossal magnetoresistance, various magnetic ordering features, ferroelectricity, thermoelectric properties etc., just to name a few.

---

[2] Although many of the oxide materials dealt in this thesis work do not directly belong the perovskite family, a discussion on the structural features of perovskites are made in order to illustrate various ordering phenomena.

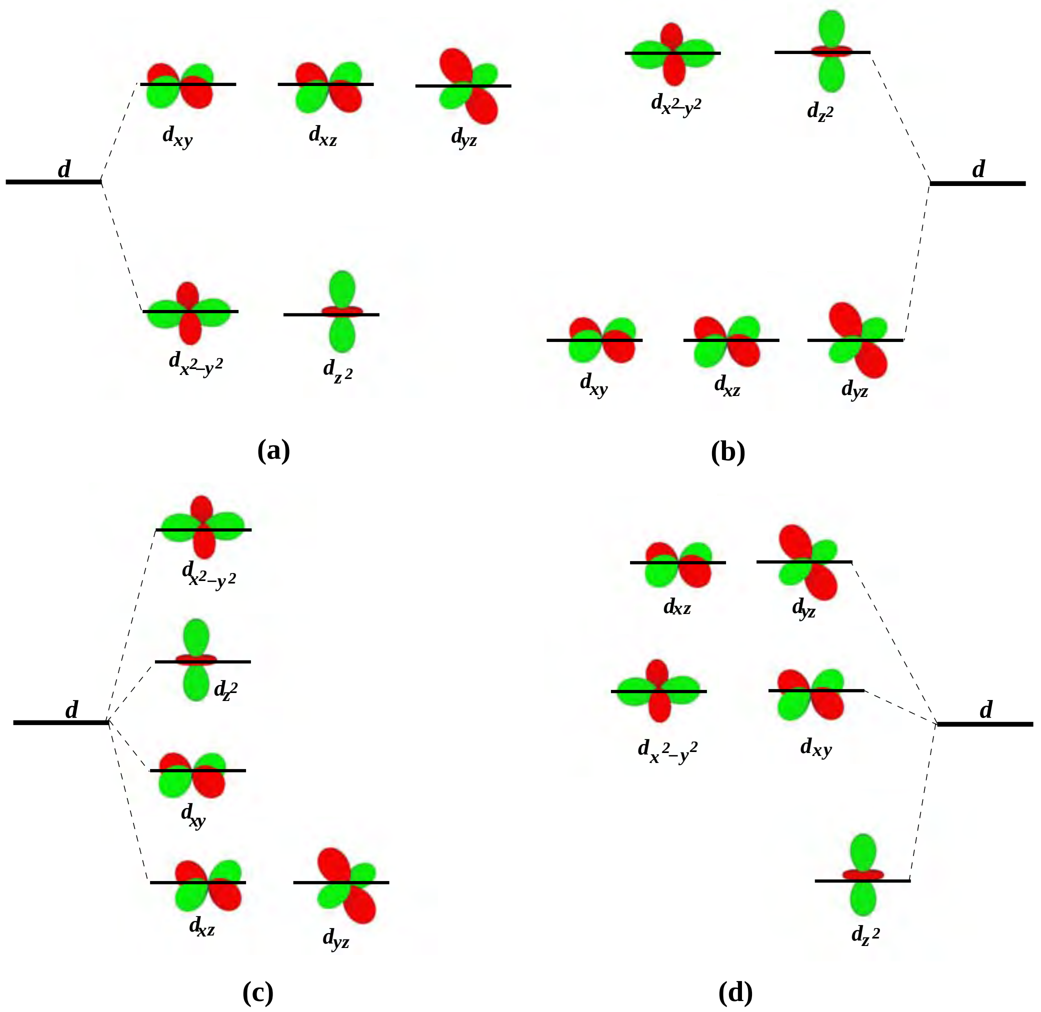

Figure 7.1: Pictorial illustration of the splitting of the d levels in (a) tetrahedral, (b) octahedral, (c) square-pyramidal, and (d) trigonal-prismatic crystal fields of idealized symmetry. No significance is to be attached to the separation between the d levels, neither within each part of the illustration nor between the different parts.

Magnetoresistance (MR) is the relative change in the electrical resistance of a material produced on the application of a magnetic field. The ratio MR [$|\Delta\rho|/\rho(0) = |\rho(H) - \rho(0)|/\rho(0)$ where $\rho(H)$ and $\rho(0)$ is the resistance at a given temperature in the presence and absence of a magnetic field (H), respectively] can be negative or positive. Large magnetoresistance, [referred to as colossal magnetoresistance (CMR)] has attracted wide attention in particular for perovskite oxides. CMR can dramatically alter the electrical resistance and related properties of a material [63] revealing some remarkable features with regard to charge and spin dynamics in addition to opening up new avenues for research. The potential industrial application has apparently accelerated the research activity, and as a result deepened our comprehension of the field.

The structure of perovskite oxides is highly compact and sensitive to the size of the cationic constituents. Consequently, efforts to go beyond the tolerance limits for the geometrical requirements, challenge the structural stability and / or cause structural distortions. The minimum Gibbs energy decisive for the stability of a phase with a certain structure is given by the relationship:

$$G = E_{\mathrm{C}} + E_{\mathrm{cf}} + E_{\mathrm{ex}} + PV - TS \tag{7.1}$$

where E_{C} is the Coulomb energy, E_{cf} the crystal-field stabilization energy, E_{ex} the exchange energy, PV the energy associated with volume change, and TS the entropy contribution. The energy content in these terms reflect the interactions between the constituents as determined by structures, valence, electronic configuration, and atomic size etc. Note that details of the structural arrangement (like the oxygen environment) may have a considerable impact on the interactions concerned. Often there is an interplay between the various contributions and this results in, among other things, preference of certain constituents for certain sites and formation of an ordered state which in general leads to the lowering of the structural symmetry.

7.2.1 Effects of Jahn-Teller distortion

One of the most-prominent structural distortion occurring in perovskite-like oxides is the co-operative Jahn-Teller distortion. The Jahn-Teller theorem [64] states that a non-linear system in an electronically degenerate state must undergo a distortion in order to remove the degeneracy, thereby lowering both the symmetry and the energy of the system. In an extended solid, where the polyhedra are linked to form a three-dimensional-bond network, the Jahn-Teller distortion that occurs at each polyhedron is felt also by the neighboring polyhedra. Consequently, the direction and size of the distortion must be co-operative throughout the crystal, an effect known as co-operative Jahn-Teller distortion (CJTD).

This diffusionless CJTD process, in fact leads to a lowering of the total symmetry of the crystal. The resulting equilibrium can be regarded as a compromise between the increase in elastic and decrease in electronic energy consequent on the distortion (since the character and extent of the distortion is strongly influenced by the structural matrix as well as the constituents). In a transition-metal oxide, where each orbital of the transition-metal constituent has different anisotropy, the displacements of the surrounding O atoms are intimately coupled to the configuration of the d orbitals. For example, when the two apical O atoms in an octahedron move toward the central atom, the d_{z^2} orbital is shifted to higher energies than the $d_{x^2-y^2}$ orbital thus lifting the degeneracy of these orbitals.

7.3 Orbital Ordering

Orbital ordering (OO) among the transition-metal oxides is concerned with the preferential occupation of electrons in specific d orbitals. The interaction of the orbital degrees of freedom among themselves and their interaction with electron spins or lattice, can give rise to long-range orbital-ordered states. Together with the charge and spin degrees of freedom they determine all the rich variety of the properties of transition-metal oxides. The orbital effects play a very important role in the physics of manganites, and also in many other transition-metal oxides. For example in an undoped rare-earth manganite, only Mn^{3+} are present at the octahedral sites and the Jahn-Teller effect determines the arrangement of the d_{z^2} orbital subsequently leading to the orbital ordering.

The orbital ordering gives rise to the anisotropy of the electron-transfer interaction. This favors or disfavors the double-exchange interaction and the super-exchange (ferromagnetic or antiferromagnetic) interaction in an orbital-direction-dependent manner and hence gives a complex spin-orbital-coupled state. According to the well known Goodenough-Kanamori-Anderson rules [65] the magnitude and even the sign of the magnetic exchange depend on the type of orbitals involved and the filling of these orbitals. If orbitals are half-filled (occupied by one electron) and directed to each other, we will have a strong AF coupling. On the other hand, if these orbitals are directed away from each other (mutually orthogonal) we would have a F interaction. The orbital degree of freedom is thought to play important roles, not only in the prominent case of CMR manganese oxides but also in the anisotropic electronic and magnetic properties of a great many transition-metal oxides. Even though a lot of attention has been paid to manganese oxides, it should be noted that the orbital physics is universal in transition-metal oxides.

7.3.1 An example$-$LaMnO$_3$

Undoped $LaMnO_3$ is well known to exhibit orbital ordering and a concomitant lattice distortion. $LaMnO_3$ in the perovskite-like structure contains the Jahn-Teller Mn^{3+} ions which are known to induce a rather strong local distortion. The e_g orbitals of the Mn^{3+} ions are ordered in such a way that at the neighboring Mn sites the d_{z^2} orbitals are ordered alternatively along the x and y directions. The transfer integral between the two neighboring Mn atoms in the crystal lattice is determined by the overlaps of the d orbitals with the p orbital of the O atom between them. The overlap between the $d_{3x^2-r^2}$ and p_z orbitals is zero because of their different orientation with respect to the xy plane. Therefore, the electron in the $d_{3x^2-r^2}$ orbital cannot hop along the z axis and the individual MnO_6 octahedra are alternatingly elongated along x and y directions. Owing to this OO, anisotropic super-exchange interaction results, viz. undoped $LaMnO_3$ has an A-type AF ordering, the spins in one xy layer exhibiting F order, and are antiparallel to the spins in the next xy layer.

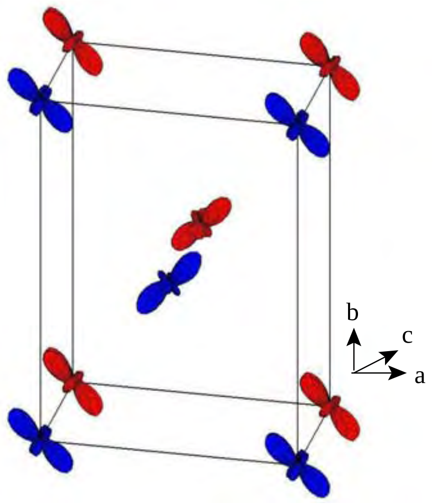

Figure 7.2: Orbital ordering in orthorhombic $\mathrm{LaMnO_3}$. In order to elucidate the antiferro-type orbital order the d_{z^2} orbitals are shown in blue and red colors. Note that the $\mathrm{MnO_6}$ octahedra are elongated along the lobes of the d_{z^2} orbital.

7.4 Charge ordering

Charge ordering (CO) is a phenomenon observed in solids wherein certain electrons defacto become localized as a result of ordering of cations of differing charges on specific lattice sites [66], thus often rendering the material insulating. CO has been known for many years in $\mathrm{Fe_3O_4}$, the transition from the CO state to the charge-disordered state in $\mathrm{Fe_3O_4}$ at 120 K (identified by Verwey [67] as early as 1939) is associated with a resistivity anomaly. In a perovskite manganite, when the trivalent cation is substituted by a divalent cation, there is variation in the amount of Mn^{3+} to Mn^{4+} ratio. When the ratio is 1:1 the OO occurs simultaneously with a long range ordering of Mn^{3+} and Mn^{4+} mediated by Coulomb interaction. Such a type of ordering can strongly modify the crystal structure and accordingly also the magnetic interactions.

Using the perovskite-like $R_{1-x}A_x\mathrm{MnO_3}$ phase as an example two correlation effects must be distinguished. First the ferromagnetic double exchange characterized by short-range electron fluctuation mediated by dynamic occupancy of the e_g orbitals. Second the structural transition driven by the orbit-lattice interaction of Mn^{3+} and controlled by the frequency of the electron hopping between Mn^{3+} and Mn^{4+} which becomes frozen in at a sufficiently low temperature. These correlation effects compete with each other and one can easily imagine that the prevailing character will depend on the geometrical arrangement of the Mn-to-O-to-Mn bonds (viz. be strongly influenced by distortion from the ideal perovskite structure). With structural deformations follow lowering of the transfer integral for the e_g electrons thus causing a weakening of the ferromagnetic interactions and a strong tendency to charge localization, viz. a preference for *charge ordering*.

The phases with the $R_{0.5}A_{0.5}\mathrm{MnO_3}$ composition is of particular interest because of the frequent observation of CO at this R:A atomic ratio. It has become clear that CO in these manganates is closely correlated with size of the A cations [68] which appears to control the Mn-O-Mn bond angle (and notably any deviation from 180°). This determines the e_g bandwidth imposed by the Mn $3d$ and O $2p$ hybridization and the hopping process . Therefore, the strength of the double-exchange mechanism is affected. For example, $\mathrm{Y_{0.5}Ca_{0.5}MnO_3}$ with the small A cation Y (ca. 1.23Å) not only has the charge-ordering transition temperature (T_{CO}) in the paramagnetic range, but also the CO is so robust that it is nearly impossible to destroy it by the application of a magnetic field [69]. On the other hand, in the regime of the larger A cations, the ferromagnetic exchange interaction increases, thereby destroying the CO state.

In the CO state of $R_{0.5}A_{0.5}\mathrm{MnO_3}$ a checkerboard arrangement of Mn^{3+} and Mn^{4+} occurs. The localized electrons of Mn^{3+} exhibit orbital degeneracy and develop an OO pattern whereas those in Mn^{4+} (t_{2g}^3) are nondegenerate. The two possible mechanisms that lead degenerate orbitals to OO is Jahn-Teller distortion and super-exchange interaction [70]. Both the CO and the OO occur simultaneously, with CO as the assumed driving force in most cases [71]. When R and A present in equal amounts, there is a strong competition between the tendency for the orbitals to order locally and the kinetic energy of the charge carriers that tends to destroy long-range order.

For the realization of the CO state, E_{C}, E_{cf}, E_{ex}, and PV (Eq. 7.1) play together simultaneously and the ordered state occurs as a consequence of the joint efforts to minimize the Gibbs energy of the crystalline phase. The different contributors to the Gibbs energy can individually distort the structure or join forces with some or all the others. In the latter case the result can not be regarded as a mere sum of the individual effects but rather as a composite effect produced by an intimate interplay between the different factors.

7.4.1 Types of charge and orbital ordering

When charges localize on specific ionic sites in perovskite-like oxides, they take up various patterns of ordering. Only the most-commonly observed ordering patterns are discussed here. In the 50% "doped" manganites, i.e., when Mn occurs in two-different valence states in equal amounts, the most-commonly seen charge ordering is of the checker-board-type where charges, for example Mn^{3+} and Mn^{4+}, order alternatively [72]. In Fig. 7.3, two different orbital ordering patterns are displayed. Fig. 7.3(a) shows **ferro-orbital order** where d_{z^2} orbital of Mn^{3+} order in phase with each other and the correspondingly empty orbital of Mn^{4+}. On the other hand in Fig. 7.3(b), d_{z^2} orbital of Mn^{3+} stack in an **antiferro**-(out-of-phase) sequence to give rock-salt arrangement.

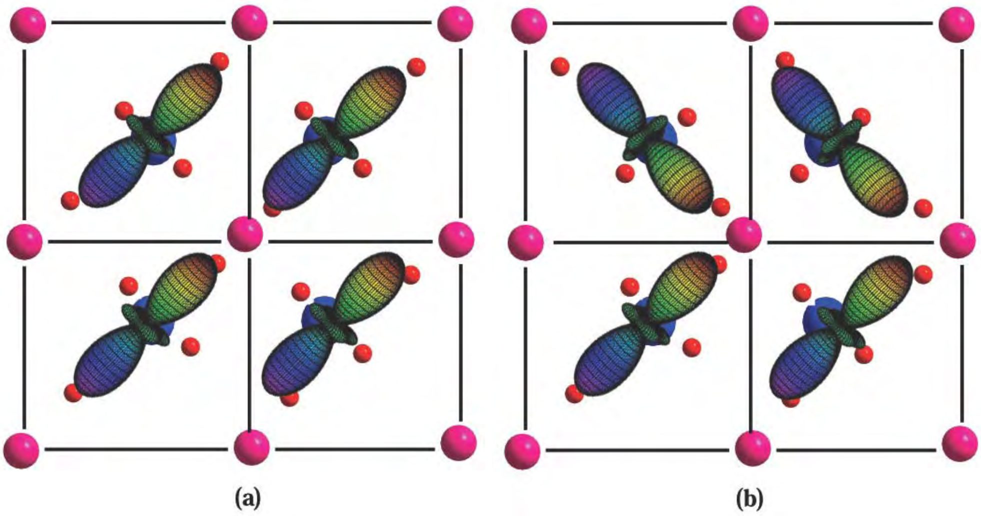

Figure 7.3: Two idealized orbital ordering patterns. (a) Ferro-orbital order and (b) antiferro-orbital order. Blue (seen behind the d_{z^2} orbital) and purple spheres represent Mn^{3+} and Mn^{4+}, respectively, in a checker-board-type charge ordered pattern.

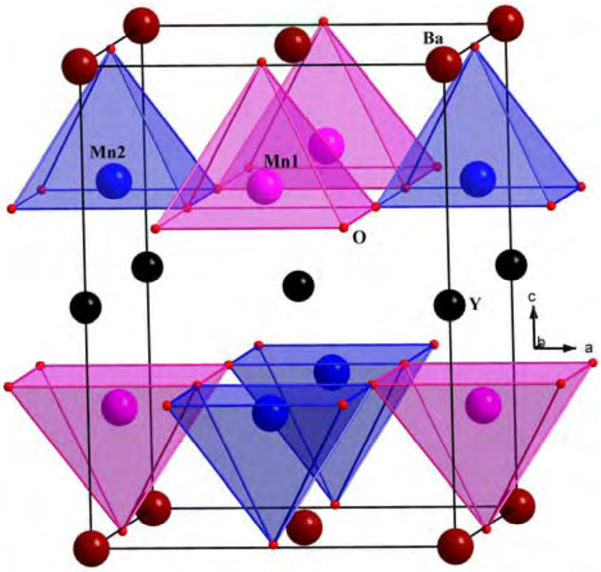

Figure 7.4: Crystal structure of $YBaMn_2O_5$ where the two different Mn atoms are shown by different-colored polyhedra. Note the oxygen vacancy in the Y layer, the occupation of which influences the electronic and transport properties of RBaMn$_2$O$_{5+\delta}$ (R = Y and rare-earths).

7.5 Charge and orbital ordering in oxygen-deficient double perovskites

Multicomponent perovskite-like oxides such as $R\text{Ba}T_2\text{O}_5$ (T = transition-metal ions) are promising candidates for versatile functional materials [73]. An ordering at the A site is typically achieved with a systematic distribution of divalent Ba and trivalent R atoms. Oxygen deficiency around the smaller R atoms is a common feature for such phases in which a square-pyramidal coordination is imposed upon the transition metal atoms as a consequence of the layered ordering of R and Ba (formally in 3+ and 2+ states). The atomic arrangement of the resulting structure (Fig. 7.4) has a characteristic appearance which has led to the name double perovskites. The base-plane oxygens of the square pyramids relax toward the R atom. It is the (still formal) R^{3+} and Ba^{2+} charge imbalance in the otherwise delicate structural arrangement which gives rise to oxygen non-stoichiometry expressed as 5+δ in the above formula. With certain rational values for δ typical ordered structure variants occur. For δ = 1/2 also an average half-integer valence state $T^{2.5+}$ is established and this can under certain conditions give rise to CO with formal valence states T^{3+} and T^{2+}.

Although a lot of experimental and theoretical attention has been paid on CO and OO in perovskite-like oxides, only a handful of studies have been made on oxygen-deficient double-perovskite oxides. Hence one of the aims of this project has been to analyze CO and OO in $\text{YBa}T_2\text{O}_5$ and $R\text{BaMn}_2\text{O}_{5+\delta}$ (T = Mn, Fe, and Co; R = Y and La; $0 \leq \delta \leq 1$).

The presence of CO and OO in a material is experimentally established by the inferences from superstructure reflections in diffraction measurements, resistivity and heat-capacity measurements, magnetic moment data, structural phase-transition (if any) etc. In our theoretical studies, we earlier made use of the calculated magnetic moments, site-projected DOS and charge-density plots within particular planes to identify the presence of transition-metal atoms in different valence states and visualize their CO features. For example, the presence of T atoms in two different valence states in $\text{YBa}T_2\text{O}_5$ with (T = Mn, Fe, and Co) is manifested as the difference in the features of their respective site-projected DOS curves (see Fig. 7.5). Similarly, the orbital-projected DOS provides evidence for the occupation of individual orbitals in the valence band. We used the d-orbital DOS to get insight into the occupancy of individual d orbitals of the T atoms (see for example Fig. 7.6 which shows the DOS of individual d orbitals for Fe in YBaFe_2O_5). With this approach we could establish the occupation of particular orbitals in the energy-range of interest. In an effort to improve the understanding on ordering phenomena, we later turned to an alternative approach based on the occupation-density matrix of d orbitals within a particular energy interval. With this new tool we are not only able to picture the filling of the orbitals, but also to establish their shape and orientation.

The occupation density in the entire valence band, and that from $-1\,\text{eV}$ to E_F enables one to visualize the CO and OO patterns directly. The occupation of the majority-, and minority-spin d levels of Mn in formally 3+ and 2+ states in YBaMn_2O_5 are shown as an example in Fig. 7.7(a, b). A clear-cut distinction between the two occupation modes is an indication for the presence of CO on the Mn atoms. Similarly, the d orbital occupancy close

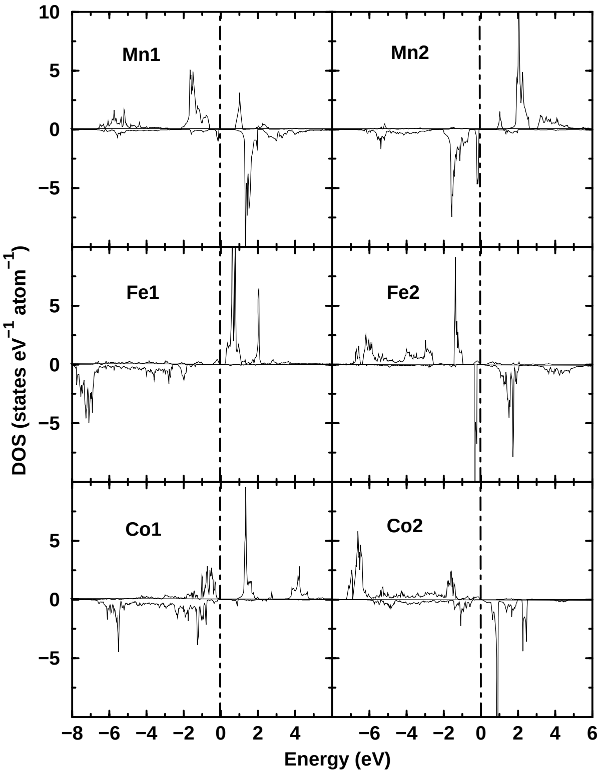

Figure 7.5: Site-projected density of states (DOS) for the T sites in YBaT_2O$_5$ (T = Mn, Fe, and Co).

to the E_F brings about that the d_{z^2} orbital on Mn^{3+} is involved whereas the d_{z^2} and $d_{x^2-y^2}$ orbitals on Mn^{2+} are seen to form a ferro-orbital-order pattern [Fig. 7.7(c)]. We have used the above-described method to visualize as well as to analyze CO and OO patterns in YBaT_2O$_5$ (as a function of d-orbital filling) and in RBaMn$_2$O$_{5+\delta}$ (as a function of the size of R and Ba as well as oxygen content). The results and the related discussions are elaborately dealt with in Publications I—V.

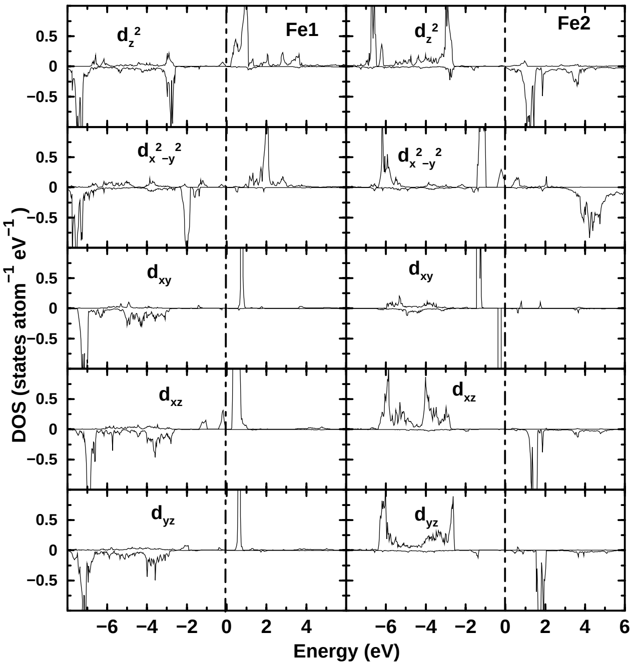

Figure 7.6: The d-orbital-projected density of states (DOS) for the Fe atoms in $YBaFe_2O_5$.

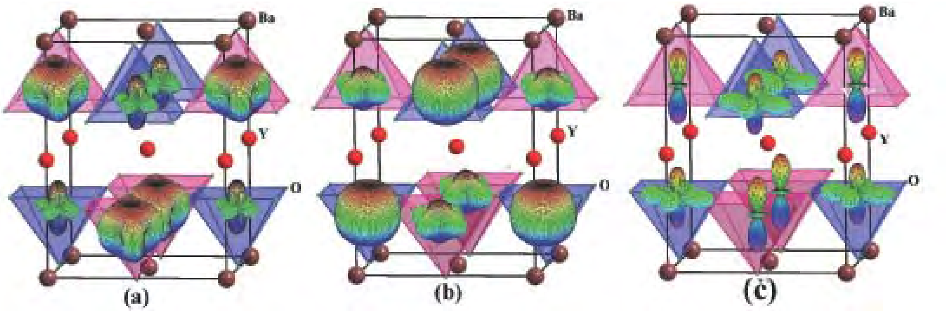

Figure 7.7: Occupation density of d orbitals of (a) majority-spin, (b) minority-spin bands, and (c) orbital ordering patterns in Mn1 and Mn2 of $YBaMn_2O_5$.

CHAPTER 8

Summing Up and Looking Ahead

> *... I seem to have been only like a boy playing on the seashore, and diverting myself now and then finding a smoother pebble or a prettier shell than ordinary, whilst the great ocean of truth lay all undiscovered before me.*
>
> *Sir Issac Newton*

As I come to the conclusive chapters of this thesis, I sit perplexed and think whether it is an end, or beginning of the end or perhaps the end of a beginning, as Sir Winston Churchil once noted. After nearly four years of research work I feel it may be the beginning of a "beginning". Among the inorganic materials, transition-metal oxides have acquired special attention owing to the vast diversity of structures and a wide spectrum of exotic properties. We have selected a narrow field, magnetic oxides in complex structures, in particular those consisting of transition-metal atoms in two different valence states. In our attempts to understand such materials, we have perhaps dealt with certain problems for too long or other fascinating problems may have come in between as interludes. Hence our work on the transition-metal oxides have spawned many ideas, some of which have evolved into separate research projects themselves. In fact, some of these are in still in progress while this concluding chapter is being written.

In this project we have considered materials such as regular- and distorted-perovskite oxides, regular- and oxygen-deficient double-perovskite oxides, complex one-dimensional oxides, and layered oxides. Even though each of these groups of compounds exhibit greatly differing properties, the common denominator for their selection has been the presence of mixed-valence transition-metal constituents.

We have used a number of highly accurate, state-of-the-art tools such as TB-LMTO, VASP, FP-LMTO, FP-LAPW (WIEN2k), and CRYSTAL03, all based on the density-functional theory. The choice of a particular tool has been made depending on the specific problem at hand. During the project period 15 articles have been written among which 8 have been already published in well reputed international journals, 2 accepted for publication and the remaining contributions are either submitted or included in the thesis in manuscript form. [In addition, I contributed as a co-author in 10 other articles on hydrides, superconducting MgB_2, and multiferroic $BiFeO_3$ (a list of which is given in appendix)].

A major theme of the project has been to understand the intrinsic properties of mixed-valence materials. Hence we have focussed on their ground-state magnetic and electronic properties, bonding behavior, and charge-, and orbital-ordering phenomena. In quite a few cases we have also paid attention on excited-state properties. The main findings of this Dr. Scient. project investigations are listed below.

8.1 Scientific highlights

⋆ Since the discovery of colossal magneto-resistance extensive works have been performed on manganese oxides. Most of the experimental and theoretical efforts have been devoted to A-site substituted perovskite oxides. Therefore we attempted to study the simultaneous presence of spin, charge, and orbital orderings using the oxygen-deficient double perovskite $YBaMn_2O_5$ as an example. The G-type ferrimagnetic insulating state is found to be the ground state in accordance with experimental findings by using both the full potential LMTO method as well as the full potential LAPW methods. The existence of the two different types of Mn atoms is visualized by differences in site- and orbital-projected DOS curves. The occurrence of checker-board-type charge ordering and ferro-type orbital ordering is established from the charge-density plots. The relatively small size of the Y atoms makes the base-plane Mn-O-Mn bond angle deviate appreciably from 180°, which in turn imposes a reduction in the e_g band width. The charge- and orbital-ordering features are believed to result from this perturbation of the e_g orbitals. We have also calculated the excited-state properties of this material and found that large anisotropy in the optical spectra originates from ferrimagnetic ordering and crystal field splitting. In order to further emphasize the different valence states of Mn, we have calculated K-edge XANE spectra. For Mn as well as O the existence of two types of valence-induced atomic species is established with the help of K-edge spectra (**Publication I**).

⋆ Over the years it has been established that hybridization interaction between Mn-d and O-p orbitals have a deciding effect on the electron localization and hence on charge and orbital orderings. Although a lot of attention has been paid to vary the d-electron count by the use of various substituents in perovskite-like solid solution systems, relatively less attention has been paid to variation in the oxygen content. Hence we have carried out model calculations on $LaBaMn_2O_{5+\delta}$ (δ = 0, 1/2, 1) and analyzed their ground-state properties in terms of the oxygen content (**Publication II**). We found that changes in the oxygen content control the valence state of Mn and the hybridization interaction between Mn and O, and consequently varies the double-exchange interactions at the expense of the competing super-exchange interactions. Therefore the electronic ground-state varies from insulator to metal on going from $LaBaMn_2O_5$ to $LaBaMn_2O_6$, with a reduced band-gap for the intermediate $LaBaMn_2O_{5.5}$ phase. In line with this drastic changes in the charge and orbital ordering phenomena have been detected.

⋆ In an effort to understand the effect of oxygen content as well as the size of R on the charge and orbital ordering, we extended the model calculations to $R$$BaMn_2O_{5+\delta}$ with R = Y and La (**Publication V**). There is a somewhat systematic variation in the electronic and magnetic properties with respect to oxygen content in these phases. However the finer features of the ordering schemes such as occupancy of particular orbitals and magnitude of the ordered charges depend largely on the size of R atoms and hence on intricate details of the atomic arrangement.

⋆ We have also analyzed the changes in ordering features in terms of d-orbital filling by for example, substituting Mn with Fe or Co in $YBaMn_2O_5$ (**Publication IV**). We found that the orbital ordering pattern does not change merely with the amount of d electrons available for ordering, but the orbital ordering is more intimately connected with the changes in the structure upon substitution. In short, it is the structural features which determines the ordering of charges and orbitals.

⋆ We have calculated the electronic and magnetic properties for the quasi-one-dimensional compound $Ca_3Co_2O_6$ for the first time (**Publication X**). The calculated ferrimagnetic ground state and Co magnetic moments were in good agreement with experimental findings. This compound is interesting since its electronic and magnetic properties appears to be tunable by application of external magnetic fields as well as by electron doping, (substituting Y for Ca). For a particular composition, $Ca_2YCo_2O_6$ we predicted a seldom observed combination of material properties viz. co-existence of ferromagnetism and insulating behaviors.

⋆ In an initial theoretical study on $Ca_3Co_2O_6$ we concluded with two different valence states for Co which we suggested to correspond to low-spin Co^{4+} and to high-spin Co^{2+} in **Publication X**. Our work clearly stimulated a lot of subsequent studies, all claiming that the assignment of different valence states for Co in this compound is inappropriate. Hence we have revisited the problem by the use different tools to analyze the valence situation of Co (**Publication XI**). Our detailed analyses show that neither our critics nor our earlier report brought out the real truth. Our fresh study concluded that the valence of the Co atoms are much smaller than the often believed 3+ state and the valence characteristics are highly directional dependent, in fact about three times more pronounced along the chains than perpendicular to the chains.

⋆ In the oxygen-deficient perovskite-like oxide $Sr_4Fe_4O_{11}$, the Fe atoms take two different co-ordinations as square pyramids and octahedra. Experimental studies on this compound were able to bring out a magnetic structure with finite magnetic moment at one of the Fe sites and almost zero moment at the other Fe site. In order to better understand this material, we have carried detailed calculations (**Publication XV**) in which we paid particular attention to the design of magnetic structure based on the calculated exchange interaction (J_{ij}) parameter values. Even though we have carried out the calculations using various tools (TBLMTO, FPLMTO, FPLAPW and VASP) all have converged to a solution where both Fe atoms have finite magnetic moments, but with a distinct difference in their values. A deeper analysis shows that, local spin frustration in one of the sites may be the reason for the observation of zero moment by neutron diffraction measurements. Among the several possibilities proposed experimentally, our theoretical results can fit to the model with Fe in square-pyramidal and octahedral environments are in formal oxidation states of 3+ and 4+, respectively.

$\star$ Although spin and orbital dynamics are not unique for manganites, they have received a lot of attention in recent years. In an effort to extend the studies to other mixed-valence transition-metal oxides, we examined for example, systems containing chromates. We have explored structures for a series of compounds ACr$_3$O$_8$ (A = H, Li$-$Cs, In, Tl, Cu, Ag, and Au) which in fact turned out to be one of the most challenging tasks of the entire project. We have predicted ground-state crystal structures for most of these compounds which agree with those established experimentally (**Publication VI $-$IX**) where-ever empirical data are available. The calculated equilibrium volumes were found to be over-estimated beyond the limit usually expected for DFT calculations. The overestimation of volume may be attributed to the layered nature of these compounds. Special attention is focussed on the valence state of Cr in these compounds which are believed to possess 3+ and 6+ valence states. However the detailed analysis of their electronic structure shows that Cr^{6+} (d^0) configuration is out of question since none of the Cr have empty d orbitals. Instead the negligible magnetic moment at the Cr site concerned (viz. the Cr atom which has led to assignment Cr^{6+}) originates from a negligible exchange splitting.

$\star$ In addition we made a particular study of Cr$_3$O$_8$ and LiCr$_3$O$_8$ which have received attention as potential candidates for cathode materials in Li-ion batteries (**Publication VII**). From the calculated total energy, a new synthesis route is suggested for Cr$_3$O$_8$. The bonding analysis shows that when Li is intercalated into the Cr$_3$O$_8$ lattice, Li retains some valence charge and does not donate its valence electron entirely to the Cr$_3$O$_8$ framework as usually believed.

$\star$ An orthorhombic perovskite-like oxide SrRuO$_3$ has a well defined ferromagnetic and metallic ground state. However, for its isostructural counterpart CaRuO$_3$ there are many controversial reports each claiming a different description of the magnetic state. In an attempt to explore the correct magnetic ground state of CaRuO$_3$, we have simulated the magnetic phase diagram for the entire Sr$_{1-x}$Ca$_x$RuO$_3$ (**Publications XII and XIII**). In addition to para, and ferromagnetic states we considered A-, C-, and G-type antiferromagnetic configurations. Around the composition x = 0.77 we found a transition from ferromagnetic-to-antiferromagnetic state. We also found that CaRuO$_3$ has a G-type antiferromagnetic ground state. However, owing to the very small energy differences between various magnetic configurations, it might have local spin frustration leading to a spin-glass-like behavior. In order to bring out a clearer picture of $CaRuO_3$, we also carried out an elaborate study on the electronic structure and excited-state properties of this compound. The calculated optical, XPS and Ru-K-edge XANE spectra showed good agreement with available experimental spectra, adding credence to our conclusion on its magnetic ground state.

⋆ We predicted huge magneto-optical effects for a series of double perovskites $A_2BB'O_6$ (A = Ca, Sr, and Ba; B = Fe; B' = Mo, W, and Re). Among these compounds, Sr_2FeWO_6 has the maximum polar Kerr rotation of 3.87° and Faraday rotation of 4.5×10^5 deg cm^{-1}. All the other compounds of this series have both Kerr and Faraday rotation more than 1° except Ca_2FeMoO_6 which has a Kerr rotation of 0.5°. It should be recalled that a Kerr rotation value greater than 0.3° is considered as technologically significant. The huge magneto-optical effects are found to result from the combined effects of large off-diagonal conductivity, refractive index, magnetic moment, spin-orbit coupling, exchange splitting, band gap, and plasma resonance. Since most of the studied compounds are attractive as potential magneto-resistive materials, our finding on their large magneto-optical effects and ferromagnetic half-metallic nature add further importance to these compounds.

8.2 General Inferences

• One of the most important lessons that we learnt from this project is that, valence states can not be approximated as simple formal oxidation states by taking only the ionic character into account. The root of the assignment problem is that part of the atomic arrangement consists of nearly pure ions whereas other parts carry a bonding skeleton of mixed bonding character. For example, the transition metal component is bonded to oxygen by mixed iono-covalent bonds. Therefore, elaborate theoretical studies should be consulted in order to assign valence states in complex systems like those handled in this project.

• In some of the earlier publication from this project the oxidation state nomenclature has been used to describe valence state, spin states, and charge ordering. In view of later gained experience such deductions should not be taken too literally until the electronic structure data have been reanalyzed with different tools.

• Many experimental oxidation / valence state assignment techniques are based on the use of reference compounds for comparative analysis with compound under investigation. Errors in the oxidation / valence state assignment for the reference substance will then automatically be carried over to the compound under examination. To remedy this defect it is suggested that potential reference substances must be subjected to electronic band structure analysis.

• The structural arrangement appears in general to be more decisive for the electronic band structure than the constituents involved. In other words compounds with equal or closely related structural arrangements obtain almost similar DOS.

• In order to establish the actual ground-state structure several related structure types were considered as inputs. In order to arrive at the correct structure, the input test structures should reasonably describe the actual atomic arrangement. Even if the test the structure does not provide all the symmetry constraints, it should be reasonably close to the real situation. This implies that the selection of proper of test input structures will simplify the structural optimization procedure.

• From the structural optimization of a couple of close packed compounds we found that the overestimation of calculated volume compared to the experimental volume is well within the limits of DFT calculations. On the other hand, the overestimation of volume is above commonly accepted limits for a series of layered compounds. Therefore, in order to estimate cohesive properties of layered compounds where van der Waals forces are more dominant, usual DFT calculations are not sufficient.

• The experimentally observed insulating/semiconducting behavior can only be computationally simulated when the experimentally observed co-operative magnetic arrangement is introduced into the input model.

• From the overall analysis one can note that the use of usual LDA and GGA were able to reproduce and explain most of the experimental findings for the compounds dealt in this project. Therefore correlation effects are not as strong in the compounds studied here as commonly believed. Therefore additional approximations such as LDA+U methods are seldom needed to explain their behavior.

8.3 Next step

As we already mentioned during the course of this project several sub-projects cropped up and also new problems have evolved. In future we plan to extend the study on spin, charge, and orbital orderings to $\mathrm{YBa}T_2\mathrm{O}_{5+\delta}$ (T = Co and Fe; δ = 1/2 and 1). An experimental measurement of XPS on $\mathrm{Ca_3Co_2O_6}$ has suggested 3+ valence states for Co constituents. Therefore we plan to simulate the XPS profile for this compound in order to evaluate the experimental claim. Moreover, for the double perovskites $A_2\mathrm{Fe}B\mathrm{O}_6$ (A = Ca, Sr, Ba; B = Mo, W, Re) half-metallic electronic structure is observed only in the ferromagnetic configuration whereas for some of these compounds ferrimagnetic configurations is proposed. So a planned extension of the present work is to carry out extensive studies on electronic and magnetic properties of the $A_2\mathrm{Fe}B\mathrm{O}_6$ series.

In the present calculations, only collinear magnetic configurations have been considered. However, non-collinear magnetic arrangements should be properly taken care of in continued projects. For the calculation of excited-state properties, excitonic effects should also be included together with improvements like GW approximations. Finally, better tools should be devised for evaluation of the real valence states of components.

BIBLIOGRAPHY

[1] C.S. Smith. On material structure and human history. *Annu. Rev. Mater. Sci.*, **16**:1, (1986).

[2] H. Hohenberg and W. Kohn. *Phys. Rev.*, **136**:864, (1964).

[3] M.T. Yin and M.L. Cohen. *Phys. Rev. B*, **51**:13987, (1982).

[4] J. Neugebauer and M. Scheffler. *Phys. Rev. B*, **46**:16067, (1992).

[5] J.L. Simonds. *Physics Today*, **48**:26, 1995.

[6] K.G. Wilson. *Rev. Mod. Phys.*, **47**(4):773, (1975).

[7] N.W. Ashcroft and N.D. Mermin. *Solid State Physics.* (Saunders College Printing, USA, 1976).

[8] W. Kohn. *Rev. Mod. Phys.*, **71**:1253, (1998).

[9] W. Kohn and L.J. Sham. *PRA*, **140**:1133, 1965.

[10] R.O. Jones and O. Gunnarsson. *Rev. Mod. Phys.*, **61**:689, (1989).

[11] D.J. Singh. *Planewaves, Psuedopotentials, and the LAPW method.* (Kluwer, USA, 1994).

[12] J.P. Perdew and Y. Wang. *Phys. Rev. B*, **45**:13244, (1992).

[13] J.P. Perdew, K. Burke, and M. Ernerhof. *Phys. Rev. Lett.*, **82**:2544, (1996).

[14] H.L. Skriver. *The LMTO Method.* (Springer, 1984, 1984).

[15] M. Methfessel. *Phys. Rev. B*, **38**:1537, (1988).

[16] O.K. Andersen. *Computational Methods in Band Theory.* (Plenum, New York, 1971).

[17] R.M. Martin. *Electronic Structure: Basic Theory and Practical Methods.* (Cambridge University Press, 2004).

[18] A. Burkhardt G. krier, O. Jepsen. *Tight Binding LMTO-ASA Program, Version 4.7.* (O. K. Andersen, Stuttgart, Germany, 1999).

[19] J.M. Wills, O. Eriksson, and M. Alouani. *in "Electronic Structure and Physical Properties of Solids", ed. by H. Dressey.* (Springer Verlag, Berlin, 2000).

[20] J. Trygg. *First Principles Studies of Magnetic and Structural Properties of Metallic Systems.* (PhD Thesis, Uppsala University, 1995).

[21] P. Blaha, K. Schwarz, and J. Luitz. *A Full Potential Linearized Augmented Planewave Package for Calculating Crystal Properties.* (Technical University Wien, Vienna, ISBN 3-9501031-0-4, 2003).

[22] M. Weinert, E. Wimmer, and A. J. Freeman. *Phys. Rev. B*, **26**:4571, (1982).

[23] N.A. Spaldin and W.E. Pickett. *J. Solid State Chem.*, **176**:615, (2003).

[24] M.L. Cohen. *Annu. Rev. Mater. Sci.*, **30**:1, (2000).

[25] P.E. Blöchl. *Phys. Rev. B*, **50**:17953, (1994).

[26] G. Kresse and J. Hafner. *Phys. Rev. B*, **47**:R6726, (1993).

[27] G. Kresse and D. Joubert. *Phys. Rev. B*, **59**:1758, (1999).

[28] F.D. Murnaghan. *Proc. Natl. Acad. Sci.*, **30**:8244, (1944).

[29] F. Birch. *Phys. Rev.*, **71**:809, (1947).

[30] F. Birch. *J. Geophys. Res.*, **83**:1257, (1978).

[31] P. Vinet, J. Ferrante, J.R. Smith, and J.H. Rose. *J. Phys. C*, **19**:467, (1986).

[32] C.D. Gelatt.Jr., A.R. Williams, and V.L. Moruzzi. *Phys. Rev. B*, **27**:2005, (1983).

[33] R. Dronskowski and P.E. Blöchl. *J. Phys. Chem.*, **97**:8617, (1993).

[34] P. Blaha J.M. Zuo and K. Schwarz. *J. Phys.: Condens. Matter*, **9**:7541, (1997).

[35] B. Silvi and A. Savin. *Nature*, **371**:683, (1994).

[36] A. Savin, A.D. Becke, J. Flad, R. Nesper, H. Preuss, and H.G. von Schnerring. *Angew. Chem. Int. Ed. Engl.*, **30**:409, (1991).

[37] A.D. Becke and K.E. Edgecombe. *J. Chem. Phys.*, **92**:5397, (1990).

[38] R.F.W. Bader. *Atoms in Molecules: A Quantum Theory*. (Clarendon Press, Oxford, 1990).

[39] R.M. Martin. *Phys. Rev. B*, **9**:1998, (1974).

[40] M.H. Cohen R. Pick and R.M. Martin. *Phys. Rev. B*, **1**:910, (1970).

[41] A. Görling. *Phys. Rev. A*, **54**:3912, (1996).

[42] F. Wooten. *Optical Properties of Solids*. (Academic, New York, 1972).

[43] R. Kubo. *J. Phys. Soc. Jpn.*, **12**:570, (1957).

[44] C.S. Wang and J. Callaway. *Phys. Rev. B*, **9**:4897, (1974).

[45] M. Born. *Principles of Optics*. (Springer, London, 1964).

[46] J. Kerr. *Phil. Mag.*, **3**:321, (1877).

[47] M. Faraday. *Phil. Trans. Roy. Soc.*, **136**:1, (1846).

[48] F.J. Kahn, P.S. Pershan, and J.P. Remeika. *Phys. Rev.*, **186**:891, (1969).

[49] W. Reim, J. Schoenes, Eds. K.H.K. Buschow, and E.P. Wohlfarth. *Ferromagnetic Materials*, **5**(Chap. 2), (1990).

[50] P.G. van Engen, K.H.J. Buschow, R. Jongebreur, and M. Erman. *Appl. Phys. Lett.*, **42**:202, (1983).

[51] P.J. Grundy. Electronic and magnetic properties of metals and ceramics. *Materials Science and Technology*, **3B**, (1994).

[52] M. Mansuripur. *The Physical Principles of Magneto-optical Recording*. (Cambridge University Press, Cambridge, 1995).

[53] A. Neckel, K. Schwarz, R. Eibler, and P. Rastl. *Microchim. Acta Suppl.*, **6**:257, (1975).

[54] C. Kittel. *Introduction to Solid State Physics*. (Wiley, New York, 1971).

[55] U. Müller. *Inorganic Structural Chemistry*. (Wiley, Chichester, 1993).

[56] C. Zener. *Phys. Rev.*, **82**:402, (1951).

[57] P.W. Anderson and H. Hasegawa. *Phys. Rev.*, **100**:675, (1955).

[58] Y. Tokura and N. Nagaosa. *Science*, **288**:462, (2000).

[59] J.M.D. Coey, M. Viret, and S. von Molnár. *Adv. Phys.*, **48**:167, (1999).

[60] A.R. West. *Solid State Chemistry and its Applications*. (Wiley, Chichester, 1984).

[61] E. Pollert. *Int. J. Inorg. Mater.*, **2**:661, (2000).

[62] M.B. Robin and P. Day. *Adv. Inorg. Chem. Radiochem.*, **10**:247, (1967).

[63] C.N.R. Rao and A.K. Cheetham. *Science*, **272**:369, (1996).

[64] H.A. Jahn and E. Teller. *Proc. R. Soc. London*, **220**:A161, (1937).

[65] J.B. Goodenough. *Magnetism and the Chemical Bond.* (Interscience, New York, 1963).

[66] C.N.R. Rao, A. Arulraj, A.K. Cheetham, and B. Raveau. *J.Phys.: Condens. Matter.*, **12**:R83, (2000).

[67] E.J.W. Verwey. *Nature (London)*, **144**:327, (1939).

[68] C.N.R. Rao and A.K. Cheetham. *Science*, **276**:911, (1997).

[69] C.N.R. Rao and P.V. Vanitha. *Curr. Opinion Solid State Mater. Sci.*, **6**:97, (2002).

[70] J. van den Brink, G. Khaliullin, D. Khomskii, and Ed.T. Chatterji. *Colossal Magnetoresistive Manganites.* (Springer, 2002).

[71] D. Khomskii and G. Sawastzky. *Solid State Commun.*, **102**:87, (1997).

[72] A.J. Williams and J.P. Attfield. *Phys. Rev. B*, **72**:024436, (2005).

[73] P.M. Woodward and P. Karen. *Inorg. Chem.*, **42**:1121, (2003).

List of Publications

List of publications

The way of progress is neither swift nor easy.
Marie Curie

I. **Spin, charge and orbital ordering in the ferrimagnetic insulator YBaMn$_2$O$_5$**
R.Vidya, P. Ravindran, A. Kjekshus, and H. Fjellvåg
Phys. Rev. B. **65**, 144422 (2002).

II. **Effect of oxygen stoichiometry on spin, charge, and orbital ordering in manganites**
R. Vidya, P. Ravindran, P. Vajeeston, A. Kjekshus, and H. Fjellvåg
Phys. Rev. B **69**, 092405 (2004).

III. **Spin, charge, and orbital ordering in oxides with dual-valent transition-metal ions**
R. Vidya, P. Ravindran, P. Vajeeston, H. Fjellvåg and A. Kjekshus
Ceramics International **30**, 1993 (2004).

IV. **Effect of d-band filling on spin, charge and orbital ordering in YBaT_2O$_5$ (T = Mn, Fe, Co)**
R. Vidya, P. Ravindran, K. Knizek, A. Kjekshus, and H. Fjellvåg
In manuscript.

V. **Spin, charge, and orbital ordering in RBaMn$_2$O$_{5+\delta}$ (R = Y, La; 0 $\leq \delta \leq$ 1) and their dependence on oxygen content and size of R constituent**
R. Vidya, P. Ravindran, A. Kjekshus, and H. Fjellvåg
In manuscript.

VI. **Structural stability, electronic structure and magnetic properties of mixed-valence ACr$_3$O$_8$ phases (A = Na, K, and Rb)**
R. Vidya, P. Ravindran, P. Vajeeston, H. Fjellvåg, and A. Kjekshus
Phys. Rev. B **72**, 014411 (2005).

VII. **Crystal and electronic structures of Cr_3O_8 and $LiCr_3O_8$: Probable cathode materials in Li batteries**
R. Vidya, P. Ravindran, H. Fjellvåg, and A. Kjekshus
Phys. Rev. B *(accepted).*

VIII. **Density-functional calculations of crystal structures and properties of $CsCr_3O_8$ and ACr_3O_8 (A = In, Tl, Cu, Ag, Au)**
R. Vidya, P. Ravindran, H. Fjellvåg, and A. Kjekshus
Submitted to Phys. Rev. B

IX. **First-principles density-functional calculations on HCr_3O_8: An exercise to better understand the ACr_3O_8 (A = alkali-metal) family**
R. Vidya, P. Ravindran, H. Fjellvåg, and A. Kjekshus
J. Electrochem. Soc. *(accepted).*

X. **Tailor-made electronic and magnetic properties in one-dimensional pure and Y-substituted $Ca_3Co_2O_6$**
R. Vidya, P. Ravindran , H. Fjellvåg, A. Kjekshus, and O. Eriksson
Phys. Rev. Lett. **91**, 186404 (2003).

XI. **Valence states and associated features of Co in quasi-one-dimensional $Ca_3Co_2O_6$**
R. Vidya, P. Ravindran, H. Fjellvåg, and A. Kjekshus
In manuscript.

XII. **Antiferromagnetic vs. ferromagnetic interactions and spin-glass-like behavior in ruthenates**
P. Ravindran, R. Vidya, P. Vajeeston, A. Kjekshus, H. Fjellvåg, and B.C. Hauback
Solid State Commun. **124**, 293 (2002).

XIII. **Magnetic properties of Ca-doped $SrRuO_3$ from full-potential calculations**
R. Vidya, P. Ravindran, A. Kjekshus, H. Fjellvåg, and B.C. Hauback
J. Solid State Chem. **177**, 146 (2004).

XIV. **Huge magneto-optical effects in half-metallic double perovskites**
R. Vidya, P. Ravindran, A. Kjekshus, and H. Fjellvåg
Phys. Rev. B **70**, 184414 (2004).

XV. **Spin- and charge-ordering in oxygen-vacancy-ordered mixed-valence $Sr_4Fe_4O_{11}$**
R. Vidya, P. Ravindran, A. Kjekshus, and H. Fjellvåg
In manuscript.

Appendix

Publications not included in this thesis

I. **Origin of multiferroic behavior in $BiFeO_3$**
P. Ravindran, R. Vidya, A. Klaveness, F. Tylholdt, H. Fjellvåg, and A. Kjekshus
Submitted to Phys. Rev. B

II. **Indicator for site preference of hydrogen in metals, alloys, and intermetallic frameworks**
P. Vajeeston, P. Ravindran, R. Vidya, H. Fjellvåg, and A. Kjekshus
Euro. Phys. Lett. **72**, 569 (2005).

III. **Ground state and excited state properties of inorganic solids from full-potential density functional calculations**
P. Ravindran, R. Vidya, P. Vajeeston, A. Kjekshus and H. Fjellvåg
J. Solid State Chemistry (review) **176**, 338-374 (2003).

IV. **Design of Potential Hydrogen-storage Material using First-principle Density-functional Calculations**
P. Vajeeston, P. Ravindran , R. Vidya, H. Fjellvåg, and A. Kjekshus
Cry. Growth & Design **4**, 471-477 (2004).

V. **Electronic Structure and Excited-state Properties of Perovskite-like Oxides**
P. Ravindran, R. Vidya, A. Kjekshus and H. Fjellvåg
J. Cryst. Growth **268**, 554-559 (2004).

VI. **A pressure-induced phase of $NaAlH_4$: A potential candidate for hydrogen storage?**
P. Vajeeston, P. Ravindran, R. Vidya, H. Fjellvåg, and A. Kjekshus
Appl. Phys. Lett. **82**, 2257 (2003).

VII. **Short hydrogen-hydrogen separation in RNiInH$_{1.333}$ (R=La, Ce, Nd)**
P. Vajeeston, P. Ravindran, R. Vidya, A. Kjekshus, H. Fjellvåg and V.A. Yartys
Phys. Rev. B **67**, 014101 (2003).

VIII. **Violation of the “2 Å rule" for Metal Hydrides**
P. Ravindran, P. Vajeeston, R. Vidya, A. Kjekshus and H. Fjellvåg
Phys. Rev. Lett. **89**, 106403 (2002).

IX. **Electronic structure, phase stability and chemical bonding in Th_2Al and Th_2AlH_4**
P. Vajeeston, R. Vidya, P. Ravindran, H. Fjellvåg, A. Kjekshus and A. Skjeltorp
Phys. Rev. B **65**, 075101 (2002).

X. **Detailed electronic structure studies on superconducting MgB_2 and related compounds**
P. Ravindran, P. Vajeeston, R. Vidya, A. Kjekshus and H. Fjellvåg
Phys. Rev. B. **64**, 224509(1-15) (2001).

Part II

List of publications

> *The way of progress is neither swift nor easy.*
> *Marie Curie*

I. **Spin, charge and orbital ordering in the ferrimagnetic insulator $\mathbf{YBaMn_2O_5}$**
R.Vidya, P. Ravindran, A. Kjekshus, and H. Fjellvåg
Phys. Rev. B. **65**, 144422 (2002).

II. **Effect of oxygen stoichiometry on spin, charge, and orbital ordering in manganites**
R. Vidya, P. Ravindran, P. Vajeeston, A. Kjekshus, and H. Fjellvåg
Phys. Rev. B **69**, 092405 (2004).

III. **Spin, charge, and orbital ordering in oxides with dual-valent transition-metal ions**
R. Vidya, P. Ravindran, P. Vajeeston, H. Fjellvåg and A. Kjekshus
Ceramics International **30**, 1993 (2004).

IV. **Effect of d-band filling on spin, charge and orbital ordering in YBaT_2O$_5$ (T = Mn, Fe, Co)**
R. Vidya, P. Ravindran, K. Knizek, A. Kjekshus, and H. Fjellvåg
In manuscript.

V. **Spin, charge, and orbital ordering in RBaMn$_2$O$_{5+\delta}$ (R = Y, La; $0 \leq \delta \leq 1$) and their dependence on oxygen content and size of R constituent**
R. Vidya, P. Ravindran, A. Kjekshus, and H. Fjellvåg
In manuscript.

VI. **Structural stability, electronic structure and magnetic properties of mixed-valence ACr$_3$O$_8$ phases (A = Na, K, and Rb)**
R. Vidya, P. Ravindran, P. Vajeeston, H. Fjellvåg, and A. Kjekshus
Phys. Rev. B **72**, 014411 (2005).

VII. **Crystal and electronic structures of Cr_3O_8 and $LiCr_3O_8$: Probable cathode materials in Li batteries**
R. Vidya, P. Ravindran, H. Fjellvåg, and A. Kjekshus
Phys. Rev. B *(accepted).*

VIII. **Density-functional calculations of crystal structures and properties of $CsCr_3O_8$ and ACr_3O_8 (A = In, Tl, Cu, Ag, Au)**
R. Vidya, P. Ravindran, H. Fjellvåg, and A. Kjekshus
Submitted to Phys. Rev. B

IX. **First-principles density-functional calculations on HCr_3O_8: An exercise to better understand the ACr_3O_8 (A = alkali-metal) family**
R. Vidya, P. Ravindran, H. Fjellvåg, and A. Kjekshus
J. Electrochem. Soc. *(accepted).*

X. **Tailor-made electronic and magnetic properties in one-dimensional pure and Y-substituted $Ca_3Co_2O_6$**
R. Vidya, P. Ravindran , H. Fjellvåg, A. Kjekshus, and O. Eriksson
Phys. Rev. Lett. **91**, 186404 (2003).

XI. **Valence states and associated features of Co in quasi-one-dimensional $Ca_3Co_2O_6$**
R. Vidya, P. Ravindran, H. Fjellvåg, and A. Kjekshus
In manuscript.

XII. **Antiferromagnetic vs. ferromagnetic interactions and spin-glass-like behavior in ruthenates**
P. Ravindran, R. Vidya, P. Vajeeston, A. Kjekshus, H. Fjellvåg, and B.C. Hauback
Solid State Commun. **124**, 293 (2002).

XIII. **Magnetic properties of Ca-doped $SrRuO_3$ from full-potential calculations**
R. Vidya, P. Ravindran, A. Kjekshus, H. Fjellvåg, and B.C. Hauback
J. Solid State Chem. **177**, 146 (2004).

XIV. **Huge magneto-optical effects in half-metallic double perovskites**
R. Vidya, P. Ravindran, A. Kjekshus, and H. Fjellvåg
Phys. Rev. B **70**, 184414 (2004).

XV. **Spin- and charge-ordering in oxygen-vacancy-ordered mixed-valence $Sr_4Fe_4O_{11}$**
R. Vidya, P. Ravindran, A. Kjekshus, and H. Fjellvåg
In manuscript.

Appendix

Publications not included in this thesis

I. **Origin of multiferroic behavior in $BiFeO_3$**
P. Ravindran, R. Vidya, A. Klaveness, F. Tylholdt, H. Fjellvåg, and A. Kjekshus
Submitted to Phys. Rev. B

II. **Indicator for site preference of hydrogen in metals, alloys, and intermetallic frameworks**
P. Vajeeston, P. Ravindran, R. Vidya, H. Fjellvåg, and A. Kjekshus
Euro. Phys. Lett. **72**, 569 (2005).

III. **Ground state and excited state properties of inorganic solids from full-potential density functional calculations**
P. Ravindran, R. Vidya, P. Vajeeston, A. Kjekshus and H. Fjellvåg
J. Solid State Chemistry (review) **176**, 338-374 (2003).

IV. **Design of Potential Hydrogen-storage Material using First-principle Density-functional Calculations**
P. Vajeeston, P. Ravindran , R. Vidya, H. Fjellvåg, and A. Kjekshus
Cry. Growth & Design **4**, 471-477 (2004).

V. **Electronic Structure and Excited-state Properties of Perovskite-like Oxides**
P. Ravindran, R. Vidya, A. Kjekshus and H. Fjellvåg
J. Cryst. Growth **268**, 554-559 (2004).

VI. **A pressure-induced phase of $NaAlH_4$: A potential candidate for hydrogen storage?**
P. Vajeeston, P. Ravindran, R. Vidya, H. Fjellvåg, and A. Kjekshus
Appl. Phys. Lett. **82**, 2257 (2003).

VII. **Short hydrogen-hydrogen separation in RNiInH$_{1.333}$ (R=La, Ce, Nd)**
P. Vajeeston, P. Ravindran, R. Vidya, A. Kjekshus, H. Fjellvåg and V.A. Yartys
Phys. Rev. B **67**, 014101 (2003).

VIII. **Violation of the “2 Å rule" for Metal Hydrides**
P. Ravindran, P. Vajeeston, R. Vidya, A. Kjekshus and H. Fjellvåg
Phys. Rev. Lett. **89**, 106403 (2002).

IX. **Electronic structure, phase stability and chemical bonding in Th_2Al and Th_2AlH_4**
P. Vajeeston, R. Vidya, P. Ravindran, H. Fjellvåg, A. Kjekshus and A. Skjeltorp
Phys. Rev. B **65**, 075101 (2002).

X. **Detailed electronic structure studies on superconducting MgB_2 and related compounds**
P. Ravindran, P. Vajeeston, R. Vidya, A. Kjekshus and H. Fjellvåg
Phys. Rev. B. **64**, 224509(1-15) (2001).

PHYSICAL REVIEW B, VOLUME 65, 144422

Spin, charge, and orbital ordering in the ferrimagnetic insulator $YBaMn_2O_5$

R. Vidya,* P. Ravindran, A. Kjekshus, and H. Fjellvåg
Department of Chemistry, University of Oslo, Box 1033, Blindern, N-0315 Oslo, Norway

(Received 4 May 2001; published 29 March 2002)

The oxygen-deficient (double) perovskite $YBaMn_2O_5$, containing corner-linked MnO_5 square pyramids, is found to exhibit ferrimagnetic ordering in its ground state. In the present work we report generalized-gradient-corrected, relativistic first-principles full-potential density-functional calculations performed on $YBaMn_2O_5$ in the paramagnetic, ferromagnetic, and ferrimagnetic states. The charge, orbital, and spin orderings are explained with site-, spin-, angular-momentum-, and orbital-projected density of states, charge-density plots, electronic structure, and total energy studies. $YBaMn_2O_5$ is found to stabilize in a G-type ferrimagnetic state in accordance with experimental results. The experimentally observed semiconducting behavior appears only when we include ferrimagnetic ordering in our calculation. We observed significant optical anisotropy in this material originating from the combined effect of ferrimagnetic ordering and crystal-field splitting. In order to gain knowledge about the presence of different valence states for Mn in $YBaMn_2O_5$ we have calculated K-edge x-ray absorption near-edge spectra for the Mn and O atoms. The presence of the different valence states for Mn is clearly established from the x-ray absorption near-edge spectra, hyperfine field parameters, and the magnetic properties study. Among the experimentally proposed structures, the recently reported description based on $P4/nmm$ is found to represent the stable structure.

DOI: 10.1103/PhysRevB.65.144422 PACS number(s): 75.50.Gg, 75.30.−m, 71.20.−b, 78.20.Ci

I. INTRODUCTION

Perovskite-type transition-metal oxides ABO_3 and their oxygen-deficient relatives exhibit a variety of interesting physical properties including high-temperature superconductivity, metal-insulator transition, and a variety of cooperative magnetic phenomena. Among them manganites have recently attracted particular attention because of the discovery of colossal negative magnetoresistance (CMR) in $La_{1-x}Sr_xMnO_3$,[1] $La_{1-x}Ba_xMnO_3$,[1] and related phases.[2–5] This renewed interest in the mixed-valence manganese perovskites such as $La_{1-x}Pb_xMnO_3$ is due to their potential technological applications.[6,7] In addition, the search for new high-temperature superconductors in mixed-oxide materials is a driving force for attention. The mechanism of high-temperature superconductivity is believed to be linked to cooperative interaction between copper $3d_{x^2-y^2}$ and $3d_{z^2}$ orbitals and oxygen $2p$ orbitals.[8] An attractive approach to obtain insight into the nature of this phenomenon is to examine the magnetic and electrical properties of non-copper-oxide analogues of known high-temperature superconducting cuprates. Manganese is a good choice for such a task, as in an octahedral perovskite-like configuration, Mn^{3+} (d^4 high spin with a single electron in an e_g orbital) will experience a similar Jahn-Teller (JT) distortion to that of Cu^{2+} [d^9 high spin with three electrons (or one hole) in the e_g orbitals]. The hole-doped manganese perovskites show some similarities to the corresponding hole-doped Cu phases in which superconductivity occurs.[9] Structural similarities between these two groups of materials suggest that new Mn analogs of the high-temperature superconducting Cu oxides may be prepared.

Since the discovery of CMR phenomena in perovskite-related manganites, extensive studies have been performed on manganese oxides with atomic arrangements related to the perovskite and pyrochlore structures over a wide variety of compositions with the aim to explore exotic spin-charge-coupled states.[10] Anisotropic CMR phenomena have also recently been reported in layered Ruddlesden-Popper variants of perovskites $(R,A)_{n+1}Mn_nO_{3n+1}$ (R=rare earth, A=alkaline earth) for $n=2$.[11] Similar effects have also been observed in the oxygen-deficient cubic pyrochlore $Tl_2Mn_2O_{7-\delta}$. The chemical features common to these materials are an intimately connected Mn-O-Mn network, within a three-dimensional or multilayered structure, and an average Mn oxidation state between 3+ and 4+ (obtained by hole-doping of Mn^{3+}).[12]

At low temperatures, manganese perovskites are characterized by the strong competition between charge-carrier itinerancy and localization. In the former case a ferromagnetic (F) metallic state is formed. In the latter case, the localized carriers tend to form charge-ordered (CO) states, which have a predominantly antiferromagnetic (AF) insulating character. Hence, we have a competition between F with metallic behavior and cooperative JT distortion with CO. The CO state can be converted into an F metallic state by the application of a magnetic field. The intriguing doping-induced, temperature-dependent metal-insulator transition and the interwoven magnetic (spin-), orbital-, and charge-ordering phenomena in mixed-valence manganese perovskites and transition-metal oxides have attracted much attention in recent years.[13] An active role of the orbital degree of freedom in the lattice and electronic response can be most typically seen in manganese perovskite oxides. As a matter of fact such properties appear to have their origin in the unique electronic structures derived from the hybridized Mn $3d$ and O $2p$ orbitals in the particular structural and chemical environment of a perovskite. The thus resulting intra-atomic exchange and the orbital degrees of freedom of the Mn $3d$ electrons play essential roles in this constellation. Furthermore, various kinds of structural distortion profoundly influence the electronic properties. The extensive studies of CMR in $R_{1-x}A_xMnO_3$ have brought forth novel features related to

©2002 The American Physical Society

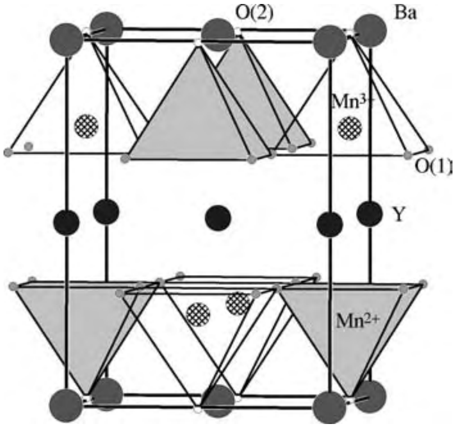

FIG. 1. The $YBaMn_2O_5$ crystal structure. The Y and Ba ions form layers along *c*. The square pyramids corresponding to Mn^{3+} and Mn^{2+} are shown by open and shaded polyhedra, respectively. The O atoms at the bases and apices of the square pyramids are denoted O(1) and O(2), respectively.

CO in these oxides. In transition-metal oxides with their anisotropic-shaped *d* orbitals, the Coulomb interaction between the electrons (strong electron correlation effect) may be of great importance. Orbital ordering (OO) gives rise to anisotropic interactions in the electron-transfer process which in turn favors or disfavors the double-exchange and the superexchange (F or AF) interactions in an orbital direction-dependent manner and hence gives a complex spin-orbital-coupled state. OO in the manganese oxides occasionally accompanies the concomitant CO.[14] The ordered oxygen-deficient double perovskites $RBaT_2O_{5+\delta}$ ($T=$transition metals like Fe, Co, and Mn) have attracted much attention as new spin-charge-orbital-coupled systems and new CMR materials. In the isostructural phases with $R=$Gd and Eu CMR effects of some 40% are observed.[15] As the experimental findings have been made available only in recent years, little theoretical work has been undertaken to understand the origin of these microscopic properties. The present study reports a detailed theoretical investigation of the electronic structure and optical properties of $YBaMn_2O_5$.

At low temperature, $YBaMn_2O_5$ is an AF insulator with CO of Mn^{3+} and Mn^{2+} accompanied by OO and spin ordering (SO).[25] The mechanism of CO and SO in manganites is not at all clear. Different authors have emphasized the importance of different ingredients such as on-site Coulomb interactions,[16–18] JT distortion,[19,20] and intersite Coulomb interactions.[21] Therefore, we have attempted to study CO, OO, and SO through full-potential linear muffin-tin orbital (FPLMTO) and full-potential linear augmented plane-wave (FPLAPW) methods. Similar to Fe_3O_4 and $SmBaFe_2O_{5+w}$ where Fe takes the conventional valence states of Fe^{3+} and Fe^{2+} at low temperature,[22,23] Mn is reported to occur as Mn^{3+} and Mn^{2+} in $YBaMn_2O_5$. Above the so-called Verwey temperature (T_V) valence-state mixing has been observed in Fe_3O_4 as well as in $SmBaFe_2O_{5+w}$. This brings in an additional interesting aspect in the study of the electronic structure and magnetic properties of Mn in $YBaMn_2O_5$. The first structural determinations based on powder x-ray (300 K) (Ref. 12) and neutron (100–300 K) (Ref. 24) diffraction data found that $YBaMn_2O_5$ crystallizes in space group $P4/mmm$, whereas a more recent powder neutron (2–300 K) (Ref. 25) diffraction (PND) study found $P4/nmm$. So a theoretical examination of the total energy for the two different structural alternatives is required.

The rest of the paper is arranged as follows: Section II gives crystal structure details for $YBaMn_2O_5$. The theoretical methods used for the calculations are described in Sec. III. The analysis of the band structure is given in Sec. IV A. Section IV B deals with the nature of the chemical bonding in $YBaMn_2O_5$, analyzed with the help of site-, spin-, angular-momentum-, and orbital-projected density of states (DOS). Section IV C discusses CO and OO in $YBaMn_2O_5$ with the help of charge-density plots. The results from calculations of optical spectra and x-ray absorption near-edge (XANE) spectra are discussed in Secs. IV D and IV E, respectively. Section IV F deals with hyperfine parameters. Finally the important conclusions are summarized in Sec. V.

II. CRYSTAL STRUCTURE

Chapman *et al.*[12] synthesized rather impure $YBaMn_2O_5$ and reported the crystal structure parameters according to space group $P4/mmm$ (described as double or ordered, oxygen-deficient perovskite, closely related to $YBaCuFeO_5$). These findings were subsequently confirmed by McAllister and Attfield[24] who also established a model for the ferrimagnetic ordering of the magnetic moments of Mn in $YBaMn_2O_5$ (still based on an impure sample). More recently Millange *et al.*[25] have succeeded in preparing phase-pure $YBaMn_2O_5$ and these authors report crystal and magnetic structure parameters according to space group $P4/nmm$.

Within the $P4/nmm$ description $YBaMn_2O_5$ crystallizes with $a=5.5359$ and $c=7.6151$ Å; Y in $2(b)$, Ba in $2(a)$, Mn(1) in $2(c)$ with $z=0.2745$, Mn(2) in $2(c)$ with $z=0.7457$, O(1) in $8(j)$ with $x=0.4911$, $y=0.9911$, and $z=0.4911$, and O(2) in $2(c)$ with $z=0.0061$. The lacking oxygens in the yttrium plane, compared with the perovskite-aristotype structure, reduces the coordination number of yttrium to 8, while barium retains the typical 12 coordination of the perovskite structure. The Mn-O network consists of double layers of MnO_5 square pyramids, corner shared in the *ab* plane and linked via their apices.

According to the $P4/nmm$ description (Fig. 1) the two kinds of MnO_5 pyramids are arranged in an ordered manner, each $Mn^{2+}O_5$ pyramid being linked to five $Mn^{3+}O_5$ pyramids. Owing to this charge ordering, each Mn^{2+} has four Mn^{3+} in-plane neighbors. Oxygen takes two crystallographically different sites. O(1) forms the base of the square pyramids, while O(2) is located at the apex of the pyramids. The interatomic Mn-O distances fall in four categories, being 1.908 and 2.086 Å for Mn^{3+}-O(1) and Mn^{2+}-O(1), respectively, whereas O(2) is 2.081 and 1.961 Å away from Mn^{3+} and Mn^{2+}, respectively. (The $P4/mmm$ description gave on the other hand, almost equal basal and apical Mn-O distances within all square pyramids.[12]) The basal plane Mn^{3+}-O(1)-Mn^{2+} angle is 157.8° and the apical Mn^{3+}-O(2)-Mn^{2+} angle is 180°. The large variation in these angles play a key role in the magnetic properties.

III. COMPUTATIONAL DETAILS

A. FPLMTO computations

The present calculations have used the FPLMTO method[26] where no shape approximation is assumed for the one-electron potential and charge density. The basis geometry consists of muffin-tin (MT) spheres centered around the atomic sites with an interstitial region in between. Inside the MT spheres the charge density and potential are expanded by means of spherical harmonic functions multiplied by a radial component. The interstitial basis function is a Bloch sum of linear combinations of Neumann or Henkel functions depending on the sign of the kinetic energy κ^2 (corresponding to the basis functions in the interstitial region). Each Neumann or Henkel function is then augmented (replaced) by a numerical basis function inside the MT spheres, in the standard way of the linear MT orbital method.[27] Since a Bloch sum of atomic centered Henkel or Neumann functions has the periodicity of the underlying lattice it may be expanded in a Fourier series, as done here. The spherical-harmonic expansion of the charge density, potential, and basis functions was performed up to $l_{max}=6$. The basis included Y $4p$, $5s$, $5p$, and $4d$ states, Ba $5p$, $6s$, $6p$, $5d$, and $4f$ states, Mn $4s$, $4p$, and $3d$ states, and O $2s$, $2p$, and $3d$ states.

Furthermore, the calculations are all electron as well as fully relativistic. The latter level is obtained by including the mass velocity and Darwin (and higher-order) terms in the derivation of the radial functions (inside the MT spheres) whereas the spin-orbit coupling was included at the variational step using an (l,s) basis. Moreover, the present calculations made use of a so-called double basis, to ensure a well-converged wave function. This means that two Neumann or Henkel functions were applied, each attached to its own radial function with an (n,l) quantum number. The integrations over the Brillouin zone (BZ) in the ground-state calculations were performed as a weighted sum, using the special point sampling,[28] with weights reflecting the symmetry of a given **k** point. We also used a Gaussian smearing width of 20 mRy for each eigenvalue in the vicinity of the Fermi level to speed up the convergence. For the DOS and optical calculations, the tetrahedron integration was employed. The calculations were performed for the experimentally determined structural parameters (see Sec. II). For the exchange-correlation functional $E_{xc}(n)$, we have used the generalized gradient approximation (GGA) where the gradient of the electron density is taken into account using the Perdew and Wang[29] implementation of the GGA. Here 192 **k** points in the irreducible part of the primitive tetragonal BZ were used for the self-consistent ground-state calculations and 352 **k** points for the optical calculations.

B. FPLAPW computations

For the XANES and orbital-projected DOS calculations we have applied the FPLAPW method[30] in a scalar-relativistic version without spin-orbit coupling. The FPLAPW method divides space into an interstitial region (IR) and nonoverlapping MT spheres centered at the atomic sites. In the IR, the basis set consists of plane waves. Inside the MT spheres, the basis set is described by radial solutions of the one-particle Schrödinger equation (at fixed energies) and their energy derivatives multiplied by spherical harmonics. The charge densities and potentials in the atomic spheres were represented by spherical harmonics up to $l=6$, whereas in the interstitial region these quantities were expanded in a Fourier series with 3334 stars of the reciprocal lattice vectors **G**. The radial basis functions of each LAPW were calculated up to $l=10$ and the nonspherical potential contribution to the Hamiltonian matrix had an upper limit of $l=4$. Atomic-sphere radii R_{MT} of 2.5, 2.8, 1.8, and 1.6 a.u. for Y, Ba, Mn, and O, respectively, were used. Since the spin densities are well confined within a radius of about 1.5 a.u, the resulting magnetic moments do not depend appreciably with the chosen atomic-sphere radii. The initial basis set included $5s$, $5p$, and $4d$ valence and $4s$ and $4p$ semicore functions for Y, $6s$, $6p$, and $6d$ valence and $5s$ and $5p$ semicore functions for Ba, $4s$, $4p$, and $3d$ valence and $3s$ and $3p$ semicore functions for Mn and $2s$, $2p$, and $3d$ functions for O. These basis functions were supplemented with local orbitals[31] for additional flexibility to the representation of the semicore states and for generalization of relaxation of the linearization errors. Owing to the linearization errors DOS are reliable only to about 1–2 Ry above E_F. Therefore, after self-consistency was achieved for this basis set we included higher-energy local orbitals: $5d$- and $4f$-like functions for Y, $6d$- and $4f$-like functions for Ba, $5s$- and $5p$-like functions for Mn, and $3p$-like functions for O. The BZ integration was done with a modified tetrahedron method[32] and we used 140 **k** points in the irreducible wedge of BZ. Exchange and correlation effects are treated within density-functional theory (DFT), using the GGA.[29]

C. Optical properties

Optical properties of matter can be described by means of the transverse dielectric function $\epsilon(\mathbf{q},\omega)$ where **q** is the momentum transfer in the photon-electron interaction and ω is the energy transfer. At lower energies one can set $\mathbf{q}=\mathbf{0}$, and arrive at the electric dipole approximation, which is assumed throughout this paper. The real and imaginary parts of $\epsilon(\omega)$ are often referred to as ϵ_1 and ϵ_2, respectively. We have calculated the dielectric function for frequencies well above those of the phonons and therefore we considered only electronic excitations. In condensed matter systems, there are two contributions to $\epsilon(\omega)$, viz., intraband and interband transitions. The contribution from intraband transitions is important only for metals. The interband transitions can further be split into direct and indirect transitions. The latter involves scattering of phonons and are neglected here, and moreover these only make small contribution to $\epsilon(\omega)$ in comparison to the direct transitions,[33] but have a temperature broadening effect. Also other effects, e.g., excitons (which normally give rise to rather sharp peaks), affect the optical properties.

The direct interband contribution to the imaginary part of the dielectric function $\epsilon_2(\omega)$ is calculated by summing all possible transitions from occupied to unoccupied states, taking the appropriate transition-matrix element into account. The dielectric function is a tensor for which all components

TABLE I. Total energy in different magnetic configurations.

Type	Paramagnetic	Ferromagnetic	Antiferromagnetic
Total energy (Ry/f.u.)	-28438.0466	-28438.2754	-28438.3125
ΔE (meV/f.u.)	3618.6	505.6	0.0
Electronic state	Metal	Metal	Semiconductor
		Calculated magnetic moment (μ_B)	
	Ferromagnetic	Antiferromagnetic	Experimental[a]
Mn^{3+}	3.45	3.07	2.91
Mn^{2+}	3.99	3.93	3.91
Saturated	7.44	0.86	0.95

[a] Reference 25.

are needed for a complete description. However, we restrict our considerations to the diagonal matrix elements $\epsilon^{\nu\nu}(\omega)$ with $\nu = x$, y, or z. The interband contribution to the diagonal elements of $\epsilon_2(\omega)$ is given by

$$\epsilon_2^{\nu\nu} = \frac{8\pi^2 e^2}{m^2\omega^2} \sum_n^{unocc} \sum_{n'}^{occ} \int_{BZ} |P^{\nu}_{nn'}(k)|^2 f_{kn}(1-f_{kn'}) \times \delta(E_n^k - E_{n'}^k - \hbar\omega) \frac{d^3k}{(2\pi)^3}, \tag{1}$$

where e is the electron charge, m its mass, f_{kn} the Fermi-Dirac distribution function, $P^{\nu}_{nn'}$ the projection of the momentum matrix elements along the direction ν of the electric field, and E_n^k one-electron energies. The evaluation of the matrix elements in Eq. (1) is done separately over the MT and interstitial regions. Further details about the evaluation of matrix elements are found in Ref. 34. The integration over BZ in Eq. (1) is performed using linear interpolation on a mesh of uniformly distributed points, i.e., the tetrahedron method. The total $\epsilon_2^{\nu\nu}$ was obtained from $\epsilon_2^{\nu\nu}$(IBZ); i.e., $\epsilon_2^{\nu\nu}$ was calculated only for the irreducible (I) part of the BZ using

$$\epsilon_2(\omega) = \frac{1}{N} \sum_{i=1}^{N} \sigma_i^T \epsilon_2(\mathrm{IBZ}) \sigma_i, \tag{2}$$

where N is the number of symmetry operations and σ_i represents the symmetry operations; for shortness, $\epsilon(\omega)$ is used instead of $\epsilon^{\nu\nu}(\omega)$. Lifetime broadening was simulated by convoluting the absorptive part of the dielectric function with a Lorentzian, whose full width at half maximum (FWHM) is equal to $0.005(\hbar\omega)^2$ eV. The experimental resolution was simulated by broadening the final spectra with a Gaussian of constant FWHM equal to 0.01 eV.

After having evaluated Eq. (2) we calculated the interband contribution to the real part of the dielectric function $\epsilon_1(\omega)$ from the Kramers-Kronig relation

$$\epsilon_1(\omega) = 1 + \frac{2}{\pi} P \int_0^{\infty} \frac{\epsilon_2(\omega')\omega' d\omega'}{\omega'^2 - \omega^2}. \tag{3}$$

In order to calculate $\epsilon_1(\omega)$ one needs a good representation of $\epsilon_2(\omega)$ up to high energies. In the present work we have calculated $\epsilon_2(\omega)$ up to 41 eV above the E_F level, which also was the truncation energy used in Eq. (3).

To compare our theoretical results with the experimental spectra we have calculated polarized reflectivity spectra using the following relation. The specular reflectivity can be obtained from the complex dielectric constant in Eq. (1) through the Fresnel's equation

$$R^{\nu\nu}(\omega) = \left| \frac{\sqrt{\epsilon(\omega)} - 1}{\sqrt{\epsilon(\omega)} + 1} \right|^2. \tag{4}$$

We have also calculated the absorption coefficient $I(\omega)$ and the refractive index n using the following expressions:

$$I(\omega) = 2\omega \left[\frac{(\epsilon_1^2(\omega) + \epsilon_2^2(\omega))^{1/2} - \epsilon_1(\omega)}{2} \right]^{1/2} \tag{5}$$

and

$$n = \left[\frac{\sqrt{\epsilon_1^2 + \epsilon_2^2} + \epsilon_1}{2} \right]^{1/2}. \tag{6}$$

IV. RESULTS AND DISCUSSION

A. Electronic band structure

The FPLMTO calculations were performed on $YBaMn_2O_5$ for three different magnetic configurations, viz., paramagnetic (P), ferromagnetic (F), and antiferromagnetic (AF). From Table I it can be seen that in the AF configuration, the spins are not canceled and hence this state is really ferrimagnetic (Ferri). Moreover, Table I shows that Ferri $YBaMn_2O_5$ has lower energy than the P and F configurations. The energy-band structure of Ferri $YBaMn_2O_5$ is shown in Figs. 2(a) and 2(b) for up- and down-spin bands, respectively. $YBaMn_2O_5$ is seen to be an indirect-band-gap semiconductor. A closer inspection of the energy-band structure shows that the band gap is between the top of the valence band (VB) at the Γ point and the bottom of the conduction band (CB) at the Z point. As the unit cell contains 18 atoms, the band structure is quite complicated and Fig. 2 therefore only depicts the energy range -7.5–7.5 eV.

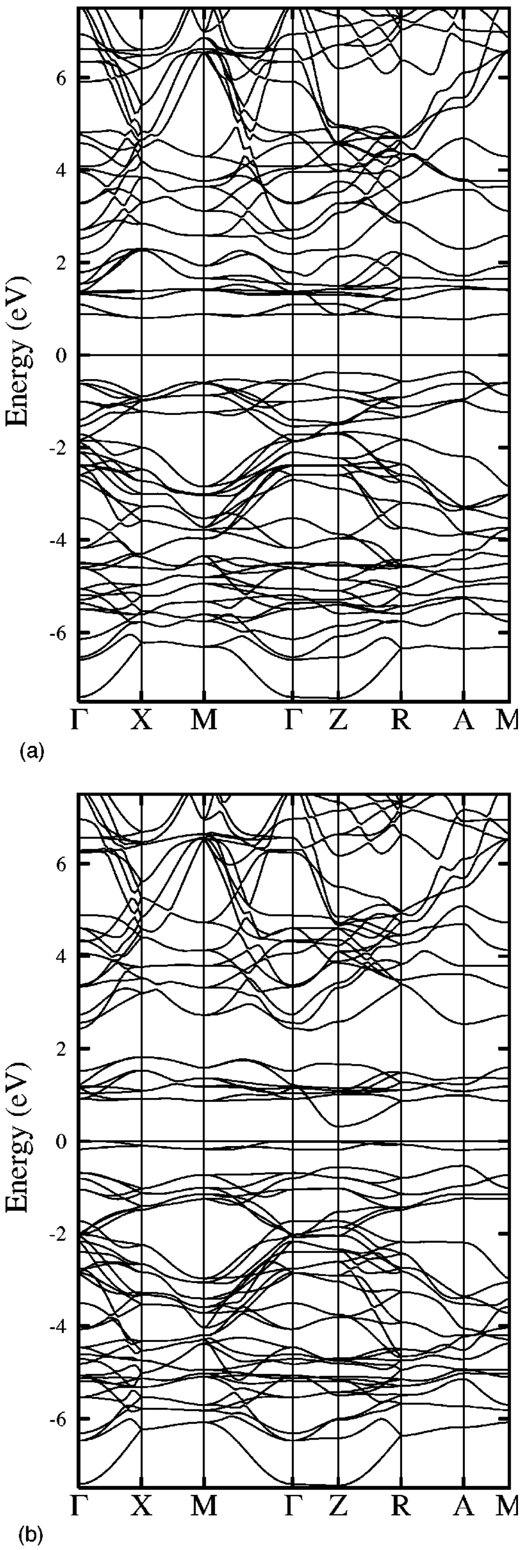

FIG. 2. The electronic band structure of $YBaMn_2O_5$ in the antiferromagnetic state: (a) up-spin bands and (b) down-spin bands. The line at 0 eV refers to the Fermi energy level.

There is a finite energy gap of 1.307 eV between the topmost-occupied VB and the bottommost-unoccupied CB in the up-spin channel. For the purpose of more clarity, it is convenient to divide the occupied portion of the band structure in the up-spin channel into three energy regions: (i) bands lying at and below -4 eV, (ii) bands lying between -4 and -2 eV, and (iii) the top of the VB, closer to E_F, viz., the range -2–0 eV. Region (i) contains 17 bands with contributions from Y $4s$, $5s$, Mn $3s$, $3d$, and O $2p$ electrons. Region (ii) comprises bands which originate from completely filled O(1) and O(2) $2p$ orbitals. Region (iii) includes 10 bands. Among them one finds delocalized (dispersed) bands originating from Y $5s$ and O $2p$ orbitals and somewhat localized bands attributed to Mn(1) d_{z^2}, $d_{x^2-y^2}$, d_{xz}, and d_{yz} orbitals. The topmost-occupied band contains electrons stemming from the Mn d_{z^2} orbital. In the unoccupied portion of the band structure, a corresponding division leads to two energy regions: (1) The bottommost CB from 0 to 2 eV and (2) the middle range of CB from 2 to 4 eV. (Above 4 eV the bands are highly dispersed and it is quite difficult to establish the origin of the bands.) There are 9 bands in region (1) which have some Y $5s$, Ba $5d$, Mn(1) $3d_{xy}$, and Mn(2) $3d$ characters. In region (2) the bands retain Y $6s$ and $4d$, Ba $7s$ and $5d$, and Mn $4s$, $4p$, and $3d$ characters.

The energy-band structure of the down-spin channel [Fig. 2(b)] has 16 bands in the region (i) up to -4 eV which arise from the s and p electrons of the Y, Ba, Mn, and O atoms. The mainly s- and p-electron character of the bands makes them appreciably dispersed. The second energy region (ii) contains 12 bands, which have Y $5s$, Ba $5p$, Mn(2) $3d$, and O(1), O(2) $2p$ character. The third region (iii) closer to E_F has 10 bands which are mainly arising from Mn(1), Mn(2) $3d$, and O(1), O(2) $2p$ orbitals. Unlike the up-spin channel the down-spin channel contains two bands at E_F which arise from the originally half-filled d_{yz}, d_{xz} orbitals of Mn(1) and the half-filled d_{xy} orbital of Mn(2).

A finite band gap of 1.046 eV opens up between the highest-occupied VB and bottommost-unoccupied CB. The unoccupied portion of the down-spin channel is quite different from that of the up-spin channel. The lowest-lying unoccupied band has Mn(2) $4s$ electrons. Between 0 and 2 eV there are 8 bands which arise mainly from Mn(1) $3d$ electrons as well as from Mn(1) and Mn(2) $4s$ electrons and O(1) and O(2) $2p$ electrons. The dispersed bands present between 2 and 4 eV have Y $5s$ and $3d$, Ba $6s$ and $5d$, and Mn(1) $3d$ characters.

B. DOS characteristics

In order to theoretically verify which of the two ($P4/mmm$ or $P4/nmm$ based) structures is energetically more stable, we performed first-principles calculations for both variants. The calculated DOS value at E_F for the P phase $P4/mmm$ variant is 192.82 states/(Ry f.u.) and for $P4/nmm$ 149 states/(Ry f.u.) in the P state. Hence, a larger number of electrons are present at E_F for the former variant, which favors the relative structural stability of the latter. Moreover, our calculations show that the $P4/nmm$ variant is 860 meV/f.u. lower in energy than the $P4/mmm$ variant. Therefore we conclude that $YBaMn_2O_5$ is more stable in space group $P4/nmm$ than in $P4/mmm$, viz., in accordance with the most recent PND-based experimental study.

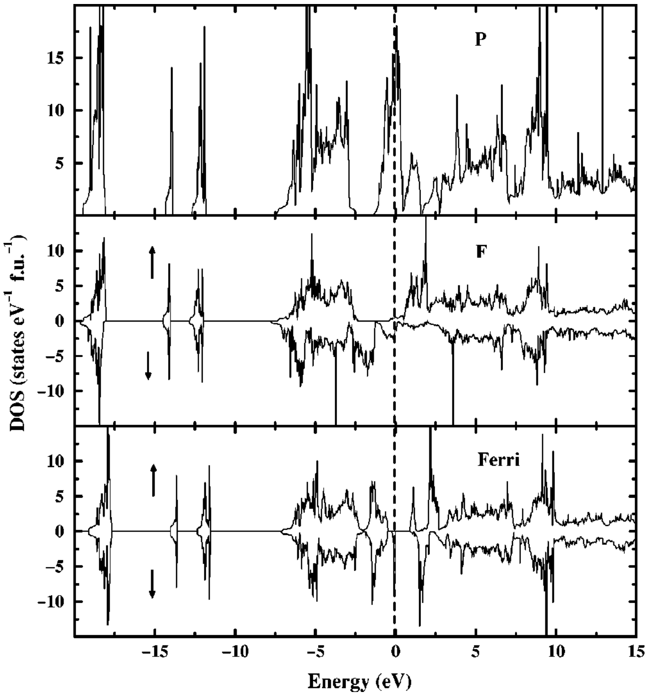

FIG. 3. Total density of states (DOS) for $YBaMn_2O_5$ in para-, ferro-, and ferrimagnetic states.

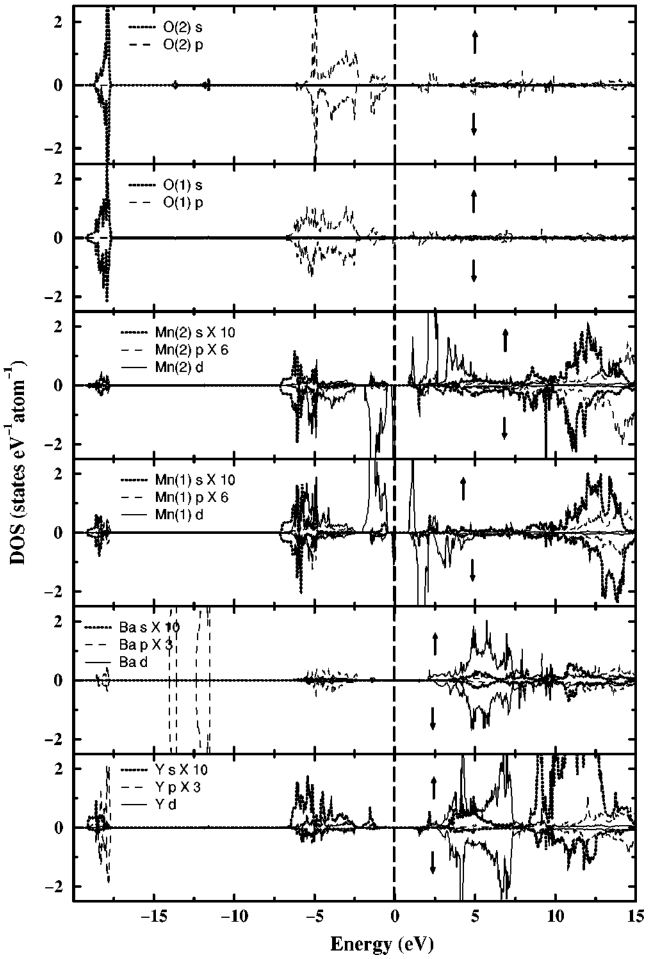

FIG. 4. Site-, spin-, and angular-momentum-decomposed DOS of $YBaMn_2O_5$ in the ferrimagnetic state, obtained by the full-potential LMTO method.

Our calculated total DOS curves for $YBaMn_2O_5$ in the P, F, and Ferri configurations are given in Fig. 3. The highest-occupied energy level in the VB, i.e., E_F, is marked by the dotted line. In the P and F cases finite DOS values are present in the vicinity of E_F. Hence, both the P and F configurations exhibit metallic character. On going from the P to F case, the electrons start to localize which is seen from the reduced number of states at E_F. Due to the electron localization, a gain in total energy of 3.1 eV (Table I) is observed when the spin polarization is included in our calculations. However, in the Ferri case, a finite band gap of 0.88 eV opens up between the top of the VB and the bottom of the CB. The experimental studies also show semiconducting behavior.[12,35] From Table I it can be seen that the Ferri configuration has lower energy than the other two configurations. The present observation of the stabilization of a Ferri ground state in $YBaMn_2O_5$ is consistent with the established magnetic structure.[25] It is interesting to note that the introduction of the Ferri configuration is essential in order to obtain the correct semiconducting state for $YBaMn_2O_5$. Unlike $LaMnO_3$ (where the energy difference between the F and AF cases is ~ 25 meV),[36] there is a large energy difference (~ 0.5 eV) between the Ferri and the F states of $YBaMn_2O_5$. So a very large magnetic field is required to stabilize the F phase and induce insulator-to-metal transition in $YBaMn_2O_5$.

In the RMnO$_3$ phases hole doping induces CE-type magnetic ordering in which the spins are F aligned in zigzag chains with AF coupling between these chains. In $YBaMn_2O_5$, the Mn spins are AF aligned within quasi-one-dimensional chains as well as between the chains. The main difference between $YBaMn_2O_5$ and RMnO$_3$ is that the latter have e_g electrons present in the vicinity of E_F and that the superexchange interaction originates from the localized t_{2g} electrons. Owing to the square-pyramidal crystal field in $YBaMn_2O_5$ both e_g (d_{xy} and d_{z^2} DOS in local coordinates) and t_{2g} (d_{yz}, d_{xz}, and $d_{x^2-y^2}$ DOS in local coordinates) electrons (Fig. 5) get localized and hence both e_g and t_{2g} electrons participate in the superexchange interaction. This is the main reason why the F state has much higher energy than the AF state in $YBaMn_2O_5$ as compared with $LaMnO_3$.

To obtain more insight into the DOS features, we show the angular-momentum-, spin-, and site-decomposed DOS in Fig. 4. The lower panels for Y and Ba show that, in spite of the high atomic numbers for Y and Ba, small DOS values are seen in VB. The Y and Ba states come high up in CB (ca. 4 eV above E_F), indicating a nearly total ionization of these atoms. They lose their valence charge to form ionic bonding with oxygen. According to the crystal structure, Y and Ba are located in layers along c, which is clearly reflected in the electronic charge-density distribution within (100) in the AF configuration (Fig. 6).

The distinction between Mn(1) and Mn(2) is clearly reflected in the different topology of their DOS curves. As seen from Table I, Mn(1) has a smaller magnetic moment

($3.07\mu_B$) than Mn(2) ($3.91\mu_B$) which leads to the conclusion that Mn(1) corresponds to Mn^{3+} and Mn(2) to Mn^{2+}, both in high-spin states. Both Mn(1) and Mn(2) have low-lying DOS features around -17 eV which can be attributed to well-localized *s* and *p* electrons originating from the covalent interaction between Mn $3d$ with O $2s$ and $2p$ states. The somewhat dispersed DOS in the energy region -7.5 to -2.5 eV is attributed to $3d$ electrons for both Mn(1) and Mn(2). As Mn(1) and Mn(2) are AF coupled, their *d*-orbital DOS have opposite character. The localized peaks closer to E_F, with a width of about 2 eV, have both $(3d)$ e_g and t_{2g} character (see below).

The top two panels of Fig. 4 show DOS for O(1) and O(2). Crystallographically O(1) is almost coplanar (in ab) with Mn, whereas O(2) is at the apex of the square pyramid (along c). The well-localized peaks in DOS for O(1) and O(2) at about -18 eV reflect the completely filled $2s$ orbitals. The spread-out DOS features between -7.5 and -0.5 eV are attributed to O $2p$ states. Figure 4 shows that the O $2p$ states are energetically degenerate with Mn $3d$ states in this energy range, implying that these orbitals form covalent bonds with Mn(1) and Mn(2) through hybridization. The presence of a strong covalent interaction between Mn and O in $YBaMn_2O_5$ is confirmed by our charge-density analysis. The almost empty DOS for O(1) and O(2) in the CB implies that the oxygen atoms are in nearly completely ionized states in $YBaMn_2O_5$.

In order to progress further in the understanding of the chemical bonding, charge, spin, and orbital ordering in $YBaMn_2O_5$, we have plotted the orbital-decomposed DOS for the $3d$ orbitals of Mn(1) and Mn(2) in Fig. 5. This illustration shows that DOS for the e_g orbitals (d_{z^2} and d_{xy}) for both Mn(1) and Mn(2) are well localized compared to that of Mn ions in $LaMnO_3$. There is a sharp peak at -5 eV in the up-spin panel for Mn(1) and in the down-spin panel for Mn(2) which correlates with a well-localized peak in DOS for O(2) (Fig. 4) This is attributed to the 180° Mn^{3+}-O(2)-Mn^{2+} bond angle which facilitates p-d σ bond to the O(2) p_z orbital and superexchange interaction.[37] As up-spin Mn(1) and down-spin Mn(2) are participating in the bonding, we infer that the superexchange interaction results in AF spin ordering between the Mn atoms involved. The peaks at ca. 1 eV in up-spin Mn(1) and down-spin Mn(2) are attributed to the (nonbonding) d_{z^2} orbitals.

Since the Mn atoms are surrounded by O atoms in a square-pyramidal arrangement and the Mn(1)-O(1)-Mn(2) bond angle is very much less than 180° (158°), the electron distributions in the e_g orbitals are very different. In particular the d_{z^2} electrons distributed closer to E_F and the d_{xy} electrons are well localized and nearly empty in the top of the VB. From Fig. 4, we see that the O $2p$ orbitals are also situated in the same energy range (-5 to 0 eV) as the d_{xy} orbitals of Mn(1) and Mn(2); thus, these orbitals and O(1) p_x and p_y orbitals form p-d σ bond. As the bond angle Mn(1)-O(1)-Mn2 is only 158°, the strength of this covalent bond is weak and consequently the AF superexchange interaction becomes weakened.[37] Despite the AF superexchange interaction, there is no exact cancellation of the spins of $Mn(1)^{3+}$ and $Mn(2)^{2+}$, and the result is a Ferri state with a finite magnetic moment of $0.85\mu_B$.

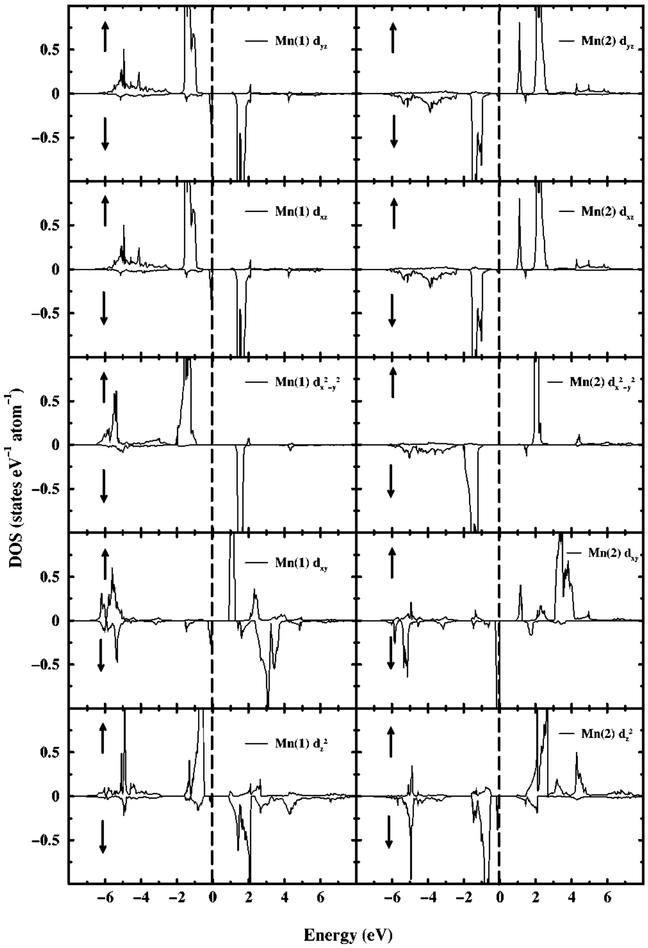

FIG. 5. Orbital (d) decomposed DOS for Mn(1) and Mn(2) in the ferrimagnetic state obtained by the full-potential FLAPW method.

Transition-metal perovskite oxides which exhibit CO like $La_{1-x}Sr_xMnO_3$ have an octahedral crystal field, whereas $YBaMn_2O_5$ has a square-pyramidal arrangement around Mn. In the former case, the t_{2g} electrons are in a well-localized state. But in $YBaMn_2O_5$ the t_{2g} electrons are closer to the E_F. Due to different nature of hybridization between the e_g orbitals and the O $2p$ state, they have a different DOS distribution as shown in Fig. 5. The t_{2g} orbitals (d_{yz}, d_{xz}, and $d_{x^2-y^2}$) of both Mn(1) and Mn(2) are energetically degenerate as clearly seen from the character of the DOS curve. The topology of orbital-projected DOS curves is similar for Mn(1) and Mn(2), except for the d_{xy} orbital. For Mn(1) the d_{xy} orbital has a very small peak at E_F whereas a finite-sized peak is observed for the same orbital of Mn(2). It is indeed the occupancy of this orbital which determines the magnetic moment of Mn(1) and Mn(2). If one considers the Goodenough-Kanamori[39] rules for magnetic interactions in manganese oxides, the expected magnetic order should be *A*-type AF (viz., F ordering within the layers and AF ordering between the layers, arising from superexchange interactions between occupied d_{xy} orbitals on Mn^{2+} and empty d_{xy} on Mn^{3+}). However, owing to the large deviation of the Mn-O-Mn bond angle from 180° along with CO, the d_{xy} orbitals for both Mn species become occupied. Hence, AF ordering is observed between Mn within the planes as well as between the planes (see Fig. 7). One Mn couples AF to its six neighboring Mn in a *G*-type AF arrangement in accordance with experimental findings.[25] Hence, the theoretical calculations have provided the correct ground state with respect to the experiments.

Magnetic susceptibility and magnetization measurements have unequivocally shown that $\mathrm{YBaMn_2O_5}$ is in a Ferri state at low temperature[12,25] with a saturated moment between $0.5\mu_B$ and $0.95\mu_B$ per $\mathrm{YBaMn_2O_5}$ formula unit.[12,25] The theoretically calculated magnetic moments for Mn are $3.07\mu_B$ and $3.93\mu_B$, repectively, giving a net magnetic moment of $0.86\mu_B$ per formula unit for the Ferri state of $\mathrm{YBaMn_2O_5}$. Our theoretically calculated value is less than the predicted (spin-only) value of $1.0\mu_B$. From the DOS analyses, we noted that there is strong hybridization between Mn $3d$ electrons and O $2p$ electrons. A finite magnetic moment of $0.0064\mu_B$/atom and $0.0032\mu_B$/atom are theoretically found to be present at O(1) and O(2), respectively. Hence, we conclude that the slight deviation in the saturated magnetic moment from that predicted by an idealized ionic model can be attributed to the strong hybridization between Mn $3d$ and O $2p$ electrons. We have also performed calculations with the room-temperature structural parameters, confirming that the two manganese atoms possess different magnetic moments at this temperature. In order to understand the role of JT distortion arising from the presence of Mn^{3+} ions in $\mathrm{YBaMn_2O_5}$, it is interesting to study the lattice relaxation effect on the electronic structure and magnetic properties of this material. However, due to the intense computations involved in such studies, it is out of scope of the present investigation.

C. Charge and orbital ordering

For the pseudocubic and layered perovskite manganese oxides, essentially three parameters control the electron-correlation strength and the resultant structural, transport, and magnetic properties:[10] First, the hole-doping level (charge-carrier density or the band-filling level of the CB). In the case of perovskite oxides the substitution of a trivalent rare earth (*R*) by a divalent alkaline earth (*A*) introduces holes in the Mn $3d$ orbitals. Second, the effective one-electron bandwidth (*W*) or equivalently the e_g electron-transfer interaction. The magnitude of *W* is directly determined by the size of the atom at the *R* and *A* sites which makes the Mn-O-Mn bond angle deviate from 180° and thus hinders the electron-transfer interaction. The correlation between CO and the size of the *R* and *A* is studied by several workers and is well illustrated by a phase diagram in Ref. 40. Third comes the dimensionality: the lowering of the electronic dimensionality causes a variety of essential changes in the electronic properties. The carrier-to-lattice coupling is so strong in manganites that the charge-localization tendency becomes very strong. Investigations on the CO state have established an intimate connection to lattice distortion. It seems to be the lattice distortion associated with OO which localizes the charge and thus initiates CO.[40]

In general the ground state of mixed-valent manganite perovskites is either F and metallic or AF and CO. In all CO systems, the magnetic susceptibility drops rapidly at the CO temperature (T_{CO}). CO drastically influences the magnetic correlations in manganites. The effect of the CO state on cooperative magnetic states is to produce insulating behavior. A high magnetic field induces a meltinglike phenomenon of the electron lattice of the CO phase, giving rise to a huge negative magnetoresistance.[41] For these reasons, it is interesting to study CO in $\mathrm{YBaMn_2O_5}$.

Charge localization, which is a prerequisite for CO, is mutually exclusive with an F state according to the double-exchange mechanism. The double-exchange mechanism requires hopping of charge carriers from one Mn to an adjacent Mn via an intervening O. The CO state is expected to become stable when the repulsive Coulomb interaction between carriers dominates over the kinetic energy of the carriers. Hence, CO arises because the carriers are localized at specific long-range-ordered sites below the CO temperature. CO is expected to be favored for equal proportions of Mn^{2+} and Mn^{3+} as in the present case, and in $\mathrm{YBaMn_2O_5}$ it is associated with the AF coupling between Mn in the ab plane. CO depends on the *d*-electron bandwidth and hence it is worth to consider this feature in some detail. On reduction of the Mn-O-Mn angle, the hopping between the Mn $3d$ and O $2p$ orbital decreases and hence the e_g bandwidth decreases. Consequently the system stabilizes in a Ferri-CO-insulating state. Usually the CO-insulating state transforms to a metallic F state on the application of a magnetic field. This may be the reason for the metallic behavior of the F phase found in our calculation. CO in $\mathrm{YBaMn_2O_5}$ is characterized by the real-space ordering of Mn^{2+} and Mn^{3+} species as shown in Figs. 6(a) and 6(b). Our calculations predict that a long-range CO of Mn^{2+} and Mn^{3+} with a rocksalt-type arrangement occurs at low temperatures. This can be viewed as chains of Mn^{2+} and Mn^{3+} running parallel to *b* and correspondingly alternating chains running along *a* and *c* (viz., a checkerboard arrangement of CO as seen from Fig. 7).

Furthermore, there exist orbital degrees of freedom for the Mn $3d$ electrons and OO can lower the electronic energy through the JT mechanism. Therefore, mixed-valent manganites can have OO in addition to CO.[42] OO gives rise to the anisotropy in the electron-transfer interaction. This favors or disfavors the double-exchange interaction and the (F or AF) superexchange interaction in an orbital-dependent manner and hence gives a complex spin-orbital-coupled state. Therefore, it is also interesting to study OO in some detail. Figures 6(a) and 6(b) show the electron charge density of $\mathrm{YBaMn_2O_5}$ in bc (100) and ab (001) planes, respectively. As the electron-charge density is plotted in the energy range where the $3d$ orbitals reside, the shape of the d_{z^2} and $d_{x^2-y^2}$ orbitals are well reproduced in Figs. 6(a) and 6(b), respectively. The transfer integral between the two neighboring Mn atoms in the crystal lattice is determined by the overlap between the $3d$ orbitals with the $2p$ orbital of O atom. In the

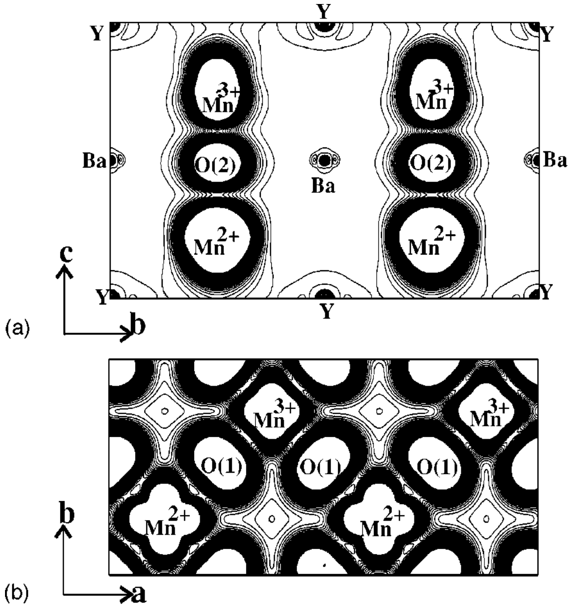

FIG. 6. Charge density distribution of $YBaMn_2O_5$ in (a) bc (100) and (b) ab (001) plane. Here 40 contours are drawn between 0 and 0.02 electrons/ a.u.^{3} The charge density is calculated in the energy range -4.57 eV to -3.42 eV in the bc plane and -9.37 eV to -3.82 eV in the ab plane in order to visualize the Mn $3d$ electrons.

bc plane the d_{z^2} orbital is ordered along c for both Mn(1) and Mn(2); this orbital hybridizes with the O(1) p_z orbital, resulting in a p-d σ bond. The finite electron density present within Mn(1)-O(2)-Mn(2) illuminates the path for the AF superexchange interaction between them. When the size of the R and A becomes smaller the one-electron bandwidth (or e_g electron-transfer interaction) decreases in value.[40] For Y^{3+} with an ionic radius of 1.25 Å [smaller than other R's like La^{3+} (1.36 Å) (Ref. 38)] the Mn(1)-O(1)-Mn(2) angle is much less than 180° so the e_g-electron bandwidth is small compared with the t_{2g}-electron bandwidth.

The overlap between the $d_{x^2-y^2}$ and p_z orbitals is zero because of their different orientation in the ab plane. Therefore, the electron in the $d_{x^2-y^2}$ orbital cannot hop along c.[37] Also the direct overlap between O $p_{x,y}$ and Mn d is minimal in the ab plane and hence the d electrons get localized and cause CO and OO. Owing to the fact that the Mn(1)-O(1) bond length is 1.908 Å compared with 2.086 Å for Mn(2)-O(1), more electronic charge is present on Mn^{2+} than on Mn^{3+}. This is visible in the orbital decomposed DOS (Fig. 5), where the d_{xy} orbital of Mn^{2+} has more states (electrons) than that of Mn^{3+}.

PND (Ref. 25) indicates that Mn^{3+} has the occupied d_{z^2} orbital extending along [001], whereas the unoccupied $d_{x^2-y^2}$ orbital extends along [110] and $[1\bar{1}0]$. A corresponding OO could be expected for Mn^{2+} with both d_{z^2} and $d_{x^2-y^2}$ orbitals occupied. Our detailed electronic structure studies show that both d_{z^2} and $d_{x^2-y^2}$ orbitals are partially occupied for Mn^{2+} as well as Mn^{3+} as shown in Fig. 5. On the other hand, according to our charge-density analysis [Figs. 6(a) and 6(b)] the d_{z^2} orbital is ordered along the bc plane and $d_{x^2-y^2}$ orbital order along the ab plane for Mn(1) and Mn(2) (Fig. 7), which is consistent with experimental findings. Both d_{z^2} and $d_{x^2-y^2}$ orbitals are aligned in the same orientation within the layer as well as between the layers as shown in Fig. 7. So this type of OO is named F type.

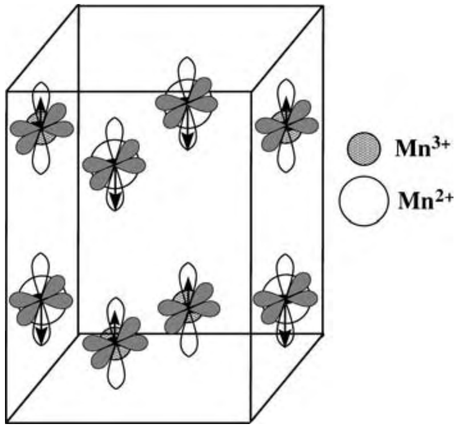

FIG. 7. Schematic diagram showing the checkerboard-type charge order (CO), F-type orbital order (OO), and G-type ferrimagnetic spin order (SO) of Mn in $YBaMn_2O_5$.

D. Optical properties

Further insight into the electronic structure can be obtained from the calculated interband optical functions. It has been earlier found that the calculated optical properties for SnI_2, $NaNO_2$, and MnX (X=As, Sb, Bi) (Refs. 44–46) are in excellent agreement with the experimental findings, and we have therefore used the same theory to predict the optical properties of $YBaMn_2O_5$. Since this material possesses unique Ferri ordering and semiconducting behavior along with a uniaxial crystal structure, it may find application in optical devices. Yet another reason for studying the optical properties is that it has been experimentally established[43] that the optical anisotropy of $Pr_{0.6}Ca_{0.4}MnO_3$ is drastically reduced above T_{CO}. It is therefore expected that the optical anisotropy will provide more insight into CO and OO in $YBaMn_2O_5$. For $YBaMn_2O_5$ with its tetragonal crystal structure, the optical spectrum is conveniently resolved into two principal directions $E\|a$ and $E\|c$, viz., with the electric field vector polarized along a and c, respectively. In the topmost panel of Fig. 8, the dispersive part of the diagonal elements of the dielectric tensor are given. The anisotropy in the dielectric tensor is clearly seen in this illustration.

In the second panel of Fig. 8, the polarized ϵ_2 spectra are shown. The spectra corresponding to $E\|a$ and $E\|c$ differ from one another up to ca. 10 eV whereas less difference is noticable in the spectra above 10 eV. Since there is a one-to-one correspondance between the interband transitions and band structures (discussed in Sec. IV A), we investigate the origin of the peaks in the ϵ_2 spectrum with the help of our calculated band structure. As $YBaMn_2O_5$ stabilizes in the Ferri state, the VB has an unequal number of bands in the up- and down-spin channels (Fig. 2), viz., 36 bands in the former and 38 in the latter. The two extra bands of the down-spin channel closer to E_F in the VB play an important role in

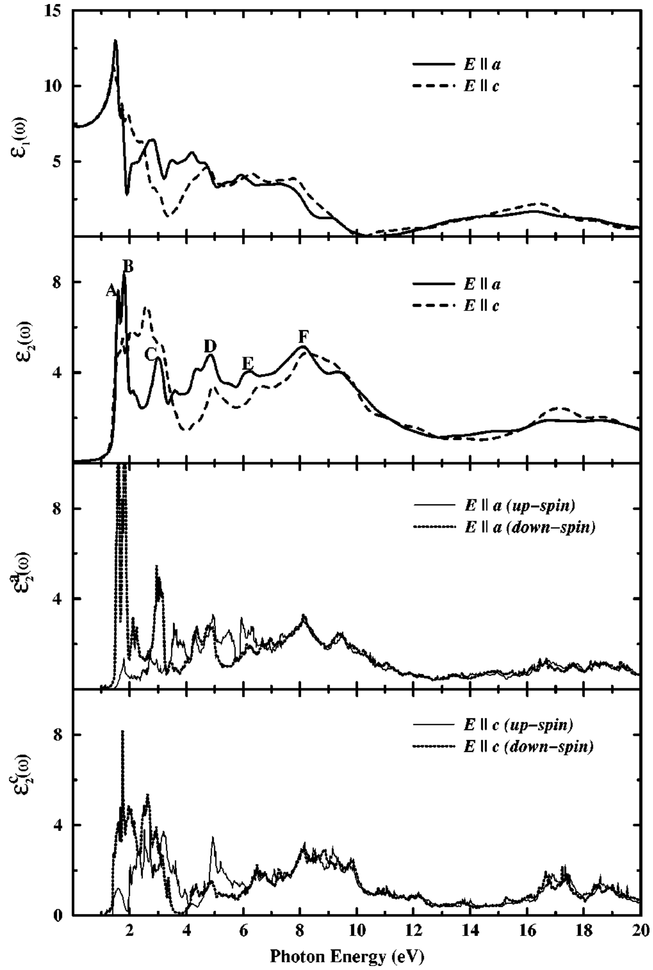

FIG. 8. Imaginary and real parts of the optical dielectric tensor of $YBaMn_2O_5$ are given in the first and second panels, respectively (note that the spectra are broadened). The spin-projected imaginary part of dielectric tensor along *a* and *c* directions are given in third and fourth panels, respectively.

the transitions as discussed below. We name the topmost band of the VB as No. 38 and bottommost band of the CB as No. 39. The lowest-energy peak *A* results from interband transitions [Nos. 35–41, mostly O(1) $2p$ to Mn(2) d_{z^2}, and Nos. 35–39, mostly Mn(1) d_{z^2} to Mn(2) $4p$] and peak *B* results from transitions (Nos. 38–48 and 36–49, mostly Mn $3d$ to Mn $4p$). Peak *C* originates from many transitions, including O $2p$ to Mn $3d$, Y $5s$ to Y $5p$, etc. Peaks *D*, *E*, and *F* are contributed by several transitions including O $2p$ to Mn $3d$ and Y $5s$ to Y $5p$. Further, a very small peak is present in the higher-energy region (~ 17 eV) of ϵ_2 which is due to transitions from lower-lying occupied levels to higher-lying unoccupied levels. The accumulation of broad Y $4d$ and Ba $5d$ bands in the high-energy part of the CB results in very little structure in the higher-energy part of the optical spectra. The optical gaps for $E\|a$ and $E\|c$ are approximately the same indicating that the effective intersite Coulomb correlation is the same for the in-plane and out-of-plane orientations for the Ferri phase. This can be traced back to the *G*-type Ferri coupling in this material.

In order to understand the origin of the optical anisotropy in $YBaMn_2O_5$ we have also made optical property calculations for the F phase, which show that (in contrast to the Ferri phase) the ϵ_2 spectrum for $E\|a$ is shifted some 3.5 eV to higher values than $E\|c$. Further, the ϵ_2 components of $E\|c$ for the F phase is much smaller than that for the Ferri phase, indicating that the large optical anisotropy in $YBaMn_2O_5$ is originating from the *G*-type Ferri ordering.

To emphasize the above finding, we have also plotted the spin-projected ϵ_2 spectra along the a $[\epsilon_2^a(\omega)]$ and c $[\epsilon_2^c(\omega)]$ directions (third and fourth panels of Fig. 8, respectively). Although the optical gap is approximately same for $E\|a$ and $E\|c$ in the ϵ_2 spectrum, there is a finite difference in the optical gaps related to up- and down-spin electrons in the $\epsilon_2^a(\omega)$ and $\epsilon_2^c(\omega)$ spectra. The optical gap for the down-spin case is smaller than that for up-spin case owing to the presence of the two narrow bands very close to E_F in the down-spin channel of the VB. There is a large difference between the spectra for up and down spins up to ca. 7 eV. The $\epsilon_2^a(\omega)$ spectrum resulting from the up-spin states has somewhat more dispersed peaks than that from down-spin states. The $\epsilon_2^a(\omega)$ spectrum resulting from the down-spin states has four well-defined peaks: two prominent peaks in the region 1.75–2 eV and two additional peaks at ca. 2.25 and 3 eV. The magnitude of the down-spin peaks are higher than those of the up-spin peaks in the $\epsilon_2^a(\omega)$ spectrum. The $\epsilon_2^c(\omega)$ spectrum originating from up- and down-spin states have appreciable differences up to ca. 6 eV. The down-spin part has two well-defined peaks at ca. 1.75 and 2.75 eV. The up-spin part has dispersed peaks of lower magnitude than the down-spin part, the magnitude of the up-spin peaks in $\epsilon_2^c(\omega)$ being generally higher than in $\epsilon_2^a(\omega)$. The optical anisotropy is noticeable in the direction- as well as spin-resolved ϵ_2 spectra. Hence, it is verified that the optical anisotropy originates both from crystal-field effects as well as from the Ferri ordering. As the reflectivity, absorption coefficient, and refractive index are often subjected to experimental studies, we have calculated these quantities and reproduced them in Fig. 9. We now advertice for experimental optical studies on $YBaMn_2O_5$.

E. XANES studies

X-ray absorption spectroscopy (XAS) has developed into a powerful tool for the elucidation of the geometric and electronic structure of amorphous and crystalline solids.[47] X-ray absorption occurs by the excitation of core electrons, which makes this technique element specific. Although the XANES only provides direct information about the unoccupied electronic states of a material, it gives indirect information about the valence of a given atom in its particular environment and about occupied electronic states. This is because the unoccupied states are affected by the occupied states through interaction with the neighbors.

The oxygen atoms are in two different chemical environments in $YBaMn_2O_5$ as clearly seen in PDOS in Fig. 4. The calculated *K*-edge spectra for O(1) and O(2) shown in Fig. 10 involve transition from the $1s$ core state to the unoccupied p state. In this context the Mn *K* edge mainly probes the

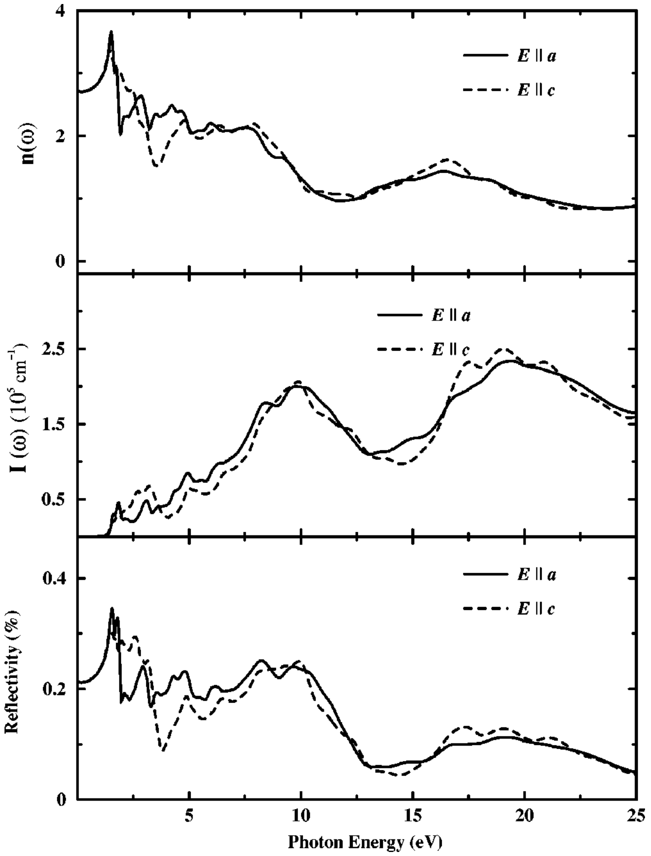

FIG. 9. Calculated reflectivity spectra, absorption coefficient $[(I(\omega)$ in 10^5 $\mathrm{cm}^{-1})]$ and refractive index $[n(\omega)]$ along *a* and *c* for $\mathrm{YBaMn_2O_5}$.

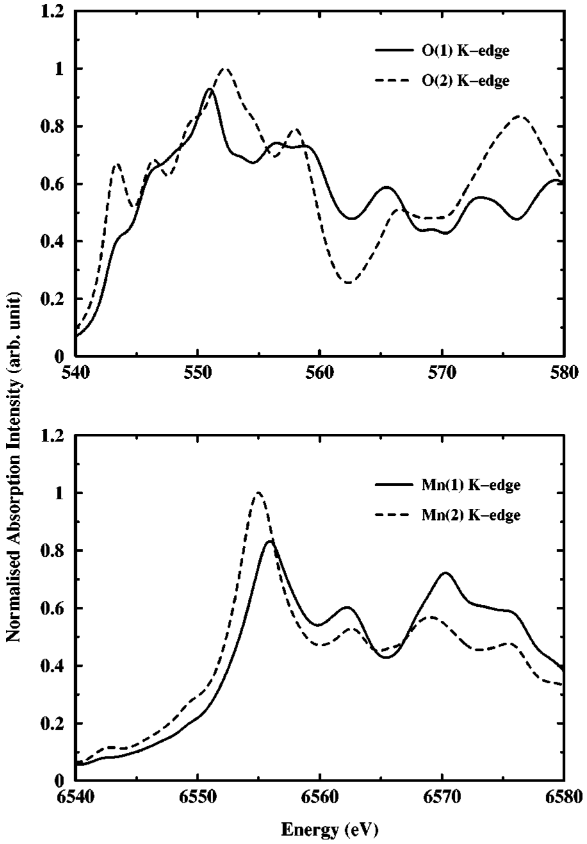

FIG. 10. Calculated *K*-edge spectra for Mn(1) and Mn(2) as well as O(1) and O(2) of $\mathrm{YBaMn_2O_5}$.

unoccupied Mn 4*p* states. It is generally accepted that O *K*-edge spectra are very sensitive to the local structure of transition-metal oxides as documented for $\mathrm{Fe_2O_3}$ (Ref. 48) and $\mathrm{TiO_2}$ (Ref. 49). The *K*-edge spectra for O(1) and O(2) (Fig. 10) show appreciable differences throughout the whole energy range. In particular there are two peaks appearing in the O(2) spectrum between 540 and 550 eV that are absent for O(1). Within 3 Å, 2 Mn, 2 Y, and 6 O surround O(1) whereas, 2 Mn, 4 Ba, and 5 O surround O(2). It is this different chemical environment which causes the differences in the *K*-edge XANES spectra of O(1) and O(2).

$\mathrm{YBaMn_2O_5}$ contains Mn in the valence states Mn^{3+} and Mn^{2+} which, as discussed in Sec. IV C, experience CO. An experimental technique to visualize CO is not available. In order to visualize the presence of different oxidation states for Mn, we have theoretically calculated the XANES *K*-edge spectra for Mn(1) and Mn(2) and presented them in Fig. 10. Both Mn atoms are seen to have four peaks within the energy range considered, reflecting that both are surrounded by five O within 2.08 Å. However, owing to the different valence states, there are intensity differences as well as energy shifts (some 1 eV) of these peaks. For example, the lower-energy peak has large intensity in the Mn(2) *K*-edge spectrum compared with that for Mn(1). On the contrary, the three higher-energy peaks in the Mn(2) *K*-edge spectrum are less intense than in the Mn(1) *K*-edge spectrum. When experimental XANES spectra become available for $\mathrm{YBaMn_2O_5}$ the above features should be able to confirm the two different valence states for Mn.

F. Hyperfine parameters

The calculation of hyperfine parameters is useful to characterize different atomic sites in a given material. Many experimental techniques such as Mössbauer spectroscopy, nuclear magnetic and nuclear quadrupole resonance, and perturbed angular correlation measurements are used to measure hyperfine parameters. Hyperfine parameters describe the interaction of a nucleus with electric and magnetic fields created by its chemical environment. The resulting splitting of nuclear energy levels is determined by the product of a nuclear and an extra-nuclear quantity. In the case of quadrupole interactions, it is the nuclear quadrupole moment that interacts with the electric field gradient (EFG) produced by the charges outside the nucleus.[50] The EFG is a ground-state property of a material which depends sensitively on the asymmetry of the electronic charges. The direct relation of the EFG and the asphericity of the electron density in the vicinity of the probe nucleus enables one to estimate the quadrupole splitting and the degree of covalency or ionicity of the chemical bonds provided the nuclear quadrupole moment is known. Quantities describing hyperfine interactions (e.g., EFG and isomer shift) are widely studied nowadays both experimentally and theoretically.

TABLE II. Calculated (FLAPW method) principal component of the electric field gradient (EFG) V_{zz} in units of 10^{21} V/m^2 and the Fermi contact hyperfine field (HFF) in kG at the atomic sites in ferro- and ferrimagnetic configurations.

	Ferromagnetic		Ferrimagnetic	
Atom	EFG	HFF	EFG	HFF
Y	0.17	45.90	0.48	21.01
Ba	10.50	−19.24	10.08	38.85
Mn(1)	2.41	−73.36	0.09	−179.54
Mn(2)	−0.98	−210.98	1.01	318.79
O(1)	5.36	64.42	4.95	−42.59
O(2)	3.86	97.06	5.06	21.96

Blaha *et al.*[51] have showed that the linear augmented plane wave (LAPW) method is able to predict EFG's in solids with high precision. The charge distribution of complex materials such as $YBa_2Cu_3O_7$, $YBa_2Cu_3O_{6.5}$, and $YBa_2Cu_3O_6$ has been studied theoretically by Schwarz *et al.*[52] by this approach. In this study, we have attempted to establish the different valence states of Mn in $YBaMn_2O_5$ with the help of the EFG and the hyperfine field calculated using the FPLAPW method as embodied in the WIEN97 code.[30]

The total hyperfine field (HFF) can be decomposed in three terms: a dominant Fermi contact term, a dipolar term, and an orbital contribution. We limit our consideration to the contact term, which in the nonrelativistic limit is derived from the spin densities at the nuclear site:

$$H_c=\frac{8}{3}\pi\mu_B^2[\rho_\uparrow(0)-\rho_\downarrow(0)]. \tag{7}$$

The EFG is defined as the second derivative of the electrostatic potential at the nucleus, written as a traceless tensor. This tensor can be obtained from an integral over the nonspherical charge density $\rho(r)$. For instance the principal component V_{zz} is given by

$$V_{zz}=\int d^3r\rho(\mathbf{r})\frac{2P_2(\cos\theta)}{r^3}, \tag{8}$$

where P_2 is the second-order Legendre polynomial. A more detailed description of the calculation of the EFG can be found elsewhere.[53]

The calculated EFG and HFF at the atomic sites in $YBaMn_2O_5$ are given in Table II which confirm that there is a finite difference in the value of both the EFG and HFF between the two Mn atoms. So we can conclude that their charge distribution is quite different. The higher value of the EFG and HFF in Mn^{2+} than in Mn^{3+} is justified because more charge is found on the latter. This can be seen from the orbital-projected DOS as well as from the magnetic moments possessed by the two ions. The HFF for Mn^{3+} in $LaMnO_3$ is found to be −198 kG,[36] which is quite close to −179 kG found for Mn^{3+} in our case. Consequently we substantiate that Mn(1) corresponds to Mn^{3+}. The two oxygen ions also differ mutually in their values for the EFG and HFF (Table II), suggesting that the strength of the covalent bond formed by them with Mn(1) and Mn(2) is different.

V. SUMMARY

Like hole-doped $RMnO_3$-based CMR materials $YBaMn_2O_5$ also carries mixed-valence states of manganese, ferrimagnetic ordering, and charge ordering and apparently undergoes a combined insulator-to-metal and ferrimagnetic-to-ferromagnetic transition. Hence $YBaMn_2O_5$ may be a potential CMR material which deserves more attention.

We have made a detailed investigation of the electronic properties of $YBaMn_2O_5$ using the full-potential LMTO method as well as the full-potential LAPW method and conclude the following.

(i) The *G*-type ferrimagnetic semiconducting state is found to be the ground state in accordance with experimental findings.

(ii) The existence of the two different types of Mn atoms is visualized by differences in site- and orbital-projected DOS curves. In order to further emphasize the different valence states of Mn, we have calculated *K*-edge XANE spectra. For Mn as well as O the existence of two types of valence-induced atomic species is established with the help of *K*-edge spectra.

(iii) The occurrence of checkerboard-type charge ordering and F-type orbital ordering is seen from the charge-density plots. The small size of Y^{3+} makes the Mn-O-Mn bond angle deviate from 180°, which in turn imposes a reduction in the e_g bandwidth. The charge- and orbital-ordering features are believed to result from this perturbation of the e_g orbitals.

(iv) As $YBaMn_2O_5$ is a ferrimagnetic semiconductor, it is useful to probe its optical properties for potential applications. We have analyzed the interband contributions to the optical properties with the help of the calculated electronic band structure features. We found large anisotropies in the optical spectra originating from ferrimagnetic ordering and the crystal field splitting. No experimental optical study of $YBaMn_2O_5$ is hitherto available.

(v) Hyperfine parameters such as hyperfine field and electric field gradients have also been calculated showing very large differences in the computed values for the crystallographically different manganese and oxygen atoms. This substantiates that Mn exists in two different valence states in $YBaMn_2O_5$.

ACKNOWLEDGMENTS

This work has received support from The Research Council of Norway (Program for Supercomputing) through a grant of computing time. R.V. wishes to thank Professor John Wills, Professor Peter Blaha, and Professor Karlheinz Schwarz for supplying their computer codes used in this study and Professor Olle Eriksson for useful communications. R.V. kindly acknowledges Professor L. Veseth and P. Vajeeston for useful discussions.

*Electronic address: ravindran.vidya@kjemi.uio.no

[1] A. Fujimori, T. Mizokawa, and T. Saitoh, in *Colossal Magnetoresistance, Charge Ordering and Related Properties of Manganese Oxides*, edited by C.N.R. Rao and B. Reveau (World Scientific, Singapore, 1998), p. 279.

[2] R. Mahendiran, A.K. Raychaudhuri, A. Chainani, D.D. Sarma, and S.B. Ray, Appl. Phys. Lett. **66**, 233 (1995).

[3] J.Z. Liu, I.C. Chang, S. Irons, P. Klavins, R.H. Shelton, K. Song, and S.R. Wasserman, Appl. Phys. Lett. **66**, 3218 (1995).

[4] G.Q. Gong, C. Canedy, G. Xiao, J.Z. Sun, A. Gupta, and W.J. Gallagher, Appl. Phys. Lett. **67**, 1783 (1995).

[5] V. Caignaert, A. Maignan, and B. Raveau, Solid State Commun. **95**, 357 (1995).

[6] N. Furukawa, J. Phys. Soc. Jpn. **63**, 3214 (1994); Y. Tokura, A. Urushibara, Y. Moritomo, T. Arima, A. Asamitsu, G. Kido, and N. Furukawa, *ibid.* **63**, 3931 (1994).

[7] A.J. Millis, P.B. Littlewood, and B.I. Shraiman, Phys. Rev. Lett. **74**, 5144 (1995).

[8] M.A. Dixon, Physica C **174**, 117 (1991).

[9] J.B. Torrance, A. Bezinge, A.I. Nazzal, T.C. Huang, S.S.P. Parkin, D.T. Keane, S.L. La Placa, P.M. Horn, and G.A. Held, Phys. Rev. B **40**, 8872 (1989).

[10] H. Kuwahara and Y. Tokura, in *Colossal Magnetoresistance, Charge Ordering and Related Properties of Manganese Oxides* (Ref. 1), p. 217.

[11] Y. Moritomo, A. Asamitsu, H. Kuwahara, and Y. Tokura, Nature (London) **380**, 141 (1996).

[12] J.P. Chapman, J.P. Attfield, M. Mölgg, C.M. Friend, and T.M. Beales, Angew. Chem. Int. Ed. Engl. **35**, 2482 (1996).

[13] T. Vogt, P.M. Woodward, P. Karen, B.A. Hunter, P. Henning, and A.R. Moodenbaugh, Phys. Rev. Lett. **84**, 2969 (2000).

[14] Y. Tokura and N. Nagaosa, Science **288**, 462 (2000).

[15] C. Martin, A. Maignan, D. Pelloquin, N. Nguyen, and B. Raveau, Appl. Phys. Lett. **71**, 1421 (1997).

[16] V.I. Anisimov, I.S. Elfimov, M.A. Korotin, and K. Terakura, Phys. Rev. B **55**, 15 494 (1997).

[17] W. Koshibae, Y. Kawamura, S. Ishihara, and S. Okomoto, J. Phys. Soc. Jpn. **66**, 957 (1997).

[18] T. Mizokawa and A. Fujimori, Phys. Rev. B **56**, R493 (1997).

[19] J. Lee, J. Yu, and K. Terakura, J. Korean Phys. Soc. **33**, S55 (1998).

[20] I. Solovyev, N. Hamada, and K. Terakura, Phys. Rev. Lett. **76**, 4825 (1996).

[21] J.D. Lee and B.I. Min, Phys. Rev. B **55**, R14 713 (1997).

[22] P. A. Cox, *Transition Metal Oxides* (Clarendon, Oxford, 1992); E.J.W. Verwey and P.W. Haayman, Physica (Amsterdam) **8**, 979 (1941).

[23] J. Linden, P. Karen, A. Kjekshus, J. Miettinen, T. Pietari, and M. Karppinen, Phys. Rev. B **60**, 15 251 (1999).

[24] J.A. McAllister and J.P. Attfield, Mater. Sci. Forum **278-281**, 744 (1998).

[25] F. Millange, E. Suard, V. Caignaert, and B. Raveau, Mater. Res. Bull. **34**, 1 (1999).

[26] J. M. Wills (unpublished); J.M. Wills and B.R. Cooper, Phys. Rev. B **36**, 3809 (1987); D.L. Price and B.R. Cooper, *ibid.* **39**, 4945 (1989).

[27] O.K. Andersen, Phys. Rev. B **12**, 3060 (1975).

[28] D.J. Chadi and M.L. Cohen, Phys. Rev. B **8**, 5747 (1973); S. Froyen, *ibid.* **39**, 3168 (1989).

[29] J. P. Perdew, in *Electronic Structure of Solids*, edited by P. Ziische and H. Eschrig (Akademie Verlag, Berlin, 1991), p. 11; J.P. Perdew, K. Burke, and Y. Wang, Phys. Rev. B **54**, 16 533 (1996); J.P. Perdew, K. Burke, and M. Ernzerhof, Phys. Rev. Lett. **77**, 3865 (1996).

[30] P. Blaha, K. Schwarz, and J. Luitz, computer code WIEN97, Vienna University of Technology, 1997 [an improved and updated Unix version of the original copyrighted code published by P. Blaha, K. Schwarz, P.I. Sorantin, and S.B. Trickey, Comput. Phys. Commun. **59**, 399 (1990)].

[31] D. Singh, Phys. Rev. B **43**, 6388 (1991).

[32] P.E. Blöchl, O. Jepsen, and O.K. Andersen, Phys. Rev. B **49**, 16 223 (1994).

[33] N.V. Smith, Phys. Rev. B **3**, 1862 (1971).

[34] M. Alouani and J.M. Wills, Phys. Rev. B **54**, 2480 (1996).

[35] T.P. Beales, M. Mölgg, J. Jutson, and C.M. Friend, Phys. Status Solidi A **161**, 271 (1997).

[36] P. Ravindran, A. Kjekshus, H. Fjellvågr, A. Delin, and O. Eriksson, Phys. Rev. B **65**, 064445 (2002).

[37] J.B. Goodenough, *Magnetism and the Chemical Bond* (Wiley, New York, 1963).

[38] H. Sawada and K. Terakura, Phys. Rev. B **58**, 6831 (1998).

[39] J.B. Goodenough, Phys. Rev. **100**, 564 (1955); J. Kanamori, J. Phys. Chem. Solids **10**, 87 (1959).

[40] C.N.R. Rao and A. K. Raychauduri, in *Colossal Magnetoresistance, Charge Ordering and Related Properties of Manganese Oxides* (Ref. 1), p. 1.

[41] Y. Tokura, H. Kuwahara, Y. Moritomo, Y. Tomioka, and A. Asamitsu, Phys. Rev. Lett. **76**, 3184 (1996).

[42] S.-W. Cheong, in *Colossal Magnetoresistance, Charge Ordering and Related Properties of Manganese Oxides* (Ref. 1), p. 241.

[43] Y. Okimoto, Y. Tomioka, Y. Onose, Y. Otsuka, and Y. Tokura, Phys. Rev. B **57**, R9377 (1998).

[44] P. Ravindran, A. Delin, R. Ahuja, B. Johansson, S. Auluck, J.M. Wills, and O. Eriksson, Phys. Rev. B **56**, 6851 (1997).

[45] P. Ravindran, A. Delin, B. Johansson, O. Eriksson, and J.M. Wills, Phys. Rev. B **59**, 1776 (1999).

[46] P. Ravindran, A. Delin, P. James, B. Johansson, J.M. Wills, R. Ahuja, and O. Eriksson, Phys. Rev. B **59**, 15 680 (1999).

[47] P. Behrens, TrAC, Trends Anal. Chem. **11**, 218 (1992).

[48] J.H. Paterson and O.L. Krivanek, Ultramicroscopy **32**, 313 (1990).

[49] V.S. Lusvardi, M.A. Barteau, J.G. Chen, J. Eng Jr., and A.V. Teplyakov, Surf. Sci. **397**, 237 (1998).

[50] H.M. Petrilli, P.E. Blöchl, P. Blaha, and K. Schwarz, Phys. Rev. B **57**, 14 690 (1998).

[51] P. Blaha, K. Schwarz, and P. Herzig, Phys. Rev. Lett. **54**, 1192 (1985).

[52] K. Schwarz, C. Ambrosch-Draxl, and P. Blaha, Phys. Rev. B **42**, 2051 (1990).

[53] P. Blaha, K. Schwarz, and P.H. Dederichs, Phys. Rev. B **37**, 2792 (1988); C. Ambrosch-Draxl, P. Blaha, and K. Schwarz, **44**, 5141 (1991); K. Schwarz and P. Blaha, Z. Naturforsch., A: Phys. Sci. **47**, 197 (1992).

II

PHYSICAL REVIEW B **69**, 092405 (2004)

Effect of oxygen stoichiometry on spin, charge, and orbital ordering in manganites

R. Vidya,* P. Ravindran, P. Vajeeston, A. Kjekshus, and H. Fjellvåg
Department of Chemistry, University of Oslo, P.O. Box 1033 Blindern, N-0315 Oslo, Norway

(Received 8 September 2003; published 18 March 2004)

Using full-potential density-functional calculations we show that oxygen stoichiometry plays an important role on spin, charge, and orbital ordering in manganites. The electronic structure and magnetic properties of $LaBaMn_2O_{5+\delta}$ have been studied for $\delta = 0$, 0.5, and 1; for $\delta = 0$ and 0.5 the system exhibits charge, orbital, and antiferromagnetic spin ordering, whereas at $\delta = 1$ the charge and orbital orderings disappear but the spin ordering remains. We also bring out an insulator-to-metal transition upon going from $\delta = 0$ to 1. The study suggests that one can manipulate the charge and orbital orderings in certain perovskite-like oxides by merely varying the oxygen stoichiometry and hence design oxides with desired electrical and magnetic properties.

DOI: 10.1103/PhysRevB.69.092405 PACS number(s): 71.15.Nc, 71.20.−b, 81.05.Je, 81.40.Rs

There has been an upsurge of interest in perovskite-like manganese-based oxides since the discovery of colossal magnetoresistance (CMR). The CMR manganites display a fascinating diversity of behaviors including several forms of spin, charge, and orbital orderings (hereafter SO, CO, and OO).[1] The electronic, magnetic, and CMR features of a given material are largely determined by the chemical composition and crystal structure and these properties may be quite sensitive to even tiny changes in the atomic architecture. Hence an improved understanding of how composition and structure affect transport and magnetism and this may guide the search for new CMR materials.[2]

The interplay between the crystal symmetry and the atomic orbitals plays a crucial role in the conductivity of the e_g electrons in manganites. The transfer integral (t) of e_g electrons between neighboring Mn sites is mediated by the O-2p orbitals and hence depends on the degree of hybridization between Mn-3d and O-2p orbitals. The substitution of divalent cations on the A site of $REMnO_3$ (RE stands for rare earth) perovskites (e.g., the parent CMR material $LaMnO_3$) induces holes in the e_g band. Many studies have addressed the effect of A-site-substituted cations on SO, CO, and OO. Although it is well known that the long-range CO and the transfer efficiency of CMR materials are very sensitive to the oxygen stoichiometry, a complete picture of the role of the oxygen content and localization is lacking. In an attempt to partly remedy this situation we have studied the SO, CO, and OO in the model system $LaBaMn_2O_{5+\delta}$ ($\delta = 0$, 0.5, and 1). In addition to a significant CMR effect, ferromagnetic ordering (viz., T_C) close to room temperature is considered essential for technological applications of manganites. Ba-substituted $LaMnO_3$ offers interesting features[3] with T_C near room temperature and large resistance changes just above [e.g., $T_C \approx 362$ K (Ref. 4) for $La_{0.65}Ba_{0.35}MnO_3$]. Hence the studies on $LaBaMn_2O_{5+\delta}$ may prove to be of basic as well as applied scientific interest.

$LaBaMn_2O_5$ crystallizes in the tetragonal double-perovskite-type structure[3] [space group $P4/nmm$, see Fig. 1(a)]. It consists of double layers of apex-sharing MnO_5 pyramids interleaved by oxygen-empty layers (Ba^{2+} are in the oxygen-apical layers and La^{3+} in the oxygen-empty layers). The Mn-O distances in the polyhedra are influenced by the size difference between La^{3+} and Ba^{2+} owing to their arrangement along c. Two crystallographic types of Mn and O atoms are present and reflected in different O-Mn-O angles (apical $= 161°$; equatorial $= 180°$). $LaBaMn_2O_{5.5}$ is orthorhombic[5] [space group $Ammm$; see Fig. 1(c)]. The additional oxygen atoms for $\delta = 0.5$ are at the oxygen-empty layers of the $LaBaMn_2O_5$-type variant. Hence $LaBaMn_2O_{5.5}$ has square pyramidal [around Mn(1)] as well as octahedral [around Mn(2)] coordinations of Mn. $LaBaMn_2O_6$ also has a tetragonal structure[3] [space group $P4/mmm$; see Fig. 1(e)]. The added oxygen atoms complete the conversion from square pyramidal coordination around Mn(1) at $\delta = 0$ to octahedral at $\delta = 1$. The interesting aspect of $LaBaMn_2O_{5+\delta}$ is that the arrangement of La^{3+} and Ba^{2+} remains unchanged, hence the similarity between the three structures is reinforced.

We have calculated the total energy of $LaBaMn_2O_{5+\delta}$ in the para- (P), ferro- (F), and antiferromagnetic (AF) configurations for the experimentally reported structural parameters. The full-potential linear muffin-tin orbital (FPLMTO) calculations[6] presented in this paper are all-electron, and no shape approximation to the charge density or potential has been used. The basis set is comprised of augmented linear muffin-tin orbitals.[7] The calculations are based on the generalized-gradient-corrected (GGA) density-functional theory as proposed by Perdew *et al.*[8] Spin-orbit coupling is included directly in the Hamiltonian matrix elements for the part inside the muffin-tin spheres. We used a multibasis in order to ensure a well-converged wave function, i.e., several Hankel or Neumann functions, each attached to its own radial function, have been used. Hence the basis included are $6s$, $6p$, $5p$, $5d$, and $4f$ orbitals for La and Ba, $4s$, $4p$, and $3d$ orbitals for Mn, and $2s$, $2p$, and $3d$ orbitals for O. The spherical-harmonic expansion of the charge density, potential and basis functions was performed up to $\ell_{max} = 6$. For the total-energy study the **k**-space integration is done using the special point method with 192 **k** points in the irreducible part of the first Brillouin zone. For the F and AF calculations, the magnetization axes are chosen in accordance with experimental findings.[3,5] In the AF calculation for $LaBaMn_2O_{5.5}$, an explicit supercell with 38 atoms is considered. In order to verify the results obtained from the FPLMTO method and to calculate the occupation matrix of each of the Mn-3d orbitals, we have done similar calculations by the full-potential linearized-augmented plane-wave (FPLAPW) method as implemented in WIEN97.[9] Atomic-sphere radii of 2.8 a.u.

0163-1829/2004/69(9)/092405(4)/$22.50 ©2004 The American Physical Society

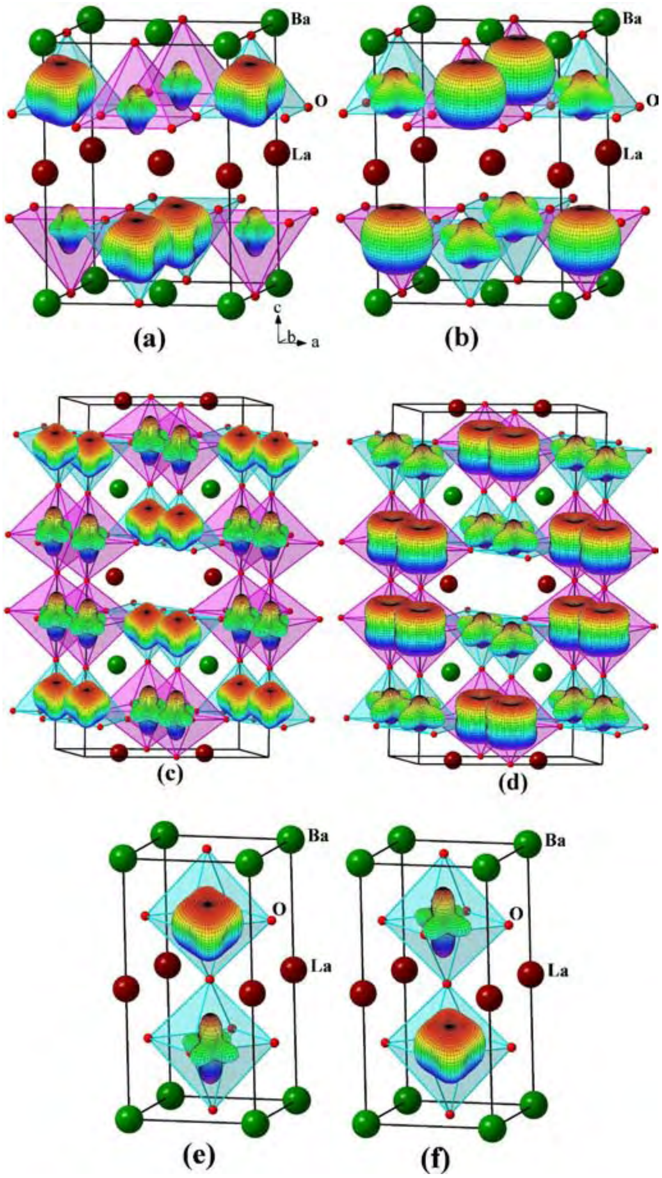

FIG. 1. (Color online) The majority- and minority-spin Mn-3d-electron distribution in (a,b) $LaBaMn_2O_5$, (c,d) $LaBaMn_2O_{5.5}$, and (e,f) $LaBaMn_2O_6$. Atoms inside cyan-colored square pyramids correspond to Mn(1) (Mn in e,f) and those inside pink-colored square pyramids/octahedra correspond to Mn(2).

for La and Ba and 2.0 and 1.6 a.u. for Mn and O, respectively, were used. Exchange and correlation effects are treated using the GGA.[8] The charge densities and potentials in the atomic spheres were represented by spherical harmonics up to $\ell=6$, whereas in the interstitial region these quantities were expanded in a Fourier series. The radial basis functions of each LAPW were calculated up to $\ell=10$ and the nonspherical potential contribution to the Hamiltonian matrix had an upper limit of $\ell=4$. From the ℓ,m projected charge density the CO and OO ordering in these materials are analyzed. For further computational details see Ref. 10.

In $RE_{1-x}AE_xMnO_3$ (AE stands for alkaline earth) compounds the one-electron bandwidth (W) of the Mn-d electrons decreases with decreasing size of the A-site cation, and leads in turn to CO and/or OO. In addition, the A-site substitution changes the valence of the Mn ions. Similarly the variation of the oxygen stoichiometry modifies W and the valence of the Mn ions and this may be used to manipulate SO, CO, and OO in perovskite-like oxides as shown here for the $LaBaMn_2O_{5+\delta}$ phase.

Table I shows the results of FPLMTO calculations performed for the P, F, and AF configurations of $LaBaMn_2O_{5+\delta}$ (similar results were obtained from the FPLAPW method). For all three compositions the AF state is found to have the lowest energy. Table II shows that AF $LaBaMn_2O_5$ has a finite total moment of 0.97 μ_B, implying that it is in fact ferrimagnetic (Ferri). The Ferri ground state and the calculated magnetic moment are in good agreement with the experimental findings.[3] From the difference in the ionic size and magnetic moment, it is experimentally established that Mn(1) corresponds to Mn^{3+} and Mn(2) to Mn^{2+} both in high spin (HS) states. This picture for $LaBaMn_2O_5$ agrees fully with the outcome of the present calculations. In order to analyze changes in the electronic structure with respect to the oxygen stoichiometry, the density of states (DOS) in the ground-state configurations of $LaBaMn_2O_{5+\delta}$ is given in Fig. 2. An energy gap (E_g) of ca. 0.84 eV opens up between the valence and conduction bands in $LaBaMn_2O_5$ [Fig. 2(a)], giving an insulating state in accordance with the experiments. The Ferri ordering leads to significant topological differences in the up- and down-spin DOS.

In general, local-density approximation including Coulomb correlations effects (LDA+U) calculations[11] are thought to be necessary to study the electronic and magnetic properties of transition-metal oxides. However, our calculations show that the insulating behavior and magnetic properties are correctly reproduced by the usual density-functional calculations for the manganites considered in the present study.

As mentioned, t depends on the degree of the hybridization between the Mn-3d and O-2p orbitals, which in turn makes this parameter sensitive to the oxygen stoichiometry. The Jahn-Teller (JT) distortion (associated with HS Mn^{3+}) induces an anisotropy in the interaction between Mn-d and O-p orbitals. Moreover, owing to the size difference between La^{3+} and Ba^{2+} and the oxygen vacancies in the La^{3+} layer, the degree of hybridization between the Mn-d and O-p orbitals is reduced. Hence t and consequently W also decrease. Moreover, the differences in Mn-O-Mn bond angles and Mn-O bond lengths promote significant distinctions between t within and perpendicular to the basal plane of $LaBaMn_2O_5$. The decreases in t and W reduce the double-exchange (DE) interaction, and hence the superexchange interaction overcomes the DE, thus favoring the insulating AF/Ferri CO and/or OO state. Therefore, in addition to Ferri SO, CO occurs with the equal amounts of Mn^{3+} and Mn^{2+} in $LaBaMn_2O_5$. In order to elucidate the effect of oxygen stoichiometry on CO and OO, we show the spatial 3d-electron distribution at each Mn site for the majority and minority spins in Figs. 1(a) and 1(b). The appreciable difference in the distribution of majority and minority d electrons between Mn^{3+} and Mn^{2+} in $LaBaMn_2O_5$, implies the presence of CO.

TABLE I. Total energy (relative to the lowest-energy state in meV/f.u.) in $LaBaMn_2O_{5+\delta}$ for the P, F, and AF phases using FPLMTO with GGA and spin-orbit coupling included.

Composition	P	F	AF
$LaBaMn_2O_5$	3922	438	0
$LaBaMn_2O_{5.5}$	3850	593	0
$LaBaMn_2O_6$	2625	6	0

It is well established that OO plays a crucial role in the magnetic and electronic properties of manganites. As electrons closer to the Fermi level (E_F) participate more in hopping interaction and determine the electronic properties, we show the orbital distribution of such electrons for $LaBaMn_2O_5$ in Fig. 3(a). Owing to the Mn-O-Mn bond angle of 161° for Mn(1), the transfer of the $3d$ electrons is not complete and these electrons therefore tend to localize in a certain pattern over the Mn sites of $LaBaMn_2O_5$. According to the orbital-projected DOS, the d_{xy}, d_{xz}, and d_{yz} orbitals of Mn^{3+} and the $d_{x^2-y^2}$ orbital of Mn^{2+} are found in the energy range -1 eV to E_F, leading to the ordering of these orbitals as shown in Fig. 3(a).

For $LaBaMn_2O_{5.5}$, the ground-state SO is found to be AF, in perfect agreement with the experimental findings.[5] Further, the Mn atoms in the square pyramidal and octahedral coordinations take a HS Mn^{3+} state. The system remains insulating on going to $LaBaMn_2O_{5.5}$, but E_g is reduced to 0.26 eV [Fig. 2(b)]. As half of the square pyramids at $\delta=0$ has been converted into octahedra at $\delta=0.5$, half of the O vacancies in the La layers is filled, and the overlap interaction between Mn-d and O-p orbitals is thereby increased. The bandwidth in turn increases, reducing the band gap. The difference in the crystal fields of square pyramids and octahedra and the accompanied JT distortion increase the carrier-to-lattice coupling and result in localization of charges. Figures 1(c) and 1(d) illustrate the difference in the distribution of majority and minority d electrons between the Mn ions at $\delta=0.5$, indicating the presence of CO. As the orbital degeneracy is lifted due to the JT effect, and anisotropy in the electron-transfer interaction results due to the partial stuffing of the oxygen vacancies, OO occurs. The square pyramidal Mn of $LaBaMn_2O_{5.5}$ have $d_{x^2-y^2}$ and d_{z^2} orbitals near E_F, whereas the octahedral Mn have only $d_{x^2-y^2}$ in the vicinity of E_F. Therefore these orbitals localize to form an OO pattern as shown in Fig. 3(b).

TABLE II. Calculated magnetic moment (in μ_B per Mn atom) for $LaBaMn_2O_{5+\delta}$ in the AF ground state. Total refers to the total magnetic moment per formula unit.

	AF			Experimental		
Composition	Mn(1)	Mn(2)	Total	Mn(1)	Mn(2)	Total
$LaBaMn_2O_5$	3.13	3.99	0.97	2.71[a]	3.21	0.70
$LaBaMn_2O_{5.5}$	3.30	3.34	0.0	3.03[b]	3.43	
$LaBaMn_2O_6$	2.98		0.0	3.50[a]		

[a] Low-temperature neutron-diffraction data, Ref. 3.

[b] Low-temperature neutron-diffraction data, Ref. 5.

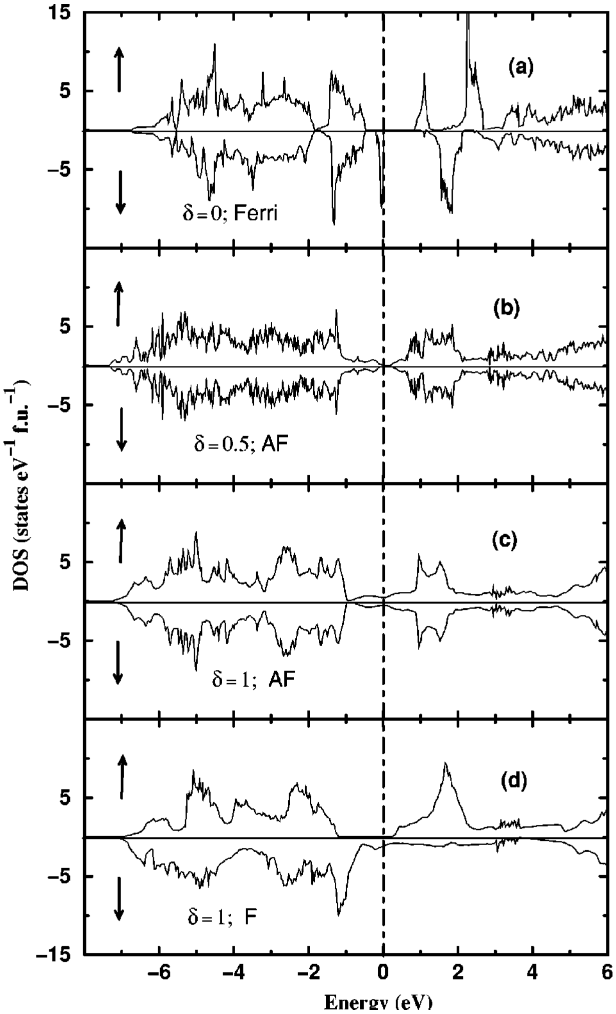

FIG. 2. Total DOS of $LaBaMn_2O_{5+\delta}$ in the magnetic configurations denoted on the illustration. The Fermi level is marked with the dotted line.

Experimentally, F ordering is found[5] for $LaBaMn_2O_6$, whereas our (FPLMTO and FPLAPW) calculations give AF as the ground state. However, recent experimental studies conclude that both F and CE-type AF ordering coexist in $LaBaMn_2O_6$ below 150 K.[12] Moreover, as the calculated energy difference between the F and AF states of $LaBaMn_2O_6$ is very small, a little perturbation may flip the spin arrangement either to F or AF. Hence the coexistence of F and AF states must be considered as a viable outcome. $LaBaMn_2O_6$ contains only one crystallographic type of Mn with an average valence state between 3+ and 4+. The Mn-d exchange splitting is found to be around 3.3, 3.0, and 2.5 eV for $LaBaMn_2O_5$, $LaBaMn_2O_{5.5}$, and $LaBaMn_2O_6$, respectively. The systematic decrease appears to reflect the increasing Mn-d and O-p hybridization interaction and the reduction in magnetic moment of Mn due to increase in its valence state, in the said sequence.

As the oxygen vacancies are filled to the $\delta=1$ limit, the electron bands are broadened and more overlap between the Mn-d and O-p bands is seen. Moreover, the small energy difference between the F and AF states implies that the DE

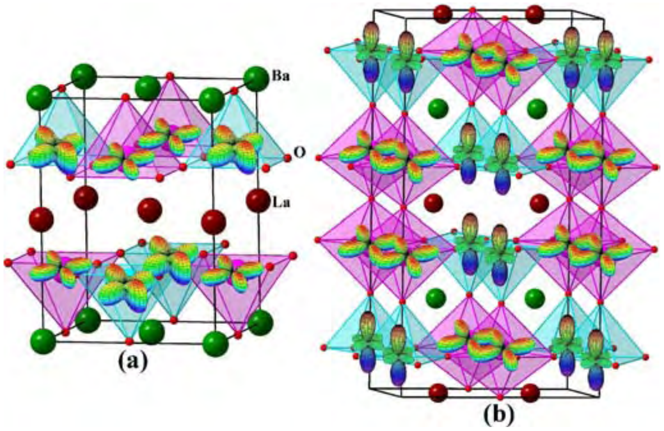

FIG. 3. (Color online) Orbital ordering in (a) $LaBaMn_2O_5$ and (b) $LaBaMn_2O_{5.5}$.

interaction increases (compared with the $\delta=0$ and 0.5 cases), again a consequence of the increased hybridization interaction. Hence the CO state disappears and metallicity appears in $LaBaMn_2O_6$ in accordance with the experimental findings.[3] The metallic behavior of $LaBaMn_2O_6$ can be seen from the small, but finite number of states in DOS at E_F [Fig. 2(c)]. The similarly shaped *d*-electron distributions [see Figs. 1(e) and 1(f)] on the Mn ions also indicate that CO and OO are absent in $LaBaMn_2O_6$.

All three compositions exhibit half-metallicity in the F state (HMF), (with E_g of 2.2, 1.92, and 1.45 eV in the minority-spin channel for $\delta=0$, 0.5, and 1, respectively). The HMF state of $LaBaMn_2O_6$ gains more importance owing to the small energy difference between the F and AF states, which may enable easier conversion from metallic AF to HMF [Fig. 2(d)]. In addition to exchange splitting, the JT distortion as in $LaMnO_3$[13] may play an important role for the occurrence of the HMF in $LaBaMn_2O_6$.

In DE systems, insulator to metal transitions accompanied by disappearance of CO and/or OO due to increased *W* can be achieved by application of external field or pressure. *Since the band characteristics t and W, as well as the valence state of Mn change more drastically with the oxygen contents than by A-site cation substitution in* $(RE,AE)MnO_3$, *one can tune an insulator-to-metal transition from the AF or Ferri CO and/or OO state to a metallic F state by merely varying the oxygen stoichiometry.* Practice has shown that such a conversion may be accompanied by resistivity changes of several orders of magnitude (the CMR effect).

In conclusion, variations in the spin, charge, and orbital orderings by changes in the oxygen content have been illustrated with $LaBaMn_2O_{5+\delta}$ as an example. The changes in the oxygen stoichiometry controls the valence state of Mn and the hybridization interaction between Mn and O. Hence, a reduction in oxygen stoichiometry narrows the bandwidth and consequently decreases the double-exchange interactions at the expense of the competing superexchange interactions. Consequently the ferromagnetic state becomes destabilized relative to the antiferromagnetic state with localized spin, charge, and orbital order as well as Jahn-Teller-type electron-lattice coupling. Therefore by adjusting the oxygen stoichiometry in manganites one can convert the insulating antiferromagnetic charge- and/or orbital-ordered state into a metallic ferromagnetic state.

The authors are grateful to the Research Council of Norway for financial support. Part of these calculations were carried out on the Norwegian supercomputer facilities.

---

*Electronic address: vidya.ravindran@kjemi.uio.no

[1] A.J. Millis, in *Colossal Magnetoresistance Oxides*, edited by Y. Tokura (Gordon and Breach, Singapore, 2000), p. 53.

[2] J.F. Mitchell, D.N. Argyriou, and J.D. Jorgensen, in *Colossal Magnetoresistance Oxides*, edited by Y. Tokura (Gordon and Breach, Singapore, 2000), p. 1.

[3] F. Millange, V. Caignaert, B. Domengés, and B. Raveau, Chem. Mater. **10**, 1974 (1998).

[4] A. Barnabe, F. Millange, A. Maignan, M. Hervieu, G. Van Tendeloo, and B. Raveau, Chem. Mater. **10**, 252 (1998).

[5] V. Caignaert, F. Millange, B. Domengés, and B. Raveau, Chem. Mater. **11**, 930 (1999).

[6] J.M. Wills, O. Eriksson, M. Alouani, and D.L. Price, in *Electronic Structure and Physical Properties of Materials*, edited by H. Dreysse (Springer, Berlin, 2000), p. 148.

[7] O.K. Andersen, Phys. Rev. B **12**, 3060 (1975).

[8] J.P. Perdew, S. Burke, and M. Ernzerhof, Phys. Rev. Lett. **77**, 3865 (1996).

[9] P. Blaha, K. Schwarz, and J. Luitz, computer code WIEN97 (Vienna University of Technology, Vienna, 1997) [an improved and updated Unix version of the original copyrighted code published by P. Blaha, K. Schwarz, P.I. Sorantin, and S.B. Trickey, Comput. Phys. Commun. **59**, 399 (1990)].

[10] R. Vidya, P. Ravindran, A. Kjekshus, and H. Fjellvåg, Phys. Rev. B **65**, 144422 (2002).

[11] V.I. Anisimov, J. Zaanen, and O.K. Andersen, Phys. Rev. B **44**, 943 (1991).

[12] T. Nakajima (private communication).

[13] P. Ravindran, A. Kjekshus, H. Fjellvåg, A. Delin, and O. Eriksson, Phys. Rev. B **65**, 064445 (2002).

III

Ceramics International 30 (2004) 1993–1998

CERAMICS INTERNATIONAL

www.elsevier.com/locate/ceramint

Spin, charge, and orbital orderings in oxides with dual-valent transition metal ions

R. Vidya*, P. Ravindran, P. Vajeeston, H. Fjellvåg, A. Kjekshus

Department of Chemistry, University of Oslo, Box 1033 Blindern, N-0315 Oslo, Norway

Received 8 November 2003; received in revised form 9 December 2003; accepted 22 December 2003

Available online 2 July 2004

Abstract

Using generalized-gradient-corrected full-potential density-functional calculations, we have studied the electronic structure and magnetic properties of $YBaMn_2O_5$, $Sr_4Fe_4O_{11}$, and $Ca_3Co_2O_6$. In these phases, the 3*d* transition metal ions have dual valence. We have studied the electronic structure using site-, angular momentum-, and orbital-projected density of states. The charge and orbital ordering are analyzed in terms of the calculated electron-density distribution, charge density, and electron localization function. The oxygen vacancy, cation radii, and crystal-field effects are found to play an important role for the various ordering phenomena in these compounds.

© 2004 Elsevier Ltd and Techna Group S.r.l. All rights reserved.

Keywords: C. Magnetic properties; D. Transition metal oxides; Spin, charge, and orbital ordering

1. Introduction

Since the discovery of colossal magnetoresistance (CMR) in perovskite-like manganites there have been increased activities on related oxides with dual-valent transition metal constituents. Beside the technological interest in the CMR effect, other related phenomena (attractive from more fundamental points of view) have been established for dual-valent compounds. A very interesting phenomenon is the tendency displayed by many transition metal oxides to adopt the kind of charge distribution known as charge ordering (CO). Although covalence effects in such compounds can be significant, the ionic picture describes it as a real-space ordering of charges and/or orbitals. In general, the Coulomb repulsion between the charges and the elastic energy perturbation owing to cooperative Jahn–Teller (JT) distortions favor the CO. Large radius of (what may be conveniently named) A-site cations (R_A) and wide e_g bandwidths, favor the mobility of the electrons through the lattice, while smaller R_A and narrow e_g bandwidths, favor localization [1]. CO is interesting because double-exchange gives rise to metallicity along with ferromagnetism (F) while the CO state can be associated with insulating and antiferromagnetic (AF) behavior. Hence, there is a competition between F with metallic behavior and insulating AF character with CO. Orbital ordering (OO) gives rise to anisotropic interactions in the electron-transfer process which in turn favor or disfavor the double- and super-exchange (F or AF) interactions in an orbital direction-dependent manner. Understanding of the CO, OO, and spin ordering (SO) processes, provides a foundation for deeper penetration into the complex behaviors of CMR materials.

In the present work, we analyze the spin, charge, and orbital orderings present in the dual-valent oxides (with crystal structure more or less related to the perovskite-type) $YBaMn_2O_5$ (YBMO), $Sr_4Fe_4O_{11}$ (SFO), and $Ca_3Co_2O_6$ (CCO). We have used full-potential density-functional calculations to understand the electronic and magnetic properties and the various orderings present in these phases.

2. Computational details

The full-potential linear muffin-tin orbital (FPLMTO) calculations [2] presented in this paper are all-electron, and no shape approximation to the charge density or potential has been used. The basis set is comprised of augmented linear muffin-tin orbitals [3]. The calculations

---

* Corresponding author.
E-mail address: vidya.ravindran@kjemi.uio.no (R. Vidya).
URL: http://folk.uio.no/ravindrv.

0272-8842/$30.00 © 2004 Elsevier Ltd and Techna Group S.r.l. All rights reserved.
doi:10.1016/j.ceramint.2003.12.198

are based on the generalized-gradient-corrected (GGA) density-functional theory as proposed by Perdew et al. [4]. Spin–orbit coupling is included directly in the Hamiltonian matrix elements for the part inside the muffin-tin spheres, hence for spin-polarized cases the size of the secular matrix is doubled. We used a multi-basis in order to ensure well-converged wave functions. This means that several Hankel or Neumann functions, each attached to its own radial function, have been used. The basis included are Y 4*p*, 5*s*, 5*p*, and 4*d*, Ba 5*p*, 6*s*, 6*p*, 5*d*, and 4*f*, Mn 4*s*, 4*p*, and 3*d*, and O 2*s*, 2*p*, and 3*d* for YBMO, Sr 5*s*, 4*p*, 4*d*, and 4*f*, as well as pseudo-core 5*p*, Fe 4*s*, 4*p*, and 3*d*, and O 2*s*, 2*p*, and 3*d* for SFO, and Ca 4*s*, 4*p*, and 3*d*, Co 4*s*, 4*p*, and 3*d*, and O 2*s*, 2*p*, and 3*d* for CCO. For the total-energy study the ***k***-space integration is done with 192, 144, and 90 ***k*** points for YBMO, SFO, and CCO, respectively, in the irreducible part of the first Brillouin zone. For the magnetic calculations, the easy magnetization axis is chosen in accordance with experimental findings [5–7].

3. Results and discussion

3.1. YBaMn$_2$O$_5$

The ordered oxygen-deficient double perovskites $R\mathrm{Ba}T_2\mathrm{O}_5$ (R = rare-earth and T = Mn, Fe, or Co) have attracted much attention as new spin–charge–orbital coupled CMR materials. CMR effects of some 40% are observed in the isostructural phases with R = Gd or Eu [8]. At low temperature, YBMO is an AF insulator with CO of Mn^{3+} and Mn^{2+} accompanied by OO and SO. The crystal structure (Fig. 1) is described in the space group *P*4/*nmm* with two kinds of MnO$_5$ pyramids arranged in an ordered manner, each Mn^{2+}O$_5$ pyramid being linked to five Mn^{3+}O$_5$ pyramids and vice versa [5]. Oxygen takes two crystallographically different sites with O(1) at the base of the square pyramids, and O(2) at the apex. The basal plane Mn^{3+}–O(1)–Mn^{2+} angle is 157.8° and the apical Mn^{3+}–O(2)–Mn^{2+} angle is 180°. The large difference in these angles play a key role in the magnetic properties.

Table 1
Calculated magnetic moment (in μ_B per T atom at 0 K) for YBMO, SFO, and CCO in the ground-state configuration

Compound	Theory			Experiment		
	T(1)	T(2)	Total	T(1)	T(2)	Total
YBaMn$_2$O$_5$ (YBMO)	3.07	3.93	0.86	2.91	3.91	0.95
Sr$_4$Fe$_4$O$_{11}$ (SFO)	2.86	3.35	0.00	0.00	3.00	0.0
Ca$_3$Co$_2$O$_6$ (CCO)	0.17	2.63	1.21	0.08	3.00	1.3

Total refers to the total magnetic moment per formula unit. The experimental values are taken from Refs. [5–7].

Among the paramagnetic (P), F, and AF configurations considered for calculations [9], AF is found to have the lowest total energy. The ferromagnetic configuration is 505 meV/f.u. higher in energy than the AF configuration. Table 1 shows that the total magnetic moment is not completely canceled, resulting in a ferrimagnetic (Ferri) state. Mn(1) has a smaller magnetic moment (3.07 μ_B) than Mn(2) (3.91 μ_B) implying that Mn(1) corresponds to Mn^{3+} and Mn(2) to Mn^{2+}, both in high-spin states. The electronic structure indicates that it is an indirect band-gap semiconductor with a band gap of 0.88 eV, in agreement with experimental findings [10,11].

CO is expected to be favored when equal proportions of Mn^{2+} and Mn^{3+} are present like in YBMO. On reduction of the Mn–O–Mn angle, the hopping between the Mn 3*d* and O 2*p* orbitals decreases and hence the e_g bandwidth decreases. Consequently the system stabilizes in a Ferri-CO-insulating state. In order to visualize the presence of CO and Ferri SO in YBMO we show the calculated *d*-electron-density distribution for the Mn ions in the up- and down-spin channels in Fig. 1a and b. The CO in YBMO is characterized by the real-space ordering of Mn^{2+} and Mn^{3+}. The significant difference in the electron-density distribution for the Mn ions clearly indicates that there occurs two different valence states with different orbital occupation. This feature ensures that the spins do not cancel exactly, resulting in the Ferri ordering (Fig. 1c).

The exchange interaction between Mn^{2+} and Mn^{3+} along *c* is AF owing to the 180° bond angle which facilitates *p*–*d* σ bonding with the O(2) p_z orbital as well

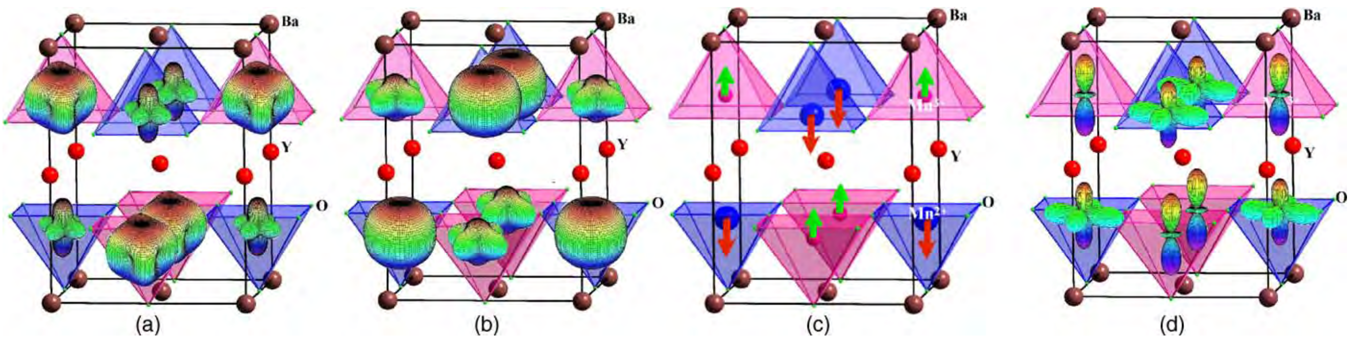

Fig. 1. The calculated Mn *d*-electron-density distribution of (a) up- and (b) down-spin electrons in YBaMn$_2$O$_5$. (c) The G-type ferrimagnetic spin ordering and (d) orbital ordering in YBaMn$_2$O$_5$.

as super-exchange interaction [12]. With a bond angle of only 157° within the basal plane, the d(Mn)–p(O) covalent bond is weak and moreover due to the HS state of Mn^{3+} in the square-pyramidal crystal field, the $d_{x^2-y^2}$ orbital at the Mn^{3+} site is almost empty whereas that at Mn^{2+} is half filled. Hence, the AF super-exchange interaction between Mn^{2+} and Mn^{3+} within the basal plane is weaker than that along c.

In order to visualize the OO in YBMO we show in Fig. 1d the electrons distribution at the Mn sites between −1 eV and E_F (viz. the electrons mainly participating in the hopping interactions). In the bc plane the d_{z^2} orbital is ordered along c for both Mn^{3+} and Mn^{2+}, and this orbital hybridizes with the O(1) p_z orbital resulting in σ bonding. There is virtually no overlap between the $d_{x^2-y^2}$ and p_z orbitals because of their different orientation in the c direction. Therefore, the electron in the $d_{x^2-y^2}$ orbital can not hop along c. Moreover, the direct overlap between O $p_{x,y}$ and Mn d is small in the ab plane ($d_{x^2-y^2}$ is almost empty for Mn^{3+} and only partly occupied for Mn^{2+} due to the JT distortion) and hence the d electrons become localized resulting in CO and OO.

3.2. $Sr_4Fe_4O_{11}$

SFO is also an oxygen-deficient perovskite-like material which crystallizes in the space group *Cmmm* [13]. It is an antiferromagnet with $T_N \approx 230$ K. Fe has square-pyramidal [Fe(1)] and octahedral [Fe(2)] coordination polyhedra. Owing to the oxygen vacancy in the structure and different crystal-field effects Fe takes the dual-valent states Fe^{3+} and Fe^{4+}.

According to powder neutron diffraction data (at 8 K) this compound has an unusual magnetic structure; Fe(1) do not exhibit any magnetic ordering whereas Fe(2) ions have a G-type AF arrangement [7]. The room-temperature Mössbauer spectrum is reported [14] to show two symmetrical doublets of equal intensity. From the isomer-shift values (0.35 and $-0.08\,\mathrm{mm\,s^{-1}}$) the two components are assigned to Fe^{3+} and Fe^{4+}. A hyperfine splitting and low flux density value has been observed for the Fe^{3+} component, whereas only a linewidth broadening is observed for the Fe^{4+} component below T_N. This suggests a partially frustrated AF structure [14]. Furthermore, a strong divergence between zero-field-cooled and field-cooled magnetic susceptibility curves is observed, implying spin-glass-like behavior [15].

We have carried out density-functional calculations in F as well as A-, C-, and G-type AF configurations and found that G-AF has the lowest energy. C-AF is the next stable state with 2.54 eV higher energy than the G-AF state. Our calculations show that G-AF configuration with zero magnetic moment for Fe(1) is higher in energy (1.85 eV) than that with a magnetic moment of 2.8 μ_B for Fe(1), indicating that the former may represent a meta-stable state. However, we have not considered temperature effects and oxygen vacancy ordering in our calculations which may play important roles for the magnetic properties. The unusual magnetic properties of SFO can be related to the crystal structure and the CO of the Fe ions. In order to be able to draw a more firm conclusion regarding the magnetic structure, further calculations including structural optimization is in progress.

A correct assignment of valence states to the Fe ions is essential to understand the relationship between the crystal structure and the electronic and magnetic properties. The Mössbauer studies appear to point to the presence of Fe^{3+} and Fe^{4+} ions. Crystal-field stabilization energy and the relative values of the bond-strength sums [13] indicate that Fe^{4+} should be assigned to square-pyramidal and Fe^{3+} to octahedral coordinations. If Fe(1) were an Fe^{4+} ion, it should be either in an intermediate-spin (IS; $t_{2g}^4 e_g^0$; 2 μ_B) state or in a low-spin (LS; $t_{2g}^4 e_g^0$; 0 μ_B) state. The octahedral Fe(2) should be Fe^{3+} in IS ($t_{2g}^4 e_g^1$; 3 μ_B). An IS state for Fe(2) agrees very well with the theoretical and experimental magnetic moment and is consistent with the JT distortion observed.

The electronic structure of SFO in the G-AF state is consistent with metallic conductivity with a low density of states (DOS) at the Fermi level (E_F). The partial DOS analysis shows that the Fe 3d and O 2p states are energetically degenerate leading to covalent interaction between them. However, as the topology of the DOS curves for Fe(1) and Fe(2) is different (Fig. 2), the magnitude of the covalent interaction is also different. In the G-AF state with the zero magnetic moment for Fe(1), the up- and down-spin DOS of Fe(1) are similar, implying that the up- and down-spin channels have the same occupancy, viz. complying with the zero magnetic moment. This emphasizes the fact that Fe(1) exists in an Fe^{4+} LS state. The majority spin channel of Fe(2) has more states than the minority spin channel, giving a finite magnetic moment (also seen for Fe(1) in the G-AF situation where Fe(1) takes a finite magnetic moment). As the Fe(2)–O bond length (2.04 Å) is longer than the Fe(1)–O bond length (1.85 Å), the Fe(2)–O bond strength is weaker than that of Fe(1)–O. On the other hand, more unpaired 3d states are localized on Fe(2) than on Fe(1). Moreover, as the Fe(1)–O–Fe(2) bond angle is less than 180°, the super-exchange interaction is incomplete like the Mn(1)–O–Mn(2) super-exchange interaction in YBMO. These features lead to the CO in addition to the SO in SFO.

3.3. $Ca_3Co_2O_6$

CCO belongs to the family of one-dimensional (1-D) oxides. Inorganic structures with 1-D atomic arrangements are in the limelight owing to their unique electronic and magnetic properties [16]. The crystal structure of CCO consists of parallel 1-D Co–O chains separated by Ca^{2+} ions. The chains are built by alternating face-sharing CoO_6 octahedra and trigonal prisms along the hexagonal c axis. The resulting short metal–metal intrachain distance (2.59 Å) (compared to the interchain distance of 5.24 Å) reinforces the 1-D character of the structure along the c axis. Mag-

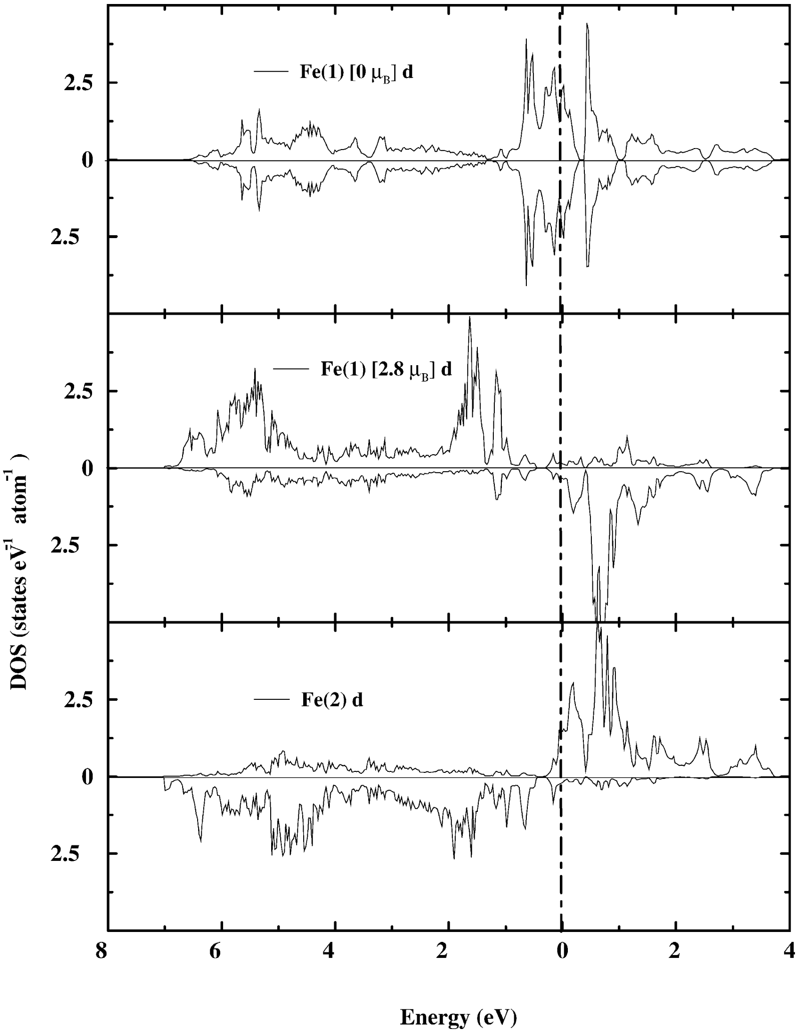

Fig. 2. The site- and angular momentum-projected density of states for Fe(1) and Fe(2) of $Sr_4Fe_4O_{11}$. The *s* and *p* partial DOSs are only about 10% of the *d* states shown.

netic studies show F intrachain ordering ($T_{C1} = 24\,K$) with AF interchain coupling ($T_{C2} = 10\,K$) [6]. For every two F-aligned Co chains, there is one AF-aligned chain giving a resultant Ferri structure.

Our total-energy study [17] shows that Ferri state of CCO has the lowest energy in perfect agreement with experimental findings [6,18]. The Ferri state is 114 meV/f.u. lower in energy than the F state. The electronic structure shows [17] a finite DOS at E_F in both spin channels, implying a metallic character consistent with the experimental conductivity study [19]. Our partial DOS analysis shows that the states in the vicinity of E_F are mainly contributed by Co *d* states.

Different spin configurations for the crystallographically different Co ions are expected [20] as a consequence of the larger crystal field for the octahedral Co(1) than for the trigonal prismatic Co(2). Various proposals have been made for spin states of Co such as (i) Co(1): LS Co^{3+}; Co(2): HS Co^{3+}, (ii) Co(1): LS Co^{4+}; Co(2): HS Co^{2+}, and (iii) Co(1): LS Co^{2+} and Co^{4+}; Co(2): HS Co^{3+}. The calculated magnetic moments listed in Table 1 are found to be in good agreement with available low-temperature neutron diffraction and magnetization data. By taking the magnetic moments at the Co sites into consideration, together with the octahedral and trigonal-prismatic crystal fields and the calculated site- and orbital-projected DOS features, we conclude that Co(1) is Co^{4+} in LS (d^5; $t_{2g}^5e_g^0$) state and Co(2) is Co^{2+} in HS (d^7; $t_{2g}^5e_g^2$) state.

As the interatomic distance in metallic Co is 2.51 Å and the distance between Co(1) and Co(2) in CCO is 2.59 Å, a metallic interaction between Co(1) and Co(2) has been anticipated [21]. However, our charge density and electron-localization-function analyses show very weak metallic interaction between the Co atoms. Moreover as seen from Fig. 3, the topology of DOS curves for Co(1) and Co(2) are entirely different implying differences in their valence and spin states. As the O $2p$ states are energetically degenerate with Co $3d$ states, there is strong covalent

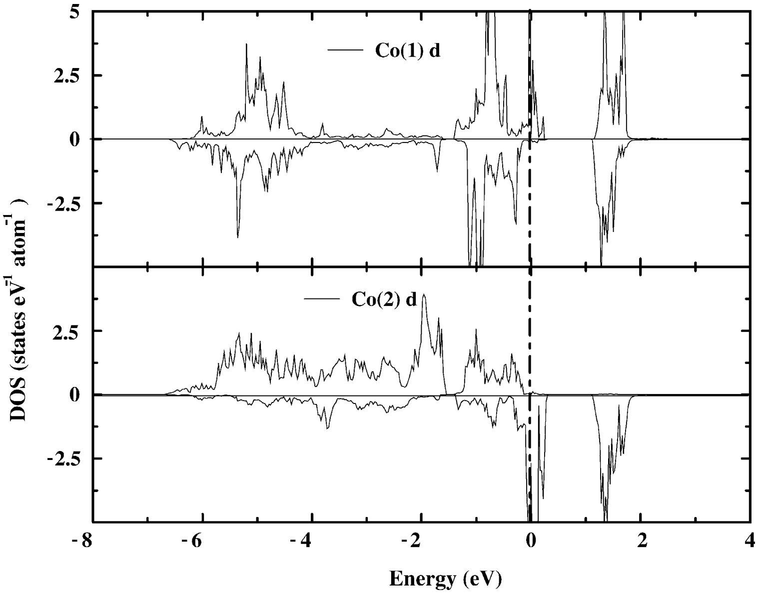

Fig. 3. The site- and angular momentum-projected density of states for Co(1) and Co(2) of $Ca_3Co_2O_6$. The Co *s* and *p* partial DOSs are only about 10% of the *d* states shown.

interaction between Co and O. However, the magnitude of covalent interaction is different for Co(1) and Co(2) owing to the difference in their crystal fields. Therefore, the localization of charges on Co(1) and Co(2) is different and leads to the ladder-type CO. Moreover, the orbital-projected DOS features show that both e_g and t_{2g} (except d_{xz}) orbitals have finite states close to E_F for Co(1) whereas only d_{xz} and d_{yz} orbitals have finite DOS in the same region for Co(2). Therefore, also the occupation of the *d* orbitals of Co(1) and Co(2) is different resulting in OO in addition to the CO and Ferri-SO situation.

4. Conclusions

We have studied the electronic and magnetic properties (in particular spin, charge, and orbital orderings) of YBMO, SFO, and CCO, using full-potential density-functional calculations. All the studied compounds have dual-valent transition metal ions which (together with at least two crystallographically non-equivalent T-atom sites) is a prerequisite for the ordering phenomena under investigation. The present study, however, shows that the phenomena are not connected to *one particular* structure type. In general, when the e_g bandwidth (determined mainly by the constituents of the compound) is small, charge ordering is favored. In YBMO, the distinction between the radii of Y and Ba together with oxygen vacancies (not discussed here) lead to difference in $T(1)$–O–$T(2)$ bond angles as well as T–O bond lengths. Hence the $T(1)$–O–$T(2)$ super-exchange interaction is not uniform in YBMO resulting in a charge ordering pattern of the checker-board type. Similarly, in SFO and CCO also the variation in the bond angles and bond lengths leads to difference in the valence states of the T ions and charge ordering. The occupancy of the *d* orbitals and hence orbital ordering is determined by the coordination polyhedra surrounding the T ions. Therefore, the crystal-field effect and hence crystal structure of a compound play an important role in orbital ordering. All in all, the constituents of a given compound, the crystal structure (including crystal-field effects), and oxygen stoichiometry determine spin, charge, and orbital orderings in this type of materials. A study of the individual effect of the just mentioned ruling parameters may reveal more insight into the ordering phenomena.

Acknowledgements

The authors are grateful to the Research Council of Norway for financial support. Part of these calculations were carried out on the Norwegian supercomputer facilities.

References

[1] C.N.R. Rao, A.K. Raychaudhuri, in: C.N.R. Rao, B. Raveau (Eds.), Colossal Magnetoresistance, Charge Ordering and Related Properties of Manganese Oxides, World Scientific, Singapore, 1998, p. 31.
[2] J.M. Wills, O. Eriksson, M. Alouani, D.L. Price, in: H. Dreysse (Ed.), Electronic Structure and Physical Properties of Materials, Springer, Berlin, 2000, p. 148.
[3] O.K. Andersen, Phys. Rev. B 12 (1975) 3060.
[4] J.P. Perdew, K. Burke, M. Ernzerhof, Phys. Rev. Lett. 77 (1996) 3865.
[5] F. Millange, E. Suard, V. Caignaert, B. Raveau, Mater. Res. Bull. 34 (1999) 1.
[6] S. Aasland, H. Fjellvåg, B.C. Hauback, Solid State Commun. 101 (1997) 187.
[7] H. Fjellvåg, unpublished.

[8] C. Martin, A. Maignan, D. Pelloquin, N. Nguyen, B. Raveau, Appl. Phys. Lett. 71 (1997) 1421.
[9] R. Vidya, P. Ravindran, A. Kjekshus, H. Fjellvåg, Phys. Rev. B 65 (2002) 144422.
[10] J.P. Chapman, J.P. Attfield, M. Mölgg, C.M. Friend, T.M. Beales, Angew. Chem. Int. Ed. Engl. 35 (1996) 2482.
[11] T.P. Beales, M. Mölgg, J. Jutson, C.M. Friend, Phys. Stat. Sol. (A) 161 (1997) 271.
[12] J.B. Goodenough, Magnetism and the Chemical Bond, Wiley, New York, 1963.
[13] J.P. Hodges, S. Short, J.D. Jorgensen, X. Xiong, B. Dabrowski, S.M. Mini, C.W. Kimball, J. Solid State Chem. 151 (2000) 190.
[14] L. Fournes, Y. Potin, J.-C. Grenier, G. Damazeau, M. Pouchard, Solid State Commun. 62 (1987) 239.
[15] T.C. Gibb, J. Chem. Soc., Dalton Trans. (1985) 1455.
[16] T.N. Nguyen, H.-C. zur Loye, J. Solid State Chem. 117 (1995) 300.
[17] R. Vidya, P. Ravindran, H. Fjellvåg, A. Kjekshus, O. Eriksson, Phys. Rev. Lett. 91 (2003) 186404.
[18] H. Kageyama, K. Yoshimura, K. Kosuge, X. Xu, S. Kawano, J. Phys. Soc. Jpn. 67 (1998) 357.
[19] A. Maignan, C. Michel, A.C. Masset, C. Martin, B. Raveau, Eur. Phys. J. B 15 (2000) 657.
[20] H. Kageyama, K. Yoshimura, K. Kosuge, H. Mitamura, T. Goto, J. Phys. Soc. Jpn. 66 (1997) 1607.
[21] H. Fjellvåg, E. Gulbrandsen, S. Aasland, A. Olsen, B.C. Hauback, J. Solid State Chem. 124 (1996) 190.

IV

Effect of d-band filling on spin, charge, and orbital ordering in $YBaT_2O_5$ (T = Mn, Fe, Co)

R. Vidya*, P. Ravindran, K. Knizek[1], A. Kjekshus and H. Fjellvåg
Department of Chemistry, University of Oslo, Box 1033 Blindern, N-0315 Oslo, Norway and
[1] *Institute of Physics ASCR, Cukrovanicka 10, 162 53 Prague, Czech Republic*

Variations in the spin, charge, and orbital ordering are analyzed in terms of the d-band filling for $YBaT_2O_5$ (T = Mn, Fe, Co). The calculations are performed with accurate density-functional-theory methods as implemented in the full-potential linearized-augmented plane-wave approach. We have carried out calculations for paramagnetic, ferromagnetic, and antiferromagnetic configurations. A ferrimagnetic ground state has been established for $YBaMn_2O_5$ whereas $YBaFe_2O_5$ and $YBaCo_2O_5$ have antiferromagnetic ground states in agreement with experimental findings. The electronic band characteristics are analyzed using total, site-, and orbital-projected density of states. Inclusion of spin-orbit coupling and Coulomb correlation effects are found to be important for $YBaFe_2O_5$ and $YBaCo_2O_5$ in order to reproduce the experimentally established semiconducting behavior. The different types of charge and orbital ordering in these compounds are visualized by making use of the energy-projected density matrices of the d electrons. Substantial differences in ordering patterns then emerge with respect to the d-band filling.

PACS numbers: PACS numbers: 71., 81.05.Je, 71.15.Nc, 71.20.-b, 81.40.Rs

The concept of colossal magnetoresistance (CMR) has received immense attention in recent years. CMR materials display a fascinating diversity in behaviors including several forms of spin, charge, and orbital ordering (abbreviated SO, CO and OO, respectively) [1]. A detailed study on these properties has appealed to both basic and applied scientists alike. The electrical and magnetic properties in relation to CMR behavior are largely determined by the chemical composition and crystal structure of the given material, and such properties are often quite sensitive to even tiny changes [2].

In transition-metal (T) oxides, the surroundings of the T atoms are conveniently described in terms of the coordination polyhedra constituted by the oxygen ligands. The polyhedra are sometimes distorted, for example by elongation of certain bonds relative to others, thereby converting the energy-degenerate d levels of the central T atom into non-degenerate levels. Such a process is actually referred to as Jahn-Teller distortion (JTD) [3] and the effect is to lower the symmetry as well as the total energy of the material. Owing to such distortion the electrons are often localized at particular atomic sites, resulting accordingly in CO. In other words, the preferential occupation of d orbitals by electrons (normally resulting in OO) is believed to be one of the driving forces in JTD and the associated CO. SO is intimately connected with JTD and as such quite sensitive to changes in the d-orbital occupancy, and CO transitions are accordingly expected to be coupled with OO and SO transitions. In spite of the fact that spin and orbital dynamics are universal to all transition-metal oxides, only the manganites have so far been honored with particular attention.

We have earlier carried out a detailed analysis [4, 5] of SO, CO, and OO in $YBaMn_2O_5$ (YBMO5) and the influence of added oxygen on SO, CO, and OO in $LaBaMn_2O_{5+\delta}$ ($0 \leq \delta \leq 1$) [6]. In this work we concentrate our efforts on the effects of d-orbital filling on SO, CO, and OO in YBMO5, $YBaFe_2O_5$ (YBFO5), and $YBaCo_2O_5$ (YBCO5). Based on rigid-band consideration, the progressive filling of d orbitals should shift the Fermi level (E_F) toward the conduction band thereby reducing the band gap. Effects of added oxygen have been reported for $YBaMn_2O_{5+\delta}$ and $YBaCo_2O_{5+\delta}$. Hence there is every reason to believe that YBFO5 will exhibit oxygen-stabilized variants with the formulae $YBaFe_2O_{5.5}$ and $YBaFe_2O_6$.

The case of YBMO5 is brought into attention in this paper for two purposes. In the first place to facilitate a direct comparison of ordering phenomena [4, 5] in three so closely related phases. Second, in our earlier study on YBMO5 we analyzed the OO by considering the orbital-projected density of states (DOS) in a narrow energy region close to E_F. In this work we adopt a somewhat different method, in which we calculate the occupation density matrix of d orbitals for the T atoms from -1 eV to E_F. This approach has the advantage that we are not only able to establish the occupancy of a particular orbital within a selected energy region, but it also enables us to determine the orientation of these orbitals. Hence an additional motivation for including YBMO5 is to test the applicability and reliability of the new line of approach.

The chemical and crystallographic composition of the YBTO5 phases are interesting since equal amounts of charged T atoms in two different valence states should maximize the Coulomb stabilization energy of a CO state. At low temperature the ground state of YBMO5 [7] comprises two different types of Mn atoms with simultaneous CO and OO in addition to ferrimagnetic (Ferri) SO. A more complicated behavior is reported for YBFO5 [9] which undergoes three successive transitions from so-called class-III mixed-valence (MV; with a common two-and-a-half average valence state for all Fe atoms) via class-II MV (premonitory CO state with

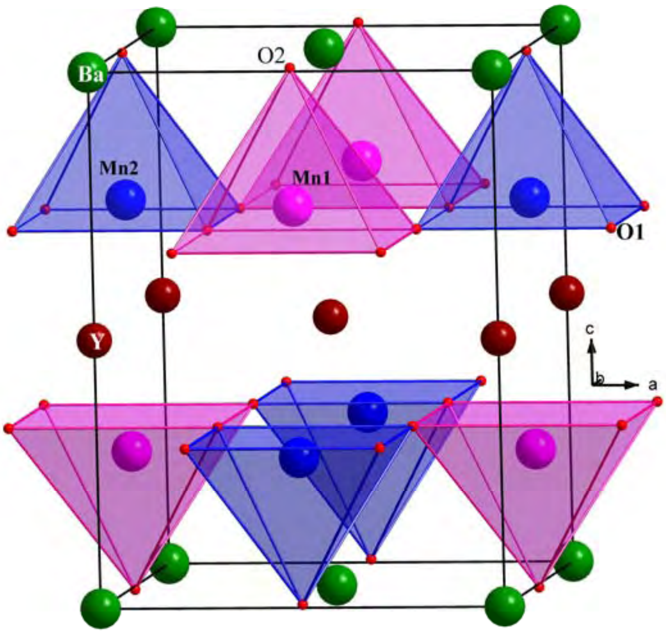

FIG. 1: (Color online) The tetragonal crystal structure of $YBaMn_2O_5$ (in the antiferromagnetic state) with Y and Ba layers interleaved by MnO_5 square pyramids. The differently colored polyhedra indicate co-ordinations with crystallographically different Mn atoms (labeled on the illustration). The Mn1 and Mn2 moments are arranged alternating along c. The structural arrangements of YBFO5 and YBCO5 are similar except for orthorhombic symmetry.

distinction between the two-and-something valence states for the crystallographically different Fe atoms) to class-I MV state (two distinct Fe^{II} and Fe^{III} valence states for Fe). The latter transition apparently triggers a number of changes in the crystal, magnetic, and electronic structures of YBFO5. YBCO5 also exhibits antiferromagnetic (AF) spin ordering as well as CO and OO. In addition, YBCO5 is reported to exhibit a low- to high-spin state transition upon cooling [10]. In spite of several experimental [11] and theoretical attempts [12–14] to clarify the situation in YBCO5, the exact spin states of Co have hitherto remained controversial. In this work we attempt to explore the spin states of the T atoms, in addition to analyzing the magnetic and electronic properties of $YBaT_2O_5$ as a function of d-orbital occupancy.

I. CRYSTAL AND MAGNETIC STRUCTURES

The overall features of the structural arrangements in these YBTO5 phases are the same, with crystal structures derived from the perovskite type with ordering of the Y and Ba atoms in layers along c and removal of oxygen exclusively from the thus obtained Y layer. This creates characteristic apically connected double layers of corner-sharing TO_5 square pyramids (Fig. 1). These double layers form the backbone of the atomic arrangement perpendicular to c axis in which Y and Ba layers intervene alternatively. Owing to the double-layered nature of the $YBaCuFeO_5$-type structure these phases are frequently referred to as double-perovskite variants. The actual structural arrangement in the YBTO5 phases varies with T, a dependence already reflected in the symmetry of the space group. Another manifestation is seen in the T-O distances in the co-ordination polyhedra which are influenced by the size and to some extent charge differences between the Y and Ba constituents. Above the co-operative magnetic ordering temperature $T_C = 165$ K YBMO5 crystallizes in the tetragonal $YBaCuFeO_5$-type structure (Ref. [7]; space group $P4/nmm$). Bond lengths and bond angles for the T-O skeleton in the YBTO5 phases are summarized in Table I.

TABLE I: Bond lengths (in Å) and bond angles (in deg) between T and O in $YBaT_2O_5$ (T = Mn, Fe, and Co).

Specification	YBMO5	YBFO5	YBCO5
$T1-O$	1 × 2.081	1 × 2.052	1 × 2.060
	4 × 1.908	2 × 1.959	2 × 1.955
		2 × 2.109	2 × 2.096
$T2-O$	1 × 1.961	1 × 1.891	1 × 1.780
	4 × 2.086	2 × 1.970	2 × 2.004
		2 × 1.976	2 × 1.894
$T1-O^a-T2$	157.8	158.6; 153.9	157.1; 164.3
$T1-O^b-T2$	180	180	180

[a] O in pyramid base plane
[b] O in pyramid apex

According to the Goodenough-Kanamori [8] rules, an A-type antiferromagnetic (hereafter A-AF) structure is expected with ferromagnetic (F) interactions between $T1$ and $T2$ in planes parallel to the ab plane and AF superexchanges along the c direction. However, owing to the large deviation of Mn1-O1-Mn2 angle from 180° in the pyramid-base plane, this interaction also becomes AF in YBMO5, resulting in a G-AF-type magnetic moment structure (in fact Ferri owing to non-cancellation of the differently sized Mn1 and Mn2 moments). The conversion to class-I MV YBMO5 (space group $Pmmm$) is reported [9] to be completed at 1.5 K; the Verwey transition (T_V) for complete conversion to class-III MV being above 300 K.

YBFO5 experiences a tetragonal-to-orthorhombic ($P4/nmmm$ to $Pmmm$) structural and magnetic transition at $T_N \approx 430$ K [9] and undergoes a further class-III to class-II MV transition from $Pmmm$ to $Pmma$ at $T_V = 308$ K (with the same chemical environment as in the P state above T_N) to $Pmma$ at 20 K (completed conversion to class-I MV; very different nearest-neighbor co-ordinations and oxidation states for Fe). The Fe1 site (said to be in a formal Fe^{III} state) has a fairly symmetric co-ordination environment at low temperature with a slight shift of Fe1 toward the apex of the square pyramid and a consequent reduction in the pyramid base-plane Fe1-O distance. On the other hand, the co-ordination of the Fe2 site (formally referred to as $\mathrm{Fe}^{\mathrm{II}}$) is very distorted as manifested by the lengthening of the pyramid-base-plane Fe-O bonds. Unlike YBMO5, the low-temperature YBFO5 structure comprises four crystallographic O atoms with different Fe-O bond lengths along the pyramid-base-plane.

The structural features of YBCO5 is similar to those of YBFO5, with a transition from tetragonal ($P4/mmm$) to orthorhombic ($Pmma$) symmetry at $T_{\mathrm{N}} = 330\,\mathrm{K}$. For YBCO5, $T_{\mathrm{V}} = 220\,\mathrm{K}$ and completed conversion to Class-I MV is reported [9] to have occurred at 50 K. Like YBFO5, class-I MV YBCO5 also exhibits alternating long and short bonds (Co1-O and Co2-O) along a doubled a axis (compared to YBMO5) and chains of either Co1-O-Co1 or Co2-O-Co2 linkages running parallel to b. This change in bond lengths along with the orthorhombic symmetry may differentiate the CO and OO patterns in YBFO5 and YBCO5 from that in YBMO5. All in all it is the average half-integer valence state of T and the corner sharing square-pyramidal framework of the oxygen-deficient perovskite-type structure which set the stage for the CO transition in these materials.

The magnetic structure of YBFO5 also transforms from the G-AF-type ordering ($\mathrm{YBaCuFeO_5}$-type) to a variant denoted as Wollan-Koehler G-AF-type magnetic arrangement. In YBFO5 and YBCO5 the isovalent Fe and Co atoms, respectively, arrange themselves in chains, but unlike YBMO5 where a given Mn site only has near Mn neighbors in a different valence state (readers are referred to Figs. 2 and 3 in Refs. [9, 10]). The magnetic structure of YBMO5 contains two formula units whereas that of YBFO5 and YBCO5 contains four formula units. In the calculations for the YBTO5 phases in AF configurations, we adopted the appropriate experimental magnetic structures.

II. COMPUTATIONAL DETAILS

The present calculations have been carried out using density-functional-theory (DFT) as implemented in the full-potential linearized-augmented plane-wave (FPLAPW-WIEN2k) method [15] in a fully relativistic version with spin-orbit coupling. The FPLAPW approach divides space into an interstitial region (IR) and non-overlapping muffin-tin (MT) spheres centered at the atomic sites. In IR, the basis set consists of plane waves. Inside the MT spheres, the basis set is described by radial solutions of the one-particle Schrödinger equation (at fixed energies), and their energy derivatives multiplied by spherical harmonics. The charge densities and potentials inside the atomic spheres were represented by spherical harmonics up to $\ell = 6$, whereas in the interstitial region these quantities were expanded in a Fourier series. Atomic-sphere radii R_{MT} of 2.2, 2.3, 1.9, and 1.6 a.u. for Y, Ba, T, and O, respectively, were used. Since the spin densities are well confined within a radius of about 1.5 a.u. the resulting magnetic moments do not depend appreciably on the chosen atomic-sphere radii. The initial basis set included 5s, 5p, and 4d valence and 4s and 4p semicore functions for Y, 6s, 6p, and 6d valence and 5s and 5p semicore functions for Ba, 4s, 4p, and 3d valence and 3s and 3p semicore functions for T, and 2s, 2p, and 3d functions for O. The Brillouin zone (BZ) integration was done with a modified tetrahedron method [16] and we used 168 $\mathbf{k}$ points in the irreducible wedge of BZ. Exchange and correlation effects are treated within density-functional theory (DFT), using GGA [17].

TABLE II: Total energy (relative to the lowest energy state in meV f.u.$^{-1}$) in $\mathrm{YBa}T_2\mathrm{O}_5$ for the para-(P), ferro-(F), and antiferromagnetic (AF) phases using FPLAPW with GGA and spin-orbit coupling included.

Phase	P	F	G-AF
$\mathrm{YBaMn_2O_5}$	3388	422	0
$\mathrm{YBaFe_2O_5}$	2588	967	0^a
$\mathrm{YBaCo_2O_5}$	873	428	0

[a] Wollan-Koehler G-AF type structure

The Coulomb correlation effects are taken into account by introducing $U = 6.0\,\mathrm{eV}$ and $J = 1.0\,\mathrm{eV}$ for Fe and Co atoms in YBFO5 and YBCO5. These GGA+U calculations [18] have also been carried out using FPLAPW method as implemented in the Wien2K program.

III. RESULTS AND DISCUSSION

A. Magnetic properties - spin ordering

In addition to confirmation of the experimentally determined AF structure, we have performed calculations for paramagnetic (P) and F configurations and established that the three compounds have AF ground states (Table II). The magnetic moments for the two Mn sites do not cancel in YBMO5 resulting in a Ferri configuration, in agreement with the experimental findings [7]. According to the calculation in terms of GGA with spin-orbit coupling included, the difference in the calculated magnetic moment values for the Fe sites in YBFO5 is small. When we include Coulomb correlation effects in the calculation ($U = 6.0\,\mathrm{eV}$ and $J = 1.0\,\mathrm{eV}$) the difference between the magnetic moments increases implying that correlation effects play an important role in YBFO5. Even though the experimental Rietveld refinements [9] were able to distinguish two different co-ordination environments for the Fe sites, the magnetic powder neutron diffraction was not able to measure separate magnetic moments for the Fe atoms. However, the theoretical calculation is able to distinguish different magnetic moments for the Fe sites and the magnetic moment value found for the Fe1 site is in fact in good agreement with the reported experimental value (Table III).

The experimental study [10] on YBCO5 has established clearly distinct magnetic moments for the Co sites

TABLE III: Calculated magnetic moment (in μ_B per T atom) for YBaT_2O$_5$ in the antiferromagnetic ground state. Total refers to the total magnetic moment per formula unit.

	YBMO5			YBFO5			YBCO5		
Composition	Mn1	Mn2	Total	Fe1	Fe2	Total	Co1	Co2	Total
GGA+Spin-orbit	2.94	3.88	0.99	3.46	3.34	0.01	1.89	1.72	0.03
GGA+U	——	——	——	3.73	3.18	0.00	2.30 (2.54)	2.68 (2.01)	(0.0)0.98
Experimental	2.90[a]	3.90	0.95	3.82[b]	–	0.0	2.70[c]	4.20	0.0

[a] Low-temperature neutron-diffraction, Ref. 7.
[b] Low-temperature neutron-diffraction, Ref. 9.
[c] Low-temperature neutron-diffraction, Ref. 10.

(AF configuration similar to that in YBFO5). However, the calculated magnetic moments are smaller than the experimental values (but note that orbital contributions are usually significant for Co [14] amounting to 1.04 and 0.40 μ_B for the Co1 and Co2 sites, respectively). As seen from Table III, inclusion of the correlation effect increases the difference between Co1 and Co2 moments and brings about a somewhat good agreement with the experimentl values. In addition when an $U = 4$ eV and $J = 0.95$ eV are used in GGA+U method, the calculated Co moments do not cancel for YBCO5 resulting in finite total moment and thus a Ferri state (the values are given in parenthesis in Table III). Moreover, around 9% of the total moment per formula unit originates from induced moments at the oxygen sites. Finally we mention that we have carried out a test calculation for YBCO5, according to the full-potential linear muffin-tin orbital (FP-LMTO) method [19] with the YBaCuFeO$_5$-G-AF-type magnetic arrangement (like in the YBMO5 variant). The results were indeed very similar to those discussed above for the G-AF case (see Tables II, III) viz. Ferri ground state and smaller magnetic moments at the Co sites than those experimentally established.

B. Electronic structure

In order to analyze the electronic structure of the YBTO5 phases we plotted total, site-, and orbital-projected density of states (DOS). In the P state, the three compounds have a finite number of states at the E_F indicating metallic character. Moreover, the E_F falls on peaks for all YBTO5 phases which suggests instability of these phases in the P state, in agreement with total energy studies (remember that the calculations refer to 0 K). In YBCO5 there has been reported [10] a pronounced upturn in the resistivity near 200 K, indicative of electron localization, that could be associated with CO on the cobalt sites. The change in resistivity may be taken as indicator for metallic character in P state of YBCO5, in agreement with our calculations. An unrestricted Hartree-Fock calculation [20] also showed metallic character for the P state of YBCO5.

At first sight, the DOS for the F state of the three phases seem to imply half-metallic character. However, a closer inspection reveals metallic character, with a considerably reduced number of states at the E_F compared with the P case. The density of the majority-spin states at the E_F progressively increases from YBMO5 to YBCO5 whereas the exchange splitting has its peak value at YBMO5 and then monotonically decreases to YBCO5.

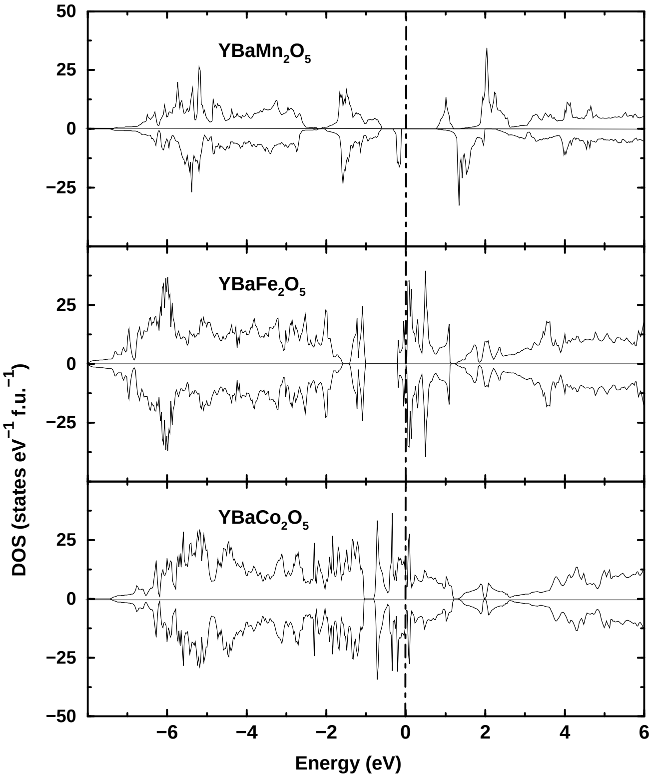

FIG. 2: Total density of states (DOS) of YBaT_2O$_5$ (T = Mn, Fe, Co) in ground-state (G-AF) magnetic configurations (see Table II).

YBMO5 is a semiconductor in the Ferri ground state with an energy gap (E_g) of 0.88 eV between the valence band (VB) and the conduction band (CB). The GGA calculations with spin-orbit coupling reproduced the correct insulating behavior of YBMO5 at 0 K. For YBFO5 and YBCO5 in GGA-type calculations without spin-orbit coupling resulted in DOS (not shown) with a finite num-

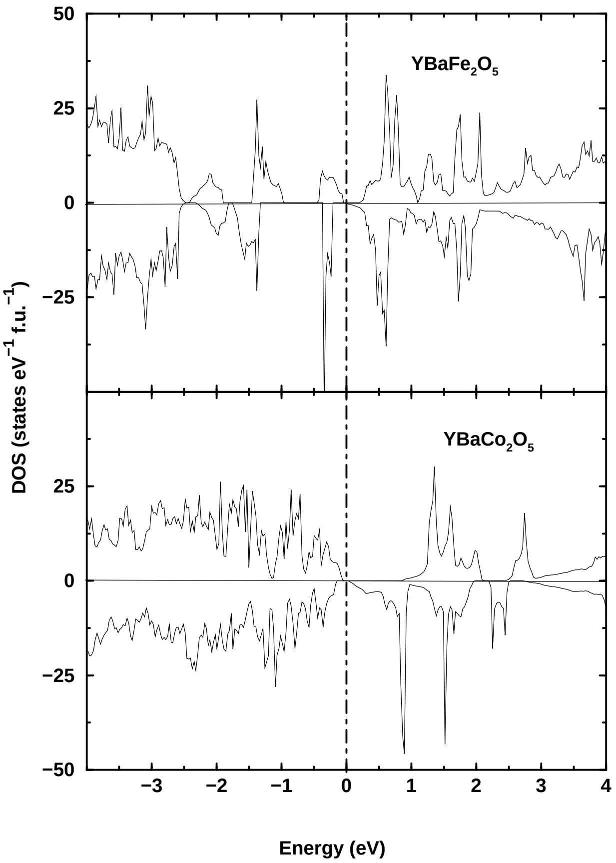

FIG. 3: Total density of states (DOS) of YBaFe$_2$O$_5$ and YBaCo$_2$O$_5$ in the antiferromagnetic configurations according to calculations which include Coulomb correlation effects.

ber of states at E_F. However, when spin-orbit coupling was included some stability was obtained in the sense that the E_F falls on a psuedo-gap-like feature for both phases (Fig. 2). Fig. 3 shows that the total DOS for YBFO5 and YBCO5 according to GGA+U calculations exhibits minute energy gaps (E_g = 0.11 and 0.13 eV, respectively). Refs. [14, 20] also report on insulating behavior for the AF state of YBCO5 on inclusion of LSDA+U in the calculations. The exchange splitting energy for YBMO5 is around 1.03 eV and that for YBFO5 is 0.97 eV. In YBCO5, the states in the majority- and minority-spin channels are so dispersed that it is quite difficult to estimate the exchange-splitting energy.

Since the site-projected DOS for the different YBTO$_5$ phases are very similar, we display only those for YBFO5 and YBCO5 according to GGA+U calculations (Fig. 4). The Y and Ba sites expose few states in VB compared with CB indicating that the Y and Ba atoms have lost their valence electrons to the T and O constituents and themselves become charged species. The two distinct T sites have topologically different DOS features which immediately signals a possible MV situation. The different types of oxygen atoms also exhibit topological differences in the −8 to −2 eV region. A heap up of T-d states are also seen in roughly the same region, implying covalent contribution to the interactions between T and O atoms with different magnitude for the different bonds.

Fig. 5 displays the DOS for the d states of the T atoms in their respective ground-state configurations. Among the three phases, YBMO5 carries the most localized T-d states. In YBFO5 the effect of GGA+U is to make the Fe2 minority-spin states more localized, and thereby bringing about a small energy gap. In YBCO5 on the other hand, the Co states remain delocalized. The influence of GGA+U is here mainly on the non-bonding electrons in the range −2 to 0 eV which are pushed down (away) from E_F. The DOS profiles reveal that the added d electron on going from YBMO5 to YBFO5 should have entered the majority-spin band, resulting in increased difference between majority- and minority-spin bands and consequently to higher magnetic moments for both sites. In the YBCO5 on the other hand it is the states closer to E_F that may have received the extra electron added when Co replaces Fe and hence this change appears to have no magnetic consequences.

C. Charge ordering

According to Ref. [9] the bond valence sums (BVS) for Mn1 and Mn2 in YBMO 5 are 2.43 and 3.10, corresponding BVS values for Fe in YBFO5 being 2.23 and 2.94, and for Co in YBCO5 2.02, 2.69. The difference in BVS for the Fe sites is larger (0.71) than that for Mn (0.67) and Co (0.67). This indicates that the coordination polyhedra around Fe in YBFO5 are comparatively more distorted than those in the corresponding Mn and Co phases. Ref. [9] attributes this distinction to so-called second order JTD. Owing to the presence of the differently charged cationic constituents Y and Ba, different valence states are to be expected for the T1 and T2. The DOS features discussed in Sec. III B supports such an inference. Our experience from previous similar projects is that the assignment of valence states is a non-trivial task for systems which exhibit mixed bonding character. We have therefore relinquished from a detailed analysis of the bonding in this case and rather concentrated on CO and OO aspects.

In order to quantify the electronic charges at each site in the structural framework we have made use of the "atoms in molecule" concept of Bader [21]. According to this approach space (in this case for a solid) is divided into regions by surfaces that run through the minima in the charge density. A given region is chosen such that at any location on a bordering surface the gradient of the charge density has no component normal to the surface. A region enclosed by such boundary surfaces is referred to as a Bader region. Each Bader region normally contains only one nucleus. By integrating the charge density within the Bader region where a given nucleus is located, and adding electronic charges in "naturally associated neighboring regions" that do not include a nucleus, the total excess charge on the atoms at a given site can be

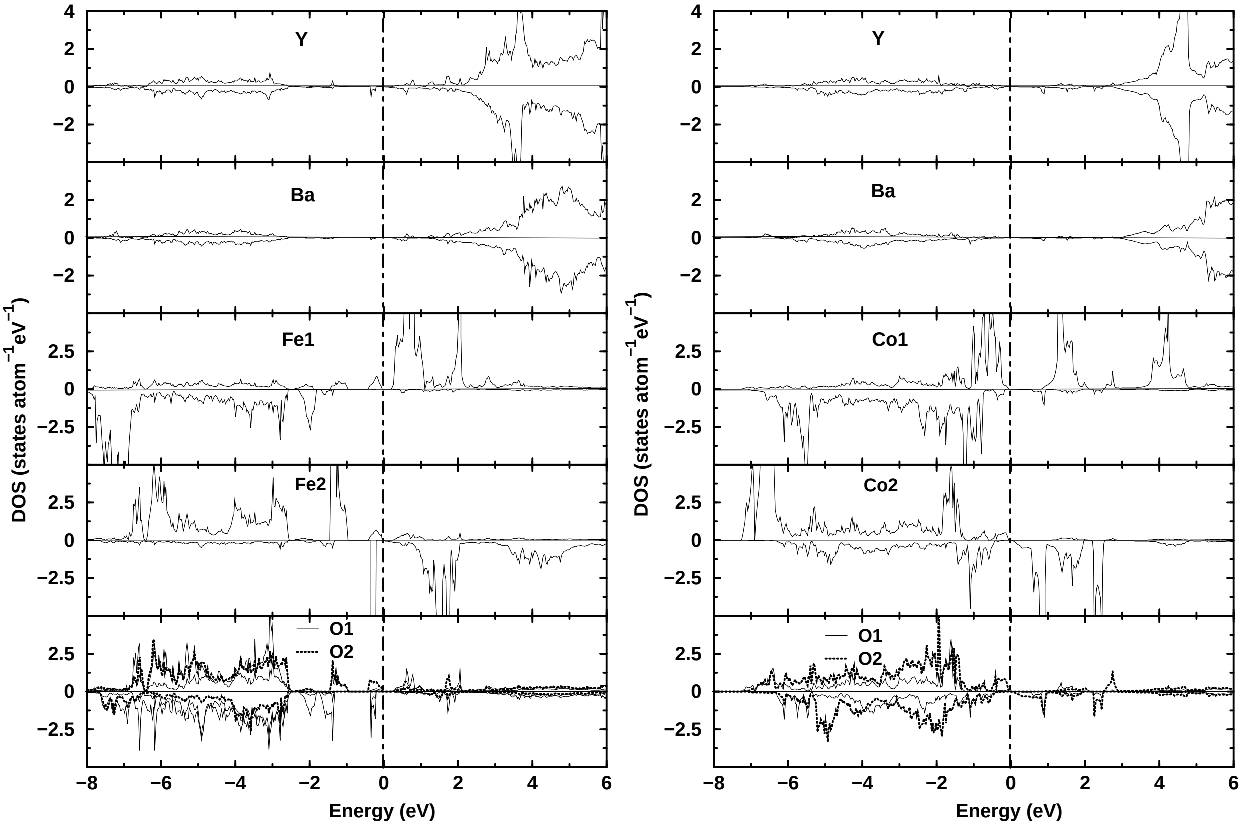

FIG. 4: Site-projected density of states (DOS) of (a) $YBaFe_2O_5$ and (b) $YBaCo_2O_5$ in the antiferromagnetic configurations; Coulomb correlation effects included in the calculations.

TABLE IV: Calculated charge (q_B) and charge heap up ($\Delta q_B = q_Z - q_B$; q_Z representing the charge of the corresponding neutral atom) inside regions defined by the Bader "atoms in molecule" concept as implemented in WIEN2k. All numbers are in units of e.

	YBMO5		YBFO5		YBCO5	
Element	q_B	Δq_B	q_B	Δq_B	q_B	Δq_B
Y	37.58	+1.42	36.84	+2.16	37.53	+1.47
Ba	54.90	+1.10	54.48	+1.52	54.82	+1.18
$T1$	24.15	+0.85	24.48	+1.52	26.35	+0.65
$T2$	24.41	+0.59	24.72	+1.28	26.23	+0.77
O1	8.80	−0.80	9.27	−1.27	8.78	−0.78
O2	8.73	−0.73	9.31	−1.31	8.80	−0.80

estimated. The advantage of this method is that the analysis is based solely on the charge density, so it is rather insensitive to the basis set used. The calculated Bader charges in Table IV support the inference that the $T1$ and $T2$ sites in these phases exhibit different charges. However, we must admit that neither this approach were able to provide quantitative assessments for the valence states of the T atoms. The root of the problem is the mixed iono-covalent bonding in these phases, a feature which not only concerns the T atoms. The conceptual shortcomings are also reflected in the Bader charges residing in the regions of Y and Ba (certainly not 3+ and 2+, respectively, as assumed for simple electron counting) and conversely O does not exhibit a completely filled valence shell (viz. not O^{2-}). However, we presume that even the small charge distinctions exposed in Table IV are large enough to occasion CO. The difference between the Bader charges for Mn1 and Mn2 (0.26) exceeds those for Fe1 and Fe2 (0.24) and Co1 and Co2 (0.12) which may give a hint for why the CO-transition temperature for YBMO5 is higher (and the CO effect is more pronounced) than that for YBFO5 and YBCO5 [9].

D. Orbital ordering

In earlier studies [4–6] on similar phases we used the integrated values of the orbital-projected DOS in a nar-

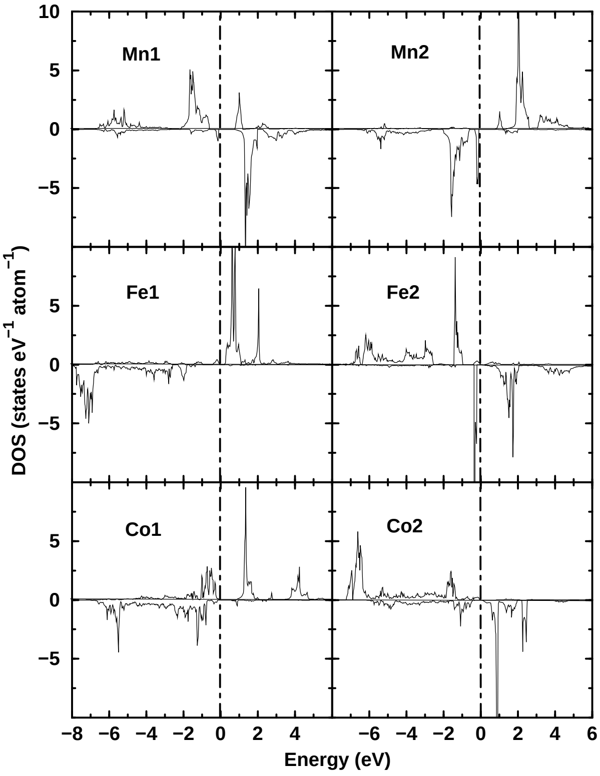

FIG. 5: Site-projected density of states (DOS) for the T sites in YBMO5, YBFO5, and YBCO5.

row energy range close to E_F (-1 to $0\,\mathrm{eV}$) to assess OO. However, we are continuously striving to make our computational efforts point more closely at the real situation in the materials under investigation. Hence we have now tested an alternative approach based on density matrices to visualize the OO by the energy-projected density matrix for the d orbitals of the T constituent. This procedure not only enables characterization of a particular d orbital close to E_F, but should also provide the correct orientation of the orbital and its degree of filling. This should in principle give more appropriate OO information. In order to evaluate such an approach, we first made OO mapping for YBMO5 and the outcome is shown in Fig. 6a. This illustration demonstrates that d_{z^2} orbital on Mn1 and d_{z^2} and $d_{x^2-y^2}$ orbitals on Mn2 order alternatively thus complying with our earlier findings (see Fig. 1d in Ref. [5]). With this affirming conclusion we proceeded to explore the OO in YBFO5 and YBCO5 by this method.

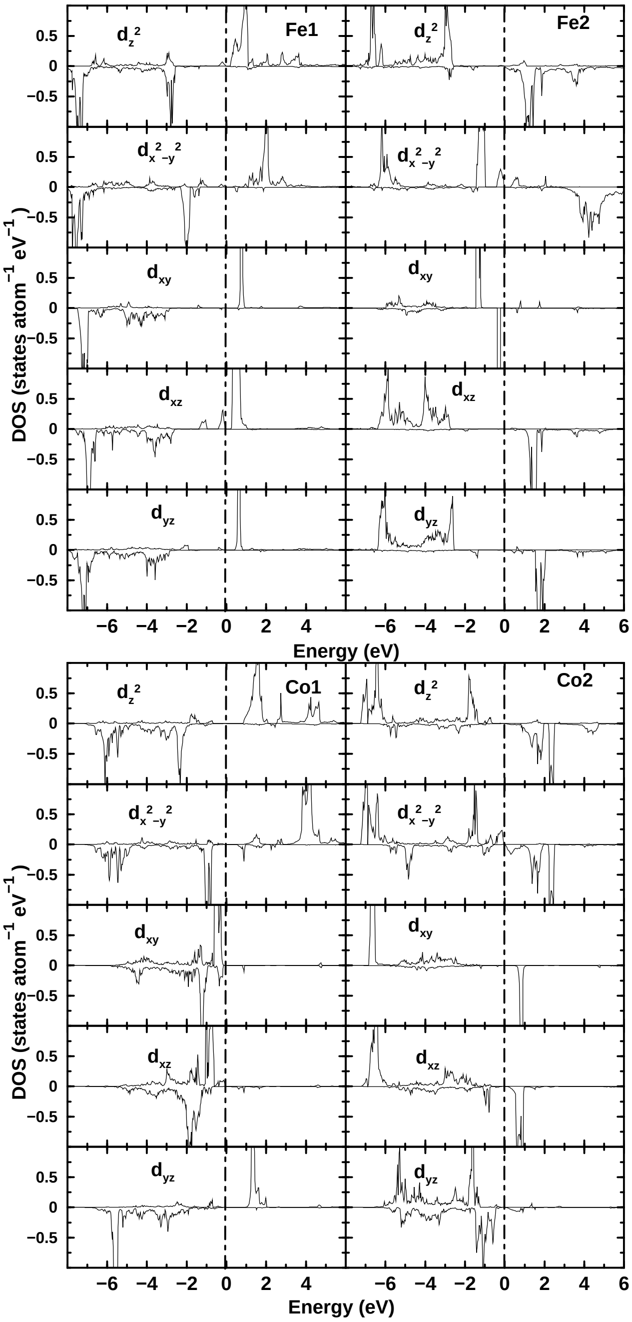

FIG. 6: Orbital-projected density of states (DOS) for T sites in YBFO5 and YBCO5.

In YBFO5 and YBCO5 a T atom at a given site has crystallographically equivalent T atoms of same valence state as nearest neighbors, arranged in chains running along the b axis [see Fig. 6(b,c)]. This arrangement is less favorable for stability of a structure, and hence such a configuration has to be supported by "extra stabilization" from OO and/or SO. According to experimental findings [9], it is claimed that Fe1 has one of its d_{xz} (pseudo-$t_{2\mathrm{g}}$) orbital stacked along the b axis. This effectively antibonding d_{xz} orbital is doubly occupied on Fe1, but only singly occupied on Fe2. The stabilization of the Fe1-d_{xz} orbital is manifested in the elongation of two of the four Fe1-O bonds in the base plane of the square pyramid (due to OO). Before going into details about the OO in the YBTO5 phases it may be appropriate to recall that the splitting of the d-orbitals on a T atom by interacting with atoms in a square-pyramidal configuration will be different from a octahedral case. In the ideal square-pyramidal configuration the d orbitals experience four-fold splitting with degenerate d_{xz} and d_{yz} orbitals

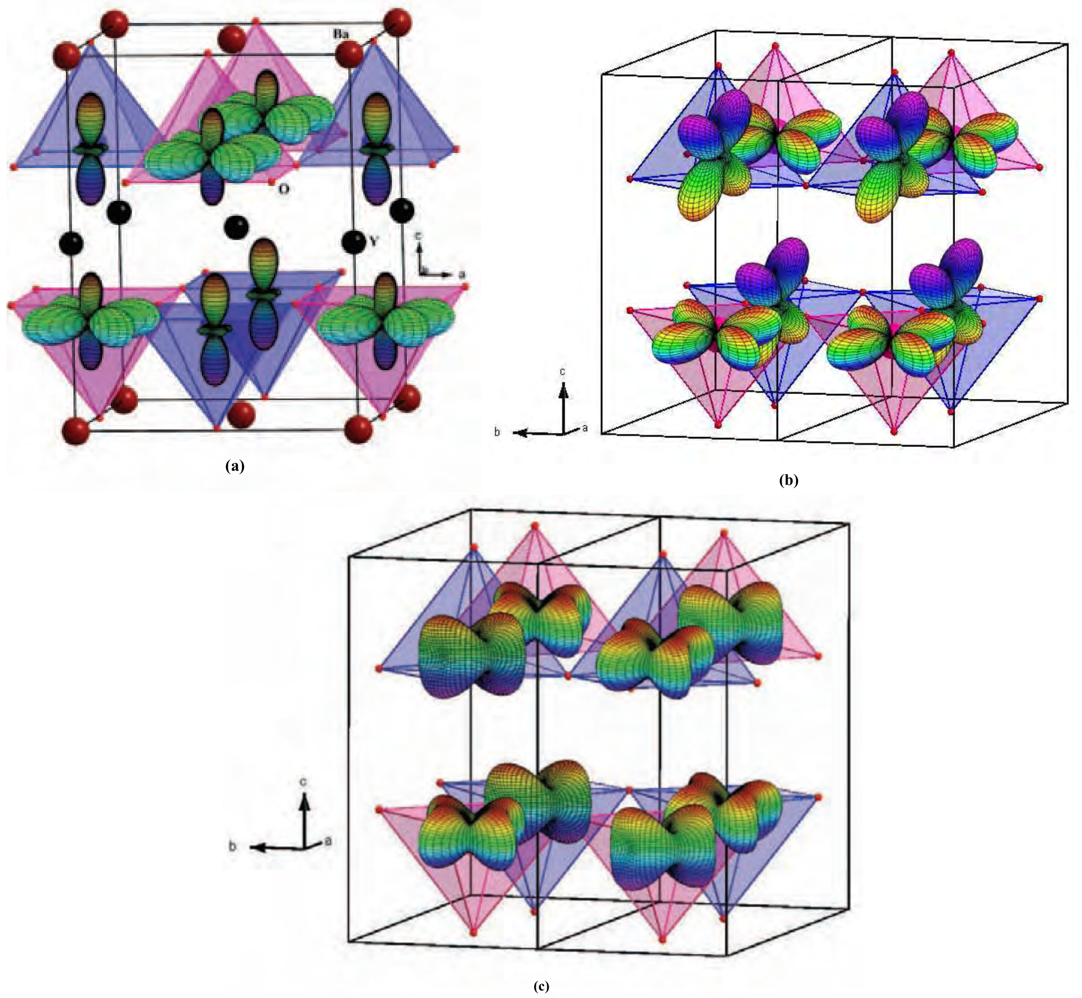

(a)

(b)

(c)

FIG. 7: (Color online) Orbital ordering patterns in (a) YBMO5, (b) YBFO5, and (c) YBCO5. The d_{z^2} in Mn1 and d_{z^2} and $d_{x^2-y^2}$ orbitals in Mn2 order in YBMO5 whereas d_{xz} on Fe1 and d_{xy} on Fe2 order in YBFO5. In Co1 of YBCO5 d_{xz}, d_{yz}, and $d_{x^2-y^2}$ orbitals order whereas d_{xy} and $d_{x^2-y^2}$ orbitals order on Co2.

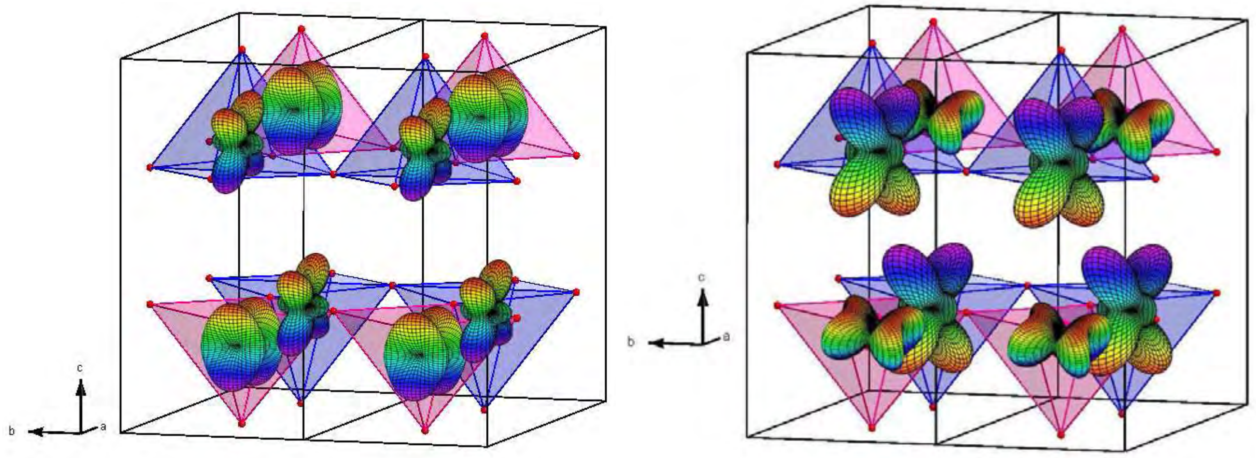

FIG. 8: (Color online) Orbital ordering patterns in (left) YBMO5 and (right) YBFO5 emerging from the rigid-band considerations on YBCO5. In both phases pseudo-t_{2g} orbitals are seen to be ordered whereas in reality, the ordering is as shown in Fig. 7.

residing at the lowest energy and d_{xy}, d_{z^2}, and $d_{x^2-y^2}$ orbitals occurring at progressively higher energies. From the orbital-projected DOS (Fig. 6a) we see that Fe1 may be ascribed a high-spin state with all d orbitals singly occupied. However, the d_{xz} orbital has the predominant presence close to E_{F}. On the other hand, since the square pyramids around Fe2 are somewhat distorted (elongation of Fe-O bonds in the pyramid-base plane; see Table I), the d_{xy} orbital is doubly occupied. Therefore this orbital has more states close to E_{F}. We observed that $d_{x^2-y^2}$ also has some states in the narrow energy region close to E_{F}. In Fig. 7a the blue colored square pyramids represent Fe1 configurations where d_{xz} orbital orders with the respective lobes pointing between the a and c axis. The Fe2 square pyramids are represented by purple color and here the d_{xy} orbital orders with its lobes between the a and b axis. In digesting these findings it must be emphasized that the d-orbital occupancy in the YBTO5 materials is different from the ideal case.

In YBCO5 two pseudo-t_{2g} orbitals on Co1 and one on Co2 are reported [10] to order. From our calculations, we found that Co1 can be associated with a high-spin state with doubly occupied d_{xz} and d_{yz} orbitals whereas Co2 correspondingly is associated with a doubly occupied d_{xy} orbital similar to that for Fe2 in YBFO5. The OO pattern in YBCO5 is different from that in YBFO5. Using the same color code as for YBFO5 to represent the two different Co sites, Fig. 7c shows that the d_{xz}, d_{yz}, and $d_{x^2-y^2}$ orbitals order for Co1 and the d_{xy} and $d_{x^2-y^2}$ orbitals order for Co2.

The overall conclusion is that the OO patterns are very different in YBMO5, YBFO5, and YBCO5. Fig. 8 shows how the OO pattern for YBMO5 and YBFO5 would evolve from the OO in YBCO5 by simply subtracting two and one electrons, respectively, according to a pure rigid-band procedure. The actual OO obtained by experiments and DFT calculations is accordingly very different from the one deduced by rigid-band considerations implying that the OO mainly depends on the structural intricacies rather than on the d orbital filling.

IV. CONCLUSION

This contribution reports on full-potential linearized-augmented plane-wave calculation for $YBaMn_2O_5$, $YBaFe_2O_5$, and $YBaCo_2O_5$ in paramagnetic, ferromagnetic, and antiferromagnetic configurations. The correct experimentally established ferrimagnetic ground state for $YBaMn_2O_5$ and the antiferromagnetic ground states are confirmed for $YBaFe_2O_5$ and $YBaCo_2O_5$ when GGA with spin-orbit coupling is included in the calculations. The GGA+U method with large U and J values gave a ferrimagnetic ground state for $YBaCo_2O_5$. Therefore additional calculations with more strict convergence criteria have been performed which yielded correct antiferromagnetic result also for this compound. The electronic semiconducting ground state is obtained correctly for $YBaMn_2O_5$ with the simple GGA spin-orbit coupling procedure whereas only the GGA+U method is able to provide semiconducting/insulating behavior for the Fe and Co variants. This implies that the Fe and Co phases are strongly correlated systems.

An attempt has been made to analyze the charge ordering phenomena with the help of density of states plots and the Bader "atom in molecule" concept. Even though different amounts of charge have been calculated in the Bader region corresponding to the transition-metal atoms, these calculations were not able to reveal quantitative values for the valence states of these atoms. On comparing the orbital ordering patterns obtained from simple rigid-band filling with those obtained from actual calculations, we found that simple rigid-band filling concept is rather inapplicable to account for and analysis of orbital ordering of these phases. The orbital ordering pattern varies depending on the structural arrangement, distortion of co-ordination polyhedra, magnetic, valence, and spin state of the transition-metal constituents.

V. ACKNOWLEDGEMENT

The authors are grateful to the Research Council of Norway for financial support. Part of these calculations were carried out on the Norwegian supercomputer facilities. R.V and P.R acknowledge J. Kunes for useful communications.

---

[*] Electronic address: **vidya.ravindran@kjemi.uio.no**

[1] A.J. Millis in *Colossal Magnetoresistance Oxides* edited by Y. Tokura (Gordan and Breach, Amsterdam, 2000).
[2] J.F. Mitchell, D.N. Argyriou and J.D. Jorgensen, in *Colossal Magnetoresistance Oxides*, edited by Y. Tokura, (Gordan and Breach, Amsterdam, 2000).
[3] H.A. Jahn and E. Teller, Proc. R. Soc. London **A161**, 220 (1937).
[4] R. Vidya, P. Ravindran, A. Kjekshus and H. Fjellvåg, Phys. Rev. B **65**, 144422, (2002).
[5] R. Vidya, P. Ravindran, P. Vajeeston, H. Fjellvåg, and A. Kjekshus, Cera. Int. **30**, 1993 (2004).
[6] R. Vidya, P. Ravindran, P. Vajeeston, A. Kjekshus, and H. Fjellvåg, Phys. Rev. B **69**, 092405 (2004).
[7] F. Millange, E. Suard, V. Caignaert, and B. Raveau, Mater. Res. Bull. **34**, 1 (1999).
[8] J.B. Goodenough, *Magnetism and the Chemical Bond*, (Interscience, New York, 1966).

[9] P.M. Woodward and P. Karen, Inorg. Chem. **42**, 1121 (2003).

[10] T. Vogt, P.M. Woodward, P. Karen, B.A. Hunter, P. Henning, and A.R. Moodenbaugh, Phys. Rev. Lett. **84**, 2969 (2000).

[11] D. Akahoshi and Y. Ueda, J. Phys. Soc. Jpn. **68**, 736 (1999).

[12] J. Wang, W. Zhang, and D.Y. Xing, Phys. Rev. B **64**, 064418 (2001).

[13] H. Wu, Phys. Rev. B **62**, R11953 (2000).

[14] S.K. Kwon, J.H. Park, and B.I. Min, Phys. Rev. B **62**, R14637 (2000).

[15] P.Blaha, K. Schwarz, G.K.H. Madsen, D. Kvasnicka, and J. Luitz, WIEN2k, revised edition 2001. Vienna University of Technology, An Augmented Plane Waves + Local Orbitals Program for Calculating Crystal Properties,Vienna, 2003.

[16] P. E. Blöchl, Phys. Rev. B **50**, 17953 (1994).

[17] J.P. Perdew, S. Burke, and M. Ernzerhof, Phys. Rev. Lett. **77**, 3865 (1996).

[18] P. Novak, F. Boucher, P. Gressier, P. Blaha, and K. Schwarz, Phys. Rev. B **63**, 235114 (2001).

[19] J. M. Wills, O. Eriksson, M. Alouani, and D. L. Price, in *Electronic Structure and Physical Properties of Materials*, edited by H. Dreysse (Springer, Berlin, 2000) p.148; J.M. Wills and B. R. Cooper, Phys. Rev. B **36**, 3809 (1987); D. L. Price and B. R. Cooper, Phys. Rev. B **39**, 4945 (1989).

[20] J. Wang, Y.C. Tao, W. Zhang, and D.Y. Xing, Phys. Rev. B **65**, 052407 (2002).

[21] R.F.W. Bader, *Atoms in Molecules A Quantum Theory* (Clarendon Press, Oxford, 1990).

V

Spin, charge, and orbital ordering in RBaMn$_2$O$_{5+\delta}$ (R = Y, La; $0 \leq \delta \leq 1$) and their dependence on oxygen content and size of the R constituent

R. Vidya*, P. Ravindran, A. Kjekshus and H. Fjellvåg
Department of Chemistry, University of Oslo, Box 1033 Blindern, N-0315 Oslo, Norway

The effect of oxygen content on spin, charge, and orbital ordering in RBaMn$_2$O$_{5+\delta}$ ($0 \leq \delta \leq 1$) is studied by density-functional-theory-based calculations as implemented in the full-potential linearized-augmented plane-wave method. Calculations have systematically been performed for paramagnetic, ferromagnetic, and antiferromagnetic configurations. For $\delta = 0$ the ground state turned out to be ferrimagnetic whereas the variants with oxygen contents $\delta = 1/2$ and 1 give rise to an antiferromagnetic ground state, all in perfect agreement with experimental findings. The electronic band characteristics are analyzed using total, site-, and orbital-projected density of states and the examination shows that the electronic structure undergoes a gradual change from semiconductor-to-metal behavior on going from $\delta = 0$ to 1. The charge and orbital ordering are analyzed with the help of the energy-projected-density matrices of the d electrons and very different ordering patterns have emerged.

PACS numbers: 71., 81.05.Je, 71.15.Nc, 71.20.-b, 81.40.Rs

So-called double perovskite variants with the general formula $R_{1-x}A_x$Mn$_2$O$_{5+\delta}$ ($0 \leq x \leq 1$; R = rare-earth element, A = alkaline-earth element; $0 < \delta < 1$) have been extensively investigated over the last decade. Potential technological application has greatly stimulated the research activity and the scientific community has benefited from these efforts in the form of improved comprehension of the systems. Many interesting features like colossal magnetoresistance, metal-insulator transitions, and spin, charge, and orbital ordering (SO, CO and OO) are certainly associated with this special class of materials. Such enchanting phenomena are believed to be caused by competition between the spin, charge, and orbital degrees of freedom.

In general, there will be disorder in the lattice when A and R in the proportion x:($1-x$) are randomly distributed in the appropriate sub-lattice of the structure. However, e.g., for $x = 1/2$, proper metal-ordered double perovskites (RAMn$_2$O$_6$) are formed with alternate stacking of layers of R and A along the c axis (this orientation of the unit cell requires in some cases space group transformation). Structural and physical properties of such a structural arrangement has been recently reported [2] for R = Y and La−Er. Owing to cation-size mismatch and Jahn-Teller distortion, RAMn$_2$O$_6$ phases undergo transition between paramagnetic-metal and antiferromagnetic-insulator states and charge-ordering transitions occur at relatively high temperatures. An interesting aspect of the RAMn$_2$O$_6$ phases with R = Y and La is their ability to form stable oxygen-deficient variants; here more conveniently represented by the reverse formula RAMn$_2$O$_{5+\delta}$ and conceptually added oxygen. The oxygen deficiencies are normally formed in the R layers of such structures.

One of the parameters used to describe CO is the transfer integral t between Mn-d and O-p states. When the t value is high, electrons are imagined to be able to hop from one Mn atom to another Mn via an appropriately arranged intervening O, giving rise to metal-like couplings between electrons known as double-exchange interaction. However when t is small, the electrons get localized on the Mn sites and this ultimately result in CO. Thus the oxygen content and the arrangement and population of the oxygen orbitals relative to the Mn-d orbitals govern the metal-insulator transitions and play an important role in the SO, CO, and OO mechanisms. We have earlier reported on the influence of oxygen occupancy on CO and OO in LaBaMn$_2$O$_{5+\delta}$ [1], and in this report we give an account for our findings for YBaMn$_2$O$_{5+\delta}$. The aim has been to evaluate the composite effects of oxygen content and size mismatch of the constituents of RAMn$_2$O$_{5+\delta}$ on CO and OO phenomena.

The composition of the present phases is chosen so that for $\delta = 0$ equal amounts of Y/La and Ba lead to equal amounts of Mn atoms in the formal ionic valence states 2+ and 3+, thus maximizing the Coulomb stabilization energy of the CO state. In the same breath, phases with $\delta = 1/2$ should exhibit only Mn^{3+} and those with $\delta = 1$ should have the formal ionic states Mn^{3+} and Mn^{4+}. In fact, experimental [3, 4] and theoretical studies have confirmed that YBaMn$_2$O$_5$ and LaBaMn$_2$O$_5$ carry two different types of Mn atoms with simultaneous CO and OO in addition to the ferrimagnetic (Ferri) spin ordering (SO). Since we have earlier analyzed the magnetic and electronic properties of YBaMn$_2$O$_5$ [8] and LaBaMn$_2$O$_5$ [1] in detail, an obvious challenge is to perform a comparative analysis of the two RAMn$_2$O$_{5+\delta}$ systems.

I. CRYSTAL AND MAGNETIC STRUCTURES

YBaMn$_2$O$_5$ and LaBaMn$_2$O$_5$ crystallize in the tetragonal YBaCuFeO$_5$-type structure (Refs. [3, 4]; space group $P4/nmm$). Oxygen-vacant Y or La and oxygen-full Ba layers are formed alternatively along the c axis [Fig. 1(a)]. Two crystallographically different Mn atoms are situated in square-pyramidal co-ordination with their oxygen neighbors. Associated with the different size of Y and Ba

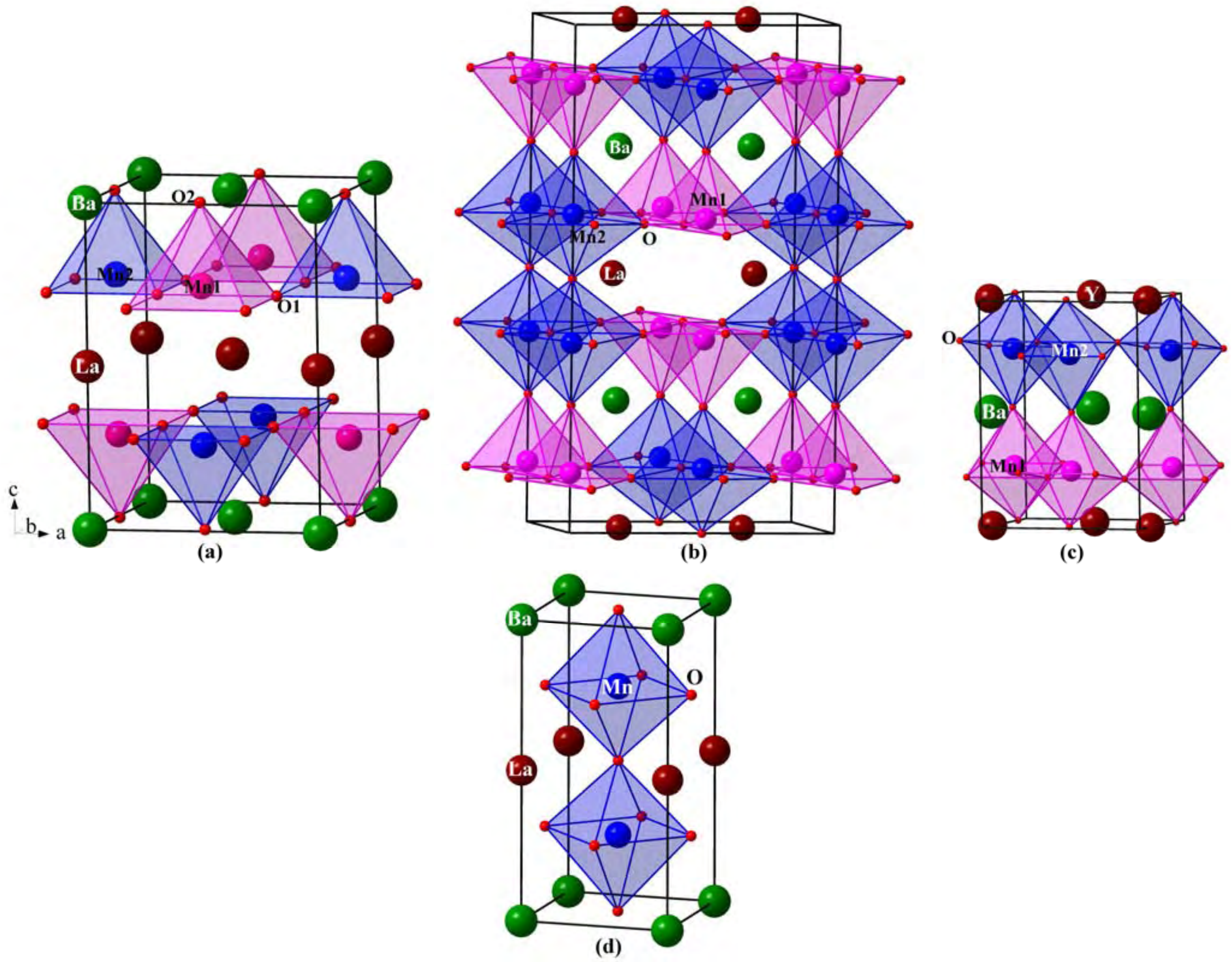

FIG. 1: (Color online) Crystal structures of (a) tetragonal $LaBaMn_2O_5$, (b) orthorhombic $LaBaMn_2O_{5.5}$ ($YBaMn_2O_{5.5}$ is virtually isostructural), (c) tetragonal $LaBaMn_2O_6$, and (d) monoclinic $YBaMn_2O_6$. Atoms of different kinds are labelled on the illustration.

the corresponding Mn-O bond lengths as well as Mn-O-Mn bond angles become appreciably different and these features are known to play crucial roles in the physical properties of these materials.

The $YBaMn_2O_{5.5}$ and $LaBaMn_2O_{5.5}$ phases are ascribed an orthorhombic structure [Refs. [4, 5]; space group *Ammm*; Fig. 1(b)]. The extra oxygen atoms compared with the $\delta = 0$ cases partially occupy the earlier oxygen-empty Y or La layers. Therefore half of the square-pyramids gain an extra oxygen atom and change their co-ordination polyhedra from square pyramids to octahedra. The structural arrangement of $LaBaMn_2O_{5.5}$ is illustrated in Fig. 1(b).

In $YBaMn_2O_6$ and $LaBaMn_2O_6$ the oxygen content of the originally oxygen-empty (viz. at $\delta = 0$) Y or La layers has become completely filled up and all the earlier square pyramids are converted into octahedra. A notable distinction between $YBaMn_2O_6$ and $LaBaMn_2O_6$ is that the former takes a low-symmetric monoclinic structure (space group $P2$; Fig. 1(c); also reported to be triclinic [7]) whereas the latter adopts a tetragonal structure [Ref. [4]; space group $P4/mmm$; Fig. 1(d)]. The influence of the size mismatch between the constituent is best seen for $\delta = 1$ where the Y-based phase exhibits highly distorted octahedra whereas those of the La variant are more regular. In $YBaMn_2O_6$ there are two crystallographically non-equivalent Mn sites (Mn1 and Mn2) and eight oxygen sites [see Fig. 1(c)] The two kinds of MnO_6 octahedra show large variation in Mn-O-Mn bond angles (157.5 to 176.8°) and a remarkable difference even in the average Mn-O distances (1.96 Å for Mn1-O and 1.93 Å for Mn2-O). The nature and magnitude of the octahedral tilting depend not only on the Y-to-Ba vs La-to-Ba mismatch but also on co-ordination preference for Y and La, covalence effects etc. Using the Goldschmidt tolerance factor as an indicator, the MnO_2 layer in $YBaMn_2O_6$

TABLE I: Bond lengths (in Å) and bond angles (in deg) between Mn and O in RBaMn$_2$O$_{5+\delta}$ (δ = 0, 1/2, and 1).

Specification	Y;δ=0	La;δ=0	Y;δ=1/2	La;δ=1/2	Y;δ=1	La;δ=1
R−O	2.406	2.530	2.568	2.642	2.773	2.716
Ba−O	2.937	2.945	2.962	2.938	2.774	2.759
Mn1−O1[a]	1.908	1.941	1.830; 1.929	1.893; 1.963	1.850; 1.810; 1.980	1.953
Mn1−O2[b]	2.081	2.004	2.107	2.025	2.080; 2.030; 2.050	1.970; 1.926
Mn2−O1	2.086	2.105	2.284; 1.888	2.231; 1.932	1.880; 1.800; 1.900; 1.990	–
Mn2−O2	1.961	1.985	1.923; 1.857	1.898; 1.942	2.090; 1.950	–
Mn1-O1-Mn2	157.8	160.8	165.53; 155.24	167.68; 168.82	172.4; 165.6; 157.5; 176.8; 162.9	174.19
Mn1-O2-Mn2	180	180	180; 174.53	180; 175.46	161.8; 172.3	180

[a] O in the base plane of the polyhedra.

[b] O at the apex of the polyhedra.

should feel opposite oriented strain forces (viz. be subjected structural frustration) from the adjacent Y-O and Ba-O layers. Because of this frustration, the structural mismatch can not be compensated by mere tilting of the MnO$_6$ octahedra. As a consequence, the shape of the octahedra becomes heavily deformed [2]. Moreover, the MnO$_2$ planar oxygen configuration is displaced toward the Y layer and away from Ba layer, resulting in shifts of the Mn and O atoms from the positions ascribed for ideal octahedral geometry. Even though the deviation from regular octahedral arrangement also has been observed in the structure of LaBaMn$_2$O$_6$, this phase only exhibits one crystallographically equivalent Mn site and the octahedra are only slightly distorted. Note that zero tilting of the co-ordination polyhedra is obtained only when there are vacant oxygen sites in the Y or La layers of YBaMn$_2$O$_5$ or LaBaMn$_2$O$_5$.

Since the experimental studies on YBaMn$_2$O$_6$ have come to structural arrangements based on different space groups, structural optimization calculations were made for both alternatives. The first set of calculations was performed with the monoclinic ($P2$) and triclinic ($P1$) arrangements described in Refs. [2] and [7], respectively, as input guess structures. These calculations terminated at structural parameters that favored the monoclinic variant by nearly 0.77 eV f.u.$^{-1}$ in terms of the total energy. However, continued calculation in which the structure was allowed to relax without the symmetry constraints of $P2$ resulted in nearly the same unit-cell dimensions, but with a somewhat different atomic arrangement which obeys the symmetry of space group Pc. The unit-cell dimensions and positional parameters for this description of the YBaMn$_2$O$_6$ structure are given in Table II. The total-energy gain on going from the experimental $P2$ to the optimized Pc variant amounts to nearly 1.01 eV f.u.$^{-1}$ Such a large gain in total energy must be appreciated on our finding that forces of nearly 3.2 eV Å^{-1} were acting on the Mn sites in the input experimental ($P2$) structure. It was indeed this fact that led us to perform the optimization of structural parameters. The difference between the calculated (Pc based atomic arrangement) and experimental unit-cell volume is ∼1.64%, well within the limit accepted for DFT calculations. We have used the optimized structural parameters in Table II to analyze magnetic and electronic properties of YBaMn$_2$O$_6$.

Owing to the different space requirement of the Y and Ba atoms, the Mn1-O and Mn2-O bond lengths and the Mn1-O-Mn2 bond angles differ considerably and these distinctions are reflected in the physical properties of the RBaMn$_2$O$_{5+\delta}$ phases. Table I displays relevant bond lengths and bond angles according to the experimental structure determinations. The Mn1-O distance (between Mn and the oxygen atoms in the "base plane" of the co-ordination polyhedra; oriented parallel to the ab plane of the lattice) is shorter in the Y phases than in the corresponding La variants. The opposite is true for Mn2-O (viz. distance to apical oxygen atoms), Y phases having generally longer bonds than their La counterparts. Moreover, the Mn1-O-Mn2 bond angles along the "base plane" of the co-ordination polyhedra deviate much from 180°. The bond angles running along the apices of polyhedra (oriented along c direction) is equal to, or deviate only little from, 180°. The deviation in bond angles from the ideal 180° is generally larger for R = Y than for La variants which in itself is a hint of an effect of the size difference between Y and La. Among the considered phases, YBaMn$_2$O$_6$ displays the overall largest distortion of the co-ordination polyhedra. The accumulated knowledge on the RBaMn$_2$O$_{5+\delta}$ phases indicates that such materials may hide a lot of yet unexplored exotic physical properties. Therefore it may be accordingly worthwhile to analyze more systematically their relevant physical properties in terms of the oxygen content and the size of the R and A constituents.

The RBaMn$_2$O$_{5+\delta}$ phases subject to this study take antiferromagnetic (AF) arrangements of the moments at low temperatures [except YBaMn$_2$O$_5$ and LaBaMn$_2$O$_5$ where the moments of Mn do not cancel, resulting in a Ferri arrangement]. An explicit magnetic structure for YBaMn$_2$O$_{5.5}$ is hitherto not reported, but LaBaMn$_2$O$_{5.5}$ takes [10] a magnetic structure with F-spin ladders along the b axis that are AF coupled along the a and c axes. This co-operative ordering pattern is used in our AF calculations for YBaMn$_2$O$_{5.5}$. However, YBaMn$_2$O$_6$ is reported [2] to take a intricate-modified CE-AF-type magnetic ordering. Since calculations on this complex magnetic arrangement appeared as a very daunting task, we here only considered the regular A-, C-, and G-AF-type magnetic structures along with the P and F arrangements. An F and CE-AF-type state is believed [6] to

TABLE II: Optimized ground-state structural parameters for $YBaMn_2O_6$ (monoclinic; space group Pc). All atoms in $2a$ positions. Experimental values taken from Ref. 2 are given in the parentheses.

Unit cell (Å or ^{o})	Atom	Positional parameters
a = 5.5536 (5.5193)	Y	0, 0.7619, 0 (0, 0.7425, 0)[a]
b = 5.5242 (5.5131)	Ba	1/2, 0.7538, 0 (1/2, 0.7635, 0)
c = 7.6487 (7.6135)	Mn1	0.2433, 0.7498, 1/2 (0.2430, 0.7565, 1/2)
β = 90.58 (90.30)	Mn2	0.7567, 0.7498, 1/2 (0.7570, 0.7565, 1/2)
V = 234.64 (231.67) Å^{3}f.u.$^{-1}$	O1	0, 0.8123, 1/2 (0, 0.7960, 1/2)
	O2	0.2006, 0.5197, 0.7711 (0.2035, 0.5015, 0.7720)
	O3	0.7994, 0.5196, 0.2290 (0.7965, 0.5015, 0.2280)
	O4	0.2421, 0.0220, 0.7298 (0.2420, 0.0135, 0.7280)
	O5	0.7579, 0.0220, 0.2702 (0.7580, 0.0135, 0.2720)
	O6	1/2, 0.7259, 1/2 (1/2, 0.7215, 1/2)

[a] In order to enable a direct comparison with the optimized parameters, experimental data are also described in Pc symmetry rather than the original $P2$ symmetry.

co-exist for $LaBaMn_2O_6$ at low temperatures, but we assumed a simple AF structure for this phase.

II. COMPUTATIONAL DETAILS

In the present calculations we have made use of the density-functional-theory (DFT) approach implemented in the full-potential linearized-augmented plane wave (FPLAPW−WIEN2k) method [12] in a fully-relativistic version (including spin-orbit coupling). In the FPLAPW method, space is divided into an interstitial region (IR) and non-overlapping muffin-tin (MT) spheres centered at the atomic sites. In the IR the basis set consists of plane waves. Inside the MT spheres the basis set is described by radial solutions of the one-particle Schrödinger equation at fixed energies, and their energy derivatives multiplied by spherical harmonics. The charge densities and potentials in the atomic spheres were represented by spherical harmonics up to $\ell = 6$, whereas in the interstitial region these quantities were expanded in Fourier series. Atomic-sphere radii R_{MT} of 2.2, 2.3, 1.9, and 1.6 a.u. for Y, La, Ba, Mn, and O, respectively, were used. We earlier noted that the resulting magnetic moments do not depend appreciably on the chosen atomic-sphere radii. The initial basis set included 5s, 5p, and 4d valence and 4s and 4p semicore functions for Y, 6s, 6p, and 6d valence and 5s and 5p semicore functions for La and Ba, 4s, 4p, and 3d valence and 3s and 3p semicore functions for Mn, and 2s, 2p, and 3d functions for O. The Brillouin zone (BZ) integration was done with a modified tetrahedron method [13] using approximately 200 **k** points in the irreducible wedge of BZ, depending on the crystal structure of the compound in question. Exchange and correlation effects are treated under the generalized-gradient-approximation (GGA) [14] including the Perdew-Burke-Ehrenkof (PBE) functional.

TABLE III: Total energy (relative to the lowest energy state in meV f.u.$^{-1}$) for $YBaMn_2O_{5+\delta}$ and $LaBaMn_2O_{5+\delta}$ with $\delta = 0$, 1/2, and 1 in para- (P), ferro- (F), and antiferromagnetic (AF) configurations using FPLAPW including GGA and spin-orbit coupling.

Compound	P	F	AF
$YBaMn_2O_5$	3388	422	0 (G-AF)
$LaBaMn_2O_5$	3421	365.4	0 (G-AF)
$YBaMn_2O_{5.5}$	3090	41.1	0 (G-AF)
$LaBaMn_2O_{5.5}$	6268	3324	0 (G-AF)
$YBaMn_2O_6$	1354	34.8	0[a] (C-AF)
$LaBaMn_2O_6$	1220	42.2	0 (Simple AF)

[a] G-AF is 20.8 meV higher in energy than C-AF.

III. RESULTS AND DISCUSSION

A. Magnetic properties

Total-energy calculations in paramagnetic (P), F and AF configurations have been performed for the phases subject to this study, and as seen from Table III the AF state is preferred in all cases. The calculated AF ground state for the Y and La phases with $\delta = 0$ and 1/2, is in perfect agreement with the experiments. As mentioned earlier, we simulated the A-, C-, and G-AF-type structures for the $YBaMn_2O_6$ phase and found that A-AF-type always converged to an F state with the G-AF-type arrangement at higher energy than the C-AF variant (see also Table III).

A Curie temperature of ($T_C =$) 335 K is experimentally reported [6] for $LaBaMn_2O_6$. This F state could not be confirmed by our calculations. Our earlier full-potential linear muffin-tin orbital (FP-LMTO) calculations as well as the present calculations clearly show that this phase should take an AF ground state. For this phase also coexistence between F and CE-AF-type is proposed. This may be taken as a hint that the F state (which rules the macroscopic behavior of experimental samples) is introduced by kinetic effects, and likely originates from chemical or physical imperfections.

TABLE IV: Calculated and experimental magnetic moment (in μ_B per Mn atom) for RBaMn$_2$O$_{5+\delta}$ in antiferromagnetic ground state (see Table III). Total refers to the total magnetic moment per formula unit.

	Theory			Experiment		
Compound	Mn1	Mn2	Total	Mn1	Mn2	Total
YBaMn$_2$O$_5$	2.94	3.79	0.99	2.90[a]	3.90	0.95
LaBaMn$_2$O$_5$	2.99	3.88	1.03	2.71[b]	3.21	0.70
YBaMn$_2$O$_{5.5}$	3.24	3.36	0.03	–	–	–
LaBaMn$_2$O$_{5.5}$	3.15	3.25	0.00	3.03[c]	3.43	0.00
YBaMn$_2$O$_6$	2.84	2.86	0.01	–	–	–
LaBaMn$_2$O$_6$	2.93	2.93	0.00	3.50[b]	–	–

[a] Experimental data taken from Ref. [3].
[b] Experimental data taken from Ref. [4].
[c] Experimental data taken from Ref. [10].

The calculated magnetic moments given in Table IV are seen to be in good agreement with the available experimental data. As also mentioned earlier, the Y and La phases with $\delta = 0$ have non-zero total moments and these accordingly take a Ferri ground state, whereas the other phases have zero or negligible total moments and these deserve classification as AF. Table IV shows that the difference between the magnetic moments at the Mn1 and Mn2 sites decreases gradually on increasing δ from 0 to 1/2. Differences in magnetic moments are commonly used as an indicator for different valence states. In this case the target is the valence states of Mn1 and Mn2 (and subsequently the question of CO). The magnetic moment data alone suggest different Mn valence states at $\delta = 0$ and valence equalization at $\delta = 1/2$ and 1. A detailed analysis of the electronic structure parameters shows that the situation is not so simple (see below). However, it seems safe to conclude that co-operative magnetic properties are determined by the oxygen contents of these phases rather than by the size and other features associated with Y and/or La.

From the calculated magnetic moments we infer that, the Mn atoms in RBaMn$_2$O$_5$ can be categorized as in the class-I mixed-valence (MV) [16] configuration where the Mn sites take different valence states. When the oxygen content increases (to $\delta = 1/2$), the Mn atoms can be regarded as converting to a class-II MV category where two different valence states exist together but with only slight difference between them. When the oxygen atoms completely fill the R layer, the Mn atoms may convert to the class-III MV category where the distinction in the co-ordination and valence states completely disappears. In YBaFe$_2$O$_5$ [17] the conversion from class-III to class-II and finally to class-I MV situation takes place on reducing the temperature. However, in the present case we witness such an occurrence on changing the oxygen stoichiometry.

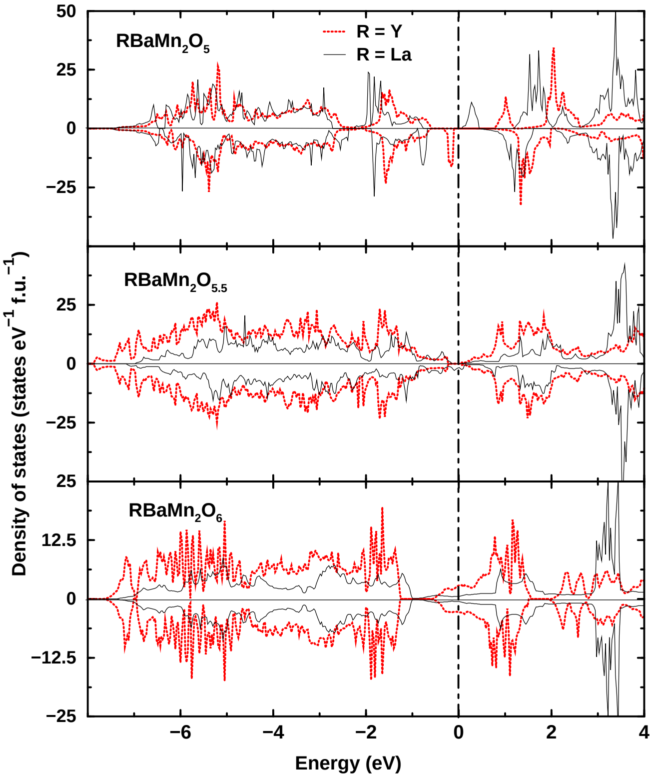

FIG. 2: (Color online) Total density of states (DOS) of RBaMn$_2$O$_{5+\delta}$ with R = Y (black), La (red) and δ = 0, 1/2, 1 in the ground-state AF configurations.

B. Electronic structure

The electronic structures of the RBaMn$_2$O$_{5+\delta}$ phases are analyzed with the help of total, site-, and orbital-projected density of states (DOS) plots. In the higher-energy P state all phases exhibit metallic character with finite number of states at the Fermi level (E_{F}). The RBaMn$_2$O$_5$ phases also exhibit a small number of states at the E_{F} in the F state, whereas the remaining phases have half-metallic behavior with a finite number of states at the E_{F} in one spin channel and an energy gap at the E_{F} in the other spin channel. The size of the gap in the minority-spin channel is 2.12, 1.83, 1.61, and 1.36 eV for YBaMn$_2$O$_{5.5}$, LaBaMn$_2$O$_{5.5}$, YBaMn$_2$O$_6$, and LaBaMn$_2$O$_6$, respectively. The decrease in the gap on going from $\delta = 0$ to 1 is already an indication of covalent bonding interaction between Mn-d and O-p states and a resulting dispersion of minority-spin states.

The total DOS of RBaMn$_2$O$_{5+\delta}$ in the ground-state AF configurations are displayed in Fig. 2. The RBaMn$_2$O$_5$ phases are semiconducting with an energy gap of 0.88 and 0.86 eV for R = Y and La, respectively. When oxygen is filled to $\delta = 1/2$ in the R layer, the gap decreases to 0.22 eV for YBaMn$_2$O$_{5.5}$ and 0.26 eV for LaBaMn$_2$O$_{5.5}$, and when the oxygen content is filled up to $\delta = 1$ the band gap has completely disappeared and a finite number of states is clearly seen at the E_{F}

in Fig. 2. The states at or near the E_F originate from Mn-*d* and O-*p* orbitals which implies that enhanced hybridization interaction between the electrons concerned leads to increased metallic character. According to Fig. 2 it can also be seen that $\mathrm{YBaMn_2O_6}$ has more states at E_F than $\mathrm{LaBaMn_2O_6}$ which may be correlated with the structural finding [2] that the former is more distorted than the latter [see Fig. 1(c, d)]. It is worthwhile to recall that the former compound has highly distorted octahedra compared to those in $\mathrm{LaBaMn_2O_6}$. Moreover, the oxygen atoms in the "base planes" of the co-ordination polyhedra are gradually more displaced toward the Y layers with increasing δ. Thereby the corresponding Mn-O distances are decreased and the hybridization interaction increases and so does the number of states at the E_F.

Nakajima et al. [2] claim successive phase transitions for $\mathrm{YBaMn_2O_6}$ from a P-metallic state via a P-insulating state to an AF-insulating state. The latter conversion is said to take place below 200 K. Although our calculations refer 0 K, we used input lattice parameters corresponding to those measured at 350 K. Hence our choice of lattice parameters could have influenced the calculated properties, and this may in principle explain why we obtained metal rather than insulating ground state for the $R\mathrm{BaMn_2O_6}$ phases. We also mention that, in the case of $\mathrm{LaMnO_3}$ [18], we only obtained the correct insulating ground-state when the experimentally-established A-AF-type configuration was taken into account in the calculations. Hence we believe that, one may also obtain insulating behavior for the $R\mathrm{BaMn_2O_6}$ phases on including the experimentally inferred *CE*-AF-type ordering in the calculations.

For the phases with $\delta = 0$ and 1/2, we found that the GGA with spin-orbit coupling is able to provide the correct insulating behaviors and magnetic ground states. Hence we had expected the same outcome for the $R\mathrm{BaMn_2O_6}$ phases. Fair enough, our calculations gave AF ground states for these compounds, but with metallic rather than insulating behavior. This result may of course be an indication for stronger correlation effects than anticipated. Therefore a possible extension of the studies on these phases would be to try to account for correlation effects by performing LDA+U calculations.

C. Site-projected density of states

Since the site-projected DOS for $R\mathrm{BaMn_2O_5}$ phases are reported already in Refs. [1, 8], we concentrate the present analyses on the phases with $\delta = 1/2$ and 1. From Fig. 3(a,), it is evident that the R and Ba atoms have largely donated their valence electrons to the other constituents and themselves entered ionic states [evident from the small number of states in the valence band (VB) and a larger number of states in the conduction band (CB)]. In the phases with $\delta = 1/2$, Mn1 is associated with the Mn atom with square-pyramidal co-ordination and Mn2 with the octahedral co-ordination. Although the topology of the DOS curves for Mn have similar features for the $R\mathrm{BaMn_2O_{5.5}}$ phases, the Mn atoms of the La variant have more states in the range from -6 to -4 eV than the Y variant (see Fig. 3). The most prominent localized Mn states are seen from -2 eV to E_F for both phases. The bulk of the oxygen states is found in the range -6 to -1 eV for both phases. Since the Mn and O states cover more or less the same energy region, there must be hybridization and appreciable degrees of covalent bonding between them. A comparison of the Y and La phases with $\delta = 1/2$ shows that the latter carries more localized states than the former, and accordingly that the covalent bonding interaction between Mn and O is stronger in $\mathrm{LaBaMn_2O_{5.5}}$ than in $\mathrm{YBaMn_2O_{5.5}}$. This may give a hint to explain the smaller magnetic moments at the Mn sites in the La phase than that in the Y phase, since electrons are confined to participate either in magnetic interaction or in bonding interaction.

The oxygen-filled-up $R\mathrm{BaMn_2O_6}$ variants do not have very different site-projected DOS features (Fig. 4). The DOS features for these two phase are similar to those for $\delta = 0$ and $\delta = 1/2$ in the sense that R and Ba have few states in the VB, indicating as already mentioned appreciable ionic character. Although there are two types Mn in $\mathrm{YBaMn_2O_6}$, the Mn-O bond lengths and magnetic moments at the Mn sites do not exhibit much distinction. This is reflected in their DOS in the sense that both Mn atoms have almost similar DOS features. Even though there is chemically only one type of Mn available in the $\mathrm{LaBaMn_2O_6}$ structure, we show DOS curves [Fig. 4(b)] for the magnetically different Mn atoms, to facilitate comparison with Mn situations in the corresponding phases with $\delta = 0$ and 1/2. The metallic conductivity of $R\mathrm{BaMn_2O_6}$ is originating from the Mn-*d* states. The most prominent localized Mn states are found close to E_F (from -2 to -1 eV) whereas more dispersed states are found from -7 to -2 eV. The Mn atoms of $\mathrm{YBaMn_2O_6}$ have larger peaks around -1.5 eV compared to the Mn states of $\mathrm{LaBaMn_2O_6}$. The oxygen atoms of the two phases also have prominent states in the same energy range (-7 to -2 eV), again evidencing covalent bonding interaction between the Mn and O atoms. It is interesting to note that more Mn-*d* and O-*p* states are present at the E_F for $\mathrm{YBaMn_2O_6}$ than for $\mathrm{LaBaMn_2O_6}$. This implies stronger covalent interaction between Mn and O atoms in the former phase, thus reducing the magnetic moments at Mn compared to the latter phase.

The above detailed analysis on the electronic structures of the phases under investigation leads one to believe that, the overall features of electronic structure vary more as a response to the oxygen content than to the size of R constituents. However, finer details of electronic structure also depends on the Mn-O-Mn bond angle which is determined by the size of the R constituents.

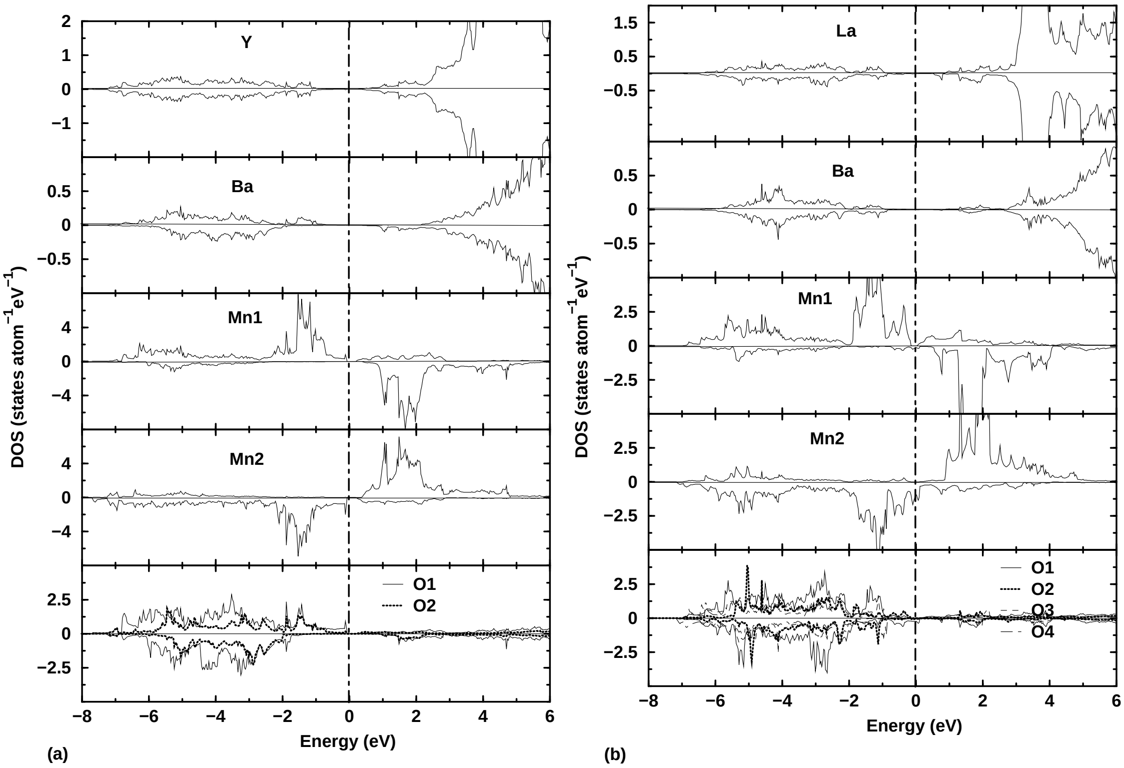

FIG. 3: Site-projected density of states (DOS) for RBaMn$_2$O$_{5.5}$ [R = (a) Y and (b) La] in the antiferromagnetic configurations.

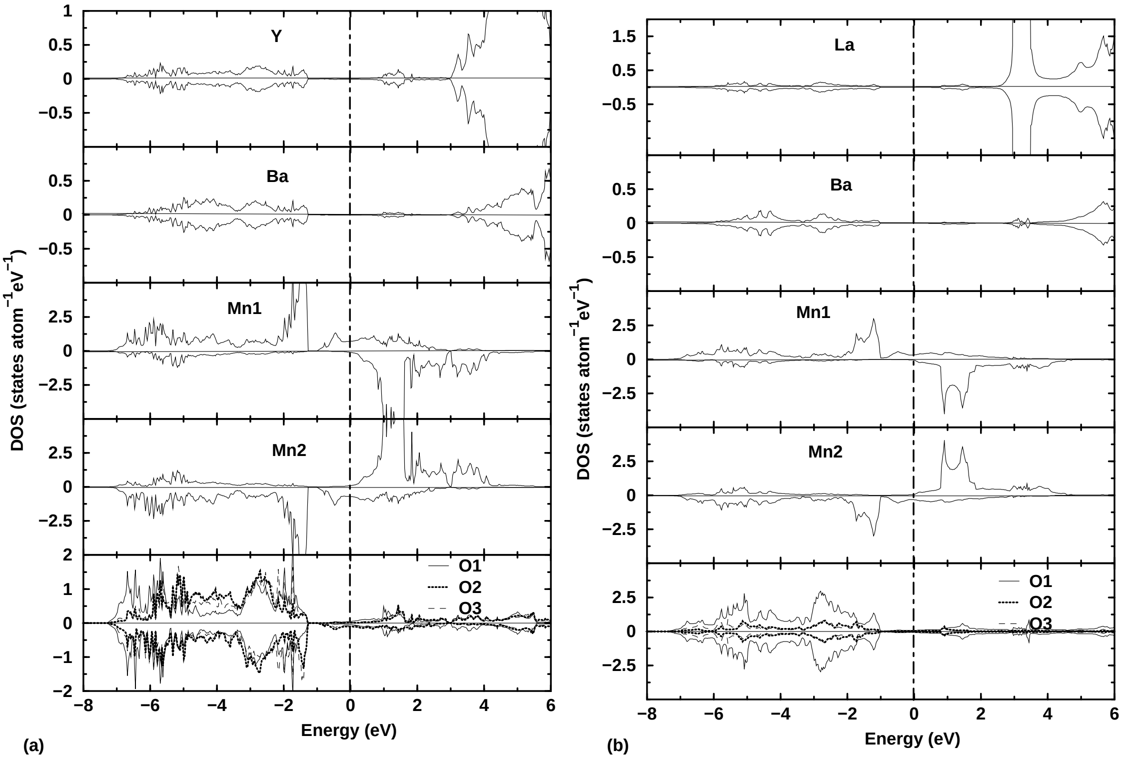

FIG. 4: Site-projected density of states for RBaMn$_2$O$_6$ (R = Y and La) in the antiferromagnetic configurations.

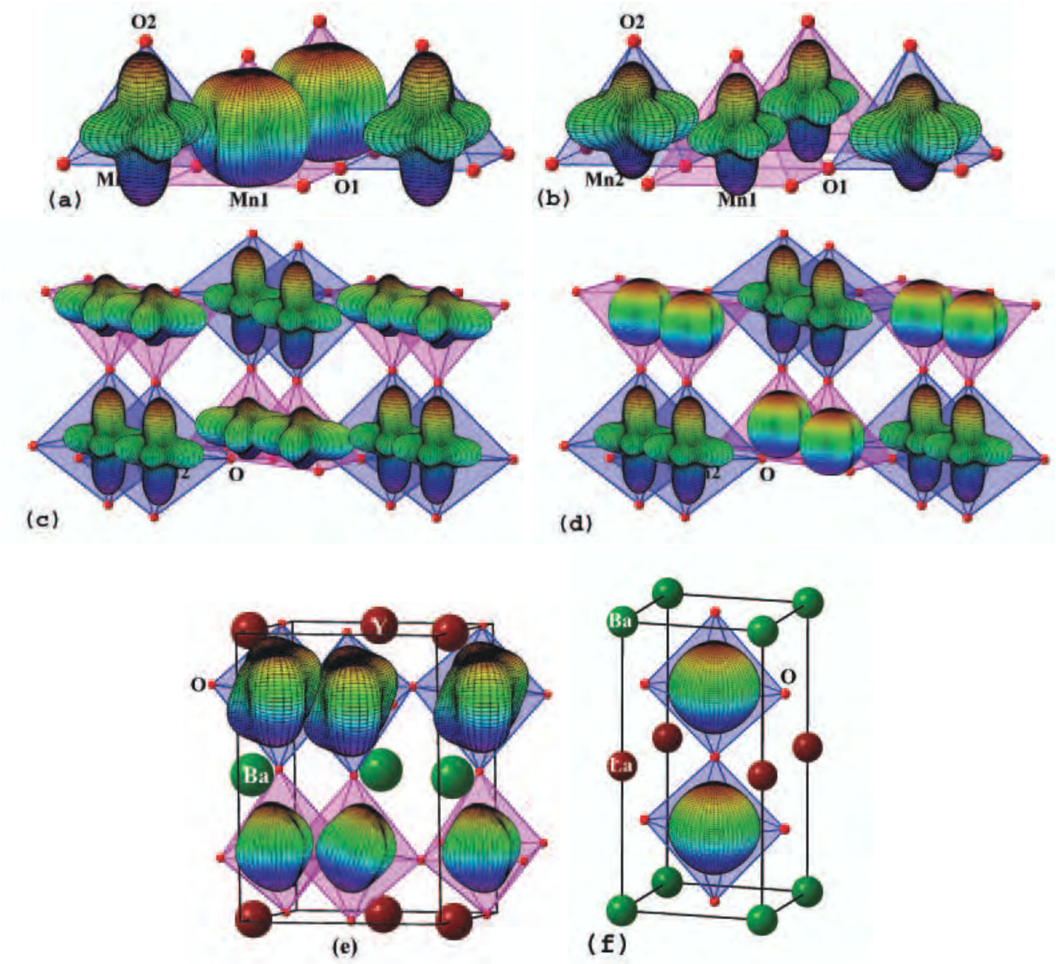

FIG. 5: (Color online) The charge ordering pattern obtained from the occupation matrices of majority-spin d orbitals in (a) $YBaMn_2O_5$, (b) $LaBaMn_2O_5$, (c) $YBaMn_2O_{5.5}$, (d) $LaBaMn_2O_5$, (e) $YBaMn_2O_6$ and (f) $LaBaMn_2O_6$. The purple-colored polyhedra contain Mn1 and blue-colored polyhedra containn Mn2 as central atoms. The degree or filling of d orbitals is indicated by their radial extension.

IV. CHARGE AND ORBITAL ORDERING

In order to analyze the CO phenomena in these phases, we take the above findings as a starting point and in addition we make use of orbital-projected DOS plots. The atomic arrangements of the $R\mathrm{BaMn_2O_5}$ phases have Mn-O-Mn bond angles deviating from 180^o in the square-pyramid base plane which hinders the transfer of electrons and tends to localize the electrons on the Mn sites. In these phases, a checker-board-type CO is established (see Fig. 5.

In our earlier report [1] we determined the OO pattern for $LaBaMn_2O_5$ from its orbital-projected DOS. The t_{2g}-like orbitals were believed to be ordered subject to slight variations in the location of E_F. In the present study we make use of the energy-projected occupation density matrix to evaluate the CO and OO. From this new approach we are not only able to identify occupation of a particular orbital in a particular energy range but also we obtain their orientation. Hence we believe that this new approach may be more appropriate to visualize the OO features. According to this new approach, we find no difference in the OO patterns of $YBaMn_2O_5$ and $LaBaMn_2O_5$ [see Fig. 5(a,b)]. The d-orbital-projected DOSs for $R\mathrm{BaMn_2O_5}$ (Fig. 7) display almost similar features in the sense that, the d_{z^2} orbital on Mn1 and d_{z^2} and $d_{x^2-y^2}$ orbitals on Mn2 occur close to the E_F. Therefore these orbitals order according to a pattern named [7] as ferro-orbital order (Fig. 6) in which same type of OO is established for both $R\mathrm{BaMn_2O_5}$ phases.

When oxygen atoms half fill the R layer in the $\delta = 1/2$ phases, half of the square pyramids become octahedra. As already pointed out, the degree of structural distortion is larger in the Y phase than in the La phase. Owing to the different types of Mn-O co-ordinations and the associated differences in bond angles and bond lengths the charges localize on the Mn sites and leads to a CO state. Fig. 5(c,d) show the so-called stripe-type CO pattern in $YBaMn_2O_{5.5}$ and $LaBaMn_2O_{5.5}$, respectively.

The corresponding OO patterns in $YBaMn_2O_{5.5}$ and

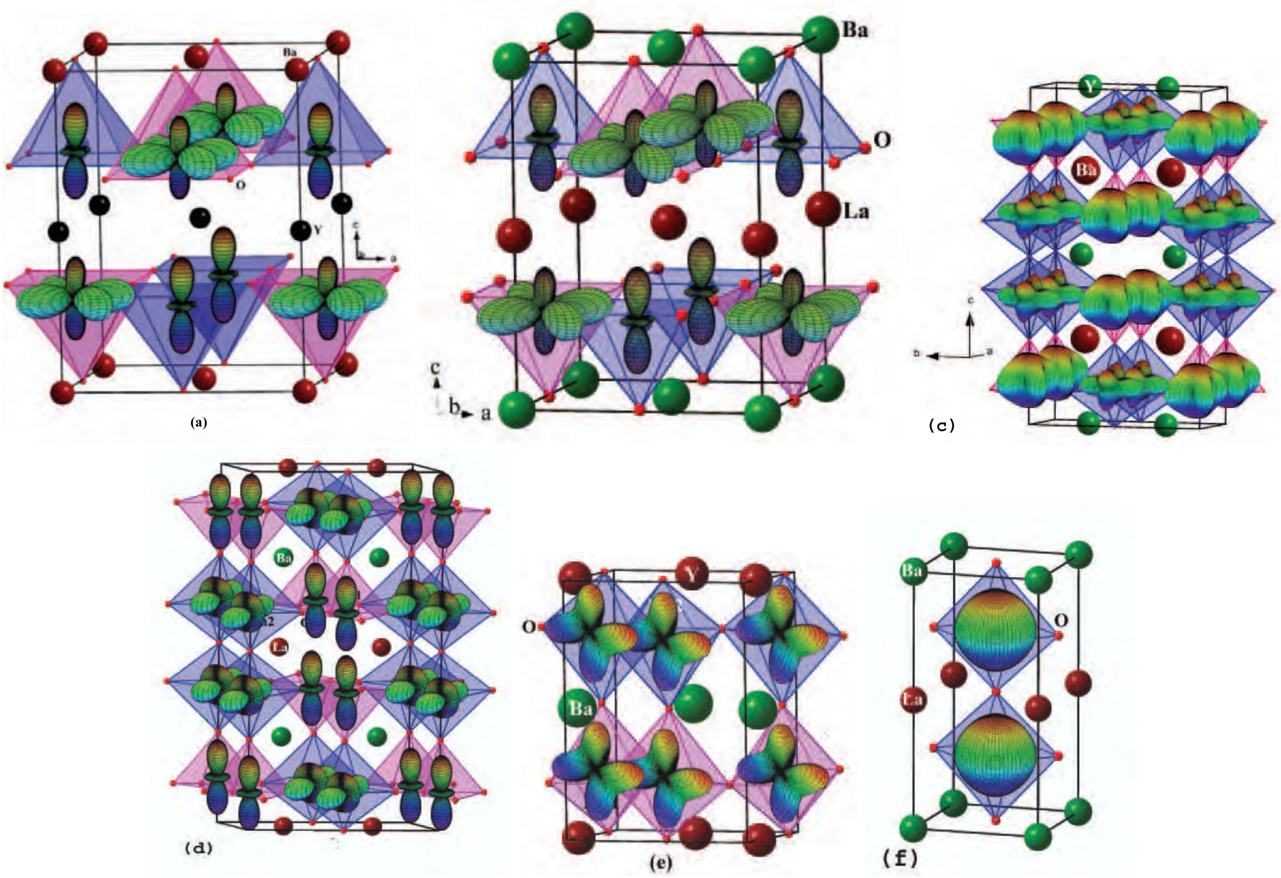

FIG. 6: (Color online) The orbital ordering pattern obtained from the occupation matrices of *d* states close to the Fermi level in (a) $YBaMn_2O_5$, (b) $LaBaMn_2O_5$, (c) $YBaMn_2O_{5.5}$, (d) $LaBaMn_2O_{5.5}$, (e) $YBaMn_2O_6$, and (f) $LaBaMn_2O_6$. The purple-colored polyhedra contain Mn1 and blue-colored polyhedra containn Mn2 as central atoms. The degree or filling of *d* orbitals is indicated by their radial extension.

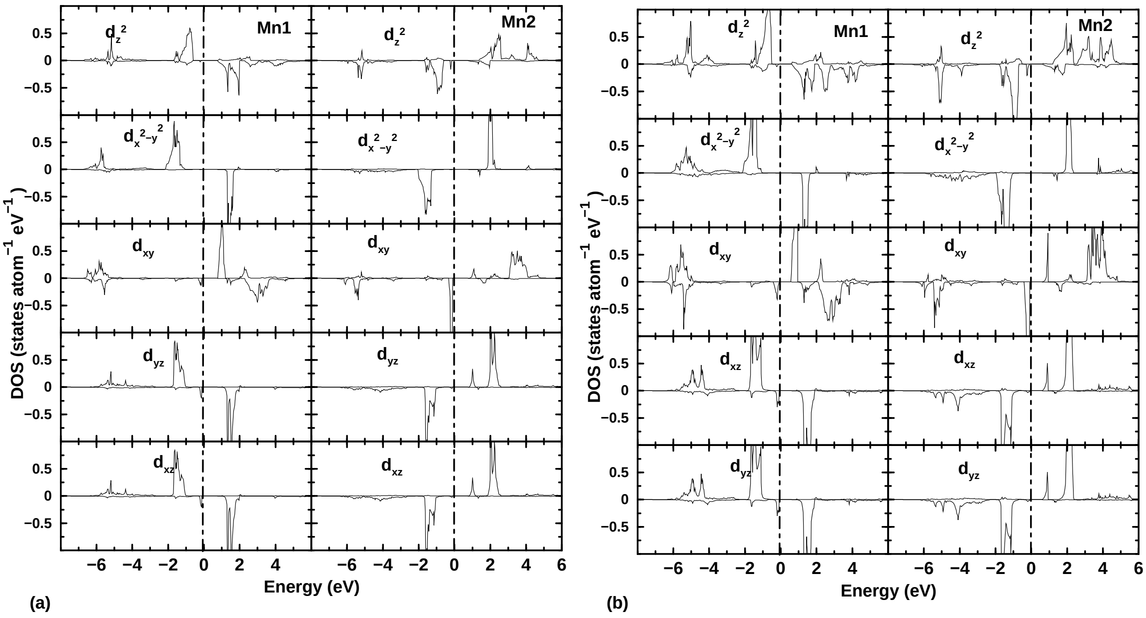

FIG. 7: The *d* orbital-projected density of states for (a) $YBaMn_2O_5$ and (b) $LaBaMn_2O_5$ in the antiferromagnetic configurations.

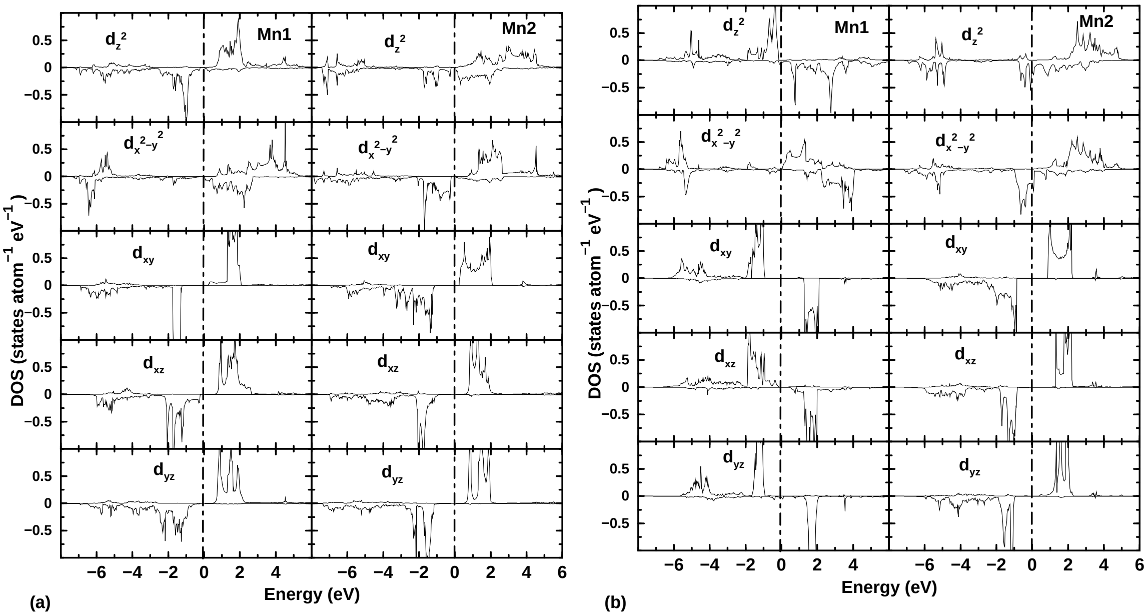

FIG. 8: The d-orbital-projected density of states for (a) $YBaMn_2O_{5.5}$ and (b) $LaBaMn_2O_{5.5}$ in the antiferromagnetic configurations.

$LaBaMn_2O_{5.5}$ are displayed in Fig. 6(c,d). Even though the charges order in more or less similar manners in these phases, the OO expose significant differences. The Mn1-O distances in the "base plane" of the square pyramids in $YBaMn_2O_{5.5}$ are shorter than those in $LaBaMn_2O_{5.5}$. The opposite is true for the Mn1-O distances along the apices of the square pyramids. Therefore, there will be large interaction between the t_{2g}-like orbitals of Mn1 (and also to some extent the Mn1-d_{z^2} orbital) and the p orbitals of O. Thus the ordered orbitals on the Mn1 site in $YBaMn_2O_{5.5}$ have t_{2g} character (and some d_{z^2} character). However, owing to the shorter Mn1-to-apical-oxygen distance in $LaBaMn_2O_{5.5}$, the interaction between Mn1-d_{z^2} and O-p orbitals is enhanced compared to that between the Mn1-t_{2g} and O-p orbitals. Therefore, the d_{z^2}-orbital orders at Mn1 in $LaBaMn_2O_{5.5}$. The orbital-projected DOS features (Fig. 8) also agree with the above inference. At the Mn2 site, both e_g (d_{z^2} and $d_{x^2-y^2}$) orbitals order for both phases, however, owing to the different distortion of the co-ordination octahedra, the orientations become different in the R = Y and La two phases.

The CO on the Mn sites in $YBaMn_2O_6$ and $LaBaMn_2O_6$ is displayed in Fig. 5(e,f). In the case of $YBaMn_2O_6$ a small difference is seen between the ordered charges on Mn1 and Mn2 whereas for $LaBaMn_2O_6$ only spherical distribution of charges is seen with no special ordering pattern. The orbital-projected DOS for these phases are shown in Fig. 9, respectively. A relatively large amount of DOS close to the E_F is contributed by electrons in the $d_{x^2-y^2}$ and d_{xz} orbitals at the Mn sites of $YBaMn_2O_6$. Therefore these orbitals order on the Mn sites [Fig. 6(e)]. As mentioned earlier, the large deviations from 180° of the Mn-O-Mn bond angles along the base plane of the square pyramids and octahedra are believed to obstruct the transfer of charges leading to their localization in different ordering patterns.

The orbital-projected DOS for $LaBaMn_2O_6$ depicted in Fig. 9(b) shows that d_{z^2} and $d_{x^2-y^2}$ orbitals at the Mn sites are formed close to E_F . Therefore the ordering of these orbitals in fact are seen as spherical distributions similar to the CO features of this phase. However, it should be remembered that the RBaMn$_2$O$_6$ phases have metallic character. Hence charge localization, the main requirement for charge ordering should be absent in these phases. Experimental work [2] on $YBaMn_2O_6$ reported a metal-to-insulator transition below 230 K and a modified-CE-type charge ordering. Even though our calculations show some signs of charge ordering in $YBaMn_2O_6$, its metallic character shrouds this interpretation in a cloud of uncertainty. Therefore, the calculations on the experimentally-suggested modified-CE-AF-type structure becomes mandatory in order to establish the correct properties of these phases. Until such calculation come at hand, our findings should be regarded as qualitative and significance should certainly not be attached to band structure details.

V. CONCLUSIONS

In order to evaluate the combined effect of oxygen content and size of the R constituents on spin, charge, and orbital orderings accurate electronic-band structure calculations have been carried out on RBaMn$_2$O$_{5+\delta}$ (R = Y, La; δ = 0, 1/2, 1) phases. Full-potential linearized augmented plane-wave methods have been employed for the study. The calculated magnetic moments are found to be

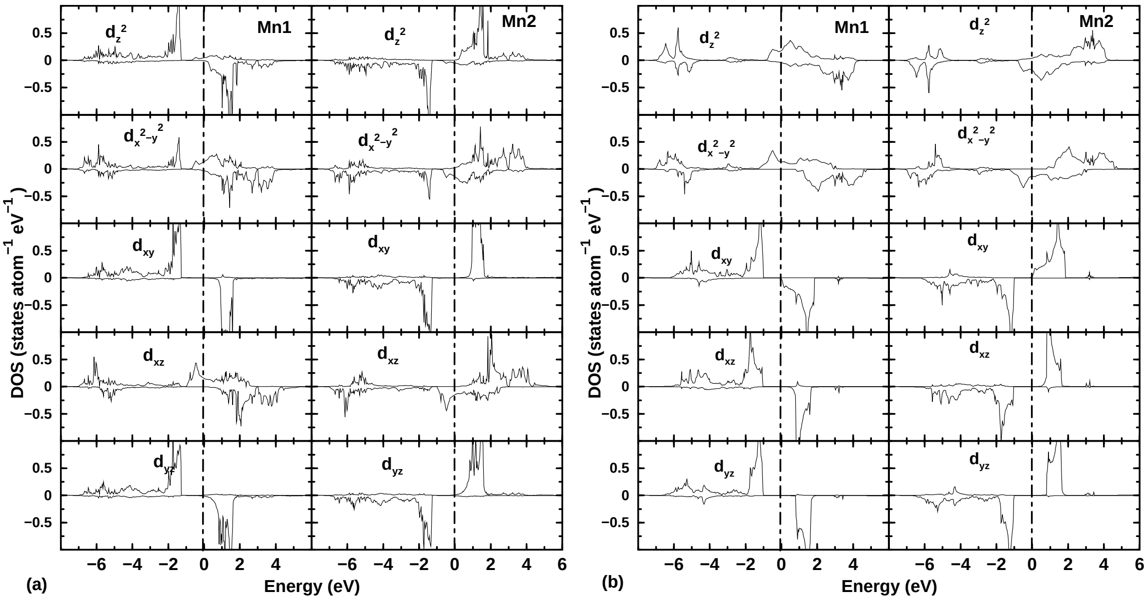

FIG. 9: The d-orbital-projected density of states for (a) $YBaMn_2O_6$ and (b) $LaBaMn_2O_6$ in the antiferromagnetic configurations.

in close agreement with available experimental data. The studied phases are seen to undergo gradual changes from so-called class-I via class-II to class-III mixed-valence situations on increasing the oxygen content from $\delta = 0$ via 1/2 to 1. The electronic structure is also found to vary from semiconductor to metal on going from $\delta = 0$ to 1, with a decrease in the band gap for the intermediate $\delta = 1/2$ phases. Since the $\delta = 1$ phases are reported to be insulating from experimental studies, inclusion of the correct co-operative magnetic order in the calculations seems to be important.

The overall physical properties such as magnetic and electronic properties change as a function of the oxygen content. The influence of the oxygen content on the Mn-O framework appears to be the origin of this relationship, notably through facilitation or obstruction of charge transfer and/or exchange interactions. We also found that the size of R constituent plays a role in determining the shape and the related distortions of the coordination polyhedra such as elongation or shortening of particular Mn-O bond(s) which in turn influences occupancy or vacancy of a particular d orbital(s). Therefore, intricate details of charge and orbital ordering (such as occupation of a particular orbital in a particular energy region, with resulting orbital ordering etc.) are found to vary with the size of the R constituent.

VI. ACKNOWLEDGEMENT

The authors are grateful to the Research Council of Norway for financial support. Part of these calculations were carried out on the Norwegian supercomputer facilities.

---

[*] Electronic address: **vidya.ravindran@kjemi.uio.no**
[1] R. Vidya, P. Ravindran, P. Vajeeston, A. Kjekshus, and H. Fjellvåg, Phys. Rev. B **69**, 092405 (2004).
[2] T. Nakajima, H. Kageyama, M. Ichihara, K. Ohoyama, H. Yoshizawa, and Y. Ueda, J. Solid State Chem. **177**, 987 (2004).
[3] F. Millange, E. Suard, V. Caignaert, and B. Raveau, Mater. Res. Bull. **34**, 1 (1999).
[4] F. Millange, V. Caignaert, B. Domenges, and B. Raveau, Chem. Mater. **10**, 1974 (1998).
[5] M. Karppinen, H. Okamoto, H. Fjellvåg, T. Motohashi, and H. Yamauchi, J. Solid State Chem. **177**, 2122 (2004).
[6] T. Nakajima, H. Kageyama, H. Yoshizawa, and Y. Ueda, J. Phys. Soc. Jpn. **71**, 2843 (2002).
[7] A.J. Williams and J.P. Attfield, Phys. Rev. B **72**, 024436 (2005).
[8] R. Vidya, P. Ravindran, A. Kjekshus, and H. Fjellvåg, Phys. Rev. B **65**, 144422, (2002).
[9] R. Vidya, P. Ravindran, P. Vajeeston, H. Fjellvåg, and A. Kjekshus, Cera. Int. **30**, 1993 (2004).
[10] V. Caignaert, F. Millange, B. Domenges, B. Raveau, and E. Suard, Chem. Mater. **11**, 930 (1999).
[11] J.B. Goodenough, Magnetism and the Chemical Bond, (Interscience, New York, 1966).
[12] P.Blaha, K. Schwarz, G.K.H. Madsen, D. Kvasnicka, and J. Luitz, WIEN2k, revised edition 2001. Vienna Univer-

sity of Technology, An Augmented Plane Waves + Local Orbitals Program for Calculating Crystal Properties,

[13] P. E. Blöchl, Phys. Rev. B **50**, 17953 (1994).

[14] J.P. Perdew, S. Burke, and M. Ernzerhof, Phys. Rev. Lett. **77**, 3865 (1996).

[15] J. M. Wills, O. Eriksson, M. Alouani, and D. L. Price, in *Electronic Structure and Physical Properties of Materials*, edited by H. Dreysse (Springer, Berlin, 2000), p. 148; J.M. Wills and B. R. Cooper, Phys. Rev. B **36**, 3809 (1987); D. L. Price and B. R. Cooper, Phys. Rev. B **39**, 4945 (1989).

[16] M.B. Robin and P. Day, Adv. Inorg. Chem. Radiochem. **10**, 247 (1967).

[17] P.M. Woodward and P. Karen, Inorg. Chem. **42**, 1121 (2003).

[18] P. Ravindran, A. Kjekshus, and H. Fjellvåg, A. Delin, and O. Eriksson, Phys. Rev. B **65**, 064445 (2002).

VI

PHYSICAL REVIEW B **72**, 014411 (2005)

Structural stability, electronic structure, and magnetic properties of mixed-valence $A\mathrm{Cr}_3\mathrm{O}_8$ phases (A = Na, K, Rb)

R. Vidya,* P. Ravindran, P. Vajeeston, H. Fjellvåg, and A. Kjekshus
Department of Chemistry, University of Oslo, Box 1033 Blindern, N-0315 Oslo, Norway

(Received 11 January 2005; revised manuscript received 5 April 2005; published 5 July 2005)

The structural stability, electronic structure, and magnetic properties are studied for $A\mathrm{Cr}_3\mathrm{O}_8$ (A=Na, K, Rb; Cr in two formally different valence states) using accurate density-functional calculations. The calculations show that at 0 K and high pressures $\mathrm{NaCr}_3\mathrm{O}_8$ remains a ferromagnetic insulator whereas $\mathrm{KCr}_3\mathrm{O}_8$ and $\mathrm{RbCr}_3\mathrm{O}_8$ undergo an antiferromagnetic-insulator-to-ferromagnetic-insulator transition, the transition pressure decreasing with increasing radius of A^+ from $\mathrm{KCr}_3\mathrm{O}_8$ to $\mathrm{RbCr}_3\mathrm{O}_8$. Indirect Cr1-to-Cr1 exchange interaction via two intervening oxygen atoms is the origin of the antiferromagnetism. The calculated structural parameters are consistent with the experimental values, actual deviations being discussed.

DOI: 10.1103/PhysRevB.72.014411 PACS number(s): 78.20.Ls, 78.20.Ci

I. INTRODUCTION

Compounds with mixed-valent transition-metal ions are interesting as they exhibit exotic properties such as charge ordering, high-temperature superconductivity, and colossal magnetoresistance (CMR). Since the discovery of CMR, a lot of attention has been paid to mixed-valent manganese compounds. Most frequently studied are 3d transition-metal oxides with Mn, Fe, Co, or Cu atoms. Cr substitution for Mn in $\mathrm{Pr}_{0.5}\mathrm{Ca}_{0.5}\mathrm{Mn}_{1-x}\mathrm{Cr}_x\mathrm{O}_3$ (x=0.02) is found[1] to destroy charge ordering and induces a semiconductor-to-metal transition with only compositional means (viz., without the application of a magnetic field). It may therefore be of interest to study oxides containing mixed-valent Cr. In most studies on mineralogy and petrology of mantle rocks, Cr appears to take only the trivalent state whereas all formal valence states from $\mathrm{Cr}^{\mathrm{II}}$ to $\mathrm{Cr}^{\mathrm{VI}}$ are known for man-made compounds. However, $\mathrm{Cr}^{\mathrm{III}}$ and $\mathrm{Cr}^{\mathrm{VI}}$ are by far the most common chromium valences for oxides, typically in octahedral and tetrahedral coordination, respectively. For example, Cr has octahedral environment and valence III in spinel-type oxides and tetrahedral environment and valence VI in chromates. In the $A\mathrm{Cr}_3\mathrm{O}_8$ (A=Na, K, Rb) compounds considered here, Cr takes both octahedral and tetrahedral coordination with formal ionic valence states believed to be Cr^{3+} and Cr^{6+}. Hence a detailed study of the valence states, electronic structures, and magnetic properties of these compounds is of considerable interest.

II. STRUCTURAL ASPECTS

The crystal structure of $A\mathrm{Cr}_3\mathrm{O}_8$ (A=Na, K, Rb) is summarized in Table I and depicted in Fig. 1. X-ray powder diffraction studies[2,3] have revealed that the three compounds are isostructural and crystallize in the monoclinic space group $C2/m$. The $A\mathrm{Cr1}^o\mathrm{Cr2}^t_2\mathrm{O}_8$ structure consists of two types of Cr atoms arranged in octahedral (o) and tetrahedral (t) environments. There are three crystallographically different O atoms. Cr1 forms six bonds with O atoms, two with O1 and four with O3, in a fairly regular octahedral arrange-

TABLE I. Optimized structural parameters, bulk modulus (B_0), and the derivative of bulk modulus (B_0') for $A\mathrm{Cr}_3\mathrm{O}_8$ (A=Na, K, Rb). Space group $C2/m$: A and Cr1 in positions 2a (0,0,0) and 2c (0,0,1/2), respectively, Cr2, O1, and O2 in 4i, and O3 in 8i. Values given in parentheses refer to experimental data quoted from Ref. 3.

Compound	Unit cell (Å or deg)	Atom	x	y	z	B_0 (GPa)	B_0'
$\mathrm{NaCr}_3\mathrm{O}_8$	a=8.6223 (8.4957)	Cr2	0.6386 (0.6360)	0	0.2731 (0.2709)	36.56	5.43
	b=5.5249 (5.4763)	O1	0.2277 (0.2256)	0	0.5562 (0.5574)		
	c=6.9214 (6.7991)	O2	0.7158 (0.7118)	0	0.0628 (0.0616)		
	β=90.347 (91.412)	O3	0.0256 (0.0235)	0.2451 (0.2461)	0.2999 (0.3000)		
$\mathrm{KCr}_3\mathrm{O}_8$	a=8.8965 (8.5716)	Cr2	0.6385 (0.6248)	0	0.2958 (0.2919)	29.38	4.96
	b=5.4633 (5.4625)	O1	0.2091 (0.2279)	0	0.5699 (0.5591)		
	c=7.8733 (7.6234)	O2	0.6840 (0.6863)	0	0.0984 (0.0884)		
	β=93.493 (95.199)	O3	0.0362 (0.0162)	0.2558 (0.2509)	0.3289 (0.3079)		
$\mathrm{RbCr}_3\mathrm{O}_8$	a=8.9135 (8.6162)	Cr2	0.6347 (0.6265)	0	0.3028 (0.2994)	26.27	3.84
	b=5.4757 (5.4584)	O1	0.2103 (0.2224)	0	0.5688 (0.5596)		
	c=8.1557 (7.9612)	O2	0.6751 (0.6769)	0	0.1111 (0.1021)		
	β=94.657 (95.813)	O3	0.0373 (0.0125)	0.2552 (0.2599)	0.3356 (0.3194)		

©2005 The American Physical Society

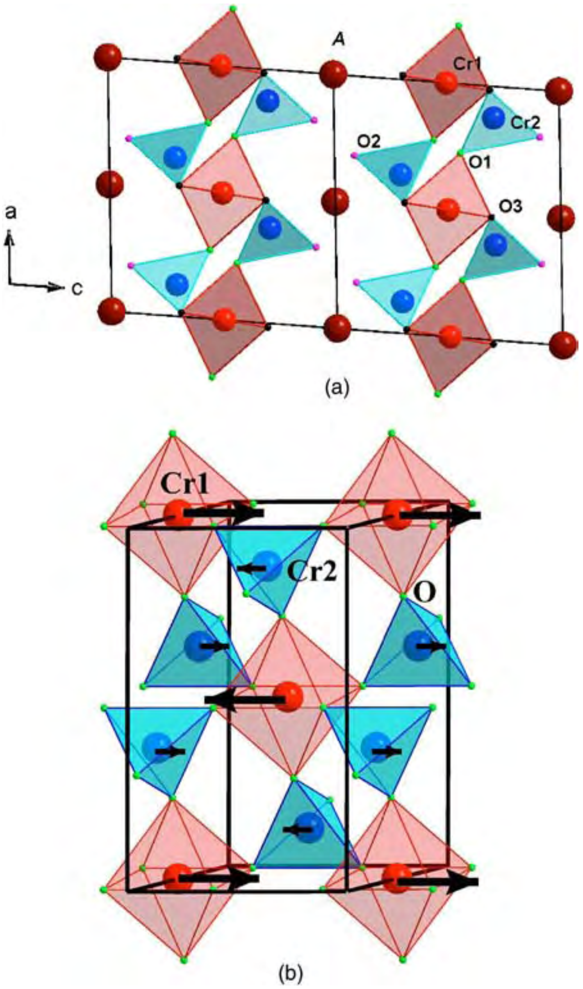

FIG. 1. (Color online) (a) Crystal structure of $A\mathrm{Cr}_3\mathrm{O}_8$ (A=Na, K, Rb), viewed along [010]. Crystallographically different atoms are labeled on the illustration; see also Table I. Note the distinct $\mathrm{Cr}_3\mathrm{O}_8$ layers. (b) The antiferromagnetic (AF) configuration of Cr2 is indicated by arrows; the size is related to the outcome of the calculations. A ions are omitted.

ment. Similarly, Cr2 takes a fairly regular tetrahedral coordination, forming one bond each with O1 and O2 and two bonds with O3. The octahedra and tetrahedra are arranged in layers parallel to the a,b plane by corner sharing. The thus generated layers are held together by the alkali-metal cations which have ten nearest oxygen neighbors. The expansion of the c axis on going from A=Na to Rb in the $A\mathrm{Cr}_3\mathrm{O}_8$ series is mainly due to the increased size of A^+.

III. COMPUTATIONAL DETAILS

The results presented here are based on density-functional theory (DFT) calculations according to the projected augmented plane-wave[4] (PAW) method as implemented in the VASP code (Vienna *ab initio* simulation package).[5] In this approach the valence orbitals are expanded as plane waves and the interactions between the core and valence electrons are described by pseudopotentials. The optimization of the atomic geometry is performed via a conjugate-gradient algorithm by minimization of the forces and stresses acting on the system. During the simulations, atomic coordinates and axial ratios are allowed to relax for different volumes of the unit cell. These parameters are changed iteratively so that the sum of the lattice energy and the electronic free energy converges to a minimum value. The ground state is calculated exactly for each set of atomic positions and the electronic free energy is taken as the quantity to be minimized. The experimental structural parameters[3] are used as the initial input. Convergence minimum with respect to atomic shifts is assumed to have occurred when the energy difference between two successive iterations is less than 10^{-7} eV f.u.$^{-1}$ and the forces acting on the atoms are less than 1 meV Å^{-1}. The generalized-gradient approximation[6] (GGA) is used to obtain accurate exchange and correlation energies for a particular atomic configuration. The calculations were carried out using a $4\times8\times8$ **k**-point Monkhorst-Pack grid, equivalent to 64 **k** points in the irreducible Brillouin zone. A further increase in the number of **k** points proved to have negligible effect on the total energy. A plane-wave energy cutoff of 550 eV was used in all calculations. In order to avoid ambiguities in the free-energy results we have used same energy cutoff and **k**-point density in all calculations. The structural optimizations were performed in paramagnetic (P), ferromagnetic (F), and antiferromagnetic (AF) configurations for all the three compounds. We have calculated the total energy of the compounds as a function of volume for ten different volumes, fitted the results to the so-called universal equation of state,[7] and therefrom extracted the bulk modulus (B_0) and its pressure derivative (B_0').

IV. RESULTS AND DISCUSSION

A. Structural optimization

The results discussed in the following sections refer to $\mathrm{KCr}_3\mathrm{O}_8$ unless otherwise specifically mentioned. The structural optimization in the P, F, and AF configurations shows that the AF configuration has the lowest total energy and represents accordingly the ground state for $\mathrm{KCr}_3\mathrm{O}_8$ (Fig. 2). This is in agreement with the magnetic susceptibility data[8,9] which show AF ordering below T_N (Néel temperature) $=125\pm4$ K. The calculations show that $\mathrm{RbCr}_3\mathrm{O}_8$ also has an AF ground state whereas $\mathrm{NaCr}_3\mathrm{O}_8$ has a F ground state. The optimized lattice parameters and atomic positions along with the experimental values are given in Table I, showing reasonably good agreement between the two sets of data. The calculated cell parameters agree well for $\mathrm{NaCr}_3\mathrm{O}_8$, but for $\mathrm{KCr}_3\mathrm{O}_8$ and $\mathrm{RbCr}_3\mathrm{O}_8$ the unit-cell parameters are up to some 3.8% larger than the experimental values. The PAW method with the GGA generally gives up to 3% overestimated volumes in some cases.[10] In order to check the deviations between the computational and experimental structural parameters for these compounds, we repeated the calculations with more **k** points, higher energy cutoff, and also including the semicore K p and Cr p states in the valence configuration. None of these calculations significantly changed the values from those listed in Table I. We also carried out a similar set of calculations using the local-density

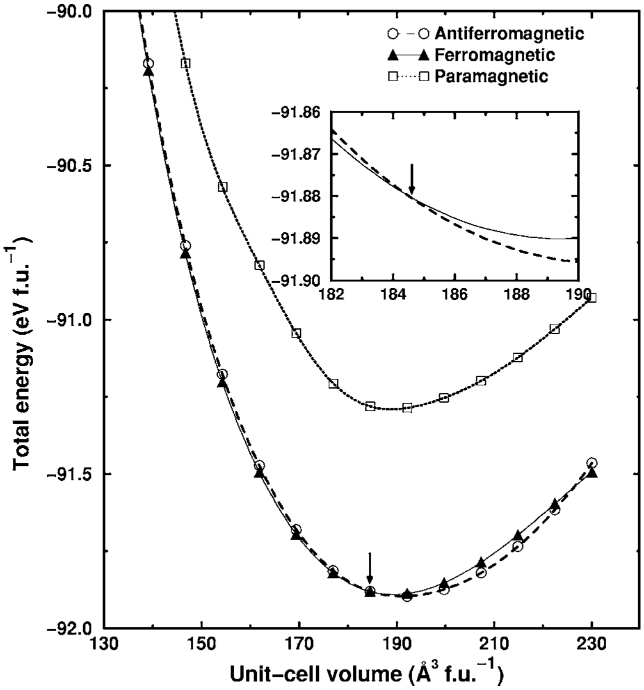

FIG. 2. Calculated unit-cell volume vs total energy for KCr_3O_8 in different magnetic configurations. The arrows indicate the antiferromagnetic-to-ferromagnetic transition.

approximation (LDA) instead of the GGA. In this case, the obtained equilibrium parameters are up to 3.6% underestimated.

In order to check the effect of the Cr PAW potential on the lattice parameters we also carried out test calculations with different potentials for CrO_2, which is an archetype for half-metallic ferromagnets. We correctly obtained the F half-metallic ground state and the equilibrium unit-cell volume (see Table II) varied around 2%, viz., well within the limit of the accuracy for DFT calculations. In all calculations the derived magnetic moment per Cr atom in CrO_2 came out as $\sim 2.0\mu_B$ as expected for Cr^{IV} (d^2). Hence the choice of potentials for the constituent elements does not significantly influence the optimized lattice parameters.

As noted earlier, the studied systems have a layered arrangement within a,b planes. It is noteworthy that the largest deviations in lattice parameters between experiment and theory are found precisely for the a direction (3.8% and 3.5% for KCr_3O_8 and $RbCr_3O_8$, respectively). Moreover, for KCr_3O_8 the deviation in a is considerably smaller in the P case (2.8%) than the AF case (3.8%). The significance of the latter finding lies in the fact that the experimental values refer to the P state at room temperature. The variation of b is almost negligible for the P and F states ($\sim$0.02%) and somewhat larger for the AF state (0.44%), whereas that for c is more appreciable for all (P, F, and AF) states (3.2–3.4 %; see Fig. 3). From Table III, it is seen that the calculated average bond length $Cr1^o$-O for the three compounds is some 2% smaller than the experimental value. On the other hand, the calculated and experimental bond lengths $Cr2^t$-O are almost the same. Cr1 has a finite magnetic moment whereas that for Cr2 is negligible (see Sec. IV B). The strongly bonded tetrahedral $Cr2O_4$ units are not affected by either external pressure or magnetic interactions whereas the octahedral $Cr1O_6$ units are influenced by such perturbations. Hence, the discrepancy between the calculated and experimental lattice parameters may be attributed to the layered structure, the strongly bonded macromolecularlike Cr_3O_8 units within the layers, and/or magnetoelastic effects. As the experimental values refer to room temperature (well above the magnetic transition temperature) and the calculations correspond to 0 K, low-temperature neutron-diffraction studies on the crystal and magnetic structures of these compounds are needed to shed light on this situation.

TABLE II. Optimized unit-cell parameters for CrO_2 using different potentials in the computation: GGA-PBE1 corresponding to pseudopotential for Cr with 3d electrons in the valence state, GGA-PBE2 to pseudocore 2p electrons also in the valence state, and LDA (see Sec. III).

Unit cell	Experiment (Ref. 11)	GGA-PBE1	GGA-PBE2	LDA
a (Å)	4.4190	4.4212	4.4204	4.4348
c (Å)	2.9154	2.9125	2.9135	2.8946
V (Å^3)	56.93	58.13	58.30	55.70

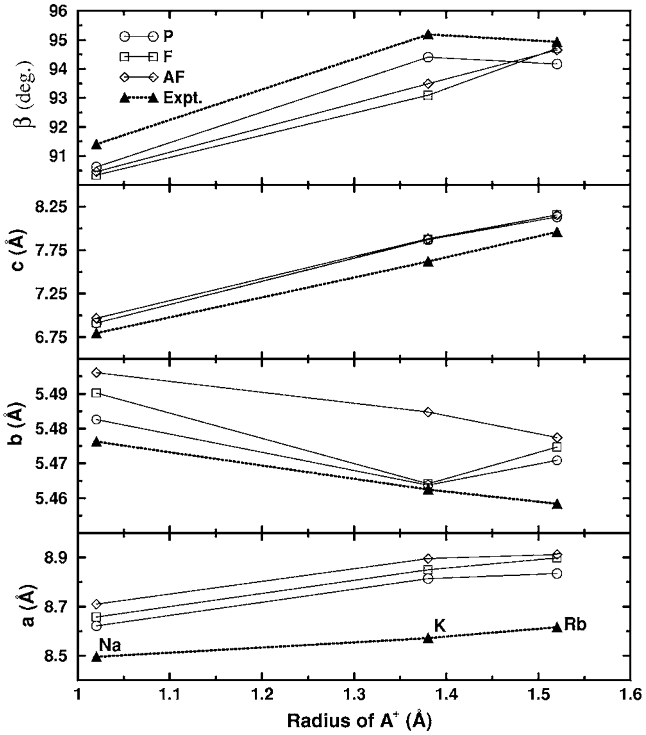

FIG. 3. Calculated unit-cell parameters for ACr_3O_8 as function of the radius of A^+ (standard values). Open and closed symbols represent calculated and experimental values, respectively. Note the enlarged scale along b.

The change in total energy as a function of unit-cell volume for KCr_3O_8 is shown in Fig. 2. This shows that a transition from the AF to the F state takes place at a pressure of 2.36 GPa, associated with a volume discontinuity of 6.4%. As the energy difference between the AF and F states is

TABLE III. Bond lengths between Cr and O (in Å) in the ground-state configurations of ACr_3O_8.

	$NaCr_3O_8$ (F)		KCr_3O_8 (AF)		$RbCr_3O_8$ (AF)	
Bonds	Calc.	Expt.	Calc.	Expt.	Calc.	Expt.
2 $Cr1^o$-O1	1.94	1.95	1.90	1.95	1.89	1.92
4 $Cr1^o$-O3	1.97	2.00	1.98	2.02	1.93	2.03
1 $Cr2^t$-O1	1.64	1.63	1.62	1.62	1.63	1.63
2 $Cr2^t$-O3	1.69	1.69	1.66	1.66	1.65	1.65
1 $Cr2^t$-O2	1.66	1.65	1.69	1.69	1.68	1.68

small (Table IV), it should be easy for this magnetic transition to occur. Similarly, $RbCr_3O_8$ also undergoes a transition from the AF to the F state at 1.31 GPa, whereas no pressure-induced magnetic transition is revealed for $NaCr_3O_8$ which remains in the F state throughout the pressure range studied.

B. Magnetic properties

We have calculated the total energy for P, F, and AF configurations as well as three different types of ferrimagnetic (Ferri) ordering. However, all Ferri configurations finally ended up with either F or AF solutions. Two different AF arrangements were considered of which that depicted in Fig. 1(b) came out 300 meV f.u.$^{-1}$ lower in energy. We have also calculated the Liechtenstein exchange parameters[12,13] for the Cr atoms based on the formalism implemented in the TBLMTO-47 code[14] and made use of the findings as guidelines to construct the magnetic cell. From the calculated exchange parameters we found that the indirect Cr1-to-Cr1 and Cr2-to-Cr2 interactions via intervening O atoms are AF (magnitudes 64.5 and 0.03 meV, respectively), whereas the corresponding Cr1-to-Cr2, interactions are F (magnitude −2.74 meV). The mutual exchange interaction between the Cr1 and Cr2 sublattices is accordingly very small. Moreover, as Cr2 carries a minor moment (see below) the net macroscopic effect of AF ordering (as assumed in the computational model) or paramagnetic disordering of the Cr2 moments will virtually be the same. Note that the Cr-Cr separation in the compounds ($\geqslant 3.38$ Å for KCr_3O_8) exceeds the critical value[15] for direct Cr-Cr interaction. The most likely superexchange-interaction path from Cr1 to Cr1 is via O3 atoms with an O3-O3 separation of 2.72 Å and a Cr1-O3-O3 angle of 133°.

At first sight the calculated magnetic moments (Table V) appear to confirm that Cr1 corresponds to nearly Cr^{III} (d^3) and Cr2 to nearly Cr^{VI} (d^0) in agreement with their octahedral and tetrahedral coordinations.[3] However, a closer investigation of the bonding situation reveals that (see below and Sec. IV D) the assignment of formal valence states to Cr in the studied systems is nontrivial. Owing to the presence of nearly three unpaired d electrons, Cr1 may be concluded as Cr^{III}, but all d electrons from Cr2 are clearly not transferred to the oxygen atoms [as is to be expected for an ideal Cr^{VI} (d^0) state]. A small magnetic moment (Table V) is associated with Cr2, and owing to hybridization interaction between Cr d and O p, the oxygen atoms also possess small magnetic moments. [This leads to total moments in the F state (see Table V) exceeding the simple sum of the moments on Cr1 and Cr2.]

TABLE IV. Total energy (relative to the lowest-energy state in meV f.u.$^{-1}$) for ACr_3O_8 in P, F, and AF states.

Compound	P	F	AF
$NaCr_3O_8$	680	0	14.5
KCr_3O_8	619	21.4	0
$RbCr_3O_8$	652	21.6	0

The magnetic moments of Cr1 are lower than the ideal spin-only values owing to strong covalent Cr-O interaction. The old findings of Klemm[8] established Curie-Weiss behavior for KCr_3O_8, but gave a somewhat larger resultant paramagnetic moment [$(4.0\text{–}4.2)\mu_B$ f.u.$^{-1}$] than the spin-only paramagnetic moment ($3.72\mu_B$ f.u.$^{-1}$ which "accidentally" coincides with the theoretical spin-only moment for a d^3 configuration) calculated from the total cooperative-magnetic moment for KCr_3O_8 in Table V. Unpublished measurements by Fjellvåg[9] found $\mu_P = (4.05 \pm 0.03)\mu_B$ and $(4.08 \pm 0.04)\mu_B$ f.u.$^{-1}$ for $NaCr_3O_8$ and KCr_3O_8, respectively. However, according to Ref. 9 $NaCr_3O_8$ takes an AF arrangement below $T_N = 91 \pm 2$ K (rather than the F arrangement arrived at computationally) and moreover both $NaCr_3O_8$ and KCr_3O_8 have a black appearance (see also Ref. 8). The latter observation suggests that these substances should be metallic rather than semiconducting. A metallic behavior can in this case easily be imagined to arise from nonstoichiometry in the oxygen content of the bona fide samples. There are also other reports[16] of paramagnetic moments in excess of $4\mu_B$ per Cr^{III} for chromic compounds. For example, the related binary oxides Cr_2O_5 and Cr_3O_8 (which also formally are believed to comprise Cr^{3+} and Cr^{6+}) are reported[17] to exhibit AF order-

TABLE V. Calculated magnetic moment for Cr1 and Cr2 (in μ_B per Cr atom) of ACr_3O_8 in F and AF states. Total refers to the total magnetic moment per formula unit.

	F			AF	
Compound	Cr1	Cr2	Total	Cr1	Cr2
$NaCr_3O_8$	2.451	0.241	2.868	2.391	0.013
KCr_3O_8	2.449	0.228	2.859	2.330	0.016
$RbCr_3O_8$	2.453	0.224	2.857	2.336	0.003

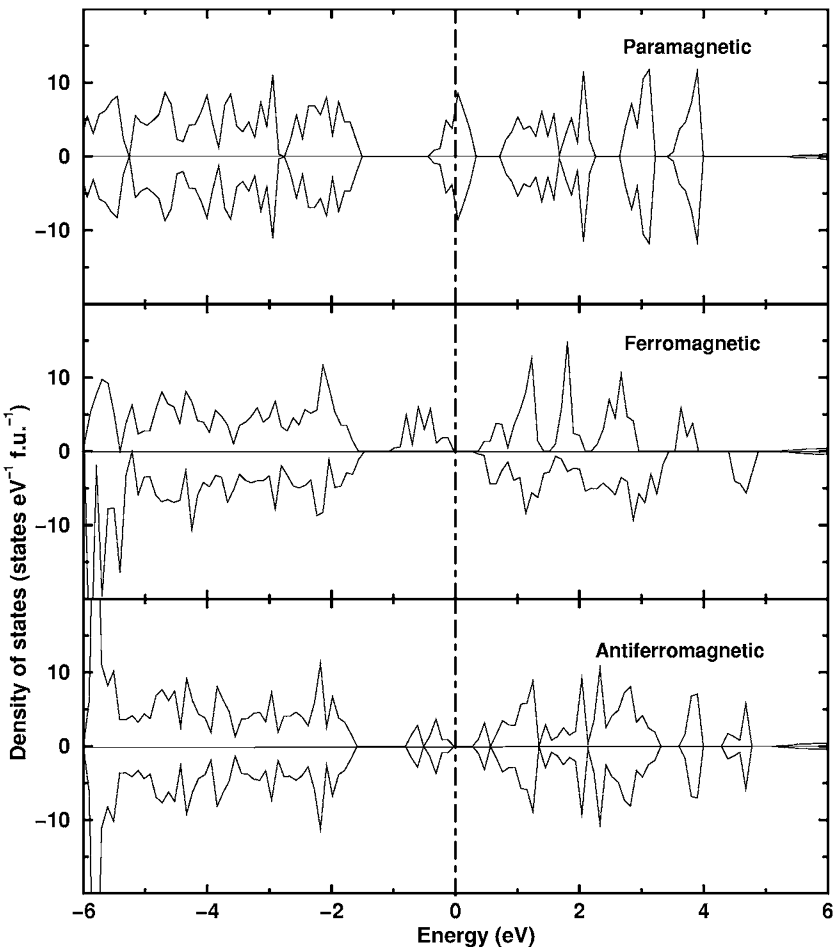

FIG. 4. Total density of states for KCr_3O_8 in different magnetic configurations. The Fermi level (E_F) is indicated by vertical dashed line.

ings at low temperature with paramagnetic moments of $(4.30\pm0.04)\mu_B$ and $(4.35\pm0.02)\mu_B$ f.u.$^{-1}$, respectively.

A number of manganese-containing compounds has been found to transform from an AF insulating (semiconducting) phase to a F metallic phase with an associated CMR effect on application of magnetic fields. The present calculations predict that KCr_3O_8 and $RbCr_3O_8$ stabilize in the F insulating phase (note at 0 K) on application of a sufficiently large field. Transport-property studies on these materials as a function of magnetic field should be particularly interesting because of the occurrence of insulating (semiconducting) states in both AF and F phases. The resistivity of the AF phase should be larger than that of the F phase owing to the enhanced scattering of the electrons by the AF-aligned spins. Hence, the measurement of changes in resistivity as a function of magnetic field should provide evidence of contributions from spin scattering alone. (Note that for the manganese-containing compounds both spin scattering and contributions from conduction electrons set free by the establishment of the metallic state will contribute to the field-dependent resistivity.) In order to penetrate further into the origin of the CMR effect, it would be useful to concentrate on cases where only one of the components contributes.

C. Electronic structure

From the total density of states (DOS) for KCr_3O_8 in Fig. 4, it is evident that the P state with a finite DOS at the Fermi level (E_F) has metallic character. However, since the E_F falls on a peak of the DOS curve, stabilization in the P configuration is not favorable, in agreement with the total energy findings. Interestingly, the F state of KCr_3O_8 is insulating (semiconducting) with a band gap (E_g) of 0.31 eV. F insulators attract much attention owing to their potential application in spintronics devices. The presently studied compounds may be the first examples of Cr-containing oxides with F insulating behavior other than spinels. (Earlier, we[18] have predicted F insulating behavior in $Ca_2YCo_2O_6$ where Co takes the valence states Co^{II} and Co^{IV}.) Also in the AF configuration KCr_3O_8 is an insulator with a reduced E_g of 0.26 eV. A small energy gap (between −1.5 and −1.0 eV) is seen within the valence band (VB) of the F state, whereas the gap is somewhat larger (between −1.8 and −1.0 eV) in the AF state where more DOS is localized. The electronic structure of all the three compounds is similar in the sense that they have metallic character in the P state and insulating (semiconducting) character in the F and AF states. $NaCr_3O_8$ has $E_g=0.36$ eV in the F ground state and 0.41 eV in the (metastable, if at all realizable) AF state, whereas $RbCr_3O_8$ has $E_g=0.39$ eV in its AF ground state and 0.33 eV in the high-pressure F state.

As seen from Fig. 5, the K states are almost empty (scale multiplied by a factor of 10). This implies that K has donated almost all its electrons to oxygen and becomes ionic. Cr and O states are energetically degenerate implying strong cova-

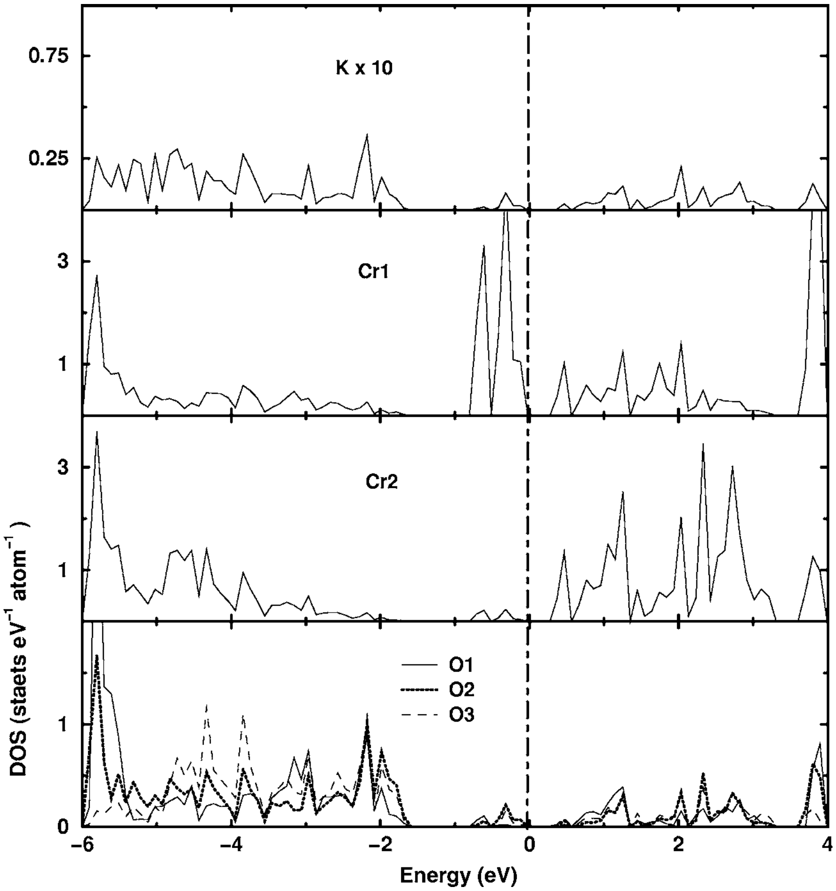

FIG. 5. Site-projected DOS for KCr_3O_8 in the antiferromagnetic state. The vertical line denotes the Fermi level (E_F).

lent interaction between them. The different valence states of the Cr ions are also obvious from their different DOS curves. The hybridization of the Cr2 *d* and O *p* states results in well-localized bonding states (−6 to −4 eV) in the VB and antibonding states in the conduction band (CB). Although the three different O atoms have states in the same energy region, they show significant topological differences in their DOS curves.

The partial DOSs for Cr1 and Cr2 are displayed in Fig. 6. As the contributions to the VB and CB from both Cr1 and

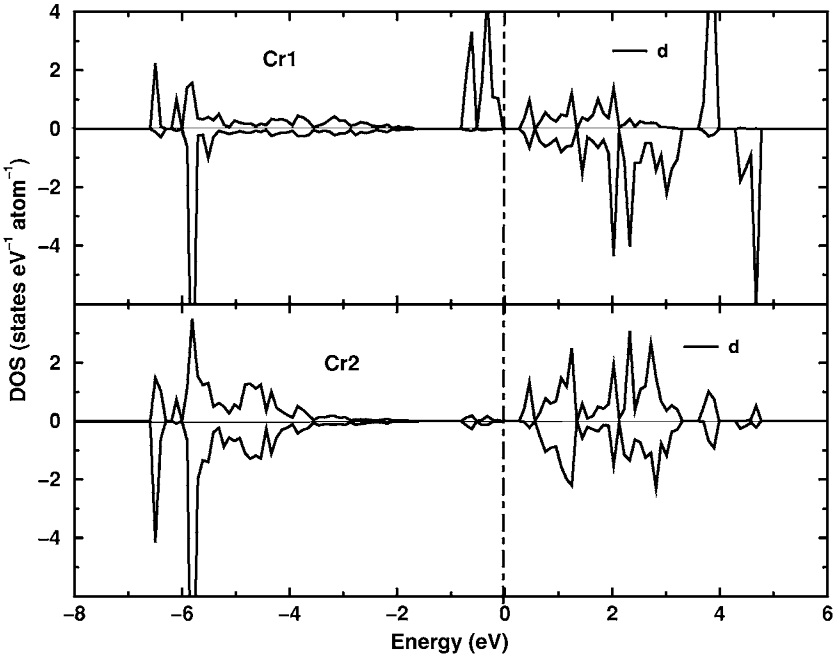

FIG. 6. Partial DOS of Cr1 and Cr2 in KCr_3O_8. The vertical line denotes E_F.

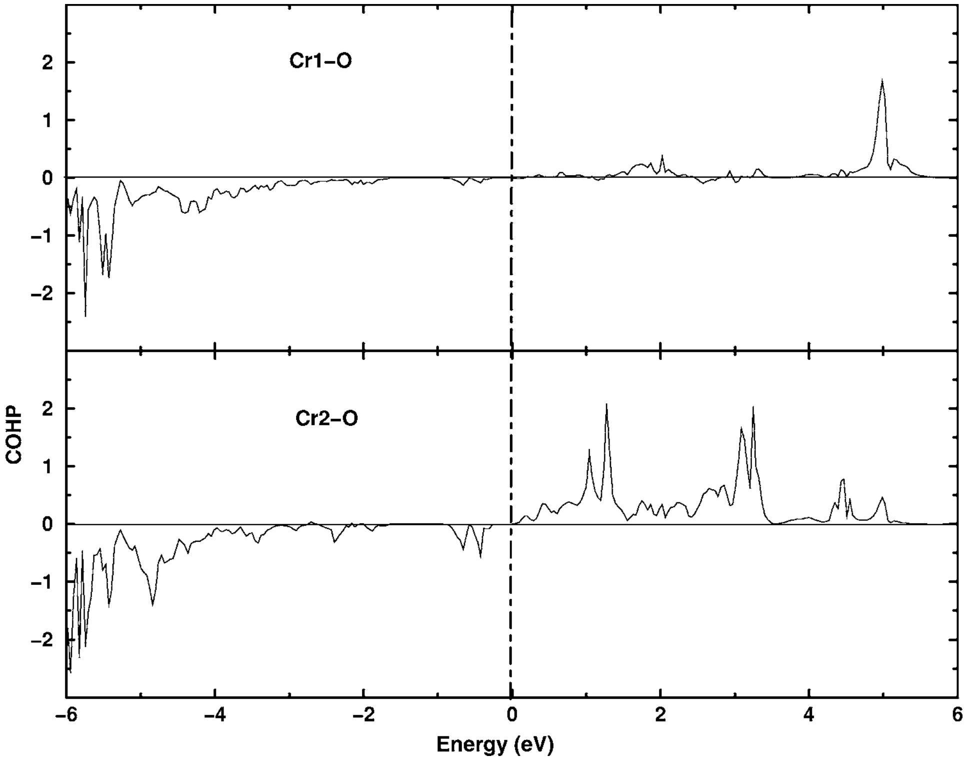

FIG. 7. Calculated COHP curves for Cr1 and Cr2 in KCr_3O_8. (The illustration refers strictly speaking to Cr1-O1 and Cr2-O2, but the profiles for Cr1-O3, Cr2-O2, and Cr2-O3 are very similar.) The vertical line denotes E_F.

Cr2 are mainly made up from *d* electrons (*s* and *p* are scarcely visible even after appreciable magnification) we here display only the *d*-electron DOS. The significant differences in the topology of the *d*-DOS curves and the integrated DOS values (4.2 states for Cr1 and 4.8 states for Cr2) reflect their different valence states. The majority-spin channel of Cr1 has more occupied states than its minority-spin channel. Moreover, if Cr2 really had been in the Cr^{VI} (d^0) state it should have an empty *d* band. Instead, it exhibits a considerable number of well-localized states with more or less equal occupancy in both spin channels. Hence it can be inferred that the almost-zero magnetic moment of Cr2 in these compounds is not due to a genuine Cr^{VI} (d^0) state, but results from negligible exchange splitting. The *lm*-projected DOS (not shown) also exhibits different occupancy of *d* orbitals for Cr1 and Cr2. As the studied systems have monoclinic crystal structure, the *d*-orbital splitting is not like that in a perfect cubic crystal field. After applying the proper rotation matrix, the octahedrally coordinated Cr1 does not exhibit perfect triply degenerate t_{2g} and doubly degenerate e_g orbitals. In the case of Cr1, the prominent peaks around −6 to −4 eV stem from t_{2g}-like orbitals whereas those closer to E_F come from e_g-like orbitals. The *lm*-projected DOS for Cr2 shows that all the *d* orbitals have almost equally filled majority- and minority-spin channels localized between −6 and −4 eV. Prominent peaks are seen for Cr1, Cr2, O1, and O3 in the energy range of −6 to −4 eV. This signals appreciable hybridization interaction between Cr and O.

D. Bonding characteristics

Crystal orbital Hamiltonian population (COHP, the DOS weighted by the corresponding Hamiltonian matrix elements) analysis[19,20] is a valuable tool to quantify the number of bonding and antibonding states. It may be recalled that a positive sign of the COHP indicates antibonding character and a negative sign bonding character. The calculated COHP for Cr1 and Cr2 is displayed in Fig. 7. For both kinds of Cr atoms the VB consists of bonding states and the CB of antibonding states indicating that both have strong bonding interaction with their surrounding O ions. The integrated COHP value (which provides a measure of bond strength) for Cr1 and Cr2 is 1.53 and 2.60 eV, respectively. Hence, the tetrahedral Cr2 atoms have stronger bonding interaction with its O neighbors than the octahedral Cr1 atoms consistent with the conclusion arrived from bond-length analysis.

A combined analysis of charge density, charge transfer, and electron localization function (ELF) plots gives additional insight into the bonding characteristics of solids.[21,22] A charge-density plot (distribution of charges in real space) together with a charge-transfer plot (difference between charge density of the solid and that of the atoms forming the solid) provides an overall idea about the transfer of charges involved in the formation of the solid. An ELF plot[23] helps to further characterize the different types of bonding involved, the ELF being defined between 0 and 1, and high values of ELF are found in covalent bonds and lone electron pairs.

As the DOS and COHP analyses clearly establish different valence states for Cr, we attempted to look for other signs of charge ordering through examination of charge-density plots [Fig. 8(a)]. For Cr1, charges are directed toward the octahedrally coordinated O ions, implying a degree of covalent Cr1-O interaction between them. In the case of Cr2, the charges are also directed toward the surrounding O ions, but here the charge is denser compared to those associated with Cr1, in agreement with the COHP analysis. The shorter Cr2-O bond length (1.62–1.69 Å) compared to the Cr1-O

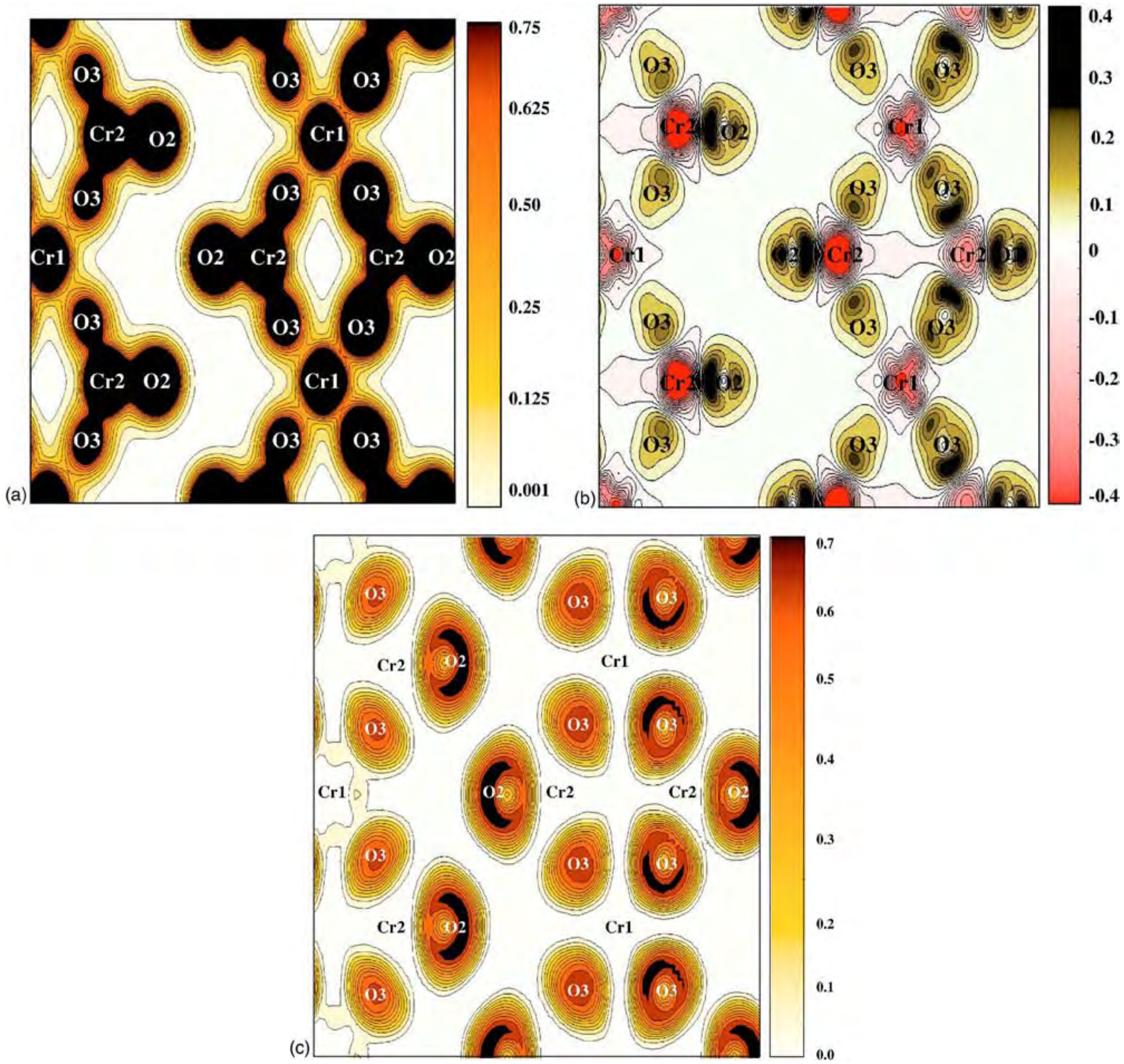

FIG. 8. (Color online) Plots in a,c plane of (a) charge density, (b) charge transfer, and (c) electron localization function for KCr_3O_8.

bond length (1.90–1.98 Å) and the enhanced charge density between Cr2 and O3 suggest strong covalent interaction. However, a closer look at the charge-transfer plot [Fig. 8(b)] paints a different picture. The anisotropic charge transfer from Cr1 to O3 implies that the Cr1-O3 bonds are of the coordinate covalent type where the shared electrons are supplied solely by Cr1. Moreover, Fig. 8(b) also shows transfer of charges from Cr2 to O3. If the Cr2-O3 bond only had covalent character, the charge-transfer plot should have shown positive charges between Cr2 and O3. However, the denser charge region between Cr2 and O3 in Fig. 8(a), does not imply a strong covalent bond (as customary thinking leads one to believe) but rather results from the presence of nonbonding *d* electrons on Cr2 (which are duly absent in the charge-transfer plot). Even though the ELF values for the Cr1-O and Cr2-O bonds [see Fig. 8(c)] are almost the same, the contours around the O3 atoms are directed toward Cr1 and away from Cr2. This suggests that the Cr1-O3 bond has some degree of directional character, whereas the Cr2-O3 bonds have both ionic and some degree of covalent character.

From the analyses of magnetic moments, *d*-orbital occupancies, and various means of bond characterization, it seems reasonable to conclude with Cr^{3+} as an approximate valence state for Cr1 whereas Cr^{6+} (as earlier studies have inferred) is certainly inappropriate for Cr2. Within the framework of the ionic picture it may be suggested that the actual charges associated with Cr2 should justify the label Cr^{2+} (with O^{1-} for all O atoms; Mulliken effective charges from the CRYSTAL03 program showed that O atoms have accepted around 0.9 electrons). The origin of the inferred deviation from the traditional formal valence scheme for charge allocation (where adoption of 2− as the valence state for O forms a basic postulate) is the appreciable covalent contribution to the Cr2-O bonding.

V. CONCLUSION

It is predicted that a combination of ferromagnetic and insulating (at 0 K) behavior may be found in formally mixed-valent chromium compounds. The calculated structural parameters are in reasonable agreement with experimental values for $NaCr_3O_8$, KCr_3O_8, and $RbCr_3O_8$. The ground states of KCr_3O_8 and $RbCr_3O_8$ should exhibit antiferromagnetic insulating (semiconducting) behavior and on application of pressure a transformation to ferromagnetic-insulating (semiconducting) states is predicted. The energy difference between the antiferromagnetic and the ferromagnetic states of these compounds is very small. Hence, by application of a small magnetic field one can transform the antiferromagnetic-insulating (semiconducting) KCr_3O_8 and $RbCr_3O_8$ into ferromagnetic insulators (semiconductors). Experimental studies including magnetic, transport, and spectroscopic properties are recommended because these compounds are likely to exhibit exciting features.

ACKNOWLEDGMENTS

The authors are grateful to the Research Council of Norway for financial support and computer time at the Norwegian supercomputer facilities. The authors are grateful to Professor A. I. Liechtenstein for fruitful discussions on exchange parameters and R.V. wishes to acknowledge Arne Klaveness for his help.

---

*Electronic address: vidya.ravindran@kjemi.uio.no

[1] B. Raveau, A. Maignan, and C. Martin, J. Solid State Chem. **130**, 162 (1997).
[2] K.-A. Wilhelmi, Acta Chem. Scand. (1947-1973) **12**, 1958 (1965); Chem. Commun. (London) **1966**, 4371966.
[3] M. J. Saavedra, C. Parada, and E. J. Baran, J. Phys. Chem. Solids **57**, 1929 (1996).
[4] P. E. Blöchl, Phys. Rev. B **50**, 17953 (1994);G. Kresse and D. Joubert, *ibid.* **59**, 1758 (1999).
[5] G. Kresse and J. Furthmuller, Comput. Mater. Sci. **6**, 15 (1996).
[6] J. P. Perdew, K. Burke, and Y. Wang, Phys. Rev. B **54**, 16533 (1996);J. P. Perdew, K. Burke, and M. Ernzerhof, Phys. Rev. Lett. **77**, 3865 (1996).
[7] P. Vinet, J. H. Rose, J. Ferrante, and J. R. Smith, J. Phys.: Condens. Matter **1**, 1941 (1989).
[8] W. Klemm, Z. Anorg. Allg. Chem. **301**, 323 (1959).
[9] H. Fjellvåg (unpublished).
[10] U. Häussermann, H. Blomqvist, and D. Noréus, Inorg. Chem. **41**, 3684 (2002).
[11] P. Porta, M. Marezio, J. P. Remeika, and P. D. Dernier, Mater. Res. Bull. **7**, 157 (1972).
[12] A. I. Liechtenstein, M. I. Katsnelson, V. P. Antropov, and V. A. Gubanov, J. Magn. Magn. Mater. **67**, 65 (1987).
[13] V. I. Anisimov, F. Aryasetiawan, and A. I. Liechtenstein, J. Phys.: Condens. Matter **9**, 767 (1997).
[14] O. K. Andersen and O. Jepsen, Phys. Rev. Lett. **53**, 2571 (1984).
[15] J. B. Goodenough, *Magnetism and the Chemical Bond* (Interscience, New York, 1963).
[16] E. Konig, in *Magnetic Properties of Coordination and Organometallic Transition Metal Compounds*, edited by K. H. Hellwege, Landolt-Bornstein, New Series, Group II, Vol. 2 (Springer, New York, 1966).
[17] T. A. Hewston and B. L. Chamberland, J. Magn. Magn. Mater. **43**, 89 (1984).
[18] R. Vidya, P. Ravindran, H. Fjellvåg, A. Kjekshus, and O. Eriksson, Phys. Rev. Lett. **91**, 186404 (2003).
[19] R. Dronskowski and P. E. Blöchl, J. Phys. Chem. **97**, 8617 (1993).
[20] G. Krier, O. Jepsen, A. Burkhardt, and O. K. Andersen, computer code Tight Binding LMTO-ASA, Version 4.7 (Stuttgart, Germany, 1999).
[21] P. Ravindran, P. Vajeeston, R. Vidya, A. Kjekshus, and H. Fjellvåg, Phys. Rev. Lett. **89**, 106403 (2002).
[22] P. Vajeeston, P. Ravindran, R. Vidya, H. Fjellvåg, and A. Kjekshus, Phys. Rev. B **68**, 212101 (2003).
[23] A. Savin, R. Nesper, S. Wengert, and T. Fässler, Angew. Chem., Int. Ed. Engl. **36**, 1809 (1997).

VII

Accepted in Phys. Rev. B

Crystal and electronic structures of Cr_3O_8 and $LiCr_3O_8$: Probable cathode materials in Li batteries

R. Vidya*, P. Ravindran, A. Kjekshus and H. Fjellvåg
[1]*Department of Chemistry, University of Oslo, Box 1033 Blindern, N-0315 Oslo, Norway*

Ground-state crystal structures are predicted for Cr_3O_8 and $LiCr_3O_8$ from accurate first-principles density-functional calculations by considering several (25 for the former and 12 for the latter phase) related structure types. Both phases are stabilize in monoclinic ($C2/m$) structures with slight variations in the atomic arrangement of the chromium-oxygen framework. Structural optimization is also performed for Cr_8O_{21}, the obtained structural parameters being in good agreement with the experimental values. A possible synthesis route for Cr_3O_8 is suggested from total energy studies. Electronic structure studies indicate insulating behavior with very small band gaps for Cr_8O_{21} and $LiCr_3O_8$ whereas Cr_3O_8 has pseudogap-like features. Magnetic property and partial density of states analyses indicate two different formal valence states for Cr in all studied phases (except CrO_3). Bonding characteristics and effects of Li intercalation in Cr_3O_8 are also analyzed with the help of charge density and charge transfer plots.

I. INTRODUCTION

Oxides containing mixed-valent transition metals have attracted much attention since the discovery of colossal magnetoresistance phenomena. The present authors have previously reported [1] on the electronic and magnetic properties of $A\mathrm{Cr}_3\mathrm{O}_8$ (A = Na, K, Rb) which formally contains Cr in mixed-valence states. In this communication we present the results of first-principles density-functional theory (DFT) calculations on the related phases Cr_3O_8 and $LiCr_3O_8$. In addition to the mixed-valence aspects associated with chromium, these phases are also of considerable interest in relation to application as cathode material in batteries (see Ref. [2] and references therein).

Rechargeable lithium batteries are attractive for use in light-weight, high-energy-density-storage devices with applications ranging from small portable electronics to larger mobile electrical units. Batteries consist of an anode and a cathode separated by a suitable electrolyte. In lithium batteries, the anode comprises Li at a high chemical potential, e.g., Li metal, Li-Al alloys or Li dissolved in carbon. A low Li chemical potential is established at the cathode which may have its chemical anchoring in a suitable metal oxide or sulfide that can intercalate Li. Li ions are intercalated into the cathode when the battery is discharged and deintercalated when it is charged. The open cell voltage of the battery is directly proportional to the chemical potential difference between the Li in anode and cathode [3]. An appreciable amount of research has been made to find possible Li cathode materials based on lithium-intercalated transition-metal oxides since these materials generally appear to exhibit quite high cell voltages and the series $\mathrm{Li}_x M\mathrm{O}_2$ (M = Ti-Zn) has, e.g., been subjected to a number of first-principles theoretical studies [3–5].

The insertion of Li in chromiun oxides by both chemical and electrochemical means was apparently first demonstrated by Koksbang and Norby [6]. Chromium oxides as constituents for cathodes are particularly attractive because of their high energy density and high capacity at low discharge rates. For example, the calculated energy density for the couple Li/Cr_3O_8 is reported to be about twice that of the couple Li/TiS_2 [7]. Moreover, the couple Li/Cr_3O_8 has open circuit and averaged discharge voltages of 3.8 and 3.0 V, respectively, as well as a cell voltage comparable to that of already commercially available lithium batteries. Several studies (see Refs. [2] and [8]) have shown that Cr_3O_8 cathodes exhibit good performance for the reversible cycling which involve Li intercalation/deintercalation, and the high energy density and good rechargeability have indeed made it a promising cathode material for Li batteries. It may be mentioned that the maximum charge transfer estimated [8] for the Li/Cr_3O_8 couple is more than 50% larger than the average charge transfer accepted for the batteries developed by the Varta company [9]. At room temperature Cr_3O_8 (as well as CrO_3 and Cr_8O_{21} which will enter in the consideration below) is insensitive to overdischarging and can be cycled even at voltages of 2 V [10]. A disadvantage which the Li/Cr_3O_8 couple has in common with other battery constructions based on intercalation mechanisms is slow kinetics.

In general, the suitability of different host matrices as secondary intercalation cathodes in lithium cells depends on their crystal structure and electronic properties [11]. Further the Li ions mobility is mainly related to the atomic architecture of the host structure and more specifically to the electrostatic interaction between Li ions and relevant parts of the host. The maximum lithium uptake is related to the number of sites that can accommodate Li and/or to the number of electronic states available for the corresponding electrons. High Li^+ uptake is clearly beneficial for high energy density, but may be accompanied by serious structural changes of the host. In fact, the interior structure and external morphology of the host may in general suffer appreciably during the intercalation and deintercalation reactions. For example, the repeated cycling of Li/Cr_3O_8 cathodes under battery conditions is reported [12] to give rise to increasingly disordered materials (viz. gradual deterioration toward an amorphous state [2]).

In this scenario, it is likely that structural studies on Cr_3O_8 and $LiCr_3O_8$ can provide crucial information for the understanding of the structural stability and other physical properties of these materials and in turn lead ways to improve their battery performance. However, experimental structural studies on Cr_3O_8 and $LiCr_3O_8$ are hitherto rather limited [13–16], which may be due to difficulties involved in preparation of single crystals. Hence we have undertaken a detailed study on structural stability, electronic structure, magnetic structure, and bonding characteristics for these materials using accurate DFT calculations. The advantage of *ab initio* calculations is that we require only the atomic numbers of the constituents of the phase under investigation and suitable guess structures.

II. COMPUTATIONAL DETAILS

The main aim of the present work has been to establish the ground-state crystal structures of Cr_3O_8 and $LiCr_3O_8$, and for this purpose a number of possible guess structures have been considered in the structural optimization calculations using the projected augmented plane-wave (PAW) [17] method as implemented in the Vienna *ab initio* simulation package (VASP) [18]. In this approach the valence orbitals are expanded as plane waves and the interactions between the core and valence electrons are described by pseudopotentials. The optimization of the atomic geometry was performed via a conjugate-gradient minimization of the total energy, using Hellmann-Feynman forces on the atoms and the stresses in the unit cell. During the simulations, atomic coordinates and axial ratios are allowed to relax for different volumes of the unit cell. These parameters are changed iteratively so that the sum of the lattice energy and the electronic free energy converges to a minimum value. The ground state is calculated exactly for each set of atomic positions and the electronic free energy is taken as the quantity to be minimized. Convergence minimum with respect to atomic shifts was assumed to have been attained when the energy difference between two successive iterations was less than 10^{-7} eV per unit cell and the forces acting on the atoms were less than 1 eV Å^{-1}. The generalized-gradient approximation (GGA) [19] was used to obtain the accurate exchange and correlation energy for all the atomic configurations. The calculations were carried out using $4 \times 8 \times 8$ Monkhorst-Pack **k**-points grid, equivalent to 64 **k** points in the irreducible Brillouin zone. Any further increase in the number of **k** points proved to have negligible effect on the total energy. A plane-wave energy cutoff of 550 eV was used in all calculations. In order to avoid ambiguities in the free-energy results we have used same energy cutoff and **k**-point density in all calculations. Calculations were performed for paramagnetic (P), ferromagnetic (F), and antiferromagnetic (AF) configurations of all guess structures with favorably low total energy (notably CrO_3, Cr_3O_8-I and -II, Cr_8O_{21}, and $LiCr_3O_8$-I and -II). We have calculated the total energy of the compounds as a function of volume for ten different volumes, fitted the results to the so-called "universal equation of state" [20], and extracted the bulk modulus (B_0).

III. STRUCTURAL CONSIDERATIONS

The first structural study [15] of Cr_3O_8 indexed the x-ray diffraction pattern of a sample with the said (not documented) composition on the basis of an orthorhombic unit cell, with unspecified space group and without any information on atomic positions. The most recent study [16] was performed on a sample with the slightly different composition Cr_8O_{21} and describes the structure as triclinic ($P\overline{1}$) on the basis of information from powder diffraction using conventional x-ray, neutron, and x-ray synchrotron radiation. (The fact that the unit-cell volume reported in Ref. [15] is related to that in Ref. [16] by a factor of nearly four suggests that the sample of the former study in reality may have consisted of Cr_8O_{21}.) According to Norby et al. [16] the Cr_8O_{21} structure consists of $Cr^{III}O_6$ octahedra and $Cr^{VI}O_4$ tetrahedra. These polyhedra form sheets which are held together by tetrachromate $Cr_4^{VI}O_{13}$ groups to form a three-dimensional framework [(Fig. 1(d)].

Despite the difference in composition, the Cr_8O_{21} structure was an obvious choice of guess structure for the structural optimization calculations. Two other equally obvious choices were the oxide segments (designated Cr_3O_8-I and -II) that remain after stripping-off K from the KCr_3O_8-type [1, 21, 22] structure [Fig.1(b); space group $C2/m$], and Li from the $LiCr_3O_8$ structure [Fig. 1(c); space group $Cmcm$ with random distribution of the Li atoms and one third of the Cr atoms [13]] and also the oxide framework of other structures considered for the optimization of $LiCr_3O_8$ (see below). Similarly we considered a guess structure based on a modified HI_3O_8 ($P2_1/m$) [23] arrangement in which H is omitted and I is replaced by Cr. In order to have larger platform for the exploration of the ground state structure of Cr_3O_8, we extended the selection of guess structures to other alternatives with 3 : 8 stoichiometry, being perfectly aware that some of these are rather unlikely for an oxide like Cr_3O_8. We considered the structure types [23] of the following reasonably related compounds as inputs in the structural optimization calculations: Nb_3Cl_8 ($P\overline{3}m1$), Rh_3Se_8 ($R\overline{3}$), α-W_3O_8 ($C222$), β-W_3O_8 ($Pbam$), Ir_3Se_8 ($R\overline{3}$), α-U_3O_8 ($P\overline{6}2m$), β-U_3O_8 ($Cmcm$), γ-U_3O_8 ($P2_1/m$), δ-U_3O_8 ($P\overline{3}$), and ϵ-U_3O_8 ($Amm2$). In the course of the study it also seemed appropriate to perform structural optimization on CrO_3 [24] which comprises a virtually one-dimensional arrangement of strings of corner sharing CrO_4 tetrahedra [Fig. 1(a)].

We considered also a number of different structure

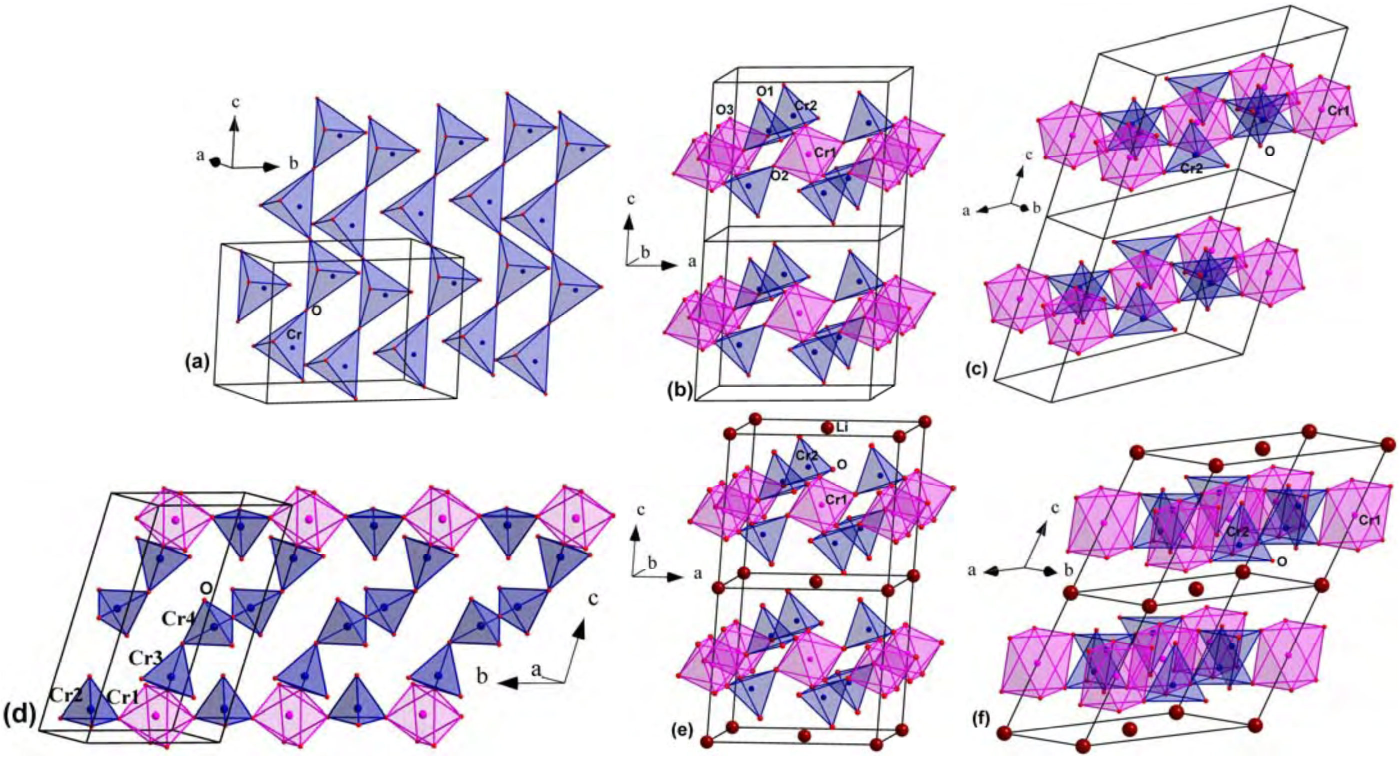

FIG. 1: (Color online) Crystal structure of (a) CrO_3 ($Ama2$), (b) Cr_3O_8-I ($C2/m$), (c) Cr_3O_8-II ($C2/m$), (d) Cr_8O_{21} ($P\overline{1}$), (e) $LiCr_3O_8$-I ($C2/m$), and (f) $LiCr_3O_8$-II ($C2/m$). Crystallographically different chromium atoms are labeled on the illustrations. Tetrahedral and octahedral Cr-O polyhedra are distinguished by different shading (color).

types as inputs to establish the ground-state structure of $LiCr_3O_8$. Obviously one starting point had to be the experimentally reported [13] $LiCr_3O_8$ structure based on $Cmcm$ symmetry. This structure is described as built up of somewhat staggered strings of (Li,Cr)O_6 octahedra connected by edge sharing in the c direction, the strings being in turn linked via corner-sharing CrO_4 tetrahedra to give the structure a certain three-dimensional character. The present simulations of the $LiCr_3O_8$ structure [Fig. 1(f); designated $LiCr_3O_8$-II] were performed in a supercell which also took care of the cooperative magnetic order. Another atomic arrangement which had to come on the top of the priority list was the KCr_3O_8-type structure [Fig. 1(e); space group $C2/m$ with K exchanged by Li; designated $LiCr_3O_8$-I] which is adopted by the succeeding elements A = Na, K, and Rb in the ACr_3O_8 series [1, 21, 22]. In addition to these structure types, the following variants [23] were considered: HI_3O_8 ($P2_1/m$; Li at the H site, and Cr at the I site), LiV_3O_8 ($P2_1/m$), $LiNb_3O_8$ ($P2_1/c$), α-$LiTa_3O_8$ ($C2/c$), β-$LiTa_3O_8$ ($Pmma$), α-$NaNb_3O_8$ ($Ibam$), β-$NaNb_3O_8$ ($Pba2$), KNb_3O_8 ($Cmcm$), ZnV_3O_8 ($Iba2$), $CuNb_3O_8$ ($P2_1/c$), $AgBiCr_2O_8$ ($I\overline{4}$), TlV_3O_8, ($P2_1/m$), and $CsCr_3O_8$ ($Pnma$).

IV. RESULTS AND DISCUSSION

A. Structural aspects

Among the different test-structural arrangements considered for chromium oxides with 3 : 8 stoichiometry, that derived by omitting K from the KCr_3O_8-type structure (viz. Cr_3O_8-I; in AF state) came out with the lowest calculated total energy [see Fig. 2(a) and Table I for structure specifications]. Other variants with the 3 : 8 stoichiometry came out with moderate [e.g., LiV_3O_8 type minus Li; $\Delta E = 0.43$ eV per Cr_3O_8 unit] to much higher total energies [e.g., Ir_3O_8 type; $\Delta E = 7.52$ eV per Cr_3O_8 unit]. A particular relevant test structure for comparison with the ground-state Cr_3O_8-I variant is Cr_3O_8-II derived by omitting Li from $LiCr_3O_8$-II [see below and Figs. 1(e) and 2(c)]. As seen from Fig. 2(a) Cr_3O_8-II exhibits an appreciably higher energy than Cr_3O_8-I, in fact, Cr_3O_8-II is located well above the mentioned Li-stripped-off variant of the LiV_3O_8-type structure.

The experimentally established Cr_8O_{21} phase on the other hand, takes a slightly different composition and an appreciably different structural arrangement from Cr_3O_8-I [see Fig. 1(b,c)]. The total energy (E) vs unit-

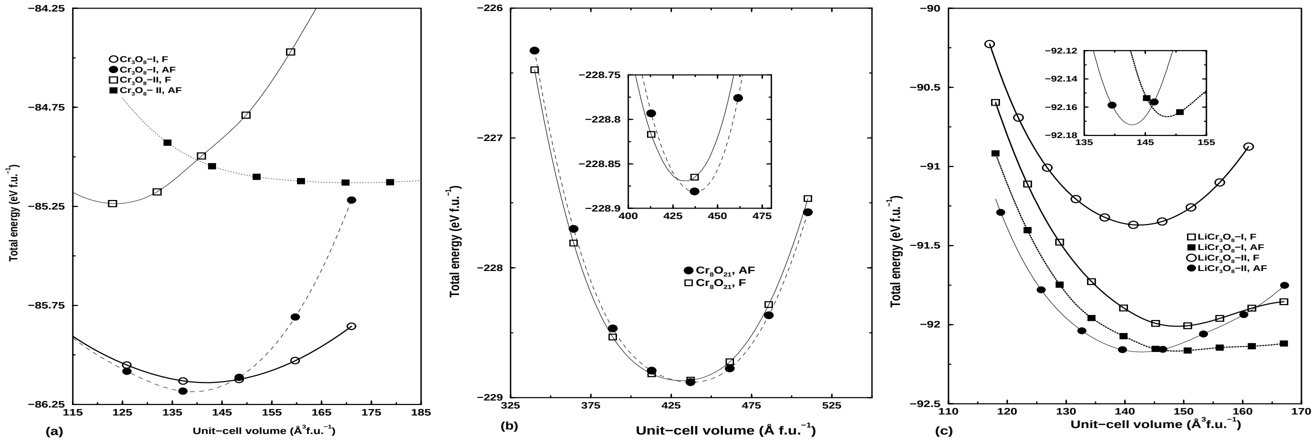

FIG. 2: Calculated unit-cell volume vs total energy for (a) Cr_3O_8-I and -II, (b) Cr_8O_{21}, and (c) $LiCr_3O_8$-I and -II in ferro- and antiferromagnetic configuration. See Fig. 1 and Table I for structural information.

TABLE I: Optimized structure parameters and bulk modulus (B_0) for Cr_3O_8-I, and -II, Cr_8O_{21} and $LiCr_3O_8$-I and -II. All structures, except Cr_8O_{21} ($P\bar{1}$), are described in space group $C2/m$ with Li in $2a$ and Cr1 in $2c$ (not included in the listing). Values given in parentheses refer to the experimental data for Cr_8O_{21} [16]. For comments about the experimental data for $LiCr_3O_8$-II ([13], see text).

Compound	Unit cell (Å or deg)	Atom	Site	x	y	z	B_0 (GPa)
Cr_3O_8-I	a = 8.4067	Cr2	4i	0.5528	0	0.2598	34.743
	b = 5.2656	O1	4i	0.2007	0	0.5884	
	c = 6.0462	O2	4i	0.2971	0	0.9770	
	β = 91.03	O3	8j	0.0495	0.2433	0.3083	
Cr_3O_8-II	a = 6.7524	Cr2	4i	0.3675	0	0.5930	4.396
	b = 5.6422	O1	$4i$	0.2205	0	0.6579	
	c = 7.7150	O2	$4i$	0.7184	0	0.6399	
	β = 117.85	O3	$8j$	0.9769	0.2460	0.6595	
Cr_8O_{21}	a = 5.434 (5.433)	Cr1	2i	0.852 (0.859)	0.211 (0.211)	0.069 (0.068)	21.424
	b = 6.637 (6.557)	Cr2	2i	0.296 (0.280)	0.235 (0.234)	0.899 (0.898)	
	c = 12.546 (12.117)	Cr3	2i	0.347 (0.358)	0.368 (0.377)	0.248 (0.258)	
	α = 105.86 (106.36)	Cr4	2i	0.731 (0.721)	0.793 (0.799)	0.529 (0.528)	
	β = 95.36 (95.73)	O1	2i	0.813 (0.800)	0.500 (0.504)	0.066 (0.060)	
	γ = 77.70 (77.96)	O2	2i	0.423 (0.426)	0.817 (0.835)	0.036 (0.049)	
		O3	1f	1/2 (1/2)	0 (0)	1/2 (1/2)	
		O4	2i	0.132 (0.127)	0.238 (0.250)	0.173 (0.182)	
		O5	2i	0.374 (0.381)	0.725 (0.727)	0.814 (0.812)	
		O6	2i	0.329 (0.304)	0.855 (0.859)	0.231 (0.243)	
		O7	2i	0.910 (0.911)	0.897 (0.899)	0.055 (0.057)	
		O8	2i	0.385 (0.383)	0.328 (0.358)	0.382 (0.397)	
		O9	2i	0.026 (0.038)	0.116 (0.115)	0.412 (0.406)	
		O10	2i	0.189 (0.183)	0.385 (0.372)	0.583 (0.591)	
		O11	2i	0.262 (0.261)	0.617 (0.632)	0.255 (0.255)	
$LiCr_3O_8$-I	a = 8.3394	Cr2	4i	0.3570	0	0.2613	49.102
	b = 5.4749	O1	4i	0.2278	0	0.4572	
	c = 6.4185	O2	4i	0.2599	0	0.0425	
	β = 90.43	O3	8j	0.4733	0.2575	0.2757	
$LiCr_3O_8$-II	a = 9.8811	Cr2	4i	0.3741	0	0.6199	53.522
	b = 5.6842	O1	4i	0.2423	0	0.7135	
	c = 6.1364	O2	4i	0.2329	0	0.6953	
	β = 123.91	O3	8j	0.9913	0.2458	0.7248	

cell volume (V) relationship for Cr_8O_{21} [Fig. 2(b)] shows nearly the same ground-state energy ($E = -85.83$ eV per $Cr_3O_{7.875}$) as Cr_3O_8-I ($E = -86.06$ eV per Cr_3O_8) whereas the corresponding cell volumes differ appreciably ($V = 163.25$ Å^3 per $Cr_3O_{7.875}$ and 139.01 Å^3 per Cr_3O_8). However, a proper comparison between Cr_8O_{21} and Cr_3O_8 has to take into account the difference in oxygen content as brought out by the reaction equation:

$$\frac{3}{8}Cr_8O_{21} + \frac{1}{16}O_2 = Cr_3O_8 \qquad (1)$$

The oxidation energy (ΔE) follows from the relation:

$$\Delta E = E(Cr_3O_8) - \frac{3}{8}E(Cr_8O_{21}) - \frac{1}{16}E(O_2) \qquad (2)$$

which upon introduction of the calculated values for Cr_3O_8, Cr_8O_{21}, and the dioxygen molecule ($E = -9.8607$

eV) gives $\Delta E = -0.39$ eV per Cr_3O_8 at 0 K). This confirms that the experimentally established Cr_8O_{21} phase is the real ground-state phase for the oxide in question. However, as will be argued below there are reasons to believe that Cr_3O_8-I can be obtained as a metastable phase under electrochemical conditions.

So far all attempts [2, 6, 8, 12–16] to synthesize Cr_3O_8 have made use of thermal decomposition of CrO_3 as a key element in the preparational procedure:

$$3CrO_3 = Cr_3O_8 + \frac{1}{2}O_2 \tag{3}$$

According to the present total energy data (see Fig. 2) Cr_3O_8 should be obtainable according to Eqn. 3 already at 0 K ($\Delta E = -5.20$ eV per Cr_3O_8 or -1.73 eV per $CrO_{2.667}$). However, formation of Cr_8O_{21} should be even more favorable ($\Delta E = -1.86$ eV per $CrO_{2.625}$). We will return to a possible synthesis route to Cr_3O_8 after the presentation of our findings for $LiCr_3O_8$. It should be noted that our attempts to perform DFT structural optimization for CrO_3 proved rather unsuccessful. In the first place the calculations converged rather slowly and oscillating, and also they terminated at unit-cell dimensions and positional parameters much different from the experimental values [24]. We believe that the root of the problem is the distinct one-dimensional character of the CrO_3 structure which may obscure the DFT calculation. It is well known that the DFT approach (in particular GGA) underestimates intermolecular, van-der-Waals-type binding.

As seen from Fig. 2(c), two of the selected test structures for $LiCr_3O_8$ (variants I and II) came out with virtually the same total energy at the minimum in the $E(V)$ relationship ($\Delta E \approx -5.6$ meV per $LiCr_3O_8$) with variant II as the energetically favored phase. Variant II has also the smallest equilibrium volume ($V = 143.19$ and 148.44 Å^3 per $LiCr_3O_8$ for variant II and I, respectively). As seen from Table I, both $LiCr_3O_8$-I and -II belong to the space group $C2/m$, even though the initial guess structures were different. We simply allotted the KCr_3O_8 type to variant I and the experimentally determined $LiCr_3O_8$ structure to variant II. According to Wilhelmi's [13] description for the $LiCr_3O_8$-II structure in space group $Cmcm$, Li and one third of the Cr atoms are randomly distributed in a fourfold position. In order to bring the disorder aspect into the computations, we constructed a supercell with periodic arrangements of Li and Cr1 to mimic the experimentally reported structure. At the start of the calculations it was detected that forces of around 2.6 eVÅ^{-1} were acting at the oxygen sites which clearly signaled certain defects in the experimental $LiCr_3O_8$-II structure. This suspicion was further reinforced during the calculations which finally converged with a gain of more than 1.3 eV f.u.$^{-1}$ in total energy and structural parameters that were "miles away" from the input values. On careful analysis of our computed $LiCr_3O_8$-II structure it turned out that this really belongs to space group $C2/m$ rather than $Cmcm$. Although this is "accidentally" the same space group as adopted by variant I, the atomic arrangement is quite different. With our retrospective wisdom we tried to convert Wilhelmi's structure to space group $C2/m$, but the efforts were in vain. Hence the calculated structure specification included in Table I represents an appreciably modified version of Wilhelmi's structure, and it is pertinent to ask what can possibly have gone wrong in Wilhelmi's single-crystal x-ray determination of the $LiCr_3O_8$-II structure. We believe that the root of the discrepancy is associated with the chemically rather unrealistic postulate that Li and Cr atoms should be randomly distributed over one and the same site in such structures. On the basis of the present theoretical findings it is strongly recommended that the $LiCr_3O_8$-II structure is subjected to an experimental redetermination.

From Fig. 1(e,f) it is seen that $LiCr_3O_8$-I and -II carries a close structural relationship, both exhibiting characteristic layer features. Wilhelmi [13] used relatively strong synthetical means (hydrothermal conditions at high temperatures) to obtain the $LiCr_3O_8$-II phase. On modifying the preparational procedure (inter alia relinquishing single-crystal production and rather imitating the synthesis procedures for the other ACr_3O_8 (A = Na, K, Rb) phases [22] it seems quite likely that the $LiCr_3O_8$-I phase will materialize. With the $LiCr_3O_8$-I phase at hand, it is easy to prescribe an apparently safe synthesis route to Cr_3O_8-I. $LiCr_3O_8$-I is simply introduced as cathode in a suitable battery setup and the unit is subjected to charging conditions.

The structural feature which makes the $LiCr_3O_8$-I phase particularly suitable for battery purposes is its pronounced layer character (like monoclinic $LiMnO_2$ [25] where the structure allows withdrawal of large amounts of Li) and the direct correspondence between the structures of Cr_3O_8-I and $LiCr_3O_8$-I [see Fig. 1(b,e)] which should facilitate lithium intercalation/deintercalation. It is the close structural relationship which will allow preparation of Cr_3O_8-I as a metastable phase at the expense of the energetically more favorable Cr_8O_{21} (see above). The synthesis of Cr_8O_{21} has been made with use of CrO_3 as starting material and it is indeed possible to imagine that Cr_3O_8-I as well as Cr_8O_{21} can be formed by reconstructions from structural fragments obtained by partial thermal decomposition of CrO_3. However, thermal decomposition requires elevated temperature and under these conditions the energetically favored Cr_8O_{21} is formed. On the other hand, under the far milder electrochemical conditions during deintercalation of $LiCr_3O_8$-I, Cr_3O_8-I should be favored by kinetics. Since the energy barrier between Cr_3O_8-I and Cr_8O_{21} is higher than the energy made available by room temperature, the activation energy needed to promote the conversion from the former to the latter is simply not available.

Table I shows that Li intercalation from Cr_3O_8-I to $LiCr_3O_8$-I leads to relatively small changes in the a and b axes (-0.8% and 3.1%, respectively) whereas there occurs an appreciable increase in the c axis

TABLE II: Calculated magnetic moment (in μ_B per Cr atom) for crystallographically non-equivalent Cr atoms (see Fig. 1 and Table I) for CrO_3, Cr_3O_8-I, Cr_3O_8-II, Cr_8O_{21}, $LiCr_3O_8$-I, and $LiCr_3O_8$-II in F and AF states . Total refers to the total magnetic moment per formula unit.

	F			AF	
Phase	Cr1	Cr2	Total	Cr1	Cr2
CrO_3	1.91	–	1.87	1.36	–
Cr_3O_8-I	1.78	0.17	1.94	1.67	0.02
Cr_3O_8-II	1.93	0.18	1.96	1.83	0.05
Cr_8O_{21}	2.39	0.26[a]	5.61	2.34	0.04[b]
$LiCr_3O_8$-I	2.55	0.22	2.89	2.45	0.02
$LiCr_3O_8$-II	2.60	0.22	2.87	2.57	0.04

[a] For Cr3: 0.21 and Cr4: 0.15

[b] For Cr3: 0.21 and Cr4: 0.02

(6.2%). This nicely illustrates the requirements to a good cathode battery material based on intercalation/deintercalation mechanisms and emphasizes why the pair Cr_3O_8-I/$LiCr_3O_8$-I constitutes a good combination. Considerations of the structural information in Fig. 1 and Table I suggest why this pair should be better than other chromium-oxygen combinations: CrO_3 appears to be rather unsuitable for intercalation/deintercalation associated with its one-dimensional structure, Cr_8O_{21} exhibits too much three-dimensional character, whereas Cr_3O_8-II carries a more irregular arrangement than Cr_3O_8-I. Moreover, most of the cathode materials tested hitherto [2, 8, 10, 25–28] appear to have contained a mixture of CrO_3, Cr_3O_8 (most likely Cr_8O_{21} according to the preparational conditions), Cr_5O_{12}, and/or Cr_2O_5, of which CrO_3, Cr_5O_{12}, and Cr_2O_5 as well as the lower oxides CrO_2 and Cr_2O_3 are all reported [2] to decrease the performance of lithium chromium oxides as battery materials. Most of the attention has been focussed on poorly characterized samples with the composition Cr_3O_8. Since these materials probably consisted of Cr_8O_{21} it is only natural that the capacity of Li intercalation is found to increase with increasing degree of amorphous character of these samples [8]. Even with its probable shortcomings (compared to Cr_3O_8-I) unspecified Cr_3O_8 is reported [8] to exhibit a quite large chemical diffusion coefficient for Li^+ ($\sim 10^{-8}\,\mathrm{cm}^2\,\mathrm{s}^{-1}$). This appears to vouch for an appreciably higher diffusion of Li^+ during intercalation/deintercalation of Cr_3O_8-I, which we still regard as a very promising battery cathode material.

B. Magnetic properties

During the structural optimization, we also took into account cooperative magnetic ordering and performed simulations for P, F, and AF configurations. [Our experience from the calculations of magnetic states for the closely related ACr_3O_8 (A = Na, K, Rb) series showed [1] that tested configurations with ferrimagnetic arrangements invariably ended up with F or AF solutions. Accordingly, such variants were not considered in this study.] As seen from Fig. 2, the AF arrangements came out as the ground states for all phases, except Cr_3O_8-II which takes F ordering as the lower-energy state. The energy difference between the AF and F states is small in all cases (between $\sim$ 4 and $160\,\mathrm{meV\,f.u.}^{-1}$). These findings suggest that some of the considered phases may be subjected to an AF-to-F transition on application of a magnetic field.

According to Table II one of the Cr sites in all these phases carries a substantial magnetic moment ($1.4-2.5\,\mu_B$ per Cr atom for the AF states at 0 K and ambient pressure) whereas the other Cr sites only exhibit small moment(s). On considering Table II it should be born in mind that the oxygen atoms also carry small induced magnetic moments. Some of these turned out to be oppositely aligned in the F cases, hence the total moments for Cr_3O_8-I and -II came out smaller than the sum of the moments at the Cr1 and Cr2 sites.

Experimental magnetic data are very scarce for these phases: limited to $\mu_\mathrm{P} = 4.2 \pm 0.1\,\mu_B$ per Cr atom, $\Theta = -165 \pm 5\,\mathrm{K}$, and T_N around 100 K for Cr_8O_{21} [16], and $\mu_\mathrm{P} = 4.35\,\mu_B$ per Cr atom, $\Theta = -170\,\mathrm{K}$, and T_N around 80 K for Cr_3O_8 (unspecified) [15]. [Note that these data refer to P states with numerical values extracted from Curie-Weiss relationships and thus follow a different definition of magnetic moment; according to the "spin-only" approximation specified as: $\mu_P = \sqrt{8C_{mol}} = 2\sqrt{S(S+1)}$]. However, powder neutron diffraction was only able to unveil a few very weak magnetic reflections at low temperatures (10−100 K) for Cr_8O_{21} [16]. Perhaps the clear indication of Néel temperatures in the magnetic susceptibility data for these phases reflects conversion to two- rather than three-dimensional cooperative magnetic ordering.

The magnetic moments at the Cr1 (Cr for CrO_3) sites in these phases are lower than the "spin-only" values for a $\mathrm{Cr}^{\mathrm{III}}$ (d^3) valence state, owing to strong Cr-O interactions (see Sec. IV D). Without our prior experience from the study of the ACr_3O_8 phases we might at first been tempted to take the observation of very low magnetic moments at the Cr2 sites as indications of a $\mathrm{Cr}^{\mathrm{VI}}$ (d^0) valence state. (The fact that we then would have overlooked that $\mathrm{Cr}^{\mathrm{VI}}$ is the formal valence state for CrO_3 is another story.) However, we know [1] that the almost zero moments of Cr2 in the ACr_3O_8 phases do not reflect a d^0 state, but rather results from very small exchange splitting. The large moments at the Cr1 sites, on the other hand, reflect precisely the opposite, viz. strong exchange interaction. The overall size and variation of the magnetic moments in Table II, clearly demonstrate that little physical significance should be attached to considerations based on formal valence states (see also Sec. IV D). It is interesting to note that the magnetic moment at Cr1 increases by approximately $1\,\mu_B$ from Cr_3O_8-I and -II to $LiCr_3O_8$-I and -II, respectively. This should not be interpreted as a trivial change in oxidation state from, say, $\mathrm{Cr}^{\mathrm{VI}}$ to $\mathrm{Cr}^{\mathrm{III}}$ but mostly as another evidence for effects of exchange splitting. In this perspective the impacts of differences in the valence states of Cr1 and Cr2 have far less significance.

C. Electronic structure

The total and site-projected DOSs for $\mathrm{CrO_3}$, $\mathrm{Cr_8O_{21}}$, $\mathrm{Cr_3O_8}$-I, and $\mathrm{Cr_3O_8}$-II are displayed in Fig. 3. The total DOS for $\mathrm{CrO_3}$ [Fig. 3(a)] with a significant number of states at the E_{F} implies metallic character contrary to the insulating behavior expected for a $\mathrm{Cr}^{\mathrm{VI}}$ state. This confirms that Cr is not in a simple $\mathrm{Cr}^{\mathrm{VI}}$ state, in agreement with magnetic moment study.

The total DOS for $\mathrm{Cr_8O_{21}}$ [Fig. 3(b)] shows insulating behavior with around 0.25 eV band gap between the valence band (VB) and conduction band (CB) which provides another evidence of the relative stability of this oxide compared with $\mathrm{Cr_3O_8}$-I and -II. $\mathrm{Cr_8O_{21}}$ comprises four crystallographically non-equivalent Cr and eight O atoms. Since the energetic distribution of the electronic states for Cr3 and Cr4 are almost same as that for Cr2, illustrations of the site-projected DOS for the former sites are not included in Fig. 3(b). Only an overall DOS is shown for the oxygen atoms of $\mathrm{Cr_8O_{21}}$. The E_{F} in $\mathrm{Cr_3O_8}$-I [Fig. 3(c)] falls on a pseudogap-like feature. Pseudogaps are known [29] to result from covalent hybridization, exchange splitting, charge transfer, *d* resonance etc., and the presence of a pseudogap appears to be favorable for stability. The $\mathrm{Cr_3O_8}$-II phase, for which both F and AF configurations occur at higher energy than the $\mathrm{Cr_3O_8}$-I phase [see Fig. 2(a)], exhibits a very small band gap [0.04 eV; Fig. 3d] and accordingly insulating behavior at 0 K. The band gap of $\mathrm{Cr_8O_{21}}$ is considerably larger lending further support to the conclusion that $\mathrm{Cr_8O_{21}}$ is more stable than the two $\mathrm{Cr_3O_8}$ variants, viz. in agreement with findings from the total energy study.

The DOS for the Cr atoms in $\mathrm{Cr_3O_8}$-I and -II as well as in $\mathrm{Cr_8O_{21}}$ show different topology indicating difference in their valence states. The partial DOS of Cr1 in all three phases are similar in the sense that the most prominent peaks are seen in the region −6 to −4 eV and in a narrow region just below the E_{F}. The majority- and minority-spin channels of Cr2 are almost equally filled, and this implies as mentioned above negligible exchange splitting and consequently a negligible moment at Cr2. The x-ray photo-emission (XPS) study [8] on $\mathrm{Cr_3O_8}$ samples (unspecified phase) reported two prominent peaks which were interpreted as evidence for Cr^{6+} and Cr^{3+}. Although assignment of valence states is not appropriate using XPS, the site-projected DOS of Cr1 and Cr2 in Fig. 3(b-d) show two such prominent peaks in VB. Owing to the presence of energetically degenerate Cr *d* and O *p* states and the layered nature of these phases, the covalent interaction between these atoms is distinct, and indeed it is this interaction which is responsible for the small magnetic moments at the oxygen sites.

The electronic structures of $\mathrm{LiCr_3O_8}$-I and -II (Fig. 5) are largely similar. Compared with $\mathrm{Cr_3O_8}$-I and -II, $\mathrm{LiCr_3O_8}$-I and -II may be said to have the states more localized. Insulating behavior is seen for both phases with band gaps of around 0.34, and 0.81 eV, respectively. Clearly visible Li states occur in the VB for $\mathrm{LiCr_3O_8}$-I whereas the Li DOS profile for $\mathrm{LiCr_3O_8}$-II becomes visible only after appreciable magnification, indicating that Li in $\mathrm{LiCr_3O_8}$-I is less ionic than that in $\mathrm{LiCr_3O_8}$-II. Similar to the corresponding $\mathrm{Cr_3O_8}$-I and -II variants, the two types of Cr atoms in $\mathrm{LiCr_3O_8}$-I and -II exhibit topologically different partial DOS. The three kinds of oxygen atoms show differences in the DOS curves like those in $\mathrm{Cr_3O_8}$-I and -II. The partial DOS of Cr and O are energetically degenerate also for the lithium phases (viz. hybridized). As is to be expected on the basis of the close structural correspondence between $\mathrm{LiCr_3O_8}$-I and -II and the $A\mathrm{Cr_3O_8}$ [1] compounds, there are also pronounced similarities in the electronic structures of these phases.

According to formal electron counting, the valence of Cr1 should be 4+ and that of Cr2 6+ in $\mathrm{Cr_3O_8}$. When Li is intercalated into $\mathrm{Cr_3O_8}$ an extra electron, formally donated by Li, goes to Cr1 and changes its valence to 3+. However, the present computations show that, for all compounds, the VB contains a large (roughly equal) number of states for Cr1 and Cr2 (certainly no way near the d^0 configuration required for a Cr^{6+} state). Owing to the hybridization interaction with O 2*p*, the states at the Cr2 site could at first sight seem to originate from back-donation. However, the orbital-projected DOSs (Fig. 5) for Cr1 and Cr2 in $\mathrm{Cr_3O_8}$ and $\mathrm{LiCr_3O_8}$ demonstrates a definite number of *d* states (integrated counts gave 3 to 5 electrons; *s* and *p* states are negligibly small and not included in the illustrations). It must therefore be concluded that, it would be inappropriate to assign valence states for Cr according to the conventional approach.

D. Bonding characteristics

The information on the chemical bonding in the compounds under investigation is largely gathered from careful analysis of the structural, magnetic, and DOS properties (Sec. III A-C) together with charge density and charge transfer plots. The insight already gained [1] on the chemical bonding in the closely related compounds $A\mathrm{Cr_3O_8}$ (A = Na, K, Rb) constitutes a firm basis for the present deductions. Our very broadly directed study of the $A\mathrm{Cr_3O_8}$ compounds included the use of electron localization function and crystal orbital Hamiltonian population analyses as additional tools. However, since the extra tools largely served to confirm the findings from the charge density and charge transfer plots, it was decided to concentrate the efforts on the latter means to illuminate bonding for the present compounds.

In the following we will focus the attention on the

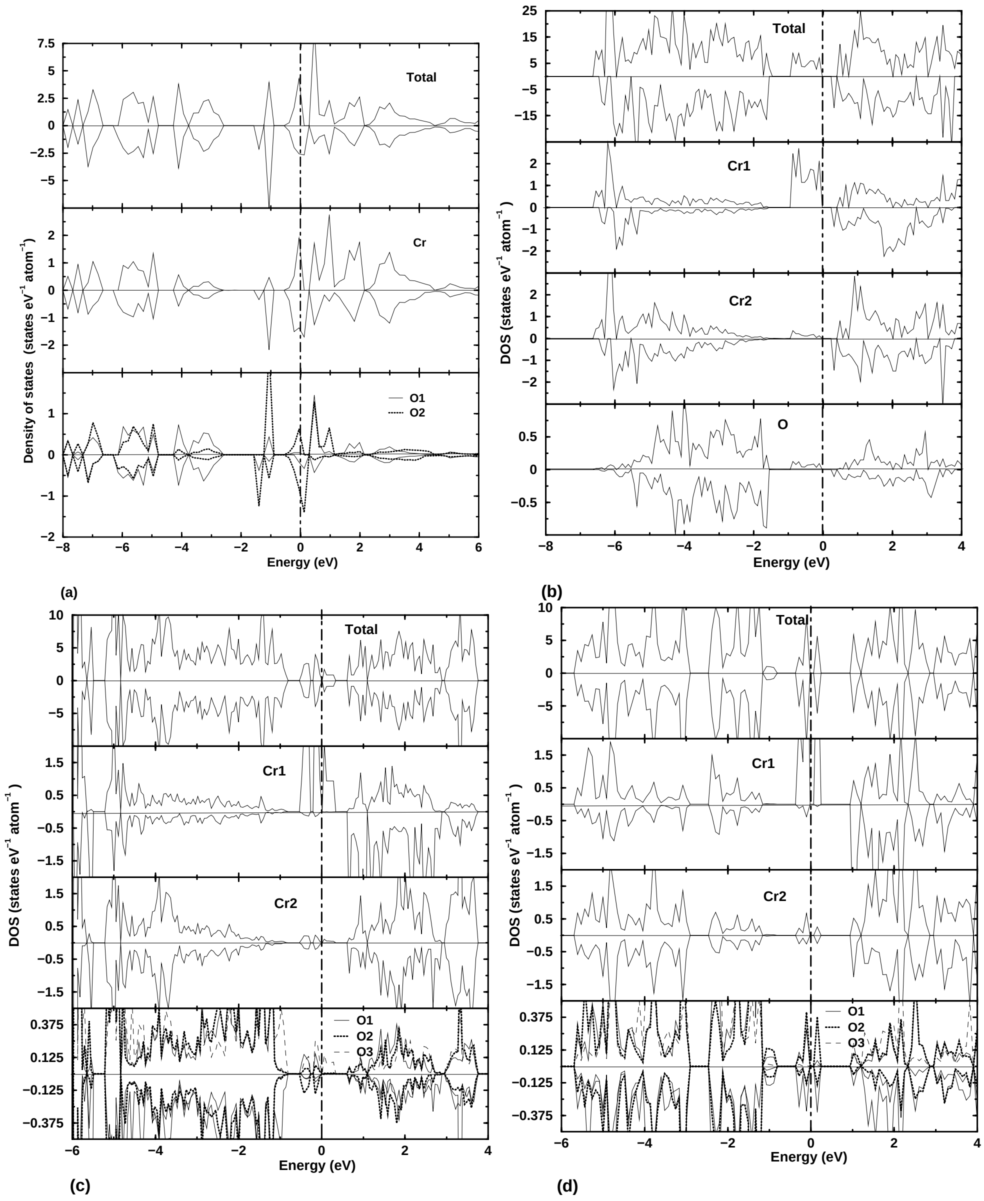

FIG. 3: Total and site-projected density of states for (a) CrO_3 (based on experimental structural parameters), (b) Cr_8O_{21}, (c) Cr_3O_8-I, and (d) Cr_3O_8-II; in AF configurations for the three former oxides and F configuration for the latter. The vertical line denotes E_F.

bonding situation in Cr_3O_8-I and $LiCr_3O_8$-I. There are two main reasons for this choice. First, $LiCr_3O_8$-I is properly isostructural with the ACr_3O_8 compounds which allows us to draw heavily on the experience from our earlier study [1] and Cr_3O_8-I constitutes the "anion" skeleton of these compounds. Second, the Cr_3O_8-I/$LiCr_3O_8$-I pair are of considerable interest in relation to battery aspects, both for pure model considerations and also for potential practical utilization. Moreover, we believe that insight gained on the bonding in Cr_3O_8-I and $LiCr_3O_8$-I has large carry-over value for illustration of our findings for the closely related phases subject to this study.

Fig. 6 shows plots of charge density and charge transfer (difference between the actual charge in the crystalline solid under investigation and the superposed atomic charge at the corresponding atomic position) for Cr_3O_8-I and $LiCr_3O_8$-I. The charge density within the Cr_3O_8-I skeleton [Fig. 6(a)] suggests that, the octahedral Cr1 exhibits considerable covalent interaction with the neighboring basal plane oxygen atoms whereas the charge density between Cr2 and oxygen implies even stronger covalent interaction. However, the charge transfer plot [Fig. 6(b)] does not fully comply with these inferences. The anisotropic charge distribution at Cr1 points to coordinated covalent bonding. The absence of charges in regions between Cr2 and O (an indicator for covalent bonding) and more positive charges at the oxygen sites

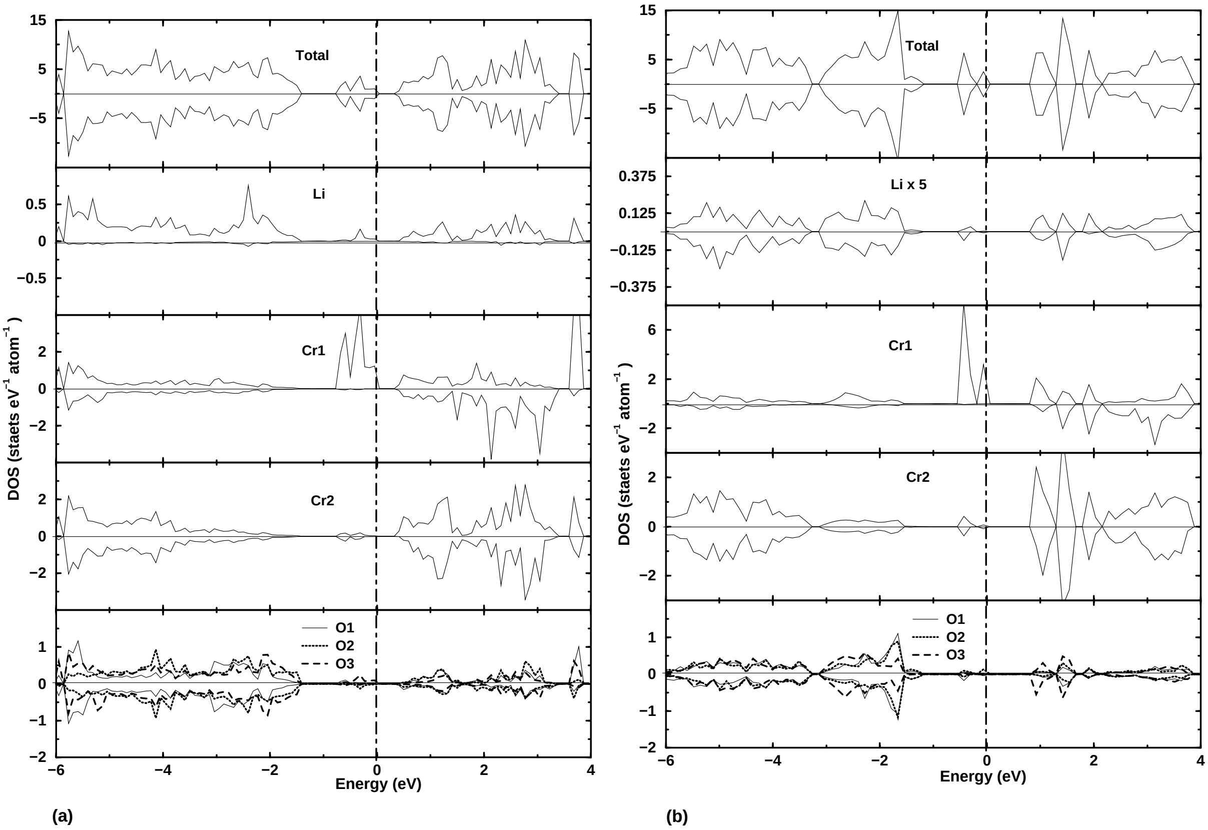

FIG. 4: Total and site-projected density of states for (a) $LiCr_3O_8$-I and (b) $LiCr_3O_8$-II in AF state. The vertical line denotes E_F.

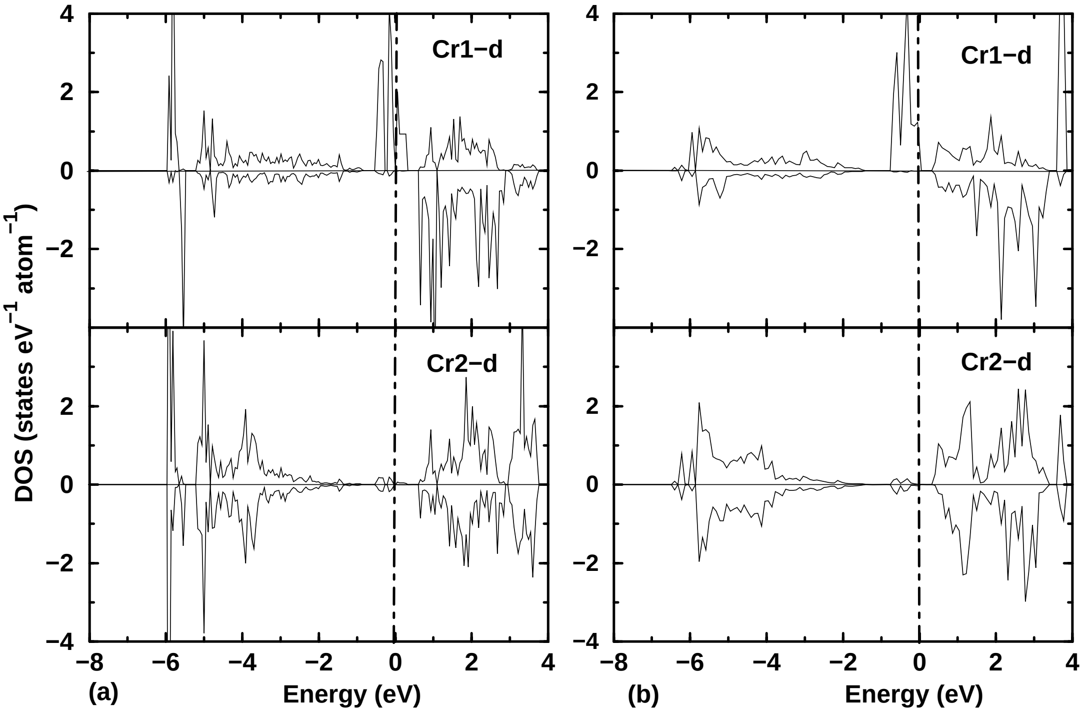

FIG. 5: d-orbital-projected density of states for Cr1 and Cr2 of (a) Cr_3O_8-I and (b) $LiCr_3O_8$-I in AF state. The vertical line denotes E_F.

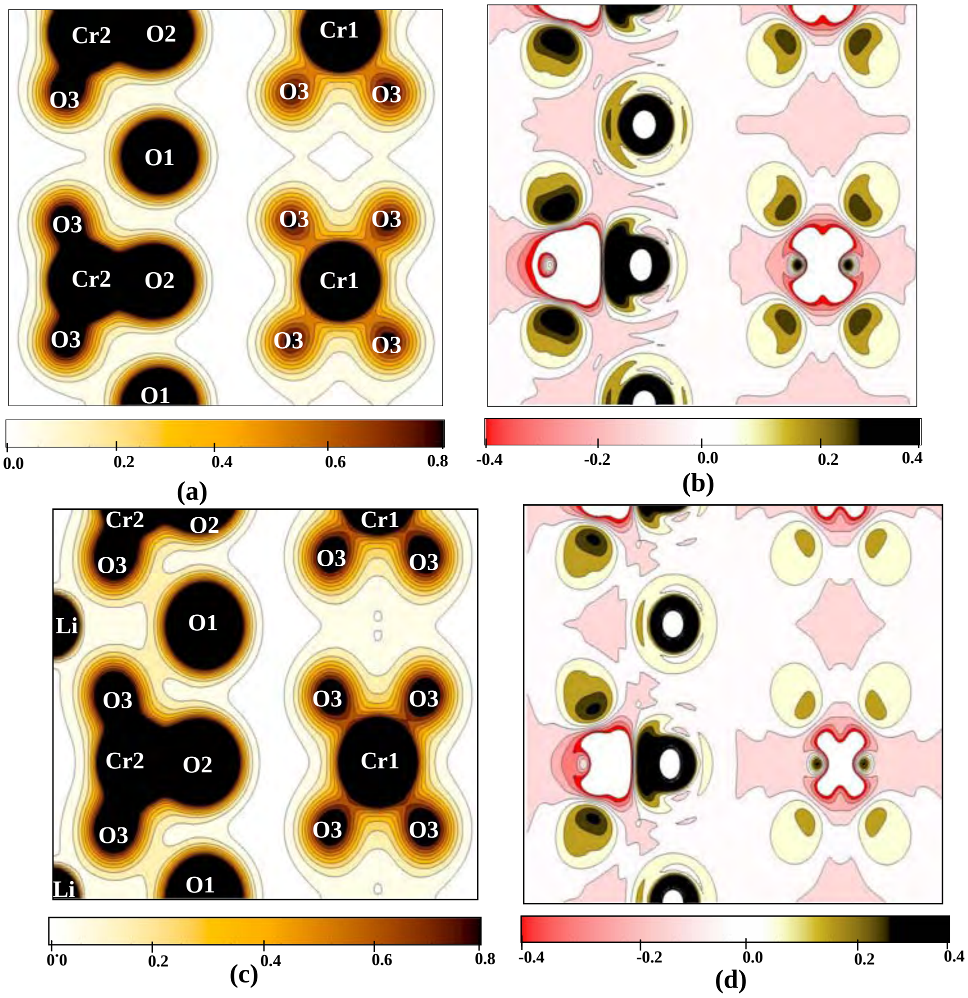

(a) (b) (c) (d)

FIG. 6: (Color online) Plots in a, c plane of (a) charge density and (b) charge transfer for Cr_3O_8-I. Corresponding plots for $LiCr_3O_8$-I are shown in c and d, respectively.

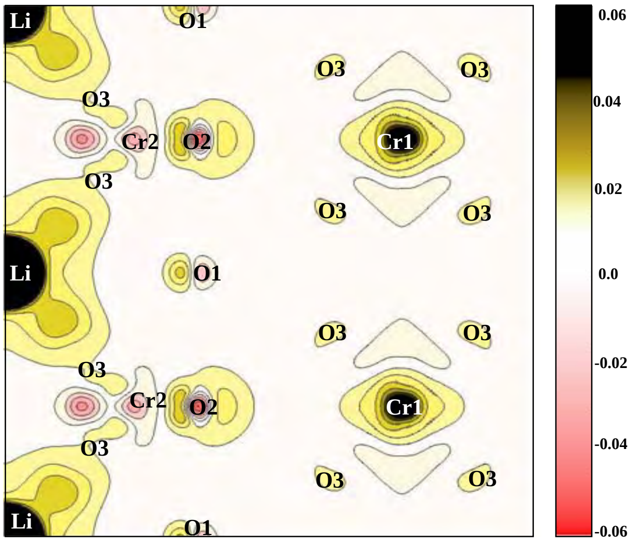

FIG. 7: Calculated charge density differences between $LiCr_3O_8$-I and Cr_3O_8-I. The calculations were performed for the fixed, relaxed geometry of $LiCr_3O_8$-I.

imply that Cr2 exhibits a distinct degree of iono-covalent interaction with its oxygen neighbors (viz. the Cr2-O bonds signal both charge transfer and directional covalent bonding). In $LiCr_3O_8$-I [see Fig. 6(c,d)], the Li site carries charge; the charges around O2 showing a somewhat larger span than that in Cr_3O_8-I, and Cr2-O exhibits higher charge density between the atoms. Except for these distinctions, the overall features of the charge density distribution are the same for Cr_3O_8-I and $LiCr_3O_8$-I.

Similar to Na, K, and Rb in the ACr_3O_8 compounds, it is appropriate to refer to Li in $LiCr_3O_8$-I as a cation. The same applies to Li in $LiCr_3O_8$-II although the picture is a little more unclear owing to its more irregular structural arrangements. In Cr_3O_8-I and -II as well as in the lithium containing compounds, Cr and O electronic states are energetically degenerate demonstrating strong covalent interaction between them. The different valence states of the Cr atoms in these compounds are seen from their different DOS curves. However, the difference is, in all phases, far smaller than indicated by the formal ionic valences Cr^{3+} and Cr^{6+}. As for the ACr$_3$O$_8$ compounds the octahedrally coordinated Cr1 may to a reasonable approximation be regarded as Cr^{3+} whereas the tetrahedrally coordinated Cr2 appears to be closer to Cr^{2+} than Cr^{6+}. The charges associated with oxygen in the presently considered compounds appear close to -1. The general feature is that the Cr-O bonds of octahedral configurations have more covalent character than those in tetrahedral arrangements.

Effect of Li intercalation

In order to illustrate the effect of Li intercalation in the Cr_3O_8-I lattice, we show the charge density difference between $LiCr_3O_8$-I and Cr_3O_8-I in Fig. 7. The charge difference has been calculated for the same unit-cell dimensions and atomic positions as that of the optimized $LiCr_3O_8$-I phase, so that the electron densities can be subtracted point by point in real space. According to the classic inorganic chemistry viewpoint: When Li is intercalated into the Cr_3O_8-I host lattice, Cr will absorb the extra charge and change oxidation state(s). If this had been the case, one would have expected appreciable modification in the electronic structure. From Fig. 6(a,c) it is however seen that there occurs no significant change at the site allocated for Li when it enters the Cr_3O_8-I host to form $LiCr_3O_8$-I, and the amount of charges present on Cr remains essentially the same. Hence the entire valence electron of Li is not transferred from it to the Cr_3O_8-I host. Fig. 7 suggests that charges are present between the Li and O3 sites. The oxygen electrons are polarized toward the Li site in an "attempt" to establish covalent bonding with Li. In accordance with this, there occurs an increase in the Cr1-O3 bond length from 1.88 Å in Cr_3O_8-I to 1.91 Å in $LiCr_3O_8$-I. If the "attempted" Li-O covalent bond had been established as a strong bond, Li deintercalation would have been hampered. However, experimental studies on Cr_3O_8 (unspecified) appears to indicate that the rechargeability and cyclability is quite good, suggesting that the covalency of the Li-O bond is weak. It is worthwhile to note that the O p states span up to E_F in Cr_3O_8-I, whereas in $LiCr_3O_8$-I they become more localized and occur between -6 to -2 eV. Moreover the participation of O p states will give rise to higher cell voltage as more energy is needed to release the electrons from the lower O p band [30] during the Li to Li^+ conversion.

As already emphasized, the conventional picture of Li donating its valence electron to the host is not applicable here. The mechanism is rather that the lattice undergoes a "self-regulating response" which minimizes the effect of the external perturbations via rehybridization [5]. This is seen as noticeable modifications in the charges around Cr and O atoms in Figs. 6(c) and 7. The Cr-O bonds undergo changes in hybridization so that Cr1 gains some charges whereas Cr2 depletes some charges (The integrated charge at the Cr1 site is 10.42 e in Cr_3O_8-I and 10.52 e $LiCr_3O_8$-I whereas that at the Cr2 site is 11.64 e in Cr_3O_8-I and 11.62 e in $LiCr_3O_8$-I.) A similar situation appears to occur in LiCuSn [31] where the Cu sites is mainly affected by the Li intercalation. As the Cr1-O bond length increases from Cr_3O_8-I to $LiCr_3O_8$-I, the strength of the covalent interaction decreases. In general it may be said that the valence electrons on a particular atom participate either in bonding or in magnetism. As the Cr1-O bond length increases, the Cr1 electrons contribute more to magnetism which in turn result in increased magnetic moment at Cr1. The situation for Cr2 is different since the average Cr2-O bond length (1.66 Å) remains almost the same in Cr_3O_8-I and $LiCr_3O_8$-I, and consequently no noticeable change in either the bonding interaction or the magnetism takes place.

V. CONCLUSION

On considering a number of different guess structures in structural optimizations of Cr_3O_8 and $LiCr_3O_8$, it is established that both compounds stabilize with the structural arrangements described in space group $C2/m$ with certain modifications in the atomic arrangements. The optimized structural parameters for Cr_8O_{21} are found to be in good agreement with the available experimental values. From total energy studies it is shown that Cr_8O_{21} is energetically more favorable than different variants of Cr_3O_8. It is proposed that Cr_3O_8 can be stabilized as a metastable phase when electrochemical conditions are imposed on $LiCr_3O_8$. Electronic structures have been explored by investigating total and site-projected density of states and it is confirmed that the electronic structure of $LiCr_3O_8$ has similarities with the structurally related ACr$_3$O$_8$ (A = Na, K, Rb) phases. Detailed analyses of the bonding situation reveal that on intercalation of Li into Cr_3O_8, Li does not donate its valence electron to the Cr_3O_8 host. On the contrary, the Cr_3O_8 host undergoes a so-called "self-regulating response" by modifying the iono-covalent character of the Cr-O bonds. In all the studied systems Cr exists in two different valences as evident from differences in magnetic moment and electronic structure details. Cr in octahedral coordination can be referred to as Cr^{III} whereas Cr in tetrahedral configuration can not properly be considered as Cr^{VI}. The suitability of $Cr_3O_8/LiCr_3O_8$ combinations as possible cathode materials has been examined from structural points of view. Owing to their potential significance in this respect, experimental studies on structural and magnetic properties are strongly recommended.

VI. ACKNOWLEDGEMENT

The authors are grateful to the Research Council of Norway for financial support and computer time at the Norwegian supercomputer facilities.

[*] Electronic address: **vidya.ravindran@kjemi.uio.no**

[1] R. Vidya, P. Ravindran, P. Vajeeston, H. Fjellvåg, and A. Kjekshus, Phys. Rev. B. **72**, 014411 (2005).

[2] R.P. Ramasamy, P. Ramadass, B.S. Haran, and B.N. Popov, J. Power Sources **124**, 155 (2003).

[3] G. Ceder, M.K. Aydinol, and A.F. Kohan, Comput. Mater. Sci. **8**, 161 (1997).

[4] M.K. Aydinol, A.F. Kohan, G. Ceder, K. Cho, and J. Joanhopaulos, Phys. Rev. B. **56**, 1354 (1997).

[5] C. Wolverton and A. Zunger, Phys. Rev. Lett. **81**, 606 (1998).

[6] R. Koksbang and P. Norby, Electrochim. Acta **36**, 727 (1991).

[7] D.W. Murphy, P.A. Christian, F.J. Disalvo, and J.N. Carides, J. Electrochem. Soc. **126**, 497 (1979).

[8] O. Yamamoto, Y. Takeda, R. Kanno, Y. Oyabe, and Y. Shinya, J. Power Sources **20**, 151 (1987).

[9] H. Laucklnd and S.C. Nijhawan, Prog. Batteries Solar Cells **5**, 61 (1984).

[10] R. Koksbang, D. Fauteux, P. Norby, and K.A. Nielsen, J. Electrochem. Soc. **136** 598 (1989).

[11] J.O. Besenhard and R. Schöllhorn, J. Electrochem. Soc. **124**, 968 (1977).

[12] Y. Takeda, R. Kanno, T. Tsuji, and O. Yamamoto, J. Power Sources **9**, 325 (1983).

[13] K.-A. Wilhelmi, Arkiv Kemi **6**, 131 (1967); Chem. Commun. 437 (1966).

[14] K.-A. Wilhelmi, Doctoral Thesis, University of Stockholm (Stockholm, 1966); Acta Chem. Scand. **22**, 2565 (1968).

[15] T. A. Hewston and B. L. Chamberland, J. Magn. Magn. Mater. **43**, 89 (1984).

[16] P. Norby, A. N. Christensen, H. Fjellvåg, and M. Nielsen, J. Solid State Chem. **94**, 281 (1991).

[17] P. E. Blöchl, Phys. Rev. B **50**, 17953 (1994); G. Kresse and D. Joubert, *ibid.* **59**, 1758 (1999).

[18] G. Kresse and J. Furthmuller, Comput. Mater. Sci. **6**, 15 (1996).

[19] J. P. Perdew, K. Burke, and Y. Wang, Phys. Rev. B **54**, 16533 (1996); J. P. Perdew, K. Burke, and M. Ernzerhof, Phys. Rev. Lett. **77**, 3865 (1996).

[20] P. Vinet, J.H. Rose, J. Ferrante, and J.R. Smith, J. Phys.: Condens. Matter **1**, 1941 (1989).

[21] K.-A. Wilhelmi, Acta Chem. Scand. **12**, 1965 (1958).

[22] M. J. Saavedra, C. Parada, and E. J. Baran, J. Phys. Chem. Solids **57**, 1929 (1996).

[23] Inorganic Crystal Structure Database, Version 2004.2.

[24] J.S. Stephens and D.W.J. Cruickshank, Acta Crystallogr., Sec. B **26**, 222 (1969).

[25] A.R. Armstrong and P.G. Bruce, Nature **381**, 499 (1996).

[26] Y. Takeda, R. Kanno, T. Tsuji, and O. Yamamoto, J. Electrochem. Soc. **131**, 2006 (1984).

[27] P. Arora, D. Zhang, B.N. Popov, and R.E. White, Electrochem. Solid-State Lett. **1**, 249 (1998).

[28] D. Zhang, B.N. Popov, Y.M. Podrazhansky, P. Arora, and R.E. White, J. Power Sources **83**, 121 (1999).

[29] P. Ravindran and R. Asokamani, Bull. Mater. Sci. **20**, 613 (1997).

[30] Y. Liu, T. Fujiwara, H. Yukawa, and M. Morinaga, Int. J. Mater. & Prod. Tech. **SPM1**, 89 (2001).

[31] S. Sharma, L. Fransson, E. Sjöstedt, L. Nordström, B. Johansson, and K. Edström, J. Electrochem. Soc. **150**, A330 (2003).

VIII

Submitted to Phys. Rev. B

Density-functional calculations on crystal structures and properties of $CsCr_3O_8$ and ACr_3O_8 (A = In, Tl, Cu, Ag, Au)

R. Vidya*, P. Ravindran, A. Kjekshus and H. Fjellvåg
[1] *Department of Chemistry, University of Oslo, Box 1033 Blindern, N-0315 Oslo, Norway*

Accurate *ab initio* density-functional calculations are performed to predict ground-state crystal structures and to gain understanding of electronic structure and magnetic properties of $CsCr_3O_8$ and ACr_3O_8 (A = In, Tl, Cu, Ag, Au). $CsCr_3O_8$ stabilizes in an orthorhombic (prototype; $Pnma$) structure in agreement with experimental findings whereas the remaining compounds stabilize in the monoclinic KCr_3O_8-type ($C2/m$) structure. All compounds exhibit antiferromagnetic ordering in the ground state at 0 K. The electronic structures are analyzed with the help of density-of-states, charge-density, and electron-localization-function plots. All compounds (except $InCr_3O_8$) are found to be semiconductors (insulators at 0 K) with very small band gaps, and Cr atoms in different environments consistently take different valence states.

I. INTRODUCTION

Oxide materials with transition metal constituents in mixed-valence states have attracted much attention in recent years since they exhibit exotic phenomena like colossal magnetoresistance (CMR) and spin, charge, and orbital ordering [1]. Transition-metal compounds with mixed-valence Mn, Cu, and Co are widely studied, whereas others with say, Cr and Ni are less explored. In an effort to gain understanding of mixed-valence Cr compounds, we have earlier [2–4] studied structural stability, electronic structure, and magnetic properties for compounds with the general formula ACr_3O_8 (A = H, Li, Na, K, Rb as well as A absent) where Cr formally takes two different valence states. In the first report [2] we used accurate density-functional theory (DFT) calculations to analyze electronic, magnetic, and bonding characteristics of ACr_3O_8 (Na, K, Rb) and later [3] we explored the ground-state structures of Cr_3O_8 and $LiCr_3O_8$ which are of considerable interest as cathode materials in rechargeable Li-ion batteries. In Ref. [4] we report the findings for the highly hypothetical compound HCr_3O_8. In the present work we analyze the structural behavior, electronic structure, and magnetic properties of the corresponding ACr_3O_8 phases with A = Cs, In, Tl, Cu, Ag, and Au, with some special emphasis on $CsCr_3O_8$.

II. COMPUTATIONAL DETAILS

The results presented here are based on density-functional calculations according to the projected-augmented plane-wave (PAW) [5] method as implemented in the VASP (Vienna *ab initio* simulation package) [6]. In this approach the valence orbitals are expanded as plane waves and the interactions between the core and valence electrons are described by pseudopotentials. Since one of the main aims of the present work is to determine ground-state structures for ACr_3O_8, we have performed structural optimizations. We considered around 12 different structure types as inputs for each compound and evaluated the total energy for these test structures. A detailed listing of all the considered input structures are given elsewhere [2, 3]. The optimization of the atomic geometry is performed via a conjugate-gradient minimization of the total energy, using Hellmann-Feynman forces on the atoms and stresses in the unit cell. During the simulations, atomic coordinates and axial ratios are allowed to relax for different volumes of the unit cell. These parameters are changed iteratively so that the sum of lattice energy and electronic free energy converges to a minimum value. Convergence minimum with respect to atomic shifts is assumed to have been attained when the energy difference between two successive iterations is less than 10^{-7} eV per cell and the forces acting on the atoms are less than 1 meVÅ^{-1}. The structure with the lowest total energy is taken as the ground-state structure. The generalized gradient approximation (GGA) [7] includes the effects of local gradients in the charge density for each point in the materials and which generally gives better equilibrium structural parameters than the local density approximation (LDA). Hence, the GGA [7] is used to obtain the accurate exchange and correlation energy for a particular atomic configuration. The calculations are carried out using 64 **k** points in the irreducible Brillouin zone for the monoclinic C2/m structure. We have used same energy cutoff and **k**-point density in all calculations. The above calculations are performed in paramagnetic (P), ferromagnetic (F), and antiferromagnetic (AF) configurations. We have calculated the total energy of the compounds as a function of volume for ten different volumes, fitted the results to the so-called "universal equation of state" [8], and extracted the bulk modulus (B_0).

III. RESULTS AND DISCUSSION

A. Structural optimization

Among the different atomic arrangements used as inputs in the calculations for $CsCr_3O_8$, the experimentally established [9] structure (prototype; $Pnma$) and the KCr_3O_8-type ($C2/m$) variant came out with lower ener-

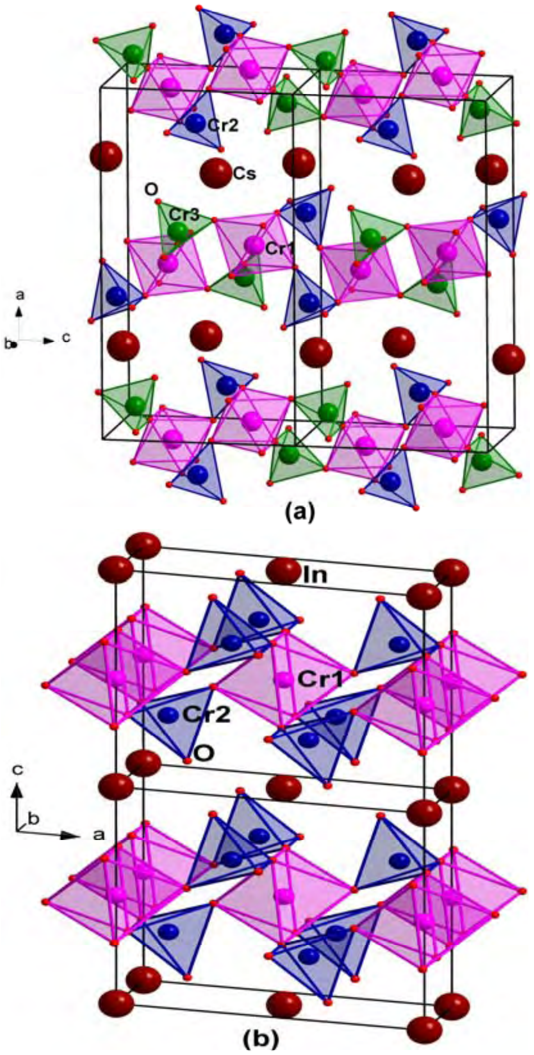

FIG. 1: (Color online) The optimized crystal structures of (a) $CsCr_3O_8$ (prototype; *Pnma*) and (b) $InCr_3O_8$ (KCr_3O_8 type; $C2/m$).

gies [Fig. 2(a)] than the other considered alternatives. Among these the experimental arrangement has the lowest energy and represents the ground state. The structure [Fig. 1(a)] comprises three crystallographic types of Cr and six types of O atoms which form $Cr1O_6$ octahedra, $Cr2O_4$ tetrahedra, and $Cr3O_4$ tetrahedra. These polyhedra are linked by corner sharing to form layers extending parallel to the *bc* plane, separated by Cs atoms which occupy interlayer positions. The calculated lattice parameters and atom positions for $CsCr_3O_8$ are found to be in reasonable agreement with the available experimental values [9], except that *a* shows nearly 5.5% deviation between theory and experiment (see Table I). Note that the $CsCr_3O_8$ structure arranges the Cr-O polyhedral layers along the *a* direction. It is in this direction one also finds the interlayer interactions that are governed by the weaker van-der-Waals-type forces, which are not accounted properly by the DFT calculations. This may be the reason for overestimation of *a* and consequently for the somewhat too large equilibrium volume (remembering that GGA alone [10] is likely to overestimate volume by 2-3 %).

Among the considered structures for $CuCr_3O_8$, our structural optimization shows that KCr_3O_8-type ($C2/m$), $LiCr_3O_8$-II-type, and ZnV_3O_8-type ($Iba2$) structures are present at the lower energy region in the total energy vs volume curve. On the other hand, the other ACr_3O_8 compounds under consideration ($A = $ In, Tl, Ag, Au) have lower energies for KCr_3O_8-type, $LiCr_3O_8$-type, and LiV_3O_8-type ($P2_1/m$) structures [see Fig. 2(b,c); for the sake of clarity higher-energy structures are left out]. Hence the ACr_3O_8 compounds with $A = $ In, Tl, Cu, Ag, and Au stabilize in the KCr_3O_8-type structure like the alkali-metal derivatives of the family [2–4, 11]. The KCr_3O_8-type structure [Fig. 1(b)] consists of two types of Cr atoms arranged in fairly regular octahedral and tetrahedral environments of O neighbors. These polyhedra form layers parallel to the *a*,*b* plane by corner sharing and the *A* atoms in interlayer positions. The atomic arrangement in $CsCr_3O_8$ (*Pnma*) is similar to that in the KCr_3O_8-type structure, except that the orientation of half of the tetrahedra of the former is different, and every second layer is rotated by 180° compared with the layers in the KCr_3O_8-type structure. There is a significant distinction between the Cr-O distances in CrO_6 octahedra and CrO_4 tetrahedra in these structures, which immediately points to a mixed-valence situation for Cr.

Optimized structural parameters for the ground state of the ACr_3O_8 compounds are given in Table I. Except for a rough linear relationship between the cell volume and the ionic radius of *A* (Fig. 3) there appears to be no clear cut overall trend in the structural parameters for the ACr_3O_8 series as a whole (despite the fact that all members except $CsCr_3O_8$ are formally isostructural). Among the ACr_3O_8 compounds with $A = $ In, Tl, Cu, Ag, and Au, only $AgCr_3O_8$ and $TlCr_3O_8$ has been synthesized and characterized by magnetic measurements (but structural determination has not been attempted). Thus, the compounds with $A = $ In, Cu, and Au hitherto remain hypothetical.

B. Magnetic properties

Cooperative magnetism with P, F, and AF configurations was taken into account in the structural optimization calculations. As seen from Fig. 2 all the studied compounds stabilize in the AF state. According to the measured [12] magnetic susceptibility data, $AgCr_3O_8$ orders antiferromagnetically at low temperatures; magnetic moment derived from the Curie-Weiss relationship gives $\mu_P = 3.95 \pm 0.03\mu_B$ f.u.$^{-1}$ Calculated magnetic moments for the studied compounds in their ground-state structures are listed in Table 2. It is evident that the octahedral Cr1 site carries an appreciable magnetic moment whereas the tetrahedral Cr2 site (as well as Cr3 for $CsCr_3O_8$) has an

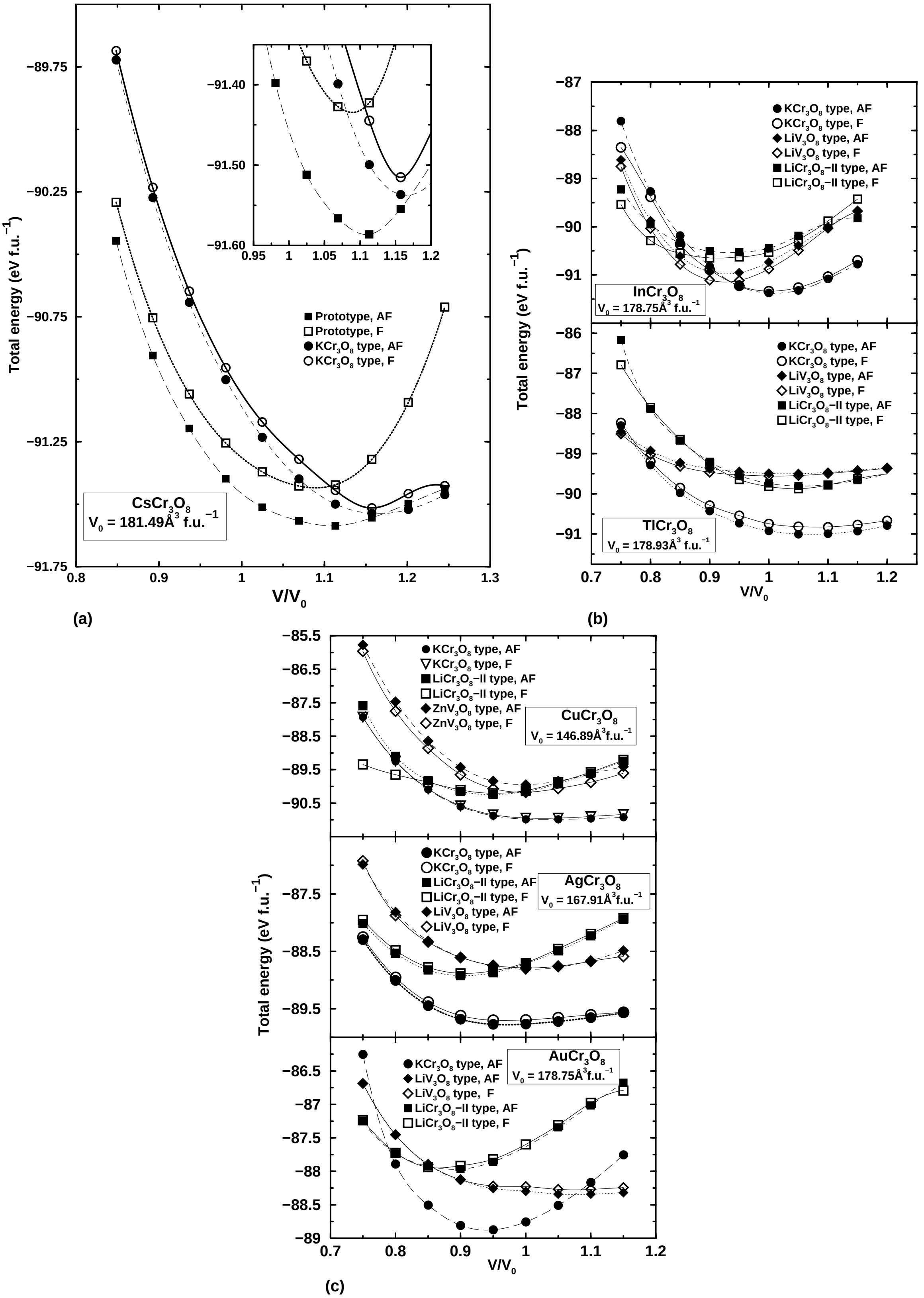

FIG. 2: Calculated cell volume vs total energy for $A\mathrm{Cr_3O_8}$ with (a) A = Cs, (b) A = In and Tl, and (c) A = Cu, Ag, and Au.

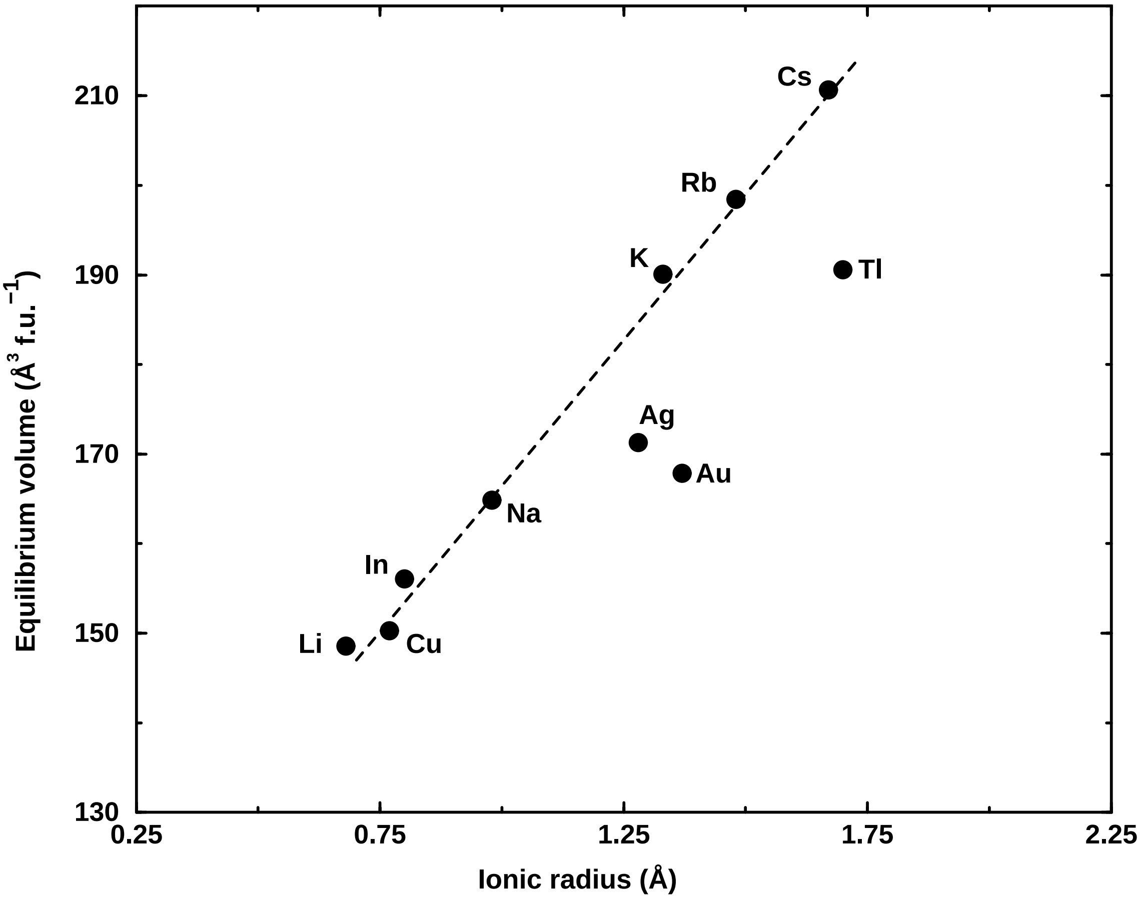

FIG. 3: Optimized equilibrium volume for ACr$_3$O$_8$ (A = Li, Na, K, Rb, Cs, In, Tl, Cu, Ag, and Au) as a function of A^+ radius (standard values).

almost negligible magnetic moment (more significant but still small at the Cr2 and Cr3 sites in CsCr$_3$O$_8$).

InCr$_3$O$_8$ represents a special case in that the magnetic moment on Cr2 in the F state is appreciable (1.06 μ_B) whereas it follows the trend for the rest of the series for the AF state (which is 0.20 eV lower in energy than the F state). The d electrons in InCr$_3$O$_8$ may, e.g., be said to participate more in magnetism than in bonding interaction as indicated by the larger Cr2-O bond length in InCr$_3$O$_8$ (1.68 Å) than that in the other compounds (e.g., 1.63 Å in TlCr$_3$O$_8$), whereas Cr1-O distance (1.91 Å) is almost equal (1.92 Å in TlCr$_3$O$_8$). A general feature for the entire ACr$_3$O$_8$ family is that the oxygen atoms also possess small magnetic moments which originate from Cr d and O p hybridization, and this results in somewhat higher total moment values for the F cases than the sum of the Cr moments. The different size of the Cr magnetic moments is a clear indication of different valence states. However, our prior experiences [2–4] show that assignment of formal valence states for Cr from their magnetic moments is not straightforward.

C. Electronic structure

All ACr$_3$O$_8$ compounds (except InCr$_3$O$_8$), exhibit insulating behavior at 0 K with small, but distinct band gaps (E_g) between the valence band (VB) and conduction band (CB). The E_g values for the compounds under consideration are included in the Table 2. InCr$_3$O$_8$ has a pseudogap-like feature at the Fermi level (E_F). The presence of pseudogap-like features in DOS is considered as favorable for stability, but this indicator can not be taken in support of a probable materialization of such a compound. In fact, compounds with monovalent In are relatively uncommon (for instance, only 114 compounds with monovalent In are reported in the ICSD database [13] compared to 1072 compounds with In in the trivalent state) and a standard ionic radius for In$^+$ is not available. In order to get insight into the occurrence of the higher magnetic moment at the Cr2 site in InCr$_3$O$_8$ than the other ACr$_3$O$_8$ compounds we have examined the total and site-projected DOS for this phase (not shown). Interestingly, this exercise showed a half-metallic behavior with filled band in the majority-spin channel and a 2.6 eV energy gap in the minority-spin channel. The exchange-splitting energy for Cr1 is around 1.5 eV whereas that for

TABLE I: Optimized ground-state structural parameters and bulk modulus (B_0) for $A\mathrm{Cr_3O_8}$ (A = Cs, In, Tl, Cu, Ag, and Au) at 0 K. Except $\mathrm{CsCr_3O_8}$ (space group $Pnma$) these compounds stabilize in $\mathrm{KCr_3O_8}$-type structure; space group $C2/m$ with A in $2a$ (0 0 0) and Cr1 in $2c$ (0 0 1/2) positions.

Compound	Unit cell (Å or ^{o})	Positional parameters	B_0 (GPa)
$\mathrm{CsCr_3O_8}$	a = 16.8322 (15.9570)[a]	Cs ($4c$): 0.2301, 1/4, 0.0150 (0.2137, 1/4, 0.0064)	18.96
	b = 5.5226 (5.5050)	Cr1 ($4c$): 0.4608, 1/4, 0.2575 (0.4524, 1/4, 0.2407)	
	c = 8.5903 (8.264)	Cr2 ($4c$): 0.6046, 1/4, 0.9516 (0.6104, 1/4, 0.9581)	
		Cr3 ($4c$): 0.9198, 1/4, 0.8714 (0.9205, 1/4, 0.8627)	
		O1 ($4c$): 0.8340, 1/4, 0.7831 (0.8370, 1/4, 0.7619)	
		O2 ($4c$): 0.1799, 1/4, 0.4294 (0.1822, 1/4, 0.4101)	
		O3 ($4c$): 0.0185, 1/4, 0.4515 (0.0110, 1/4, 0.4699)	
		O4 ($4c$): 0.3996, 1/4, 0.4345 (0.3842, 1/4, 0.4459)	
		O5 ($8d$): 0.3884, 0.9979, 0.1619 (0.3766, 0.9887, 0.1570)	
		O6 ($8d$): 0.0294, 0.0006, 0.1759 (0.0242, 0.0009, 0.1743)	
$\mathrm{InCr_3O_8}$	a = 8.4711	Cr2 ($4i$): 0.3576, 0, 0.2641	83.32
	b = 5.6404	O1 ($4i$): 0.7771, 0, 0.5478	
	c = 6.5323	O2 ($4i$): 0.7428, 0, 0.9571	
	β = 90.04	O3 ($8j$): 0.9721, 0.7614, 0.2741	
$\mathrm{TlCr_3O_8}$	a = 8.9606	Cr2 ($4i$): 0.3604, 0, 0.2942	27.91
	b = 5.5066	O1 ($4i$): 0.7918, 0, 0.5729	
	c = 7.7331	O2 ($4i$): 0.6834, 0, 0.9082	
	β = 92.84	O3 ($8j$): 0.9630, 0.7541, 0.3271	
$\mathrm{CuCr_3O_8}$	a = 8.3412	Cr2 ($4i$): 0.3462, 0, 0.2707	20.17
	b = 5.5182	O1 ($4i$): 0.7727, 0, 0.5360	
	c = 6.5480	O2 ($4i$): 0.7708, 0, 0.9434	
	β = 94.32	O3 ($8j$): 0.9631, 0.7577, 0.2797	
$\mathrm{AgCr_3O_8}$	a = 8.6410	Cr2 ($4i$): 0.3444, 0, 0.2848	23.34
	b = 5.5211	O1 ($4i$): 0.7840, 0, 0.5525	
	c = 7.1954	O2 ($4i$): 0.7473, 0, 0.9219	
	β = 93.80	O3 ($8j$): 0.9566, 0.7553, 0.3064	
$\mathrm{AuCr_3O_8}$	a = 8.7686	Cr2 ($4i$): 0.3412, 0, 0.2796	68.04
	b = 5.4699	O1 ($4i$): 0.7860, 0, 0.5484	
	c = 7.0013	O2 ($4i$): 0.7577, 0, 0.9254	
	β = 91.50	O2 ($8j$): 0.9543, 0.7551, 0.3006	

[a] Experimental value from Ref. [9].

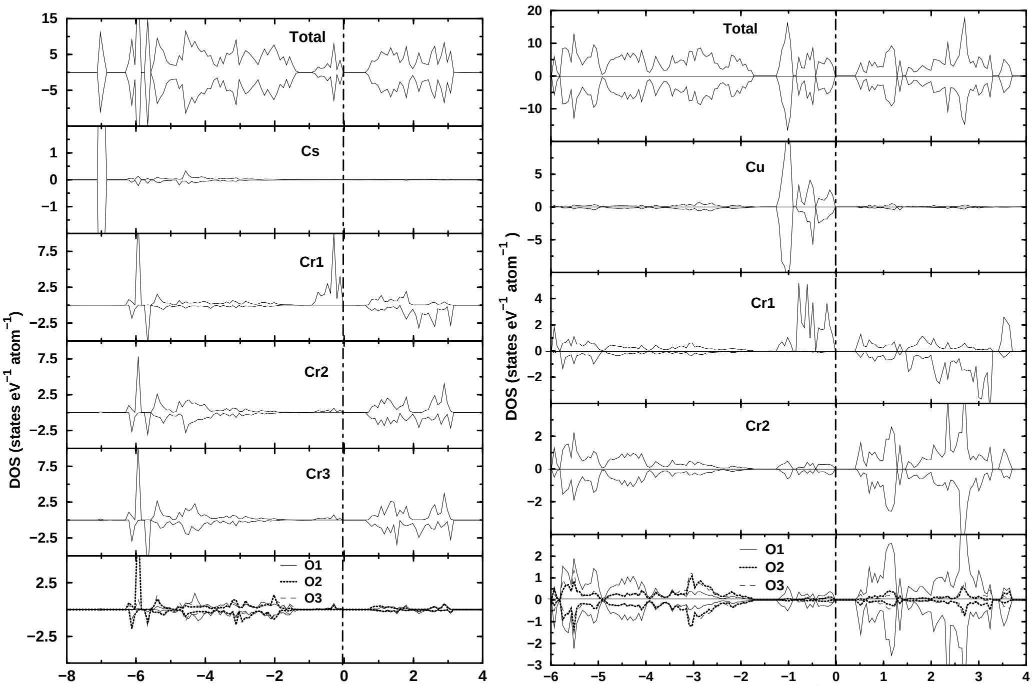

(a) (b)

FIG. 4: Total and site-projected density of states for $\mathrm{CsCr_3O_8}$ (prototype) and $\mathrm{CuCr_3O_8}$ ($\mathrm{KCr_3O_8}$ type). The Fermi level (E_F) is indicated by vertical dashed line.

TABLE II: Calculated magnetic moment (in μ_B per Cr atom) for ACr$_3$O$_8$ in F and AF states. Total refers to the total magnetic moment per formula unit. Band gap (E_g) is given in units of eV.

	F			AF		E_g
Compound	Cr1	Cr2	Total	Cr1	Cr2	
CsCr$_3$O$_8$[a]	2.488	0.231	2.866	2.481	0.233	0.61
CuCr$_3$O$_8$	2.608	0.231	2.888	2.533	0.018	0.41
AgCr$_3$O$_8$	2.518	0.249	2.879	2.476	0.000	0.58
AuCr$_3$O$_8$	2.422	0.226	2.854	2.476	0.011	0.45
InCr$_3$O$_8$	2.750	1.063	4.776	2.579	0.673	psuedogap
TlCr$_3$O$_8$	2.495	0.212	2.868	2.422	0.016	0.53

[a] Moment at Cr3 is 0.208 and 0.212 in F and AF states, respectively.

Cr2 is 0.8 eV. It is the latter distinct exchange splitting which is responsible for the sizeable magnetic moment at the Cr2 site. Hence, provided InCr$_3$O$_8$ can be obtained its properties appear to deserve a closer attention.

Fig. 4 shows the total and site-projected DOS profiles for CsCr$_3$O$_8$ together with CuCr$_3$O$_8$ as representative for the ACr$_3$O$_8$ compounds with KCr$_3$O$_8$-type structure. The well-localized states around -7 eV in Fig. 4(a) originate from Cs p orbitals. Cr d and O p states are present from -6 eV up to E_F. It is interesting to note that all the Cr atoms have well-defined sharp peaks in DOS around -6 eV and that the O atoms also have similar features in the same energy region. This implies covalent hybridization interaction between them. The states closer to E_F (from -0.9 eV to E_F) in Cr1 originate from unpaired electrons in $t_{2\mathrm{g}}$-like orbitals which are responsible for the substantial magnetic moment. On the other hand, the majority- and minority-spin channels of Cr2 and Cr3 are more or less equally filled, resulting in the small magnetic moments.

According to our calculations CuCr$_3$O$_8$ should be a semiconductor with a 0.41 eV band gap. The prominent states for Cu close to E_F is associated with completely filled d states. The almost empty s and p bands indicate that Cu has donated its valence electron to the oxygen atoms. The two types of Cr atoms have topologically different DOS profiles. The overall features are similar to the findings for the alkali-metal members of the ACr$_3$O$_8$ [2, 3] family. Cr1 has sharp peaks close to E_F (from -1.5 to E_F) with more states in the majority-spin channel than in the minority-spin channel. On the other hand, both the majority- and minority-spin channels of Cr2 for CuCr$_3$O$_8$ are almost equally filled, resulting in negligible exchange splitting and hence in a negligible magnetic moment. From this observation we conclude that small magnetic moment at the Cr2 site is not due to small amount of electrons at the Cr2 state (6+ valence state has been expected by experimentalists). Moreover, the states at the Cr2 site are more localized than those at the Cr1 site [see the -6 to -2 eV range in Fig. 4(b)]. If Cr2 had been in the Cr^{6+} (d^0) state, its d band should have been empty. However, the appreciable DOS seen in the VB of Cr2 demonstrates that the valence state of Cr2 is certainly not Cr^{6+} as expected experimentally. Similar to the findings for the other ACr$_3$O$_8$ compounds with KCr$_3$O$_8$-type structure, the O atoms exhibit somewhat different DOS profiles, even though they are energetically degenerate with themselves and with the Cr atoms. The result is distinct covalent hybridization.

D. Bonding characteristics

In spite of the fact that the CsCr$_3$O$_8$ structure possesses 48 atoms in the unit cell which certainly obscures the clarity of the picture, we have attempted to elucidate its bonding characteristics using charge-density and ELF plots. (see Refs. [2–4, 14, 15] for background information and utilization of these tools for other members of the ACr$_3$O$_8$ family). It is seen from Fig. 5(a) that the covalent interaction between Cr2 and O is stronger than that between Cr1 and O. The ionic nature of Cs at the inter-layer position is clearly evident from the more or less spherically distributed charge around Cs. The ELF is negligible at the Cr sites whereas it attains local maximum values at the O sites; another manifestation of covalent interaction. The bonding situation in CsCr$_3$O$_8$ is similar to that seen for other members of ACr$_3$O$_8$ family in the sense that chromium and oxygen atoms form iono-covalent-bonded subunits whereas Cs has distinct ionic character. This may be one of the reasons for characteristic magnetic features observed in these compounds.

IV. CONCLUSION

The prediction of ground-state crystal structures for the ACr$_3$O$_8$ series have been extended to A = In, Tl, Cu, Ag, and Au considering several potential structure types. The calculated ground-state structure for CsCr$_3$O$_8$ (space group $Pnma$) is found to be in good agreement with experimental data. Except NaCr$_3$O$_8$ all members of the ACr$_3$O$_8$ family exhibit antiferromagnetic ordering as the ground-state configurations and the electronic structures show that all compounds (except InCr$_3$O$_8$) are insulators at 0 K; a pseudogap-like feature is established for InCr$_3$O$_8$. Different magnetic moments and DOS profiles for the Cr atoms clearly confirm mixed-valence situations. Bonding analysis undertaken using density-of-states, charge-density and electron-localization plots indicate ionic behavior for the A atoms whereas the Cr and O atoms mutually experience largely covalent interaction, however, with different degree of covalence for Cr1 and Cr2.

V. ACKNOWLEDGEMENT

The authors are grateful to the Research Council of Norway for financial support and computer time at the

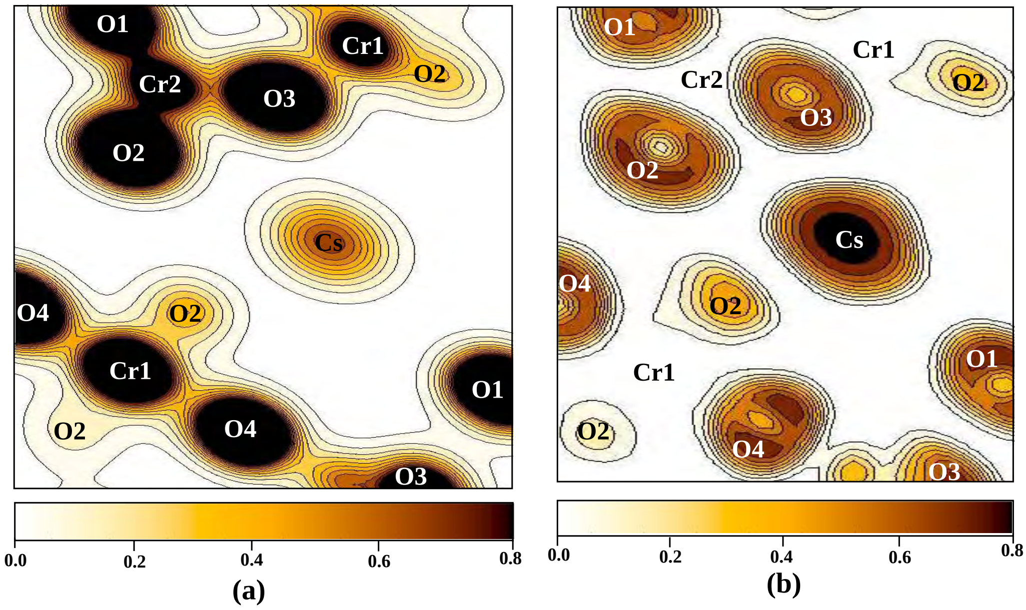

FIG. 5: (Color online) Calculated (a) charge density and (b) electron-localization function for $CsCr_3O_8$.

Norwegian supercomputer facilities.

---

[*] Electronic address: **vidya.ravindran@kjemi.uio.no**

[1] C.N.R. Rao and A.K. Raychauduri in *Colossal Magnetoresistance, Charge Ordering and Related Properties of Manganese Oxides*, edited by C.N.R. Rao and B. Raveau (World Scientific, Singapore, 1998), p. 1.

[2] R. Vidya, P. Ravindran, P. Vajeeston, H. Fjellvåg, and A. Kjekshus, Phys. Rev. B **72**, 014411 (2005).

[3] R. Vidya, P. Ravindran, A. Kjekshus, and H. Fjellvåg, Phys. Rev. B (accepted).

[4] R. Vidya, P. Ravindran, A. Kjekshus, and H. Fjellvåg, J. Electroceramics (submitted).

[5] P. E. Bløchl, Phys. Rev. B **50**, 17953 (1994); G. Kresse and D. Joubert, *ibid.* **59**, 1758 (1999).

[6] G. Kresse and J. Furthmuller, Comput. Mater. Sci. **6**, 15 (1996).

[7] J. P. Perdew, K. Burke, and Y. Wang, Phys. Rev. B **54**, 16533 (1996); J. P. Perdew, K. Burke, and M. Ernzerhof, Phys. Rev. Lett. **77**, 3865 (1996).

[8] P. Vinet, J.H. Rose, J. Ferrante, and J.R. Smith, J. Phys.: Condens. Matter **1**, 1941 (1989).

[9] K.-A. Wilhelmi, Arkiv Kemi **26**, 141 (1966); Chem. Commun. 437 (1966); Doctoral Thesis, University of Stockholm, (Stockholm, 1966).

[10] U. Häussermann, H. Blomqvist, and D. Noréus, Inorg. Chem. **41**, 3684 (2002).

[11] M. J. Saavedra, C. Parada, and E. J. Baran, J. Phys. Chem. Solids **57**, 1929 (1996).

[12] H. Fjellvåg, Unpublished results.

[13] Inorganic Crystal Structure Database, Version 2004.2.

[14] P. Ravindran, P. Vajeeston, R. Vidya, A. Kjekshus, and H. Fjellvåg, Phys. Rev. Lett. **89**, 106403 (2002).

[15] A. Savin, R. Nesper, S. Wengert, and T. Fässler, Angew. Chem. Int. Ed. Engl. **36**, 1809 (1997).

IX

Accepted in J. Electrochem. Soc.

First-principles density-functional calculations on HCr_3O_8: An exercise to better understand the ACr_3O_8 (A = alkali metal) family

R. Vidya*, P. Ravindran, A. Kjekshus and H. Fjellvåg
Department of Chemistry, University of Oslo, Box 1033 Blindern, N-0315 Oslo, Norway

Accurate *ab initio* density-functional calculations are performed to understand structural stability, electronic structure, and magnetic properties of the ACr_3O_8 (A = H, Li, Na, K, Rb, Cs) series. The ground-state structures for the compounds with A = Li−Rb take the same KCr_3O_8-type atomic arrangement (space group $C2/m$) whereas $CsCr_3O_8$ adopts a modified atomic architecture (prototype; space group $Pnma$), in agreement with available experimental findings. The hypothetical compound HCr_3O_8 is found to stabilize in an LiV_3O_8-type structure (space group $P2_1/m$), with an unexpectedly large equilibrium volume. The electronic structures of these compounds are analyzed using density-of-states, charge-density, and electron-localization-function plots, and all are found to exhibit semiconducting (insulating at 0 K) properties with very narrow band gaps. The Cr atoms occur in two different valence states and all compounds (except $NaCr_3O_8$) are found to exhibit antiferromagnetic ordering of the magnetic moments at 0 K.

Keywords: Density-functional calculations, Mixed valence, Semiconductivity, Magnetic properties

Introduction

Owing to exotic phenomena like colossal magnetoresistance (CMR) and spin, charge, and orbital ordering [1], oxides comprising transition-metal atoms in mixed-valence states attract much attention. Mixed-valence compounds with Mn, Co, and Cu are widely studied, whereas compounds with, say, Cr and Ni are less explored. In an effort to understand better the mixed-valence Cr compounds, we have studied structural stability, electronic structure, and magnetic properties within the series ACr_3O_8 (A = H, Li, Na, K, Rb, and Cs) where Cr formally exists in two different valence states. The study has been undertaken using accurate density-functional-theory (DFT) calculations. In an earlier contribution [2] we have reported on electronic, magnetic, and bonding characteristics of ACr_3O_8 with A = Na, K, and Rb and more recently [3] we have explored the ground-state structures of Cr_3O_8 and $LiCr_3O_8$ which are of considerable interest in relation to cathode material for rechargeable Li-ion batteries. In the present work we consider overall trends in structural behavior, electronic structure, and magnetic properties for these compounds, with some special attention on the highly hypothetical HCr_3O_8.

Computational details

The results presented here are based on DFT calculations according to the projected-augmented plane-wave (PAW) [4] method as implemented in the VASP (Vienna *ab initio* simulation package) [5]. In this approach the valence orbitals are expanded as plane waves and the interactions between the core and valence electrons are described by pseudopotentials. In order to determine the ground-state structures for the ACr_3O_8 compounds, we have performed structural optimizations. We considered the experimentally established structures as the first choice for guess structures where such information is available. To broaden the structural platform for the series, and for compounds without explicit experimental structure data in particular, a considerable number of seemingly relevant structural arrangements were considered as test structures. The optimization of the atomic geometry is performed via a conjugate-gradient minimization of the total energy, using Hellmann−Feynman forces on the atoms and stresses in the unit cell. During the simulations, atomic coordinates and axial ratios are allowed to relax for different volumes of the unit cell. These parameters are changed iteratively so that the total energy converges to a minimum value. Convergence minimum is assumed to have been attained when the energy difference between two successive iterations is less than 10^{-7} eV per cell and the forces acting on the atoms are less than 1 meV Å^{-1}. The structure with the lowest total energy is taken as the ground-state structure. The generalized-gradient approximation (GGA) [6] is used to obtain the accurate exchange and correlation energy for a particular atomic configuration. The calculations are carried out using 64 **k** points in the irreducible Brillouin zone. We have used same energy cutoff and **k**-point density in all calculations. All calculations are performed for paramagnetic (P), ferromagnetic (F), and antiferromagnetic (AF) configurations.

Results and discussion

Structural optimization

For $LiCr_3O_8$, a relatively old single-crystal x-ray diffraction study [7, 8] concluded with an orthorhombic (space group $Cmcm$) structure with random distribution of Li and one third of the Cr atoms over one and the same crystallographic site. In order to partially mimic such a disorder computationally, we constructed a supercell with an ordered arrangement of the Li and Cr atoms concerned. The complete random distribution of these Li and Cr atoms had to be abolished because our programs do not allow random distribution of different atoms at one site. Hence our optimizations had to end with a more regular arrangement of Li and Cr atoms than postulated by Wilhelmi [7] (the energy gain between the input and resulting relaxed structure exceeding 1.3 eV f.u.$^{-1}$). The resulting structure [designated $LiCr_3O_8$-II; the same space group ($C2/m$) as for $LiCr_3O_8$-I, but a somewhat different atomic arrangement] has the lowest energy compared to other structure types considered [3]. The $LiCr_3O_8$-I atomic arrangement, which is isostructural with that of succeeding members of the ACr_3O_8 series is, in fact, found to be slightly higher in energy than $LiCr_3O_8$-II. The ACr_3O_8 compounds with A = Na, K, and Rb are found to stabilize in the experimentally determined [9] KCr_3O_8-type structure [space group $C2/m$; $A(Cr1)(Cr2)_2O_8$] which comprises two types of Cr atoms arranged in fairly regular octahedral and tetrahedral environments of O neighbors. There are three crystallographically different O atoms. The octahedra and tetrahedra are arranged in layers parallel to the a,b plane by corner sharing. The layers are held together by alkali-metal ions.

According to our calculations, $CsCr_3O_8$ is found to stabilize in the prototype structure with $Pnma$ symmetry in agreement with the experimental findings [10]. The atomic arrangement is similar to the KCr_3O_8-type forerunners in the ACr_3O_8 series with layers of CrO_6 octahedra and CrO_4 tetrahedra joined at corners. However, the orientation of half of the tetrahedra is different, and every second layer is rotated 180° compared with the layers in the KCr_3O_8-type structure.

The ACr_3O_8 structures exhibit a significant difference between the Cr$-$O distances in the CrO_6 octahedra and CrO_4 tetrahedra which immediately points at a mixed-valence situation for the Cr atoms, conventionally interpreted as the ionic valence states Cr^{3+} and Cr^{6+}, respectively. Rigid-band considerations and preliminary electronic structure studies on ACr_3O_8 (A = Li$-$Cs) suggest insulating behavior for all members. In order to further elucidate the rigid-band deductions we also included the highly hypothetical compound HCr_3O_8 in the considerations.

Among the twelve different structural arrangements considered in the structural optimization for HCr_3O_8, the KCr_3O_8, $LiCr_3O_8$-II, and LiV_3O_8 ($P2_1/m$) types came out with the lower total energies. Among the tested alternatives, inputs according to the types $NaNb_3O_8$ ($Ibam$) and $LiTa_3O_8$ ($Pmma$) came out with the highest total energies; these and variants which fall in the intermediate energy range are not included in Fig. 2. The illustration shows that the LiV_3O_8-type structure has the lowest total energy (~1.62 eV f.u.$^{-1}$ lower than the KCr_3O_8-type variant), however, with a much larger equilibrium volume (191.91 vs 133.68 Å^3 f.u.$^{-1}$). Possible reasons for such an unexpected large cell volume will be discussed later. Although an HI_3O_8-type arrangement could have been a more likely structural arrangement for HCr_3O_8 from a chemical point of view, our calculations show that this variant comes out with about 6.42 eV higher total energy than the LiV_3O_8-type structure.

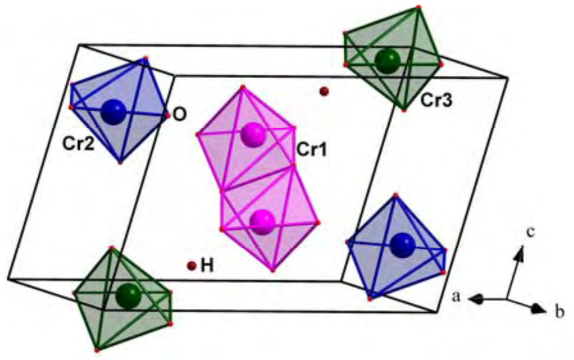

FIG. 1: (Color online) The optimized crystal structure of HCr_3O_8 in LiV_3O_8-type atomic arrangment. Crystallographically different Cr atoms are labeled on the illustration.

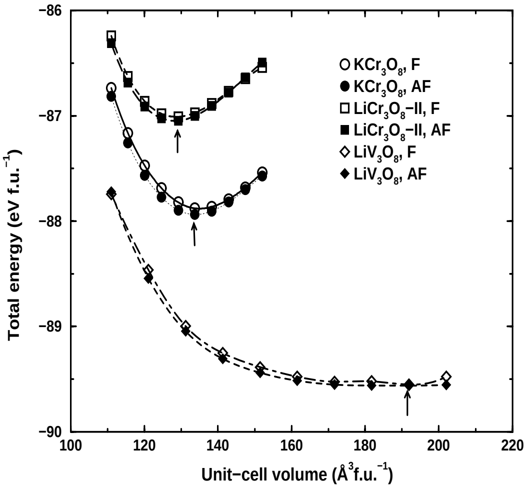

FIG. 2: Calculated cell volume vs total energy for HCr_3O_8. Structure type inputs are specified in the illustration. Arrow points at total energy minimum.

Optimized structural parameters for HCr_3O_8 are given in Table. 1. The structure comprises three types of Cr atoms and eight types of O atoms. The three types of Cr atoms exhibit different Cr$-$O interatomic distances in configurations which are of the trigonal bipyramidal form. The polyhedra around Cr1 share edges whereas those around Cr2 and Cr3 share corners along the a direction. These polyhedra form Cr$-$O molecular-like units with H in intermediate positions.

The calculated equilibrium volume for ACr_3O_8 (A=Li$-$Cs) increases roughly linearly with the radius of A. The equilibrium structural parameters vary some 2$-$4% from the available experimental values, in the range of accuracy of the GGA (which overestimate volume by around 3 % [11]). The calculated equilibrium volumes for the alkali-metal members of the ACr_3O_8 se-

TABLE I: Optimized ground-state structure parameters for HCr_3O_8 in LiV_3O_8-type structure space group $P2_1/m$; all atoms are in position $2e$ where $y = 1/4$.

Unit cell	Atom	x	z
$a = 13.8287$ Å	H	0.3022	0.8413
$b = 3.8235$ Å	Cr1	0.4741	0.6529
$c = 6.9332$ Å	Cr2	0.9148	0.7468
$\beta = 100.37^o$	Cr3	0.1398	0.9714
$V = 191.91$ Å^3	O1	0.5168	0.4120
	O2	0.0951	0.2021
	O3	0.3591	0.6840
	O4	0.8486	0.5341
	O5	0.5492	0.8566
	O6	0.0458	0.7660
	O7	0.2612	0.9551
	O8	0.8665	0.9760

TABLE II: Calculated magnetic moment (in μ_B per Cr atom) for ACr_3O_8 compounds in F and AF states. Total refers to the total magnetic moment per formula unit.

	F			AF	
Compound	Cr1	Cr2	Total	Cr1	Cr2
HCr_3O_8[a]	0.390	1.394	2.878	0.348	1.448
HCr_3O_8[b]	2.566	0.207	2.857	2.507	0.004
$LiCr_3O_8$	2.600	0.222	2.886	2.578	0.032
$NaCr_3O_8$	2.451	0.241	2.868	2.391	0.013
KCr_3O_8	2.449	0.228	2.859	2.330	0.016
$RbCr_3O_8$	2.453	0.224	2.857	2.336	0.003
$CsCr_3O_8$	2.478	0.238	2.867	2.479	0.237

[a] LiV_3O_8-type structure; Cr3 moment 1.521 and 1.282 μ_B in F and AF states, respectively.

[b] KCr_3O_8-type structure.

ries are even in this perspective too large compared with the experimental volumes. This may originate from the somewhat open and layered nature of the structural arrangements where interlayer interactions are more governed by van der Waals forces which are unfortunately not accounted properly in DFT calculations of today.

The equilibrium volumes for HCr_3O_8 in the $LiCr_3O_8$-II- and KCr_3O_8-type structural arrangements fit reasonably well into the approximate linear relation between ionic radius and cell volume for the ACr_3O_8 compounds with alkali-metal cations (Fig. 3). However, the total energy for these variants is much higher than that for the ground-state LiV_3O_8-type structure (see Fig. 2). On the other hand, the cell volume for the ground-state atomic arrangement is so high that it is not really comparable with the findings for the other compounds at all. A likely inference of these findings is that a compound like HCr_3O_8 would be so acidic that it should not possible to stabilize it as a salt-like structure. Another fact which must be taken into account is that the structure prescribed for our hypothetical HCr_3O_8 (Fig. 1) consists of molecular-like Cr-to-O strongly covalent-bonded subunits. Hence, when the hydrogen and their chromium-oxygen counterparts atoms are allowed to relax, they may arrange themselves relatively freely in an "abundance" of space. It should also be mentioned that experimental studies [12] on Li intercalation in Cr_3O_8 have shown that when the concentration of Li is increased, the intercalated "$LiCr_3O_8$" framework gradually becomes amorphous. The unexpected large equilibrium volume observed for HCr_3O_8 with LiV_3O_8-type structure may be an omen indicating that "such a compound" really prefers the amorphous state.

Magnetic properties

The structural optimizations performed for P, F, and AF configurations show that all compounds stabilize in the AF state, except $NaCr_3O_8$. The calculated AF ground state for KCr_3O_8 is in agreement with the magnetic susceptibility data [13, 14] which shows AF ordering below a Néel temperature of 125 ± 4 K. Magnetic property data are not available for the other compounds.

The magnetic moment values listed for HCr_3O_8 in Table 2 refer both to the LiV_3O_8-type ground-state structure and the excited-state KCr_3O_8-type arrangement, the latter to facilitate comparison with the ACr_3O_8 compounds of the alkali metals. Owing to Cr-d and O-p hybridization, the oxygen atoms also possess small magnetic moments, resulting in somewhat higher total moments than the sum of the Cr moments in the F case. The different magnetic moments immediately support different valence states for the Cr atoms in these compounds, and at first sight the findings appear to confirm the formal electron counting picture that Cr1 corresponds to Cr^{3+} (d^3) and Cr2 to Cr^{6+} (d^0). However, a closer investigation of the bonding situation reveals that the assignment of formal valence states to Cr in these compounds is non-trivial.

Electronic structure

The compounds under consideration are all semiconductors (insulators at 0 K) with very small band gaps (E_g ranging from 0.12 to 0.63 eV). The hypothetical HCr_3O_8 would exhibit the smallest $E_g = 0.12$ eV, in agreement with rigid-band considerations. As the band structure of these compounds exhibit similar features we only display the total and site-projected DOS profiles for the ground-state structures of $RbCr_3O_8$ and HCr_3O_8 (Fig. 4). Fig. 4(a) shows that $RbCr_3O_8$ is a semiconductor with $E_g = 0.33$ eV. In common with A for the other ACr_3O_8 compounds, the Rb states are almost empty (visible only after appreciable multiplication) emphasizing pronounced ionic character. Cr and O states are energetically degenerate indicating considerable covalent interaction between them.

The different valence states of Cr are also evident from the differences in their DOS curves. The majority-spin channel for Cr1 (Cr2 and Cr3 for HCr_3O_8) has more occupied states than the corresponding minority-spin channel demonstrating larger exchange splitting and

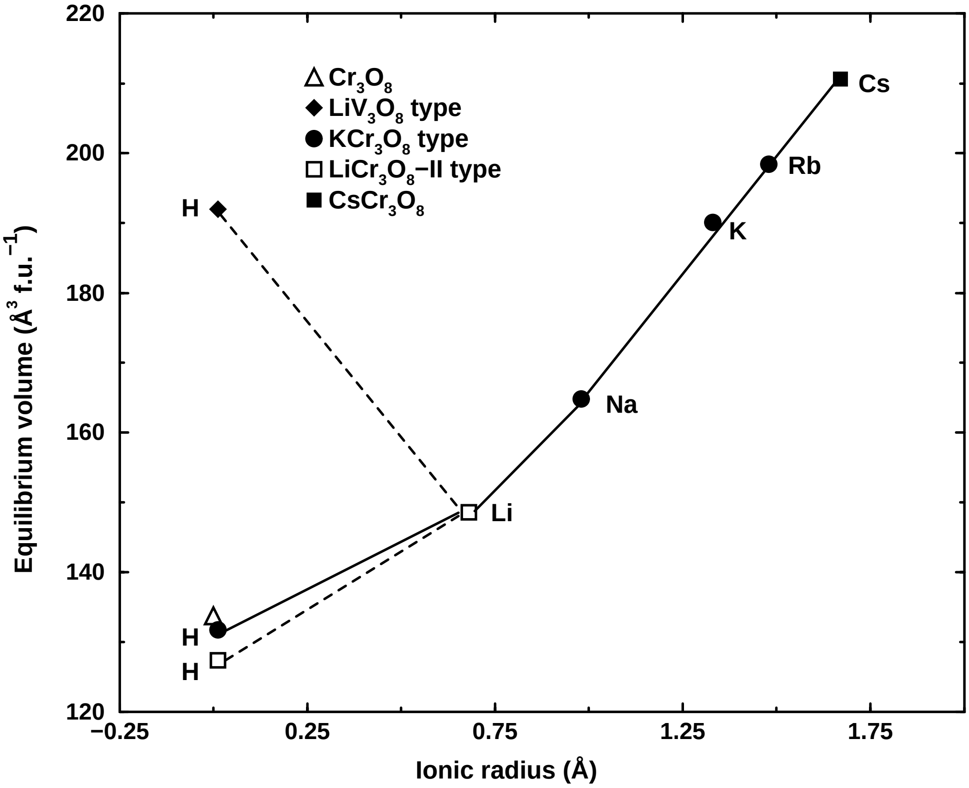

FIG. 3: Equilibrium volume for the ACr$_3$O$_8$ series as a function of ionic radius (standard values). The data for HCr$_3$O$_8$ expose volumes for LiV$_3$O$_8$-, KCr$_3$O$_8$-, and LiCr$_3$O$_8$-II-type structural arrangements (see Fig.2).

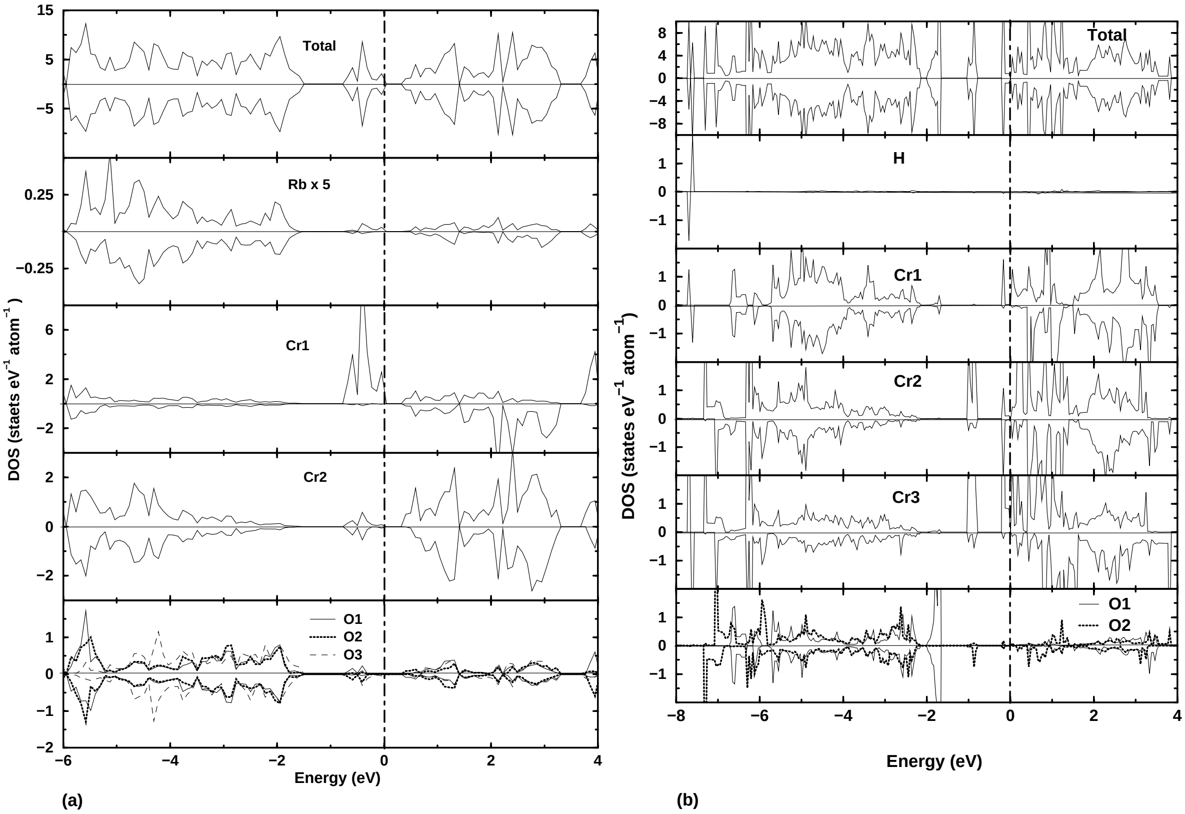

(a)

(b)

FIG. 4: Total and site-projected density of states for (a) RbCr$_3$O$_8$ in KCr$_3$O$_8$-type and (b) HCr$_3$O$_8$ in LiV$_3$O$_8$-type structures; both in AF state. The Fermi level is indicated by vertical dashed line.

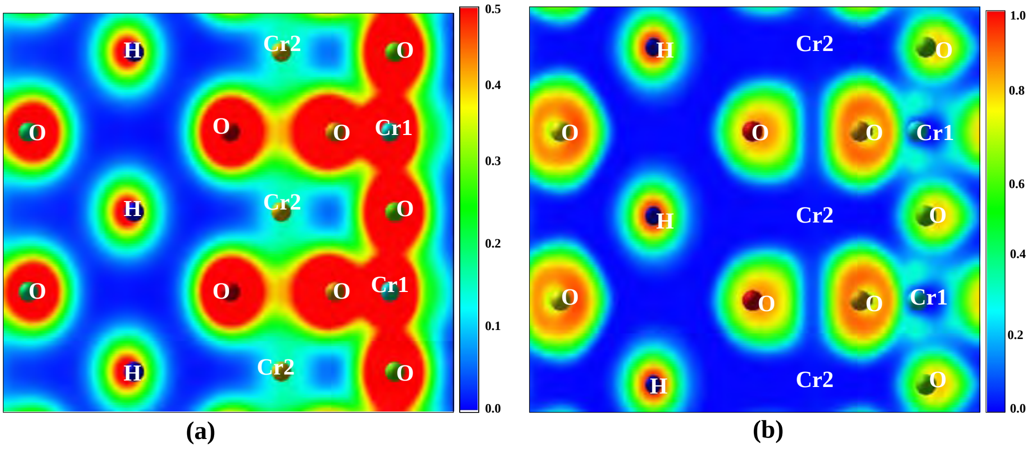

FIG. 5: Calculated (a) charge-density and (b) electron-localization-function plots for the ground-state structure of HCr_3O_8.

hence a sizeable magnetic moment(s). Moreover, if Cr2 (Cr1 for HCr_3O_8) really had been in the Cr^{6+} (d^0) state it should have exhibited an empty d band. Instead, it shows a considerable number of well-localized states with more or less equal occupancy in both spin channels. Hence for Cr2 (Cr1 for HCr_3O_8) it can be inferred that its almost zero magnetic moment is not due to a genuine Cr^{6+} (d^0) state, but results from negligible exchange splitting. All crystallographically different O atoms have states in the same energy region, but they display significant topological differences in the DOS curves.

Bonding in HCr_3O_8

In order to gain understanding of the unusually large equilibrium volume for the ground-state structure of HCr_3O_8, we display charge-density (distribution of charges in real space) and electron-localization-function (ELF; see Refs. [15, 16]) plots in Fig. 5. A distinct charge density at the H site indicates that it retains some localized electronic charge which does not participate in bonding interaction with the other constituents of HCr_3O_8. On the other hand, large charges seen between Cr1 and the surrounding O atoms as well as a substantial ELF at O directed toward Cr1 imply strong covalent interaction. The large value and spherical shape of the ELF at H, lead one to believe that H remains more or less aloof as $H^{\delta+}$ ($\delta < 1$) in the structure whereas the chromium and oxygen atoms form distinct, largely covalent-bonded subunits in a somewhat open structure. The result appears to provide a reasonable explanation of the unexpected much larger volume for LiV_3O_8-type ground-state structure than for the KCr_3O_8- and Li_3O_8-II-type variants of HCr_3O_8.

Conclusions

From accurate first-principles density-functional calculations, it is found that the hypothetical HCr_3O_8 compound stabilizes in an LiV_3O_8-type atomic arrangement, ACr_3O_8 with A = Li–Rb in KCr_3O_8-type frameworks, and $CsCr_3O_8$ in an orthorhombic (prototype) structure. The theoretically calculated ground-state structures for $NaCr_3O_8$, KCr_3O_8, $RbCr_3O_8$, and $CsCr_3O_8$ are in good agreement with available experimental results. The Cr atoms in all these compounds occur in two different valence states, one kind having large and the other small or negligible exchange splittings. All these compounds are found to be semiconductors with very small band gaps. The somewhat aloof nature of H in the ground-state structure of HCr_3O_8 and the formation of Cr-to-O covalent-bonded subunits arise as possible explanations for the large equilibrium volume.

From our calculation exercise on the hypothetical HCr_3O_8 compound we have learnt the following: Although "H^+" is believed to be considerably smaller than the alkali-metal ions, the volume of the ground-state structure of HCr_3O_8 suggests that "H^+" under equilibrium condition takes up an effective size comparable with that of K^+. However, in the excited-state KCr_3O_8- and $LiCr_3O_8$-II-type structures the volume of "H^+" appears to be comparable with that of the vacancy in Cr_3O_8 with a K-stripped-off KCr_3O_8-type structure. This stresses the significance of the structural arrangement in this kind of considerations. The LiV_3O_8-type ground-state structure of HCr_3O_8 comprises distinct Cr-to-O largely covalent-bonded subunits with "H^+" at somewhat aloof locations in the lattice whereas the KCr_3O_8-type structure exhibits characteristic chromium-oxygen layers with alkali-metal ions in between. This distinction also manifests itself in the charge distribution. The hydrogen atoms retains some electronic charge in HCr_3O_8 whereas the valence electrons of the alkali-metal constituents in ACr_3O_8 are scarcely visible in DOS and charge-density plots, emphasizing a more significant ionic contribution from the alkali-metal representatives to the compound formation. The findings for HCr_3O_8 show that the magnetic features of the ACr_3O_8 series originate largely from the Cr_3O_8 subunits and that the A constituents have negligible impact on the magnetic properties. It is interesting to note that it is just A = H and Cs (viz. " the small and large cations") which do not manage to keep the KCr_3O_8-type structure.

Acknowledgement

The authors are grateful to the Research Council of Norway for financial support and computer time at the Norwegian supercomputer facilities.

---

[*] Electronic address: **vidya.ravindran@kjemi.uio.no**

[1] C.N.R. Rao and A.K. Raychauduri in *Colossal Magnetoresistance, Charge Ordering, and Related Properties of Manganese Oxides*, edited by C.N.R. Rao and B. Raveau (World Scientific, Singapore, 1998).

[2] R. Vidya, P. Ravindran, P. Vajeeston, H. Fjellvåg, and A. Kjekshus, Phys. Rev. B **72**, 014411 (2005).

[3] R. Vidya, P. Ravindran, A. Kjekshus, and H. Fjellvåg, Phys. Rev. B (accepted).

[4] P.E. Blöchl, Phys. Rev. B **50**, 17953 (1994); G. Kresse and D. Joubert, *ibid.* **59**, 1758 (1999).

[5] G. Kresse and J. Furthmuller, Comput. Mater. Sci. **6**, 15 (1996).

[6] J.P. Perdew, K. Burke, and Y. Wang, Phys. Rev. B **54**, 16533 (1996); J.P. Perdew, K. Burke, and M. Ernzerhof, Phys. Rev. Lett. **77**, 3865 (1996).

[7] K.-A. Wilhelmi, Arkiv Kemi **6**, 131 (1967); Chem. Commun. 437 (1966).

[8] K.-A. Wilhelmi, Doctoral Thesis, University of Stockholm (Stockholm, 1966); Acta Chem. Scand. **22**, 2565 (1968).

[9] M.J. Saavedra, C. Parada, and E.J. Baran, J. Phys. Chem. Solids **57**, 1929 (1996).

[10] K.-A. Wilhelmi, Acta Chem. Scand. **12**, 1065 (1958).

[11] U. Häussermann, H. Blomqvist, and D. Noréus, Inorg. Chem. **41**, 3684 (2002).

[12] Y. Takeda, R. Kanno, T. Tsuji, and O. Yamamoto, J. Electrochem. Soc. **131**, 2006 (1984).

[13] W. Klemm, Z. Anorg. Allg. Chem. **301**, 323 (1959).

[14] H. Fjellvåg, Unpublished results.

[15] P. Ravindran, P. Vajeeston, R. Vidya, A. Kjekshus, and H. Fjellvåg, Phys. Rev. Lett. **89**, 106403 (2002).

[16] A. Savin, R. Nesper, S. Wengert, and T. Fässler, Angew. Chem. Int. Ed. Engl. **36**, 1809 (1997).

X

Tailor-Made Electronic and Magnetic Properties in One-Dimensional Pure and Y-Substituted $Ca_3Co_2O_6$

R. Vidya,* P. Ravindran, H. Fjellvåg, and A. Kjekshus
Department of Chemistry, University of Oslo, Box 1033 Blindern, N-0315 Oslo, Norway

O. Eriksson
Department of Physics, Uppsala University, Box 530, 75121 Uppsala, Sweden

(Received 12 March 2003; published 30 October 2003)

Full-potential density-functional calculations show that the electronic structure of one-dimensional ferrimagnetic $Ca_3Co_2O_6$ varies from metal to half metal to insulator as its magnetic ordering changes from the ferrimagnetic through the ferromagnetic to the paramagnetic state. The present Letter is the first to establish the occurrence of half metallicity in one-dimensional oxides. Moreover, the electronic and magnetic properties of this material can be tuned by substitution of Y for Ca, as shown by our detailed study on $Ca_{3-x}Y_xCo_2O_6$ ($x = 0$, 0.3, 0.75, and 1). The Co ions are in two different valence states [Co^{4+} (low-spin) and Co^{2+} (high-spin)], and hence the occurrence of charge ordering in addition to spin ordering is established. For specific Y concentrations we predict a rarely seen combination of ferromagnetic and insulating behavior.

DOI: 10.1103/PhysRevLett.91.186404 PACS numbers: 71.20.Ps, 75.50.Ee, 78.20.Ci

Inorganic structures with one-dimensional (1D) atomic arrangements are in the limelight because of their unique electronic and magnetic properties [1]. Investigations into the nature of the magnetism in these materials have proved particularly rewarding because of the combination of highly anisotropic structures and phenomena such as ferromagnetism (F), antiferromagnetism (AF), and more complex magnetic behavior [2]. Low-dimensional materials are currently in the focus because of their technological significance. For example, magnetoresistance effects have been evidenced in layered Bi-based cobaltites [3,4] and a high figure of merit for the conversion of thermoelectric energy is found [5] in the two-dimensional $Ca_3Co_4O_9$.

A large number of oxides have been synthesized with 1D structures [6]. However, most of their physical properties and the theoretical interpretations about them remain largely unexplored because of their complex crystal and magnetic structures. The present exploration based on density-functional full-potential calculations is expected to open up new avenues where new materials of fundamental and technological significance can be found. In this Letter we report the first *ab initio* results on electronic structure and magnetic properties of pure and Y-substituted 1D $Ca_3Co_2O_6$. We show that $Ca_3Co_2O_6$ transforms into a half-metallic ferromagnet by application of magnetic fields as well as by substituting Y for Ca. When the concentration of Y increases, the system prefers to be an F insulator.

$Ca_3Co_2O_6$ belongs to the A'_3ABO_6 class ($A' = \mathrm{Ca, Sr}$, $A = \mathrm{Co, Ni, Cu, Zn}$, $B = \mathrm{Co, Ir, Pt}$) with Sr_3NiIrO_6-type structure [7]. The structure consists of parallel Co-O chains separated by Ca^{2+} ions. The chains are built by alternating face-sharing CoO_6 octahedra and trigonal prisms along the hexagonal c axis. The resulting short metal-metal intrachain distance (2.59 Å) [compared to the interchain distance (5.24 Å)] reinforces the 1D character of the structure along the c axis. Each Co chain is surrounded by six chains constituting a hexagonal pattern in the basal plane. $Ca_3Co_2O_6$ behaves as a planar Ising-like Heisenberg AF triangular lattice where each chain acts as if it carries a single localized spin. Magnetic studies show F-type intrachain ordering ($T_{C1} = 24$ K) with AF-interchain coupling ($T_{C2} = 10$ K) [8]. For every two F-aligned Co chains, there is one AF-aligned chain giving a resultant ferrimagnetic (Ferri) structure. A low-temperature neutron-diffraction examination [9] has shown that $Ca_3Co_2O_6$ possesses a long-range Ferri order below 10 K.

The different possible oxidation states of cobalt in cobalt oxides together with its various spin configurations such as low spin (LS), intermediate spin, and high spin (HS) are responsible for various phenomena such as temperature-/hole-doping-induced spin-state transitions in $LaCoO_3$ [10], giant magnetoresistance in $La_{1-x}Sr_xCoO_3$, and insulator-to-metal transition as well as magnetoresistance properties in $Ln\mathrm{BaCo_2O_{5.5}}$ [11]. Although the magnetic properties of $Ca_3Co_2O_6$ have been clarified to some extent [8,9], the exact electronic state of the Co ions remains controversial. Kageyama *et al.* [12] proposed Co^{3+} for both Co1 and Co2 with Co1 being nonmagnetic and Co2 carrying an effective moment of $1\mu_B$. The three models proposed for the Co-spin states by Aasland *et al.* [8] do not completely fit the observed magnetic moments and high-field magnetization data. In this Letter we attempt to settle the

0031-9007/03/91(18)/186404(4)$20.00 © 2003 The American Physical Society

controversy over the valence and spin state of the Co ions in $Ca_3Co_2O_6$.

$Ca_3Co_2O_6$ is described in the space group $R\bar{3}c$ with $a = 9.079$ and $c = 10.381$ Å [7]. For the paramagnetic (P) and F calculations, we have considered the rhombohedral unit cell (consisting of 22 atoms). For the Ferri case we have taken into account a hexagonal supercell (consisting of 66 atoms) as shown in Fig. 1. Structural parameters for $Ca_{3-x}Y_xCo_2O_6$ are taken from low-temperature neutron-diffraction data [13], but for $Ca_2YCo_2O_6$, we obtained the structural parameters [14] by force and stress minimization in the F state using the projected augmented wave implementation of the Vienna *ab initio* simulation package (VASP) [15] as experimental data are hitherto not available. The virtual crystal approximation (VCA) has been applied for calculating the total energies for Y-substituted $Ca_3Co_2O_6$ systems. VCA has been quite successful in explaining magnetic properties of cobaltates [16]; hence its use in the present study seems justified. However, for $Ca_2YCo_2O_6$ we considered an explicit supercell with periodic replacement of Ca by Y.

The full-potential linear muffin-tin orbital (LMTO) calculations [17] presented in this Letter are all electron, and no shape approximation to the charge density or potential has been used. The basis set is comprised of augmented linear muffin-tin orbitals [18]. The spherical-harmonic expansion of the charge density, potential, and basis functions were carried out up to $\ell = 6$. The calculations are based on the generalized-gradient-corrected (GGA) density-functional theory (DFT) as proposed by Perdew *et al.* [19]. The spin-orbit coupling term is included directly in the Hamiltonian matrix elements for the part inside the muffin-tin spheres; hence for spin-polarized cases the size of the secular matrix is doubled. The basis set included Ca $4s$, $4p$, $3d$; Co $4s$, $4p$, $3d$; O $2s$, $2p$, $3d$; and Y $4p$, $4d$, $5s$ states. For the total-energy study the **k**-space integration is done using the special point method with 90 **k** points in the irreducible part of the first Brillouin zone. As the experimental [8] magnetization studies on $Ca_3Co_2O_6$ show that the easy magnetization axis is along c, we have chosen [001] as the magnetization axis for all our spin-polarized calculations. The density of states (DOS) was calculated using the linear tetrahedron technique. Since the effect of strong electron-electron interactions for transition-metal oxides have been discussed in the past, we have also used the LDA + U method (LDA is local-density approximation). The inclusion of the Coulomb correlation effect through the LDA + U method does not improve the results indicating that the usual DFT calculations are sufficient to describe the properties of these materials. Because of space limitation we have not included the results of the LDA + U calculations.

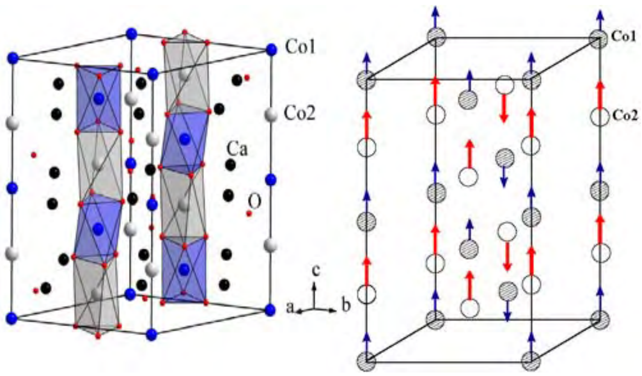

FIG. 1 (color online). Left: crystal structure of one-dimensional $Ca_3Co_2O_6$. Right: schematic representation of ferrimagnetic ordering in hexagonal $Ca_3Co_2O_6$, consisting of 66 atoms per unit cell; only Co ions are shown. (Note that the Ferri arrangement involves two F and one AF aligned chains.)

We list the calculated total energy for undoped and electron-doped samples in Table I. $Ca_3Co_2O_6$ stabilizes in the Ferri state in perfect agreement with experimental findings [8,9]. The F state in which all Co moments are aligned parallel with respect to each other is 114 meV higher in energy than the Ferri state. According to experimental magnetization measurements the magnetic field required for the Ferri-to-F transition is 2.2 T. The exchange splitting increases the band energy (component of total energy) and helps to stabilize the Ferri phase. The gain in band energy is 514 meV/f.u. for the Ferri case compared with the P state. When we include other contributions to the total energy, the Ferri phase is 673 meV/f.u. lower in energy than the P phase. Hence the P phase represents an energetically unfavorable configuration even though it is found to be insulating. From Table I it is clear that when electrons are doped into the system, the F state is stabilized.

A finite DOS (Fig. 2) is present at the Fermi level (E_F) in both spin channels in the Ferri phase implying a metallic character. This finding is consistent with the experimental conductivity study [11]. Our partial DOS analysis shows that the states in the vicinity of E_F are mainly contributed by Co d states. With Ferri ordering these d states are considerably delocalized, so electrons are transferred within and between the chains resulting in metallic behavior.

The second panel of Fig. 2 shows the total DOS of $Ca_3Co_2O_6$ in the F state. A finite DOS is present in the up-spin channel at E_F, whereas an energy gap of 0.09 eV opens up in the down-spin channel, resulting in

TABLE I. Total energy (relative to the lowest energy state in meV/f.u.) in $Ca_{3-x}Y_xCo_2O_6$ for the P, F, and Ferri phases using FLMTO including GGA and spin-orbit coupling.

Composition	P	F	Ferri
$Ca_3Co_2O_6$	673	114	0
$Ca_{2.7}Y_{0.3}Co_2O_6$	693	0	224
$Ca_{2.25}Y_{0.75}Co_2O_6$	1027	0	481
$Ca_2YCo_2O_6$	753	0	352

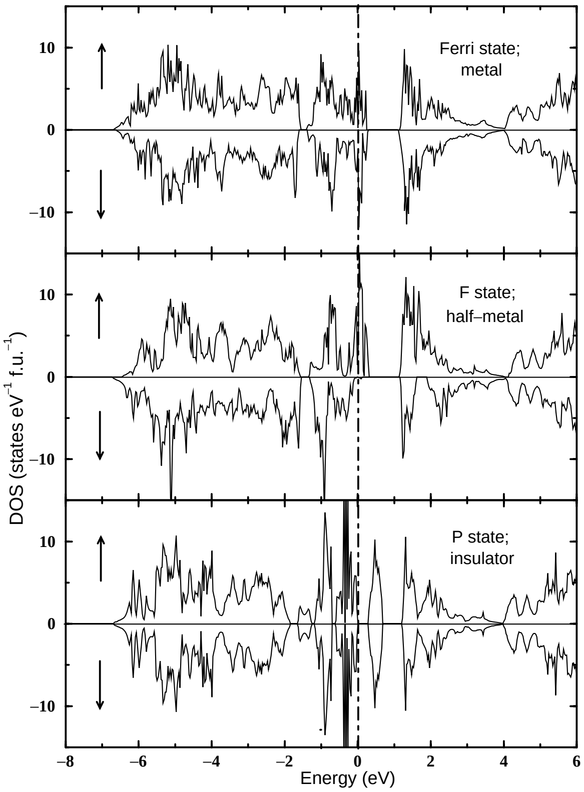

FIG. 2. Total DOS for $Ca_3Co_2O_6$ in the Ferri, F, and P states.

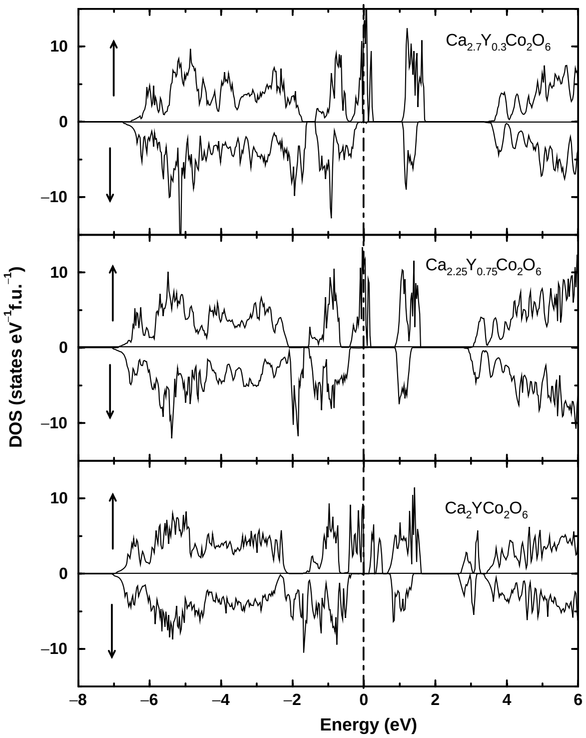

FIG. 3. Total DOS of Y-doped $Ca_3Co_2O_6$ in the F ground state configurations.

half-metallic character. Half-metallic ferromagnetic (HMF) oxides attract much attention due to their potential applications in magnetoelectronic [20] and magneto-optical recording devices. *The present Letter is, to the best of our knowledge, the first to point out the occurrence of HMF behavior in 1D oxides.* The strong covalent bonding between Co and O apart from the exchange splitting contributes to the half-metallic (HM) nature. When the long-range magnetic ordering disappears (viz. in the P state), an energy gap opens up in both spin channels with a magnitude of 0.3 eV resulting in an insulator. The DOS analysis shows that relatively many nonbonding $3d$ electrons from Co exist just below E_F in the P case, reducing its stability over Ferri and F cases.

Table I shows that the Ferri-to-F transition can be achieved by electron doping (substituting Y for Ca) in addition to the application of magnetic field. However, it is to be noted that a spin-glass behavior or noncollinear magnetism has not been considered in our calculations, though triangular lattice formation is often found to induce such complicated magnetic states.

The total DOS of Y-substituted $Ca_3Co_2O_6$ in the F ground state is shown in Fig. 3. $Ca_{2.7}Y_{0.3}Co_2O_6$ and $Ca_{2.25}Y_{0.75}Co_2O_6$ are found to exhibit HM properties with an energy gap in the down-spin channel of 0.156 and 0.375 eV, respectively. If the down-spin channel has not been perturbed by the added electrons, the total magnetic moment is expected to increase. But in contrast, additional states appear around -2 eV in the down-spin channel of Y-substituted $Ca_3Co_2O_6$ (see Fig. 3), and hence the magnetic moments decrease. As the electrons become more localized, the HMF situation occurs. A rigid-band analysis shows that if we replace one Ca atom by one Y per formula unit, an insulating material with F ordering should be realized — a combination of material properties that is rarely encountered. Hence we have performed total-energy calculations for $Ca_2YCo_2O_6$ also in P, F, and Ferri configurations. From Table I it is seen that this material indeed prefers F ordering and from Fig. 3 it is clear that it shows an insulating electronic structure with a band gap of 0.139 eV (0.467 eV according to our LDA + U calculation), consistent with the rigid-band analysis. Efforts are being made to synthesize this phase [13] which may prove to be the first example of an F insulator in this type of 1D oxide.

Let us now turn our attention to the valence and spin states of Co. Different spin configurations for the crystallographically different Co ions are expected [21] as a consequence of the larger crystal field for octahedral Co1 than for trigonal prismatic Co2. The calculated magnetic moments listed in Table II are found to be in very good agreement with available low-temperature neutron-diffraction and magnetization data. By taking into consideration the magnetic moments at the Co sites, the octahedral and trigonal prismatic crystal fields, and the calculated site- and orbital-projected DOS features (not shown), we conclude that Co1 is indeed Co^{4+} in the LS (d^5; $t_{2g}^5e_g^0$) state and Co2 is Co^{2+} in the HS (d^7; $t_{2g}^5e_g^2$) state. The charge density and electron localization

TABLE II. Calculated magnetic moment (in μ_B per Co atom) for $Ca_{3-x}Y_xCo_2O_6$ in the F and Ferri states. Total refers to the total magnetic moment per formula unit.

	F			Ferri			Experimental		
Composition	Co1	Co2	Total	Co1	Co2	Total	Co1	Co2	Total
$Ca_3Co_2O_6$	0.179	2.638	3.639	0.169	2.632	1.209	0.08[a]	3.00[a]	1.3[a]
$Ca_{2.7}Y_{0.3}Co_2O_6$	0.171	2.614	3.521	0.161	2.607	1.172	0.15[b]	2.41[b]	⋯
$Ca_{2.25}Y_{0.75}Co_2O_6$	0.124	2.488	3.216	0.116	2.485	1.070	⋯	⋯	⋯
$Ca_2YCo_2O_6$	0.065	2.407	2.992	0.138	2.369	0.985	⋯	⋯	⋯

[a]Low-temperature neutron-diffraction data, Ref. [8]. [b]Low-temperature neutron-diffraction data, Ref. [13].

function show weak metallic interaction between the Co atoms and strong covalent interaction between Co and O. Because of the latter feature, a finite moment (around $0.1\mu_B$) is found at the O sites. Also, due to this hybridization between Co and O the magnetic moments at Co are smaller than the ideal spin-only values.

In $Ca_2YCo_2O_6$, the additional electron contributed by Y is expected (see the decreasing trend in magnetic moment values in Table II) to go to Co1 and convert this ion into LS, nonmagnetic Co^{3+} ($t_{2g}^6e_g^0$). However, the detailed charge-density analysis shows that the extra electrons mainly go into interstitial regions and are otherwise uniformly distributed on all constituents. It is indeed the strong Co-O bonding interaction which is responsible for the almost vanishing magnetic moment at the Co1 site rather than a valence transition. As equal amounts of Co ions are in two different valence and spin states with localized $3d$ electrons, ladder-type charge and spin ordering must be present in these materials.

In conclusion, for the first time we have shown the occurrence of HMF and insulating F behavior in fairly complex one-dimensional oxides using accurate density-functional full-potential methods. The metallic Ferri state is found to be the ground state for $Ca_3Co_2O_6$ in accordance with experiments. Various proposals have been made for spin states of Co such as (i) Co1:LS Co^{3+}; Co2: HS Co^{3+}, (ii) Co1: LS Co^{4+}; Co2: HS Co^{2+}, and (iii) Co1: LS Co^{2+} and Co^{4+}; Co2: HS Co^{3+}. By analyzing electronic structure with various tools we conclude that Co1 corresponds to LS Co^{4+} and Co2 to HS Co^{2+}. We have shown that tailor-made electronic and magnetic properties can be obtained in 1D oxides by magnetic field or electron doping. We predict a seldom observed combination of material properties, namely, a ferromagnetic insulator. Because of the complexity in the crystal and magnetic structures of the considered phases, more studies may reveal new features.

The authors are indebted to Dr. John Wills for providing the computer program used in this study. The authors are grateful to the Research Council of Norway for financial support and computer time at Norwegian supercomputer facilities. O. E. is grateful to the Swedish Research Council (VR) and the Foundation for Strategic Research (SSF).

*Electronic addresses: vidya.ravindran@kjemi.uio.no
http://folk.uio.no/ravindrv

[1] T. N. Nguyen and H.-C. zur Loye, J. Solid State Chem. **117**, 300 (1995).

[2] M. D. Smith and H.-C. zur Loye, Chem. Mater. **12**, 2404 (2000).

[3] D. Groult, C. Martin, A. Maignan, D. Pelloquin, and B. Raveau, Solid State Commun. **105**, 583 (1998).

[4] T. Yamamoto, I. Isukada, and K. Uchinokura, Jpn. J. Appl. Phys., Part 1 **38**, 1949 (1999).

[5] I. Matsubara, R. Funahashi, T. Takeuchi, S. Sodeoka, T. Shimizu, and K. Ueno, Appl. Phys. Lett. **78**, 3627 (2001).

[6] K. E. Stitzer, J. Darriet, and H.-C. zur Loye, Curr. Opin. Solid State Mater. Sci. **5**, 535 (2001).

[7] H. Fjellvåg, E. Gulbrandsen, S. Aasland, A. Olsen, and B. C. Hauback, J. Solid State Chem. **124**, 190 (1996).

[8] S. Aasland, H. Fjellvåg, and B. Hauback, Solid State Commun. **101**, 187 (1997).

[9] H. Kageyama, K. Yoshimura, K. Kosuge, X. Xu, and S. Kawano, J. Phys. Soc. Jpn. **67**, 357 (1998).

[10] P. Ravindran, H. Fjellvåg, A. Kjekshus, P. Blaha, K. Schwarz, and J. Luitz, J. Appl. Phys. **91**, 291 (2002).

[11] A. Maignan, C. Michel, A. C. Masset, C. Martin, and B. Raveau, Eur. Phys. J. B **15**, 657 (2000).

[12] H. Kageyama, K. Yoshimura, K. Kosuge, M. Azuma, M. Takano, H. Mitamura, and T. Goto, J. Phys. Soc. Jpn. **66**, 3996 (1997).

[13] V. Miksch, H. Fjellvåg, A. Kjekshus, and B. C. Hauback (private communication); H. Fjellvåg, A. Kjekshus, and B. C. Hauback (unpublished).

[14] The optimized structural parameters for $Ca_2YCo_2O_6$ are $a = 9.034$ and $c = 10.731$ Å; atom positions of Ca: 0.3665 0.00 0.25; Y: 0.8829 0.25 0.6171; O: 0.1920 0.0265 0.1300; Co positions and the space group are given as in Ref. [7].

[15] G. Kresse and D. Joubert, Phys. Rev. B **59**, 1758 (1999).

[16] P. Ravindran, P. A. Korzhavyi, H. Fjellvåg, and A. Kjekshus, Phys. Rev. B **60**, 16423 (1999).

[17] J. M. Wills, O. Eriksson, M. Alouani, and D. L. Price, in *Electronic Structure and Physical Properties of Materials*, edited by H. Dreysse (Springer, Berlin, 2000), p. 148.

[18] O. K. Andersen, Phys. Rev. B **12**, 3060 (1975).

[19] J. P. Perdew, K. Burke, and M. Ernzerhof, Phys. Rev. Lett. **77**, 3865 (1996).

[20] L. Pinsard-Gaudart *et al.*, J. Appl. Phys. **87**, 7118 (2000).

[21] H. Kageyama, K. Yoshimura, K. Kosuge, H. Mitamura, and T. Goto, J. Phys. Soc. Jpn. **66**, 1607 (1997).

XI

Valence states and associated features of Co in quasi-one-dimensional $Ca_3Co_2O_6$

R.Vidya,[*] P.Ravindran, H.Fjellvåg, and A.Kjekshus
Department of Chemistry, University of Oslo, Box 1033 Blindern, N-0315 Oslo, Norway

The valence state of the constituents of $Ca_3Co_2O_6$ has been analyzed using accumulated charge in atomic spheres and Bader regions as well as Born effective charges, and the results are compared with the situation in CoO and $LaCoO_3$ where Co takes a divalent and trivalent state, respectively. Moreover, the role of the covalent contribution to the bonding between Co and O and the possible metallic bonding between the Co atoms on the magnetic ordering and valence states has been investigated with the help of orbital-projected DOS, charge density, charge transfer, and electron-localization function. Born-effective-charge analyses show that the actual valence of the Co atoms are much smaller than the often believed 3+ state and the valence characteristics are highly directional dependent, in fact about three times more pronounced along the chains than perpendicular to the chains.

PACS numbers: 71., 71.20.Ps, 75.50.Ee, 78.20.Ci

I. INTRODUCTION

Low-dimensional structures have long been acknowledged to exhibit intriguing transport and magnetic properties. Recently, attention has been focused on quasi-one-dimensional phases [1] with the general formula A_3T1T2O_6 (A = Ca, Sr, Ba; $T1$,$T2$ = transition metal) where transition-metal-oxygen polyhedra form well separated chains running parallel to the trigonal axis of the crystal structure. In $Ca_3Co_2O_6$, which is the target of this study, each chain consists of alternating, face-sharing CoO_6 octahedra ($Co1O_6{}^o$) and CoO_6 trigonal prisms ($Co2O_6{}^t$). Typically, the ratio of the interchain to intrachain metal-metal distance is of the order of two giving the structure its quasi-one-dimensional character. The Ca atoms are located in the regions between the chains. Within this class of oxides, $Ca_3Co_2O_6$ is the only representative in which $T1$ and $T2$ refer one and the same element. Magnetic properties of $Ca_3Co_2O_6$ have been clarified to some extent, whereas aspects like valence states are still open for considerable debate. The fact that there are two different Co sites in the crystal structure makes it difficult to fully penetrate the nature of the electronic state of the individual Co atoms.

The possible valence states for Co are one, two, three, and four associated with various spin states such as low-spin (LS), intermediate-spin (IS) or high-spin (HS), and different spin, charge, and orbital ordering with different structural dimensionality. These are responsible for various interesting phenomena such as the temperature-induced spin-state transition in $LaCoO_3$ [2], the colossal magnetoresistance in $La_{1-x}Sr_xCoO_3$ [3], the insulator-to-metal transition and magnetoresistance properties in the oxygen-deficient perovskite phase $LaBaCo_2O_{5.5}$ [4], and the high figure of merit for the conversion of thermoelectric energy in the two-dimensional material $Ca_3Co_4O_9$ [5].

The crystal structure of $Ca_3Co_2O_6$ is related to the K_4CdCl_6-type structure [6] (space group $R\bar{3}c$) and consists of $(Co_2O_6)_\infty$ chains of alternating face sharing $Co1O_6$ octahedra and $Co2O_6$ trigonal prisms along the hexagonal c axis. Each $(Co_2O_6)_\infty$ chain is surrounded by six corresponding chains forming a triangular net in the ab plane. The adjacent $Co2^t$ atoms experience strong ferromagnetic (F) coupling within the chains whereas the interchain coupling is weakly antiferromagnetic (AF) [7–11]. Thus, relevant magnetic properties of $Ca_3Co_2O_6$ can be described in terms of a planar Ising hexagonal lattice in which the magnetic moment of each $(Co_2O_6)_\infty$ chain can be rationalized with one accumulated spin.

We have earlier reported electronic structure calculations for $Ca_3Co_2O_6$ in the ground-state ferrimagnetic (Ferri) structure [12], and the calculated total moment was found to be in very good agreement with low-temperature powder neutron diffraction [7] and the magnetization measurements [13]. Even though several theoretical studies [14–19] have been performed on $Ca_3Co_2O_6$, nobody (except our previous work [12]) has attempted to base the study on the experimental ground-state Ferri structure of this compound. This neglect is of course explicable on the ground of the complex magnetic structure which makes the electronic structure computations quite demanding. So, our previous report [12] represents the only theoretical account for $Ca_3Co_2O_6$ in the correct ground state.

It is generally agreed that Ca will be in the 2+ state and O in the 2− state in this class of compounds. Hence, in order to make charge balance, Co1 and Co2 take here either a pure ionic 3+ state (alternatively 2+ and 4+ states) or less than 3+ if the bonding with the O neighbors takes a significant degree of covalent character. On the basis of the $T1$-O/$T2$-O bond lengths in $Ca_3Co_2O_6$ [6] and corresponding phases [20, 21] it was predicted that the $Co2^t$ has a much lower oxidation state than $Co1^o$ because the Co-O bonds in the trigonal prisms are longer than those in the octahedra. An implicit assumption made during these deductions is that the $T2$-O

---

[*] Electronic address: `vidya.ravindran@kjemi.uio.no`; URL: `http://folk.uio.no/ravindrv`

bond length is not affected by the magnetic state and/or covalent bonding interaction. The higher-lying d levels for the $T2O_6$ configuration has a stronger antibonding character and more of these levels are occupied in a high-moment (HM; note that we by purpose avoid the conventional notation HS) state than in a low-moment (LM) state. As a result the TO_6 configuration should have longer T-O bond lengths in a HM state than a LM state.

In our previous study [12] we concluded that Co1^o and Co2^t in $Ca_3Co_2O_6$ are in valence state four and two, respectively. We will now elaborate on reasons behind this inference. It is established that one can substitute Co with four-valent species such as T = Mn, Ru, Rh, or Ir up to (or near) the composition Ca_3CoTO_6 [22–25]. It is also shown that it is possible to simultaneously substitute both two- and four-valent species in this structural framework [26–28]. These observations suggest that it is chemically plausible to have Co ions with valence states two and four in $Ca_3Co_2O_6$.

In an octahedral (cubic) crystal field the Co-d levels will split into triply degenerate t_{2g} (d_{xy},d_{xz},d_{yz}) and doubly degenerate e_g ($d_{x^2-y^2}$,d_{z^2}) levels. Owing to trigonal distortion of the octahedral co-ordination, the t_{2g} levels further split into a non-degenerate 1a level and doubly degenerate 1e levels. With Co in the 4+ oxidation state there will be five d electrons to accommodate in these levels. The spin moment according to a pure ionic description will then be 1, 3, and 5 μ_B per Co for low-spin (LS; $t_{2g}^5e_g^0$), intermediate-spin (IS; $t_{2g}^4e_g^1$), and high spin (HS; $t_{2g}^3e_g^2$) configuration, respectively. In practice, materials often have covalent hybridization between the transition metal and surrounding atoms, and this will reduce the spin moment owing to the fact that some of the electrons participate in bonding rather than in magnetism. So, one mostly gets non-integer value for the spin moments at the transition metal sites and also small induced moments at the sites of the surrounding atoms.

A powder neutron diffraction study [7] of $Ca_3Co_2O_6$ shows that, in the ordered magnetic state, the magnetic moment at the Co1^o site is $0.08 \pm 0.04\,\mu_B$. The calculated spin moment for the Co1^o site obtained from accurate density-functional calculation is $0.169\,\mu_B$ [12] (note that calculated magnetic moments generally are smaller than those obtained by magnetization measurements). With Co in a 3+,LS state ($t_{2g}^6e_g^0$) one expects zero spin moment at the Co1^o site. However, the t_{2g} states should have been completely filled and the e_g states completely empty; features not seen in any of the reported orbital-projected density-of-states (DOS) data [14, 19]. We laid decisive weight on the DOS evidences and concluded [12] that Co1^o is in a 4+,LS state. The too small value for the spin moment compared with the ionic picture was attributed to the strong covalent contribution to the bonding between Co1^o and O.

In a trigonal prismatic crystal field d levels will split into non-degenerate 1a (d_{z^2}), doubly degenerate 1e (d_{xy}, $d_{x^2-y^2}$), and doubly degenerate 2e (d_{xz},d_{yz}) levels. With Co in the 2+ oxidation state there will be seven d electrons to be accommodated in these levels. The spin moment for Co2^t in LS ($1a^21e^42e^1$) and HS ($1a^21e^32e^2$) configurations will then be 1 and 3 μ_B, respectively, for the pure ionic case. The powder neutron diffraction study [7] gave an ordered magnetic moment at the Co2^t site of $3.00 \pm 0.05\,\mu_B$, whereas the density-functional calculation gave a somewhat smaller spin moment ($2.632\,\mu_B$). The calculated total moment for $Ca_3Co_2O_6$ in the Ferri state came out in very good agreement with the experimental value (1.209 vs 1.30 μ_B). As the calculated spin moment for both Co atoms came out in reasonable to good agreement with ionic Co^{4+},LS and Co^{2+},HS states we jumped to the conclusion of 4+ and 2+ oxidation states for Co1^o and Co2^t in LS and HS configurations, respectively. Recently there have appeared several experimental [8, 25, 30, 31] and theoretical [14–16, 19, 32, 33] reports claiming that the valence states of both Co atoms in $Ca_3Co_2O_6$ are in fact 3+. So, in order to get more insight into the valence states of Co we have now made more detailed theoretical analyses of the Co valence situation in $Ca_3Co_2O_6$.

II. COMPUTATIONAL DETAILS

The crystal-orbital-Hamiltonian-population (COHP) and electron-localization-function (ELF) data were calculated using the TBLMTO program [34]. For the DOS calculations we have applied the full-potential linearized-augmented plane-wave method implemented in the WIEN2k package [35] including spin-orbit coupling. The Born-effective-charge calculations were performed using the Vienna *ab-initio* simulation package (VASP) [36] within the projector-augmented-wave (PAW) method [37] as implemented by Kresse and Joubert [38]. Structural optimizations were continued until the forces on the atoms had converged to less than 1 meV Å^{-1} and the pressure on the cell had minimized within the constraint of constant volume. The optimized structure has been used for the Berry-phase calculations. The atoms involved in the calculations required extra care; either large basis sets within a pseudo-potential scheme or an all-electron scheme. So we have used very large basis sets with 875 eV for the plane-wave cutoff. For the **k**-space integrations in the Berry-phase calculations, a uniform 8 × 8 × 8 **k**-point mesh was found to be adequate. For $LaCoO_3$ and CoO, we have used the LDA+U approach with an U value of 5 and 8 eV, respectively, for Co in order to reproduce the insulating behavior.

III. RESULTS AND DISCUSSION

Before we pursue our renewed findings we will give a brief account of the recent development in the view on the spin and valence situation in $Ca_3Co_2O_6$. The status on magnetism is largely unchanged from that prevailing when we published our previous report [12]. At least two magnetic transitions are recognised at quite low temperatures. One around 24 K can rather unambiguously be attributed to F ordering within the chains and another around 10 K appears to be associated with Ferri coupling between the chains [7, 8]. The origin of the latter transition remains a matter of dispute [7, 8, 22, 28, 39, 40], some reports favoring a more regular Ferri situation with interchain AF coupling between the F chains [7, 39] while others point at spin-glass freezing within every third chain [41]. On the basis of a moment of 4 μ_B per $Ca_3Co_2O_6$ formula unit from magnetization measurements [42], it has been conjectured that both Co atoms are in a 3+ state with $Co1^o$ as LS (non-magnetic) and $Co2^t$ as HS (magnetic).

The effective moment has been extracted from the temperature dependence of the magnetic susceptibility and explained as a 1:1 HS and IS configurations of Co in 3+ states [8]. This interpretation is in the first place contradictory to the neutron diffraction results [7] and secondly stabilization of the IS configuration requires lowering of the symmetry of the $Co1^o$ co-ordination in order to provide the required additional splitting of the e_g levels. Also, Co in a pure 3+,IS state should have a moment of $2\,\mu_B$ and introduction of covalence should reduce the moment, but probably not below $1\,\mu_B$ (see Ref. [2]). All in all, the fresh magnetic data suffer from exactly the same weaknesses as the older data with regard to evaluation of the valence states for $Co1^o$ and $Co2^t$ (see below).

X-ray photoemission spectroscopy (XPS) data on Ca_3CoTO_6 (T=Co, Rh, Ir) have been interpreted [25] as evidence for a 3+ valence state for $Co1^o$ and $Co2^t$ in LS and HS configuration, respectively. XPS profiles comprise information about the density of states of the electrons, but it is very difficult to judge oxidation states from such data alone. Even extraction of qualitative valence-state information from XPS data requires the use of suitable standards for comparison. Such references have apparently not been used in this case. As mentioned before, the crucial information needed to decide the valence state is the orbital-projected DOS and that can not be extracted from the XPS. Moreover, the XPS measurements were carried out at room temperature and at this temperature it is quite possible that Co has in any case reached a common average valence state. Hence, the conclusion advanced from XPS measurements can not be taken as conclusive evidence for a 3+ universal oxidation state for both Co atoms in $Ca_3Co_2O_6$.

Low-temperature field-sweep ^{59}Co NMR measurements on $Ca_3Co_2O_6$ have also been interpreted [30] as evidence for the presence of non-magnetic Co in the 3+,LS state. A serious drawback with this study is that only the signal from one of the two Co sites is detected and even this signal could only be observed in a very narrow temperature range from 7 to 15 K. The key questions in this connection are then why the signal from the companion 3+,HS state is not detected and what happens to the signal from the claimed 3+,LS state below 7 and above 15 K. Before these questions are satisfactorily answered the NMR findings can not be taken in favor of anything. However, one further comment of direct relevance for the present communication should be made. It is not possible to have completely non-magnetic Co species in $Ca_3Co_2O_6$ for the following reason. The shortest Co-Co distance within the chains is about 2.59 Å which is comparable to that in the closest Co-Co distance in hcp Co (2.51 Å). Both experimental [7] and theoretical [12] studies clearly demonstrate that $Co2^t$ carries a large spin moment. Hence, one can not conceive a situation with a completely non-magnetic $Co1^o$; the large moment at $Co2^t$ site and the short Co1-Co2 distance, should certainly have led to an induced moment at the $Co1^o$ site.

Recently two reports [18, 19] have appeared dealing with LDA+U calculations on $Ca_3Co_2O_6$. It is therefore appropriate to consider any drawbacks using the LDA+U method on $Ca_3Co_2O_6$. The degree of localization of the electrons at the $Co1^o$ and $Co2^t$ sites are not the same and hence the use of the same U and J values for both sites is not appropriate. Furthermore, the quasi-one-dimensional nature of the atomic arrangement also gives the band dispersion a one-dimensional character. So, in order to treat the strong correlation effect in $Ca_3Co_2O_6$ appropriately one need to account for the $\mathbf{k}$ dependence of U, viz. the Mott-Hubbard correction terms in the LDA+U methods must contain local character, features missing in the currently available LDA+U approach. With these deficiencies, the LDA+U calculations will inevitably reveal that the relative stability of the intrachain F and AF arrangements depends on the chosen U value and the "initial density" employed for the calculations [18]. For example, the intrachain F arrangement is more stable than the intrachain AF arrangement for U = 3 and 4 eV, but the opposite is true for U = 2 and 5 eV. Moreover, the LDA+U calculation gave a too large spin moment for the F state of $Ca_3Co_2O_6$ [19] (5.66 μ_B f.u.$^{-1}$) compared with the magnetization measurements ($4\,\mu_B$ f.u.$^{-1}$) [42]. The use of LDA+U calculations for Na_xCoO_2 [43] shows that caution must be taken in order to avoid worse agreement with experimental data than by the use of simple LDA calculations. In addition, it should be recalled that U is an empirical parameter. We have shown earlier [12], that the magnetic properties of $Ca_3Co_2O_6$ can be correctly be described by the use of GGA itself. Therefore, in the following we will focus only on results obtained by GGA calculations.

Both the neutron-diffraction study [7] and our earlier total-energy calculations [12] show that $Ca_3Co_2O_6$ has a Ferri ground state. Specific heat [28] and transport measurements [44] show metallic behavior for $Ca_3Co_2O_6$. In contrast, the recent theoretical study [19] incorrectly concluded that this material is an F insulator. In our previous report we emphasized that all results reported had been obtained from relativistic full-potential GGA calculations with spin-orbit coupling (SOC) included. However, Ref. [19] wrongly cited that SOC had not been included in our calculations. All in all, we strongly believe

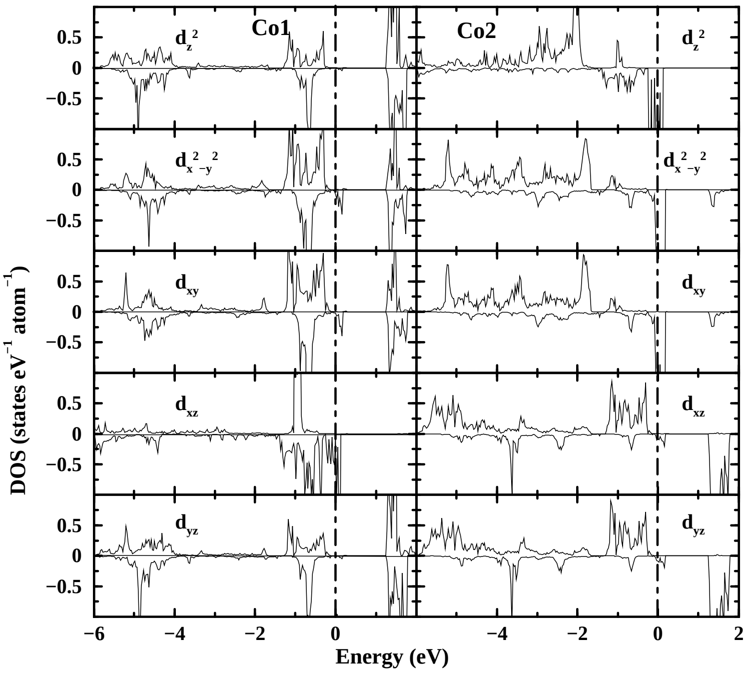

FIG. 1: Calculated orbital-projected density of states (DOS) for Co1^o and Co2^t in $Ca_3Co_2O_6$ for the ground-state ferrimagnetic configuration. The Fermi level is set to zero.

that the GGA approach with spin-orbit coupling is sufficiently accurate to describe the electronic structure and magnetic properties of $Ca_3Co_2O_6$ and proceed our analysis accordingly.

To obtain firm pictures of the valence states of atoms in compounds, the key information one really needs is how many electrons that are present at each site in the atomic arrangement. This information is very difficult to extract unambiguously from usual DFT calculations owing to the fact that the integrated charges at a given site depends not only on the chosen radius for the enclosing atomic sphere, but also involve charges in the surrounding interstitial regions. In order to remedy this situation we have now consulted several tools, viz. charge density, charge transfer, electron-localization function, angular-momentum and orbital-projected DOS, crystal-orbital-Hamiltonian population, Bader charge, and Born effective charge. These analyses were carried out not only for $Ca_3Co_2O_6$, but also for CoO and $LaCoO_3$ (for which the valence states of Co are more unambiguous) in order to cross check their resolving capabilities.

More insight into the spin and valence states of the Co1^o and Co2^t atoms in $Ca_3Co_2O_6$ is provided by the orbital-projected d-electron DOS (Fig. 1). This illustration clearly convey the message that Co1^o is in a LM state, and Co2^t conversely in a HM state. If Co1^o had been in a proper ionic 3+,LS state one should expect that three d orbitals would have been completely filled and two d orbitals completely empty. On the contrary Figs. 1 and 2 show almost equal amounts of DOS in all d orbitals, thus confirming that Co1 is certainly not in an ionic 3+,LS state. However, the partial DOS for Co1^o and Co2^t (Fig. 2) are sufficiently different to defend the characterization as different valence states. The partial DOS for Ca (Fig. 2) clearly demonstrates a nearly empty valence band and consequently an ideal 2+ state with negligible amounts of valence electrons at the Ca site.

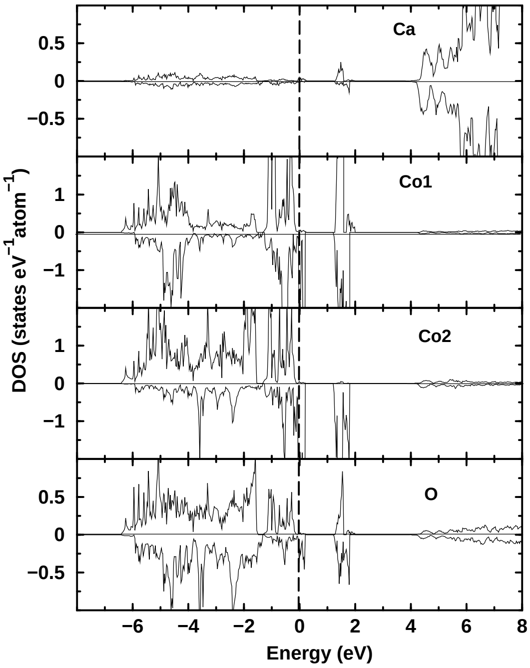

FIG. 2: Calculated site-projected density of states (DOS) for $Ca_3Co_2O_6$ in the ground-state ferrimagnetic configuration. The Fermi level is set to zero.

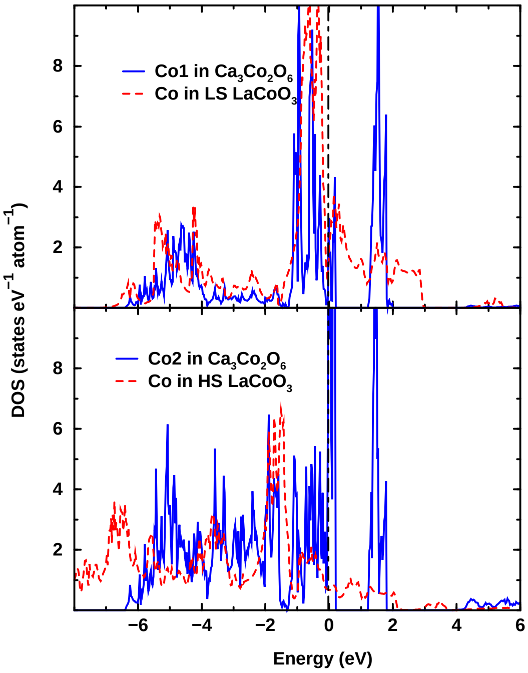

FIG. 3: (Color online) Calculated partial (d) density of states (DOS) for Co1^o and Co2^t in Ca$_3$Co$_2$O$_6$ for the ferrimagnetic ground-state phase superimposed with the calculated profiles for Co^{3+} in LS and HS modifications of LaCoO$_3$, respectively. The Fermi level is set to zero.

The energetically degenerate nature of the Co-d and O-p states conveys evidence for appreciable covalent interaction between Co and O, and as a result of this hybridization interaction there occur an induced spin moment of around 0.13 μ_B at the oxygen sites.

LaCoO$_3$ provides an example of Co^{3+} in an LS state with completely filled t_{2g} states and empty e_g states and a resulting semiconducting behavior with a band gap of about 0.2 eV. As part of the control tests for Ca$_3$Co$_2$O$_6$ we have now calculated the DOS for the 3+,LS state for Co in LaCoO$_3$ and compared it with the DOS for the Co1^o site. A similar comparison have been made for the DOS for the 3+,HS state of Co in LaCoO$_3$ (obtained from the fixed-spin calculation reported earlier [2]) in relation to that for Co2^t in Ca$_3$Co$_2$O$_6$. These comparisons can be appraised in Fig. 3, which shows that there is certainly no correspondence between the Co DOSs obtained for the different modifications of LaCoO$_3$ and those for different sites in Ca$_3$Co$_2$O$_6$. The Co partial DOSs for Ca$_3$Co$_2$O$_6$ occur in narrower energy regions than those for the LaCoO$_3$ reference materials, overall features which we attribute to the quasi-one-dimensional nature of the crystal structure of Ca$_3$Co$_2$O$_6$.

If a given material exhibits a significant amount of covalence in its bonding, the simple oxidation state approach can not be used to estimate the valence states. All earlier studies on Ca$_3$Co$_2$O$_6$ have ignored the covalent contribution to the bonding and most of them have in fact made the valence assessment only on the observed size of the magnetic moments at the Co sites. Whangbo *et al.* [14, 18] made spin-polarized electronic band-structure calculation for Ca$_3$Co$_2$O$_6$ on the basis of the room-temperature crystal structure in F configuration. From partial DOS analyses these authors concluded that both Co1^o and Co2^t are 3+ ions in LS and HS state, respectively. However, this inference contradicts their own findings: (i) Despite the fact that the calculations gave a magnetic moment of 0.3 μ_B at the Co1^o site they proceed as if the moment is zero. (It is worthwhile to record that DFT-calculated moments generally come out smaller than according to the pure ionic scheme due to the covalent interaction between constituents.) (ii) In an octahedral crystal field, proper Co^{3+} ions in the LS state should exhibit completely filled t_{2g}^6 levels and completely empty e_g levels. However, the orbital-projected DOS of Whangbo *et al.* closely resembles our findings (Figs. 1 and 2) which is clearly incompatible with a 3+,LS state.

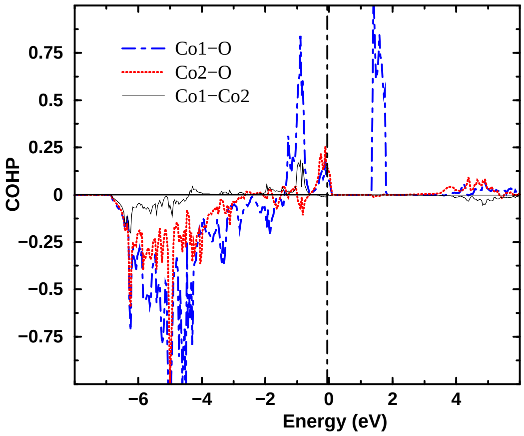

FIG. 4: (Color online) Crystal-orbital-Hamilton population (COHP) for Co1-to-O, Co2-to-O, and Co1-to-Co2 interactions in an assumed non-magnetic state of Ca$_3$Co$_2$O$_6$.

Strength of bonding interaction between the constituents of a compound is often assessed from COHP plots. The COHP is the DOS weighted by the corresponding Hamiltonian matrix elements and is also indicative of the character of a bond (negative COHP indicating bonding; positive COHP antibonding interaction [34, 45]). The calculated COHP for the Co1-to-O, Co2-to-O, and Co1-to-Co2 interactions in Ca$_3$Co$_2$O$_6$ are illustrated in Fig. 4 which shows that the strongest bonding interaction is between Co1 and O. This is consistent with the experimental findings in the sense that the Co1-O bond length is shorter than the Co2-O bond length. The integrated COHP yielded bond strength of -1.39, -0.77 and -0.08 eV for the Co1-to-O, Co2-to-O, and Co1-to-Co2 interaction, respectively. Since the covalent Co1-to-Co2 interaction is weak, the intrachain F interaction has to be attributed to metallic type of bonding. The strong covalent interaction between Co1 and O could explain why the spin moment at the Co1^o site is quenched.

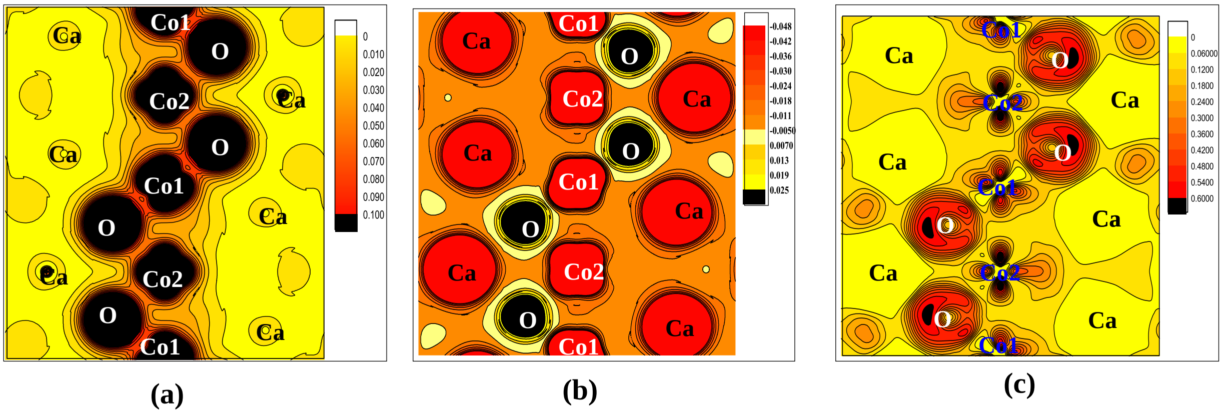

FIG. 5: (Color online) Calculated (a) charge density, (b) charge transfer, and (c) electron-localization function for $Ca_3Co_2O_6$. The illustrations refer to the (110) plane.

More details about the bonding interactions between constituents can be obtained from charge-density, charge transfer, and ELF analyses. The charge-density distribution in $Ca_3Co_2O_6$ [Fig. 5(a)] shows that only a negligibly small charge is left at the Ca site, thus confirming the presence of ionic bonding between Ca and the $(Co_2O_6)_\infty$ chains. The atoms within the chain exhibit appreciable covalent character as already manifested by the one-dimensional appearance. Although the interatomic Co1-Co2 distance is short, the interaction between these atoms are largely of metallic character. The charge-transfer distribution [Fig. 5(b)] shows that electrons are transferred from both Ca and Co atoms to the oxygen sites, viz. in accordance with an ionic conception. However, if the bonding interaction between Co and O had been purely ionic one would have expected an isotropic charge-transfer distribution. Hence, the anisotropic distribution between Co and O in the charge-transfer plot supports the inference that there is an appreciable degree of covalence in the Co-to-O bonding interaction. If one had known the amount of electrons transfer from Co to O, one could have estimated a more exact valence state for Co. According to Fig. 5(b) it is clear that both Co atoms have donated electrons to the oxygen sites, but the degree of charge transfer is different for $Co1^o$ and $Co2^t$. In conclusion, it is difficult to judge the valence of Co from the charge-transfer distribution alone.

ELF is an informative tool to distinguish different bonding interactions in solids [46]. The ELF for $Ca_3Co_2O_6$ [Fig. 5(c)] exhibits only a small numerical value between Ca and the other constituents which is another indication for the ionic character of the Ca-to-$(Co_2O_6)_\infty$ bonding. The maximum value of the ELF at the O sites and minimum values at the Ca and Co sites reconfirms that charge has been transferred from Ca and Co to O. The polarization with different orientation of ELF at the Co sites indicates different orientation of the orbitals residing at $Co1^o$ and $Co2^t$. Although the charge-density plot exposes a relatively large amount of charge at the Co sites, the small value of ELF show that these charges are mainly of *d* character. The conclusion from the charge-density, charge-transfer, and ELF analyses is accordingly that the bonding interaction between Ca and O is mainly ionic and that between Co and O is ionic with appreciable covalent woof. This conclusions is further supported by the findings from the Born-effective-charge analysis (see below).

Everybody agrees that the number of electrons at a given atomic site is the key quantity for evaluation of the valence state. The accumulated charges inside the appropriately chosen atomic sphere are 18.11, 24.97, 24.76, and 7.16 (all in units of e) for Ca, $Co1^o$, $Co2^t$, and O, respectively. Since there are ambiguities associated with the definition of the boundary of an atomic sphere and no clear-cut distinction between cationic and anionic charges, we turned our attention to the "atom-in-molecule" approach introduced by Bader. Bader gave an elegant approach to this problem with his "interatomic surface" [47] concept, according to which the space in a solid is divided into regions established by surfaces that run through minima in the charge density. A given region is chosen such that at any location on the bordering surface the gradient of the charge density has no component normal to the surface. A region enclosed by such boundary surfaces is referred to as a Bader region. Each Bader region normally contains only one nucleus. By integrating the charge density within the Bader region where a given nucleus is located, and adding electronic charges in "naturally associated neighboring regions" that do not include a nucleus, the total excess charge on the atom at a given site can be estimated and this charge is named as Bader charge. The advantage of this method is that the analysis is based solely on the charge density, so it is rather insensitive to the basis set used. The Bader charge difference (Δq_B relative to the corresponding neutral atom) at each atomic site in $Ca_3Co_2O_6$ are listed in Table I together with values for the reference substances CoO and $LaCoO_3$. The Bader charge differences for CoO and $LaCoO_3$ give much smaller valence states than the expected values according to a pure ionic model, but provide correct qualitative measures for the transfer of electrons from one site to another.

The Born-effective charge gives information about how much electrons are polarized on application of an electric field. If ions behaves like closed-shell ions, they should carry an effective charge close to their nominal ionic value. On the contrary, a large amount of non-rigid delocalized charge will flow across the skeleton of a compound with covalent directed bonds when the lattice is subjected to displacement [48, 49]. Owing to this covalence effect, one usually obtains larger Born-effective charges than the nominal ionic values. So, one can consider the Born-effective charge as an upper limit for the valence in a given system. The Born-effective charge is indeed a macroscopic concept [50, 51], which involves the polarization of the valence electrons as a whole, while the charge "associated with" a given atom is an ill-defined concept. High Born-effective-charge values indicate that the relative displacements of neighboring ions against each other trigger highly polarized electrons. Roughly speaking, a large amount of delocalized charge is responsible for higher values for the Born-effective charge than the nominal ionic values. As the Born-effective charge concept gives more reasonable values for the valence of the Co atoms in well known systems than the Bader-charge approach, it seemed worthwhile to attempt to use this tool to resolve the valence situation for Co in $Ca_3Co_2O_6$. The average value of the Born-effective charge (see Table I) for Co in CoO and $LaCoO_3$ is 2.17 and 3.35, respectively, and are reasonably close to the respective formal valence of two and three.

The calculated Born-effective charge for $Ca_3Co_2O_6$ (Table I) once again confirm that both Ca and Co donate electrons and O accepts electrons in accordance with the traditional ionic picture. However, for a pure ionic system one expects more isotropic values for the Born-effective charges than that obtained for $Ca_3Co_2O_6$. Considerable anisotropy in the diagonal components of the Born-effective-charge tensor (Table I) along with the noticeable off-diagonal components at the O sites confirm the presence of covalent bonding between oxygen and the neighboring Co atoms. Our other chemical-bonding-analysis tools discussed above also show that there is considerable covalent bonding between Co and O. Born-effective-charge analyses account for the anomalous contributions (defined as the excess charge relative to the accepted value for the ion in question) to the effective charges. The almost equal value of the xx and yy components of the Born-effective charge at the Co sites reflects the one-dimensional character of the atomic arrangement. The average value of the diagonal components of the Born-effective charge for Ca, Co1, Co2, and O are 2.637, 1.800, 2.269, and −2.01, respectively, indicating that the average valence state of $Co1^o$ and $Co2^t$ are similar. It is interesting to note that the Bader charges at $Co1^o$ and $Co2^t$ are in fact almost equal. On the other hand, the zz component (along the chain) of the Born-effective charge at $Co1^o$ and $Co2^t$ are appreciably different (2.8 vs 4.2) indicating that the *nature of the valence state of the two sites are indeed different.* However, because of the appreciable degree of covalence in the Co-to-O bonding, the ionic-based valence count for both Co sites comes out much smaller than the expected formal valence of 3+ for Co in $Ca_3Co_2O_6$.

IV. CONCLUSION

In conclusion, the large difference in the magnetic moment between the Co atoms is due to different degree of covalent character between Co and the surrounding oxygens. The $Co1^o$ and $Co2^t$ atoms are not in conventional 3+,LS and 3+,HS state, respectively. Our detailed analyses show that the actual valence states are much smaller than three. We maintain that formal valence concept works well for insulators with pure ionic bonding. If the material under consideration has finite degree of covalent character along with the ionic, the simple ionic picture can not be used to predict the valence states correctly. Our Born-effective-charge analyses suggest that in low-dimensional phases like $Ca_3Co_2O_6$ the valence electrons are distributed highly anisotropically. As a consequence, the simple formal valence picture can not be used to describe the electronic structure and magnetic properties properly.

V. ACKNOWLEDGEMENT

The authors are grateful for the financial support from the Research Council of Norway. Parts of these calculations were carried out at the Norwegian supercomputer facilities.

---

[1] K.E. Stitzer, J. Darriet, and H.-C. zur Loye, Curr. Opin. Solid State Mater. Sci. **5**, 535 (2001).

[2] P. Ravindran, H. Fjellvåg, A. Kjekshus, P. Blaha, K. Schwarz, and J. Luitz, J. Appl. Phys. **91**, 291 (2002).

[3] G. Briceno, H. Chang, X. Sun, P.G. Schultz, and X.D. Xiang, Science **270**, 273 (1995).

[4] C. Martin, A. Maignan, D. Pelloquin, N. Nguyen, and B. Raveau, Appl. Phys. Lett. **71**, 1421 (1997).

[5] L. Li, R. Funakaski, I. Matsubara, K. Ueno, and H. Yamada, J. Mater. Chem. **9**, 1959 (1999).

[6] H. Fjellvåg, E. Gulbrandsen, S. Aasland, A. Olsen, and B.C. Hauback, J. Solid State Chem. **124**, 190 (1996).

[7] S. Aasland, H. Fjellvåg, and B. Hauback, Solid State Commun. **101**, 187 (1997).

TABLE I: Calculated Bader charge difference (Δq_B; see text) and Born effective charge tensor (Z^*_{ij}) for non-magnetic $Ca_3Co_2O_6$, $LaCoO_3$ and antiferromagnetic CoO

Specification	Δq_B	Z^*_{xx}	Z^*_{yy}	Z^*_{zz}	Z^*_{xy}	Z^*_{xz}	Z^*_{yx}	Z^*_{yz}	Z^*_{zx}	Z^*_{zy}
$Ca_3Co_2O_6$										
Ca	1.51	2.993	2.586	2.334	0.023	−0.076	−0.013	−0.008	−0.500	−0.001
Co1	1.33	1.290	1.303	2.809	−0.008	0.000	0.007	−0.005	0.000	0.000
Co2	1.36	1.290	1.317	4.202	−0.013	0.002	0.002	0.002	0.000	0.000
O	−1.20	−2.264	−1.427	−2.358	0.508	0.282	0.426	−0.041	0.007	0.034
CoO										
Co	0.74	2.269	2.269	1.971	0.000	0.000	0.000	0.000	0.000	0.000
O	−0.74	−2.275	−2.275	−1.972	0.000	0.000	0.000	0.000	0.000	0.000
$LaCoO_3$										
La	2.09	4.478	4.501	4.035	−0.021	0.002	−0.005	−0.009	0.000	0.000
Co	1.71	3.453	3.454	3.166	1.687	0.000	−1.687	0.000	0.000	0.000
O	−1.26	−3.377	−1.929	−2.408	−0.004	0.868	0.060	0.081	0.817	−0.013

[8] A. Maignan, C. Michel, A.C. Masset, C. Martin, and B. Raveau, Eur. Phys. J. B **15**, 657 (2000).

[9] V. Hardy, S. Lambert, M.R. Lees, and D.M. Paul, Phys. Rev. B **68**, 014424 (2003).

[10] H. Kageyama, K. Yoshimura, K. Kosuge, X. Xu, and S. Kawano, J. Phys. Soc. Jpn. **67**, 357 (1998).

[11] B. Martinez, V. Laukhin, M. Hernando, J. Fontcuberta, M. Parras, and J.M. Gonzalez-Calbet, Phys. Rev. B **64**, 012417 (2001).

[12] R. Vidya, P. Ravindran, H. Fjellvåg, A. Kjekshus, and O. Eriksson, Phys. Rev. Lett. **91**, 186404 (2003).

[13] M.N. Baibich, J.M. Broto, B. Raquet, H. Rakoto, M. Costes, A. Maignan, S. Lambert, and D. Grebille, Physica B **320**, 337 (2002).

[14] M.-H. Whangbo, D. Dai, H.-J. Koo, and S. Jobic, Solid State Commun. **125** 413 (2003).

[15] V. Eyert, C. Laschinger, T. Kopp, and R. Fresard, Chem. Phys. Lett. **385**, 249 (2004).

[16] R. Fresard, C. Laschinger, T. Kopp, and V. Eyert, Phys. Rev. B **69**, 140405 (2004).

[17] J. An and C.-W. Nan, Solid State Commun. **129**, 51 (2004).

[18] A. Villesuzanne and M.-H. Whangbo, Inorg. Chem. **44**, 6339 (2005).

[19] H. Wu, M.W. Hu, D.I. Khomskii, and L.H. Tjeng, Phys. Rev. Lett. 95, 186401 (2005).

[20] O. Gaurdon, V. Petricek, M. Dusek, P. Bezdicka, S. Durovic, D. Gyepesova, and M. Evain, Acta Crystallogr., Sec. B **55**, 841 (1999).

[21] M. Evain, F. Boucher, O. Gourdon, V. Petricek, M. Dusek, and P. Bezdicka, Chem. Mater. **10**, 3068 (1998).

[22] H. Kageyama, K. Yoshimura, and K. Kosuge, J. Solid State Chem. **140**, 14 (1998).

[23] S. Rayaprol, K. Sengupta, and E.V. Sampathkumaran, Phys. Rev. B **67**, 180404(R) (2003).

[24] V.G. Zubkov, G.V. Bazuev, A.P. Tyutynnik, and I.F. Berger, J. Solid State Chem. **160**, 293 (2001).

[25] K. Takubo, T. Mizokawa, S. Hirata, J.-Y. Son, A. Fujimori, D. Topwal, D.D. Sarma, S. Rayaprol, and E.V. Sampathkumaran, Phys. Rev. B **71**, 073406 (2005).

[26] C.L. Onnerud, M. Sigrist, and H.-C. zur Loye, J. Solid State Chem. **127**, 25 (1996).

[27] A. Niazi, E.V. Sampathkumaran, P.L. Paulose, D. Eckert, A. Handstein, and K.-H. Müller, Phys. Rev. B **65**, 064418 (2002).

[28] V. Hardy, M.R. Lees, A. Maignan, S. Hebert, D. Flahaut, C. Martin, and D.M. Paul, J. Phys.: Condens. Matter **15**, 5737 (2003).

[29] A. Maignan, S. Hebert, C. Martin, and D. Flahaut, Mat. Sci. Eng. B **104**, 121 (2003).

[30] E.V. Sampathkumaran, N. Fujiwara, S. Rayaprol, P.K. Madhu, and Y. Uwatoko, Phys. Rev. B **70**, 014437 (2004).

[31] A. Maignan, V. Hardy, S. Hebert, M. Drillon, M.R. Lees, O. Petrenko, D.M. Paul, and D. Khomskii, J. Mater. Chem. **14**, 1231 (2004).

[32] C. Laschinger, T. Kopp, V. Eyert, and R. Fresard, J. Magn. Magn. Mater. **272-276**, 974 (2004).

[33] D. Dai and M.-H. Whangbo, Inorg. Chem. **44**, 4407,(2005).

[34] G. Krier, O. Jepsen, A. Burkhardt, and O.K. Andersen, *Tight Binding LMTO-ASA Program Version 4.7* , Stuttgart, Germany 1999.

[35] P.Blaha, K. Schwarz, G.K.H. Madsen, D. Kvasnicka, and J. Luitz, WIEN2k, revised edition 2001.

[36] G. Kresse and J. Hafner, Phys. Rev. B **47**, R6726 (1993); G. Kresse and J. Furthmuller, Comput. Mater. Sci. **6**, 15 (1996).

[37] P.E. Blöchl, Phys. Rev. B **50**, 17953 (1994)

[38] G. Kresse and J. Joubert, Phys. Rev. B **59**, 1758 (1999).

[39] H. Kageyama, K. Yoshimura, K. Kosuge, H. Mitamura, and T. Goto, J. Phys. Soc. Jpn. **66**, 1607 (1997).

[40] S. Rayaprol, K. Sengupta, and E.V. Sampathkumaran, Solid State Commun. **128**, 79 (2003).

[41] S. Rayaprol, K. Sengupta, and E.V. Sampathkumaran, Proc. Indian Acad. Sci. (Chem. Sci.) **115**, 553 (2003).

[42] H. Kageyama, K. Yoshimura, K. Kosuge, M. Azuma, M. Takano, H. Mitamura, and T. Goto, J. Phys. Soc. Jpn. **66**, 3996 (1997).

[43] M.D. Johannes, I.I. Mazin, and D.J. Singh, Phys. Rev. B **71**, 205103 (2005).

[44] B. Raquet, M.N. Baibich, J.M. Broto, H. Rakoto, S. Lambert, and A. Maignan, Phys. Rev. B **65**, 104442 (2002).

[45] R. Dronskowski and P.E. Blochl, J. Phys. Chem. **92**, 5397 (1993).

[46] A. Savin, R. Nesper, S. Wengert, and T.F. Fässler, Angew. Chem. Int. Ed. Engl. **36**, 1808 (1997).

[47] R.F.W. Bader *Atoms in Molecules: A Quantum Theory*

(Clarendon Press, Oxford, 1990).

[48] M. Posternak, R. Resta, and A. Baldereschi, Phys. Rev. B **50**, 8911 (1994).

[49] W. Zhong, R.D. King-Smith, and D. Vanderbilt, Phys. Rev. Lett. **72**, 3618 (1994).

[50] R.M. Martin, Phys. Rev. B **9**, 1998 (1974).

[51] R. Pick, M.H. Cohen, and R.M. Martin, Phys. Rev. B **1**, 910 (1970).

XII

PERGAMON

Solid State Communications 124 (2002) 293–298

solid
state
communications

www.elsevier.com/locate/ssc

Antiferromagnetic vs. ferromagnetic interactions and spin-glass-like behavior in ruthenates

P. Ravindran[a,*], R. Vidya[a], P. Vajeeston[a], A. Kjekshus[a], H. Fjellvåg[a], B.C. Hauback[b]

[a]Department of Chemistry, University of Oslo, P.O. Box 1033, Blindern, N-0315 Oslo, Norway
[b]Institute of Energy Technology, P.O. Box 40, Kjeller N-2007, Norway

Received 18 July 2002; accepted 21 August 2002 by C.N.R. Rao

Abstract

We have made a series of gradient-corrected relativistic full-potential density-functional calculations for Ca-substituted and hole-doped $SrRuO_3$ in para, ferro, and A-, C-, and G-type antiferromagnetic states. Magnetic phase-diagram data for $Sr_{1-x}Ca_xRuO_3$ at 0 K are presented. Neutron diffraction measurements combined with total energy calculations show that spin-glass behavior with short-range antiferromagnetic interactions rules in $CaRuO_3$. The substitution of Sr by Ca in $SrRuO_3$ decreases the ferromagnetic interaction and enhances the G-type antiferromagnetic interaction; the G-AF state is found to stabilize around $x = 0.75$ consistent with experimental observations. Inclusion of spin–orbit coupling is found to be important in order to arrive at the correct magnetic ground state in ruthenates. © 2002 Elsevier Science Ltd. All rights reserved.

PACS: 75; 81.05.Je; 75.10.Nr; 71.20. − b

Keywords: A. Ruthenates; C. Spin-glass-behavior

Ever since unconventional superconductivity was observed in Sr_2RuO_4 [1], ruthenates have attracted much interest. Substitution [2] of the smaller Ca for Sr in Sr_2RuO_4 leads to an antiferromagnetic (AF) Mott insulator with a staggered moment of $S = 1$. Coexistence of ferro- and antiferromagnetic fluctuations in Ca_2RuO_4 and competition between p- and d-wave superconductivity in Sr_2RuO_4 have also been reported [3]. Recently coexistence of magnetism and superconductivity is discovered [4] in ruthenium-based layered cuprates such as $RRuSr_2Cu_2O_8$ (R = Eu, Gd). Lee et al. [5] reported the existence of a pseudogap (PG) in $BaRuO_3$ reminiscent of the PG in high-T_c superconductors. As in f-electron-based intermetallics, non-Fermi-liquid (NFL) behavior has recently been observed in $La_4Ru_6O_{19}$ [6]. Critical magnetic fluctuations associated with metamagnetism is reported for $Sr_3Ru_2O_7$ [7] and a metallic AF phase with temperature induced insulator-to-metal transition is found for $Ca_3Ru_2O_7$ [8].

Poorly metallic NFL-behaving $SrRuO_3$ is the only known ferromagnetic (F; $T_C = 160$ K) 4d transition-metal oxide [9,10]. $CaRuO_3$ is also metallic, but experimental and theoretical studies conclude contradictory regarding the nature of the magnetic ground state (e.g. AF [9,11,12], nearly F [13], exchange enhanced paramagnetic (P) [14], Curie–Weiss P [15], verge of F instability [16], spin glass (SG) [17] etc.) and this controversy is not settled yet. Some of these reports indicate a lack of long-range magnetic order whereas others suggest evidence for an AF ground state with a Néel temperature (T_N) of ~110 K [11]. The striking difference in the magnetic properties of $SrRuO_3$ and $CaRuO_3$ makes magnetic phase diagram studies on $Sr_{1-x}Ca_xRuO_3$ quite interesting.

$CaRuO_3$ and $SrRuO_3$ are isostructural and isoelectronic, differing structurally only in the degree of the small orthorhombic distortion (lattice constants within 2%). Hence, insight into the magnetic properties of these compounds is expected to increase the general knowledge on magnetic phenomena in perovskite oxides, and

---

[*] Corresponding author. Tel.: +47-22-855-606; fax: +47-22-85-5441.
E-mail address: ravindran.ponniah@kjemi.uio.no (P. Ravindran).

0038-1098/02/$ - see front matter © 2002 Elsevier Science Ltd. All rights reserved.
PII: S0038-1098(02)00472-6

Table 1
Total energy (relative to the lowest energy state; in meV/f.u.) for $CaRuO_3$ in P, F, and A-, C-, and G-AF states with orthorhombic and undistorted cubic (designated cubic) structures

Method	P	F	A-AF	C-AF	G-AF
GGA + SO	26	19.8	6	4	0
GGA + SO (cubic)	1307	1249	1292	1299	1303
GGA	38	0	9	10	7

ruthenates in particular. The density-functional calculations [16,18] for $CaRuO_3$ which conclude with 'verge of F instability' have the weakness that AF interactions were not considered. In this report, we present the intriguing result that SG behavior with short-range AF interaction occurs in metallic $CaRuO_3$.

The present full-potential linear-muffin–tin orbital [19] (FPLMTO) calculations are all-electron, and no shape approximation to the charge density or potential has been used. The basis functions, charge density and potential were expanded in spherical harmonic series inside the muffin-tin spheres and in Fourier series in the interstitial regions. The calculations are based on the generalized-gradient-corrected (GGA) density-functional theory as proposed by Perdew et al. [20]. Spin–orbit (SO) terms are included directly in the Hamiltonian matrix elements for the part inside the muffin-tin spheres. The basis set contained semi-core 4p and valence 5s, 5p, and 4d states for Sr, 4s, 4p, and 3d states for Ca, 5s, 5p, and 4d for Ru, 2s, 2p, and 3d states for O, and 4s, 4p, and 3d states for K. All orbitals were contained in the same energy panel. The self consistency was obtained with 284 k points in the irreducible part of the first Brillouin zone for the orthorhombic structure and the same density of k points were used for the cubic structure as well as for the supercells. Structural parameters for $Sr_{1-x}Ca_xRuO_3$ are taken from the X-ray diffraction data reported by Kobayashi et al. [21]. Details about the experimental reexamination of $CaRuO_3$ will be presented in the full account of our findings [22].

There are three possible magnetic arrangements according to the interplane and intraplane couplings in perovskite

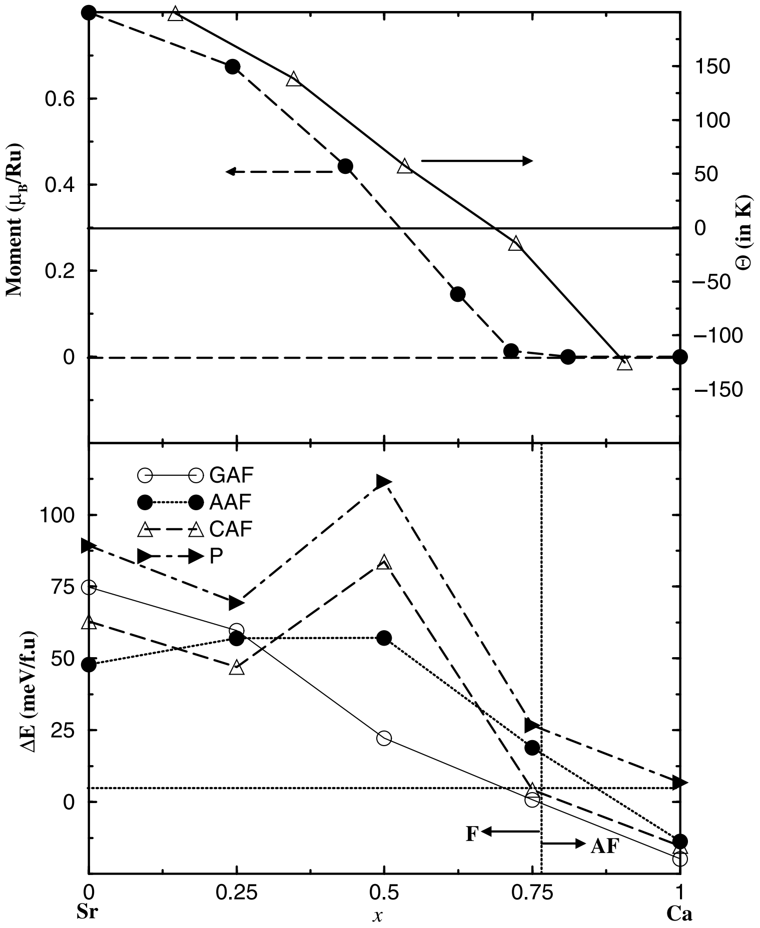

Fig. 1. Magnetic phase diagram data for $Sr_{1-x}Ca_xRuO_3$. Energies are given with respect to the total energy for the F phase.

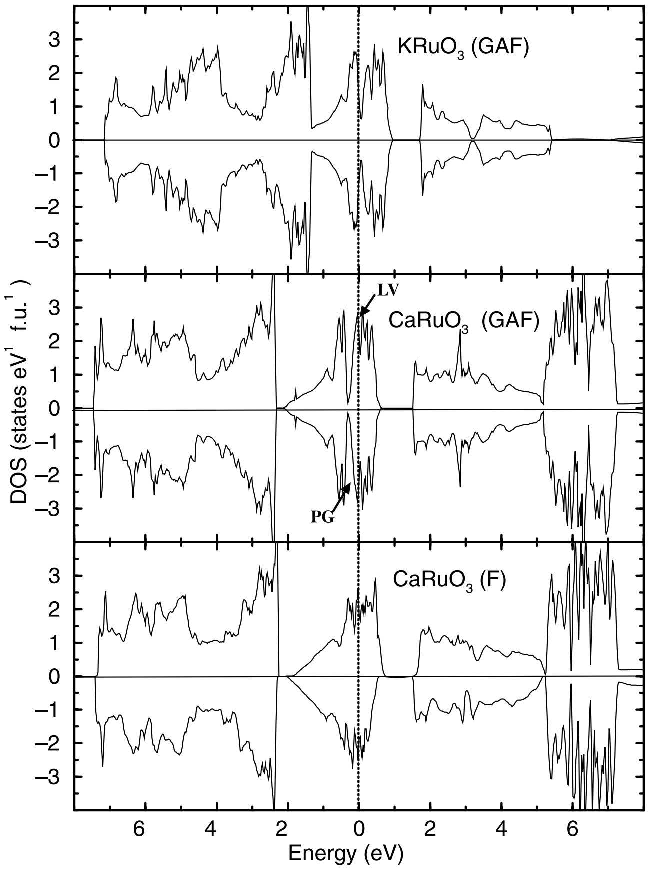

Fig. 2. Total DOS for $CaRuO_3$ in F and G-AF states and hypothetical $KRuO_3$ in G-AF state. Fermi level is set to zero.

oxides. (i) With interplane AF coupling and intraplane F coupling the A-AF structure arises. (ii) The opposite arrangement with interplane F coupling and intraplane AF coupling is called C-AF structure. (iii) If both the inter- and intraplane couplings are AF the G-AF structure arises. In the G-type AF lattice, each Ru atom will be surrounded by six Ru neighbors whose moments are antiparallel to that of the chosen reference atom. The details about the calculations on magnetic and excited state properties can be found elsewhere [23]. We have placed the magnetic moment direction along [001] in all calculations to comply with the out-of-plane easy axis observed for $Sr_{1-x}Ca_xRuO_3$ [24]. The energy differences between the various magnetic configurations are very small and extreme computational accuracy is therefore needed. The theoretical method used in the present study is capable of reproducing energy differences of the order of μeV [25].

The calculated total energy for $CaRuO_3$ from the GGA calculation with (GGA + SO) and without SO coupling are given in Table 1 relative to the corresponding ground state. From this table it is clear that the G-AF phase is the ground state for $CaRuO_3$. The total energy differences between the different AF phases are as already mentioned very small. If we disregard the orthorhombic distortion, the F phase is seen to have the lowest energy indicating that strong magneto-elastic couplings are present in $CaRuO_3$. We also see large energy gains when we include the orthorhombic distortion in the calculation consistent with experimental observation. The F phase is found to be the ground state with 7 meV/f.u. lower energy than the G-AF phase when SO interactions are neglected. Hence, SO coupling appears to play an important role in deciding the magnetic properties of ruthenates.

The calculated magnetic moment at the Ru site in $SrRuO_3$ is 0.92 μ_B/atom is in good agreement with 0.85 μ_B/atom obtained from magnetization measurements [9]. Goodenough [26] has argued that, in general, a spontaneous change between F and AF states are expected when $\mu_F \approx \mu_{AF}$, the stable magnetic phase being the one with the highest atomic moment. Our findings are consistent with this viewpoint in that the larger magnetic moments are found for the stable magnetic configuration of $Sr_{1-x}Ca_xRuO_3$ (viz. for $x < 0.724$ the F phase has highest magnetic moment and for $x > 0.724$ G-AF has the highest moment). The hyperfine field at the Ru site in G-AF state $CaRuO_3$ is 263 kOe/μ_B in agreement with the experimental value of 222 ± 50 kOe/μ_B obtained from Knight shift measurements [27].

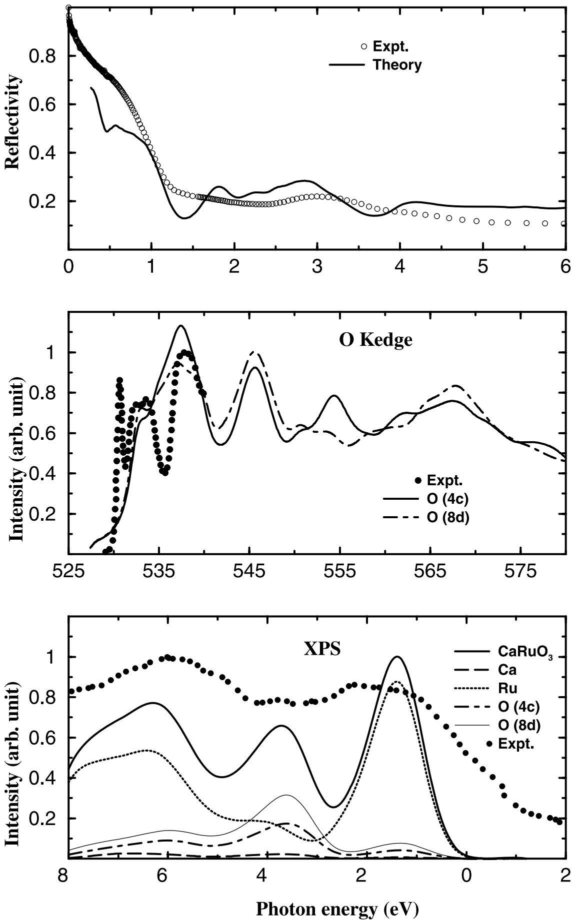

Fig. 3. Calculated valence band XPS, O K-edge XANES, and optical reflectivity spectrum for G-AF state $CaRuO_3$. Experimental XPS, XANES and reflectivity spectra are taken from Refs. [30,31].

The experimentally found spontaneous magnetic moment [13] and Weiss temperature [28] for $Sr_{1-x}Ca_xRuO_3$ are given in Fig. 1 along with the calculated total energy difference relative to that of the F phase for the various magnetic configurations. An increase in x decreases the F interaction and increases the G-AF interaction. Because of the smaller ionic radius of Ca compared with Sr (0.99 vs. 1.18 Å), tilting of the octahedra occur when one substitutes Ca for Sr in $SrRuO_3$ which in-turn affects the magnetic properties. Fig. 1 shows that the F to G-AF transition takes place around $x = 0.75$ both experimentally and theoretically. This confirms the presence of AF interactions in $CaRuO_3$. One of the interesting aspects of Fig. 1 is that at $x = 0.5$, there is large gain in the total energy of the F phase compared with the P, A- and C-AF phases. DOS analyses show that the F phase of $Sr_{0.5}Ca_{0.5}RuO_3$ is nearly half-metallic with a gap of 0.73 eV in the majority spin channel which gives extra contribution to the stability. Moreover, E_F is at peaks in the DOS curves of the P, A- and C-AF phases (which further contribute to the enhanced energy difference relative to the F state).

The lower total energy for the G-AF state for $x > 0.724$ compared with the other magnetic configurations can be understood as follows. The spin-projected total DOS curve for $CaRuO_3$ in the F and G-AF phases are shown in the lower and middle panel of Fig. 2. In the F case E_F is at a peak-like feature in the DOS curve. This infers an instability to the lattice. However, for the G-AF phase a deep valley-like (PG-like) feature appears in the DOS curve. This will give an extra contribution to lattice stability [29] and hence $CaRuO_3$ is expected to stabilize in the G-AF phase. The calculated excited-state properties such as reflectivity, O K-edge spectra and XPS spectra for $CaRuO_3$ in the G-AF phase are found to be in good agreement with experimental spectra (see Fig. 3), indicating that the ground state is correctly assigned. The creation of a PG-like feature on introduction of G-AF ordering gives an extra contribution to the band energy term of the total energy (66 meV/f.u.) which stabilizes the G-AF phase over the F phase. However, our neutron powder diffraction diagrams at 298 and 8 K show no sign of extra Bragg reflections at 8 K, which should have been the proof of long-range AF ordering. (A full account of the neutron diffraction findings will be given in the forthcoming article [22].) Hence, the magnetic exchange interactions must have only short-range influence. Closer examination of the DOS curve for the G-AF phase shows that E_F is located on a shoulder of a peak-like feature (an unfavorable condition for stability) with a local valley (LV, see Fig. 2) situated just 40 meV above E_F. This may explain why there is no established long-range magnetic ordering in this material. Recent magnetization measurements [17] show distinctions between the zero-field-cooled and field-cooled characteristics which confirm the presence of SG behavior with finite moments at the Ru sites. So, we conclude that $CaRuO_3$ exhibits short-range AF ordering which manifests itself in SG behavior at low temperature.

Rigid-band-filling analysis shows that an addition of 0.136 electrons/f.u. will bring E_F to LV with the expected effect of long-range G-AF ordering. In fact, long-range magnetic ordering has been observed for $CaRu_{1-x}Rh_xO_3$ with $x > 0.015$ where Rh acts as an electron donor for $CaRuO_3$ [32]. Rigid-band-filling analysis also show that removal of exactly one electron from $CaRuO_3$ will bring E_F to a PG. In order to test this possibility we have made additional calculations for hypothetical $KRuO_3$ with the structural parameters for $CaRuO_3$. Consistent with the rigid-band-filling findings E_F is found at PG for the G-AF phase of hypothetical $KRuO_3$ (see upper panel of Fig. 2). When E_F is at PG, all bonding states would be filled and all antibonding states empty, implying extra contributions to stability. Total energy calculations show that the G-AF phase is 21.7 meV/f.u. lower in energy than the F phase for hypothetical $KRuO_3$, viz. a larger difference than that for $CaRuO_3$ indicating that one really should expect G-AF long-range ordering in $KRuO_3$ at low temperature. Further the G-AF phase is 38.6 meV/f.u. lower in energy than the P phase for hypothetical $KRuO_3$ indicating that T_N should be reasonably high. It is worth to recall that according to Goodenough [33] the sign of the transfer integral for 180° cation–anion–cation superexchange interactions between octahedral-site cations are predicted to give AF for Ru^{5+}–O–Ru^{5+}. Ru^{5+} ions with enhanced AF interaction has recently been established for $CaRu_{0.95}Cu_{0.05}O_3$[34]. Moreover, the change in the oxidation state of $Sr_3Ru_2O_7$ from Ru^{4+} to Ru^{5+} by fluorine addition stabilizes G-AF ordering [35]. Oxygen non-stochiometry and hole doping can accordingly bring E_F toward PG and stabilize the G-AF ordering. This may explain why long-range AF ordering has been reported for some experimentally studied $CaRuO_3$ samples [11] and Na doped $CaRuO_3$ [36].

In the SG state the moments are arranged in a certain equilibrium oriented pattern, but without long-range order. Some characteristics of SG materials are: (i) Existence of local moment as we have found with spin-polarized calculations. (ii) No magnetic Bragg scattering at low temperature as our neutron diffraction study show. (iii) A history-dependent magnetic response as the recent magnetization measurements [17] have shown. (iv) Both long-range and short-range terms in the Hamiltonian [37]. In accordance with our calculations we believe that short-range nearest-neighbor AF interactions are dominant in $CaRuO_3$.

Two important ingredients necessary to produce SG behavior are frustration and partial randomness of the interaction between the magnetic moments [38]. Owing to the small total energy differences between the AF and F phases of $CaRuO_3$ (see Table 1 and Fig. 1), there will be a competition among the different AF and F interactions, in the sense that no single configuration of the moments is uniquely favored by all interactions (viz. frustration). In other words, the AF moments can arrange themselves randomly in small domain-like regions with minimal loss in energy. The Ru ions which are responsible for the magnetic properties of $CaRuO_3$ are in a strictly periodic order. Hence, structural disorder cannot be responsible for the SG behavior. The SG state of $CaRuO_3$ is characterized by a predominant AF situation with random spin arrangement. AF systems with SG-like transition have been observed in ruthenates with pyrochlore-like structures such as $R_2Ru_2O_7$ for which recent experimental results indicate that the atomic arrangement does not participate in the P-to-SG transition which is solely associated with the Ru moments [39]. The small energy differences between the different AF states bring disordering of the moments and hence SG behavior to $CaRuO_3$ at low temperature. In fact, SG behavior has been found for $CaRuO_3$ doped with small amounts of Sn [40] or Rh [32]. The calculated excited state properties for $CaRuO_3$ in the G-AF state are in good agreement with the experimental measurements indicating that the electronic structure does not differ significantly between the SG and G-AF phases.

We conclude that $CaRuO_3$ exhibits short-range AF interaction with SG behavior. The hitherto hypothetical $KRuO_3$ is expected to exhibit long-range G-AF ordering. We have demonstrated that the relative strengths of the F and AF exchange interactions can be varied by varying the Ca content of $Sr_{1-x}Ca_xRuO_3$.

Acknowledgements

PR is grateful to the Research Council of Norway for financial support. Part of these calculations were carried out on the Norwegian supercomputer facilities.

References

[1] Y. Maeno, H. Hashimoto, K. Yoshida, s. Nisizaki, T. Fujita, J.G. Bednorz, F. Lictenber, Nature 372 (1995) 532.

[2] S. Nakatsuji, Y. Maeno, Phys. Rev. Lett. 84 (2000) 2666.

[3] I.I. Mazin, D.J. Singh, Phys. Rev. Lett. 82 (1999) 4324.

[4] L. Bauernfeind, W. Widder, H.F. Braun, Physica C 254 (1995) 151.

[5] Y.S. Lee, J.S. Lee, K.W. Kim, T.W. Noh, Y. Jaejun, E.J. Choi, G. Cao, J.E. Crow, et al., Europhys. Lett. 55 (2001) 280.

[6] P. Khalifah, K.D. Nelson, R. Jin, Z.Q. Mao, Y. Liu, Q. Huang, X.P.A. Gao, A.P. Ramirez, R.J. Cava, Nature 411 (2001) 669.

[7] R.S. Perry, L.M. Galvin, S.A. Grigera, L. Capogna, A.J. Schofield, A.P. Mackenzie, M. Chiao, S.R. Julian, S.I. Ikeda, S. Nakatsuji, Y. Maeno, C. Pfleiderer, Phys. Rev. Lett. 86 (2001) 2661.

[8] G. Cao, S. McCall, J.E. Crow, R.P. Guertin, Phys. Rev. Lett. 78 (1997) 1751.

[9] A. Callaghan, C.W. Moeller, R. Ward, Inorg. Chem. 5 (1966) 1572.

[10] P. Kostic, Y. Okada, N.C. Collins, Z. Schlesinger, J.W. Reiner, L. Klein, A. Kapitulnik, T.H. Geballe, M.R. Beasley, Phys. Rev. Lett. 81 (1998) 2498.

[11] J.M. Longo, P.M. Raccah, J.B. Goodenough, J. Appl. Phys. 39 (1968) 1327.

[12] J.L. Martinez, C. Pricto, J. Rodriguez-Carvajal, A. de Andres, M. Vallet-Regi, J.M. Gonzalez-Calbet, J. Magn. Magn. Mater. 140–144 (1995) 179.

[13] T. Kiyama, K. Yoshimura, K. Kosuge, H. Mitamura, T. Goto, J. Phys. Soc. Jpn 68 (1999) 3372.

[14] K. Yoshimura, T. Imai, T. Kiyama, K.R. Thurber, A.W. Hunt, K. Kosuge, Phys. Rev. Lett. 83 (1999) 4397.

[15] T.C. Gibb, R. Greatrex, N.N. Greenwood, P. Kaspi, J. Chem. Soc., Dalton Trans. (1973) 1253.

[16] I.I. Mazin, D.J. Singh, Phys. Rev. B 56 (1997) 2556.

[17] I. Felner, I. Mowik, I. Bradaric, M. Gospodinov, Phys. Rev. B 62 (2000) 11332.

[18] G. Santi, T. Jarlborg, J. Phys.: Condens. Matter 9 (1997) 9563.

[19] J.M. Wills, O. Eriksson, M. Alouani, D.L. Price, in: H. Dreysse (Ed.), Electronic Structure and Physical Properties of Solids, Springer, Berlin, 2000, p. 148.

[20] J.P. Perdew, S. Burke, M. Ernzerhof, Phys. Rev. Lett. 77 (1996) 3865.

[21] H. Kobayashi, M. Nagata, R. Kanno, Y. Kawamoto, Mater. Res. Bull. 29 (1994) 1271.

[22] R. Vidya, P. Ravindran, A. Kjekshus, H. Fjellvåg, B.C. Hauback (unpublished).

[23] P. Ravindran, H. Fjellvåg, A. Kjekshus, A. Delin, O. Eriksson, Phys. Rev. B (2002) in press.

[24] G. Cao, S. McCall, M. Shepard, J.E. Crow, R.P. Buertin, Phys. Rev. B 56 (1997) 321.

[25] P. Ravindran, A. Kjekshus, H. Fjellvåg, P. James, L. Nordström, B. Johansson, B. Eriksson, Phys. Rev. B 63 (2001) 144409.

[26] J.B. Goodenough, et al., in: J.T. Lopuszanski, J.T. Pekalski, J. Przystawa (Eds.), Magnetism in Metals and Metallic Compounds, Plenum Press, New York, 1974, p. 35.

[27] H. Mukuda, K. Ishida, Y. Kitaoka, K. Asayama, R. Kanno, M. Takano, Phys. Rev. B 60 (1999) 12279.

[28] F. Fukunaga, N. Tsuda, J. Phys. Soc. Jpn 63 (1994) 3798.

[29] P. Ravindran, R. Asokamani, Bull. Mater. Sci. 20 (1997) 613.

[30] M.V. Rama Rao, V.G. Sathe, D. Sornadurai, B. Panigrahi, T. Shripathi, J. Phys. Chem. Solids 62 (2001) 797.

[31] J.S. Lee, Y.S. Lee, T.W. Noh, K. Char, J. Park, S.-J. Oh, J.-H. Park, C.B. Eom, T. Takeda, R. Kanno, cond-mat/0107375, 2001.

[32] G. Cao, F. Freibert, J.E. Crow, J. Appl. Phys. 81 (1998) 3884.

[33] J.B. Goodenough, Magnetism and the Chemical Bond, Wiley, New York, 1963.

[34] I.M. Bradaric, I. Felner, M. Gospodinov, cond-mat/0107170, 2001.

[35] R.K. Li, C. Greaves, Phys. Rev. B 62 (2000) 3811.

[36] M. Shepard, G. Cao, S. McCall, F. Freibert, J.E. Crow, J. Appl. Phys. 79 (1996) 4821.

[37] D. Chowdhury, Spin Glasses and Other Frustrated Systems, World Scientific, Singapore, 1986, p. 7.

[38] K.H. Fischer, J.A. Hertz, Spin Glasses, Cambridge University Press, Cambridge, 1997, p. 2.

[39] M. Ito, Y. Yasui, M. Kanada, H. Harashna, S. Yoshii, K. Murata, M. Sato, H. Okumura, K. Kakurai, J. Phys. Chem. Solids 62 (2001) 337.

[40] G. Cao, S. McCall, J. Bolivar, M. Shepard, F. Freibert, P. Henning, J.E. Crow, T. Yuen, Phys. Rev. B 54 (1996) 15144.

XIII

ACADEMIC PRESS

Available online at www.sciencedirect.com

SCIENCE DIRECT®

Journal of Solid State Chemistry 177 (2004) 146–158

JOURNAL OF SOLID STATE CHEMISTRY

http://elsevier.com/locate/jssc

Magnetic properties of Ca-doped $SrRuO_3$ from full-potential calculations

R. Vidya,[a] P. Ravindran,[a,*] A. Kjekshus,[a] H. Fjellvåg,[a] and B.C. Hauback[b]

[a] *Department of Chemistry, University of Oslo, Box 1033, Blindern, N-0315, Oslo, Norway*
[b] *Institute for Energy Technology, P.O.Box 40, Kjeller, N-2007, Norway*

Received 18 March 2003; received in revised form 6 June 2003; accepted 3 July 2003

Abstract

We have carried out accurate generalized-gradient-corrected fully-relativistic full-potential calculations for $Sr_{1-x}Ca_xRuO_3$ ($x = 0$, 0.25, 0.5, 0.75, and 1) in para-, ferro-, and *A*-, *C*-, and *G*-type antiferromagnetic configurations. We have performed electronic structure calculations for the experimentally observed orthorhombic structure as well as the hypothetical cubic structure. Our results are analyzed with the help of total, site-, spin-, and orbital-projected density of states. The total-energy studies show that $CaRuO_3$ stabilizes in the *G*-type antiferromagnetic state. The octahedral tilting owing to the relatively small radius of Ca^{2+} leads to weak hybridization between Ru 4*d* and O 2*p*. This weak hybridization along with exchange splitting causes a pseudogap-like feature close to the Fermi level, which should stabilize *G*-type antiferromagnetic ordering in $CaRuO_3$. However, powder neutron diffraction data on $CaRuO_3$ taken at 8 and 298 K do not show any magnetic peaks, implying that $CaRuO_3$ exhibits a spin-glass-like state with dominant short-range antiferromagnetic interaction. The calculated magnetic ground state of $Sr_{1-x}Ca_xRuO_3$ is found to be consistent with the experimental findings. We have also calculated optical spectra as well as X-ray and ultra-violet photoemission spectra and Ru and O *K*-edge X-ray absorption spectra for *G*-type $CaRuO_3$ and found good agreement with available experimental spectra.

© 2003 Elsevier Inc. All rights reserved.

PACS: 71.; 71.20.-b; 75.50.Ee; 78.20.Ci

Keywords: Ruthenates; Magnetic properties; Spin-glass behavior; Excited properties

---

1. Introduction

Although oxides containing 4*d* and 5*d* metals have been known for a long time, their physical properties remain largely unexplored. However, since the discovery of superconductivity for some such oxides, this class of compounds have been studied intensively. The ruthenium-based perovskite $CaRuO_3$ is found to fulfill some of the requirements to an electrode material for solid-oxide fuel cells such as metallic conductivity and high chemical stability [1,2]. Moreover its high topotactic reduction/oxidation properties [3] make it interesting for catalysis purposes and its possible technological significance is enhanced by the observation of a strain induced metal–insulator transition in thin films [4]. $CaRuO_3$ epitaxial thin films have easy growth, good stability (with characteristics similar to those of single crystals), and only a small lattice mismatch with $YBa_2Cu_3O_{7-\delta}$ substrates. Hence, it is one of the most promising candidates for formation of epitaxial heterostructures with other perovskites, say, like electrodes for superconductor-to-normal-metal-to-superconductor junctions [5], field-effect transistors with oxide-superconductor channels, ferroelectrics [6], and magnetic multilayers. Particularly, the ferroelectric material $Bi_4Ti_3O_{12}$ has a low lattice mismatch with $CaRuO_3$ making it suitable as substrate for bottom electrodes of a ferroelectric random-access memory [7].

In order to exploit $CaRuO_3$ for technological applications, knowledge about its ground- and excited-state properties is essential. Although $SrRuO_3$ and $CaRuO_3$ are similar both structurally and chemically, their magnetic properties appear to be different. $SrRuO_3$ is a metallic conducting ferromagnet (F) [8,9], whereas the magnetic ground state of $CaRuO_3$ is still

---

[*] Corresponding author.
E-mail address: ponniah.ravindran@kjemi.uio.no (P. Ravindran).

0022-4596/$ - see front matter © 2003 Elsevier Inc. All rights reserved.
doi:10.1016/S0022-4596(03)00386-4

shrouded under controversy, but certainly not a clear-cut F state.

According to Callaghan et al. [8] $CaRuO_3$ follows Curie–Weiss law at high temperatures with negative Weiss constant (Θ). Longo et al. [9] were the first to "identify" a Néel temperature of 110 ± 10 K. The recent value for Θ is -160 K and the deviation from Curie–Weiss law classifies it as antiferromagnetic-like (AF) [10]. However, Mössbauer spectroscopic data collected [11] down to 4.2 K did not show magnetic splitting, and the absence of magnetic peaks in powder neutron diffraction (PND) diagrams [12] at 1.5 K appears to preclude the existence of long-range AF ordering in $CaRuO_3$. Martinez et al. [12] also report a clear departure from Curie–Weiss law behavior below 70 K which is interpreted as an indication of short-range AF correlations.

The low-temperature resistivity of $CaRuO_3$ shows [13] non-Fermi-liquid (NFL) behavior, a phenomenon theoretically expected near a quantum-critical point induced by a 0 K phase transition to an AF state. However, the measured magnetoresistance (MR) is positive at 5 K and low fields and becomes negative above ~ 40 K. In non-magnetic pure metals and alloys MR is generally positive and shows a quadratic dependence on the magnetic field. MR can be negative in magnetic materials as a result of suppression of the moment disorder by the magnetic field [14]. However, a transition to positive MR at low temperature while the magnetic susceptibility still increases is less expected. This suggests that changes in the behavior of the magnetic moments may occur.

Ab-initio calculations have so far not been able to resolve the contradictory experimental findings on the magnetic properties of $CaRuO_3$. Santi et al. [15] have performed extensive TBLMTO calculation on $CaRuO_3$ and obtained an F ground state, but without considering the possibility of AF states. They noted that the orthorhombic distortion favors cooperative magnetic states such as F, Ferri, and AF. Mazin and Singh [16] carried out full-potential LAPW calculation for the paramagnetic (P) and F states, and found that $CaRuO_3$ is in P state, but on the verge of F ordering. Their fixed-moment calculations show that the total energy of $CaRuO_3$ is nearly independent of magnetization up to 1 μ_B. Some of the present authors have earlier obtained the correct *A*-AF insulating ground state for $LaMnO_3$ [17], the *C*-AF state for $LaVO_3$ [18], and the *G*-AF state for $LaFeO_3$ [18]. This motivated us to probe the magnetic structure of $CaRuO_3$ by adopting the same procedure (accurate state-of-the-art relativistic-full-potential total-energy calculations), for all possible magnetic orderings with the interplane and intraplane ferro/AF exchange interactions. However, noncollinear magnetic configurations are not considered in the present study. We have done extensive electronic structure calculations on $Sr_{1-x}Ca_xRuO_3$ which may provide insight into why the isostructural $SrRuO_3$ and $CaRuO_3$ phases can take entirely different magnetic ground states. Since the magnetic ordering is contributed by the 4*d* electrons of Ru, relativistic effects such as spin–orbit (SO) coupling may be significant for this material. The reliability of the results can be improved by including inhomogeneity effects through the generalized-gradient approximation (GGA) [17]. Therefore, we have used a fully-relativistic full-potential method (with GGA) for the experimentally observed orthorhombic $GdFeO_3$-type (distorted perovskite) structure for $Sr_{1-x}Ca_xRuO_3$ as well as a postulated (hypothetical) ideal cubic perovskite structure for $CaRuO_3$. In an earlier study [19] the optical transition in $CaRuO_3$ is interpreted as a Mott–Hubbard transition, indicating that the compound is a strongly correlated material. However, a recent experimental optical property study [20] suggests that correlation effects are less significant. Hence a theoretical optical properties study has also been undertaken.

The rest of the paper is organized as follows. Structural aspects are described in Section 2.1, computational and experimental details are given in Sections 2.2 and 2.3, respectively. In Section 3 we discuss the magnetic ground state and electronic structure with the help of band structure, total, site-, and angular-momentum projected as well as orbital-projected density of states (DOS) curves. Excited state properties such as optical, ultra-violet photoemission (UPS), X-ray photoemission (XPS), and Ru and O *K*-edge X-ray absorption (XANE) spectra are considered in Section 4, and Section 5 summarizes the important findings.

2. Structural aspects, computational and experimental details

2.1. Crystal structure

$CaRuO_3$ stabilizes in the orthorhombic $GdFeO_3$-type structure comprising four formula units. The structural parameters obtained from PND and single-crystal X-ray diffraction data [3] are given in Table 1. The orthorhombic structure can be viewed as a highly distorted cubic perovskite structure with a quadrupled unit cell ($a_c\sqrt{2}$, $a_c 2$, $a_c\sqrt{2}$ where a_c is the lattice parameter of the cubic perovskite). The relatively small size of Ca^{2+} leads to tilting of the octahedra in order to fill the space efficiently. The tilted octahedra form zig-zag chains through the corner-sharing linkage. The tolerance factor is a measure of tilting of the octahedra which is defined as $(R_A + R_O)/[\sqrt{2}(R_M + R_O)]$, where R_A, R_M, and R_O are the ionic radii for *A*, *M*, and O, respectively. The tolerance factor for $CaRuO_3$ is 0.88 which may be taken as another measure for the quite large distortion of this particular atomic arrangement. The Ru–O–Ru bond angle is ~150° and the O–Ru–O angle ~92° at 293 K. The deviation of the Ru–O–Ru angle from 180° plays an important role for the ground-state properties of $CaRuO_3$. In order to evaluate the role of the orthorhombic distortion on electronic structure and ground-state properties, we have done calculations also for a hypothetical undistorted cubic perovskite structure. For the calculations on the ideal cubic variant we have used the experimental equilibrium volume of the orthorhombic structure. We found that it is important to use a consistent structure for different magnetic configurations to avoid the errors arising from the computational parameters. So, we have expressed the cubic structure into an equivalent orthorhombic structure with four formula units (i.e. $a = c = a_c\sqrt{2}$ and $b = 2a_c$). For the electronic structure calculations of $Sr_{1-x}Ca_xRuO_3$ we have used the structural description given in Ref. [21]. We have constructed a supercell consisting of four formula units and periodically replaced Sr by Ca. For example, $Sr_{0.25}Ca_{0.75}RuO_3$ contains one Sr and three Ca atoms in the supercell considered for calculations.

Four magnetic arrangements are possible depending on the interplane and intraplane couplings in perovskite oxides like $Sr_{1-x}Ca_xRuO_3$ (Fig. 1). (i) The ferromagnetic case where both inter- and intraplane couplings are F. (ii) With interplane AF coupling and intraplane F coupling the *A*-AF structure arises. (iii) The opposite arrangement with interplane F coupling and intraplane AF coupling is called *C*-AF structure. (iv) If both the inter- and intraplane couplings are AF the *G*-AF structure arises. A more detailed description of the different AF orderings is found in Ref. [17].

Table 1
Crystallographic data for $CaRuO_3$ derived by Rietveld analysis of PND data collected at 8 K

Parameter	PND; 8 K	SXD; 296 K
a (Å)	5.5311(2)	5.524(1)
b (Å)	7.6460(3)	7.649(2)
c (Å)	5.3408(2)	5.354(1)
Ca *x*	0.9443(4)	0.9448(4)
z	0.0125(7)	0.0139(2)
O(1) *x*	0.0218(4)	0.0258(6)
z	0.5939(4)	0.5920(6)
O(2) *x*	0.2020(3)	0.2021(5)
y	0.4514(2)	0.4518(3)
z	0.1980(3)	0.1973(4)

Space group *Pnma*; Ca and O(1) in 4*c*, Ru in 4*b*, and O(2) in 8*d*. Calculated standard deviations are given in parantheses. Single-crystal X-ray diffraction (SXD) data taken from Ref. [3] are included for comparison.

2.2. Computational details

The full-potential LMTO calculations [22] presented in this paper are all electron, and no shape approximation to the charge density or potential has been used. The base geometry in this computational method consists of muffin-tin and interstitial parts. The basis set is comprised of augmented linear muffin-tin orbitals [23]. Spherical-harmonic expansion of the charge density, potential, and basis functions were carried out up to $\ell = 6$. The calculations are based on the generalized-gradient-corrected density-functional theory as proposed by Perdew et al. [24].

The SO term is included directly in the Hamiltonian matrix elements for the part inside the muffin-tin spheres, hence for a spin-polarized case the size of the secular matrix is doubled. The present calculations made use of the so-called multi basis, which is important to obtain a reliable description of the higher lying unoccupied states, especially for the optical properties. The basis included 4*s*, 4*p*, and 3*d* states for Ca, 5*s*, 5*p*, and 4*d* states for Ru, and 2*s*, 2*p*, and 3*d* states for O. Earlier studies [16,15] have shown that the magnetic properties of ruthenates are very sensitive to the **k**-point density and hence the **k**-space integration for the total energetics was done using the special point method with 284 **k** points in the irreducible part of the first Brillouin zone (IBZ) for both the orthorhombic and cubic structure. The test calculations show that we have used well-converged **k**-point set. The experimental studies on single crystal show that the easy magnetization axis is along *c* for $CaRuO_3$ [25] as well as $Sr_{1-x}Ca_xRuO_3$ [26] and hence we have chosen [001] as the magnetization axis for all spin-polarized calculations. Using the derived self-consistent potentials, the imaginary part of

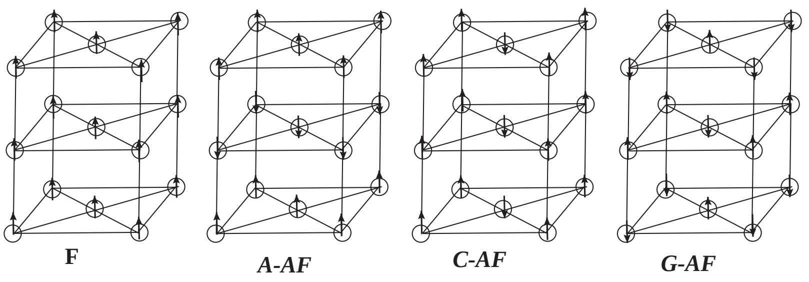

Fig. 1. The different types of magnetic ordering considered for the calculations of $Sr_{1-x}Ca_xRuO_3$.

the optical dielectric tensor and the band structure of $CaRuO_3$ were calculated for the *G*-AF state. The DOS was calculated using the linear tetrahedron technique. For the calculations of optical properties 584 **k** points are used in IBZ. The knowledge of both the real and imaginary parts of the dielectric tensor allows calculations of reflectivity, absorption coefficient, electron energy-loss spectrum (EELS), and refractive index. For this purpose we follow the definitions given in Ref. [27].

For metals, the intraband contribution to the optical dielectric tensor influences the lower-energy part of the spectra. This has been calculated using the unscreened plasma frequency obtained from Fermi surface integration according to the description in Ref. [27]. In order to calculate the unscreened plasma frequency and orbital-projected DOS (for *G*-AF state orthorhombic $CaRuO_3$) we have used the full-potential linearized augmented plane-wave (FPLAPW) method [28] in a scalar-relativistic version, without SO coupling. For these calculations we used atomic sphere radii (R_{MT}) of 2.1, 2.0, and 1.7 a.u. for Ca, Ru, and O, respectively. The charge density and the potentials are expanded into lattice harmonics up to $L = 6$ inside the spheres and into Fourier series in the interstitial region. The basis set included 4*s* valence states for Ca, 5*s*, 5*p*, and 4*d* for Ru, and 2*s* and 2*p* for O. Exchange and correlation are treated within GGA using the parameterization scheme of Perdew et al. [24]. To ensure convergence, 244 **k** points in IBZ were used. The results discussed in the following sections refer to the orthorhombic structure except where specifically mentioned as cubic.

2.3. Experimental

The synthesis of $CaRuO_3$ was performed by a standard solid-state reaction between well mixed fine powders of $CaCO_3$ (p.a., Merck; dried at 450°C for 1 day) and RuO_2 (99.9%, Aldric). The powder mixture was pelletized and calcined at 1200°C for 2 days in air. After cooling to room temperature the sample was carefully grinded, repelletized and the heat treatment was repeated.

The thus obtained sample was characterized by powder X-ray diffraction at 25°C with a Siemens D5000 diffractometer with reflection geometry using monochromatic Cu$K\alpha_1$ radiation from an incident beam Ge monochromator. The sample was mounted on a single crystal Si sample holder, the detector was a Brown PSD, and the diffraction pattern was collected over the 2θ range 10–90°. All reflections were indexed in accordance with the structural data for $CaRuO_3$ and the sample was accordingly considered phase pure.

The sample was also subjected to thermogravimetric analysis with a Perkin-Elmer TGA7 system in air. A silica-glass container was used as sample holder. The heating rate was $10°C\ min^{-1}$ and the sample size was ~ 50 mg. The heating sequence (temperature in °C was): $25 \rightarrow 1200 \rightarrow 500$ (held for 5 h) $\rightarrow 25$. This heat treatment exposed no mass changes which could have been an indication of variation in oxygen stoichiometry.

High-resolution PND data (Fig. 2) for $CaRuO_3$ were collected at 8 and 298 K with the PUS two-axis diffractometer [$\lambda = 1.555$ Å, focussing Ge(511) monochromator] accommodated at the JEEP II reactor,

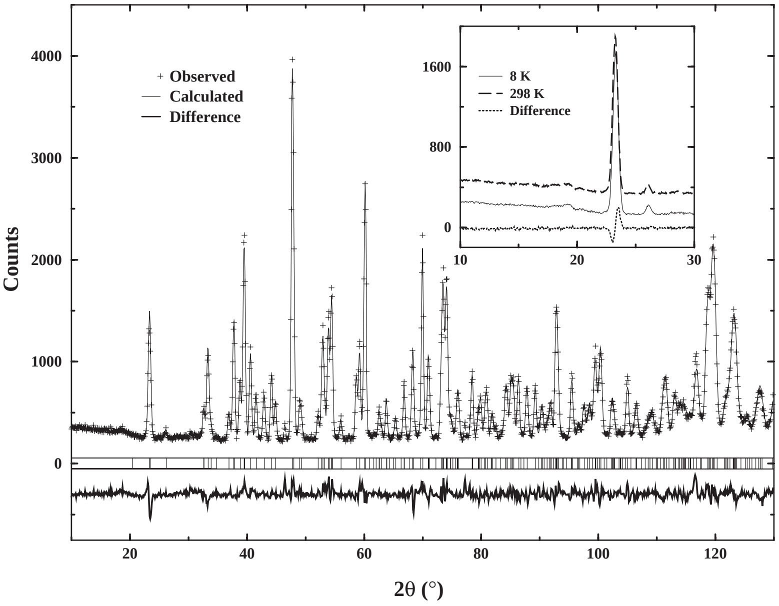

Fig. 2. Observed (crosses) and calculated (solid line) PND intensity profiles for $CaRuO_3$ at 8 K. The vertical lines indicate the positions for Bragg reflections and the lower part of figure shows the difference plot, I(obs)−I(calc). Inset shows enlarged portion of the low-angle parts of diagrams taken at 8 and 98 K with higher resolution than for the structure determination.

Kjeller, Norway. The sample was contained in a cylindrical vanadium holder with 3 mm inner diameter. A Displex cooler was used at 8 K. The diffraction pattern was registered by means of two detector banks, each covering 20° in 2θ and each containing a stack of seven position sensitive detectors [29]. The General Structure Analysis System ((GSAS) [30]) was used for Rietveld refinements of the PND data. Nuclear scattering lengths were taken from the GSAS library. The background was modelled as a cosine Fourier series polynomial (12 terms). The peak shape was modelled by a pseudo-Voight function. The PND data used for the least-squares refinements included 2400 data points (2θ range 10–30°, step length 0.05°).

3. Results and discussion

3.1. Magnetic properties

The total energy for different magnetic configurations obtained from our calculations are given in Table 2. From this table, it is obvious that $CaRuO_3$ should stabilize in the *G*-AF state. The FPLMTO method used in these calculations is capable of resolving total energy differences of the order of μRy [31] and we conclude that the energy differences of the order of meV between different magnetic configurations are significant. We are gaining around 26 meV when we include *G*-AF in the calculations. Owing to the small exchange splitting in this material, the energy difference between the different magnetic configurations is small compared to isostructural $LaMnO_3$ [17].

Table 3 shows that the Ru magnetic moment of the *G*-AF state is larger than that of F state for orthorhombic $CaRuO_3$. The magnetic moments at the O(1) and O(2) sites in the direction of Ru are 0.000 and 0.005 μ_B, respectively, in the *G*-AF state, and in the F state, 0.034 and 0.032 μ_B, respectively. The enhanced moment at the Ru site in the F state induces more moment in the O site than that in the AF state. In order to check whether the octahedral tilting plays a role in stabilizing *G*-AF, we have done similar calculations for the hypothetical cubic perovskite structure of $CaRuO_3$, in all five magnetic configurations. The results show that one loses a large amount of total energy in the cubic case indicating that the energetics associated with the octahedral tilting are higher than the magnetic energy. Interestingly, the

Table 2
Total energies (relative to the lowest energy state in meV/f.u.) of $Sr_{1-x}Ca_xRuO_3$ for the orthorhombic phase in P, F, *A*-, *C*-, and *G*-AF states using FLMTO with GGA and SO coupling

Compound	P	F	*A*-AF	*C*-AF	*G*-AF
$SrRuO_3$	89	0	48	63	75
$Sr_{0.75}Ca_{0.25}RuO_3$	69	0	57	47	59
$Sr_{0.5}Ca_{0.5}RuO_3$	111	0	57	84	22
$Sr_{0.25}Ca_{0.75}RuO_3$	27	0	19	4	0.79
$CaRuO_3$	26	19.8	6	4	0
$CaRuO_3$ (GGA without SO)	38	0	9	10	7
$CaRuO_3$ (cubic)	1307	1249	1292	1299	1303

Data for the hypothetical cubic phase of $CaRuO_3$ are included for comparison. For the cubic phase the total energies are given relative to orthorhombic *G*-AF phase.

Table 3
Calculated magnetic moment (in μ_B/Ru atom) for $Sr_{1-x}Ca_xRuO_3$ in F and *A*-, *C*-, and *G*-AF state

Compound	F	*A*-AF	*C*-AF	*G*-AF	Total	Literature
$SrRuO_3$	0.92	0.67	0.57	0.52	1.43	0.79[1], 0.85[2]
$Sr_{0.75}Ca_{0.25}RuO_3$	0.78	0.33	0.50	0.33	1.20	0.67[1]
$Sr_{0.5}Ca_{0.5}RuO_3$	0.99	0.78	0.66	0.66	1.51	0.35[1]
$Sr_{0.25}Ca_{0.75}RuO_3$	0.62 (0.38)[3]	0.30	0.53	0.53	0.77	0.01
$CaRuO_3$	0.28	0.53	0.54	0.59	0.44	1.93[4], 1.8[5]
$CaRuO_3$ (GGA without SO)	0.65	0.60	0.60	0.62	1.00	—
$CaRuO_3$ (cubic)	0.76	0.43	0.40	0.37	1.20	—

Total refers to the total magnetic moment per formula unit in the F state. The magnetic moments are calculated with FLMTO, GGA, and SO coupling. Data for the hypothetical cubic phase of $CaRuO_3$ are included for comparison.

[1] From TB-LMTO-ASA calculations. Ref. [15].

[2] From experiment, Ref. [32].

[3] Ru atoms have different magnetic moments depending upon the nearest-neighbors, see text.

[4] Measured spontaneous magnetic moment per Ru atom, Ref. [33].

[5] From magnetization measurement, Ref. [8].

ground state of the hypothetical cubic phase is F indicating the presence of strong magneto-elastic coupling in this material. In order to understand the role of the SO coupling on the magnetic properties of ruthenates we have made total-energy studies for all five magnetic configurations of $CaRuO_3$ neglecting the SO coupling. For orthorhombic $CaRuO_3$ without inclusion of SO coupling, the F state represents the lowest energy configuration with 7 meV/f.u. lower energy than the *G*-AF state (Table 2). This strongly suggests that the SO coupling plays an important role in deciding the magnetic properties of ruthenates.

The establishment of *G*-AF as the most probable ground state motivated a redetermination of $CaRuO_3$ by the PND technique. However, a very careful examination of the 8 and 298 K PND diagrams (Fig. 2) [32,35] showed no sign of cooperative long-range AF ordering at low temperatures (in agreement with Refs. [11,12]). Hence, the exchange interactions in $CaRuO_3$ must be short ranged. Recent magnetization measurements [25] show irreversibility in the zero-field-cooled and field-cooled characteristics indicating spin-glass (SG) behavior. Compared with the energy difference between the *G*-AF and F states of $SrRuO_3$ (Table 2), the energy differences between the magnetic states of $CaRuO_3$ are small indicating that SG is a very likely state for $CaRuO_3$. Some of the common characteristics of SG states are: (i) Existence of a local moment. (ii) Absence of long-range magnetic order. (iii) Higher susceptibility with field-cooled than zero-field cooled treatment. $CaRuO_3$ is found to possess all these characteristics (present results and Ref. [25]). In addition, as a result of the small energy difference between the magnetic states of $CaRuO_3$, the SG behavior of this material may also be facilitated by small perturbations from, say, oxygen nonstoichiometry (MnO exhibits AF ordering, $MnO_{1.01}$ shows SG behavior [34]), impurities (SG behavior is reported in Sn- [35] and Rh-doped [36] $CaRuO_3$), etc. It may also be recalled that SG behavior has been observed in La_2MnRuO_6 [37].

The main reason for SG behavior (magnetic frustration) of $CaRuO_3$ is the delicate balance between the F and (various) AF nearest-neighbor interactions. The energy difference between *A*-, *C*-, and *G*-AF states are small. Hence a competition among different AF interactions leads to a situation where no single configuration of the moments is uniquely favored by all interactions. This situation is nothing but magnetic frustration. A real SG material is expected to have both long- and short-range terms in the Hamiltonian [38]. Our calculations suggest that AF terms dominate the cooperative magnetic states of $CaRuO_3$, but PND data does not reveal any long-range magnetic ordering, leading to the belief that the AF interactions should be short-range. So we conclude that $CaRuO_3$ exhibits SG-like behavior with short-range *G*-AF ordering. This observation is consistent with experimental results such as the susceptibility measurements [10] which suggest a Weiss temperature of around 160 K and deviations from Curie–Weiss law which indicate short-range AF interactions (because no long range AF ordering is seen in PND).

We have performed similar magnetic calculations for the series $Sr_{1-x}Ca_xRuO_3$ ($x = 0$, 0.25, 0.5, 0.75, and 1). The calculated total energy and magnetic moments are given and compared with available literature data in Tables 2 and 3. From the magnetic phase diagram data in Ref. [39] it is clear that the AF-to-F transition takes place around $x = 0.75$ (from experimental studies) and $x = 0.724$ from our theoretical study. This provides additional support for the proposed dominant AF interactions in $CaRuO_3$.

According to Goodenough [40] a change between F and AF states may be expected when $\mu_F \approx \mu_{AF}$, the stable magnetic phase being the one that has highest magnetic moment. Our calculated results are consistent with this viewpoint in that the magnetic moments are found to be larger for the stable magnetic configuration in $Sr_{1-x}Ca_xRuO_3$ (see Table 2). Ru obtains two different moments (0.62 and 0.38 μ_B/Ru atom) for the F ground state of $Sr_{0.25}Ca_{0.75}RuO_3$, (Ru with two Ca atoms at close distance having the higher moment, the other value refers to Ru with one Sr and one Ca at close distance). No such distinction between Ru moments was found for the compositions $Sr_{0.5}Ca_{0.5}RuO_3$ and $Sr_{0.75}Ca_{0.25}RuO_3$. The special situation for $Sr_{0.25}Ca_{0.75}RuO_3$ being clearly related to the closeness of this composition to the change-over between dominant F and AF interaction (see above).

The calculated magnetic moment at the Ru site for $SrRuO_3$ is 0.92 μ_B/Ru atom in good agreement with 0.85 μ_B/Ru atom obtained from magnetization measurements [8]. As the Ca content decreases in $Sr_{1-x}Ca_xRuO_3$, the F interaction becomes stronger [21] (there are only insignificant changes in the Ru–O bond distance), following the decrease in the Ru–O–Ru bond angle from 164° to 150°. It is the thus weakened covalent Ru–O interaction (compared to that in $SrRuO_3$) which makes the *G*-AF state more stable than the F state. The crystal orbital Hamiltonian population (COHP) gives a quantitative measure of the bonding interaction between two constituents of a compound [41,42]. The (calculated) integrated COHP for the Ru–O covalent bond in $CaRuO_3$ and $SrRuO_3$ are 0.22 and 0.23 Ry per unit cell, respectively. Therefore we conclude that the increased tilting of the RuO_6 octahedra resulting from the smaller size of Ca^{2+} plays an important role in stabilizing an AF situation in the SG state of Ca-rich $Sr_{1-x}Ca_xRuO_3$. It is to be noted that a the sister-compounds Ca_2RuO_4 [43] and $Ca_3Ru_2O_7$ [26] take AF arrangements at low temperature. We have also made F state calculations for the closely related compounds $BaRuO_3$ [11] and $LaRuO_3$ [10] and found no spontaneous magnetism in these materials (see also Refs. [10,11,44]). So, long-range magnetic ordering or SG-like behavior is not a general feature for ruthenates.

3.2. Band structure

Since we have established that the short-range interaction is of the *G*-AF type in orthorhombic $CaRuO_3$, we here present the electronic structure for this phase. The experimentally determined [44] single-crystal electrical resistivity classifies $CaRuO_3$ as a poor metallic conductor ($\rho = 3.7 \times 10^{-3}\ \Omega\,\mathrm{cm}^{-1}$ at room temperature with a positive temperature coefficient). Fig. 3 shows that a finite number of bands cross the Fermi level (E_F), implying consistency between experiment and theory. For simplicity only bands in the energy region −8 to 8 eV are shown in Fig. 3. As Ca appears to be in a completely ionized state, only Ru and O have a predominant presence in the valence band (VB). Around −8 eV, Ru-5*s* and O-2*p* electrons show some presence. In the energy from −8 to −2.5 eV both Ru 4*d* and O 2*p* are dominant and they are hybridized. The bands in the energy range from −2 to 0.75 eV mainly originate from Ru 4*d* with small contributions from O 2*p*. From the orbital-projected DOS, it is found that the bands at E_F have predominant Ru-4*d* (t_{2g}-like) character. The well-dispersed bands from 1.5 to 5 eV in the conduction band (CB) stem mainly from Ca-4*s* and Ru-4*d* (e_g-*like*) electrons. Above 5 eV the bands have mixed character which makes it quite difficult to establish their origins.

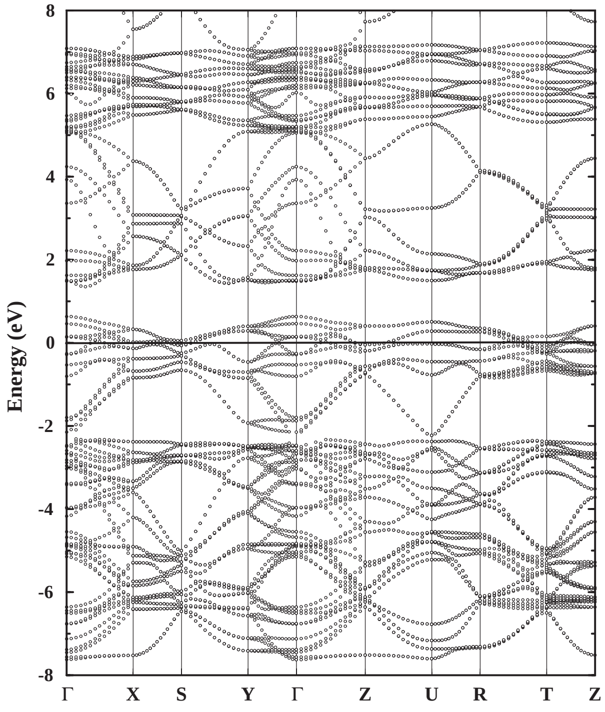

Fig. 3. Band structure of orthorhombic $CaRuO_3$ in *G*-type AF state. The solid horizontal line denotes the Fermi level.

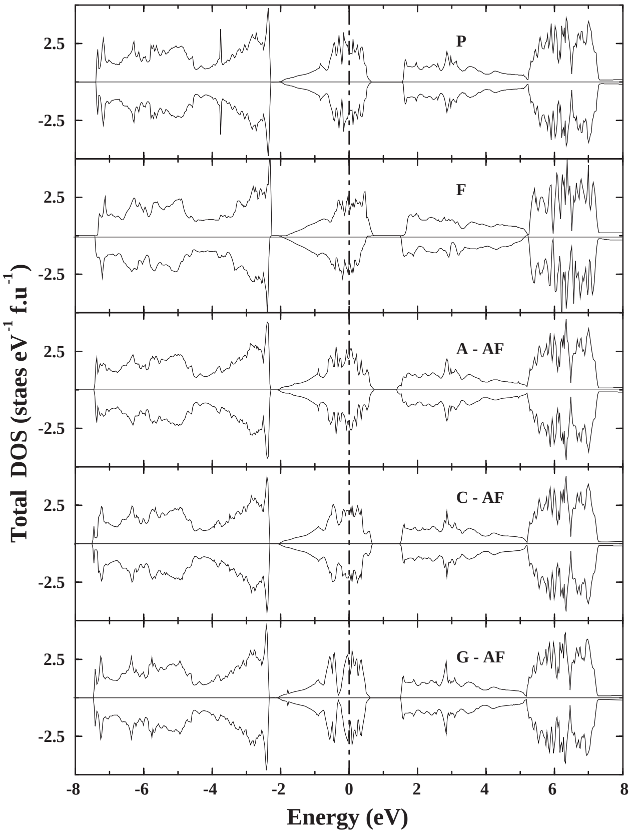

Fig. 4. Total DOS of orthorhombic $CaRuO_3$ in different magnetic configurations.

3.3. DOS

The total DOS for $CaRuO_3$ in all considered magnetic configurations are shown in Fig. 4. Although these DOS profiles appear to be similar with respect to energy, they show appreciable topological differences. In all five cases, DOS is spread out from −7.75 to −2.5 eV in VB and a small but finite gap of ~0.25 eV opens up around the latter energy region. An interesting aspect of DOS for the *C*- and *G*-AF states is the occurrence of a valley-like feature (pseudogap-like feature, called PG-like, hereafter) in the vicinity of E_F (around −0.31 eV). It should be noted that similar pseudogap feature is observed [45] experimentally for the closely related phase $BaRuO_3$. As the PG-like feature is also favorable for stability, one should expect orthorhombic $CaRuO_3$ to stabilize in a *C*- or *G*-AF magnetic structure. A pseudogap is known to occur due to covalent hybridization, exchange splitting, charge transfer, and/or *d* resonance [46]. If the valence electrons of the constituents of a compound exist in the same energy region, their wave functions will mix strongly with each other and this covalent hybridization increases the bond strength by pulling the electrons concerned to lower energy and thereby produce a pseudogap. In the present case, apart from the Ru-4*d* and O-2*p* hybridization which splits the t_{2g}-like electrons, the exchange splitting by the *C*/*G*-AF ordering causes the PG-like feature. Moreover, the PG-like feature is predominant in the *G*-AF phase indicating that the nearest neighbor AF interaction plays an important role in its creation. The presence of the PG-like feature will contribute to the total energy as a gain in band energy. Our calculations show that the gain in the band energy is 66 meV for *G*-AF compared with the F state. This finding clearly shows that the PG-like feature is responsible for the stabilization of the *G*-AF phase over the other phases considered.

However, a closer investigation of the DOS profile for the *G*-AF state shows that the PG-like feature is not exactly at E_F (which would have enhanced the stability) and the location of E_F close to a sharp peak-like feature may in fact, induce a degree of instability to the phase. This provides an additional hint as to why long-range antiferromagnetic ordering is lacking in $CaRuO_3$. Oxygen nonstoichiometry and hole doping can bring E_F towards the PG-like feature and stabilize the *G*-AF-type ordering. This may explain why long-range AF ordering has been reported for some $CaRuO_3$ samples [9]; Na-doped [32] and 1%-Fe-doped $CaRuO_3$ (Mössbauer spectroscopy at 4.1 K [25]). The calculated DOS at E_F $[N(E_F)]$ for the *G*-AF phase is 58.4 states/(Ry f.u.) and this yields a electronic specific-heat coefficient of $10.13\ \mathrm{mJ/mol\ K^2}$ without including electron-phonon mass-enhancement effect and spin fluctuations. The experimental electronic specific-heat [25] at low temperature for a single crystal is $77.5\ \mathrm{mJ/mol\ K^2}$.

The total DOS of cubic $CaRuO_3$ for all five magnetic configurations is shown in Fig. 5. Substantial differences in the DOS profiles are seen between the cubic and orthorhombic phases (Fig. 4, 5). Notably the small band gap of ~0.25 eV around −2 eV and the sharp peak-like feature at −2.25 eV are absent for the cubic phases. However, more significantly, E_F falls on a peak for all AF states of the cubic variant (an exchange splitting of ~0.5 eV is seen for the F state). As the location of E_F at a peak in DOS is unfavorable for stability, $CaRuO_3$ does not take the cubic arrangement. The total energy for all magnetic configurations of the cubic phase is moreover higher than those of the orthorhombic phase (see Table 2). Another interesting aspect is the absence of the PG-like feature for the cubic phase which implies that the occurrence of the feature in the orthorhombic AF phases is mainly due to octahedral tilting and further deepened by the exchange splitting. The exchange splitting of Ru 4*d* in *G*-AF orthorhombic $CaRuO_3$ is ~0.38 eV compared with 3.34 eV for Mn 3*d* in *A*-AF $LaMnO_3$ [17]. This is because, owing to the broader nature of 4*d* compared with 3*d* states, the magnetic moments of 4*d* elements (0.58 μ_B for Ru in *G*-AF $CaRuO_3$) is smaller than those of 3*d* elements (3.43 μ_B for Mn in *A*-AF $LaMnO_3$ [17]). On going from *A*- to *G*-AF orthorhombic $CaRuO_3$ the magnetic moment at the Ru site increases. Our calculated value for the exchange energy of $CaRuO_3$ is comparable with that for the closely related $SrRuO_3$ (0.5 and 0.65 eV from experimental [47] and theoretical [48] studies, respectively). Further, due to the tilting of the RuO_6 octahedra, the Ru–O hybridization interaction in $CaRuO_3$ is smaller than that in $SrRuO_3$ and hence the Ru-4*d* electrons are more localized and favor AF ordering for $CaRuO_3$.

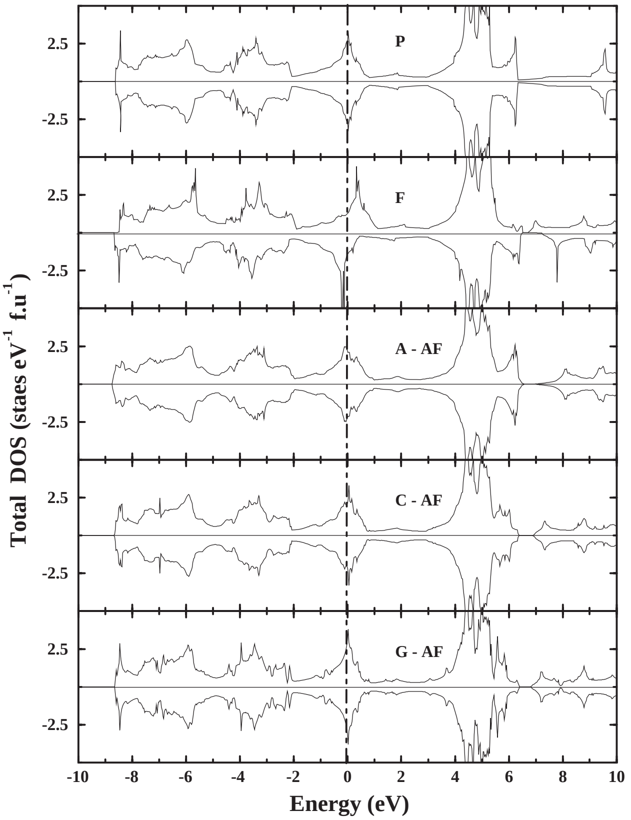

Fig. 5. Total DOS of hypothetical cubic $CaRuO_3$ in different magnetic configurations.

More insight into the electronic structure can be obtained by looking at the site-, spin-, and angular-momentum-projected DOS (Fig. 6). Ca-4*s* and -4*p* electrons have only feeble presence in VB, the indication that Ca is in a completely ionized state, donating almost all its electrons to O 2*p*. In the lowest energy range (−20 to −17 eV) the DOS is dominated by O-2*s* electrons with small contribution from Ru-5*s* and -5*p* electrons. The predominant presence of Ru-4*d* and O-2*p* states between −7.5 and E_F implies hybridization between these electrons. The PG-like feature is present both in Ru 4*d* and O 2*p*, indicating that the *d*–*p* hybridization is one of the reasons for the occurrence of the PG-like feature. The two O positions have somewhat different DOS. The

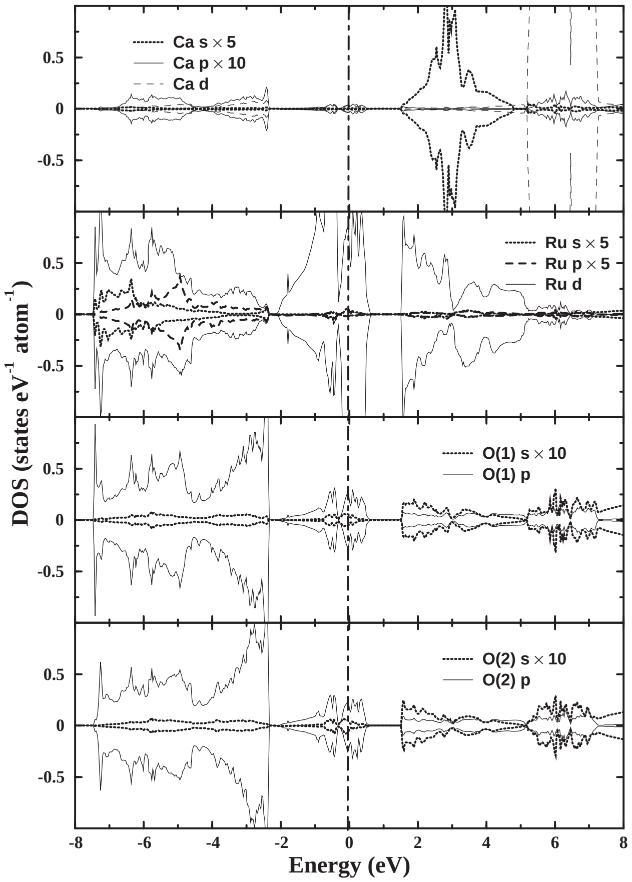

Fig. 6. Site- spin- and angular-momentum-projected DOS for orthorhombic *G*-AF $CaRuO_3$ obtained from FPLMTO method.

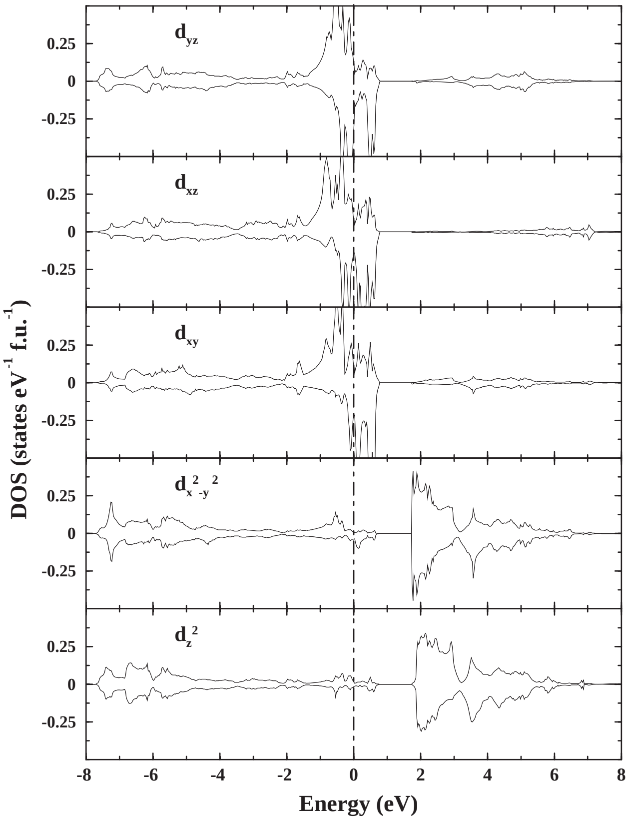

Fig. 7. Orbital-projected DOS of Ru 4*d* for orthorhombic *G*-AF $CaRuO_3$ from FPLAPW method.

sharp peak around −7.8 eV is not so well-defined for O(2) as for O(1), indicating formation of *p*–*d* σ bonding along *c*.

Earlier studies show that [1] the direct Ru–Ru interaction has been ruled out by the larger Ru–Ru separation (5.60 Å) compared with, say, 2.65 Å in metallic Ru. However, our calculations show that more than 50% of the DOS at E_F (4.29 states eV^{-1} f.u.$^{-1}$) is contributed by the Ru-4*d* electrons. This indicates that the Ru-4*d* electrons participate appreciably in the metallic conduction. Compared with $CaRuO_3$, the magnetic moment at the O site in $SrRuO_3$ is very large [16] (some 40% of the total moment resides at the O site) and this distinction is due to the tilting of octahedra in $CaRuO_3$ and also the AF ordering which yields lower induced moments at the neighbors.

In order to obtain more insight about the Ru-4*d* states in $CaRuO_3$, we show the orbital-projected DOS in Fig. 7. In the hypothetical cubic crystal structure, the *d* orbitals split into doubly-degenerate e_g-like (d_{z^2} and $d_{x^2-y^2}$; we call it e_g; usually close to E_F) and triply-degenerate t_{2g}-like (d_{xy}, d_{xz}, and d_{yz}; we call it t_{2g}; usually well-localized) states. However, owing to the large tilting of the octahedra in orthorhombic $CaRuO_3$, the t_{2g} orbitals lie close to E_F while the e_g orbitals are spread out over a wide energy range in VB and CB. From Fig. 7 it is clear that t_{2g}-electrons mainly participates in the magnetism of $CaRuO_3$. The crystal-field-splitting energy (10Dq) obtained from our orbital-projected DOS is around 2.5 eV and this value is comparable with 3.0 eV obtained from optical measurements [20] and in agreement with 2.5 eV obtained for $SrRuO_3$ by Singh [48] from LAPW calculations. The fact that 10Dq for $CaRuO_3$ is larger than that calculated for *A*-AF $LaMnO_3$ (~1.2 eV [17]) reflects the extended nature of 4*d* orbitals compared with 3*d* orbitals. Also, the strong orthorhombic distortion along with the anisotropic Coulomb potential due to the surrounding oxygen ions could influence the Ru-4*d* orbitals appreciably. The large contribution from t_{2g} over e_g electrons at E_F indicates that the t_{2g} electrons are mainly responsible for not only the magnetic properties but also for transport properties. (In $LaMnO_3$ the t_{2g} electrons contribute to magnetism and the e_g electrons to the transport properties.) Another notable aspect of the DOS profiles is that the PG-like feature is present for all t_{2g} orbitals. Owing to the tilting of octahedra, the t_{2g} orbitals participate more than the e_g orbitals in the covalent bonding with O 2*p*, and hence each of them has different DOS profiles depending upon their orientation whereas the topology of the DOS curves for the e_g

electrons do not differ much and these electrons do not participate much in the magnetism of $CaRuO_3$.

From the optical properties study [19] it has been suggested that Ru ions are in a low spin $t_{2g}^4 e_g^0$ configuration. In this case the e_g states would be empty and the t_{2g} states would have around 4 electrons. Our orbital-projected DOS (Fig. 7) shows that around 1.3 electrons are present in the e_g states and their contribution to the magnetism is negligibly small ($\sim 0.03\ \mu_B$/Ru atom). Our calculation shows that around 3.3 electrons are present in the t_{2g} states and that they are responsible for the magnetism ($\sim 0.55\ \mu_B$/Ru atom). So, the Ru ions are clearly not in a low-spin state in $CaRuO_3$ and the relatively small moment in this compound originates from the smaller exchange splitting which in turn reflects the extended nature of the 4*d* orbitals.

4. Excited state properties

4.1. Optical properties

A deeper understanding of electronic structures can be obtained by studying optical spectra which not only give information about the occupied and unoccupied states, but also about the character of bands. Therefore we have calculated optical properties for orthorhombic *G*-AF $CaRuO_3$ (Fig. 8) and compared them with available experimental data by [20,47,49–53]. Since $CaRuO_3$ is a metallic conductor, it is important to take into account the intraband contributions to the optical transitions in addition to the interband transitions. We have made use of the FPLAPW (WIEN97) code [28] for this purpose. The calculated unscreened plasma frequency (ω_p) along the crystallographic directions *a* (0.86 eV) and *b* (0.83 eV) are almost the same. However, ω_p along *c* takes a somewhat smaller value (0.66 eV) indicating some anisotropy in the transport properties. Due to the PG-like feature near E_F in $CaRuO_3$ the ω_p values are much smaller than in other transition-metal compounds. The wavelength corresponding to ω_p along *c* (5323 cm^{-1}) is somewhat larger than that (4115 cm^{-1}) obtained from infrared reflectivity measurement [50]. The discrepancy between experiment and theory can be due to thin films used in the experiments while our results are for a perfect single crystal at low temperature. Moreover, the plasma frequency obtained experimentally is estimated from the free-electron approximation which is not strictly valid for transition-metal compounds.

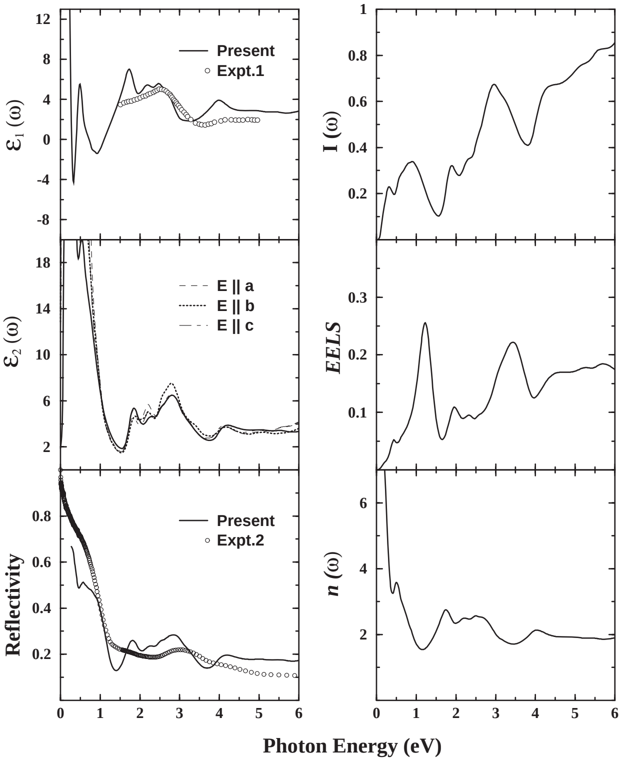

Fig. 8. Linear optical properties for orthorhombic *G*-AF $CaRuO_3$: The left panel shows reflectivity, imaginary $[\varepsilon_2(\omega)]$ and real part of optical dielectric tensor $[\varepsilon_1(\omega)]$. The right panel shows refractive index $[n(\omega)]$, electron energy loss function (EELS), and absorption coefficient [$I(\omega)$ in $10^5\ cm^{-1}$]. Experimental data are taken from Ref. [49] (Expt. 1) and Ref. [53] (Expt. 2).

As there should be one-to-one correspondence between band structure and optical spectra, we look first at the imaginary part of the optical dielectric tensor $[\varepsilon_2(\omega)]$. The transitions between the Ru-4*d* states should be forbidden for an isolated atom. However, in $CaRuO_3$, owing to the hybridization between Ru 4*d* and O 2*p* and the local lattice distortions, optical transitions between the Ru-4*d* states are possible [47]. The peak around 1.8 eV (interpreted as on-site Coulomb-repulsion energy) in $\varepsilon_2(\omega)$ is due to such intra-atomic transitions and is in good agreement with the value 1.7 eV obtained from optical measurements [20]. The smaller value of *U* for $CaRuO_3$ compared with that obtained [17] for $LaMnO_3$ ($\sim$2.22 eV) indicates that the correlation effects for $CaRuO_3$ is of little significance compared with 3*d* transition-metal oxides. A sharp peak in the lower-energy region ($<$1 eV) in the spectrum originates from intraband transitions facilitated by the metallic nature of $CaRuO_3$. However, in the experimental spectrum [49] for thin films no such peak is found, whereas such a peak-like feature is observed for $SrRuO_3$ films where it is attributed to Drude-like carrier absorption. The fact that no peak is observed for $CaRuO_3$ films is explained [49] by closeness to a metal–insulator boundary. Strain induced substitution of the small Ru^{4+} by the larger Ca^{2+} leads to metal–insulator transition in epitaxial thin films of $CaRuO_3$ [4]. However, as the electronic structure calculations and experimental transport properties [26] predict metallic features for a single crystal of $CaRuO_3$ one should really expect a peak in the experimental single-crystal spectra at the energy concerned. Consistent with this expectation a recent reflectivity measurement [53] has found such a feature (see the experimental reflectivity spectrum in Fig. 8). The two-peak features at 1.84 and 2.80 eV in the $\varepsilon_2(\omega)$ spectra originate from transitions from Ru $4d(t_{2g})$ to O $2p$ (interband) and from O $2p$ to unoccupied Ca-*s* and Ru-$4d$ (e_g) states, respectively. In order to check whether optical anisotropy is present in orthorhombic *G*-AF $CaRuO_3$, we have calculated direction-resolved spectra and show them in the same panel of Fig. 8. Some anisotropy is present in the energy range 2–4 eV, otherwise the spectrum is isotropic in whole energy region shown. We have also calculated the optical properties for the F case, and observed negligible optical anisotropy. The calculated optical $\varepsilon_1(\omega)$ spectrum is compared in Fig. 8 with available experimental data [49]. It is in good agreement with the experimental results in the energy range 1.5–5 eV. Our findings show well-dispersed bands in CB between 2 and 4 eV (Fig. 3), consequently the peaks above 3 eV are not very sharp.

The calculated reflectivity spectrum shows a good correspondence with that experimentally obtained below 5 eV for $CaRuO_3$ thin films [53]. The present calculations of the dielectric function only pertain to the electronic response and do not include the effects of lattice vibrations which dominate the lower-energy part of the spectrum. Consistent with the predicted metallic behavior, $CaRuO_3$ shows a large reflectivity in the lower-energy region. The overall good agreement between the theoretical and experimental optical spectra implies that the present calculations are able to well reproduce the electronic structure of $CaRuO_3$.

The refractive indices for a crystal are closely related to the electronic polarizability of the constituents and the local field inside the crystal. The calculated refractive indices [$n(\omega)$; resembling the real part of the dielectric tensor] for $CaRuO_3$ is shown in the lower-right panel of Fig. 8. The calculated electron energy loss spectrum (EELS; resembling the imaginary part of the dielectric tensor) in Fig. 8 shows peaks at 1.2 and 3.3 eV correspond to the screened plasma frequencies. The calculated absorption coefficient [$I(\omega)$] is shown in the top-right panel. No experimental data for these optical characteristics are available.

4.2. UPS, XPS, and XANES

The fully relativistic angle-resolved intensity of the spectrum is obtained as a product of partial, angular-momentum-dependent cross-sections and partial DOS. The relativistic cross-sections are calculated using the muffin-tin part of the potential over the energy range of the DOS functions for the fixed incident-photon energy. This has been evaluated for the potentials and DOS functions from the self-consistent fully-relativistic full-potential LMTO calculations. However, for the sake of brevity we have not presented the details of the elaborate theoretical method used and refer instead to Ref. [17] for a description. To be consistent with the reported photoemission spectra (PES), we have made all calculations with a fixed incident photon energy of 21.2 eV (corresponding to He(I) source) for UPS and 1486.6 eV (corresponding to Al$K\alpha$ source) for X-ray photoemission spectra (XPS). The calculated spectra enable us to compare our band-structure findings with the available experimental results. Moreover, the origin of the experimentally observed peaks can be determined by site-resolved PES. From the upper panel of Fig. 9, it is seen that our calculated spectrum correctly reproduces the experimental spectra [51,52] in the energy region −6 to 0 eV. In both theoretical and experimental spectra E_F is fixed at 0 eV. A small shoulder-like peak closer to E_F (at ~1.6 eV) is due to the presence of the O(1)-2*s* and Ru-4*d* electrons. The strongest peak near −4 eV (which is observed in both experimental studies) has main contributions from O(1) electrons at the apex of the octahedron. From the partial DOS analysis we have already seen that although O(1) and O(2) fall in the

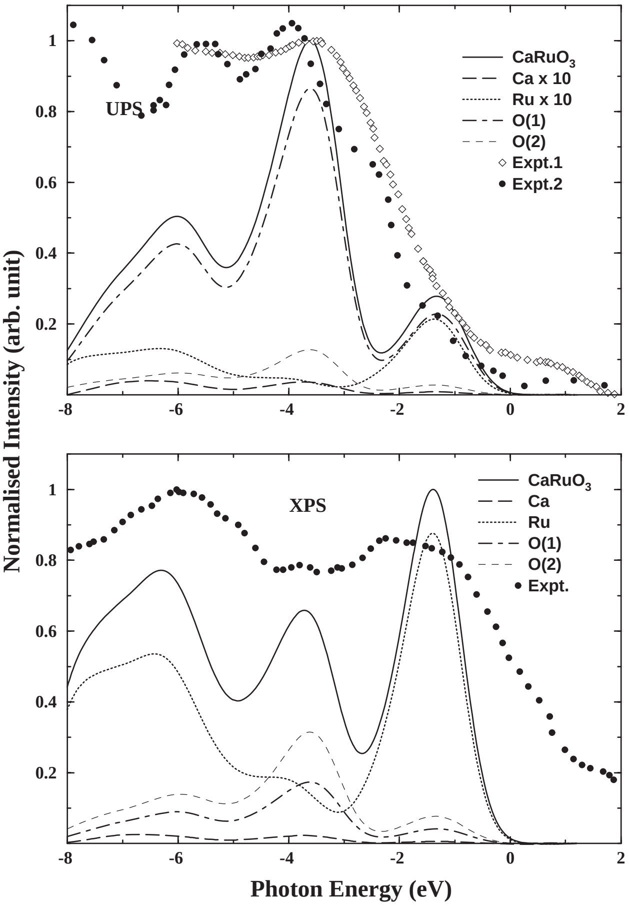

Fig. 9. Calculated UPS and XPS spectra for orthorhombic *G*-AF $CaRuO_3$. The experimental UPS data (Expt. 1 and 2) are taken from Refs. [51,52], respectively. The experimental XPS data are taken from Ref. [51].

same energy region, they exhibit notable differences. It should further be emphasized that O(2) contributes very little to the peak under consideration. Since Ca^{2+} does not have a considerable number of electrons in VB, its contribution to the spectra in the whole energy range is negligible.

The valleys around -5 eV in the calculated UPS is absent in both experimental spectra due to the following fact. Experimental UPS usually include contributions from inelastically scattered secondary electrons at lower energies which are not taken into account in the theoretical spectrum. Consistent with this viewpoint Cox et al. [52] found a strong peak-like feature at -8 eV which is attributed to the inelastically scattered secondary electrons.

The calculated XPS is shown in the lower panel of Fig. 9 which shows that the peak features in the calculated spectrum agrees extremely well with the experimental spectrum [51] over the entire energy range. As mentioned above, the intensity of the peaks depends upon the partial DOS as well as cross-sections of the constituents of the compound. The first peak around -6 eV is mainly contributed by Ru-4*d* (e_g-like) electrons. The second peak at -4 eV reflects the combined contributions of the O-2*p* and Ru-4*d* electrons. The prominent peak at ~ -1 eV is due to narrow Ru-4*d* (t_{2g}-like) electrons which are also responsible for the magnetism of this material. As the UPS and XPS give information about electronic distribution in VB only, the intensity contributions above E_F in the experimental spectra have no physical meaning and hence this aspect is not commented here.

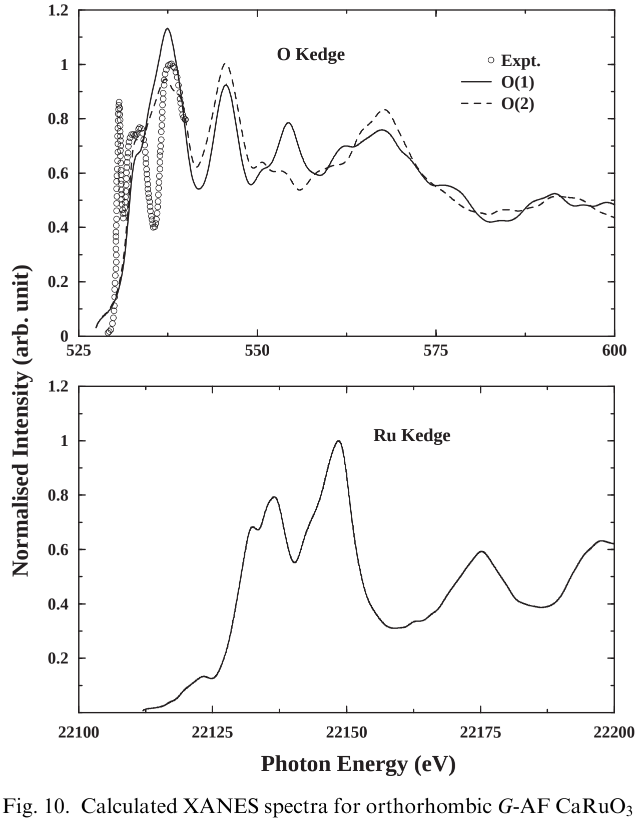

Fig. 10. Calculated XANES spectra for orthorhombic *G*-AF $CaRuO_3$. The experimental O *K*-edge spectrum is taken from Ref. [20].

The calculated O *K*- and Ru *K*-edge XANES for orthorhombic $CaRuO_3$ is shown in Fig. 10. The theoretical O *K*-edge XANES is found to be in good agreement with the experimental spectra in the lower-energy region. No experimental Ru *K*-edge XANES is available for comparison.

5. Conclusions

In order to settle the controversy about the magnetic ground state of $CaRuO_3$, we have carried out generalized-gradient-corrected fully-relativistic full-potential calculations for $Sr_{1-x}Ca_xRuO_3$ ($x = 0$, 0.25, 0.5, 0.75, and 1) in P, F, and *A*-, *C*-, and *G*-AF magnetic configurations for the experimentally observed orthorhombic as well as a hypothetical cubic (perovskite aristotype) $CaRuO_3$ and summarized our results as follows.

1. Among the five different magnetic configurations, the orthorhombic *G*-AF phase is found to have the lowest total energy and highest Ru magnetic moment. However, as low-temperature powder neutron diffraction examination has not shown any magnetic peaks, we conclude that $CaRuO_3$ is in a spin-glass state with dominant short-range antiferromagnetic interactions.
2. Owing to the relatively small size of Ca^{2+} the RuO_6 octahedra are tilted which in turn lead to weak hybridization between the Ru-4*d* and O-2*p* electrons resulting in AF ordering. The *G*-AF type exchange interaction produces a pseudogap-like feature in close vicinity of E_F for orthorhombic $CaRuO_3$ which gives extra contribution to stability in this system.
3. The cubic $CaRuO_3$ phase would be stabilized in the F state and the total energies for different magnetic configurations of the cubic phase are much higher than those of the corresponding orthorhombic phases implying that orthorhombic phase is the ground state.
4. The total-energy and magnetic-property studies for $Sr_{1-x}Ca_xRuO_3$ show that this solid-solution phase obeys Goodenough's supposition that magnetic compounds stabilize in the state with the highest magnetic moment.
5. Ru in $CaRuO_3$ are not in the low-spin state. The relatively low magnetic moment of $CaRuO_3$ is due to the small exchange splitting resulting from the extended nature of the 4*d* orbitals.
6. The electronic structure study shows that $CaRuO_3$ is metallic in agreement with experimental findings.
7. The orbital-projected DOS shows that the t_{2g} electrons mainly contribute to the magnetic and transport properties of $CaRuO_3$.

8. The calculated optical properties of orthorhombic *G*-AF $CaRuO_3$ are found to be in good agreement with available experimental spectra. Our theoretically calculated spectral data for orthorhombic *G*-AF and F $CaRuO_3$ are found to be nearly isotropic.

9. The calculated ultra-violet photoemission and X-ray photoemission spectra are in good agreement with experimental spectra in the energy range considered. The same applies to the O *K*-edge X-ray absorption spectrum (the Ru *K*-edge spectrum has also been calculated, but no experimental data are available for comparison).

Acknowledgments

The authors wish to acknowledge Dr. John Wills, Professor K. Schwarz, and Professor Peter Blaha for providing the programs used in this study, and Dr. A. Delin, Dr. H.W. Brinks, and Dr. O.H. Hansteen for useful communications. The authors are grateful for the financial support from the Research Council of Norway. Part of these calculations were carried out on the Norwegian supercomputer facilities.

References

[1] P.R. Van Loan, Am. Ceram. Soc. Bull. 51 (1972) 231.

[2] T. Takeda, R. Kanno, Y. Kawamoto, Y. Takeda, O. Yamamoto, J. Electrochem. Soc. 147 (2000) 1730.

[3] W. Bensch, H.W. Schwalle, A. Reller, Solid State Ionics 43 (1990) 171.

[4] R.A. Rao, Q. Gan, C.B. Eom, R.J. Cava, Y. Suzuki, J.J. Krajewski, S.C. Gausepohl, M. Lee, Appl. Phys. Lett. 70 (1997) 3035.

[5] K. Char, L. Antognazza, T.H. Geballe, Appl. Phys. Lett. 63 (1993) 2420.

[6] G.L. Catchen, T.M. Rearick, D.G. Schlom, Phys. Rev. B 49 (1994) 318.

[7] N. Higashi, N. Okuda, H. Funakubo, Jpn. J. Appl. Phys. 39 (2000) 2780.

[8] A. Callaghan, C.W. Moeller, R. Ward, Inorg. Chem. 5 (1966) 1572.

[9] J.M. Longo, P.M. Raccah, J.B. Goodenough, J. Appl. Phys. 39 (1968) 1327.

[10] T. Sugiyama, N. Tsuda, J. Phys. Soc. Jpn. 68 (1999) 3980.

[11] T.C. Gibb, R. Greatrex, N.N. Greenwood, P. Kaspi, J. Chem. Soc., Dalton Trans. (1973) 1253.

[12] J.L. Martinez, C. Prieto, J. Rodriguez-Carvajal, A. de Andrés, M. Vallet-Regi, J.M. Gonzaler-Calbet, J. Magn. Magn. Mater. 140–144 (1995) 179.

[13] L. Klein, L. Antognazza, T.H. Geballe, M.R. Beasley, A. Kapitulnik, Phys. Rev. B 60 (1999) 1448.

[14] C.N.R. Rao, in: C.N.R. Rao, B. Raveau (Eds.), Colossal Magnetoresistance, Charge Ordering and Related Properties of Manganese Oxides, World Scientific, Singapore, 1998.

[15] G. Santi, T. Jarlborg, J. Phys: Condens. Matter 9 (1997) 9563.

[16] I.I. Mazin, D.J. Singh, Phys. Rev. B 56 (1997) 2556.

[17] P. Ravindran, A. Kjekshus, H. Fjellvåg, A. Delin, O. Eriksson, Phys. Rev. B 65 (2002) 064445.

[18] P. Ravindran, A. Kjekshus, H. Fjellvåg, unpublished.

[19] J.S. Ahn, J. Bak, H.S. Choi, T.W. Noh, J.E. Han, Y. Bang, J.H. Cho, Q.X. Jia, Phys. Rev. Lett. 82 (1999) 5321.

[20] J.S. Lee, Y.S. Lee, T.W. Noh, K. Char, J. Park, S.-J. Oh, J.-H. Park, C.B. Eom, T. Takeda, R. Kanno, cond-mat/0107375, 2001.

[21] H. Kobayashi, M. Nagata, R. Kanno, Y. Kawamoto, Mater. Res. Bull. 29 (1994) 1271.

[22] J.M. Wills, O. Eriksson, M. Alouani, D.L. Price, in: H. Dreysse (Ed.), Electronic Structure and Physical Properties of Materials, Springer, Berlin, 2000, p. 148;
J.M. Wills, B.R. Cooper, Phys. Rev. B 36 (1987) 3809;
D.L. Price, B.R. Cooper, Phys. Rev. B 39 (1989) 4945.

[23] O.K. Andersen, Phys. Rev. B 12 (1975) 3060.

[24] J.P. Perdew, K. Burke, M. Ernzerhof, Phys. Rev. Lett. 77 (1996) 3865.

[25] I. Felner, I. Nowik, I. Bradaric, M. Gospodinov, Phys. Rev. B 62 (2000) 11332.

[26] G. Cao, S. McCall, M. Shepard, J.E. Crow, R.P. Guertin, Phys. Rev. B 56 (1997) 321.

[27] P. Ravindran, A. Delin, B. Johansson, O. Eriksson, J.M. Wills, Phys. Rev. B 59 (1999) 1776.

[28] P. Blaha, K. Schwarz, J. Luitz, WIEN97, Vienna University of Technology, Vienna, Austria 1997; Improved and updated version of the original copyrighted WIEN code, which was published by P. Blaha, K. Schwarz, P. Sorantin, S.B. Trickey, Comput. Phys. Commun. 59 (1990) 399.

[29] B.C. Hauback, H. Fjellvåg, O. Steinsvoll, K. Johansson, O.T. Buset, J. Jørgensen, J. Neutron Res. 8 (2000) 25.

[30] A.C. Larson, R.B. Von Dreele, General Structure Analysis System (GSAS), LANSCE, MS-H 805, Los Alamos National Laboratory, Los Alamos, NM, USA, 1998.

[31] P. Ravindran, A. Kjekshus, H. Fjellvåg, P. James, L. Nordström, B. Johansson, O. Eriksson, Phys. Rev. B 63 (2001) 144409.

[32] M. Shepard, G. Cao, S. McCall, F. Freibert, J.E. Crow, J. Appl. Phys. 79 (1996) 4821.

[33] T. Kiyama, K. Yoshimura, K. Losige, H. Mitamura, T. Goto, J. Phys. Soc. Jpn. 68 (1999) 3372.

[34] J.J. Hauser, J.V. Waszczak, Phys. Rev. B 30 (1984) 5167.

[35] G. Cao, S. McCall, J. Bolivar, M. Shepard, F. Freibert, P. Henning, J.E. Crow, T. Yuen, Phys. Rev. B 54 (1996) 15144.

[36] G. Cao, F. Freibert, J.E. Crow, J. Appl. Phys. 81 (1998) 3884.

[37] N. Kamegashira, T. Mori, A. Imamura, Y. Hinatsu, J. Alloys Compd. 302 (2000) L6.

[38] D. Chowdhury, Spin Glasses and Other Frustrated Systems, World Scientific, Singapore, 1986, p. 7.

[39] P. Ravindran, R. Vidya, P. Vajeeston, A. Kjekshus, H. Fjellvåg, B.C. Hauback, Solid State Commun. 124 (2002) 293.

[40] J.B. Goodenough, in: J.T. Lopusanski, J.T. Pekalski, J. Przystawa (Eds.), Magnetism in Metals and Metallic Compounds, Plenum, New York, 1976.

[41] F. Boucher, R. Rousseau, Inorg. Chem. 37 (1998) 2351.

[42] R. Dronskowski, P.E. Blöchl, J. Phys. Chem. 97 (1993) 8617.

[43] G. Cao, S. McCall, J.E. Crow, R.P. Guertin, Phys. Rev. Lett. 78 (1997) 1751.

[44] R.J. Bouchard, J.L. Gillson, Mater. Res. Bull. 7 (1972) 873.

[45] Y.S. Lee, J.S. Lee, K.W. Kim, T.W. Noh, J. Yu, E.J. Choi, G. Cao, J.E. Crow, Europhys. Lett. 55 (2001) 280.

[46] P. Ravindran, R. Asokamani, Bull. Mater. Sci. 20 (1997) 613.

[47] J.H. Jung, K.H. Kim, D.J. Eom, T.W. Noh, E.J. Choi, J. Yu, Y.S. Kwon, Y. Chung, Phys. Rev. B 55 (1997) 15489.

[48] D.J. Singh, J. Appl. Phys. 79 (1996) 4818.

[49] H.S. Choi, J. Bak, J.S. Ahn, N.J. Hur, T.W. Noh, J. Korean Phys. Soc. 33 (1998) 185.

[50] F.P. de la Cruz, N.E. Massa, V.M. Nassif, S.L. Cuffini, R.E. Carbonio, H. Salva, Phys. Stat. Sol. B 220 (2000) 603.

[51] M.V. Rama Rao, V.G. Sathe, D. Sornadurai, B. Panigrahi, T. Shripathi, J. Phys. Chem. Solids 62 (2001) 797.

[52] P.A. Cox, R.G. Egdell, J.B. Goodenough, A. Hamnett, C.C. Naish, J. Phys. C: Solid State Phys. 16 (1983) 6221.

[53] J.S. Lee, T.W. Noh, Private communication.

XIV

PHYSICAL REVIEW B **70**, 184414 (2004)

Huge magneto-optical effects in half-metallic double perovskites

R. Vidya,* P. Ravindran, A. Kjekshus, and H. Fjellvåg
Department of Chemistry, University of Oslo, Box 1033, Blindern, N-0315, Oslo, Norway

(Received 16 July 2004; published 10 November 2004)

Using generalized-gradient-corrected full-potential density-functional calculations we have studied the magneto-optical properties of double perovskites $A_2BB'O_6$, A=Ca, Sr, and Ba; B=Fe; and B'=Mo, W, and Re. Sr_2FeWO_6 has the maximum polar Kerr rotation of 3.87° and specific Faraday rotation of 4.5×10^5 deg cm^{-1}. All other compounds have Kerr rotation more than 1°, except Ca_2FeMoO_6 which has maximum Kerr rotation of 0.5°. Our electronic structure studies show that all these compounds are half-metallic in the ferromagnetic configuration. The large Kerr rotation is found to be due to the combined effects of relatively large exchange splitting from Fe, large spin-orbit coupling due to 4d or 5d elements, large offdiagonal conductivity, and half-metallicity.

DOI: 10.1103/PhysRevB.70.184414 PACS number(s): 78.20.Ls, 71.20.−b, 78.20.Ci

Materials with large magneto-optical (MO) effects have attracted a lot of attention in both basic and applied research. The motivation stems from desire to develop erasable MO memories and high density disks with MO readout. However, it is still a challenging problem to find a material with large MO rotation and also possessing a collection of necessary magnetic properties.

The interaction of electromagnetic radiation with magnetized matter manifests itself as MO effects. The MO effect due to reflection is called MO Kerr effect (MOKE) and that due to transmission is called MO Faraday effect. Plane-polarized light, when reflected from a metal surface or transmitted through a thin film that has nonzero magnetization will become elliptically polarized with ellipticity (ϵ_K in reflection mode and ϵ_F in transmission mode). The major axis is rotated by the angle θ (θ_K in reflection mode and θ_F in transmission mode) relative to the polarization axis of the incident beam. The MOKE is of three major types, polar, longitudinal, and equatorial. The polar Kerr effect for which the direction of the macroscopic magnetization of the ferromagnetic material and the propagation direction of plane polarized incident beam are perpendicular to the plane of the surface, is the most interesting case and used in practical applications. Digital information, which is suitably stored in a magnetic material can be read out using MOKE. In a transmission mode larger values of the Faraday rotation (θ_F) are clearly an advantage for technological applications.[1]

Transition-metal oxides with ordered double-perovskite structure, $A_2BB'O_6$ (A=Ca, Sr, and Ba; B=Fe, and B'=Mo, W, and Re) have begun to attract the interest of material scientists as magnetoresistive (MR) materials. These compounds are considered as an attractive alternative to the manganese compounds. As MR in manganites is observed near the ferromagnetic transition temperature (T_C), normally below room temperature, it is difficult to fully exploit the potential of manganites.[2]

A lot of efforts have been paid to study the magnetic and MR properties of $A_2BB'O_6$. A majority of these compounds are half-metallic ferromagnets (HMF) or ferrimagnets with T_C in the range of 300–450 K. These compounds also have large perpendicular magnetic anisotropy due to noncubic structure, large magnetic moment on B, large spin-orbit (SO) coupling from B', and various possibilities to substitute the A, B, or B' ions. As they have many of the salient features of potential MO materials, we attempt to study the MO properties of these materials. From full-potential density-functional calculations we show that, in addition to MR applications, $A_2BB'O_6$ can be considered as potential candidates for MO applications. We found good agreement between the calculated and the available experimental MOKE spectra which motivates us to predict MO properties for other compounds in this series. Sr_2FeWO_6 (SFWO) is found to have the maximum polar Kerr rotation (−3.87°) and all other compounds have more than 1°, except Ca_2FeMoO_6 (CFMO; −0.5°). Interestingly, maximum specific Faraday rotation (θ_F) of all the compounds is found to be more than 1×10^5 deg cm^{-1}. The present work is the first to find such a large MO effect among perovskitelike and double perovskite oxides.

In the ordered double perovskites $A_2BB'O_6$, the transition-metal sites are occupied alternatively by different cations B and B'. Oxygen atoms bridge between B and B', forming alternating octahedra with B or B' as central atom. Owing to the smaller ionic size of Ca^{2+}, alternating FeO_6 and $B'O_6$ (B'=Mo, W and Re) octahedra are tilted considerably, leading to a monoclinic structure (space group $P2_1/n$). Sr_2FeMoO_6 (SFMO) and SFWO are tetragonal with space group $P4_2/n$ and $I4/m$, respectively, whereas Sr_2FeReO_6 (SFRO) is cubic with space group $Fm\bar{3}m$ like other Ba-containing compounds. The monoclinic and tetragonal arrangements have two formula units and the cubic variants have one formula unit per unit cell. For Ca_2FeWO_6 (CFWO), Ba_2FeWO_6 (BFWO), and SFRO, though the crystal structure is known as cubic, explicit structural parameters are not available. Hence we have obtained the optimized structural parameters by force and stress minimization using the projected augmented wave implementation of the Vienna *ab initio* simulation package (VASP).[3] All the studied compounds except SFWO are experimentally found to be ferrimagnetic metals or half-metals with antiparallel spin alignment between Fe and B' moments. SFWO is found to be an antiferromagnetic insulator[4] with $T_N \approx 37$ K. Readers are referred to Refs. 5–10 for a detailed crystal and magnetic structure informations.

©2004 The American Physical Society

The full-potential linear muffin-tin orbital (FPLMTO) calculations[11] presented in this paper are all electron, and no shape approximation to the charge density or potential has been used. The basis set is comprised of augmented linear muffin-tin orbitals.[12] The calculations are based on the generalized-gradient-corrected density-functional theory as proposed by Perdew *et al.*[13] The SO coupling term is included directly in the Hamiltonian matrix elements for the part inside the muffin-tin spheres, hence for spin-polarized cases the size of the secular matrix is doubled. We used a multibasis in order to ensure a well-converged wave function. As experimental polar Kerr rotation is measured by applying an external magnetic field in order to bring about the perpendicular anisotropy, we calculated the MO spectra in the ferromagnetic configuration. For ferromagnetic calculations, the easy magnetization axis is considered along [001]. For the total-energy study the **k**-space integration is done using a minimum of 192 **k** points in the irreducible part of first Brillouin zone (IBZ) and for the optical and MO studies a minimum of 420 **k** points were used in IBZ, depending on the crystal structure.

Because of the metallic nature, a dominant contribution to the optical tensor comes from intraband transitions in the lower-energy region. The intraband contribution to the diagonal components of the conductivity is normally described by the Drude formula,

$$\sigma_D(\omega) = \frac{\omega_{\mathrm{P}}^2}{4\pi\left(\frac{1}{\tau} - i\omega\right)}, \tag{1}$$

where ω_P is the unscreened plasma frequency and τ is the relaxation time which characterizes the scattering of charge carriers, depends on the amount of vacancies and other defects, and therefore varies from sample to sample. Our experience show that if we use τ around 0.3 eV we get good agreement with the experimental spectra. So, we have used τ as a parameter with the value 0.3 eV for all our calculations. The ω_P depends on the concentration of charge carriers. The extraction of Drude parameters from the experimental data requires a free-electronlike region in the optical spectra which does not exist for the compounds studied here. As the experimental determination of Drude parameters is intrinsically difficult, we have chosen an alternative path. We have calculated the spin resolved unscreened plasma frequency by integrating over the Fermi surface using the full-potential linearized augmented plane-wave method as implemented in WIEN2K.[14] The calculations yield the unbroadened absorptive part of the optical conductivity tensor. The interband transitions are affected by scattering events which are phenomenologically described by using a finite lifetime. Since the lifetime of an excited state generally decreases with increased excitation energy, it is relevant and more appropriate to broaden with a function whose width increases with excitation energy. Thus, broadening the calculated optical spectra was performed by convoluting the absorptive optical conductivity with a Lorentzian, whose full width at half maximum (FWHM) was set to 0.01 eV, at photon energy 1 eV. The experimental resolution was simulated by broadening the final spectra with a Gaussian of constant FWHM equal to 0.02 eV. The dispersive parts of the components of the optical conductivity were calculated with a Kramers-Kronig transformation.

With the magnetic moment in the [001] direction of the crystal, the form of the optical conductivity tensor is

$$\sigma = \begin{pmatrix} \sigma_{xx} & \sigma_{xy} & 0 \\ -\sigma_{xy} & \sigma_{xx} & 0 \\ 0 & 0 & \sigma_{zz} \end{pmatrix}. \tag{2}$$

The Kerr rotation (θ_K) and Kerr ellipticity (ϵ_K) can be written as

$$\theta_K + i\epsilon_K = \frac{-\sigma_{xy}}{\sigma_{xx}\sqrt{1 + \frac{4\pi i}{\omega}\sigma_{xx}}}. \tag{3}$$

Similarly, the Faraday rotation (θ_F) and Faraday ellipticity (ϵ_F) are given by,

$$\theta_F + i\epsilon_F = \frac{\omega d}{2c}(n_+ - n_-), \tag{4}$$

where d is the thickness of the film, c is the velocity of light in vacuum, and n_+ and n_- are the refractive indices of the circular waves and given by the eigenvalues of the dielectric tensor. In terms of conductivities they are given as

$$n_{\pm}^2 = 1 + \frac{4\pi i}{\omega}(\sigma_{xx} \pm i\sigma_{xy}). \tag{5}$$

A detailed description of optical and MO calculation is given in Refs. 15 and 16.

The ferromagnetic calculations of all the compounds converge to be ferrimagnetic, viz., the magnetic moments of Fe and B' are antiparallel to each other. The magnetic moment of Fe is found to be around $3.5\mu_B$ with SFMO having the maximum Fe moment of $3.57\mu_B$. The magnetic moment of B' ranges from -0.1 to $-0.7\mu_B$ with maximum moment possessed by Re ions. The total magnetic moment is nearly an integer, i.e., 3.06 or $3.99\mu_B/\mathrm{f.u.}$ Our electronic structure studies show that all the compounds are half-metallic (HM) in the ferromagnetic state. They have a small band gap (E_g) in the majority-spin channel and a finite number of states at the Fermi level (E_F) in the minority-spin channel. The magnitude of E_g of all the compounds is given in Table I. The calculated electronic structure and magnetic moments are in good agreement with other ferromagnetic calculations[19,20] for $Sr_2FeB'O_6$, where B' = Mo, W, and Re. The E_g value for SFMO, SFWO, and SFRO is 0.59, 1.36, and 0.56 eV, respectively. The site-projected density of states for the abovementioned compounds is shown in Fig. 1. In all the three compounds Sr is completely ionized, hence electrons are in the conduction band from 4 to 8 eV. Below E_F, the majority-spin channel is mainly occupied by Fe 3d orbitals and O 2p orbitals. In particular, Fe e_g orbitals are closer to E_F (from -2 to 0 eV) and Fe t_{2g} orbitals are present from -8 to -2 eV with prominent densities from -4 to -2 eV. The B' orbitals are antibonding in the majority-spin channel with t_{2g} orbitals above E_F (from 0.25 to 2 eV) and e_g orbitals are higher-lying (from 4 to 7 eV). The W antibonding t_{2g} orbitals in SFWO are present between 1–2 eV, making its E_g larger

TABLE I. Magnitude of energy gap (E_g) in majority-spin channel, maximum Kerr rotation $\theta_{K\max}$, maximum specific Faraday rotation $\theta_{F\max}$, and maximum figure of merit (FOM; in Kerr configuration) for $A_2FeB'O_6$ (where A=Ca, Sr, and Ba; B'=Mo, W, and Re.) The values in the parenthesis indicate the energy (in eV) at which the maximum occurs.

Composition	E_g(eV)	$\lvert\theta_{K\max}\rvert$(deg)	$\lvert\theta_{F\max}\rvert$($10^5$ deg cm^{-1})	FOM(deg)
Ca_2FeMoO_6	1.02	0.50 (1.25)	1.73 (3.20)	0.23 (2.06)
Ca_2FeWO_6	1.09	1.32 (1.89)	2.28 (1.00)	0.50 (1.90)
Ca_2FeReO_6	0.19	1.04 (1.43)	3.15 (2.48)	0.62 (1.10)
Sr_2FeMoO_6	0.59	1.21 (1.96)	1.04 (1.91)	0.44 (1.92)
Sr_2FeWO_6	1.36	3.87 (1.55)	4.50 (1.48)	1.63 (1.50)
Sr_2FeReO_6	0.56	1.84 (1.72)	3.67 (4.83)	0.90 (1.80)
Ba_2FeMoO_6	0.93	1.46 (0.87)	2.05 (3.25)	0.62 (1.60)
Ba_2FeWO_6	1.80	1.70 (2.83)	4.43 (3.15)	0.69 (2.60)
Ba_2FeReO_6	0.53	1.51 (1.54)	3.10 (2.90)	0.65 (1.54)

compared to the other two compounds, whereas the Re t_{2g} orbitals are just above E_F (from 0.25 to 1.4 eV). In both spin channels O $2p$ orbitals are present from -8 to -2 eV. The B' d orbitals are well hybridized with O $2p$ orbitals so that the bonding states are well-localized (from -8 to -6 eV) and antibonding states are above E_F. The states present at E_F in the minority-spin channel is due to the hybridized Fe and B' t_{2g} orbitals. A more detailed analysis of magnetic and electronic properties will be given elsewhere.[21]

The polar Kerr rotation and Kerr ellipticity spectra for $Ca_2FeB'O_6$, $Sr_2FeB'O_6$, and $Ba_2FeB'O_6$ are given in Figs. 2–4. The peak value of the Kerr rotation for each compound along with the energy at which it occurs is given in Table I. The calculated Kerr spectra are compared with the available experimental spectra for A_2FeMoO_6 (where A=Ca, Sr, and Ba). The magnitude of the calculated Kerr rotation peaks for CFMO and SFMO agrees very well with that of experiment (at 101 K), but for BFMO theoretical calculations overestimate the magnitude. The position of theoretical MOKE peaks are somewhat shifted in relation to the experimental ones. In general, the peaks of calculated optical conductivities and polar Kerr spectra are displaced toward higher energies with respect to experimental spectra.[16] This may be due to the fact that DFT overestimates the $3d$-band width which in turn affects the optical and MO spectra peaks to shift toward higher energy. This can be artificially corrected by increasing lattice parameters which gives narrower bands or

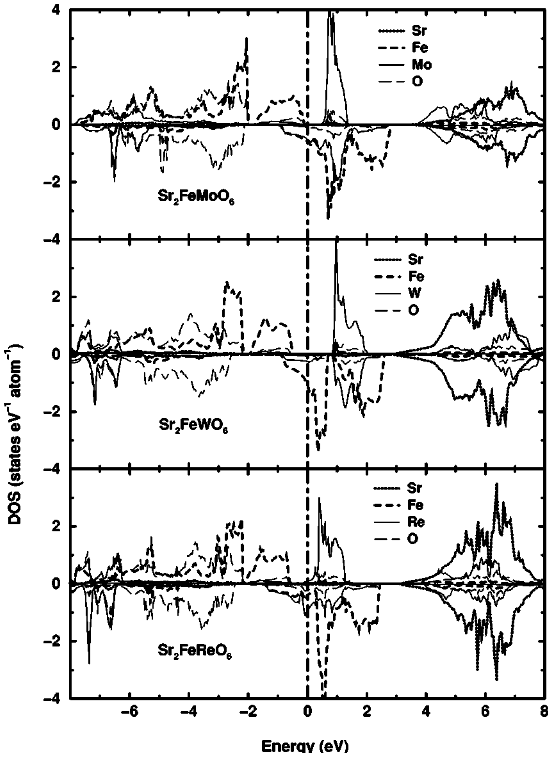

FIG. 1. Site-projected density of states for $Sr_2FeB'O_6$ where B'=Mo, W, and Re.

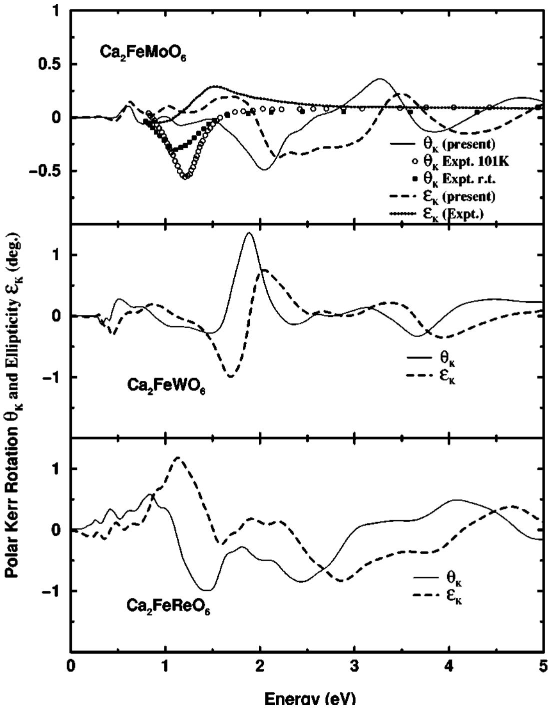

FIG. 2. Polar Kerr rotation (θ_K) and Kerr ellipticity (ϵ_K) spectra for $Ca_2FeB'O_6$ where B'=Mo, W, and Re. Experimental data for CFMO are from Ref. 17.

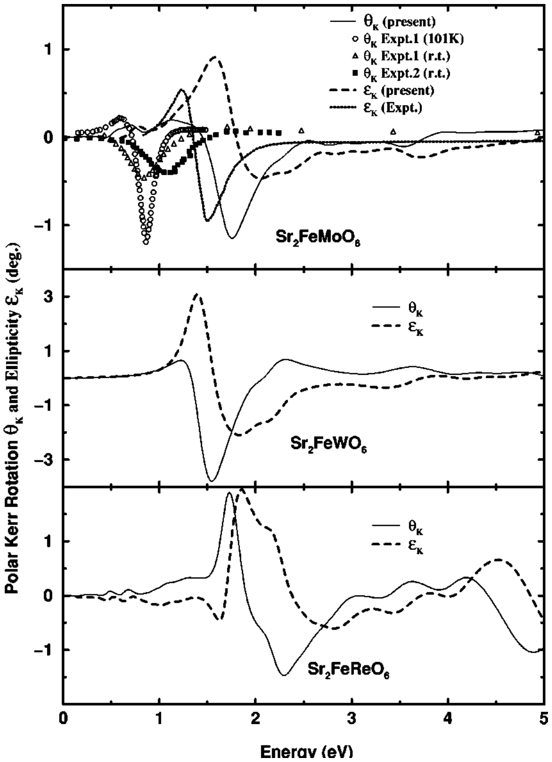

FIG. 3. Polar Kerr rotation (θ_K) and Kerr ellipticity (ϵ_K) spectra for $Sr_2FeB'O_6$ where B'=Mo, W, and Re. Experimental data for SFMO are taken from Ref. 17 (Expt. 1) and Ref. 22 (Expt. 2).

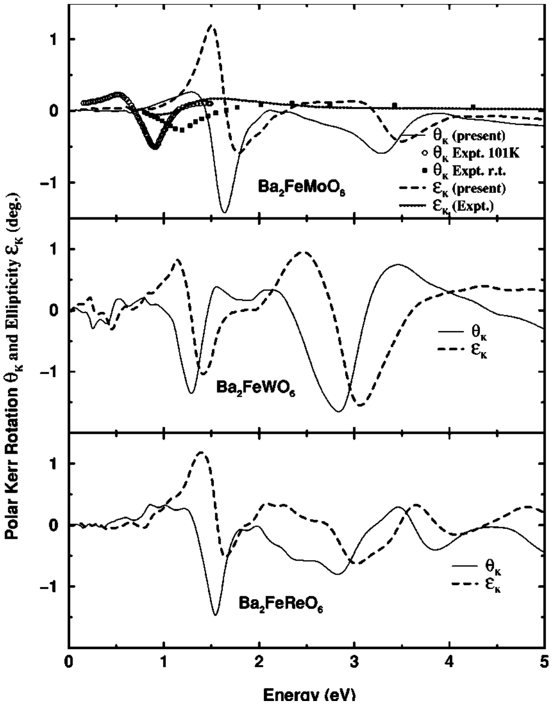

FIG. 4. Polar Kerr rotation (θ_K) and Kerr ellipticity (ϵ_K) spectra for $Ba_2FeB'O_6$ where B'=Mo, W, and Re. Experimental data for BFMO is taken from Ref. 17.

by performing GW-corrected calculations of MO spectra. However, it has to be mentioned that the experimental peak positions are sample-dependent[23] (see for example the PtMnSb case in Ref. 24) and appear to depend on stoichiometry, homogeneity, impurities, etc., whereas the magnitude depends on sample preparation, annealing, etc. One month after polishing samples exhibit a marked aging effect compared to the sample just after polishing.[18] The magnitude is enhanced by a factor of 1.5 and the center (or zero-crossing) shifts toward the longer wavelength side.[17] Moreover, we can see that the experimental Kerr rotation peaks for A_2FeMoO_6 are almost doubled at 101 K compared to that at room temperature. It has to be mentioned that we have calculated the MO properties for single crystals at low temperature and hence it is more appropriate to compare our results with the experimental spectra measured at low temperatures for single crystals.

In an attempt to understand the reason for huge MO effects on the studied compounds, we show reflectivity and conductivity spectra for $A_2FeB'O_6$ in Fig. 5. In the top-left panel reflectivities of SFMO, SFWO, and SFRO are shown along with the available experimental spectra for SFMO. Though the essential features of the theoretical spectrum are comparable to that of experimental spectra, the former is shifted by ~0.5 eV toward higher energy region. However, it has to be noted that even the experimental spectrum measured at 10 K is shifted toward higher energy in relation to that measured at 300 K. As mentioned earlier, it would be more appropriate to compare our theoretical spectra with experimental spectra at low temperature. Moreover, the reflectivity spectra exhibit remarkable aging effects due to oxidation of the surface of the samples (similar to Kerr spectra). The amplitude of reflectivity for the sample just after polishing is more than two times larger than that of the sample one month after polishing (as seen in the experimental spectra for SFMO in Fig. 5). A dip in the reflectivity spectra in the lower energy region (around 1.7 eV) has been experimentally interpreted as due to the plasma resonance of conduction electrons in the crystal since the diagonal and offdiagonal elements of the dielectric tensor is expected to exhibit an anomaly near the plasma edge.[25] Therefore both reflectivity and Kerr spectra are affected by this. In order to check whether the dip around 1.7 eV is really due to plasma resonance, we have also calculated the electron energy loss spectrum (EELS). The function representing characteristic energy losses (or plasmon oscillations) is proportional to the probability that a fast electron moving across a medium loses energy per unit length. Generally speaking, plasma resonances manifest themselves as rather distinct peaks in the EELS,[26] and are thus a feature easily observed experimentally. The EELS for SFMO, SFWO, and SFRO show prominent peaks at 1.62, 1.49, and 1.14 eV, respectively. The reflectivity spectra of SFWO and SFRO also show a dip at 1.3 and 1.6 eV, respectively. Hence, the dip observed in these compounds is due to the plasma resonance. However, no experimental reflectivity spectra are available for SFWO and SFRO to compare our theoretical spectra with. As Kerr spectra show peaks for all these compounds in the energy region 1–2 eV, plasma resonance also plays an important role in the $\theta_{K\max}$ values (Fig. 5).

The real part of diagonal conductivity of SFMO is in reasonable agreement with the available experimental spectra,

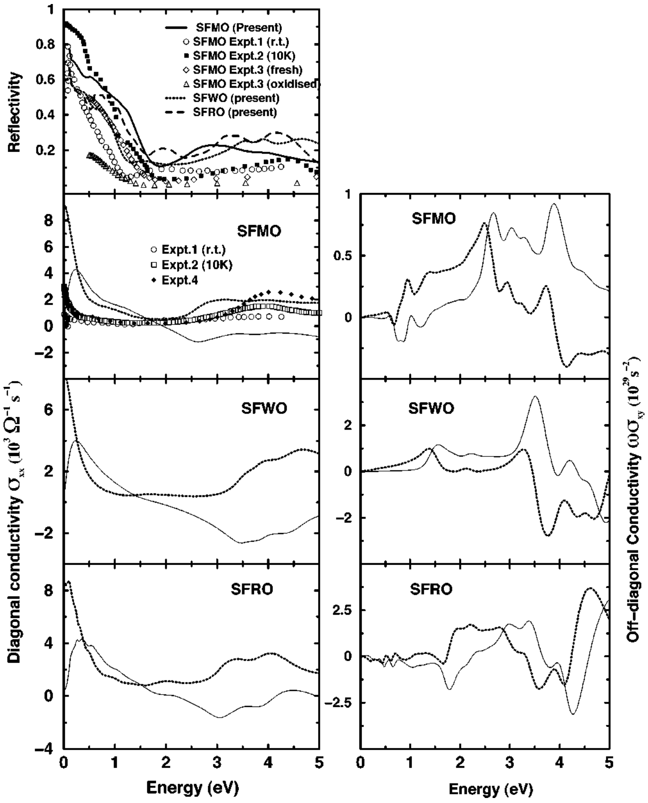

FIG. 5. Reflectivity and conductivity spectra for Sra$_2$FeB'O$_6$ where B'=Mo W, and Re. Experimental data for SFMO are taken from Ref. 27 (Expt. 1), Ref. 28, (Expt. 2), Ref. 18 (Expt. 3), and Ref. 29 (Expt. 4).

except that the amplitude of theoretical spectra is higher than that of experimental spectrum in the lower energy region. As experimental spectra are derived through Kramers-Kronig transformation of reflectivity spectra, there is slight discrepancy. The Drude component is involved in the theoretical conductivities, which will enhance the amplitude in the lower energy region. Around 0.5 eV, a small bump is observed which is due to Fe $e_g^{\uparrow}$ to Mo $t_{2g}^{\uparrow}$ transition. The peak at 4 eV observed by experiments is shifted to 3 eV, instead a small bump is seen at 4 eV. This peak is attributed to the O 2p to hybridized $t_{2g}^{\downarrow}$ of Fe and Mo. In the case of SFWO, two prominent peaks occur around 4 and 4.5 eV. The first peak is due to O 2p to Fe $t_{2g}^{\downarrow}$ transition and the second peak is due to O 2p to W $t_{2g}^{\uparrow}$ transition. Around five peak structures appear for SFRO. An experimental study[30] is available for this compound up to 0.8 eV. However, no prominent structure exists within that narrow energy region to be compared with our theoretical spectrum. The lower energy peaks at 0.6 and 0.8 eV can be attributed to the interband (Fe $e_g^{\uparrow}$ to Re $t_{2g}^{\uparrow}$) transition. The peaks at 2 and 3.25 eV are due to O 2p to Fe and Re hybridized $t_{2g}^{\downarrow}$ transition. The peak around 4 eV is due to O 2p to $t_{2g}^{\uparrow}$ transition. From the figure it can be seen that the overall topology of the diagonal conductivity for the three compounds is somewhat similar. As experimentalists often display $\omega\sigma_{xy}$ instead of σ_{xy}, we also show $\omega\sigma_{xy}$ in the right panel of Fig. 5. From Eq. (3) it can be seen that the Kerr rotation can be enhanced by a larger off-diagonal conductivity and a smaller diagonal conductivity. The diagonal conductivity of all three compounds shows a minimum around 1.5–2 eV where maximum of θ_K is observed. The off-diagonal conductivity of SFWO and SFRO show higher values than that of SFMO, implying that the high Kerr rotation of these compounds also result from high off-diagonal conductivity. The influence of intraband effects on the MOKE is restricted to energies smaller than 1–2 eV.

The MOKE signal is proportional to $f \cdot M$, where f is determined by the complex refractive index at the probe frequency and M is the magnetization.[22] The refractive index of SFMO, SFWO, and SFRO in the energy region 1–2 eV (where $\theta_{K\max}$ occurs) is 1.56, 1.88, and 1.98, respectively. Though the refractive index of SFWO is slightly smaller than SFRO, its magnetic moment is 3.99μ_B whereas SFRO has 3.07μ_B. So it has larger $\theta_{K\max}$ than SFMO and SFRO. The fact that the Kerr rotation correlates with the atomic magnetic moment of spin should not be surprising since the MO effect involves spin-orbit interaction.[31] Incident photons excite the 3d valence electrons of the transition metals by altering their orbital angular momenta. When the electrons fall back from their excited states, the emitted photons are polarized and characteristic of both spin orientation and magnitude. Thus, the SO interaction couples the momentum of the electron with its spin and provides the link for the circularly-polarized electromagnetic waves to couple to the magnetization of the material. The heavier the atom, the stronger will be the SO interaction. Thus, all the studied compounds have large MO effects. Moreover, SFWO has maximum exchange splitting of 3.1 eV and its band gap in the majority spin channel is 1.36 eV. So the electrons are highly spin polarized in the HMF state. Therefore, larger off-diagonal conductivity, refractive index, magnetic moment, SO coupling, exchange splitting, band gap, and plasma resonance combine to give huge MO values for all the studied compounds, and in particular to SFWO. The polar Kerr ellipticity is a measure of how the shape of the wave has changed upon reflection and depends only on the absolute magnitudes of the reflection coefficients. As the reflectivities of these compounds are also large, they also have large polar Kerr ellipticity.

The Kerr rotation peaks of all the studied compounds lie in the energy region of infrared to visible radiation. An intense search is going on for materials with MO peaks in the lower wavelength region for use in high-density storage.[1] Among the studied compounds CFRO (−0.89° at 2.47 eV), SFRO (−1.5° at 2.3 eV), BFWO (−1.70° at 2.83 eV), and BFRO (−0.86° at 2.83 eV) have large peaks in the green-violet energy region. It has to be noted that a large polar Kerr rotation, typically greater than about 0.2° is clearly of benefit in reading information stored in a thermo-MO thin film.[1] The strong SO coupling results in a large uniaxial anisotropy which is one of the essential requirements for a MO storage device. The magnitude of the uniaxial anisotropy depends on structural anisotropy and hence noncubic systems usually possess large magnetic anisotropy. Moreover flexibility to substitute or dope A, B or B' elements will be useful to tune the MO properties according to the need. In that perspective the present compounds may be of relevance for high-density storage applications.

In a transmission mode, large Faraday rotation is desirable for applications.[32] Materials with large Faraday rotation are used in devices called optical isolators.[33] Therefore we predict the specific Faraday rotation and ellipticity of $A_2\mathrm{Fe}B'\mathrm{O}_6$ (not shown), experimental Faraday spectra are hitherto not available for comparison. In Table I we have given the maximum of specific Faraday rotation for each compound. Specific Faraday rotation of all the studied compounds is greater than 1×10^5 deg cm^{-1}. It is interesting to note that SFWO has the maximum Kerr as well as Faraday rotation among $A_2\mathrm{Fe}B'\mathrm{O}_6$.

In order to detect the written information in a MO medium easily, and to make the signal-to-noise ratio as high as possible, the MO figure of merit (FOM) should be large.[1] FOM is defined[34] as FOM $\approx \sqrt{R(\theta_K^2+\epsilon_K^2)}$, where R, is reflectivity and θ_K and ϵ_K as defined earlier. For the sake of simplicity, in Table I we have given the maximum of FOM and the corresponding energy at which it occurs. The FOM calculated for the present compounds is comparable with that of the well-known MO material PtMnSb. In spite of the fact that FOM is often used to characterize the performance of a MO medium and the factors determining FOM depend on the structure on which magnetic material is embedded, we believe that the given large FOM values may motivate more MO studies on these systems.

In conclusion, the presently studied compounds have many of the basic requirements[35] for a MO medium, such as presence of uniaxial magnetic anisotropy, T_C ranging between 300 and 600 K, large Kerr rotation, large Faraday rotation, large FOM, HMF at room temperature, long term stability, etc. For the first time, using full-potential density functional calculations, we have shown that $A_2BB'\mathrm{O}_6$ have the huge MO effects among the oxides and can be considered as potential candidates for MO applications. The huge magneto-optical effects are found to result due to combined effects of large off-diagonal conductivity, refractive index, magnetic moment, SO coupling, exchange splitting, band gap, and plasma resonance.

The authors are grateful to the Research Council of Norway for financial support and computer time at the Norwegian supercomputer facilities. R.V. and P.R. wish to acknowledge Dr. J. Wills and Dr. A. Delin for providing the computer programs used in this study, and Professor Claudia Ambrosch-Draxl and Dr. S. Sharma for useful discussions.

---

*Electronic address: vidya.ravindran@kjemi.uio.no

[1] P.J. Grundy, in *Electronic and Magnetic Properties of Metals and Ceramics*, Materials Science and Technology, edited by K.H.J. Buschow (VCH, FRG, 1994), Vol. 3B, p. 575.

[2] O. Chmaissem, R. Kruk, B. Dabrowski, D.E. Brown, X. Xiong, S. Kolesnik, J.D. Jorgensen, and C.W. Kimball, Phys. Rev. B **62**, 14 197 (2000).

[3] G. Kresse and J. Hafner, Phys. Rev. B **47**, 558 (1993); G. Kresse and J. Furthmuller, Comput. Mater. Sci. **6**, 15 (1996).

[4] G. Blasse, Philips Res. Rep. **20**, 327 (1965); H. Kawanaka, I. Hase, S. Toyoma, and Y. Nishihara, J. Phys. Soc. Jpn. **68**, 2890 (1999).

[5] K.-I. Kobayashi, T. Kimura, H. Sawada, K. Terakura, and Y. Tokura, Nature (London) **395**, 677 (1998).

[6] C. Ritter, M.R. Ibarra, L. Morellon, J. Blasco, and J.M. De Teresa, J. Phys.: Condens. Matter **12**, 8295 (2000).

[7] J. Gopalakrishnan, A. Chattopadhyay, S.B. Ogale, T. Venkatesan, R.L. Greene, A.J. Millis, K. Ramesha, B. Hannoyer, and G. Marest, Phys. Rev. B **62**, 9538 (2000).

[8] Y. Moritomo, S. Xu, A. Machida, T. Akimoto, E. Nishibori, M. Takata, M. Sakata, and K. Ohoyama, J. Phys. Soc. Jpn. **69**, 1723 (2000).

[9] W. Prellier, V. Smolyaninova, A. Biswas, C. Galley, R.L. Greene, K. Ramesha, and J. Gopalakrishanan, J. Phys.: Condens. Matter **12**, 965 (2000).

[10] L. Pinsard-Gaudart, R. Suryanarayanan, A. Revcolevschi, J. Rodriguez-Carvajal, J.-M. Greneche, P.A.I. Smith, R.M. Thomas, R.P. Borges, and J.M.D. Coey, J. Appl. Phys. **87**, 7118 (2000).

[11] J.M. Wills, O. Eriksson, M. Alouani, and D.L. Price, in *Electronic Structure and Physical Properties of Materials*, edited by H. Dreysse (Springer, Berlin, 2000), p. 148.

[12] O.K. Andersen, Phys. Rev. B **12**, 3060 (1975).

[13] J.P. Perdew, K. Burke, and M. Ernzerhof, Phys. Rev. Lett. **77**, 3865 (1996).

[14] P. Blaha, K. Schwarz, G.K.H. Madsen, D. Kvasnicka, and J. Luitz, WIEN2k, revised edition, 2001.

[15] P. Ravindran, A. Delin, P. James, B. Johansson, J.M. Wills, R. Ahuja, and O. Eriksson, Phys. Rev. B **59**, 15 680 (1999).

[16] A. Delin, O. Eriksson, B. Johansson, S. Auluck, and J.M. Wills, Phys. Rev. B **60**, 14 105 (1999).

[17] K. Shono, M. Abe, M. Gomi, and S. Nomura, Jpn. J. Appl. Phys., Part 1 **21**, 1720 (1982).

[18] K. Shono, M. Abe, M. Gomi, and S. Nomura, Jpn. J. Appl. Phys. **20**, L426 (1981).

[19] I.V. Solevyev, Phys. Rev. B **65**, 144446 (2002).

[20] Z. Fang, K. Terakura, and J. Kanamori, Phys. Rev. B **63**, 180407 (2001).

[21] R. Vidya, P. Ravindran, H. Fjellvåg, and A. Kjekshus (unpublished).

[22] T. Kise, T. Ogasawara, M. Ashida, Y. Tomioka, Y. Tokura, and M. Kuwata-Gonokami, Phys. Rev. Lett. **85**, 1986 (2000).

[23] U. Rüdiger, M. Rabe, G. Güntherodt, H.Q. Yin, R.I. Dass, and J.B. Goodeneough, Appl. Phys. Lett. **77**, 2216 (2000).

[24] K. Takanashi, K. Sato, J. Watanabe, Y. Sato, and H. Fujimori, Jpn. J. Appl. Phys., Part 1 **30**, 52 (1991).

[25] G. Dresselhaus, A.F. Kip, and C. Kittel, Phys. Rev. **100**, 618 (1955).

[26] P. Ravindran, A. Delin, R. Ahuja, B. Johansson, S. Auluck, J.M. Wills, and O. Eriksson, Phys. Rev. B **56**, 6851 (1997).

[27] Y. Moritomo, S. Xu, A. Machida, T. Akimoto, E. Nishibori, M. Takata, and M. Sakata, Phys. Rev. B **61**, R7827 (2000).

[28] Y. Tomioka, T. Okuda, Y. Okimoto, R. Kumai, K.-I. Kobayashi, and Y. Tokura, Phys. Rev. B **61**, 422 (2000).

[29] J.H. Jung, S.-J. Oh, M.W. Kim, T.W. Noh, J.-Y. Kim, J.-H. Park, H.-J. Lin, C.T. Chen, and Y. Moritomo, Phys. Rev. B **66**,

104415 (2002).

[30] H. Kato, T. Okuda, Y. Okimoto, Y. Tomioka, K. Oikawa, T. Kamiyama, and Y. Tokura, Phys. Rev. B **65**, 144404 (2002).

[31] P.M. Oppeneer, T. Maurer, J. Sticht, and J. Kübler, Phys. Rev. B **45**, 10 924 (1992).

[32] J. Schones, in *Electronic and Magnetic Properties of Metals and Ceramics*, Materials Science and Technology, edited by K.H.J. Buschow (VCH, FRG, 1994), Vol. 3B, p. 233.

[33] D.K. Wilson, Mater. Res. Soc. Symp. Proc. **517**, 541 (1998).

[34] M. Mansuripur, *The Physical Principles of Magneto-Optical Recording* (Cambridge University Press, Cambridge, 1995), p. 206.

[35] P. Hansen, J. Magn. Magn. Mater. **83**, 6 (1990).

XV

Spin- and charge-ordering in oxygen-vacancy-ordered mixed-valence $Sr_4Fe_4O_{11}$

R.Vidya,[*] P.Ravindran, H.Fjellvåg, and A.Kjekshus
Department of Chemistry, University of Oslo, Box 1033 Blindern, N-0315 Oslo, Norway

Structural, electronic, and magnetic properties of the vacancy-ordered mixed-valence $Sr_4Fe_4O_{11}$ phase have been investigated using spin-polarized electronic-structure total-energy calculations. The optimized structural parameters obtained from accurate total-energy calculations are found to be in very good agreement with low-temperature neutron-diffraction findings. Among the different spin configurations considered for $Sr_4Fe_4O_{11}$, the *G*-type antiferromagnetic configuration is found to represent the magnetic ground state. The calculations show finite magnetic moments at both Fe sites and this is against the conclusions arrived at from Mössbauer and low-temperature powder neutron-diffraction measurements, but consistent with the results from the magnetization measurements. The present study clearly show that one of the magnetic sub-lattices is frustrated and hence $Sr_4Fe_4O_{11}$ can be considered as a phase-separated system with one phase in the *G*-type antiferromagnetic state and the other in a spin-glass-like state. Our theoretical results show unambiguously that the Fe atoms with the square pyramidal environment has a lower oxidation state than that in the octahedral co-ordination. However, the presence of covalent interaction between Fe and the neighboring oxygen atoms makes the actual oxidation state considerably smaller than the formal oxidation state 3+ and 4+ for square pyramidal and octahedral coordination, respectively. $Sr_4Fe_4O_{11}$ is found to be semiconducting in the antiferromagnetic ground state.

PACS numbers: 71., 71.20.Ps, 75.50.Ee, 78.20.Ci

I. INTRODUCTION

Perovskite-type oxides exhibiting ionic or mixed electronic/ionic conductivity are of considerable interest for potential application in high-temperature electrochemical devices, e.g., as electrodes for high-temperature solid-oxide fuel cells, sensor materials,[1–3] membranes separating oxygen from air, and catalyst for the conversion of hydrocarbons [4–7]. One of the most essential features of such materials is the high oxygen mobility and another attraction is the catalytic activity of oxygen vacancies. However, the oxygen mobility usually drops appreciably at temperatures below $\sim 600-800^o$ C and hence many, at first sight, seemingly promising materials turn out to be unsuitable for practical purposes. Therefore, the development of oxygen ionic conductors that retain appreciable oxygen mobility at ambient operating temperatures is of considerable interest. Since it is documented [8] that oxide ion conductivity is closely related to the ordering of oxygen vacancies in the crystal structure, it seems worthwhile to look more closely at the properties of oxygen deficient perovskites.

The high-temperature phase $SrFeO_{3-x}$ $(2.5 \leq x \leq 3.0)$ exhibits appreciable mixed electronic and ionic conductivities and the materials derived from this phase are considered to be of potential interest [9] for application in many of the device catagories mentioned above. From the scientific point of view, it is vital to explore properties of phases with different oxygen stoichiometry as they form different structural distortions, exotic valences, spin, charge, and orbital ordering.

The orbital distribution of the *d* electrons of higher-valence Fe species is very versatile, changing not only with the kind and amount of other constituents (in particular alkali, alkaline-earth or rare-earth elements) but also temperature as, e.g., observed for $Ca_{1-x}Sr_xFeO_3$ and $Sr_{1-x}La_xFeO_3$ [10]. Another influential factor is the oxygen content as revealed for the $SrFeO_{3-x}$ [9], $LaBaMn_2O_{5+\delta}$[11], and $YBaMn_2O_{5+\delta}$ [12] phases. Oxygen deficiency formally increases the number of electrons per Fe atom and modifies (at least locally), the electron exchange between the Fe atoms. Subsequently it perturbs the electronic band structure and varies the band filling of the transition-metal ion and also structural arrangement simultaneously.

The preparation and characterization of oxygen-deficient specimens of $SrFeO_{3-x}$ have been subjected to numerous studies [9, 13–15]. One of the curiosities which is commonly associated with the $SrFeO_{3-x}$ phase (more specifically with the highly electropositive element Sr) is the occurrence of Fe in a rare, formal oxidation state of 4+ and a wide-range of oxygen nonstoichiometry. Systematic studies [13, 14] have established the existence of a series of ordered Ruddlesden-Popper-type phases $Sr_nFe_nO_{3n-1}$ with $n = \infty$, 8, 4, and 2 corresponding to the formulae $SrFeO_3$, $SrFeO_{2.875}$ ($Sr_8Fe_8O_{23}$), $SrFeO_{2.75}$ ($Sr_4Fe_4O_{11}$), and $SrFeO_{2.5}$ ($Sr_2Fe_2O_5$), respectively. Hence the variable-valence $SrFeO_{3-x}$ phase may provide an instructive model system for a closer examination of the effects of oxygen-vacancy ordering on structure, magnetism, and electronic properties.

The oxygen-deficient end member, $Sr_2Fe_2O_5$ is claimed [16] to exhibit well behaved Fe^{3+} cations at both tetrahedral and octahedral coordination of an orthorhombic oxygen-vacancy-ordered structure [17] and it

---

[*] Electronic address: `vidya.ravindran@kjemi.uio.no`; URL: `http://folk.uio.no/ravindrv`

is an antiferromagnetic (AF) Mott-type insulator. The other end, $SrFeO_3$, possess, as mentioned, the unusually high Fe^{4+} oxidation state according to a pure ionic model. The structure is of the regular cubic perovskite type, the magnetic ordering is of the helical-AF type, and this phase exhibits metallic conductivity [18, 19]. Between these composition limits one finds the two above-mentioned intermediate phases with oxygen-vacancy ordering [13–15, 20, 21]. The $Sr_4Fe_4O_{11}$ variant is reported to take an orthorhombic $2\sqrt{2}a_p \times 2a_p \times \sqrt{2}a_p$ (a_p refers to the lattice parameter of cubic perovskite subcell) structure [13], whereas $Sr_8Fe_8O_{23}$ has a tetragonal $2\sqrt{2}a_p \times 2\sqrt{2}a_p \times 2a_p$ structure. Both these variants exhibit AF ordering at low temperatures.

Tofield *et al.*[22] first reported that $Sr_4Fe_4O_{11}$ exists in a narrow single-phase region centered around the ideal stoichiometric composition 4:4:11. It is reported [23] to undergo charge ordering (CO) transition ($T_{\rm CO}$) below 675 K with equal amounts of Fe^{3+} and Fe^{4+} alternatively arranged in the lattice. $Sr_4Fe_4O_{11}$ is found [14, 24] to be a *G*-type AF with a Né*e*l temperature ($T_{\rm N}$) of 230 K. According to Mössbauer [14] and neutron diffraction [24] measurements, one Fe site forms long-range AF arrangement. At present it is not known whether the other Fe sub-lattice forms a spin-glass-like configuration below the $T_{\rm N}$, remains paramagnetic or possibly undergoes a separate spin-ordering (SO) transition at very low temperatures (notably below 4.2 K). In order to settle some of these issues accurate electronic structure studies is highly desirable and this demand was one of the motivations for the present study.

The hitherto conducted structural studies have clearly indicated that the Fe atoms alternatively occupy the square pyramidal ($Fe1^s$) and octahedral site ($Fe2^o$) in $Sr_4Fe_4O_{11}$. However, there is strong disagreement on the assignment of valence and spin states to the crystallographically different Fe atoms. From the calculated electronic structure and magnetic properties our study aims at resolving this controversy.

II. STRUCTURAL ASPECTS

The crystal structure of $Sr_4Fe_4O_{11}$ (Fig. 1) can be visualized as an oxygen-vacancy-ordered arrangement in a perovskite-like superstructure. It consists of one-dimensional chains of vertex-linked $Fe2O_6^o$ units cross-linked by $(Fe1O_5^s)_2$ "bow-tie" dimer units. The oxygen vacancies are ordered into strings of vacancies alternating with oxide ions along the [110] direction of the perovskite sub-cell. The interplane ordering is such that the structure contains equal amounts of Fe in square-pyramidal and octahedral co-ordination to the oxygen atoms.

The most prominent feature of this vacancy-ordered structure is the appearance of "one-dimensional channels" of apex-sharing $Fe2O_6^o$ units along *b* direction (see Fig. 1). In planes parallel to *ac*, each of these octahedra are surrounded by four (corner sharing) $Fe1O_5^s$ units.

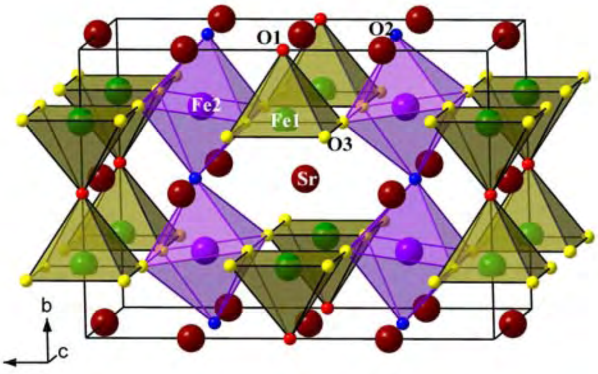

FIG. 1: (Color online) Crystal structure of $Sr_4Fe_4O_{11}$. $Fe1^s$ and $Fe2^o$ are in square-pyramidal and octahedral coordinations, respectively.

The $Fe1O_5^s$ unit consists of one O1 and four O3 atoms, (the latter forming the base of the pyramid; labelling according to Hodges et al.[14]). The O1 atom is shared by two neighboring Fe1 atoms, and it is this configuration that forms the "bow-tie" unit. The Fe1 atom is located close to the base of the pyramid. The octahedral surroundings of Fe2 are formed by two O2 and four O3 atoms. The pyramids and octahedra share the O3 atoms. For the $Fe1O_5^s$ units the increase in repulsion energy due to short O-O distances in the base is partly compensated by the relaxation effect of the longer separation between the O atoms in the base and the apex. The $Fe2O_6^o$ units are compressed at the apex, a structural distortion introduced by the "bow-tie" configuration of the pyramids. However, this distortion causes only tilting of the octahedra and does not change their shape (see Fig. 1).

III. COMPUTATIONAL DETAILS

A. Structural optimization

Two different structural arrangements (monoclinic $C2/m$ and orthorhombic $Cmmm$) are described for $Sr_4Fe_4O_{11}$ with full site occupancy [14] and we have performed structural optimization for both in order to establish the ground-state structure. These calculations have been carried out using the projected augmented plane-wave (PAW) [25] method as implemented in the Vienna *ab initio* simulation package (VASP) [26]. The optimization of the atomic geometry was performed via a conjugate-gradient minimization of the total energy, using Hellmann-Feynman forces on the atoms and the stresses in the unit cell. The atomic coordinates and axial ratios are allowed to relax for different volumes of the unit cell. These parameters are changed iteratively so that the sum of the lattice energy and the electronic free energy converges to a minimum value. The electronic free energy is taken as the quantity to be minimized and the total energy is calculated exactly for each set of atomic positions. Convergence minimum with respect to atomic shifts was assumed to have been attained when the energy difference between two successive iterations was less than 10^{-7} eV per unit cell and the forces acting on the atoms were less than 1 meV Å^{-1}. The generalized-gradient approximation (GGA) [27] was used to obtain the accurate exchange and correlation energy for a particular atomic configuration. The calculations were carried out using a $4 \times 4 \times 4$ **k**-points Monkhorst-Pack grid, equivalent to 64 **k** points in the Brillouin zone. A plane-wave energy cutoff of 875 eV was used in all calculations since high energy cutoff was found [28] to be necessary in order to describe the nuclear and magnetic structures of complex oxides unambiguously.

B. FPLAPW calculation

In order to calculate orbital-projected DOS and energy-projected occupation density matrix we made use of the full-potential linearized-augmented plane-wave (FPLAPW) method as implemented in the WIEN2k package [29] in a fully-relativistic version with spin-orbit coupling. The FPLAPW approach divides space into an interstitial region (IR) and non-overlapping muffin-tin (MT) spheres centered at the atomic sites. In the IR, the basis set consists of plane waves. Inside the MT spheres, the basis set is described by radial solutions of the one-particle Schrödinger equation (at fixed energies), and their energy derivatives multiplied by spherical harmonics. The charge densities and potentials inside the atomic spheres were represented by spherical harmonics up to $\ell = 6$, whereas in the interstitial region these quantities were expanded in a Fourier series. Atomic-sphere radii (R_{MT}) of 2.3, 1.9, and 1.6 a.u. for Sr, Fe, and O, respectively were used. The Brillouin zone (BZ) integration was carried out with a modified tetrahedron method [25] and we used 75 **k** points in the irreducible wedge of BZ for the DOS and total energy calculation. Exchange and correlation effects are treated within density-functional theory (DFT), using GGA [27].

IV. RESULTS AND DISCUSSIONS

Hodges *et al.* [14] tested different possible oxygen-ordering schemes for $Sr_4Fe_4O_{11}$ of which several gave almost equally good fits in Rietveld refinements of powder neutron diffraction (PND) data. However, all solutions except that based on the space group $Cmmm$ had to be disregarded owing to the unacceptable short Fe-O distances. From the structural optimizations, according to proposed structure models described in space groups $C2/m$ and the $Cmmm$, the variant specified in $Cmmm$ came out with around 0.433 eV f.u.$^{-1}$ lower energy than the C2/m variant. This confirms that the experimental studies have identified [14, 15, 24] the correct ground-state structure for $Sr_4Fe_4O_{11}$. For the optimized monoclinic structure, the calculated magnetic moments at the two Fe sites are almost equal (differ only by 0.3 μ_B) and also there is no noticeable difference in the integrated charge density between the Fe sites. These indicate that the charge ordering is not well pronounced in this structure and it may represent a high temperature phase with no charge ordering.

TABLE I: Optimized structural parameters for the ground-state of $Sr_4Fe_4O_{11}$ (space group $Cmmm$). Experimental data from Ref. [15] are given in parentheses.

Unit cell (Å)	Atom	Site	(x, y, z)
$a = 11.0372$ (10.9430)	Sr1	$2d$	0, 0, 1/2 (0, 0, 1/2)
$b = 7.6629$ (7.6795)	Sr2	$2c$	1/2, 0, 1/2 (1/2, 0, 1/2)
$c = 5.4930$ (5.4549)	Sr3	$4g$	0.2421, 0, 0 (0.2400, 0, 0)
$V = 464.58$ (458.41)	Fe1	$4i$	0, 0.2468, 0 (0, 0.2410, 0)
	Fe2	$4f$	1/4, 1/4, 1/2 (1/4, 1/4, 1/2)
	O1	$2a$	0, 0, 0 ($2b$; 1/2, 0, 0)
	O2	$4h$	0.2284, 0, 1/2 (0.2320, 0, 1/2)
	O3	$16r$	0.1196, 0.2773, 0.2368 (0.1190, 0.2726, 0.2410)

The reported unit-cell volume for $SrFeO_{3-x}$ at $x \approx 0.25$ varies somewhat between different reports [458.41 (x=0.247) [15], 462.21 ($x = 0.27$) [13], 462.59 (x= 0.26) [14], 463.05 ($x = 0.29$) [30], 463.15 ($x = 0.255$) Å^3 f.u.$^{-1}$ [23]]. This apparently significant variation may indicate of a small homogeneity range for the $SrFeO_{2.75}$ ($Sr_4Fe_4O_{11}$) phase as suggested in proposed phase diagrams [13]. The present optimized equilibrium volume (464.58 Å^3 f.u.$^{-1}$) for $Sr_4Fe_4O_{11}$ is somewhat larger than any of the experimental volumes but fully acceptable as good agreement (deviation less than 1.5 %) for DFT calculations. The calculated unit cell dimensions and positional parameters for the optimized ground-state structure according to space group $Cmmm$ (Table I) are in very good agreement with the low temperature PND data, once more exposing predicting power of accurate DFT calculations even for quite complex systems.

To gain insight into the relations between crystal structure and electronic and magnetic properties of $Sr_4Fe_4O_{11}$, a correct assignment of valence states to the crystallographically different Fe sites is critical. It therefore appears appropriate to give a brief account of the experimental findings for the valence- and spin-state situation for Fe in $Sr_4Fe_4O_{11}$. From low-temperature ME data it has been concluded [31] that only Fe in formal 3+ state order magnetically below, T_{N}=220 K. Room-temperature spectra comprises two symmetrical doublets of equal intensity [30], which on the basis of the isomer shifts were assigned as Fe^{3+} ($\delta = 0.35\,\mathrm{mm\,s^{-1}}$) and Fe^{4+} ($\delta = -0.08$ mm s^{-1}). Below T_{N} the spectra exhibit (hyperfine) magnetic splitting by an internal magnetic field of 46 T. The latter finding is interpreted [30] as indicative of a high spin (HS) 3+ (d^5) state for iron.

Using the results from powder x-ray diffraction and Mössbauer spectroscopic measurements Takano *et al.*[21, 32] concluded that $Fe1^s$ is in a 3+,HS state and $Fe2^o$ in a 4+, low spin (LS) state on the additional assumption that Fe2^o is subject to a residual disorder and only manifests itself in the broad background of the Mössbauer spectra. Fournes *et al.* [23] on the other hand concluded from room-temperature ME data that, Fe2^o is in the 3+, HS state (arguing with the isomer shift values for SrFeO$_{2.5}$ as reference substance) and Fe1^s in the HS 4+, state. Based on the bond-valence sums Hodges *et al.* [14] concluded that Fe1^s is in a 3+ state and Fe2^o in a 4+ state. The same authors argue that the Fe2^o sub-lattice forms an AF dominated magnetic structure, while the Fe1^s sublattice is subject to conflicting magnetic superexchange interactions and does not exhibit cooperative magnetic order (remaining either as paramagnetic or develops a spin-glass-like arrangement). From the PND and magnetization/susceptibility data over the temperature range 1.5−293 K it has also been inferred [15] that Fe1^s and Fe^o are in the 3+ and 4+ states, respectively, where Fe^{3+} order antiferromagnetically below 232 K and Fe^{4+} forms a magnetically frustrated sublattice. This conclusion was arrived at by Schmidt *et al.* [15] who drew heavily from the accumulated knowledge on Sr-Fe-O compounds. From this resume it should be obvious that there are controversies in the interpretations of the so-called experimental facts regarding the assignment of valence and spin states to the different Fe sites in Sr$_4$Fe$_4$O$_{11}$.

It is interesting to analyze why different conclusions have been arrived at experimentally about spin state and valence state assignments to the different Fe sites. The Mössbauer spectroscopic assignments [15, 31] draw heavily on isomer shift values for reference standards. However, these standards are not real standards in the sense that they do not provide a fixed value for each valence state of Fe. On the contrary, Mössbauer spectroscopy has a relatively broad range of isomer shift values at disposal for each valence state. This lack of precision is connected with the ambiguities one inevitably faces with every assignment of valence state. The bond valence deductions are also based on the use of reference standards. Neither these are universal standards, and simple bond radii for Fe^{2+} and Fe^{3+} are certainly not fixed-constant parameters. It gets even worse when it comes to Fe^{4+} where suitable reference compounds yet have not been found and hence the bond-radius of Fe^{4+} is only estimated [33].

Semiconducting behavior with an activation energy of 0.053 eV at 300 K has been reported for SrFeO$_{3-x}$ specimens with composition x=0.28 and 0.22 [34]. Hence it can be anticipated that the transport properties of SrFeO$_{3-x}$ do not change drastically over a small compositional range. The total DOS given in Fig. 2 exposes that Sr$_4$Fe$_4$O$_{11}$ (SrFeO$_{2.75}$) is a semiconductor with a band gap of 0.13 eV. The observation of semiconducting behavior is consistent with the experimental temperature-dependent electrical properties measurement [18, 34]. It should be remembered that the density-functional calculations generally yield smaller band gaps than that obtained from experimental studies like optical measurements.

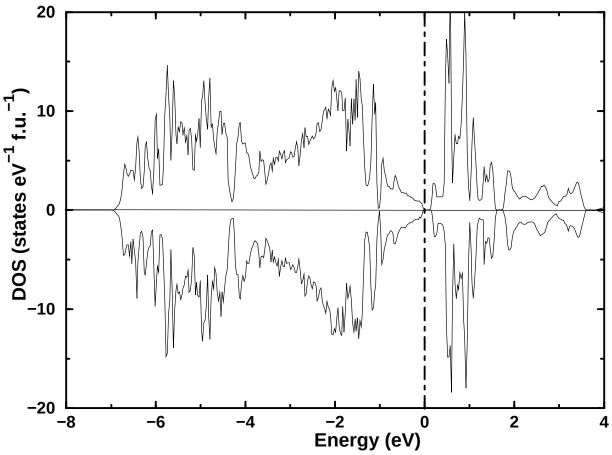

FIG. 2: Calculated total density of states (DOS) for Sr$_4$Fe$_4$O$_{11}$ in the ground-state G-AF configuration. The Fermi level is set to zero.

We now turn the attention to the assignment of the valence states for both Fe atoms based on DFT calculations. The calculated charge at the Fe1^s site is larger than that in the Fe2^o site by around 0.5 electrons. This indicates that, as a coarse approximation Fe1^s can be assigned the formal valence of 3+ and accordingly, Fe2^o 4+. Now let us see why should Fe in square-pyramid configuration prefers 3+ state rather than the 4+ state. The removal of an oxygen atom from an Fe2O$_6$ octahedron (present in system without oxygen vacancy i.e. SrFeO$_3$) is formally the same as addition of two electrons to the remaining structural framework. If one postulates that the defect is rectified mainly locally one can imagine that, among the two electrons, one electron is used to convert Fe^{4+} into Fe^{3+} and the other electron participates in bonding interaction with the neighboring O sites. Moreover, as each Fe1^s is surrounded by only 5 O compared to Fe2^o with 6 O neighbors, in a desire to have charge balance in the system, Fe1^s would prefer to have lower oxidation state than that in Fe2^o.

The calculated magnetic moment at the Fe1^s and Fe2^o sites for the G-AF configuration are 2.82 and 3.44 μ_B per Fe atom, respectively. The calculated moment at the Fe2^o site is in good agreement with the experimental moment from PND [15, 24] (see Table III). The experimentally established AF ordering in Sr$_4$Fe$_4$O$_{11}$ concerns Fe2^o atoms. However, neither PND nor Mössbauer spectroscopy were able to detect magnetic ordering of the moments at the Fe1^s site, the reason for this will be discussed below. Neither of the Fe sites in Sr$_4$Fe$_4$O$_{11}$ has a perfect local cubic environment and both sites give rise to an electric field gradient for Fe1^s and Fe2^o sites of $-1.56\ \times 10^{21}$ and $-5.64\ \times 10^{21}$ Vm^2, respectively. These calculated values are in accordance with the experimental observation of different quadrupole doublets for the two Fe sites in the Mössbauer spectra [15].

The magnetic moment at Fe2^o site in Sr$_4$Fe$_4$O$_{11}$ is analyzed along with that in SrFeO$_3$ which has a cubic perovskite structure with an AF screw spin arrangement (T_N=134 K and a moment of 3.1 μ_B/Fe at 4 K) [18, 19]. The Mössbauer spectroscopic data [16] for SrFeO$_3$ show an isomer shift of 0.05 mm/sec and a magnetic hyperfine field (HFF) of 33.1 T at 4 K which has been believed to be the typical values for Fe^{4+} in octahedral environment. Our calculated magnetic moment for the Fe2^o site (3.53 μ_B) in Sr$_4$Fe$_4$O$_{11}$ is found to be slightly larger than that in SrFeO$_3$. The larger moment value may be related to the oxygen vacancies present adjacent to the octahedra in the lattice which is likely to weaken the Fe-O bonding interactions within the Fe2O$_6$ units, hence relatively more electrons at Fe2^o site are allowed to participate in magnetism rather than in bonding. Consistent with this view point the calculated Fe−O distance at the base of the octahedra in Sr$_4$Fe$_4$O$_{11}$ is larger than that in SrFeO$_3$ (2.05 vs. 1.92 Å). Owing to the relatively large magnetic moment at the Fe2^o site the measured [13, 21, 31] HFF is found to be 46 T in Sr$_4$Fe$_4$O$_{11}$. This would have mislead the experimentalists to believe that the magnetic ordering results from Fe^{3+} rather than Fe^{4+}. We have calculated the fermi contact contribution to the HFF from our density functional calculations. This value is found to be 17 and 30 T for Fe1^s and Fe2^o sites, respectively. The larger value of HFF at the Fe2^o site reflects the higher moment at that site.

The next puzzle is the origin of the larger moment at the octahedral site than at the square-pyramidal site. If an oxygen atom is removed from a configuration with 180^o Fe-O-Fe bond angle, the electrostatic repulsive force pushes the Fe atoms apart, and the neighboring O atoms are collectively moved toward the vacancy to screen this repulsion. The optimized structural parameters show that the Fe atoms of the Fe1^s is surrounded by 4 base-plane O atoms at a distance of 1.87 Å compared with the Fe1 to apical O distance of 1.89 Å. In the Fe2O$_6^o$ structural sub-unit each Fe is surrounded by 4 base-plane O atoms at a distance of 2.05 Å and two apical O at a distance of 1.93 Å. These findings strongly suggest that the bonding interaction between Fe and O is stronger in the FeO$_5$ coordination than that in the Fe2O$_6^o$. Hence, compared with the local surrounding of Fe2O$_6^o$ relatively more of the electrons in the Fe1O$_5^s$ sub-units are participating bonding rather than magnetism. The longer Fe-O distance in the Fe2O$_6^o$ sub-units than that in the Fe1O$_5^s$ indicates that the Fe-3d electrons in the former configuration are relatively more localized and their exchange splitting correspondingly larger than those in the Fe2O$_5^s$ configuration. This appears to explain why magnetic moment at the Fe2^o is larger than the the Fe1^s site.

In order to provide more insight in the bonding between the different constituents we show the site projected DOS for Sr$_4$Fe$_4$O$_{11}$ in Fig. 3. The negligibly small DOS distribution in the valence band (VB) at the Sr site indicate pronounced ionic bonding between Sr and the other constituents. The noticeable difference in the topology of the DOS profile for the two Fe sites strongly suggests different valence states for these Fe atoms. The DOS for the minority-spin channel in the VB of both the Fe sites is almost empty indicating that these two Fe atoms are in the HS states. The broad features of the VB at the Fe sites indicate a delocalized character of these electrons and their hybridization interaction with the neighbors. The degenerate nature of the DOS for the O and Fe atoms throughout VB strongly suggest that the bonding interaction between these atoms has a distinct covalent character. The peak feature in the DOSs for Fe1 and O1 around −2 eV carrying the message of appreciable covalent contribution to the Fe1-O bond. This could explain the relatively low moment at the Fe1 site. It would be interesting to understand the microscopic origin of the larger covalent participation in Fe1^{3+}-O bond than the Fe2^4-O bond. With increasing charge and decreasing radius it is expected [18] that the Fe ion will attract electron density from neighboring oxygen and this increase the electron population of its orbitals. It appears that such a mechanism leads to increased covalent contribution to the Fe1-O bonding.

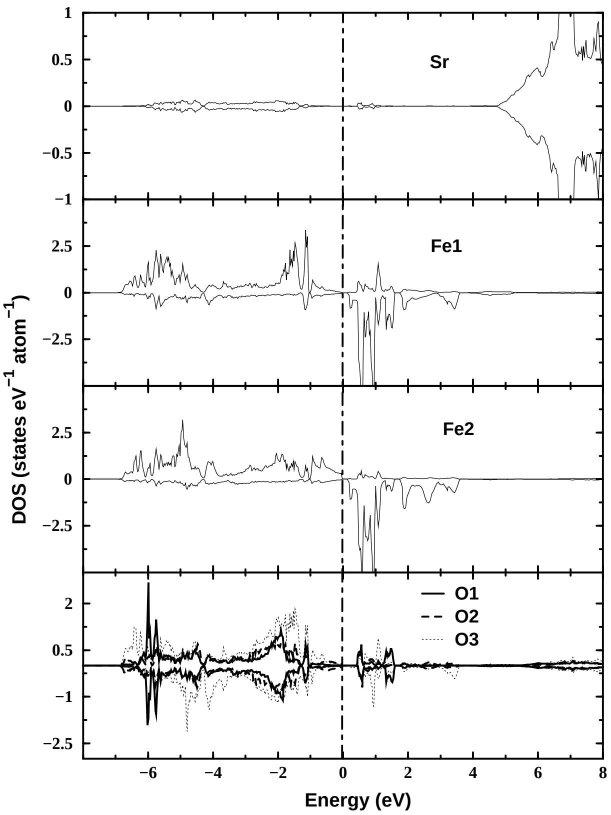

FIG. 3: Calculated site-projected density of states (DOS) for Sr$_4$Fe$_4$O$_{11}$ in the ground-state G-AF configuration. The Fermi level is set to zero.

In order to visualize the charge ordering in Sr$_4$Fe4O$_{11}$ we have given the valence d electron density at the Fe1^s and Fe2^o site for the majority and the minority spin electrons in Fig. 4. The smaller d-electron density at the minority spin channel at Fe2^o site clearly reflects the HS state. The shape of the d-electron distribution

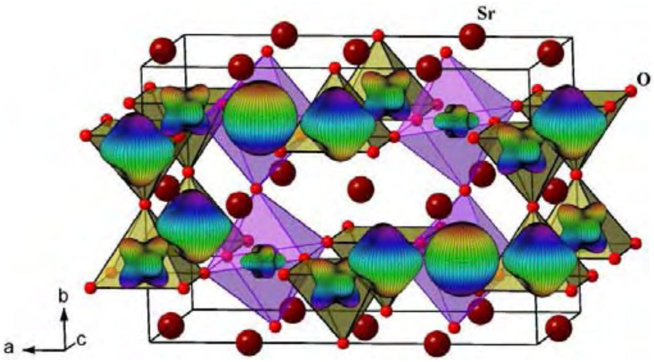

FIG. 4: (Color online) Calculated spatial distribution of valence charge density at Fe1^s and Fe2^o for the majority and minority spin electrons.

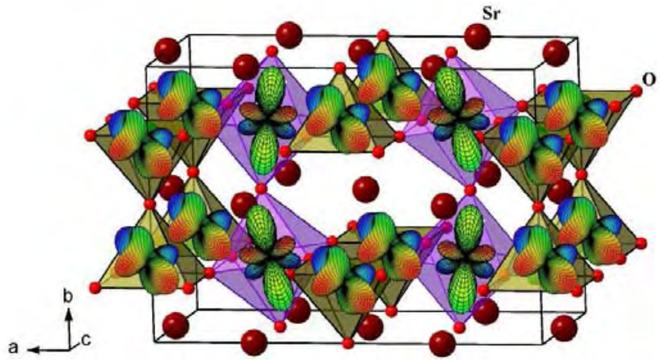

FIG. 5: (Color online) The orbital ordering pattern obtained from the occupation matrices of d states close to the Fermi level at the Fe1^s and Fe2^o sites in $\mathrm{Sr_4Fe_4O_{11}}$.

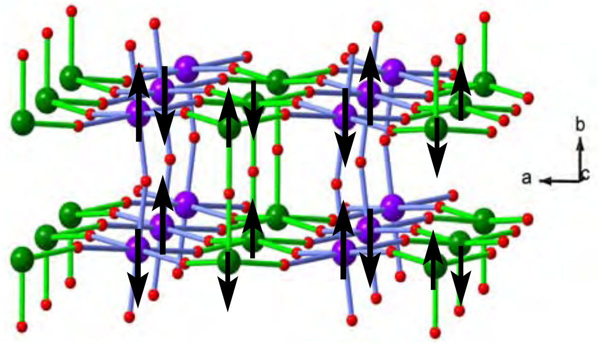

FIG. 6: (Color online) The schematic ground-state magnetic structure for $\mathrm{Sr_4Fe_4O_{11}}$ obtained from the spin-polarized total energy calculations. The longer arrow corresponds to the moment of 3.53 at the Fe2^o site and the smaller arrow reflects the moment of 2.83 μ_B at the Fe1^s site. For clarity only Fe and O atoms are shown with bonds.

at the minority spin channel for both the site is almost the same. But, the distinct topology of the distribution of d-electrons at the majority for the Fe1^s and Fe2^o sites clearly shows the different valence states of both Fe which confirms the charge ordering observed experimentally [23]. In the Fe1^s site, there is considerable amount of d-electrons present at the minority spin channel also. Hence, though there are more d-electrons at the Fe1^s than the Fe2^o the net spin density at the Fe1^s is smaller than that at the Fe2^s site. The electrons at the vicinity of Fermi level in the VB generally participate more in the hopping interactions and hence they are important for the exchange interaction between atoms. In Fig. 5 we have shown the spatial distribution for valence band d-electrons at the Fe1^s and Fe2^o sites within the 1 eV from Fermi level. The interesting feature in this figure is the orientation of d_{z^2}-like orbital along the [010] at the Fe2^o site. This clearly illuminates the super-exchange interaction path. Hence, the d-electrons at the Fe2^o sites form AF alignment via O2 resulting in the magnetic structure given in Fig. 6. On the other hand the valence d-electrons within 1 eV from Fermi level at the Fe1^s sites have complex orbital distribution. So, in spite of the bond angle for Fe1^s-O1-Fe1^s being 180^o (which should prefer AF interaction), the superexchange interaction is not as strong as that between Fe2^o. This may be one of the reasons why long range ordering is stronger between Fe2^o than between Fe1^s sites.

More insight in to the spin state of d electrons at the two Fe sites is also highly desirable. In an octahedral (cubic) crystal field the Fe-d levels are split in to triply degenerate t_{2g} (d_{xy},d_{xz},d_{yz}) and doubly degenerate e_g ($d_{x^2-y^2}$,d_{z^2}) levels. Owing to orthorhombic distortion of the octahedral co-ordination, the degeneracy of both t_{2g} and e_g levels is further split (see Fig. 7). With the Fe in the 4+ oxidation state there will be four d electrons to accommodate in these levels. The spin moment according to a pure ionic picture will then be 2 and 4 μ_B for low spin (LS; $t_{2g}^4e_g^0$) and high spin (HS; $t_{2g}^3e_g^1$) configuration respectively. In practice, materials experience covalent hybridization between the transition-metal atoms and its surrounding atoms, which reduce the spin moment owing to the fact that some of the electrons participate in bonding rather than in magnetism. Moreover, the delocalized character of the electrons (as evident from the DOS curves in Figs. 3 and 7) reduces the exchange interaction and also the moment. So, one mostly gets non-integer values for the spin moments at the transition-metal sites and noticeable induced moment at the sites of the surrounding atoms. The calculated spin moment of 3.53 μ_B at the Fe2^o site supports the inference that this site is in the 4+, HS state, as a coarse approximation. Consistent with this deduction, the calculated orbital projected DOS (Fig. 7) show an almost negligible amount of DOS in the minority spin channel. The magnetic structure with long arrow in Fe sites at Fig. 6 show the long range G-AF ordering present at the Fe2^o site. More details about magnetic structure will be discussed later.

In an ideal square-pyramidal crystal field the d levels will split into doubly degenerate e_g (d_{xz},d_{yz}) nondegenerate b_{2g} (d_{xy}), a_{1g} (d_{z^2}), and b_{1g} ($d_{x^2-y^2}$) levels (See Fig. 7). With Fe^{3+} there will be five d electrons to be accommodated in these levels. The spin moment for

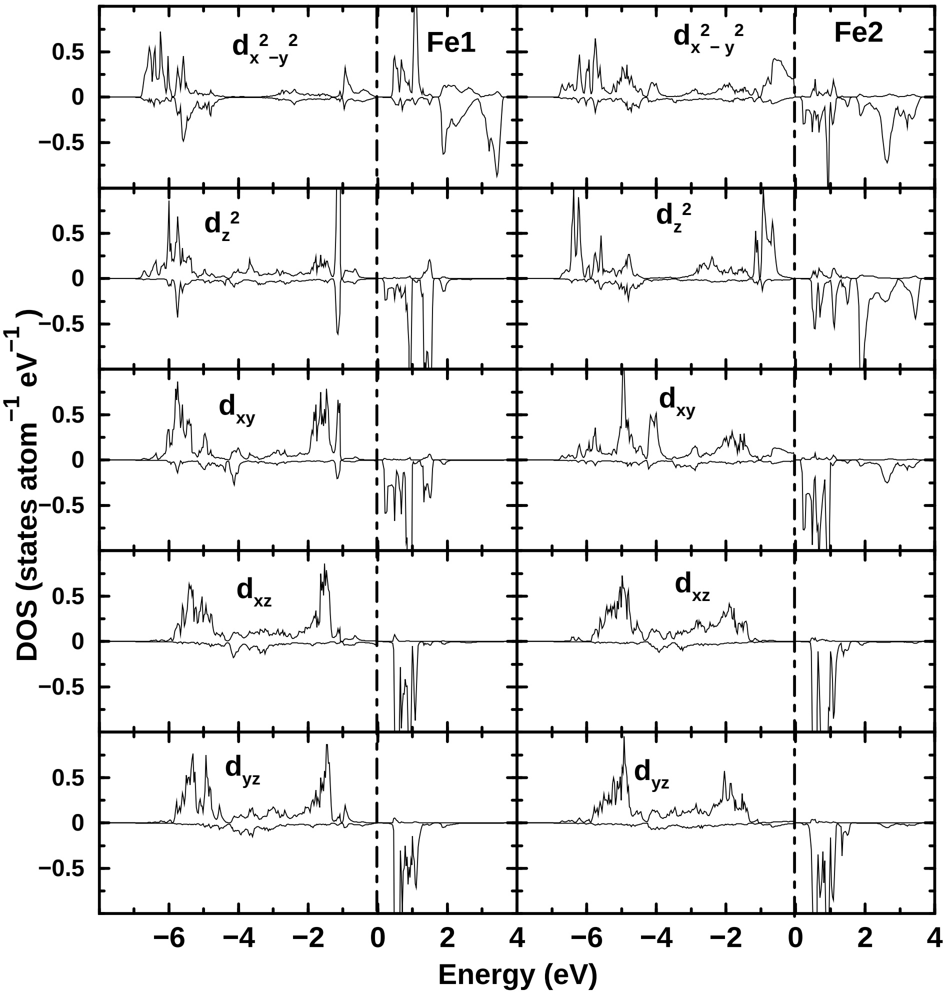

FIG. 7: Calculated orbital-projected density of states (DOS) for Fe1^s and Fe2^o in $Sr_4Fe_4O_{11}$ for the ground-state G-AF configuration. The Fermi level is set to zero.

Fe1^s in LS ($e_g^4b_{2g}^1a_{1g}^0b_{1g}^0$) and HS ($e_g^2b_{2g}^1a_{1g}^1b_{1g}^1$) configurations will then be 1 and 5 μ_B, respectively, for the pure ionic case. The powder neutron diffraction study [15, 24] and ME measurements [13, 15, 21, 23, 31] unable to detect any ordered moment at the Fe1^s site, but according to difference in the field cooled and zero field cooled magnetic susceptibility curves [15, 24] the unpaired electrons at the Fe1^s sites can be F aligned in a strong enough magnetic field. Consistent with these experimental findings density-functional calculation gave a spin moment of 2.83 μ_B (for comparison, the assumed 3+, HS state in $Sr_2Fe_2O_5$ is reported [17] to exhibit a magnetic moment of 4.5 μ_B). However, the calculated spin moment is unusually low for 3+ HS configuration. The calculated spin moment for the Fe1^s site, on the other hand, higher than for an ideal ionic 3+, LS value. Hence we have confidence in the coarse assinment of 3+, HS state to Fe1^s and that the too low value for spin moment is to be associated with the combination of partial delocalization of the 3d electrons and covalency effect.

If the Fe^{4+} at the octahedral site is in the HS state one should expect Jahn-Teller distortion (JTD). But the experimental and theoretical structural analysis show that neither the $LaMnO_3$-type [35] characteristic of structural distortion nor the $CaFeO_3$-type disproportionation reaction $2Fe^{4+}(t_{2g}^3e_g^1) \rightarrow Fe^{4-\delta}(t_{2g}^3e_g^{1+\delta}) + Fe^{4+\delta}(t_{2g}^3e_g^{1-\delta})$ characteristics of narrow band electrons [36, 37] are present in $Sr_4Fe_4O_{11}$. It is worth to note that Fe ions in $SrFeO_3$ is the typical example for HS Fe^{4+} ions. But the expected JTD is not observed down to very low temperature. The non-observation of JTD in $SrFeO_3$ is interpreted to the presence of metallic behavior, broad band features at the valence band, and the deep lying nature of the Fe 3d levels. The cooperative JTD is very active for a pure ionic system with localized electrons. The system with broad band features and finite covalent characteristics it is not necessary to have active JTD. Also, for the current system the presence of orthorhombic distortion already lift the degeneracy of the e_g states. However, we found that the FeO_6 octahedron in $Sr_4Fe_4O_{11}$ is compressed with two short (Fe−O distance 1.93 Å) and four long (Fe−O distance 2.05 Å) Fe−O bonds. This distortion is suggestive of a localized Jahn-Teller effect and therefore a HS Fe2 cation in an octahedral environment.

It is worth to analyze the reasons behind why different experimental conclusions arrived about, spin-state, valence, and coordination of different Fe ions in $Sr_4Fe_4O_{11}$. The ^{57}Fe ME at room temperature was fitted with two symmetrical doublets which were assigned to Fe^{3+} and Fe^{4+} on the basis of the isomer shift, quadrupole splitting and linewidth.[30, 31] The low saturation magnetic field of 46 T for Fe^{3+} in $Sr_4Fe_4O_{11}$ was used to argue [31] for a low coordination despite an isomer shift more typical of octahedral coordination. If the HFF is closer to 33 T, it can be interpreted to the value for the HS Fe^{4+} configuration with some degree of covalency. [16, 18] The observed HFF of 46 T is comparable to the value of 43 T in $Sr_2Fe_2O_5$ where the Fe ions are present in the 3+ state. [38] This lead the experimentalist to believe that Fe^{3+} ions are responsible for the AF ordering in $Sr_4Fe_4O_{11}$. It is important to note that the HFF at each site is depend on the magnetic field acting at each site. It will not give directly the information about the coordination number of site and also the amount of electrons at each site. Hence, it is not possible to assign the valence state of ions based on HFF alone.

The behavior of the other Fe is unusual since no resolved hyperfine splitting could be observed.[14, 21, 31] Based on the results from x-ray diffraction and ME measurements Takano *et al.*[21, 32] concluded that Fe^{4+} HS ions reflect a residual disorder and responsible for the broad background in the ME spectrum. However, our detailed analysis below indicates magnetic frustration, which is also evident in the large differences between susceptibility data from the field cooled and zero field cooled measurements.[15, 24] This magnetic behavior is much like that of a spin-glass transition as observed in a variety of Fe-containing perovskite-derived oxides. Example, in the magnetically dilute $SaAFeBO_6$ (A=Sr,Ca,Ba; B = Nb,Sb, Ta) systems where it is believed [39–41] that competing nearest-neighbors and next-nearest-neighbors exchange interactions prevent the development of long-range magnetic order.

Now we try to understand why the HFF at the $Fe2^o$ in the 4+ state is comparable with that in $Sr_2Fe_2O_5$ where Fe is in the 3+ state. The calculated Fe-O bond length at the octahedral coordination is between 1.93−2.05 Å for $Sr_4Fe_4O_{11}$ and these values are comparable with that in $Sr_2Fe_2O_5$ where the Fe-O bond length at the octahedral coordination is between 1.94 to 2.028 Å [17] The valence state of ions will decide only the number of electrons at each site. But, the magnetic moment at each site is depend on the degree of localization and the exchange splitting those are decided by the bonding interaction between the atoms and hence the bond length. So, the HFF for the $Fe2^{4+}$ in $Sr_4Fe_4O_{11}$ is comparable with Fe^{3+} in $Sr_2Fe_2O_5$ that misled to experimentalist to arrived at wrong conclusion.

TABLE II: Total energy (relative to the lowest energy state in meV/f.u.) in $Sr_4Fe_4O_{11}$ for the Para, Ferro, and $A-$, $C-$, and $G-$ AF phases obtained from VASP-PAW method.

Para	Ferro	$C-$AF	$A-$AF	$G-$AF
4099.8	3865.6	757.3	127.9	0.0

A. Magnetic structure

Magnetic exchange in perovskite-like oxides is generally assumed to take place by superexchange [42] and/or double exchange. [43] This involves exchange between magnetic ions with the nearest neighbors oxygen and leads to an antiparallel/parallel alignment. Such reliance of magnetic exchange upon anion coupling of two magnetic ions implies that oxygen nonstoichiometry should produce alternation of the magnetic properties of $Sr_4Fe_4O_{11}$. For instance, it can be imagined that anion vacancies would tend to decouple the exchange interaction and in $Sr_4Fe_4O_{11}$ it will introduce equal amount of Fe^{3+} and Fe^{4+} which results in the introduction of ferromagnetic double exchange also in to the system.

Based on the inter-plane and intra-plane exchange interactions of magnetic ions in perovskite-like oxides one often arrive ferromagnetic, A-AF, C-AF or G-AF ordering. [44] In order to arrive the ground state magnetic structure of $Sr_4Fe_4O_{11}$ we have made total energy calculations for different magnetic configurations. The calculated total energy for $Sr_4Fe_4O_{11}$ in different magnetic configurations with reference to the ground state are given in Table II. From this table it is clear that we have gained large energy when we introduce antiferromagnetic ordering into the system. We found the G-AF magnetic structure is the ground state for $Sr_4Fe_4O_{11}$ where we have AF ordering within plane as well as between the planes. Further, the A-AF ordering is only 128 meV/f.u. higher in energy than the G-AF configuration and this is associated with the possibility of having double exchange interaction between $Fe2^o$-O3-$Fe1^s$ within the plane. The calculated magnetic moments at the Fe sites from different magnetic configurations are not differ much and in particular we arrive always smaller moment at the $Fe1^s$ site than the $Fe2^o$ (see Table III). Interestingly we found large moment of around 0.17 μ_B in all the oxygen sites which results higher total moment in the ferromagnetic configuration.

The ME measurements [13, 15, 21, 31] and NPD measurements [14, 15, 24] indicated that only one sublattice orders antiferromagnetically. The observed magnetic reflections in the NPD has been fitted to two magnetic models described using the Cm′m′m′ and Cmm′m′ Shubnikov groups. [15] In the Cm′m′m′ model the magnetic moments of $Fe1^s$ are aligned along the [010] direction where the AF coupling is facilitated by a superexchange interaction via O1. In contrast, for the Cmm′m′ Shubnikov group, magnetic moments are permitted on both $F1^s$ and $Fe2^o$ sites as we have arrived at lowest energy

TABLE III: Calculated magnetic moment (in $\mu_B/atom$) per Fe atom for $Sr_4Fe_4O_{11}$ in the ferromagnetic (FM) and antiferromagnetic phases. The total moment (Total) represent the total magnetic moment per formula unit.

Configuration	Fe1	Fe2	Total
Ferro	2.78	3.26	13.92
A-AF	3.00	3.49	0.0
C-AF	2.80	3.30	0.0
G-AF	2.91	3.57	0.0
G-AF (FP-LAPW)	2.83	3.53	0.0
Exp.[15]		3.55	0.0
Exp.[24]		3.3	0.0

in the present study (see Fig. 6). In this magnetic model the superexchange interaction will take place via both O1 and O2. However, to be consistent with the observed magnetic peak intensities and the ME data which indicate only one magnetically ordered site, the moment at one of the site has to be zero. If the moment on Fe^s site is zero and the magnetic moment is constrained to be along [010], the AF would most likely be facilitated by a superexchange interaction via O2.

Hodges *et al.*[14] placed Fe^{4+} and Fe^{3+} ions on the square-pyramidal and octahedral sites respectively, based on bond strength calculations, which favor the Cmm′m′ magnetic structure. Schmidt *et al.* discussed that for complex oxides a bond-strength sum for an individual site is not meaningful and criticized the magnetic structure proposed based on bond strength calculations. Based on the argument that the Fe^{4+} state in Sr-Fe-O compounds has so far only been found to occupy octahedral site,[13, 45–47] Schmidt *et al* concluded that Fe^{3+} occupies the pyramidal site and Fe^{4+} in the octahedral site. This assignment favors the Cm′m′m′ model. However, their conclusion is inconclusive due to their statement that "the conclusions drawn from this particular model can be easily be applied to the Cmm′m′ model since the F1 and Fe2 sublattices have similar topology". Also, the refined moment with both the model yield almost the same moment.

In accordance with the reported ME data and the low temperature NPD magnetic reflections, a magnetic structure was recently proposed [24] which only involved long range magnetic ordering of $Fe2^o$ atoms. The magnetic structure for $Sr_4Fe_4O_{11}$ is given in Fig. 6. This magnetic structure show the presence of strong AF $Fe2^o$-O-$Fe2^o$ superexchange interactions within the one dimensional chains of vertex-linked $Fe2^oO_6$-octahedra along [010] (see also Fig. 5). There are no direct $Fe2^o$-O-$Fe2^o$ interactions within the *xz* planes, whereas week $Fe2^o$-O-O-$Fe2^o$ interactions possibly occurs resulting the observed magnetic ordering. Our calculations show that the apical oxygens at both octahedral and square pyramid sites are posses noticeable magnetic moment of around 0.13 μ_B. It is interesting to note that, though the interatomic distance between the apical oxygen and the Fe at the octahedral sites is shorter than the distance between Fe and the oxygen at the base, the apical oxygens have larger moment indicate that the superexchange path is along the Fe and apical oxygen (similar conclusion arrived also from the orbital ordering analysis discussed above). This would explain why we have AF exchange interaction between $Fe2^o$ along [010].

Even though our calculation show 2.83 μ_B moment at the $Fe1^s$ site, both NPD [15, 24] and ME measurements [14, 21, 31] unable to show finite moment at that site. Now we will try to understand the microscopic origin behind this observation. Each $Fe1^s$ is surrounded by four nearest neighbors $Fe2^o$ atoms within the *xz* planes, for which two of the resulting $Fe1^s$-O3-$Fe2^o$ exchange interactions are ferromagnetic and the remaining two are AF. Hence, the magnetic moments of $Fe1^s$ site become topologically frustrated within the *G*-AF $Fe2^o$ sublattice. Hence, experimentally unable to find any long range ordering for the magnetic moments at the $Fe1^s$ atoms.

It is interesting to understand why $Fe2^o$ first ordered antiferromagnetically instead of $Fe1^s$. The angle between $Fe1^s$-O1-$Fe1^s$ is exactly 180^o which will results antiferromagnetic superexchange interaction between the $Fe1^s$ along [010] (i.e. the 'bow-ties' placed in spaces between every four octahedron chains running along the *b* axis will have AF ordering). Compared with the value of magnetic moment at the $Fe2^o$ site, the moment at the $Fe1^s$ site is small and hence the exchange interaction between $Fe2^o$ will be larger than that between $Fe1^s$. Consistent with this view point our calculated Lichtenstein's exchange interaction parameter (J_{ij}) from TB-LMTO program between Fe2 is 56 meV and it is higher than that between Fe1 (41 meV). Hence, $Fe2^o$ will prefer to order first.

Our total energy calculation show that among the considered magnetic configurations, the *G*-AF ordering is found to be the ground state for $Sr_4Fe_4O_{11}$. We have made additional total energy calculations with the magnetic configuration where $Fe1^s$ is nonmagnetic (in order to mimic some of the experimental interpretations) and $Fe2^o$ with *G*-AF ordering. Interestingly we are able to stabilize such configuration with good convergence. However, this solution is found to be 1.85 eV/f.u. higher in energy than the ground state configuration. Hence, theory rules out the possibility of having nonmagnetic $Fe1^s$ in $Sr_4Fe_4O_{11}$. In this system, owing to the competition between the ferromagnetic and antiferromagnetic interactions in the $Fe1^s$ sublattice (i.e. $Fe1^s$-O1-$Fe1^s$ is superexchange AF interaction and $Fe1^s$-O3-$Fe2^o$ is double exchange ferromagnetic interaction) created frustration resulting non-observation of long range magnetic ordering at $Fe1^s$ site. As a result, this compound can be visualized as a "phase separated" system with two phases, one consists of *G*-AF ordered FeO_6 octahedra in a $SrFeO_3$-like sublattice and the other consists of spin-glass-like magnetically ordered FeO_5 square pyramids in a $Sr_2Fe_2O_5$-like sublattice.

As a summary, the magnetic structure of $Sr_4Fe_4O_{11}$ can be visualized as follows. Below the Neel temperature of 230K, the Fe2 sublattice forms an antiferromagnetic spin structure, with the coupling mediated by Fe2-O2-Fe2 superexchange interactions parallel to the [010] direction and Fe2-O3-O3-Fe2 super-superexchange interactions within the *xz*-planes. Each Fe1 will then have two Fe2 neighbors with "up" spin magnetic configuration and two with "down" spin magnetic configuration. Irrespective of whether the Fe1-O-Fe2 superexchange interactions are F or AF, the Fe1 magnetic moments will be topologically frustrated due to the opposite spin alignments of the nearest-neighbors Fe2 cations resulting no long range order in reality.

B. Conclusions

The optimized structural parameters for $Sr_4Fe_4O_{11}$ are found to be in good agreement with the low temperature NPD results. Though NPD and ME measurements unable to show magnetic moment at one of the Fe site, the susceptibility study at FC and ZFC indicate the presence of finite moment at both the Fe sites. Using accurate density functional calculations we have shown that large magnetic moments present at both the Fe sites. As our calculation show large magnetic moment at the Fe1 site, the non-observation of long range magnetic ordering in Fe1 site is associated with the spin-glass-like behavior. The origin for the magnetic frustration in $Sr_4Fe_4O_{11}$ has been analyzed. Among the experimentally reported different possibilities, the present calculation suggest that Fe^{3+} are in the square pyramid site and Fe^{4+} are in the octahedral site. The spin-state of Fe^{4+} can be assigned as HS state and the calculated moment at the Fe^{3+} site is higher than LS state and lower than HS state. Within the experimentally suggested two magnetic structures based on the Cmm′m′ and the Cm′m′m′ Shubnikov groups, we confirmed that Cmm′m′ is more appropriate to describe the magnetic structure. The unusual magnetic properties of $Sr_4Fe_4O_{11}$ can be related to the crystal structure and charge order of the Fe^{4+} and Fe^{3+} cations.

Acknowledgments

The authors are grateful for the financial support from the Research Council of Norway. Part of these calculations were carried out at the Norwegian supercomputer facilities.

[1] B.C.H. Steele, Mater. Sci. Eng. **B13**, 79 (1992).

[2] H.Y. Tu, N. Imanishi, O. Yamamoto, Solid State Ionics, **100**, 283 (1997).

[3] M.L. Post, J.J. Tunney, D: Yang, X. Du, and D.L. Singleton, Sensors and Actuators B, **59**, 190 (1999).

[4] L. Qiu, T.H. Lee, L.-M. Liu, Y.L. Yang, A. Jacobson, J. Solid State Ionics, **76**, 321 (1995).

[5] C.H. Chen, H.J.M. Bouwmeester, R.H.E. van Doorn, H. Kruidhof, A.J. Burggraaf, Solid State Ionics, **98**, 7 (1997).

[6] S. Pei, M.S. Kleefisch, T.P. Kobylinski, J. Faber, C.A. Udovich, V. Zhang-McCoy, B. Dabrowski, U. Balachandran, R.L. Mieville, R.B. Poeppel, Catal. Lett. **30**, 201 (1995).

[7] C. Schinzer, R.A. Saymeh, H.M. Asfour, Z. Naturforsch, **52B**, 927 (1997).

[8] C.E. Mohn, N.L. Allan, C.L. Freeman, P. Ravindran, and S. Stolen, Phys. Chem. Chem. Phys. **6**, 3052 (2004).

[9] B.C.H. Steele, Curr. Opin. Solid State Mater. Sci. **1**, 684 (1996).

[10] M. Takano and Y. Takeda, Bull. Inst. Chem. Res. Kyoto Univ. **61**, 406 (1983).

[11] R. Vidya, P. Ravindran, P. Vajeeston, A. Kjekshus, and H. Fjellvåg, Phys. Rev. B **69**, 092405 (2004).

[12] R. Vidya, P. Ravindran, A. Kjekshus, and H. Fjellåg (unpublished).

[13] Y. Takeda, K. Kanno, T. Takeda, O. Yamamoto, M. Takano, N. Nakayama, and Y. Bando, J. Solid State Chem. **63**, 237 (1986).

[14] J.P. Hodges, S. Short, J.D. Jorgensen, X. Xiong, B. Dabrowski, S.M. Mini, and C.W. Kimball, J. Solid State Chem. **151**, 190 (2000).

[15] M. Schmidt, M. Hofmann, and S.J. Campbell, J. Phys. Condens. Matter. **15**, 8691 (2003).

[16] P.K. Gallagher, J.B. MacChesney, and D.N.E. Buchanan, J. Chem. Phys. **41**, 2429 (1864).

[17] M. Schmidt and S.J. Campbell, J. Solid State Chem. **156**, 292 (2001).

[18] J.B. MacChesney, R.C. Sherwood, and F. Potter, J. Chem. Phys. **43**, 1907 (1965).

[19] T. Takeda, Y. Yamaguchi, and H. Watanabe, J. Phys. Soc. Jpn. **33**, 967 (1972).

[20] J. -C. Grenier, N. Ea, M. Pouchard, and P. Hagenmuller, J. Solid State Chem. **58**, 243 (1985)

[21] M. Takano, T. Okita, N. Nakayama, Y. Bando, Y. Takeda, O. Yamamoto, and J.B. Goodenough, J. Solid State Chem. **73**, 140 (1988).

[22] B.C. Tofield, C. Greaves, and B.E.F. Fender, Mater. Res. Bull. **10**, 737 (1975).

[23] L. Fournes, Y. Potin, J.C. Grenier, G. Demazeau, and M. Pauchard, Solid State Commun. **62**, 239 (1987).

[24] H. Fejellvåg, O.H. Hansteen, Y. Bréard. and B.C. Hauback (unpublished).

[25] P. E. Blöchl, Phys. Rev. B **50**, 17953 (1994).

[26] G. Kresse and J. Furthmuller, Comput. Mater. Sci. **6**, 15 (1996).

[27] J.P. Perdew, S. Burke, and M. Ernzerhof, Phys. Rev. Lett. **77**, 3865 (1996).

[28] P. Ravindran, R. Vidya, A. Klaveness, A. Kjekshus, and H. Fjellvåg (unpublished).

[29] P.Blaha, K. Schwarz, G.K.H. Madsen, D. Kvasnicka, and J. Luitz, WIEN2k, revised edition 2001. Vienna University of Technology, An Augmented Plane Waves + Local Orbitals Program for Calculating Crystal Properties,Vienna, 2003.

[30] T.C. Gibb, J. Mater. Chem. **4**, 1445 (1994).

[31] T.C. Gibb, J. Chem. Soc. Dalton Trans. 1455 (1985).

[32] M. Takano, N. Nakanishi, Y. Takeda, and T. Shinjo, in *Ferrites, Proceedings of the Int. Conf., 1980, Japan*, Eds. H. Watanabe, S. Iida, and M. Sugimoto, p.389, Center for Academic Publication, Japan (1981).

[33] J. Ziolkowski, J. Solid State Chem. **57**, 269 (1985).

[34] S. Nakamura and S. Iida, Jpn. J. Appl. Phys. **34**, L291 (1995).

[35] J. B. Goodenough, Phys. Rev. **100**, 564 (1955).

[36] J.B. Goodenough, J. Solid State Chem. **12**, 148 (1975).

[37] M. Takano, N. Nakanishi, Y. Takeda, S. Naka, and T. Takada, Mat. Res. Bull. **12**, 923 (1977).

[38] P.D. Battle, T.C. Gibb, and S. Nixon, J. Solid State Chem. **79**, 75 (1989).

[39] R. Rodriguez, A. Fernandez, A. Isalgue, J. Rodriguez, A. Labarta, J. Tejada, and X. Obradors, J. Phys. C **18**, L401 (1985).

[40] P.D. Battle, T.C. Gibb, A.J. Herod, and J.P. Hodges, J. Mater. Chem. **5**, 75 (1995).

[41] P.D. Battle, T.C. Gibb, A.J. Herod, S.H.Kim, and P.H. Munns, J. Mater. Chem. **5**, 865 (1995).

[42] P.W. Anderson, Phys. Rev. **79**, 350(1950).

[43] C. Zener, Phys. Rev. **82**, 403 (1951); P.W. Anderson and H. Hasegawa, Phys. Rev. **100**, 675 (1955); P.G. de Gennes, Phys. Rev. **118**, 141 (1960).

[44] P. Ravindran, A. Kjekshus, H. Fjellvåg, A. Delin and O. Eriksson Phys. Rev. B **65**, 064445 (2002).

[45] S.E. Dann, M.T. Waller, and D.B. Currie, J. Solid State Chem. **92** 237 (1991).

[46] S.E.Dann, M.T. Waller, and D.B. Currie, J. Solid State Chem. **97**, 179 (1992)

[47] S.E.Dann, M.T. Waller, D.B. Currie, M.F. Thomas, and A.D. Al-Rawwas, J. Mater. Chem. **3**, 1231 (1993).

Omslagsillustrasjon: Inger Sandved Anfinsen

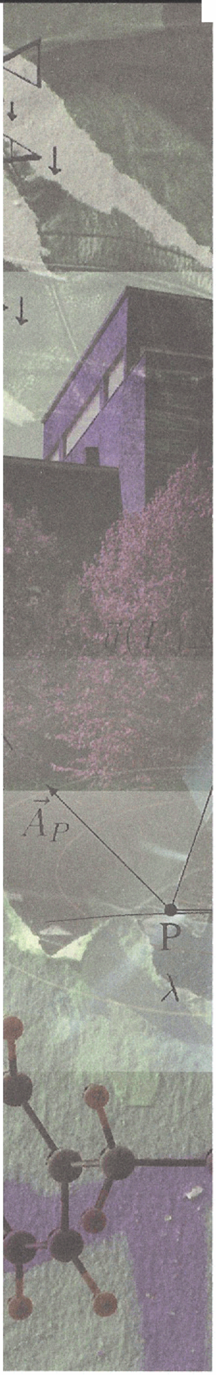

Ravindran Vidya

Theoretical Investigations on Mixed-valence Transition-metal Oxides

Dissertation for the Degree of Dr. Scient. 2005

FACULTY OF MATHEMATICS AND NATURAL SCIENCES
UNIVERSITY OF OSLO

unipubavhandlinger

ISSN 1501-7710
No. 485